3.4.4 Research Paper

Name of the teacher	Title of paper	Name of journal	Link to the recognition in UGC enlistment of the Journal	UGC-CARE Listed
Prof. Y.P.Raiwani	USING MACHINE LEARNING TO DETECT FAKE NEWS: A COMPREHENSIVE SEARCH	Journal of East China University of Science and Technology	http://hdlgdxxb.info/index.php/JE_CUST/article/view/381	YES
Prof. Y.P.Raiwani	Realization of natural language processing and machine learning approaches for text‐based sentiment analysis	Expert Systems	https://onlinelibrary.wiley.com/doi/abs/10.1111/exsy.13114	YES
Prof. Y.P.Raiwani	Review and Comparison of Various Technologies for Predicting Student's Academic Performance	Journal of Critical Reviews	https://drive.google.com/file/d/1fs4kVy0fsp_zGPTdhls6TddRP9JFUbYf/view	YES(Before 2020)
Prof. Y.P.Raiwani	Review on Prediction of Heart Diseases Using Data Mining in Healthcare System	Journal of Critical Reviews	https://drive.google.com/file/d/1fs4kVy0fsp_zGPTdhls6TddRP8KFUbYf/view	YES(Before 2020)
Prof. Y.P.Raiwani	Implementation of machine learning algorithms on CICIDS-2017 dataset for intrusion detection using WEKA	International Journal of Recent Technology and Engineering	https://www.ijrte.org/wp-content/uploads/papers/v8i3/C4587098319.pdf	YES(Before 2019)
Prof. M.M.S.Rauthan	A Survey on Multi-Objective Tasks and Workflow Scheduling Algorithms in Cloud Computing",	International Journal of Cloud Applications and Computing (IJCAC)	https://www.igi-global.com/article/a-survey-on-multi-objective-tasks-and-workflow-scheduling-algorithms-in-cloud- computing/297100	YES
Prof. M.M.S.Rauthan	SMA-LinR: An Energy and SLA-Aware Autonomous Management of Virtual Machines.	International Journal of Cloud Applications and Computing	https://www.igi-global.com/article/sma-linr-an-energy-and-sla-aware-autonomous-management-of- virtual-machines/284494	YES
Prof. M.M.S.Rauthan	CMODLB: an efficient load balancing approach in cloud computing	The Journal of Supercomputing,	https://link.springer.com/article/10.1007/s11227-020-03601-7#:~:text=Efficient%20CMODLB%20load%20balancing%20method,to%20balance%20load%20among%20VMs	YES
Prof. M.M.S.Rauthan	AntPu: a meta-heuristic approach for energy-efficient and SLA aware management of virtual machines in cloud computing,	Memetic Computing	https://link.springer.com/article/10.1007/s12293-020-00320-7	YES
Prof. M.M.S.Rauthan	Novel hybrid ANN and clustering inspired load balancing algorithm in cloud environment",	Applied Soft Computing	https://www.sciencedirect.com/science/article/abs/pii/S1568494621008851	YES
Prof. M.M.S.Rauthan	"A survey on application of machine learning to manage the virtual machines in cloud computing",	International Review of Applied Sciences and Engineering,	https://akjournals.com/view/journals/1848/11/3/article-p197.xml	YES
Prof. M.M.S.Rauthan	Analysis of Security Attacks and Security Protocols of Wireless Sensor Network: Review",	INTERNATIONAL JOURNAL OF SCIENTIFIC & TECHNOLOGY RESEARCH VOLUME	http://www.ijstr.org/final-print/jan2020/Analysis-Of-Security-Attacks-And-Security-Protocols-Of-Wireless-Sensor-Network- Review.pdf	YES(Before 2019)
Prof. M.M.S.Rauthan	The Latest Review: Scheduling Algorithms On The Cloud Computing Based Environment",	INTERNATIONAL JOURNAL OF SCIENTIFIC & TECHNOLOGY RESEARCH VOLUME	http://www.ijstr.org/final-print/jan2020/The-Latest-Review-Scheduling-Algorithms-On-The-Cloud-Computing-Based- Environment.pdf	YES(Before 2019)
Prof. M.M.S.Rauthan	Systematic Review On Vm Scheduling Algorithms	INTERNATIONAL JOURNAL OF SCIENTIFIC & TECHNOLOGY RESEARCH VOLUME	https://www.ijstr.org/final-print/mar2020/Systematic-Review-On-Vm-Scheduling-Algorithms.pdf	YES(Before 2019)
Prof. M.M.S.Rauthan	The Relative performance of Security protocols and attacks in Wireless Sensor Network	International Journal of Advanced Science and Technology	http://sersc.org/journals/index.php/IJAST/article/view/33200	YES(Before 2020)

Prof. M.M.S.Rauthan	"TOPSIS-PSO inspired Non-Preemptive Tasks Scheduling Algorithms in Cloud Computing Environment"	Cluster Computing, Springer,	https://link.springer.com/article/10.1007/s10586-019-02915-3	YES
Prof. M.M.S.Rauthan	Component based web application firewall for analyzing and defending SQL injection attack vectors	International Journal of Recent Technology and Engineering	https://www.ijrte.org/portfolio-item/c4674098319/	YES(Before 2019)
Prof. M.M.S.Rauthan	Securing Stored Biometric Template Using Cryptographic Algorithm	International Journal of Rough Sets and Data Analysis (IJRSDA)	https://www.igi-global.com/article/securing-stored-biometric-template-using-cryptographic-algorithm/214968	YES
Prof. M.P.Thapliyal	Performance Evaluation of Algorithms for Breast Cancer Prediction	Design Engineering	http://www.thedesignengineering.com/index.php/DE/article/view/4445	NO
Dr. Prem Nath	Data Congestion Control Using Offloading in IoT Network	Wireless Personal Communication	https://link.springer.com/article/10.1007/s11277-022-09649-3#:~:text=In%20the%20process%20of%20congestion,and%20the%20buffer%20is%20overflowed.	YES
Dr. Prem Nath	Resource-Cardinality Based Scheme to Reduce Resource Lookup Cost in Structured P2P Networks	Wireless Personal Communication	https://link.springer.com/article/10.1007/s11277-022-09714-x	YES
Dr. Prem Nath	A REVIEW ON ENERGY EFFICIENT LEACH PROTOCOL FOR WIRELESS SENSOR NETWORKS	JOURNAL OF EAST CHINA UNIVERSITY OF SCIENCE AND TECHNOLOGY	http://hdlgdxxb.info/index.php/JE_CUST/article/view/148	YES
Dr. Prem Nath	Data Congestion Prediction in Sensors Based IoT Network	Journal of Scientific & Industrial Research	https://pdfs.semanticscholar.org/3fc2/92b3cf2e4c24f3222d0763a3d74da70c2018.pdf	YES
Dr. Prem Nath	Analysis and modeling the effects of mobility, Churn rate, node's life span, intermittent bandwidth and stabilization cost of finger table in structured mobile P2P networks	Wireless Networks	https://link.springer.com/article/10.1007/s11276-020-02493-y	YES
Dr.Pritam Singh Negi	Implementation of machine learning algorithms on CICIDS-2017 dataset for intrusion detection using WEKA	International Journal of Recent Technology and Engineering	https://www.ijrte.org/wp-content/uploads/papers/v8i3/C4587098319.pdf	YES(Before 2019)
Dr. Om Prakash	Dense optical flow based background subtraction technique for object segmentation in moving camera environment	IET Image Processing	https://ietresearch.onlinelibrary.wiley.com/doi/10.1049/iet-ipr.2019.0960	YES
Dr. Om Prakash	Keyframe extraction using Pearson correlation coefficient and color moments	Multimedia Systems	https://link.springer.com/article/10.1007/s00530-019-00642-8	YES

J. Mountain Res. P-ISSN: 0974-3030, E-ISSN: 2582-5011
Vol. 16(3), (2021), 437-445

DOI: https://doi.org/10.51220/jmr.v16i3.43

Design of U-Shaped Slot Quad Band Patch Antenna

Kuldip Kumar[1*] • Arun S. Bahuguna[1] • Yogendra P. Pundir[1] • Don Biswas[2]

[1]Deptt. of ECE, HNB Garhwal University, Srinagar (Uttrakhand), India-246174.
[2]Deptt. of USIC, HNB Garhwal University, Srinagar (Uttrakhand), India-246174.

*Corresponding Author: kuldipkumarhnb@gmail.com

Received: 25.11.2021; Revised: 17.12.2021; Accepted: 27.12.2021
©Society for Himalayan Action Research and Development

Abstract: A four-band microstrip antenna with a U-shaped slot and two straight slots is proposed in this study. As the width of the dielectric substrate layer is extended, the frequency bands and antenna gain are observed to rise. In this current study, the suggested antenna is intended for using in wireless devices operating at frequencies between 5 GHz to 9 GHz.

Keywords: Patch Antenna, Multiband Microstrip antenna, Quad-Band Antenna, Slot Patch Antenna.

Introduction

A multi-band antenna for a multi-system handset is required due to the rapid advancement of wireless and mobile communication systems, as well as the growing demand for several applications in a single device via a single internal antenna (Rhazi et al 2018). The multi-band microstrip antenna is commonly employed as an internal antenna in wireless mobile communication system applications (Bhattacharya and Garg 1985, Nataraj et al 2017, Chaurasia and Jain 2020, Kumar and Gangwar 2016) Dual or multiple bands of frequencies (Amal et al 2016, Rhazi et al 2019, Wang et al 2018, Cao et al 2015) can be obtained by employing the U-shaped slot in the antenna patch. Figure 1 depicts the proposed multi-band microstrip antenna geometry, which includes a U-shaped slot and two linear slots. The main radiating patch, dielectric layer, ground plane, and feeding point comprise the microstrip antenna (IE3D 14, Zeland software Inc.).

The resonant frequency of the proposed antenna has been appropriately chosen to range between 5 and 9 GHz. As a result, the proposed antenna can operate at these frequencies. The maximum and minimum dimensions of the suggested antenna are calculated using the transmission line model (Bhattacharyya and Garg 1985, Garg et al 2001, Kumar and Ray 2003) for the frequency operation range of 5 GHz to 9 GHz. The dimensions obtained at the lowest frequency, f= 5 GHz, are length, L=39 mm, and width, W = 47 mm. The dielectric constant of the Teflon dielectric layer is 2.25. Because the height of the dielectric substrate

Journal of Magnetism and Magnetic Materials 551 (2022) 169161

Contents lists available at ScienceDirect

Journal of Magnetism and Magnetic Materials

journal homepage: www.elsevier.com/locate/jmmm

Comparative analysis of STT and SOT based MRAMs for last level caches

Rajesh Saha [a,*], Yogendra Pratap Pundir [a,b], Pankaj Kumar Pal [a]

[a] Department of Electronics Engineering, National Institute of Technology Uttarakhand, Srinagar (Garhwal), Uttarakhand 246174, India
[b] Department of Electronics and Communication Engineering, Hemvati Nandan Bahuguna Garhwal University, Srinagar (Garhwal), Uttarakhand 246174, India

ARTICLE INFO

Keywords:
Spin Transfer Torque (STT)
Spin-Orbit Torque (SOT)
MRAMs
Large Last Level Cache (L^3C)
Magnetic Tunnel Junction (MTJ)

ABSTRACT

In recent years, magnetic RAMs have stimulated considerable research interest due to its high area-density and low leakage-power with comparable speed that makes it a strong contender for possible replacement of conventional RAMs. However, the operational speed of MRAM is relatively lower than the SRAMs. Advanced switching mechanism such as Spin Transfer Torque (STT), Voltage-Controlled Magnetic Anisotropy (VCMA), Magneto Electric (ME) effect, and Spin-Orbit Torque (SOT) has been introduced to further improve the speed of operation. This paper explores the comparative analysis of STT and SOT-based MRAMs for the application of Large Last-Level Caches (L^3Cs). It will give an insight into the MRAM from device to architectural level, in-aspect of performance parameters such as read-write energy consumption, leakage power, chip-area and read-write latency. This research work is carried out through a benchmarked simulation framework, starting from device to architectural level. At the cell level, it is observed that STT-MRAM takes 50% less area with 74% reduction in leakage power dissipation as compared to SOT-MRAM. However, the SOT-MRAMs is 4× faster than the STT-MRAM. At the architectural level, SOT-MRAM outperforms STT-MRAM in terms of read/ write energy and latency at the cost of marginal chip-area and leakage-power. Overall, in comparison to its conventional counterpart (SRAMs), SOT MRAMs are proved to be a superior candidate at a large size of *LLCs* in all aspects.

1. Introduction

In the era of big-data, the demands of non-volatile energy-efficient caches are paramount to achieve high-performance computational systems [1,2]. Current computational systems are designed by using multi-core processors so as to improve the computational efficiency. However, such computing systems are also requiring large on-chip caches for converging large workloads [3]. Caches are the high-speed on-chip memories which hold the most frequently used instructions or programs. It is utilized by the processor to improve the computational speed of the system. Therefore, the demand for the caches is increasing in order to improve the system performance and energy consumption. Hierarchy of an on-chip caches (*L1, L2* and last level cache, *LLC)* are categorized based on the size and the operating speed, in which higher the speed (*L1 > L2 > LLC*), lower would be the size (*L1 < L2 < LLC*). The often-used conventional memory technologies for caches are SRAMs and DRAMs [4,5]. SRAMs are used for high operating speed but limit its applicability due to large occupancy of chip-area, power hungriness, and volatility. In case of DRAMs, it has a high density with moderate speed but requires complex circuitry (refreshing/control circuits etc.) and volatile in nature too [5].

Apart from the conventional RAMs, the advanced resistive based memories such as Resistive RAMs (R-RAM), Phase-Change RAMs (PC-RAM), and Magnetic RAMs (MRAMs) have been used. These technologies consist of one storage device [such as GST ($GE_2SB_2TE_5$), MIM (Metal-Insulator-Metal) and MTJ] and one driver/transistor to switch the state of a storage device. These memories are not relied on a capacitive action for storing charge in comparison to its conventional counterparts (i.e. Flash, DRAMs and SRAMs) [3]. These resistive memories have an ability of miniaturization and provide almost zero leakage currents.

Amongst the aforementioned technologies, PC-RAM is operated by switching between crystalline and amorphous phases to store the binary bits. However, a large amount of drive current is required during phase change [6,7]. The R-RAM is implementing by forming a conducting and a non-conducting path using oxide-molecules between two metal electrodes to store the bits. However, it has the disadvantages of a low write-endurance (i.e. 10^6–10^9 cycles) and unsatisfactory read/write performance for low power applications [6]. The MRAM is working based on the principle of a spin and stores the information as a magnetic moment.

* Corresponding author.
E-mail address: rajeshsaha.phd@nituk.ac.in (R. Saha).

https://doi.org/10.1016/j.jmmm.2022.169161
Received 28 June 2021; Received in revised form 6 February 2022; Accepted 9 February 2022
Available online 18 February 2022
0304-8853/© 2022 Elsevier B.V. All rights reserved.

IOP Publishing Semiconductor Science and Technology
Semicond. Sci. Technol. 36 (2020) 015010 (11pp) https://doi.org/10.1088/1361-6641/abc51e

Effect of gate length on performance of 5nm node *N*-channel nano-sheet transistors for analog circuits

Yogendra Pratap Pundir[1,2], **Rajesh Saha**[2] and **Pankaj Kumar Pal**[2]

[1] Electronics and Communication Engineering, Hemvati Nandan Bahuguna Garhwal University, Srinagar Garhwal, Uttarakhand 246174, India
[2] Electronics Engineering, National Institute of Technology Uttarakhand, Srinagar Garhwal, Uttarakhand 246174, India

E-mail: y.pratap.iisc@gmail.com

Received 17 July 2020, revised 15 October 2020
Accepted for publication 27 October 2020
Published 17 November 2020

Abstract

In this work, the effect of channel length on the performance of an *N*-channel Nano-sheet Transistor (NST) for analog circuits has been investigated. A fully-calibrated TCAD platform is used to evaluate the performance of NST devices with channel lengths ranging from 10 nm to 240 nm. The maximum transconductance measured is 0.65 mS for gate length of 24 nm. In addition, the transconductance efficiency ranging from 3 V^{-1} to 38 V^{-1} is observed. Intrinsic gain increases from 7.3 to 121.65 as the gate length is varied from 10 nm to 240 nm. For 12 nm gate length, a unit gain frequency of 565 GHz is observed. NST with 24 nm exhibits Gain Frequency Product value of 5.3 THz. The gain-to-power efficiency improvement from 0.048 μA^{-1} to 2.16 μA^{-1} is observed. A reversal of relationships of transconductance and other performance parameters with gate length is observed at 24 nm gate length.

Keywords: analog performance, intrinsic gain, nano-sheet transistor, transconductance efficiency, unit gain frequency, drain induced barrier lowering

(Some figures may appear in colour only in the online journal)

1. Introduction

Semiconductor Industry has been consistently making the transistors smaller to deliver better speed-to-power dissipation ratio in every novel technology node. As, the cell area decreases with smaller transistors, wire lengths also decrease. This results in smaller capacitances and faster circuit speeds [1]. However, to continue the downscaling of device dimensions; the transistors must reach closer to their ideal features. An ideal MOS transistor is conceptualized to be a Gate-All-Around (GAA) channel device with a high-*k* gate dielectric, and low source/drain resistances [2]. GAA devices have been reported to offer better short channel immunity than its multi-gate counterpart FinFETs [3].

Nano-sheet Transistors (NSTs), being a GAA device is a potential candidate as successor to FinFETs for sub-5 nm technology nodes [2–4]. The NSTs have the advantage of being a quasi-planar technology and provide a larger effective width per unit footprint area [5, 6]. Also, wide and thin sheets are reported to provide superior performance [7]. Unlike FinFETs, the width of NSTs can be varied, continuously as per the circuit requirements. This results in greater flexibility for circuit designers. The smallest dimension in the NST, namely sheet thickness, is controlled by the epitaxial process. Epitaxy process has better control, in contrast to the etching process used to shape fins of FinFETs. The width of fins in FinFET devices presents variability issues that become more problematic as the advanced technology nodes demand difficult aspect ratios. NSTs have also been reported to have better immunity to work-function variations [8]. The performance of NSTs for digital circuits is evaluated in [9]. AC/DC performance of NSTs is reported in [10]. The impact of nano-sheet thickness and width on its performance has been analyzed and reported in [11]. However, the effect of length on analog performance

 © 2020 IOP Publishing Ltd Printed in the UK

Impact of Size, Latency of Cache-L1 and Workload Over System Performance:

Publisher: IEEE Cite This PDF

Rajesh Saha ; Yogendra Pratap Pundir ; Sarita Yadav ; Pankaj Kumar Pal All Authors

1 Cites in Paper

215 Full Text Views

Abstract

Document Sections

I. Introduction

II. Experimental Setup and Configuration

III. Results and Discussion

IV. Conclusion

» APPENDIX

Authors

Figures

References

Citations

Keywords

Metrics

Abstract:
In this paper, a system architecture modelled to check the impact of the size of cache-L1, latency of cache-L1 and Mibench workbench on performance parameter Miss Rate and IPS is presented. Gem5 simulation tool has been used to model the system architecture and its configuration. Five applications of Mibench are basicmath, crc32, fft, stringsearch and Patricia which are used to evaluate the performance of the system. It is observed that performance of the system increases with the decrease in the latency and the increase in size of the cache-L1.

Published in: 2020 International Conference on Advances in Computing, Communication & Materials (ICACCM)

Date of Conference: 21-22 August 2020

INSPEC Accession Number: 20152157

Date Added to IEEE *Xplore*: 10 November 2020

DOI: 10.1109/ICACCM50413.2020.9213015

ISBN Information:

Publisher: IEEE

ISSN Information:

Conference Location: Dehradun, India

I. Introduction

Any computing system consists of a central processing unit (CPU) with its peripheral. Generally used Instruction Set Architecture (ISA) for CPU are 0x86 architecture (mostly used in general purpose computer) and ARM architecture (mostly used in mobile, toys, automobile, equipment's etc.). Every general purpose computing processor has inbuilt cache memory to enhance the performance of the processor. These cache memory are categorized into different sections based on their latency like L1 (0.5-5ns), last level cache or LLC (10-20ns). In the early 80's, there was no existence of cache memory in processors. At that time, processors used main memory (DRAM) to access the data and instructions, which was very slow and more expensive. Starting of the 1980's this gap began to widen quickly which can be seen in [1]. Microprocessors clock speed raised but memory access times improved far less dramatically. Researcher at IBM discovered that most of the codes are nearly similar and extremely

Mixed-mode circuit simulations with 5 nm Node Nanosheet Transistors using TCAD

1st Yogendra Pratap Pundir
Dept. of Electronics and Communication Engineering
Hemvati Nandan Bahuguna Garhwal University
Uttarakhand, India
y.pratap.iisc@gmail.com

2nd Rajesh Saha
Dept. of Electronics Engineering
National Institute of Technology
Uttarakhand, India
rajeshsaha29@gmail.com

3rd Pankaj Kumar Pal
Dept. of Electronics Engineering
National Institute of Technology
Uttarakhand, India
pankajpal86@nituk.ac.in

***Abstract*— In this work, circuit designs with 5 nm node Nanosheet Transistors (NSTs) using a calibrated TCAD platform are presented. A three-stage ring oscillator (RO) with a frequency of 49.5 GHz is reported. The observed delay for NOT gate is 6.73 ps. A cross-coupled oscillator with 5 GHz oscillation frequency and its systematic design are reported. The calculated values of inductance and capacitance for 5 GHz cross-coupled oscillator are 300 pF and 1.69 pF, respectively.**

***Index Terms*—Nanosheet Transistor, TCAD Model, Ring Oscillator, Cross-coupled Oscillator**

I. INTRODUCTION

Semiconductor Technology as an art of repetitively creating fine structures with great precision has enabled our society to realize many interesting and useful ideas in physical form. These fine structures primarily include transistors and interconnects. Of these, the Transistors in the form of signal processing and memory elements have been a key driver behind the growth of the semiconductor industry. Also, the revolution in Information Technologies has been fuelling a historic growth in the Semiconductor Industry for the last few decades. The next revolution, at the footsteps, in data centers, cyberspace, cloud computing, Internet of Things, smart automobile and personal computing devices, etc. is expected to take the semiconductor industry to a much larger scale [1]. However, these prospects are not without challenges. Some of the great challenges are related to a huge amount of data, network connectivity, and time-bound decisions and responses. These challenges necessitate a technology with faster and smaller transistors at acceptable increments in cost [2]. Every new transistor technology is made possible by innovations in lithography, materials, and processes [3]. However, today's industry is looking for a new transistor device structure, also, to replace conventional transistor technology. The new device technology while offering better performance to power dissipation ratio can be acceptable only if it comes with minimal modifications to the existing CMOS process technology.

The Semiconductor Industry has placed its bet on Nano Sheet Transistors (NSTs) as an immediate successor to the current FinFETs based technology for beyond 7nm nodes [4]. NSTs have better performance due to a larger effective width per unit footprint area than conventional FinFETs [4], [5]. Also, the NSTs have been demonstrated using very few modifications in the existing manufacturing process [4]. Nanosheet transistors consist of horizontal sheets of silicon used as channels. Multiple sheets can be stacked for realizing a device and therefore, result in larger effective widths per unit footprint area in case of Nanosheet transistors. Nanosheet transistors use gate controls from all four sides i.e. Gate All Around (GAA) to mitigate the leakages at 5nm node and beyond [6].

NSTs being planar devices offer an advantage that their sheet width can be varied, continuously, for different power and performance requirements, without any additional process difficulty. This is a big advantage over conventional FinFETs technology. Further, the GAA NST FETs can be realized with a smaller spacing among sheets and parasitic capacitances can also be scaled down while allowing higher drive current. An NST device also has the flexibility to add the number of sheets to get required ON transistor currents [7].

II. DEVICE STRUCTURE AND CALIBRATION OF MODEL FOR SIMULATION PLATFORM

An N channel and a P channel Nanosheet Transistor of 5nm technology node [4], with three vertically stacked nanosheets and a GAA structure, are created as shown in Fig. 1. N channel device uses Silicon with (100) transport direction. P channel device uses Silicon-Germanium ($Si_{(x)}Ge_{(1-x)}$ with x = 0.5). The GAA structure for nanosheet channels is shown in Fig. 1. The values of important device dimensions and physical parameters used are listed in Table I.

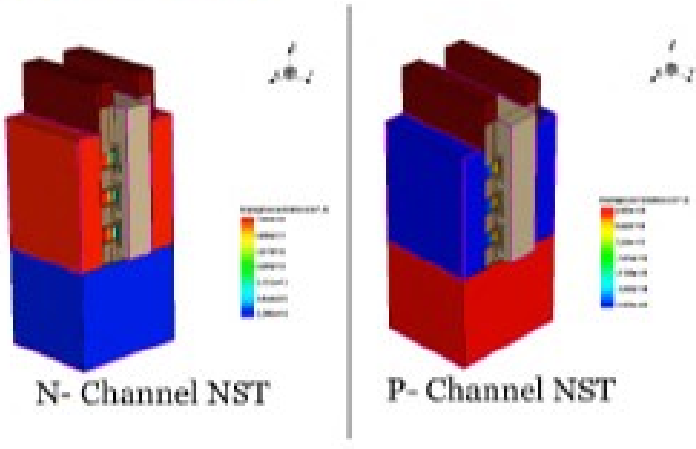

Fig. 1. Nanosheet Transistor (NST) with GAA.

978-1-7281-9785-2/20/$31.00 ©2020 IEEE

Silicon
https://doi.org/10.1007/s12633-022-01800-w

ORIGINAL PAPER

Effect of Temperature on Performance of 5-nm Node Silicon Nanosheet Transistors for Analog Applications

Yogendra Pratap Pundir[1,2] · Arvind Bisht[1] · Rajesh Saha[1] · Pankaj Kumar Pal[1]

Received: 6 December 2021 / Accepted: 1 March 2022
© The Author(s), under exclusive licence to Springer Nature B.V. 2022

Abstract

This work investigates the effects of temperature on the performance of a 5-nm node *N*-channel Nanosheet Transistor (NST) for analog applications. A fully calibrated commercial TCAD platform is used for the device as well as mixed-mode circuit simulations. The range of temperature used in the study is from 250 to 450 K. The transconductance (g_m) of the NST shows a change in the sign of its temperature coefficient (TC), from positive to negative, around a gate voltage of 0.52 V. The Output-conductance (g_{ds}) and Early-voltage (V_{EA}) parameters increase with the increase in temperature. However, the Intrinsic-gain (A_v), Transconductance-generation-efficiency (g_m/I_{DS}), Unit-gain-frequency (f_T), Gain-Frequency product (*GFP*), Transconductance–Frequency product (*TFP*), and Gain- Transconductance–Frequency product (*GTFP*) parameters are observed to deteriorate with the increasing temperature. For the increase in temperature from 250 to 450 K: the maximum g_m value is seen to decrease from 228 µS to 200 µS; the g_{ds} values increase from 24.6 µS to 27.1 µS; the early voltage (at V_{GS} = 400 mV) improves from 2.37 to 2.71 V; the f_T value decreases from 568 GHz to 524 GHz; the A_v value falls from 9.2 to 7.4; Discharge-time (t_d) value improves from 9.45 ns to 8.11 ns; the g_m/I_{DS} values degrade from 37.5 V^{-1} to 22.4 V^{-1}; the *GFP* value falls from 5.22 THz to 3.86 THz.

Keywords Analog Performance · Gain frequency product · Intrinsic gain · Nanosheet Transistor · Unit gain frequency

1 Introduction

The art of creating nano-scale semiconductor devices has been one of the most advanced technologies developed in almost half a century. From the 22-nm technology node onward, the FinFETs based semiconductor technology has successfully kept the foundation of computing technology a rock-solid one. The FinFETs of newer technology nodes use narrower and taller fins along with better junction optimizations to achieve improvements in SS and DIBL [1]. Advancements in FinFETs based technology have been made possible by technology innovations such as pitch splitting, cut masks, spacer-based patterning, fin depopulation, etc. [2]. Better fin process control, along with the use of gate-stack engineering for threshold voltage (V_{TH}) tuning, instead of implant-based V_{TH} control, has allowed the FinFETs to have lesser V_{TH} variations and a lower power supply voltage. However, it is challenging to continuously scale down the devices to improve their energy efficiency and computing performance. The challenge is primarily because of poor device electrostatics, large device parasitics, large leakage power, and sub-optimal low-voltage operation [3, 4]. Nanosheet transistor (NST) has been proposed as a successor for FinFETs, to continue the scaling of transistors and circuits [5–7]. The NSTs use wide and thin nanosheets, covered by the gate stack from all four sides, as the channels. The NSTs provide better electrostatics and a larger effective width due to their Gate-All-Around (GAA) structure and vertical stacking of nanosheet channels [8, 9]. The NSTs can also provide relief from the increasingly complex patterning required for narrower and taller fins for advanced FinFETs [10, 11] and save on the cost of scaling. NSTs are also resistant to the short channel effects and process variability [12, 13]. Furthermore, in comparison to prior nodes, the advanced technology nodes deliver a power, performance area, and cost (PPAC) advantage, but these are principally optimized for higher logic and SRAM performance to provide area and cost advantages. While the digital circuits do

✉ Yogendra Pratap Pundir
y.pratap.iisc@gmail.com

[1] National Institute of Technology Uttarakhand, Srinagar Garhwal, Uttarakhand 246174, India

[2] Hemvati Nandan Bahuguna Garhwal University, Srinagar Garhwal, Uttarakhand 246174, India

Published online: 12 March 2022

Suman Lata et al., International Journal of Research in Engineering, IT and Social Sciences, ISSN 2250-0588, Impact Factor: 6.452, Volume 07 Issue 09, September 2017, Page 22-26

Mental Health of Male and Female Professional Course Students: A Comparative Study

Suman Lata[1] and Kuldip Kumar[2]

[1](Assistant Teacher, G.P.S., Uttarakhand Government, India)

[2](Assistant Professor, HNB Garhwal University, Srinagar, India)

Abstract: *Mental health is a main factor for individuals, families and communities, and is more than simply the absence of a mental disorder. In this paper, there is a comparison between the mental health of male and female professional course students. We use null hypothesis method for observing the mental health of male and female professional course students of HNB Garhwal University, Srinagar, and Uttarakhand. We take a null hypothesis that there is no significant difference in Mental Health according to the gender of professional course students. This research is conducted on the basis of questionnaire tool "Mental Health Questionnaire as Mental Health Battery" by Arun Kumar Singh and Alpana Sen Gupta. After analyzing the collected data, our findings are there is an effect of the gender of students in emotional stability; Overall Adjustment and Security-Insecurity but we did not find any significance difference in Autonomy, Self-Concept, Intelligence and Overall Mental Health. These are the factors Mental Health.*

I. INTRODUCTION

Mental health is defined by the World Health Organization (WHO) as *"a state of well-being in which the individual realizes his or her own abilities, can cope with the normal stresses of life, can work productively and fruitfully, and is able to make a contribution to his or her community"*. Good mental health is not just the absence of mental health problems. Individuals have some virtue with good mental health:

- develop emotionally, creatively, intellectually and spiritually
- initiate, develop and sustain mutually satisfying personal relationships
- face problems, resolve them and learn from them
- are confident and assertive
- are aware of others and empathize with them
- use and enjoy loneliness
- play and have fun

The objective of this study is to compare the mental health of the students according to their gender i.e. male and female. The study was conducted on 120 professional course students of the following three colleges of HNB Garhwal central university at Chauras campus:

1. School of Engineering and Technology.
2. School of Pharmacy.
3. School of Management.

The study has been limited to the students of only three professional courses i.e. B.Tech, B.Pharm and MBA and the study is directed toward the students with in age range from 18 to 24 years.

II. METHOD

This research is conducted on the basis of questionnaire survey on the students of professional courses of different collages of the HNB Garhwal central university in chauras. We take three professional courses like B.Tech., B.Pharm., MBA for this study and categories these courses in to two part first one is under graduate and second one is post graduate level. In this study, we take samples on the basis of simple random sampling. It means that every member of the sample is selected from these three courses in such a manner that all members of these courses have essentially the probability of being selected.

Procedure

The students had to attempt total 130 questions according to the instructions given in the tool, *"Mental Health Questionnaire as Mental Health Battery"* by *Arun Kumar Singh and AlpanaSen Gupta*, which is used in this study.

In this tool, the questions are distributed according to the six different areas which are the key features of mental health. These areas are:

MultiCraft

International Journal of Engineering, Science and Technology
Vol. 11, No. 3, 2019, pp. 40-48

INTERNATIONAL JOURNAL OF ENGINEERING, SCIENCE AND TECHNOLOGY

www.ijest-ng.com
www.ajol.info/index.php/ijest
© 2019 MultiCraft Limited. All rights reserved

Microcontroller based data acquisition system using error reduction technique

Don Biswas[1*], Kuldip Kumar[2], Vishal Rohilla[3], Gambheer Singh Kathait[4], Prashant Thapliyal[5], Arun Shekhar Bahuguna[6], Yogendra Pundir[7], Vinay Prasad tamta[8]

[1,3,4,5] *Department of University Science Instrumentation Centre, Hemwati Nandan Bahuguna Garhwal University, Srinagar Garhwal, INDIA*
[2,6,7] *Department of Electronic and Communication Engineering, Hemwati Nandan Bahuguna Garhwal University, Srinagar Garhwal, INDIA*
[8] *Department of Information Technology, Hemwati Nandan Bahuguna Garhwal University, Srinagar Garhwal, INDIA*

Abstract

The application of high-speed real-time data acquisition is becoming increasingly wide spread in industrial field, and its measurement accuracy is also increasing. In the present study, the development of a USB based data acquisition system is presented here, where a microcontroller based standalone embedded system is used as data collection and also field control device. The data acquisition system has been calibrated in terms of output voltage generated in signal conditioner. The USB device system also calibrated for the error in the output result. Here USB device has been programmed as Human Interface Device (HID) class, hence not requiring any kind of device specific driver. This data acquisition system is utilized to measure the flow of a channel. The flow of water is not acidic.

Keywords: USB, microcontroller, PIC, acquisition, data acquisition, programmer, digital.

DOI: http://dx.doi.org/10.4314/ijest.v11i3.5

1. Introduction

From industrial view point, the physical parameter flow is a very critical constant for certain locations like, different types of power plant, field plant, DM plant, bottling plant, etc. Flow can be measure in two ways; one is dependent upon the volume and the other is dependent upon weight. Solid may be measured in terms of either weight per unit time or mass per unit time. The solid quantity is measured in terms of volume very rarely. The liquid quantity is characterized with the measurement of volume rate or in weight rate. The Gas quantity is normally measured in volume rate. The flow rate can be measured using different sensors like DPT type instrument, turbine flow meter. It basically measures the pressure difference between two points. The pressure difference is calibrated in terms of flow measurement. The data acquisition system has been also calibrated according to that purpose. The whole system has been calibrated using different techniques. First, we send some sinusoidal signal and analyze the correlation characteristic of the measured voltage peak data, which includes mean value, variance, standard deviation, range, deviation etc., and then finds out the influence rules of software timing error on data acquisition and measurement accuracy (Monoranjan and Sarma, 2010).

The sine-wave signal of this closed-loop test system is constructed by the SCIENTECH (ST4060) single-channel signal source, KEYSIGHT (Infiniti Vision DSO-X 2024A) oscilloscope, and data acquisition card. In the high-speed data acquisition, the repeatability and reproducibility error can be reduced. The faster, reliable, efficient data acquisition system has been introduced in the field of modern measuring instrument (Pandey and Arora, 2019). With the rapid development of various measuring instruments and equipment, the demand for accuracy, loss reduction and real-time of data acquisition measurement is also increasing (USB-IF, 2006; Song et al, 2011; Zhao et al, 2012; Niculescu et al., 2019). The popularity of Universal Serial Bus (USB) has been extended due to its inexpensive and easy-to-use nature. The short range (5m) communication medium has been used for the transfer of data from one device to another. In a regular PC (host), the communication device acts as a client (USB-IF,

Journal of Magnetism and Magnetic Materials 529 (2021) 167882

Contents lists available at ScienceDirect

Journal of Magnetism and Magnetic Materials

journal homepage: www.elsevier.com/locate/jmmm

Research articles

Design of an area and energy-efficient last-level cache memory using STT-MRAM

Rajesh Saha [a,*], Yogendra Pratap Pundir [a,b], Pankaj Kumar Pal [a]

[a] Department of Electronics Engineering, National Institute of Technology-Uttarakhand, Srinagar (Garhwal), Uttarakhand 246174, India
[b] Department of Electronics and Communication Engineering, Hemvati Nandan Bahuguna Garhwal University, Srinagar (Garhwal), Uttarakhand 246174, India

ARTICLE INFO

Keywords:
Magnetic tunnel junction (MTJ)
Gate-all-around
Spin transfer torque
MRAM
Last level cache
Energy efficient circuits

ABSTRACT

This paper presents an area and energy-efficient non-volatile Last-level Cache (LLC) using a STT-MRAM based on a state-of-art perpendicular magnetic tunnel junction (pMTJ) and an Vertical Gate-All-Around Field-Effect Transistor (GAA-FET). This work presented, in this article is carried out from device to circuit, architecture and up to the system level. A detailed analysis of STT-MRAM has been presented by comparing an Vertical GAA-FET (GA) with a bulk-FET (B) at cell level. It is observed that GA-STT-MRAM is advantageous and offers 93.10% and 60% reduction in leakage-power dissipation and area, respectively over B-STT-MRAM. Furthermore, at architecture level, 20% to 80% reduction in sizes of LLCs (ranging from 512 KB to 64 MB) is observed by using GA-STT-MRAM and around 80.70% leakage power reduction is achieved in comparison to SRAM based LLCs. In addition to the architecture level, GA-STT-MRAM is found to have 83.26% and 39.40% energy reduction compared to a B-STT-MRAM and a conventional SRAM, respectively at system level. The GA-STT-MRAM proves to be a more promising candidate to replace conventional semiconductor based LLC for next-generation energy-efficient microprocessors having on-chip non-volatility.

1. Introduction

The modern computing systems have becomes data intensive and therefore, the modern system processor requires large size in LLCs, main memories and data storage. Although, the 6T-SRAM based on-chip caches can improve the system performance, the limitation of their size restricts the system performance for IoTs, machine learning and deep neural network applications [1]. Moreover, the challenges with SRAM performance e.g. variability, retention-error and other short-channel effects (SCEs), have been increasing with the continuous device-scaling [2]. Several researchers have reported 8T, 10T, and 12T SRAM topologies to address the issues of retention errors, variability, and read disturbance [3]. However, this results in an increase in the area of cache memory that limits the usage of such topologies in caches [4]. In a nano-regime, SRAM also suffers from large leakage current, and causes increased power dissipation at array level [2,5].

A number of emerging resistive memories such as Phase-Change RAMs (PCRAM), Resistive RAMs (RRAM), and Spin Transfer Torque-Magnetic RAMs (STT-MRAMs) have been used as data storage. These memories do not rely on a capacitor for storing a charge, unlike their conventional counterparts (i.e. SRAMs, DRAMs and Flash) [1,6–7]. These technologies also have the potential to further scale down to smaller geometries and offer near zero leakage currents, as well. Amongst them, the PCRAM has been demonstrated to store binary bits by switching between crystalline and amorphous phase. However, it requires a large amount of drive current during phase transition [6,7]. The RRAM works on the principle of forming a conducting and a non-conducting paths using oxide-molecules between two metal electrodes. But it has the disadvantages of a low write-endurance (i.e. 10^6–10^9 cycles) and unsatisfactory read/write performance for low power applications [6]. The STT-MRAM is working based on principle of a spin and stores the information in the form magnetic moment. The STT MRAMs have a non-volatile nature, a good writing endurance (>10^{12} cycles), a small size, and a very low leakage current [7]. Also, the switching time values of STT-MRAMs are comparable to the conventional SRAMs [7]. It is also compatible with the CMOS fabrication process [6]. After comprehensive research, the STT-MRAM is found to be a potential candidate, to replace conventional SRAM, for last level caches.

The STT-MRAMs consists of a Magnetic Tunnel Junction (MTJ) and a driving transistor device. To meet the performance of LLCs, STT-MRAM

* Corresponding author.
E-mail address: rajeshsaha29@gmail.com (R. Saha).

https://doi.org/10.1016/j.jmmm.2021.167882
Received 23 December 2020; Received in revised form 16 February 2021; Accepted 21 February 2021
Available online 6 March 2021
0304-8853/© 2021 Elsevier B.V. All rights reserved.

IOP Publishing Semiconductor Science and Technology
Semicond. Sci. Technol. 36 (2021) 095037 (11pp) https://doi.org/10.1088/1361-6641/ac16e6

Air-spacers as analog-performance booster for 5 nm-node N-channel nanosheet transistor

Yogendra Pratap Pundir[1,2,*], Arvind Bisht[1], Rajesh Saha[1] and Pankaj Kumar Pal[1]

[1] National Institute of Technology Uttarakhand, Srinagar Garhwal, Uttarakhand 246174, India
[2] Hemvati Nandan Bahuguna Garhwal University, Srinagar Garhwal, Uttarakhand 246174, India

E-mail: y.pratap.iisc@gmail.com

Received 29 March 2021, revised 13 July 2021
Accepted for publication 22 July 2021
Published 23 August 2021

Abstract

This work investigates the use of air-spacers as an analog-performance booster for nanosheet transistors (NSTs) at 5 nm node. The NSTs with air-spacers are evaluated across the design space for analog circuits. A fully calibrated three-dimensional technology computer-aided design platform was used for the device and mixed-mode circuit simulations. The use of air-spacers improves the output impedance (r_o) from 974 kΩ to 1.32 MΩ, as well as the intrinsic gain (A_V) from 90 to 118, for the NST with L_g/W_g = 240 nm/15 nm. The air-spacers also improve analog performance parameters such as the unit-gain frequency (f_T) from 562 to 596 GHz; gain-frequency product from 4.76 to 5 THz; transconductance-frequency product from 2.11 to 2.22 THz; and the gain-transconductance-frequency product from 17.9 to 18.7 THz; for the NST with L_g/W_g value of 12 nm/15 nm. In addition, the discharge time (t_d) also improves from 1.64 to 1.5 ns, for NST with L_g/W_g = 12 nm/120 nm. The oscillation frequency of a three-stage ring-oscillator is also reported to improve from 68.3 to 88.2 GHz by the use of air-spacers.

Keywords: analog performance, nanosheet transistor, air-spacer, intrinsic gain, unit gain frequency, gain frequency product, ring oscillator

(Some figures may appear in colour only in the online journal)

1. Introduction

Semiconductor devices have steadily evolved to achieve a better performance. The performance improvements are due to the smaller dimensions of transistors as well as the shrinking of wires surrounding them [1]. However, the continued scaling of semiconductor device dimensions also resulted in the onset of many secondary effects that deteriorate the device performance known as the short-channel (SCEs) and narrow-width effects. The SCEs cause transistor devices to conduct a significant current in the OFF state. This further affects the system-level performance by wasting the electrical power and the cooling efforts. The challenge of SCEs was overcome by several novel MOS based devices such as SOI, FinFETs, nano-wire etc. The FinFETs marked a shift from a planar transistor technology to a quasi-planar multi-gate transistor structure [2–4]. The tri-gate architecture of a FinFETs helps in increasing the gate electrostatic control over the channel, and thus allowed for a low voltage operation while mitigating SCEs [2]. Consequently, the FinFETs have been a phenomenal success from 22 nm technology-node to 7 nm technology-node [5–7]. However, the FinFETs based technology may not continue to be scaled beyond 7 nm node, due to a loss of gate control, width quantization that limits its usage in circuits, and increased device parasitic due to quasi-planar nature [8–10]. A number of technology boosters have been proposed to facilitate the scaling of FinFETs beyond 7 nm, but with costly process difficulties [5, 11, 12]. Consequently, the nano-wire transistors (NWFETs), with a gate-all-around (GAA) architecture

* Author to whom any correspondence should be addressed.

Ferroelectrics

ISSN: 0015-0193 (Print) 1563-5112 (Online) Journal homepage: http://www.tandfonline.com/loi/gfer20

Temperature dependence of dielectric properties of sodium potassium niobate ceramics for different values of x ($Na_{1-x}K_xNbO_3$)

Don Biswas, Gambheer Singh Kathait, Prashant Thapliyal, Vishal Rohilla & Surendra Singh

To cite this article: Don Biswas, Gambheer Singh Kathait, Prashant Thapliyal, Vishal Rohilla & Surendra Singh (2018) Temperature dependence of dielectric properties of sodium potassium niobate ceramics for different values of x ($Na_{1-x}K_xNbO_3$), Ferroelectrics, 526:1, 168-175, DOI: 10.1080/00150193.2018.1456307

To link to this article: https://doi.org/10.1080/00150193.2018.1456307

Published online: 08 May 2018.

Submit your article to this journal

View related articles

View Crossmark data

Full Terms & Conditions of access and use can be found at
http://www.tandfonline.com/action/journalInformation?journalCode=gfer20

FERROELECTRICS
2018, VOL. 526, 168–175
https://doi.org/10.1080/00150193.2018.1456307

Taylor & Francis
Taylor & Francis Group

Check for updates

Temperature dependence of dielectric properties of sodium potassium niobate ceramics for different values of x ($Na_{1-x}K_xNbO_3$)

Don Biswas[a], Gambheer Singh Kathait[a], Prashant Thapliyal[a], Vishal Rohilla[a], and Surendra Singh[b]

[a]USIC Dept., HNB Garhwal University, Srinagar Garhwal, Uttarakhand, India; [b]Dept. of Physics, HNB Garhwal University, Srinagar Garhwal, Uttarakhand, India

ABSTRACT

Dielectric constant, loss tangent and electrical conductivity of $Na_{1-x}K_xNbO_3$ (X = 0.08 and 0.17)(SPN) ceramic pellets have been measured at 10, 100 and 1000 kHz frequencies and at temperature varying from room temperature to 425°C. The dielectric constant increases with increase of temperature up to 400°C at all the three frequencies, and thereafter, it decreases with further increase of temperature, i.e., it shows a structural transition at about 400°C. The loss tangent also shows similar behaviour as dielectric constant shows. Some variations may be due to relaxation effects and impurities etc. around the sensitive transition region, which are seem to play prominent role in this soft mode region. Electrical conductivity increases with increase in temperature at all the three frequencies.

ARTICLE HISTORY
Received 17 August 2017
Accepted 18 March 2018

KEYWORDS
Ceramics; dielectric constant; loss tangent; electrical conductivity

1. Introduction

Ferroelectricity is the phenomenon of a spontaneous polarization which exists in certain, in a certain temperature range, limited by the transition temperature (T_c), and can be reversed by applying external electric field. Ferroelectricity is characterized by a polarization –electric field (P-E) hysteresis loop. The spontaneous polarization (P_S) is the polarization which remains present in the ferroelectric material in the absence of the external electric field. Spontaneous polarization (P_S) is defined as the surface density of the bound charge on the sample surface. With increasing temperature spontaneous polarization decreases rapidly on crossing the transition temperature. Depending on the transition mechanism, ferroelectrics can be divided into two main groups, viz., order-disorder type (polarization along only one axis, up or down), and displacive type (polarization along several axes that are equivalent in the unpolar state). The most typical ABO_3 type displacive ferroelectrics are perovskite type (having $CaTiO_3$ structure), e.g., $BaTiO_3$, $KNbO_3$, $PbTiO_3$, $KTiO_3$, $PbZrO_3$, $LiNbO_3$, $LiTaO_3$, etc. [1]. In this structure cations, based on their valence states and coordination number, occupy the A or B site, normally lower valency [1–4] ions occupy A sites and high valency (3-6) cations occupy B sites.

CONTACT Don Biswas donusic06@gmail.com

Color versions of one or more of the figures in the article can be found online at www.tandfonline.com/gfer.

© 2018 Taylor & Francis Group, LLC

The perovskite (ABO_3) type compounds have attracted considerable attention due to their broad range of technologically important dielectric, piezoelectric, ferroelectric and optoelectronic properties [2]. NaNbO3, one of the important members of ABO_3 series (perovskite type), is controversial due to its property of antiferroelectricity. Initial worker [3–5] reported that it is ferroelectric having $T_C = 480°C$. But later on [6–8] it was reported that $NaNbO_3$ is antiferroelectric at room temperature and ferroelectric below about $-200°C$. a small amount of $KNbO_3$ (ferroelectric, $T_C = 435°C$) added to pure $NaNbO_3$, greatly alters its physical characteristics and gives a new system Sodium Potassium Niobate (SPN), i.e.,$Na_{1-x}K_xNbO_3$.Corresponding a fixed chemical composition ratio of Na/K, the physical properties are extremal, is generally called morphotropic phase boundary [1].

Near the morphotropic phase boundary (MPB) these ferroelectrics show excellent ferroelectric and piezoelectric properties [1, 9]. Near the morphotropic region (MR), composition exhibits a transition region, where the crystal structure changes abruptly and the physical properties are extremal. It is well known that the optimal electrical properties can be obtained when the composition lies in the MPB region, between rhombohedral and tetragonal phases, in many lead based system [9]. An example for lead based material with MPB is Lead zirconate titanate (PZT), is a lead based perovskite structure ferroelecrtric material. This is a binary solid solution of lead zirconate (PZ) an anti ferroelectric (orthorhombic structure) and lead titanate (PT) a ferroelectric (tetragonal structure) material. This material possess a morphotropic phase boundary (MPB) when the Zr/Ti $\sim$ 52/48 [1,9]. However, the toxicity of lead oxide and its high vapor pressure during processing has lead to a demand for alternative lead free piezoelectric material [11]. Therefore in the present study our focus is to search a lead free material having a morphotropic phase boundary (MPB) with better ferroelectric and piezoelectric properties comparable to their lead based counter parts. The search for alternative is now focused on alkali niobates system in which MPB occurs. Among them $(Na_{0.5}K_{0.5})NbO3$ has been consider good candidates for lead free piezoelectric ceramics because of its strong piezoelectricity and ferroelectricity [17].

The perovskite potassium sodium niobate system is of interest, because it shows a number of ferroelectric phases with high spontaneous polarization. Ferroelectric materials play an important role in piezoelectric and dielectric applications in modern engineering and ceramic technology. Their widespread applications in infrared detectors, transducers, capacitors, electro optical modulators, switching and second harmonic generations have attracted the attention of researchers. Potassium niobate ($KNbO_3$) is useful in second harmonic generation, optical waveguide and pyroelectric sensors. Efficiency of $KNbO_3$ is three times larger than that of $LiNbO_3$.

Several researchers [18–21] have established that several phase transitions with high spontaneous polarization occurs between $-200°$ to $600°C$, in this system, with the help of high temperature optical and X-ray diffraction studies.

2. Experimental details

The raw materials used for preparing the composition, for the present study, were sodium carbonate (Na_2CO_3), potassium carbonate (K_2CO_3) and niobium pentoxide (Nb_2O_5) all of 99.99% pure. Sodium- potassium niobate pellet samples were prepared by conventional solid state reaction method. First we removed the absorbed moisture from the starting materials and for that purpose the materials were dried, at $200°C$ for 1 hour. The

compositions were prepared by weighing the materials in proper stoichiometric ratio for different compositions ($Na_{1-x}K_xNbO_3$, x = 0.08 and 0.17). Using agate mullet mortar and pestle, each composition was manually dry mixed and ground for 4 hours and with acetone for another 2 hours. The mixture is calcined in a crucible in air at 900 degree C to remove carbonate. After cooling to room temperature, in dry air, the calcined mixture was weighed to ensure the complete carbonate removal from the mixture. Pre-sintered mixture was ground and pressed into disk of 8 mm diameter and having 2 mm thickness at 0.2 GPa. Pellets of $Na_{1-x}K_xNbO_3$ (x = 0.08 and 0.17) were sintered, each composition for 14 hours, at 1100°C. All the sintered pellets were taken out from the furnace when it cooled to room temperature. For dielectric measurements sintered pellets were electroded, with air drying silver paste, in metal- insulator- metal (MIM) configuration. Frequency, temperature and composition (x = 0.08 and 0.17) dependence of dielectric constant (K), dissipation factor (tan δ) and dielectric conductivity (σ) of the prepared samples were measured in MIM configuration [22], using Fluke– PM6306 RCL meter. Using a temperature controller of accuracy ±1°C, measurements were carried out between 35–500°C, in 1 KHz–1 MHz frequency range. It was found that the samples show orthorhombic structure at room temperature. The RLC meter FLUKE PM6306 is used to measure the dielectric properties.

The observed XRD patterns of the prepared $Na_{1-x}K_xNbO_3$ pellet samples with different (x = 0.08 and 0.17) values of x have been shown in Fig. 1. The XRD patterns of the prepared pellet samples show polycrystalline behavior and are in good agreement with the Joint Committee on Powder Diffraction Standards (ICSD) (calculated from ICSD using POWD-12^{++}(1997)) [23] data of $NaNbO_3$ with peaks corresponding to (100), (110), (211), etc. The perovskite subcell parameters calculated from the XRD data, using the relation provided by Azaroff [24], have been given in Table 1. The values of calculated subcell parameters closely agree with the reported results [25, 26]. In the observed composition range (x = 0.08

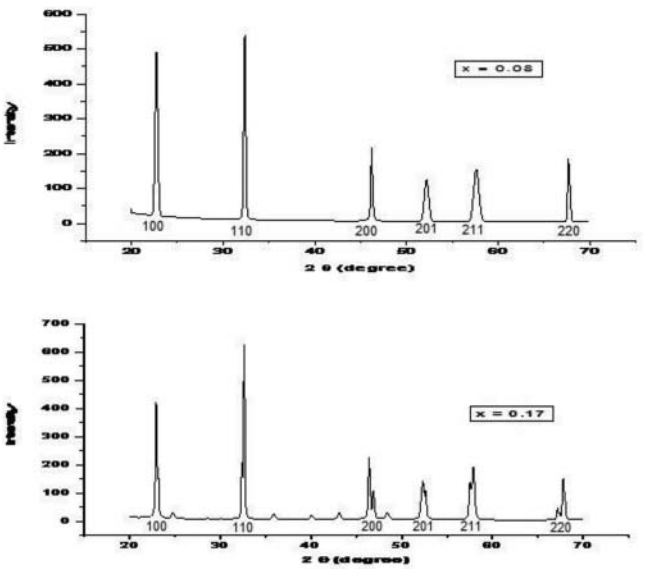

Figure 1. XRD patterns of $Na_{1-x}K_xNbO_3$.

Table 1. Lattice parameters of $Na_{1-x}K_xNbO_3$ for different x values (x = 0.08 and 0.17).

	Lattice Parameters		
Composition	a (Å)	b (Å)	c (Å)
Na0.92K0.08NbO3	7.82606	7.817992	7.8422170
Na0.83K0.17NbO3	7.884696	7.750694	7.8815470

and 0.17), a continuous shifting of the most intense peaks, (110) and (100), to higher angle was observed, with increasing potassium concentration (x value) up to x = 0.08.

Room temperature X-ray diffraction (XRD) patterns of all the prepared samples were taken by Pan Analytical X- ray Diffractometer (PW340), using Cu*K*α1 radiation of wavelength 1.54060Å. The instrument is well calibrated with silicon standard samples and the lines obtained are matching with the standard lines. Surface morphology and grain size of the prepared samples were studied using the model EVO 18 Special Edition (Switzerland) manufactured by ZEISS. From scanning electron micrographs of the prepared pellets average grain sizes were found between 6 and 8 μm.

Out of the various possible ways of characterization, X-Ray diffraction method of the powder is of special importance. Also, it is the most convenient method by which diffraction data can be obtained from the crystalline materials. These data which depend on the unit cell parameters are unique for a particular substance and can be employed for its identification. The powder method is the quickest possible means of achieving this. Room temperature X-Ray diffraction patterns of all the prepared compositions have been obtained on a Pan Analytical X- ray Diffractometer (PW340), using Cu*K*α1 radiation of wavelength 1.54060Å. The instrument is well calibrated with silicon standard samples and the lines obtained are matching with the standard lines. The perovskite subcell parameters were

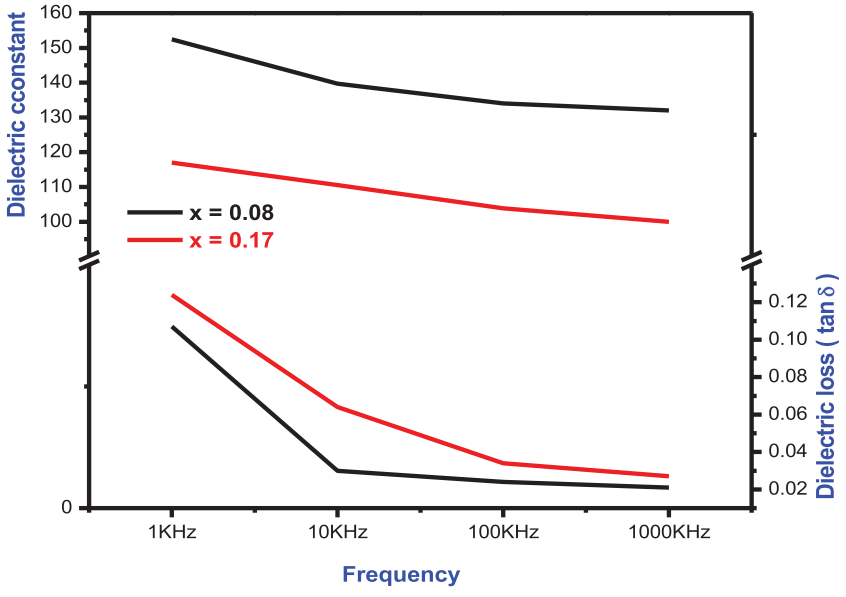

Figure 2. Variation of dielectric constant and loss tangent in SPN system (x = 0.08 and 0.17) at room temperature.

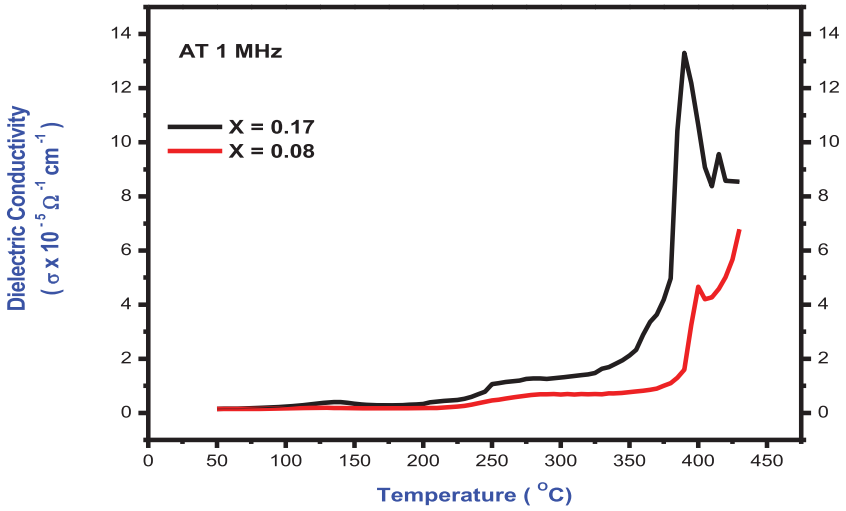

Figure 3. Temperature dependence of electrical conductivity with respect to temperature in SPN system (x=0.08 and 0.17).

obtained using the HighScore Plus computer software. It was found that the samples show orthorhombic at room temperature.

3. Results and discussion

Ceramic pellets have been prepared for $Na_xK_{1-x}NbO_3$ (x = 0.08 and 0.17) (SPN) samples by solid state reaction method. These samples have been characterized using XRD and the sublattice parameters are presented in Table 1 which are found to be in agreement with the previous results [18, 19] and are reported for pure $NaNbO_3$ and $KNbO_3$. Scanning Electron

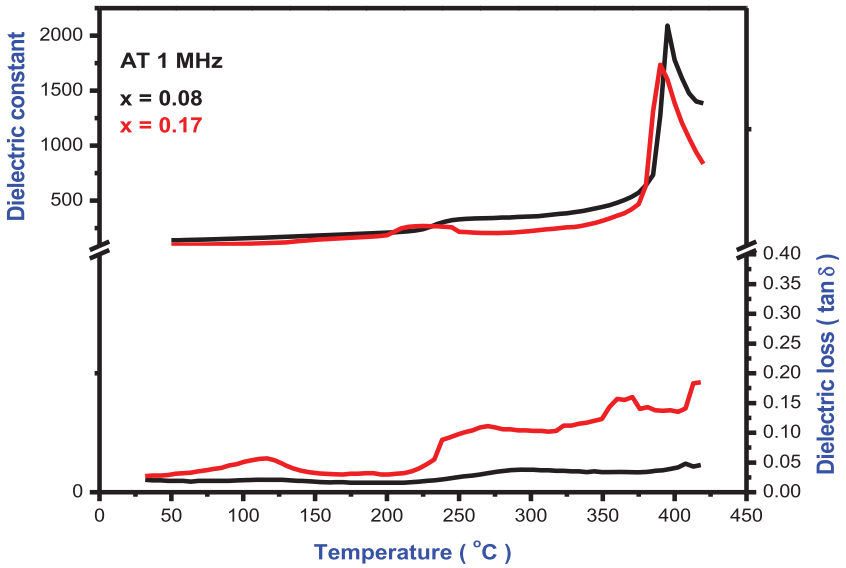

Figure 4. Temperature dependence of dielectric constant and loss in SPN system (x=0.08 and 0.17).

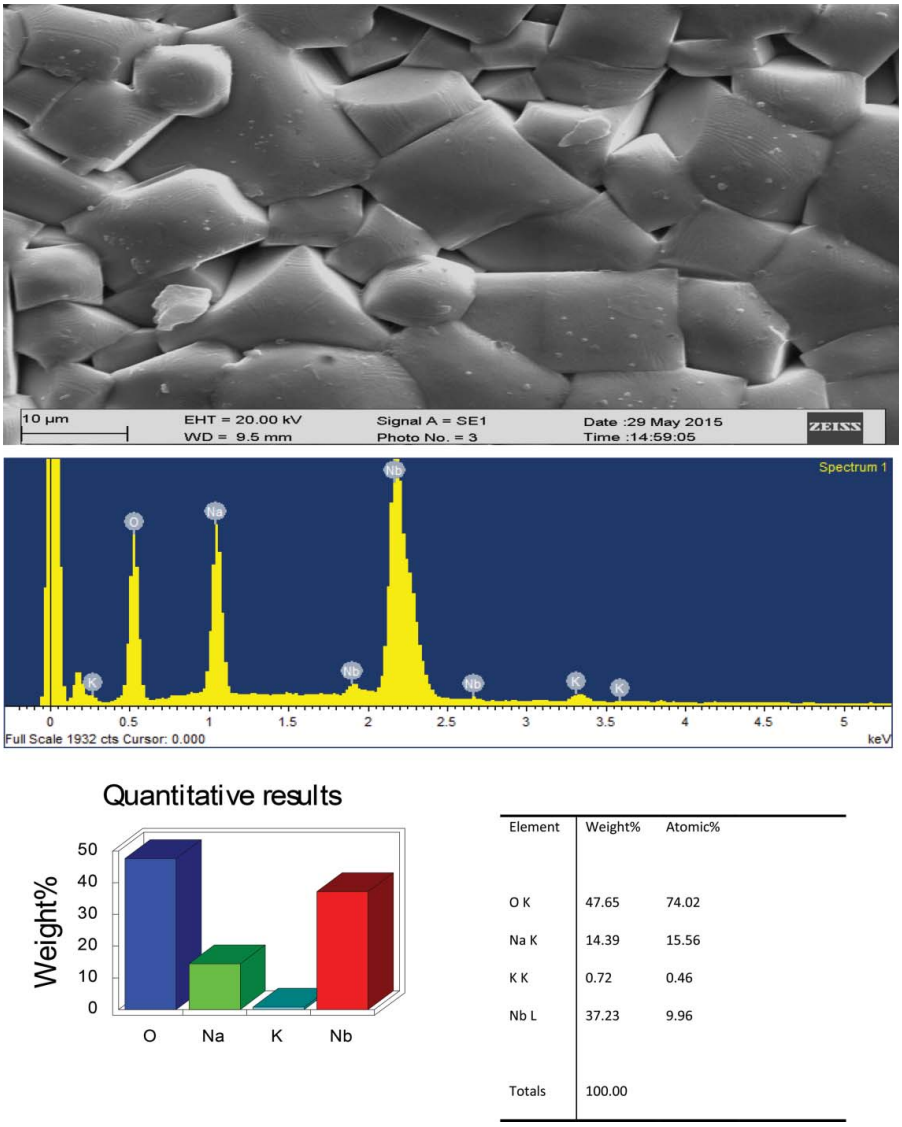

Figure 5. Quantitative analysis of the pellet samples of $Na_xK_{1-x}NbO3$ (X =0.08).

Microscopic (SEM) photograph was taken by using the model EVO 18 Special Edition by ZEISS (Switzerland). The average grain size obtained was 5 μm– 8 μm for $Na_xK_{1-x}NbO_3$ (X = 0.08 and 0.17), which was found to be in agreement with the previously reported results [27, 28]. We have measured dielectric constant, loss tangent and electrical conductivity of $Na_xK_{1-x}NbO_3$ (X = 0.08 and 0.17) ceramic pellets using RLC meter (Fluke, Germany) at 10, 100 and 1000 kHz frequencies and at temperature varying from room temperature to up to 425°C. The temperature dependence of dielectric constant, loss tangent is presented in Figure 2 (at room temperature). Figure 3 shows the temperature dependence of electrical conductivity for $Na_xK_{1-x}NbO_3$ (X = 0.08 and 0.17). It is observed from Figure 4 that the value of dielectric constant increases, with increase of temperature up to 400°C at all the

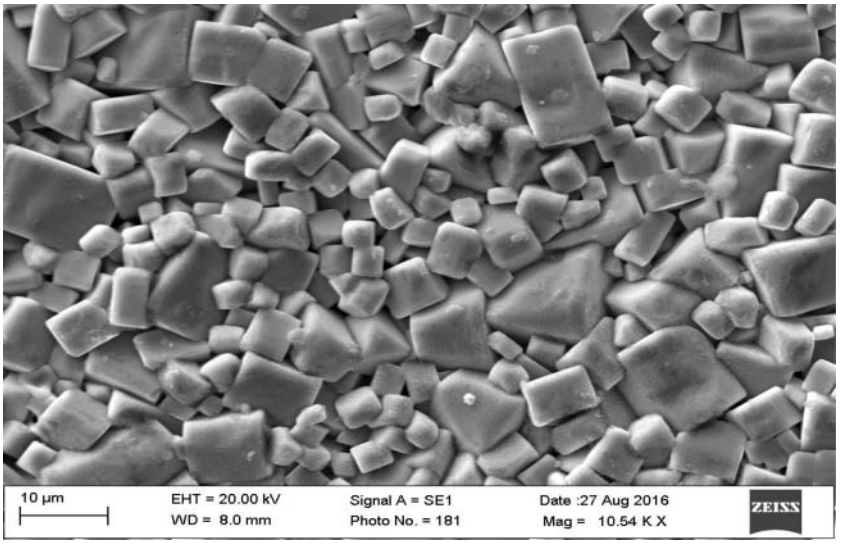

Figure 6. SEM results of the pellet samples of $Na_xK_{1-x}NbO3$ (X=0.17).

three frequencies, and thereafter, it decreases with further increase of temperature, i.e., it shows a structural phase transition (Sharp change) at about 400°C from tetragonal to cubic.

Cubic phase. For the compositions with x = 0.08, the most intense peaks were observed. In the observed composition range ($0.08 \leq \times \leq 0.17$), a continuous shifting of the most intense peaks, (110) and (100), to higher angle was observed with increasing potassium concentration (x value). Some variations may be due to relaxation effects, arising due to impurities etc. around the sensitive transition region, which seem to play prominent role in this

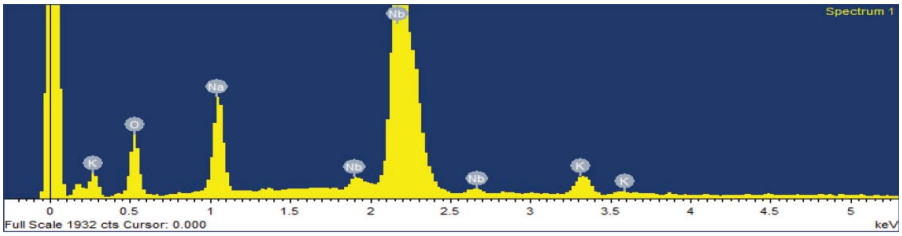

Element	Weight%	Atomic%
O K	31.87	63.82
Na K	10.91	15.21
K K	2.60	2.13
Nb L	54.63	18.84
Totals	100.00	

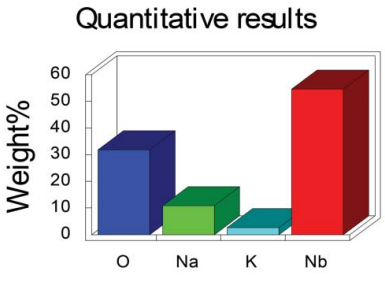

Figure 7. Quantitative analysis of the pellet samples of $Na_x K_{1-x} NbO_3$ (X = 0.17).

soft mode region. The SEM results as well as the quantitative analysis of the prepared samples have been shown in Figures 5–7.

It has been observed that the dielectric constant is higher for $Na_xK_{1-x}NbO_3$ (X = 0.08) and lower for $Na_xK_{1-x}NbO_3$ (X = 0.17) with varying temperature condition as well as at room temperature. The dielectric loss is higher for the $Na_xK_{1-x}NbO_3$ (X = 0.17) sample and lower for $Na_xK_{1-x}NbO_3$ (X = 0.08) sample. The dielectric conductivity is also higher for the $Na_xK_{1-x}NbO_3$ (X = 0.17) sample and lower for $Na_xK_{1-x}NbO_3$ (X = 0.08) sample. So from the prepared samples, the composition $Na_{0.92}K0_{.08}NbO_3$ would have appreciable interest because of its high dielectric, low loss and dielectric conductivity.

Acknowledgments

The authors are thankful to Prof. N. S. Panwar, HNB Garhwal University, Srinagar (Garhwal), for his kind suggestion. Prof. N. S. Panwar is also thankfully acknowledged for providing laboratory facilities.

References

[1] H. Nagta, N. Chikoshi, and T. takenaka, *J. Appl.phy.* **38**, 5497–5499 (1999).
[2] G. A. Samara, *ferroelectrics* **73**, 145 (1987).
[3] B. T. Mathias, *Phy Rev.* **75**, 1771 (1949).
[4] B. T. Mathias, J. P. Remeika, *Phys.Rev.* **82**, 727 (1951).
[5] E. A. Wood, *Act. Cryst.* **04**, 353 (1955).
[6] G. Shirane, and R. Newnham, R. Pepinsky, *Phys. Rev.* **96** (3), (581 (1954).
[7] L. E. Cross, and B. J. Nicholson, *Philos. Mag.* **46** (7), 453 (1955).
[8] R. H. Dungan, and R. D. Golding, *J. Am. Ceram. Soc.* **47**, 2(73 (1964).
[9] M. Suzuki, H. Nagta, J. Ohara, H. funakubo, and takenaka, *J.Appl.phys.* **42**, 6090–6093 (2003).
[10] D. W. Baker, A. P. Thomas, N. Zhang, and A. M. Glazer, *Acta. Crystal.* **B65**, 22 (2009).
[11] Alok Singh Kandari, Vijendra Lingwal, and N. S. Panwar, *sol.Stat.commun.* **150**, 74 (2010).
[12] Eiko Matsushita, and Kouichi Sugiyama, *ferroelectric* **428**, 49 (2012).
[13] V. M. Goldschmidt, Trans. *Faraday soc.* **25**, 809 (1954).
[14] Yoshihiriro Ishibashi, *ferroelctrics* **264**, 197 (2001).
[15] Alok Singh Kandari, Vijendra Lingwal, and N. S. Panwar, *Ferroelectrics* **396**, 18 (2010).
[16] B. Jaffe, R. S.. Routh, and S. Marzullo, *J. Appl.phys.* **25**, 809 (1954).
[17] Yiping Guo, Ken-ichi Kamkimoto, and Hitoshi ohsato, *j. Appl. Phys.* **85**, 4121 (2004).
[18] V. J. Tennary, and K. W. Hang, *J. Appl. Phys.* **39**, 4749 (1968).
[19] G. Shirane, R. Newnham, and R. Pipinsky, *Phys. Rev.* **96**, 581 (1954).
[20] S. Narayana Murthy, K. V. Rama Murthy, K. Umakantham, and A. Bhanumathi, *Ferroelectric* **102**, 243 (1990).
[21] L. Egerton, and D. M. Dillon, *J. Amer. Cer. Soc.* **42**, 438 (1959).
[22] V. Lingwal, and N. S. Panwar, *Ferroelectrics* **300**, 3 (2004).
[23] M. Ahtee, and A. W. Hewat, *Acta Crystallogr. Sec A: Cryst. Phys., Diffr. Theor. Crytallogr.* **31**, 846 (1975).
[24] L. V. Azaroff, *Elements of X-ray Crystallography*, (McGraw Hill Book Company, New York 1968)..
[25] V. J. Tennery, and K. W. Hang, *J. Appl. Phys.* **39**, 4749 (1968).
[26] C. N. W. Darlington, and H. D. Megaw, *Acta Cryst.* **B29**, 2171 (1973).
[27] G. H. Heartling, *J. Am. Cerm. Soc.* **50**, 330 (1967).
[28] S. Narayana Murthy, K. V. Rama Murthy, K. Umakantham, and A. Bhanumathi, *Ferroelectric* **102**, 243 (1990).

Journal of Physics and Chemistry of Solids 123 (2018) 311–317

Contents lists available at ScienceDirect

Journal of Physics and Chemistry of Solids

journal homepage: www.elsevier.com/locate/jpcs

Dielectric properties of $Na_{1-x}K_xNbO_3$, near x = 0.5 morphotropic phase region

Surendra Singh[a,*], Jyotsana Negi[a], N.S. Panwar[b]

[a] Department of Physics, India
[b] University Science Instrumentation Centre, H.N.B. Garhwal University, Srinagar, Garhwal, 246174, India

ARTICLE INFO

Keywords:
Ferroelectric
Perovskite
Dielectric properties
Morphotropic phase transition

ABSTRACT

Sodium-potassium niobate ($Na_{1-x}K_xNbO_3$) ceramic pellets, with x = 0.490, 0.495, 0.500, 0.505 and 0.510, were prepared by solid state reaction method with double sintering. With varying potassium content (x), dielectric properties and X-ray diffraction (XRD) peaks shifting pattern exhibit strong compositional dependence. Among the prepared compositions, a break in the XRD peaks shifting tendency, and minimum dielectric constant, loss tangent and Electric conductivity indicate a morphotropic phase transition type behavior, at the composition with x = 0.500.

1. Introduction

Perovskite ABO_3 type alkali metal niobates and their solid solutions show technologically potential dielectric, ferroelectric, piezoelectric and optical properties [1]. Among these perovskites sodium-potassium niobate (Na, K) NbO_3 (NKN) based lead free ferroelectrics have great potential to replace lead based compositions used in many piezo- and ferro-electric devices [2–4]. Having end members, $NaNbO_3$, an antiferroelectric, and $KNbO_3$, a ferroelectric, at room temperature; $Na_{1-x}K_xNbO_3$ solid solutions can be formed for all values of x (from 0 to 1) [5,6]. By adding even a small amount (~2 mol %) of $KNbO_3$, antiferroelectric $NaNbO_3$ becomes ferroelectric [6–8]. Solid solutions of ferroelectric materials display a composition dependent transition region, in their composition phase diagrams, known as a morphotropic phase boundary (MPB) [6,7], where the physical properties are extremal because of the abrupt change in lattice structure [6]. The high electromechanical response in this region is related to the morphotropic phase transition (MPT) [7] because of symmetry-allowed polarization rotation [9–11]. In this system, a composition dependent anomalous behavior of electrical properties has been reportedly observed near the equi-composition mixed $KNbO_3$- $NaNbO_3$ [12]. On the basis of dielectric measurements and X-ray diffraction patterns, Kandari et al. [13–15] have reportedly observed the MPT region(s), in $Na_{1-x}K_xNbO_3$, at the compositions with x = 0.17, 0.32, and 0.475. Raevskii et al. [16] have explained MPT in $Na_{1-x}K_xNbO_3$, on the basis of concentration dependence of electrical conductivity, which exhibits minima at these concentrations. A break in tendency of the peaks shifting in the XRD patterns has also been reportedly observed near MPT [16,17]. On the basis of lattice parameters, Tennery et al. [17] confirmed the three MPT regions, at x = 0.17, 0.325 and 0.475. Ye-Jing Dai et al. [18] investigated the influence of the Na/K ratio on electrical properties and phase structures of $Na_{1-x}K_xNbO_3$ compositions with x = 0.46 to 0.52, prepared by conventional solid-state reaction route, and suggested that a typical MPB exists, at x = 0.52–0.525. In the reported works, the K composition interval between neighboring samples have been either too large [12,17,19,20] or too small [2,18,21,22] to understand the detailed influence of the Na/K ratio on the phase structure and electrical behavior.

The control of material properties often becomes possible by varying the composition of the solid solution and by varying preparation conditions. The morphotropic phase boundary (MPB), which separates two ferroelectric phases with different crystallographic parameters, can lead to a great enhancement of piezoelectric activity [23,24]. In the composition-property diagram of solid solution systems, near the MPB, the ferro-composition has a two- or more-phases and has extremal electro-physical properties [25–29]. On change of composition, MPT exhibits anomalous dielectric and piezoelectric properties [30], and sharp structural change [2,26,29–34], in a solid solution.

Present study is focused on the composition dependence of dielectric properties of NKN system, near equimolar (Na, K) morphotropic niobate compositions. $Na_{1-x}K_xNbO_3$ ($0.490 \le x \le 0.510$) ceramic samples were prepared by solid state reaction route using double sintering. To investigate the MPT region closely, near x = 0.500, measurement of X-ray diffraction peaks shifting, dielectric constant, loss

* Corresponding author.
E-mail address: jhinkwan.surendra@gmail.com (S. Singh).

https://doi.org/10.1016/j.jpcs.2018.08.018
Received 24 April 2018; Received in revised form 15 June 2018; Accepted 14 August 2018
Available online 18 August 2018
0022-3697/ © 2018 Elsevier Ltd. All rights reserved.

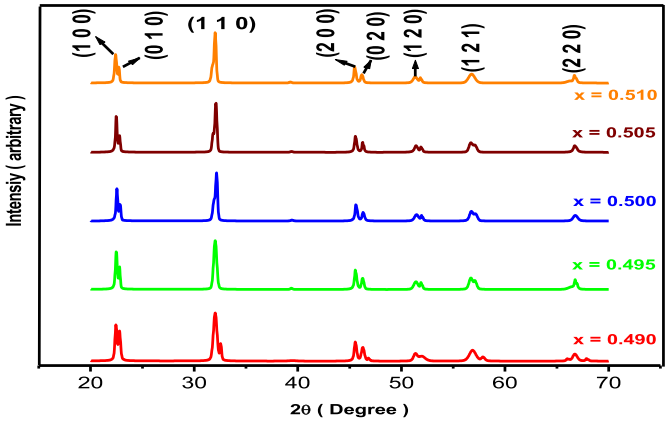

Fig. 1. XRD patterns of $Na_{1-x}K_xNbO_3$ (0.490 ≤ x ≤ 0.510).

tangent and electric conductivity were carried out in the prepared samples.

2. Methods

Ceramic pellets of $Na_{1-x}K_x$ NbO_3 (0.490 ≤ x ≤ 0.510) were prepared by conventional solid-state reaction method. The raw materials K_2CO_3, Na_2CO_3, and Nb_2O_5, with purity better than 99.9%, were dried in ambient atmosphere, at 200 °C, for 2 h to remove the absorbed moisture, and weighed precisely according to stoichiometric ratio. The stoichiometric composition was ground using agate mullet mortar and pestle. The compositions were ground, for the first half an hour wet in acetone, and then dry for 1 h. This wet and dry grinding cycle was repeated such that total wet grinding was done for 2 h and dry for 4 h. The ground power was calcined at 950 °C, for 4 h, in ambient atmosphere to remove carbon dioxide. The calcined composition was fine ground, for 2 h, and then the ground powder was pressed into 8 mm diameter and ~ 2–3 mm thick pellets, at 0.4 GPa. The melting point of $NaNbO_3$ is 1422 °C, and that of $KNbO_3$ is 1040 °C, so the sintering temperatures of the $Na_{1-x}K_xNbO_3$ compositions were chosen according to their melting points [33], and pellets of each composition were sintered for 4 h, at temperatures between 1108 and 1116 °C, with decreasing x (K content).

Some of the sintered pellets were crushed further, fine ground and pressed into pellets at 0.4 GPa, and the pellets were further sintered at the chosen temperatures according to their melting temperatures, each for 4 h. All the sintered pellets were taken out from the furnace when it cooled to room temperature. XRD measurements of all the prepared samples were taken, at room temperature, by an X-ray diffractometer

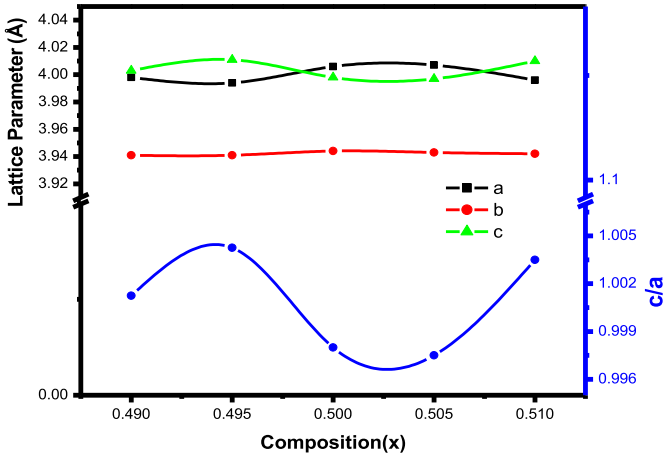

Fig. 3. Variation of lattice parameters, and c/a ratio with composition in Na1-xKxNbO3 (0.490 ≤ x ≤ 0.510).

(PANalytical, X'PERT PRO), using Cu $K_{\alpha 1}$ radiation of wavelength 1.5405980 Å radiation, in a wide range of 2θ (20° < 2θ < 70°) at a scanning rate of 6°/min. Surface morphology and grain size of the prepared samples were studied using a scanning electron microscope (CARL ZEISS, MA15/EVO18). Sintered pellets were electroded, with air dryable conducting paste of silver, in metal-insulator- metal (MIM) configuration, for dielectric measurements. Dielectric constant (ε), loss tangent (tan δ) and Electric conductivity (σ) of the prepared samples were measured, in MIM configuration, by RLC meter (Fluke, PM 6306), in the frequency range from 1 KHz to 1 MHz, at different temperatures.

3. Results and discussion

3.1. XRD results

The observed XRD patterns of different prepared compositions of $Na_{1-x}K_xNbO_3$ are shown in Fig. 1. The XRD patterns show polycrystalline behavior of the prepared samples, and have been found in good agreement with the Inorganic Crystal Structure Database - (ICSD) (00-061-0315) data of $Na_{0.5}K_{0.5}NbO_3$ with peaks corresponding to (100), (110), (211), etc. In the observed composition range (0.490 ≤ x ≤ 0.510), a continuous shifting of the most intense peaks, (100), (010), (110), (200), and (020) was observed, with varying potassium concentration (x value), Fig. 2. For compositions with x ≤ 0.500, these peaks were observed shifting to higher angles with

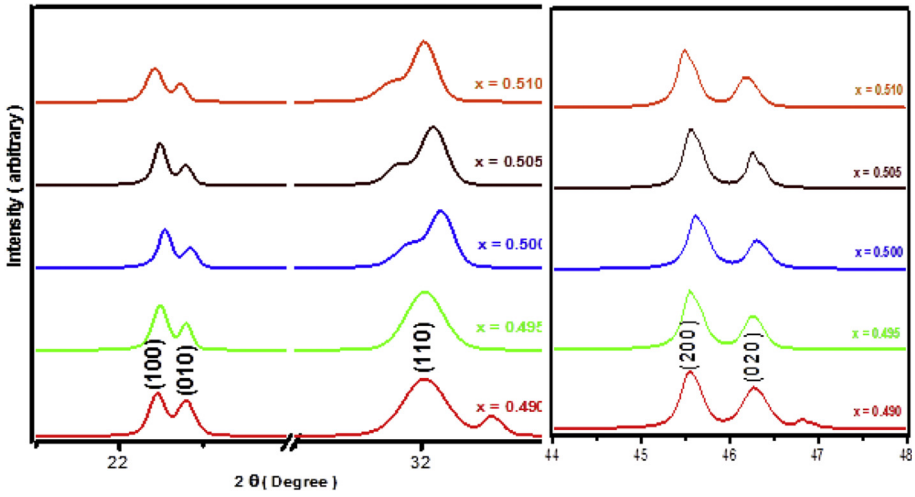

Fig. 2. XRD patterns of $Na_{1-x}K_xNbO_3$ (0.490 ≤ x ≤ 0.510), showing the peaks shifting tendency with x.

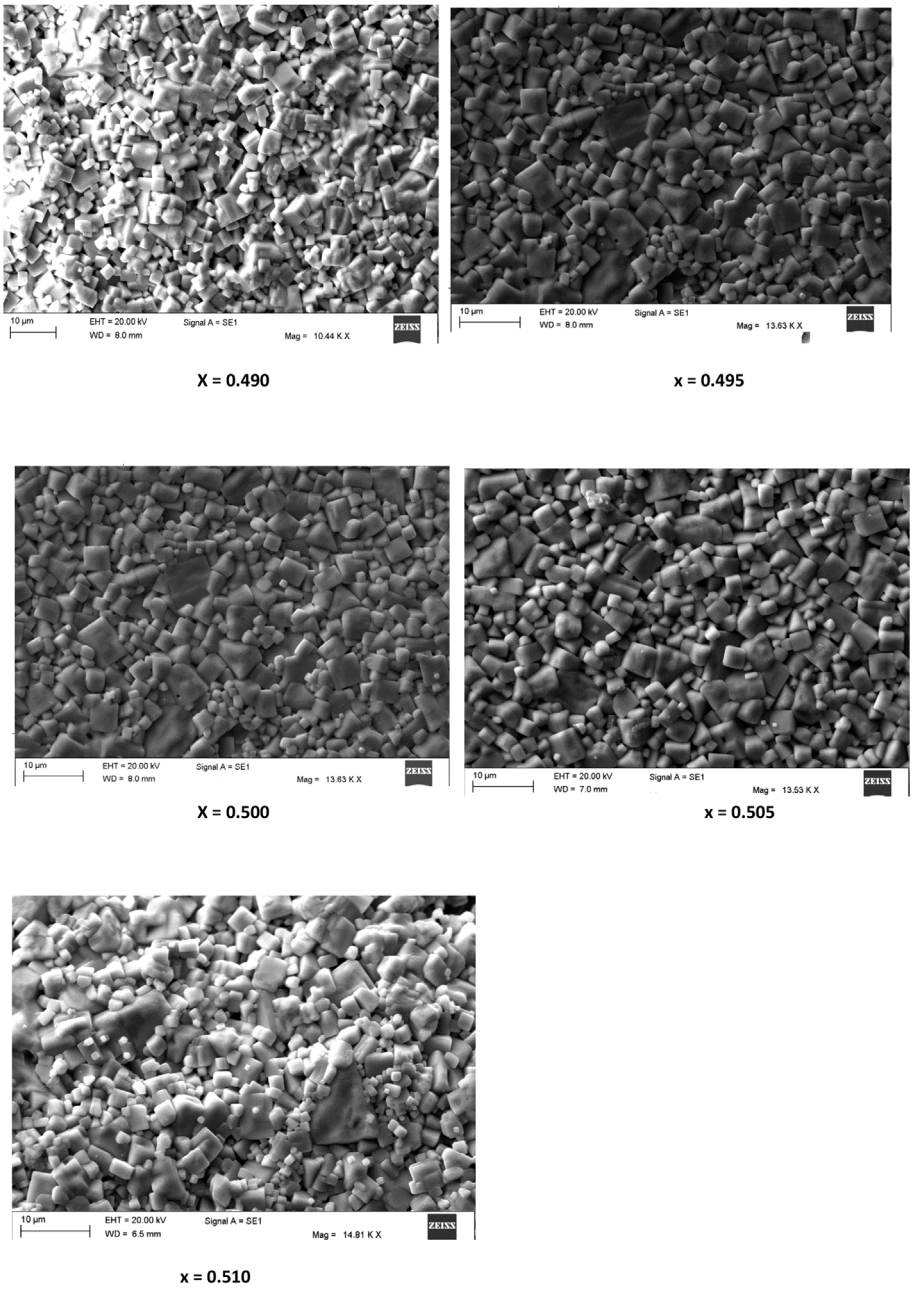

Fig. 4. SEM Photograph of prepared $Na_{1-x}K_xNbO_3$ ($0.490 \leq x \leq 0.510$) samples.

increasing x, and for the compositions with $x > 0.500$, these peaks were observed shifting to lower angles with increasing x, showing a break in the peak shifting pattern at the composition with $x = 0.500$. A break in the peak shifting tendency has been reportedly observed, in $Na_{1-x}K_xNbO_3$, near $x = 0.175$, 0.32, and 0.475 compositions [13–15].

The lattice parameters were refined by High Score Plus software, using the Rietveld method and the background was modeled using the Legendre polynom and the peaks' profiles were refined using a pseudo-Voigt function [35,36]. The chosen space group for these refinements was monoclinic Pm6 [37]. Observed variation of the cell parameters with composition (x) has been shown in Fig. 3. For the prepared compositions, generally, $a < c$, and slop of the plot of c/a ratio with x was found positive; except for the compositions $0.500 \leq x \leq 0.505$, where $a > c$ and slop of the plot of c/a ratio with composition was found negative, Fig. 3, which indicates structural anomaly in this compositional region.

3.2. SEM results

Fig. 4 shows the observed scanning electron micrographs (SEM) of the prepared samples. The SEM photographs show that the prepared samples own an average grain size of about 2.8 µm but a few have larger grains that exceed 8 µm. Variation of the average grain size with composition is shown in Fig. 5. Average grain size was found maximum (3.15 µm) for the composition with $x = 0.490$, and minimum (2.67 µm) for $x = 0.510$, among the prepared samples. Composition (x) variation

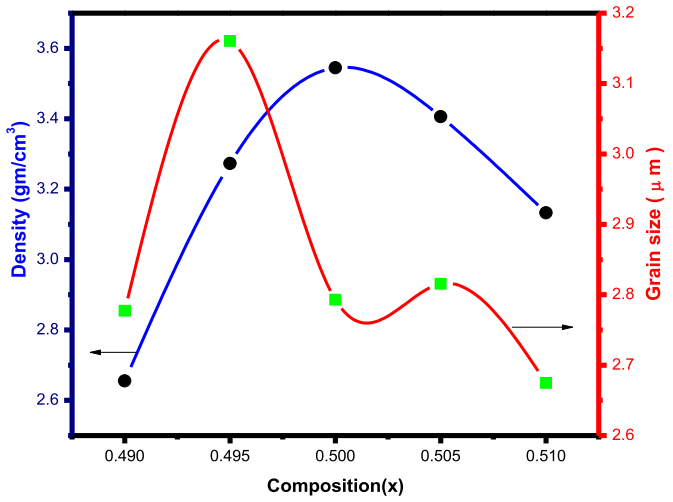

Fig. 5. Variation of grain size, and density with composition (x), in $Na_{1-x}K_xNbO_3$ ($0.490 \le x \le 0.510$).

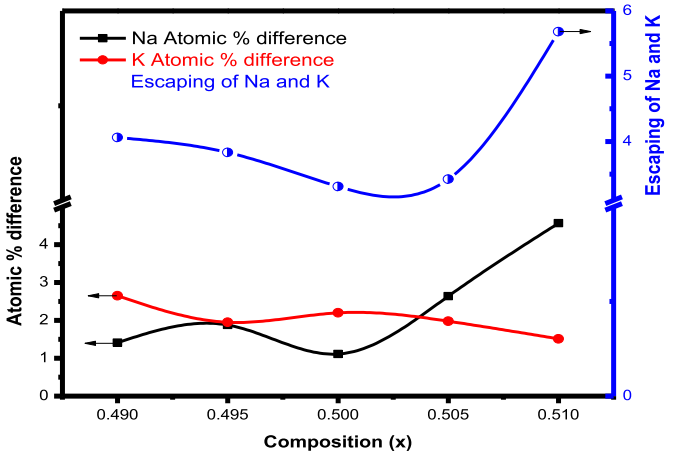

Fig. 6. Variation of escaping of Na and K (atomic %) with composition, in $Na_{1-x}K_xNbO_3$ ($0.490 \le x \le 0.510$).

Table 1
EDAX results of $Na_{1-x}K_xNbO_3$ system.

Atomic %									
x value	Observed				Calculated				Escaping of Na and K
	Na	K	Nb	O	Na	K	Nb	O	
0.490	8.79	7.15	19.51	64.55	10.2	9.8	20	60	4.06
0.495	8.22	7.95	19.52	64.31	10.1	9.9	20	60	3.83
0.500	8.89	7.80	19.25	64.06	10.0	10.0	20	60	3.31
0.505	7.46	8.12	19.17	62.25	9.9	10.1	20	60	3.42
0.510	5.63	8.69	21.61	64.08	9.8	10.2	20	60	5.68

of density of the prepared samples is shown in Fig. 5. Density of prepared samples increases from 2.65 g/cc, for x = 0.490–3.65 g/cc, for x = 0.500 (58–78% of theoretical value), and thereafter it decreases to 3.15 g/cc, for x = 0.510. The density and porosity greatly affect the dielectric properties of the samples [38,39]. Samples with x = 0.500 were found most dense, among the prepared compositions, Fig. 5. The process of grain growth and densification during sintering requires material transport, which may occur via surface diffusion, grain boundary diffusion, lattice diffusion, viscous flow and evaporation [40]. The two stage sintering was used to activate different sintering mechanisms in different temperature ranges, and to inhibit grain growth and enhance densification mechanism. But no improvement in density and microstructure was observed using this method. Chen et al. [41] reported similar observations for two-stage sintered NKN ceramics. Surface diffusion is the dominating sintering mechanism, in the NKN ceramics [40]. The low activation energy of surface diffusion results rapid grain growth during initial sintering stage, which contributes to the grain coarsening. This early grain growth reduces the driving force of sintering before the sample reaches main sintering stage, which results poor densification [42,43]. The low activation energy of surface diffusion may be related to the low lattice energy of NKN ceramics [40]. Moreover, the path of material diffusion is also determined by the defects present in ceramics. The free surfaces, fraction of grain boundaries and lattice atoms change during sintering and modify contribution of different mechanisms. Also the diffusing species are ions of different charges with different diffusion rates. Each species of ion may have different diffusion paths, diffusion rates and different vapor pressures, and their resultant effect may be attributed to the observed grain size and density of the prepared samples. However, the structural anomaly, at x = 0.500, seems facilitating the occurrence of highest density among the prepared compositions.

Table 1 shows the observed energy dispersive X-ray analysis (EDAX) results of the prepared samples. A significant escaping of alkali (Na and K) ions was observed in the sintered pellets, having lowest for the composition with x = 0.500. Among the prepared compositions, for the samples with $x \le 0.500$ escaping of potassium was observed higher than the sodium ions, which may be due the higher equilibrium vapor pressure of potassium over NKN than that of sodium [44], however, Na escaping was observed higher than that of K, in the compositions with $x > 0.500$. The minute variations in the stoichiometry very sensitively affect the density, grain size and morphology of the sintered NKN ceramic samples [45].

3.3. Dielectric properties

The observed composition ($0.490 \le x \le 0.510$) dependence of dielectric constant (ε), loss tangent (tan δ) and electric conductivity (σ) of $Na_{1-x}K_xNbO_3$ ceramics, at room temperature (RT) and different frequencies has been given in Figs. 7–9. For all the prepared compositions, generally, ε and tan δ were observed decreasing and σ increasing, with increasing frequency. These observations are in good agreement with the earlier reported results [19,46–48]. At 1 MHz, the observed composition ($0.490 \le x \le 0.510$) dependence of ε, tan δ and σ, at different temperatures, has been shown in Figs. 10 and 11. With increasing temperature, in the measured range, ε, tan δ and σ of all the prepared samples were found increasing. For all the measured temperatures, a drastic minimum in ε, tan δ and σ indicates an MPT, for the ceramics with x = 0.500. The observed composition dependence of ε, tan δ and σ, for different frequencies at RT, has been shown in Figs. 12 and 13. Again, at all the applied frequencies, a remarkable minimum in ε, tan δ and σ, at the composition with x = 0.500, indicates a strong feature-the morphotropic transition driven by the composition rather than frequency or temperature. Raevskii et al. [16] observed composition dependence of electrical conductivity and explained the MPT, for the compositions exhibiting minima, in $Na_{1-x}K_xNbO_3$. The composition dependent structural anomaly and the escape of alkali ions may be held responsible for the observed dielectric behavior of $Na_{1-x}K_xNbO_3$ ($0.490 \le x \le 0.510$) system. Because of the increased presence of non-ferroelectric low permittivity grain boundaries dielectric constant, generally, decreases with decreasing grain size [49]. The loss decreases due to the reduction in the number of grain boundaries with increasing

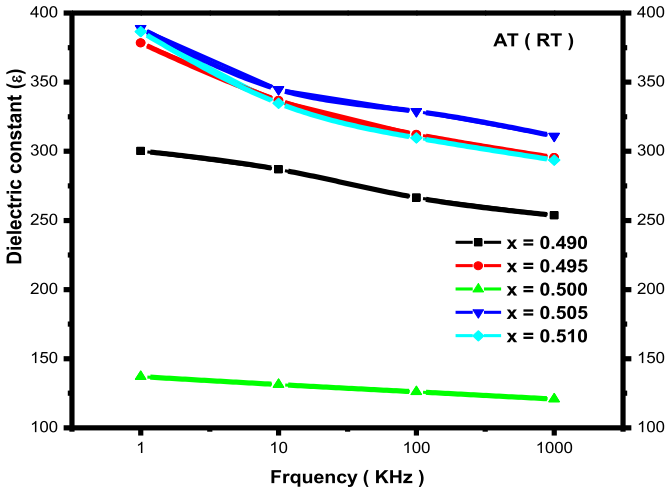

Fig. 7. Variation of dielectric constant (ε) with frequency, in $Na_{1-x}K_xNbO_3$ ($0.490 \leq x \leq 0.510$).

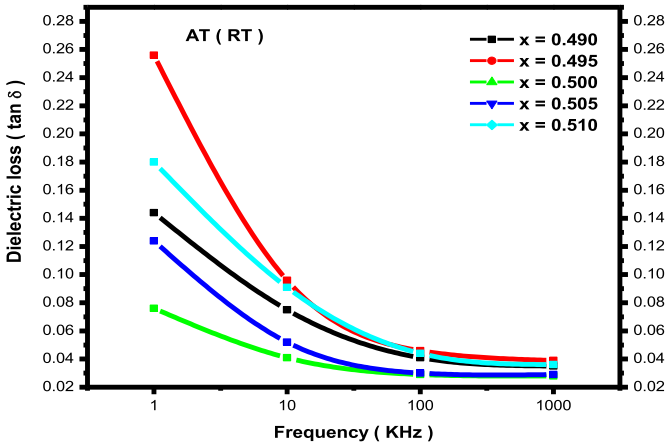

Fig. 8. Variation of dielectric loss (tan δ) with frequency, in $Na_{1-x}K_xNbO_3$ ($0.490 \leq x \leq 0.510$).

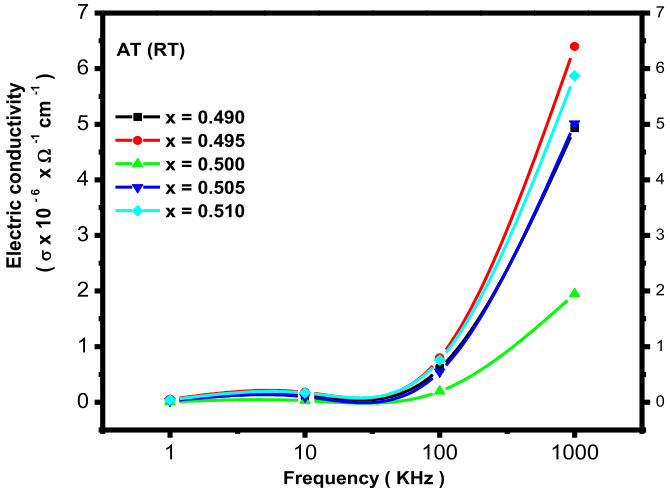

Fig. 9. Variation of Electric conductivity (σ) with frequency, in $Na_{1-x}K_xNbO_3$ ($0.490 \leq x \leq 0.510$).

grain size. Moreover, the interplay of porosity, grain size, liquid phase presence, ordering, etc. may be held responsible for the observed dielectric behavior in these perovskite ceramics.

The ABO_3 perovskites may have two major defects, *viz.*, A-site, and O− site vacancies [27], and there is no concrete evidence of vacancies reported at B− site. Electrical properties are significantly affected by the presence of these vacancies [13–15,27,33,50]. With isovalent substitution of K at Na site, antiferroelectric $NaNbO_3$ becomes ferroelectric, at room temperature, resulting increased effective polarization and thereby increase in conductivity, in general, however, near MR it is observed markedly low. In these oxides the conduction process may be explained on the basis of the majority of acceptor or donor concentration. Due to the deficiency of electron the A-site vacancy contributes 'hole', and due to the excess of electrons the O− site vacancy contributes extra electrons for conduction in the solid. In that way if there are only A-site vacancies, the solid should show p-type behavior, or if there are only O− site vacancies it should behave as n-type. Majority of A- or O− site vacancies decides the majority of charge carriers, and thereby the p- or n-type nature of the conduction. The EDAX results of the presently prepared $Na_{1-x}K_xNbO_3$ compositions show significant escaping of alkali ions, with a minimum for the composition with x = 0.500, Table 1, Fig. 6. The alkali ions escaping was observed significantly higher than oxygen escaping. Due to the excess of the vacancies at A-site than that at O− site, p-type conduction is envisaged in the present $Na_{1-x}K_xNbO_3$ compositions. The A-site vacancy attracts electron and acts as acceptor, and due to the electron deficiency the A-site vacancy behaves as 'hole' in the lattice. Due to the less escaping of the alkali ions less number of 'holes' will be available for conduction, resulting lower conductivity in the compositions with x = 0.500, than other compositions. The p-type conductivity is reportedly observed in many oxides, viz., Pb(Ti, Zr)O_3, ZrO_2, etc. [51], where 'superoxidation', i.e., excess of A-site vacancies over the O− site vacancies, is more probable. In the p-type ceramics, with increased A-site vacancy concentration, for the compositions near MR, a distinct conductivity maximum has been reportedly observed [15]. Presently, with a decrease in A-site vacancy concentration for the composition, near MR with x = 0.500, a distinct conductivity minimum was observed, which agrees with the above given supposition. For the composition near MR, it seems that during sintering of the samples the intensification of diffusion processes remarkably reduces the possibility of escape of highly volatile alkali metal ions from the lattice.

Dielectric constant of the ceramics generally increases with increasing density [52,53]. In the present study density was found maximum and dielectric constant minimum, for the composition with x = 0.500, among the prepared samples; which indicates that the occurrence of morphotropic phase is more dominating than the increased density contribution. Also the grain size effect was found meager. The properties of ceramics depend on the preparation process, and are subject to systematic and statistical fluctuations in the samples of a given batch. These fluctuations may be due to inhomogeneity in microchemistry, mechanical differences in the forming process, chemical modification and varying shrinkage at the time of sintering.

The reported and present observations show that preparation process, composition and structure greatly influence the electrical behavior of the ceramics. With p-type conduction a decrease in A-site vacancy concentration, and structural anomaly may be attributed to the observed lowest values of the dielectric constant, loss tangent, and electric conductivity of the composition with x = 0.500, among the prepared compositions.

4. Conclusion

In the prepared $Na_{1-x}K_xNbO_3$ ($0.490 \leq x \leq 0.510$) compositions, the p-type conductivity was found due to the excess of A-site vacancy concentration over the O− type vacancies. The EDAX results show decreased A-site vacancies, near x = 0.500, resulting remarkable conductivity minimum. A decrease in A-site vacancies in the p-type material and the structural anomaly dominatingly affect the dielectric properties of the prepared compositions rather than the density and grain size effect, near the MR, at x = 0.500.

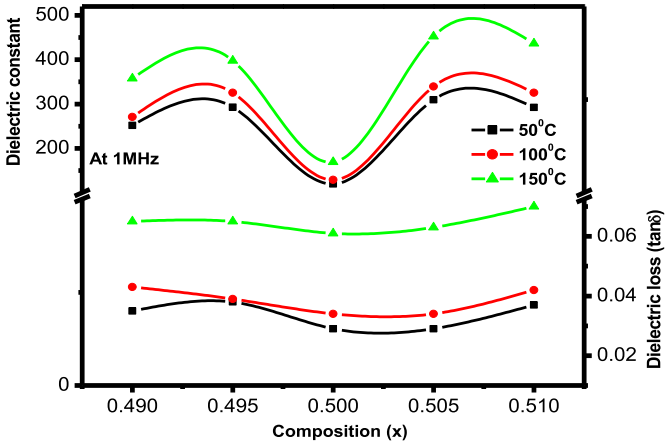

Fig. 10. Variation of dielectric constant (ε) and dielectric loss (tan δ) with composition (x), in $Na_{1-x}K_xNbO_3$ (0.490 ≤ x ≤ 0.510), at different temperatures.

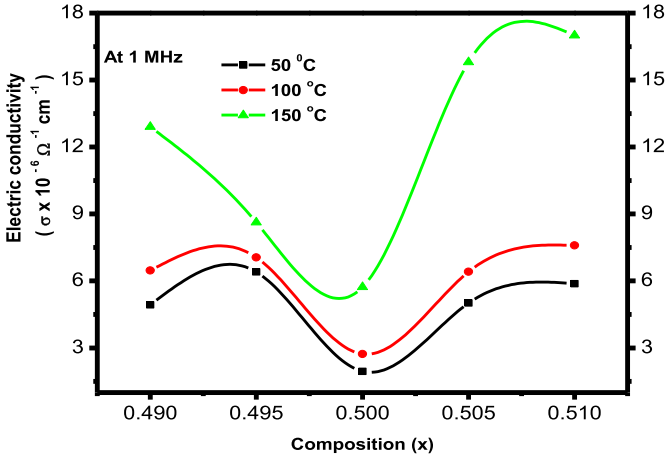

Fig. 11. Variation of Electric conductivity (σ) with composition (x), in $Na_{1-x}K_xNbO_3$ (0.490 ≤ x ≤ 0.510), at different temperatures.

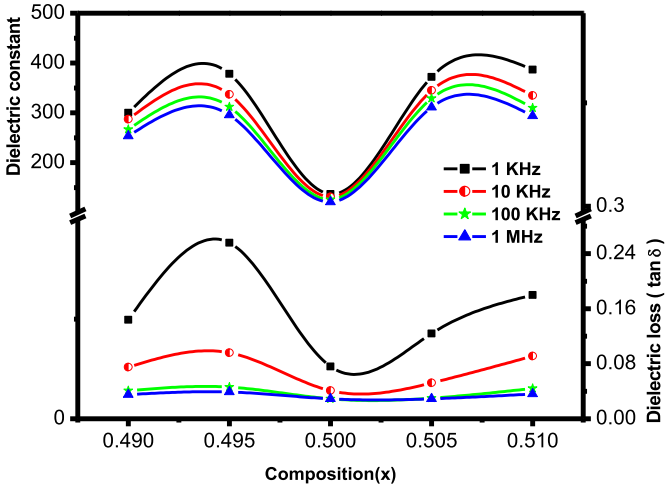

Fig. 12. Variation of dielectric constant (ε) and dielectric loss (tan δ) with composition (x), in $Na_{1-x}K_xNbO_3$ (0.490 ≤ x ≤ 0.510), at room temperature.

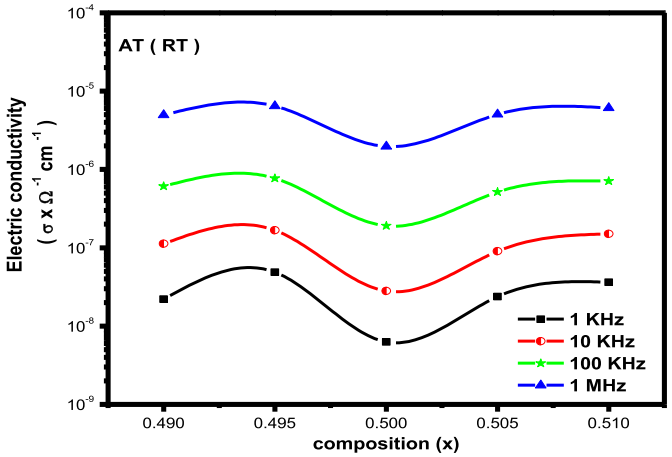

Fig. 13. Variation of electric conductivity (σ) with composition (x), in $Na_{1-x}K_xNbO_3$ (0.490 ≤ x ≤ 0.510), at room temperature.

References

[1] G.A. Samara, Effects of pressure on the dielectric properties and phase transitions of the alkali metal tantalates and niobates, Ferroelectrics 73 (1987) 145–159.
[2] Y. Saito, H. Takao, T. Tani, T. Nonoyama, K. Takatori, T. Homma, T. Nagaya, M. Nakamura, Lead-free piezoceramics, Nature 432 (2004) 84–87.
[3] M. Dawber, K.M. Rabe, J.F. Scott, Physics of thin-film ferroelectric oxides, Rev. Mod. Phys. 77 (2005) 1083–1130.
[4] L. Wang, K. Yao, W. Ren, Piezoelectric $K_{0.5}Na_{0.5}NbO_3$ thick films derived from Polyvinylpyrrolidone-modified chemical solution deposition, Appl. Phys. Lett. 93 (1–3) (2008) 092903.
[5] M. Ahtee, A.W. Hewat, Structural phase transitions in sodium-potassium niobate solid solutions by neutron powder diffraction, Acta Crystallogr. A34 (1978) 309–317.
[6] M. Ahtee, A.M. Glazer, Lattice parameters and tilted octahedra in sodium-potassium niobate solid solutions, Acta Crystallogr. A32 (1976) 434–446.
[7] R. Guo, L.E. Cross, S.E. Park, B. Noheda, D.E. Cox, G. Shirane, Origin of the high piezoelectric response in $PbZr_{1-x}Ti_xO_3$, Phys. Rev. Lett. 84 (2000) 5423–5426.
[8] G. Shirane, R. Newnham, R. Pepinsky, Dielectric properties and phase transitions of Na, 1954 $NaNbO_3$ and (Na,K)$Nb0_3$, Phys. Rev. 96 (1954) 581–588.
[9] H. Fu, R.E. Cohen, Polarization rotation mechanism for ultrahigh electromechanical response in single-crystal piezoelectrics, Nature 403 (2000) 281–283.
[10] R.E. Cohen, MATERIALS SCIENCE Relaxors go critical, Nature 441 (2006) 941–942.
[11] M. Ahart, M. Somayazulu, R.E. Cohen, P. Ganesh, P. Dera, H.K. Mao, R.J. Hemley, Y. Ren, P. Liermann, Z. Wu, Origin of morphotropic phase boundaries in ferroelectrics, Nature 451 (2008) 545–548.
[12] L. Wu, J.L. Zhang, C.L. Wang, J.C. Li, Influence of compositional ratio K/Na on physical properties in $(K_x Na_{1-x})NbO_3$ ceramics, J. Appl. Phys. 103 (1–5) (2008) 084116.
[13] A.S. Kandari, V. Lingwal, N.S. Panwar, Morphotropic phase boundary in $Na_{1-x}K_xNbO_3$, Near, x = 0.32, Solid State Commun. 150 (2010) 74–77.
[14] A.S. Kandari, K. Kandari, V. Lingwal, A.A. Bourai, N.S. Panwar, Composition dependent dielectric anomaly in $Na_{1-x}K_xNbO_3$, at x = 0.475, Ferroelectrics 393 (2009) 121–129.
[15] A.S. Kandari, V. Lingwal, N.S. Panwar, Morphotropic region in $Na_{1-x}K_xNbO_3$, between x = 0.17 and 0.18, Ferroelectrics 396 (2010) 18–26.
[16] I.P. Raevskii, L.A. Reznichenko, O.I. Prokopalo, Phase-transition and electrical-properties of, 1979 of ferroelectric sodium niobate-based solid-solutions, Izv. Akad. Nauk. SSSR, Met. 15 (1979) 872–875.
[17] V.J. Tennery, K.W. Hang, Thermal and x-ray diffraction studies of the $NaNbO_3$-$KNbO_3$ system, J. Appl. Phys. 39 (1968) 4749–4753.
[18] Y.J. Dai, X.W. Zhang, K.P. Chen, Morphotropic phase boundary and electrical properties of K_{1-x} Na_xNbO_3 lead-free ceramics, Appl. Phys. letter. 94 (1–3) (2009) 042905.
[19] R.E. Jaeger, L. Egerton, Hot pressing of potassium-sodium niobates, J. Am. Ceram. Soc. 45 (1962) 209–213.
[20] B.P. Zhang, J.F. Li, K. Wang, H. Zhang, Compositional dependence of piezoelectric properties in $Na_xK_{1-x}NbO_3$ lead-free ceramics prepared by spark plasma sintering, J. Am. Ceram. Soc. 89 (2006) 1605–1609.
[21] D.W. Baker, P.A. Thomas, N. Zhang, A.M. Glazer, Structural study of $K_xNa_{1-x}NbO_3$ (KNN) for compositions in the range x = 0.24–0.36, Acta Crystallogr. B65 (2009) 22–28.
[22] N. Zhang, A.M. Glazer, D. Baker, P.A. Thomas, Structures of $K_{0.05}Na_{0.95}NbO_3$ (50–300 K) and $K_{0.30}Na_{0.70}NbO_3$ (100–200 K), Acta Crystallogr. B65 (2009) 291–299.
[23] B. Jaffe, R.S. Roth, S. Marzullo, Piezoelectric properties of lead zirconate-lead titanate solid-solution ceramics, J. Appl. Phys. 25 (1954) 809–810.
[24] D. Damjanovic, Ferroelectric, dielectric and piezoelectric properties of ferroelectric thin films and ceramics, Rep. Prog. Phys. 61 (1998) 1267–1324.

[25] A.M. Glazer, P.A. Thomas, K.Z. Baba-Kishi, G.K.H. Pang, C.W. Tai, Influence of short- range and long-range order on the evolution of the morphotropic phase boundary in $Pb(Zr_{1-x}Ti_x)O_3$, Phys. Rev. B70 (1–9) (2004) 184123.
[26] K. Kakimoto, K. Akao, Y. Guo, H. Ohsato, Raman scattering study of piezoelectric $(Na_{0.5}K_{0.5})NbO_3$-$LiNbO_3$ ceramics, Jpn. J. Appl. Phys., Part 1 44 (2005) 7064–7067.
[27] B. Jaffe, W.R. Cook, J.H. Jaffe, Piezoelectric Ceramics, Academic, New York, 1971.
[28] Y. Ishibashi, M. Iwata, A theory of morphotropic phase boundary in solid-solution systems of perovskite-type oxide ferroelectrics, Jpn. J. Appl. Phys., Part 1 38 (1999) 800–804.
[29] N. Klein, E. Hollenstein, D. Damjanovic, H.J. Trodahl, N. Setter, M. Kuball, A study of the phase diagram of (K, Na, Li)NbO_3 determined by dielectric and piezoelectric measurements, and Raman spectroscopy, J. Appl. Phys. 102 (1–8) (2007) 014112.
[30] S.E. Park, T.R. Shrout, Ultrahigh strain and piezoelectric behavior in relaxor based ferroelectric single crystals, J. Appl. Phys. 82 (1997) 1804–1811.
[31] B. Noheda, Tructure and high-piezoelectricity in lead oxide solid solutions, Curr. Opin. Solid State Mater. Sci. 6 (2002) 27–34.
[32] Y. Guo, K.I. Kakimoto, H. Ohsato, Phase transitional behavior and piezoelectric properties of $(Na_{0.5}K_{0.5})NbO_3$ –$LiNbO_3$ ceramics, Appl. Phys. Lett. 85 (2004) 4121–4123.
[33] V. Lingwal, N.S. Panwar, Morphotropic phase transitions in mixed sodium-potassium niobate system, Ferroelectrics 300 (2004) 3–14.
[34] S.Y. Chu, W. Water, Y.D. Juang, J.T. Liaw, Properties of (Na, K)NbO_3 and (Li, Na, K) NbO_3 ceramic mixed systems, Ferroelectrics 287 (2003) 23–33.
[35] J. Tellier, B. Malic, B. Dkhil, D. Jenko, J. Cilensek, M. Kosec, Crystal structure and phase transitions of sodium potassium niobate perovskites, Solid State Sci. 11 (2009) 320–324.
[36] L.V. Azaroff, Elements of X-ray Crystallography, McGraw Hill Book Company, New York, 1968.
[37] J. Attia, L. Bellaiche, P. Gemeiner, B. Dkhil, B. Malic, Study of potassium-sodium-niobate alloys: a combined experimental and theoretical approach, J. Phys. IV France 128 (2005) 55–60.
[38] S. Kawashima, M. Nishida, I. Ueda, H. Ouchi, $Ba(Zn_{1/3}Ta_{2/3})0_3$ ceramics with low dielectric loss at microwave frequencies, J. Am. Ceram. Soc. 66 (1983) 421–423.
[39] Y. Hirata, A. Nitta, S. Sameshima, Y. Kamino, Dielectric properties of barium titanate pressing, Mater. Lett. 29 (1996) 229–234.
[40] B. Malic, J. Koruza, J. Hrescak, J. Bernard, K. Wang, J.G. Fisher, A. Bencan, Sintering of lead-free piezoelectric sodium potassium niobate ceramics, Materials 8 (2015) 8117–8146.
[41] I.W. Chen, X.H. Wang, Sintering dense nanocrystalline ceramics without final-stage grain growth, Nature 404 (2000) 168–171.
[42] J. Koruza, B. Malic, Initial stage sintering mechanism of NaNbO3 and implications regarding the densification of alkaline niobates, J. Eur. Ceram. Soc. 34 (2014) 1971–1979.
[43] R.M. German, Z.A. Munir, Surface-area reduction during isothermal sintering, J. Am. Ceram. Soc. 59 (1976) 379–383.
[44] A. Popovic, L. Bencze, J. Koruza, B. Malic, Vapour pressure and mixing thermodynamic properties of the $KNbO_3$ -$NaNbO_3$ system, RSC Adv. 5 (2015) 76249–76256.
[45] J. Acker, H. Kungl, R. Schierholz, S. Wagner, R.A. Eichel, M.J. Hoffmann, Microstructure of sodium-potassium niobate ceramics sintered under high alkaline vapor pressure atmosphere, J. Eur. Ceram. Soc. 34 (2014) 4213–4221.
[46] S. Narayana Murty, K. Umakantham, A. Bhanumathi, Ferroelectric behaviour of Lanthanum doped (NaK)$Nb0_3$ ceramics, Ferroelectrics 82 (1988) 141–147.
[47] L.E. Cross, Electric double hysteresis in $(K_xNa_{1-x})NbO3$ single crystals, Nature 181 (1958) 178–179.
[48] G.H. Haertling, Properties of hot-pressed ferroelectric alkali niobate ceramics, J. Am. Ceram. Soc. 50 (1967) 329–330.
[49] M.H. Frey, Z. Xu, P. Han, D.A. Payne, The role of Interfaces on an apparent grain size effect on the Dielectric Properties for Ferroelectric Barium Titanate ceramics, Ferroelectrics 206 (1998) 337–353.
[50] E.V. Bursyan, Nonlinear Crystal-Barium Titanate, Nauka Press, Moskva, 1974.
[51] J.Z. Rudolph, About the conduction mechanism of oxidic semiconductors at high temperatures, Naturforscher 14a (1959) 727–737.
[52] H. Chen, C. Yang, C. Fu, Li Zhao, Z. Gao, The size effect of $Ba_{0.6}Sr_{0.4}TiO_3$ thin films on the ferroelectric properties, Appl. Surf. Sci. 252 (2006) 4171–4177.
[53] Q. Xu, X.F. Zhang, H.X. Liu, W. Chen, M. Chen, B.H. Kim, Effect of sintering temperature on dielectric properties of $Ba_{0.6}Sr_{0.4}TiO_3$–MgO composite ceramics prepared from fine constituent powders, Mater. Des. 32 (2011) 1200–1204.

Temperature Dependence of Dielectric Properties in Doped Perovskites

Vijendra Lingwal[1], A S Kandari[2] & N S Panwar[3]

[1]Department of Physics, Pt. L.M.S. Govt. PG College Rishikesh, Dehradun, Uttarakhand, India
[2]Deparment of Physics, Govt. PG College New Tehri, Uttarakhand, India
[3]University Science Instrumentation Centre, HNB Garhwal University, Srinagar (Garhwal), India

ABSTRACT

Pellet samples of mixed sodium-potassium tantalate ($Na_{1-x}K_xTaO_3$), for compositions x = 0, 0.2 and 0.5 were prepared by solid-state reaction method. The calcined mixture was pressed at 0.02 MPa and sintered in a closed furnace to form 6 mm diameter pellets. Temperature variation of dielectric constant and loss tangent of the prepared samples has been studied in the frequency range from 10 KHz to 1 MHz. Dielectric anomalies have been observed near the transition temperatures of the samples. Dielectric constant and loss tangent peak heights were observed decreasing with increasing frequency, for all the compositions, which show relaxational behavior of the material.

Keywords – Dielectric constant, loss tangent, perovskites, relaxational behavior, transition temperature.

1. INTRODUCTION

Study of dielectric constant and loss tangent provides insight to the understanding of intra- and inter-molecular interactions, modes of motion and configurational changes in a solid. The perovskite (ABO_3) type alkali metal niobates and tantalates constitute an important group of oxide compounds with broad ranges of technologically important dielectric, piezoelectric, ferroelectric and optoelectronic properties[1]. Solid solutions of sodium potassium niobate ($Na_{1-x}K_xNbO_3$) and sodium potassium tantalate ($Na_{1-x}K_xTaO_3$) can be formed over the whole composition range (x = 0 to 1), which allow a high degree of tailorability of physical properties. For low x values, these systems appear to exhibit true phase transitions and their dielectric properties can be understood in terms of soft optic phonons[2-3].

Interest has centered on $Na_{1-x}K_xTaO_3$ system, especially in relation to quantum effects, suppression of the phase transition and the question of long-range order *vs* glasslike behavior[4]. $Na_{1-x}K_xTaO_3$ system has interesting end members, i.e., $NaTaO_3$ is ferroelectric with ilmenite structure at room temperature and a transition temperature (T_c) ~ 475°C, and $KTaO_3$ is paraelectric, at room temperature[5]. Na in $KTaO_3$ occurs as an off-centre impurity and makes $KTaO_3$ a wide gap incipient ferroelectric. Davis[3] has observed that, for $x \geq 0.70$, this system shows a single-phase transition from the high temperature cubic paraelectric phase to a tetragonal ferroelectric phase (CT). For $0.70 \geq x \geq 0.45$, it shows two ferroelectric transitions, a cubic to tetragonal transition followed by a lower temperature transition to a phase believed to have an orthorhombic symmetry[3]. Samara has found the pressure dependence of CT transition, in $Na_{0.28}K_{0.72}TaO_3$ single crystal, consistent with the soft mode theory[1].

$Na_{1-x}K_xTaO_3$ is a relatively less studied system. Investigators have studied the low temperature dielectric behavior of $Na_{1-x}K_xTaO_3$ single crystals[1, 3] and high temperature phases, conductivity and structure of $NaTaO_3$ and $KTaO_3$[6, 7]. In the present study dielectric measurements on $Na_{1-x}K_xTaO_3$ pellet samples, for different x values, in the temperature range from 50 to 680 °C, have been carried out.

2. PREPARATION

Materials were prepared with conventional solid-state reaction method. The starting materials were sodium carbonate (Na_2CO_3) (99.95 % pure), potassium carbonate (K_2CO_3) (99.95 % pure) and tantalum pentoxide (Ta_2O_5) (99.95 % pure), for preparing $Na_{1-x}K_xTaO_3$ system. The starting materials were initially dried at 150 ^{0}C to remove the absorbed moisture. K_2CO_3 is a hygroscopic material and hence due care was taken in its handling. Different compositions of $Na_{1-x}K_xTaO_3$ (x = 0, 0.2 and 0.5) were prepared by weighing the starting materials in stoichiometric ratio. Each composition was manually dry mixed for 1 hour and with methyl alcohol for another 1 hour using agate mortar and pestle. The mixture was calcined in an alumina crucible in ambient atmosphere at 950 ^{0}C for 2 hours, to remove carbonates present in the mixture. After cooling, in dry air, the calcined mixture was weighed to ensure complete carbonate removal from the mixture. Calcined mixture was pressed at 0.02 MPa to form the pellets of 6 mm diameter. These raw pellets were sintered in a closed furnace. All the pellet samples, except $NaTaO_3$, were placed in an alumina crucible and sintered at 1050 ^{0}C, for 15 hours. Due to their high melting point $NaTaO_3$ pellets were sintered at 1100 ^{0}C, for 15 hours. All the samples were taken out from the furnace when it cooled to room temperature.

3. MEASUREMENTS

Room temperature x-ray diffraction patterns of all the prepared samples were taken by Philips analytical x-ray diffractometer (PW3710), using $CuK_{\alpha 1}$ radiation of wavelength 1.54056Å. Peak indexing was done by using Joint Committee on Powder Diffraction Standards (JCPDS) data cards. Crystallite size of the samples was calculated from the full width at half maximum (FWHM) of the highest intensity peak in the XRD pattern[8] and the perovskite subcell parameters were obtained using the relation provided by Azaroff [9]. Sintered pellets were electroded, with air-drying silver paste, in metal-insulator-metal (MIM) configuration for dielectric measurements.

Dielectric properties of $Na_{1-x}K_xTaO_3$ ceramics vary with x and preparation conditions. Temperature and frequency dependence of dielectric properties of $Na_{1-x}K_xTaO_3$ system, for x = 0, 0.2 and 0.5, were investigated in the present study. For studying the temperature and frequency dependence of dielectric properties, measurement were made run to run on the same sample and sample to sample for all samples prepared with the similar method, in the frequency range from 10 KHz to 1 MHz, and in temperature range from 50 to 680 ^{o}C. The observations were close to each other and the values were averaged. Capacitance and dissipation factor measurements were carried out in MIM configuration, using Fluke- PM6306 RCL meter and HP-4275 Multifrequency LCR meter. Dielectric constant (K) was calculated by the relation,

$K = C/C_o$; where C and C_o are the capacitances of the electrodes with and without dielectric, respectively; C_o is given by,

$C_o = (0.0885\ \pi r^2/d)$ pF; where r (cm) is the radius of the electrodes and d (cm) distance between them.

4. RESULTS AND DISCUSSION

Fig. 1 shows room temperature x-ray diffraction patterns of $Na_{1-x}K_xTaO_3$ samples for x = 0, 0.2 and 0.5. The patterns show an orthorhombic polycrystalline structure with peaks corresponding to (101), (200), (220), etc. planes. The

diffraction peaks were observed shifting towards lower angle with increasing x value. Lattice parameters for $NaTaO_3$ were obtained as a = 5.5228, b = 7.7847 and c = 5.5451 Å; which were found comparable to the reported values[10]. Addition of potassium shows decreasing crystallite size, 0.0338, 0.0219 and 0.0108 μm for x = 0, 0.2 and 0.5, respectively, in $Na_{1-x}K_xTaO_3$ composition. The observed decrease in the crystallite size with increasing x values, in these samples, may be due to their sintering at the same temperature. All potassium incorporated samples, in the present study, were sintered at the same temperature (at 1050 ^oC). However, it is worth noting that the melting point of these materials decreases with increasing potassium content[11] and hence ideally the sintering temperature of these compositions should be varied accordingly.

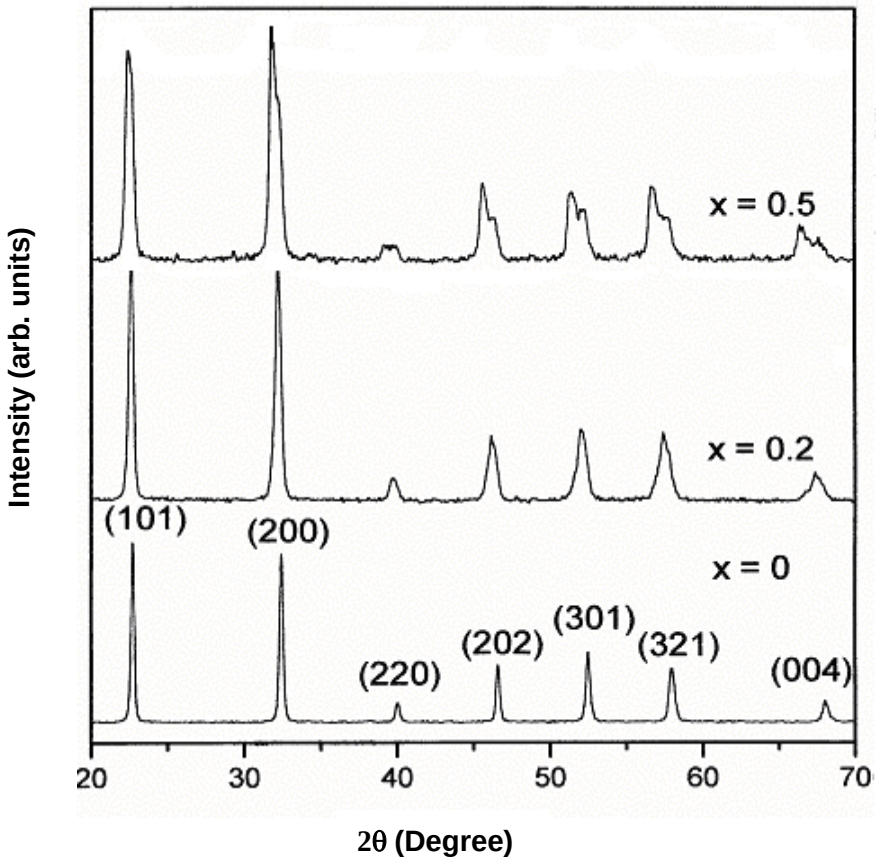

Fig. 1 - X-ray diffraction patterns of $Na_{1-x}K_xTaO_3$ samples for different x values, at room temperature

The observed temperature variation of dielectric constant and loss tangent of $Na_{1-x}K_xTaO_3$ system (for x = 0) has been shown in Figs. 2 and 3. Dielectric constant remains almost constant and shows anomaly at 480 ^oC for all the measured frequencies. The peak value of dielectric constant was observed decreasing with increasing frequency, i.e., 277, 120 and 59; at 10, 100 and 1000 KHz, respectively. Loss tangent initially decreases up to 100 ^oC, remains constant between 100 and 325 ^0C, and thereafter increases sharply near the transition temperature. Loss tangent decreases with increasing frequency. For x = 0.2, an anomaly at 150 ^oC was observed in dielectric constant and loss tangent measurements, Figs. 4 and 5.

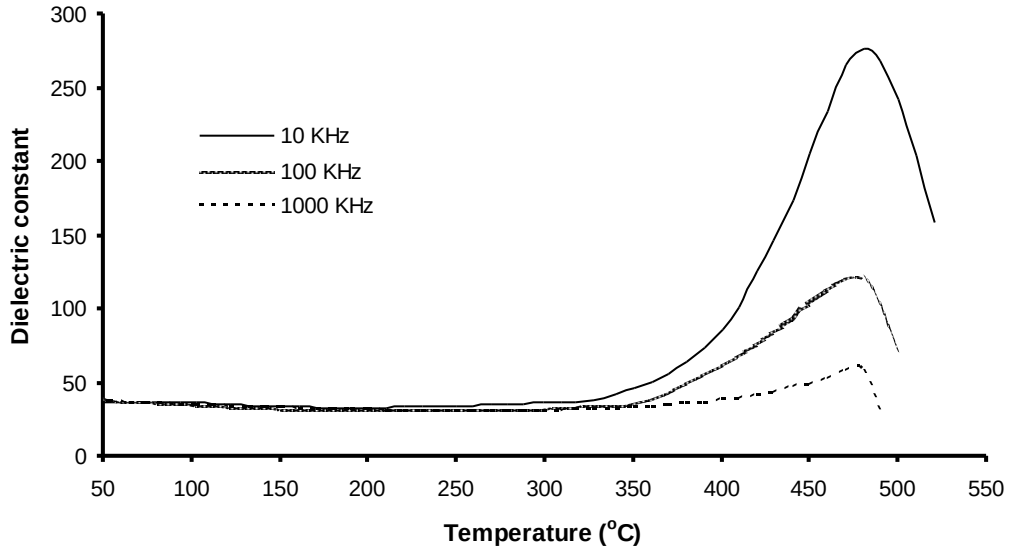

Fig. 2 Temperature dependence of dielectric constant, in $NaTaO_3$, at different frequencies.

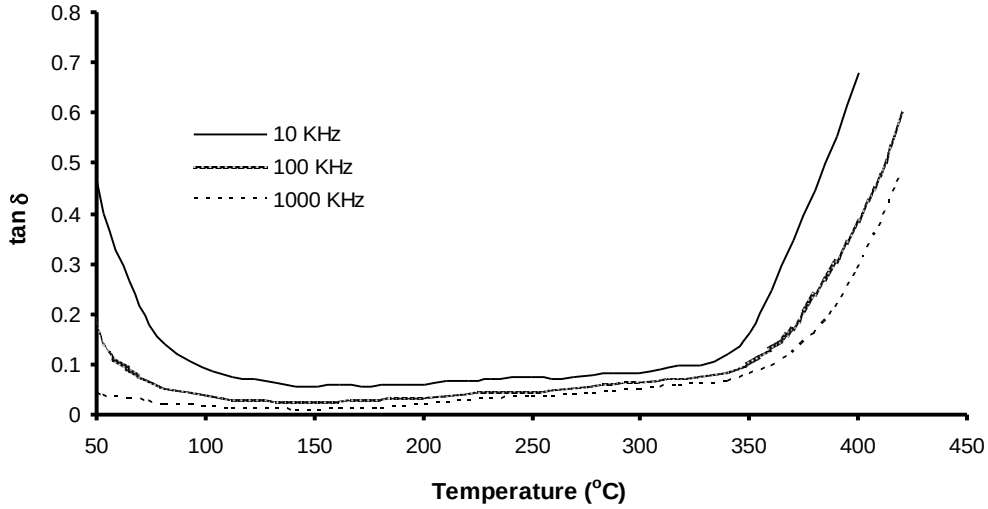

Fig. 3 Temperature dependence of loss tangent (tan δ), in $NaTaO_3$, at different frequencies.

Temperature variation of dielectric constant and loss tangent at different frequencies for x = 0.5, in $Na_{1-x}K_xTaO_3$ system, has been given in Figs. 6 and 7, respectively. An anomaly at 420 °C, followed by two small peaks at 490 and 631 °C, was observed in the dielectric constant measurements. These peaks may be associated with certain structural transitions at these temperatures.

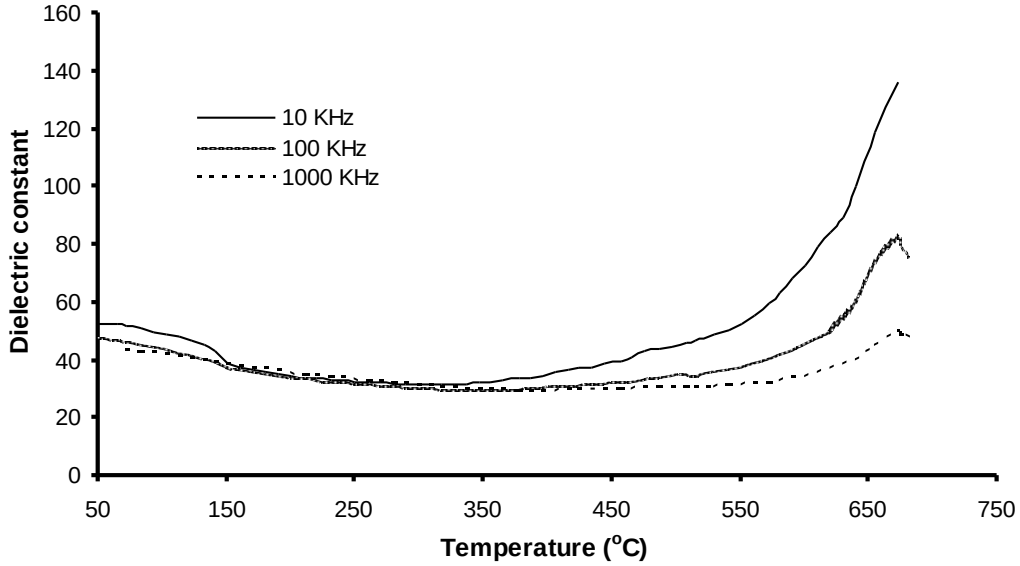

Fig. 4 Temperature dependence of dielectric constant, in $Na_{0.8}K_{0.2}TaO_3$, at different frequencies.

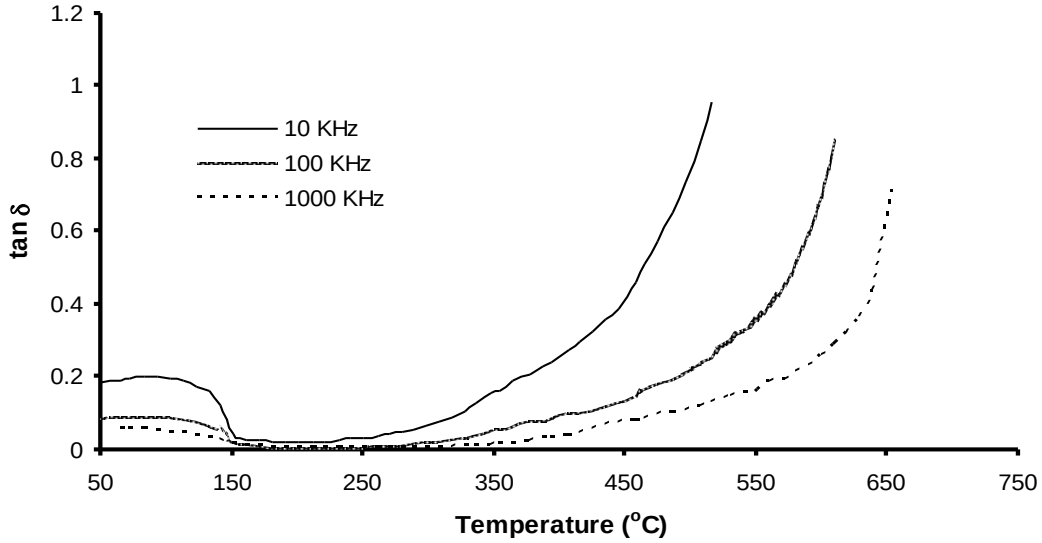

Fig. 5 Temperature dependence of loss tangent (tan δ), in $Na_{0.8}K_{0.2}TaO_3$, at different frequencies.

Dielectric constant and loss tangent peak heights decrease with increasing frequency, in the prepared samples. Decreasing nature of dielectric constant with increasing frequency may be due to the relaxational behavior of a material[12]. Lossy dielectrics can be represented by the circuit analog of a resistance in parallel with a capacitor[12]. At higher frequency the capacitor offers low reactance to the sinusoidal signal, which minimizes the conduction losses in the resistor. Hence, the value of dielectric loss decreases at higher frequencies.

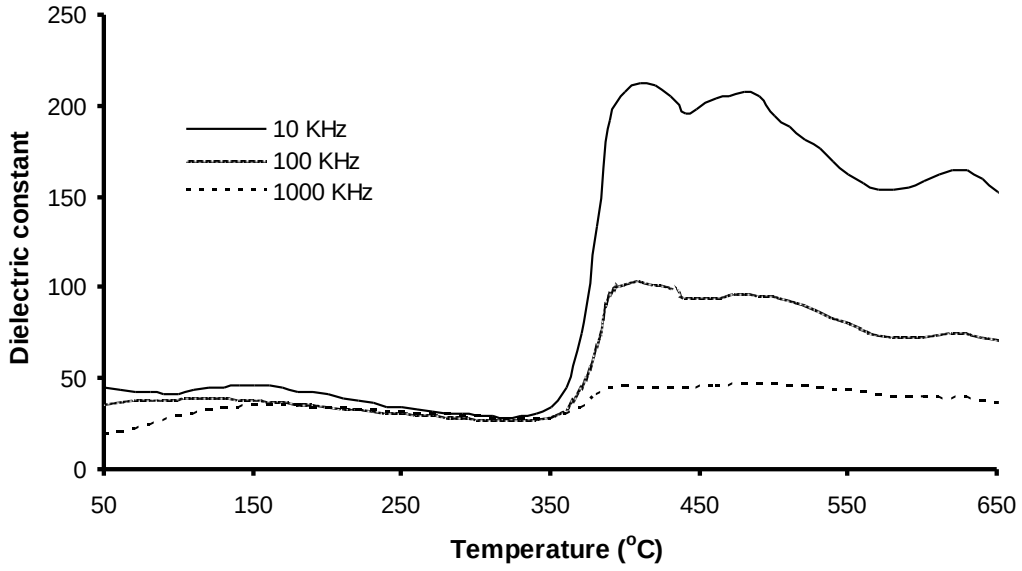

Fig. 6 Temperature dependence of dielectric constant, in $Na_{0.5}K_{0.5}TaO_3$, at different frequencies.

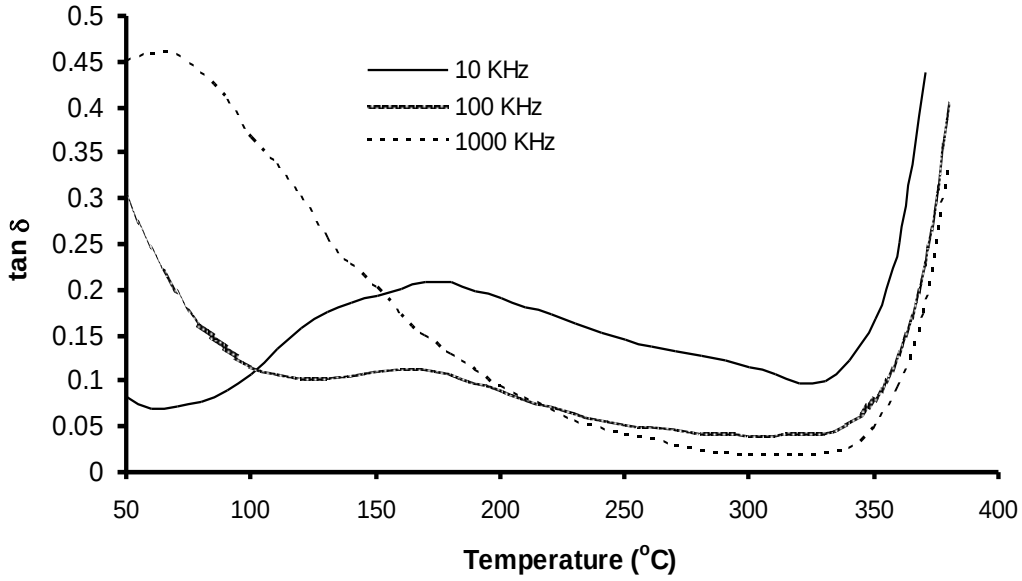

Fig. 7- Temperature dependence of loss tangent (tan δ), in $Na_{0.5}K_{0.5}TaO_3$, at different frequencies.

The damping out of successive relaxation modes is attributed to the decrease of peak height with frequency[12]. The anomalous behavior at certain temperature is due to structural change or phase transition of the material at that temperature[13, 14]. This phase transition in the perovskite type materials is, generally, assumed to be due to the instability of temperature dependent low frequency optical phonon- the soft phonon mode, at transition temperature[15]. Anharmonic interactions among different modes are held responsible for the observed temperature dependence of dielectric properties[14, 16]. At the transition temperature, frequency of the soft mode tends to zero and

the lattice displacement associated with it becomes unstable, leading to the structural change in the lattice. The observed anomalous behavior of dielectric properties of these materials can be associated with the structural change of the lattice near the transition temperature.

The frequency dispersion or change in dielectric properties with frequency and the corresponding circuit analogs for a general solid show several relaxation modes. The dielectric constant shows an expected decrease with frequency as successive polarization modes become damped out, and corresponding peaks occur in the loss spectra at the different relaxation and resonance frequencies. The resonance losses occurring for ionic and electronic oscillations at infrared and ultraviolet frequencies are associated with absorption interactions with the incident radiation at or near the natural vibration frequencies for the ions or electrons. Relaxation losses, conversely, are associated with dipolar orientation, ion jump, or electron hopping, and can occur over a wide frequency range. Contributions to the overall dielectric constant from different polarization mechanisms are related to the composition, frequency, and temperature of the dielectric.

5. CONCLUSIONS

The x-ray diffraction patterns of the prepared samples show orthorhombic polycrystalline behavior. With increasing x value in $Na_{1-x}K_xTaO_3$, the diffraction peaks were observed shifting towards lower angle. The lattice parameters calculated from the XRD pattern, for $NaTaO_3$, were found comparable to the reported values[10]. The crystallite size was found decreasing with increasing x value, which may be due to same sintering condition for all the compositions, whereas the melting point varies with varying x value. The dielectric constant and loss tangent of the prepared samples have been found decreasing with increasing frequency, which show relaxational behavior of the material. The observed dielectric anomalies in $Na_{1-x}K_xTaO_3$ system can be associated with the softening of the relaxational modes near transition temperatures[17]. Damping out of successive relaxational modes may be attributed to the decrease in dielectric peak height with increasing frequency. Dielectric constant and dielectric loss have been found lower for the present system than those for its niobate counter part[1, 18-19] and hence the former can be used in ultrasonic delay lines in place of the latter.

REFERENCES

1. G.A. Samara, *Ferroelectrics*, *73* (1987), 145.
2. G.A. Samara and P. S. Peercy, *Solid State Physics* (Academic Press, New York, 1981).
3. T.G. Davis, *Phys Rev*, *5* (1972), 2530.
4. G.A. Samara, Proceedings of the 6th International Meeting on Ferroelectricity, Kobe, Japan 1985.
5. P. Vousden, *Acta Cryst*, *4* (1951), 373.
6. C.N.W. Darlington and K. S. Knight, *Acta Cryst, 55* (1999), 24.
7. A. Arakcheeva, G. Chapuis, V. Grinevitch and V. Shamray, *Acta Cryst, 57* (2001), 157.
8. B.D. Cullity, *Elements of X-ray Diffraction* (Addison-Wesley Publishing Company Inc., 1977).
9. L.V. Azaroff, *Elements of X-ray Crystallography* (McGraw Hill Book Company, New York, 1968).
10. H.F. Kay and J.L. Miles, *Acta Cryst*, *10* (1957), 213.

11. A. Reisman and E. Banks, *J Amer Ceram Soc*, *80* (1958), 1877.
12. G. Goodman, R.C. Buchanan and T.G. Reynolds III, *Ceramic Materials for Electronics; Processing, Properties, and Application*, Ed. Relva C Buchanan, (Marcel Dekker Inc., New York, 1991).
13. E. Pytte, *Phys Rev*, *5* (1972), 3758.
14. B.S. Semwal and N.S.Panwar, *Bull Mater Sci*, *15* (1992), 237.
15. W. Cochran, *Adv Phys*, *9* (1960), 387.
16. N.S. Panwar, T.C. Upadhyay and B.S. Semwal, *Pramana J Phys*, *33* (1989), 603.
17. Vijendra Lingwal, B.S. Semwal and N.S. Panwar, *Bull Mat Sci*, *26* (2003), 619.
18. L. Egerton and D.M. Dillon, *J Amer Ceram Soc*, *42* (1959), 438.
19. S. Narayana Murty, K.V. Rama Murty, K. Umakantham and A. Bhanumathi, *Ferroelectrics*, *102* (1990), 243.

Theoretical Investigation of Dielectric Properties of Potassium Mixed Sodium Niobate Crystals

Vijendra Lingwal[1], A S Kandari[2] & N S Panwar[3]

[1]Department of Physics, Pt. L.M.S. Govt. PG College Rishikesh, Dehradun, Uttarakhand, India.
[2]Deparment of Physics, Govt. PG College New Tehri, Uttarakhand, India.
[3]University Science Instrumentation Centre, HNB Garhwal University, Srinagar (Garhwal), India.

ABSTRACT

Using experimental observed dielectric and loss behavior of potassium mixed sodium niobate crystals the temperature dependence of soft mode frequency, width, relaxation time, order parameter, fourth order coupling coefficients and anharmonic constants have been calculated. Anomaly has been observed in the behavior of soft mode frequency, width, relaxation time, and order parameter, near the transition temperatures in this compound.
Keywords – Hamiltonian, perovskites, soft mode, relaxational behavior, transition temperature.

1. INTRODUCTION

The perovskite type- ABO_3 crystals observe structural phase transition from the high temperature cubic phase to the low temperature tetragonal, rhombohedral (trigonal) or orthorhombic phase. The phase transition in perovskite crystals is, generally, assumed to be due to the instability of the temperature dependent low frequency optical phonon at transition temperature [1-3]. Depending on the relative magnitude of anharmonic interaction coefficients, different structural phases occur. By displacement of ions from special positions of the lattice of crystals having distorted perovskite structure several modes are involved in various transitions. Pytte [4] has proposed a model Hamiltonian to describe the ferroelectric transition in ABO_3 type compounds in terms of localized normal mode coordinates, elastic strains and large wavelength acoustic phonons. Expressions for free energy and normal mode frequencies have been obtained to describe the phase transition in these compounds, but the dielectric and other related properties could not be explained due to an early decoupling of various correlations in this study. Panwar and Semwal [5] modified the pytte's Hamiltonian in terms of creation and annihilation operators. Using the systematic Green's function method and Dyson's equation the normal phonon frequencies, width and soft mode dynamics of perovskite type crystals were evaluated [5-8].

In the present study, temperature dependence of phonon frequency, width, order parameter, fourth order coupling coefficient and anharmonic constants of potassium mixed sodium niobate crystals have been calculated by correlating the theoretical expressions with the experimental results on dielectric measurements.

2. THEORY

Using the model Hamiltonian [5-8], double time thermal Green's function [9] method and Dyson's equation [10], renormalized soft phonon frequency and width have been calculated [5]. Using the Kubo formalism [11], the real part of the dielectric constant is given as:

$$K'(\omega) - 1 = -\frac{8\pi N \mu^2 \Omega_\lambda(q)\left\{\omega^2 - \hat{\Omega}_\lambda^2(q)\right\}}{\left[\left\{\omega^2 - \hat{\Omega}_\lambda^2(q)\right\}^2 + \Omega_\lambda^2(q)\,\Gamma_\lambda^2(q,\omega)\right]} \quad , \tag{1}$$

Where the symbols have their usual meanings [5-8], and tangent loss (tan δ), which is the ratio of imaginary and real part of dielectric constant is given by:

$$\tan\delta = -\frac{\Omega_\lambda(q)\,\Gamma_\lambda(q,\omega)}{\left\{\omega^2 - \hat{\Omega}_\lambda^2(q)\right\}} \quad , \tag{2}$$

In the presence of resonant interaction the relaxation time (τ) with the phonon width (Γ) is related as [12]

$$\tau_\lambda(q) = \Gamma_\lambda(q) \Big/ \hat{\Omega}_\lambda^2(q) \tag{3}$$

In the experimental range of frequencies $\omega << \hat{\Omega}_\lambda(q)$; for the temperature, at which $\Omega_\lambda(q)\tau_\lambda(q) << 1$, i.e., the systems for which no relaxation effect is observed;

and using relation (3) the Eq. (1) reduces to

$$K(\omega) = \frac{8\pi N \mu^2 \Omega_\lambda(q)}{\hat{\Omega}_\lambda^2(q)} \quad , \tag{4}$$

$$\text{or } K(\omega) \cong \text{Constant} \Big/ (T - T_c) \quad ;$$

This is Curie- Weiss law.

and, using relation (3), Eq. (2) reduces to

$$\tan\delta = \frac{\Omega_\lambda(q)\tau_\lambda(q)}{\left\{1 + \Omega_\lambda^2(q)\tau_\lambda^2(q)\right\}} \cong \omega\left(\alpha + \beta T + \gamma T^2\right) \Big/ (T - T_C) \tag{5}$$

Where α is harmonic and defect contribution, β and γ are the contributions due to three- and four- phonon anharmonic interactions of the lattice, in the absence of anharmonicity they have zero value.

From Eq. (5), for small values of tan δ, one obtains

$$\tau_\lambda(q) = 1 \Big/ \{\Omega_\lambda(q)\tan\delta\} \tag{6}$$

In the first approximation the temperature dependence of phonon frequency ($\hat{\Omega}_{\lambda T}$) and width $\Gamma_{\lambda T}$ can be approximated to [7]

$$\hat{\Omega}_{\lambda T}^2 = \alpha + \beta T + \gamma T^2 \quad , \tag{7}$$

$$\Gamma_{\lambda T} = \alpha' + \beta' T + \gamma' T^2 \tag{8}$$

3. RESULTS AND DISCUSSION

Figs. 1 (a) and (b) show the temperature dependence of soft mode frequency and width for $NaNbO_3$, in orthorhombic and pseudo-orthorhombic phase, respectively; and Fig. 1 (c) shows that for $Na_{0.5}K_{0.5}NbO_3$, in

orthorhombic phase. These values have been calculated from the dielectric measurement data of references [13-15], using relation, Eqs. (4) and (2). The mode softening is visualized near the transition temperature.

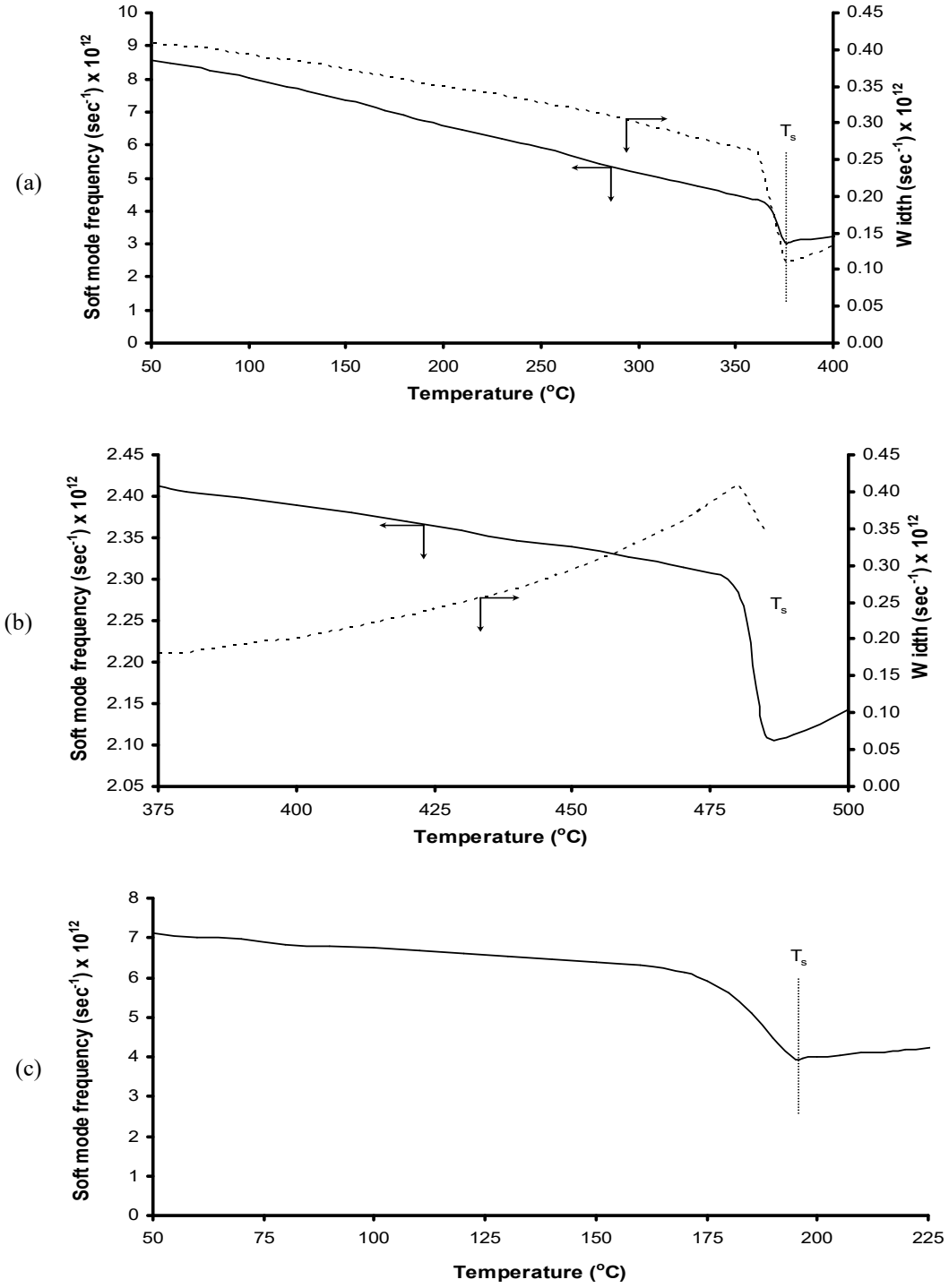

Fig. 1 Temperature dependence of soft mode frequency and width for $NaNbO_3$ system in (a) orthorhombic, (b) pseudo-orthorhombic phase; and for $Na_{0.5}K_{0.5}NbO_3$ in (c) orthorhombic phase [using data of ref. 17, 18 at 10 KHz]

The temperature variation of soft mode frequency and width, for $Na_{0.5}K_{0.5}NbO_3$, in orthorhombic and tetragonal phase, has been calculated from our own dielectric measurements [16], using Eqs. (4) and (2), and are shown in Fig 2. Using Eq. (6), calculated temperature variation of relaxation time for $NaNbO_3$-$KNbO_3$ mixed system has been given in Fig. 3. It has been observed that the relaxation time for $NaNbO_3$-$KNbO_3$ mixed system increases with increasing temperature, in the observed range.

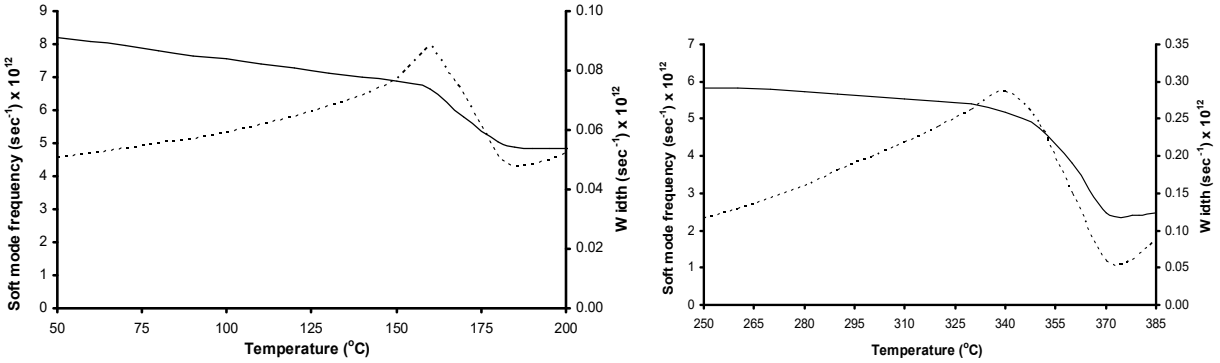

(a) (b)

Fig. 2 Temperature dependence of soft mode frequency and width for $Na_{0.5}K_{0.5}NbO_3$ system in (a) orthorhombic and (b) tetragonal phase [using our own data (16) at 100 KHz]

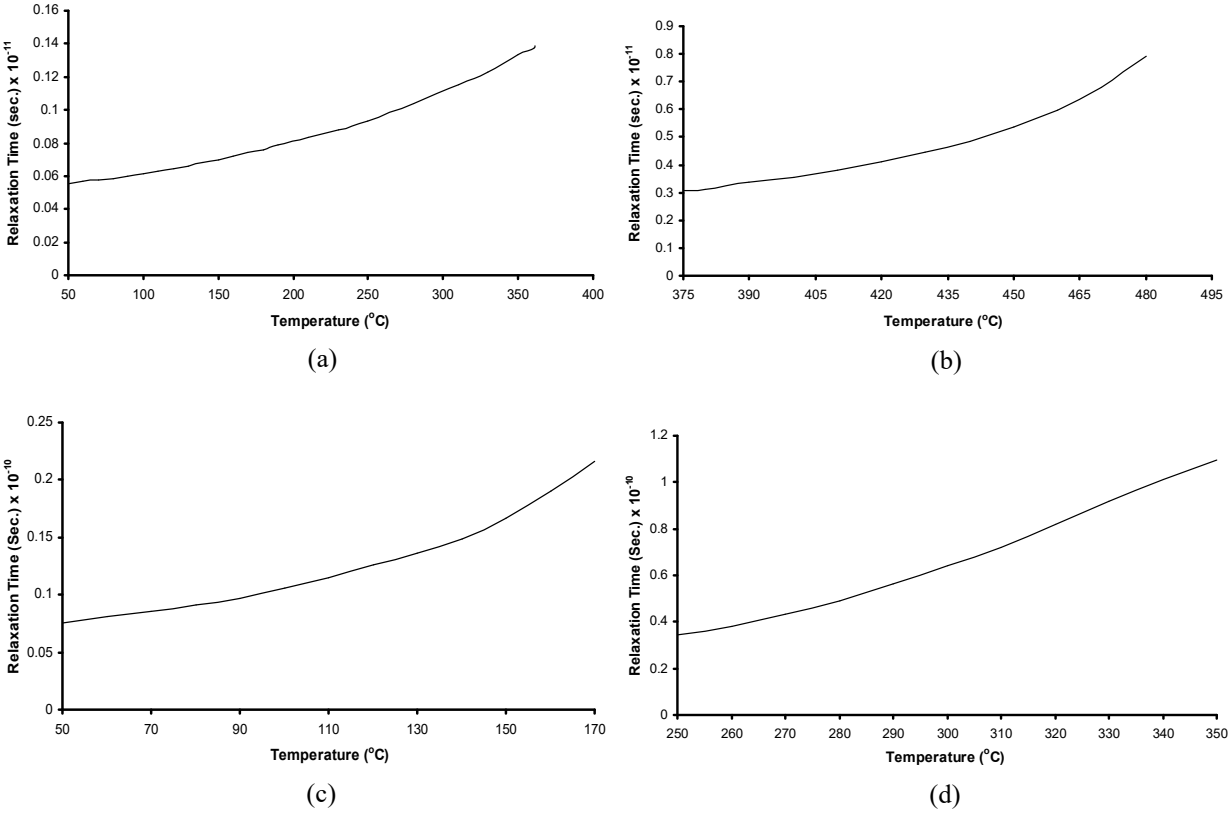

(a) (b)

(c) (d)

Fig. 3 Temperature dependence of relaxation time for $NaNbO_3$ system in (a) orthorhombic, (b) pseudo-orthorhombic phase [using data of ref. 17 at 10 KHz]; and for $Na_{0.5}K_{0.5}NbO_3$ in (c) orthorhombic and (d) tetragonal system [using our own data (16) at 100 KHz]

Fitting Eqs. (7) and (8), with the reported [17-19] and our own results of dielectric measurements [16], calculated values of α, β, γ; α', β', and γ' for different phases of $NaNbO_3$-$KNbO_3$ mixed system have been given in Tables 1 and 2.

Table 1. Values of α, β, γ for different phases [* calculated from our own data (16)]

Parameter	$NaNbO_3$		$Na_{0.5}K_{0.5}NbO_3$		$KNbO_3$	
	Ortho.	Pse. Ortho.	Ortho.	Tetra.	Ortho.	Tetra.
α (s^{-1})	1.36×10^{26}	-4.85×10^{25}	-1.06×10^{26}	-3.02×10^{26}	2.11×10^{25}	-2.31×10^{26}
	$*2.78 \times 10^{26}$	----	$*-2.50 \times 10^{25}$	----	----	----
β ($K^{-1}s^{-1}$)	-2.00×10^{23}	1.66×10^{23}	9.86×10^{23}	1.25×10^{24}	4.07×10^{22}	8.4×10^{23}
	$*-4.77 \times 10^{23}$	----	$*6.91 \times 10^{23}$	----	----	----
γ ($K^{-2}s^{-1}$)	8.08×10^{18}	-1.27×10^{20}	-1.54×10^{21}	-1.16×10^{21}	-1.26×10^{20}	-7.2×10^{20}
	$*1.10 \times 10^{20}$	----	-1.20×10^{21}	----	----	----

Table 2. Values of α', β', γ' for different phases [* calculated from our own data (16)]

Parameter	$NaNbO_3$		$Na_{0.5}K_{0.5}NbO_3$		$KNbO_3$	
	Ortho.	Pse. Ortho.	Ortho.	Tetra.	Ortho.	Tetra.
α' (s^{-1})	1.29×10^{13}	7.05×10^{12}	-1.79×10^{12}	----	-1.87×10^{11}	-1.47×10^{13}
	$*7.29 \times 10^{11}$	----	----	----	----	----
β' ($K^{-1}s^{-1}$)	-3.68×10^{10}	-2.17×10^{10}	1.17×10^{10}	----	1.35×10^{9}	5.06×10^{10}
	$*-3.11 \times 10^{9}$	----	----	----	----	----
γ' ($K^{-2}s^{-1}$)	2.57×10^{7}	1.71×10^{7}	1.66×10^{7}	----	-1.8×10^{6}	-4.19×10^{7}
	$*3.72 \times 10^{6}$	----	----	----	----	----

The Curie-Weiss behavior of tangent loss in $SrTiO_3$ and $SrTiO_3$ doped with impurity [20], shows that this contribution is due to the temperature independent term α. This suggests that imperfections cause damping. The imperfections couple the soft mode to other modes and provide a mechanism for scattering energy out of the driven mode. At higher temperatures the loss deviates strongly from the Curie-Weiss type behavior and increases linearly with temperature. This assumes that at higher temperature lattice anharmonicity is responsible for the observed loss.

The order parameter (A) is given by [20]

$$A^2 = \frac{9k_B}{m\omega_m^2}\left[T_c - \left\{1 - \frac{\hat{\Omega}}{\omega_m}\tan^{-1}\frac{\omega_m}{\hat{\Omega}}\right\}T\right], \qquad (9)$$

where ω_m is the natural frequency of the system; and m is reduced mass of the system, given by

$$m = \frac{2m_o m_{Nb}}{m_o + m_{Nb}}; \quad \text{(for Nb-O system).}$$

Using the previously calculated values of $\hat{\Omega}$, A^2 has been calculated, from Eq. (9), at different temperatures for $NaNbO_3$-$KNbO_3$ mixed system. The calculated temperature variation of order parameter (A^2) has been given in Figs. 4.

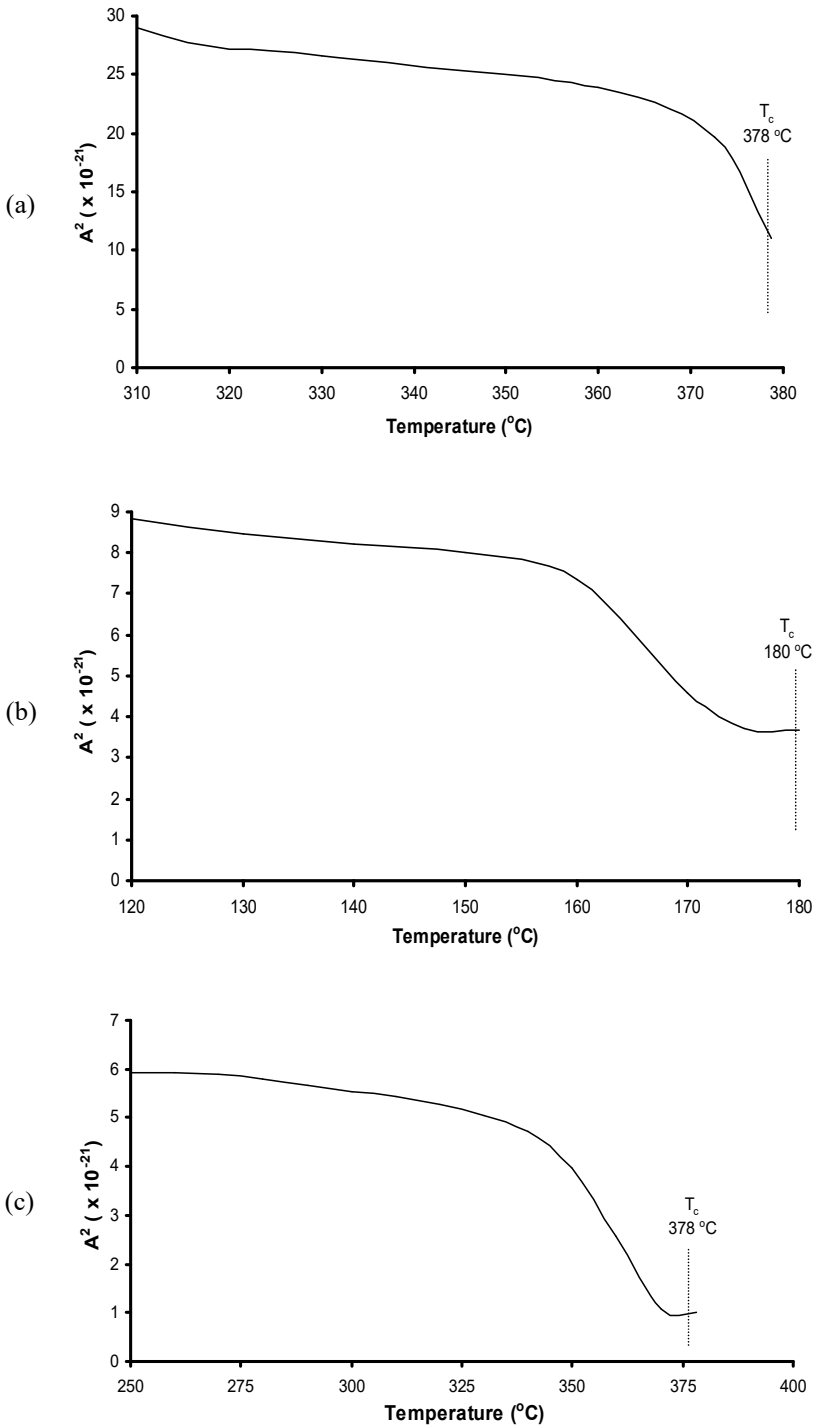

Fig. 4 Temperature dependence of A^2 for (a) $NaNbO_3$ system in orthorhombic phase [17]; and for $Na_{0.5}K_{0.5}NbO_3$ in (b) orthorhombic, and (c) tetragonal phase [calculated from our own data (16)]

Table 3 Fourth order coupling coefficients for $NaNbO_3$- $KNbO_3$ system

	$NaNbO_3$	$Na_{0.5}K_{0.5}NbO_3$	$KNbO_3$
$\Gamma_1 \times 1018$ (J/m4)	10.63	126	7.1
$\Gamma_2 \times 1018$ (J/m4)	5.31	62.76	3.52
	4.5*	----	2.9*

*Values obtained by following ref. [21].

Fourth order coupling coefficients, Γ_1 and Γ_2, have been calculated for $NaNbO_3$, $Na_{0.5}K_{0.5}NbO_3$ and $KNbO_3$, and are given in Table 3.

The fourth order coupling coefficient has been calculated, for $SrTiO_3$, by Silverman [21] with a different approach. Following Silverman [21], the fourth order coupling coefficient has been calculated for $NaNbO_3$ and $KNbO_3$. The calculated values of the fourth order coupling coefficient, obtained with the present approach and those obtained from the Silverman's approach [21], have been found close to each other, Table 3.

Thus taking all the interactions into consideration, in the model Hamiltonian proposed by Pytte [20], and using Green's function method and Dyson's equation; expressions for phonon frequencies, widths and relaxation times, and hence for the dielectric constant and loss tangent have been obtained. The calculated expressions explain well the observed dielectric behavior of $NaNbO_3$-$KNbO_3$ mixed system.

REFERENCES

1. P.W. Anderson, in *Physics of Dielectrics-1960,* Conference Proceedings, edited by G.I. Skanavi, (Academy of Sciences, Moscow, 1960), pp. 290.
2. W. Cochran, *Adv. Phys.*, *9* (1960), 387.
3. G. Shirane and Y. Yamada, *Phys. Rev.*, *177* (1969), 2.
4. E. Pytte, *Phys. Rev.* B, *5* (1972), 3758.
5. N.S. Panwar, T.C. Upadhyay and B.S. Semwal, *Indian J. Pure & Appl. Phy.*, *27* (1989), 765.
6. N.S. Panwar, T.C. Upadhyay and B.S. Semwal, *Pramana: J. Phys.*, *33* (1989), 603.
7. N.S. Panwar and B.S. Semwal, *Indian J. Pure & Appl. Phys.*, *28* (1990), 706.
8. B.S. Semwal and N.S. Panwar, *Bull. Mat. Sci.*, *15* (1992), 237.
9. D.N. Zubarev, *Phys. Uspekhi (USSR)*, *3* (1960), 2.
10. R.P. Gairola and B.S. Semwal, *J. Phys. Soc. Jpn.*, *42* (1977), 975.
11. R.J. Kubo, *J. Phys. Soc. Jpn.*, *12* (1957), 570.
12. E. Litov and C.W. Garland, *Ferroelectrics*, *72* (1987), 22; *72* (1987), 321.
13. E.A. Wood, R.C. Miller and J.P. Remeika, *Acta Cryst.*, *15* (1962), 1273.
14. A. Reisman and E. Banks, *J. Amer. Ceram. Soc.*, *80* (1958), 1877.
15. V.J. Tennery and K.W. Hang, *J. Appl. Phys.*, *39* (1968), 4749.
16. Vijendra Lingwal, "Dielectric properties of mixed $Na_{1-x}K_x(Nb,Ta)O_3$ Systems", Ph.D. Thesis, HNB Garhwal University, 2003.
17. B.T. Matthias and J. Remeika, *Phys. Rev.*, *82* (1951), 727.
18. G. Shirane, R. Newnham and R. Pepinsky, *Phys. Rev.*, *96* (1954), 581.
19. L. Egerton and D.M. Dillon, *J. Amer. Ceram. Soc.*, *42* (1959), 438.
20. E. Pytte, *Phys. Rev. Lett.*, *28* (1972), 895.
21. B.D. Silverman, *Phys. Rev.*, *125* (1962), 1921; *131* (1963), 2478; *135* (1964), 1596.

Materials Research Express

PAPER

Agriculture waste reinforced corn starch-based biocomposites: effect of rice husk/walnut shell on physicomechanical, biodegradable and thermal properties

RECEIVED
13 November 2018

REVISED
11 December 2018

ACCEPTED FOR PUBLICATION
14 January 2019

PUBLISHED
28 January 2019

Tej Singh[1,5], **Brijesh Gangil**[2,5], **Amar Patnaik**[3], **Don Biswas**[4] and **Gusztáv Fekete**[1]

[1] Savaria Institute of Technology, Eötvös Loránd University, Szombathely, 9700 Hungary
[2] Mechanical Engineering Department, H.N.B.U. Garhwal, 246174 India
[3] Department of Mechanical Engineering, M.N.I.T. Jaipur, 302017 India
[4] University Science Instrumentation Centre, H.N.B.U. Garhwal, 246174 India
[5] Authors to whom any correspondence should be addressed.

E-mail: tejschauhan@gmail.com **and** brijeshgangil@gmail.com

Keywords: cornstarch, agriculture waste, biocomposite, physicomechanical, biodegradability, thermal

Abstract

In the present work, agriculture waste based biocomposites were developed by reinforcing corn starch resin with various rice husk and walnut shell content of 5, 10 and 15 wt%. These fabricated biocomposites were investigated for physical, mechanical and thermal properties. It was found that the physical properties such as density and water absorption of the biocomposites remains in the range of 1.20–1.32 g cm^{-3} and 4.32%–8.68% respectively, while these properties decreased by the increase of rice husk and walnut shell content. The slower degradation rate of rice husk and walnut shell resulted in enhanced degradation period of the biocomposites. Thermogravimetric analysis revealed that the addition of increased rice husk and walnut shell content enhanced the thermal stability of the biocomposites. The evaluated mechanical (tensile strength, flexural strength, compressive strength, impact energy and hardness) properties were found to increase with the amount of rice husk and walnut shell content. The maximum tensile strength of 10.70 MPa, flexural strength of 19.60 MPa and impact energy of 0.362 J was observed for biocomposites with 15 wt% rice husk content. Similarly, the maximum compressive strength of 22.70 MPa and hardness of 21.31 Hv is obtained for biocomposites with 15 wt% walnut shell content. The rice husk based biocomposites gave better tensile strength, flexural strength, impact energy and thermal stability but resulted in lower hardness and compressive strength than the walnut shell based biocomposites. The biocomposites reinforced with walnut shell exhibit higher resistance to water absorption and biodegradability than those associated with rice husk. The results suggest that the developed biocomposites can be used as ecofriendly materials in lightweight applications.

1. Introduction

The rising environmental awareness has encouraged the scientists towards the development of ecofriendly materials from sustainable assets to supplant traditionally used synthetic materials in numerous applications [1–3]. It is well known that the synthetic polymers are very versatile materials with numerous applications thus their production and utilization have been expanding [4–6]. These synthetic polymers are non-biodegradable and hence pose severe environmental problems if not discarded properly [6, 7]. Therefore, researchers are continuously putting great attention to the development of new biodegradable and ecofriendly polymeric materials [8–10]. Among them, natural starch offers several advantages due to its various beneficial attributes such as biodegradability and availability [11–13]. Apart from beneficial attributes, higher water uptake capacity and inferior mechanical properties are the main disadvantages of natural starch resin-based composites [14]. For this reason, natural fibers provide good perspective as reinforcements in starch-based composites [15]. The

© 2019 IOP Publishing Ltd

main advantages of using natural fibers are their lower cost, sustainability, light in weight, nonhazardous, nonabrasive and more importantly, they do not affect the biodegradability of the composites [16].

In this regards, a lot of effort has been devoted to study the influence of natural fibers on physical and thermo-mechanical properties of starch based biocomposites. Peilei *et al* [17] added jute fibers to cassava starch and found that 15 wt% jute fibers increased the tensile strength of the biocomposite from 4.8 MPa to 22 MPa. The results also indicated that increased jute fiber content resulted in increased thermal stability and stiffness with reduced water absorption behavior. Ramirez *et al* [18] studied the influence of coir fiber on the tensile strength and water absorption behavior of corn and cassava starch based biodegradable composites. They concluded that tensile strength of the composite increased, while the water absorption decreased with the increase of coir fiber content. Hemp fiber reinforced starch-based biodegradable composites also reported to achieve outstanding mechanical properties by Ochi [19]. Excellent mechanical (tensile and compressive strength) and thermal properties were recorded for sisal fiber reinforced thermoplastic corn starch based biocomposites by Cheng *et al* [20]. Flax fibers also reported to improve the storage modulus of maize starch based biocomposites by Daniele *et al* [21]. Gironès *et al* [22] developed sisal and hemp fiber reinforced corn starch based biocomposites and showed that the incorporation of fibrous reinforcement caused an increase in the thermo-mechanical properties of the biocomposites. A tremendous improvement in tensile strength of bagasse and banana fiber reinforced corn starch biocomposites was reported by Guimaraes *et al* [23].

Apart from natural fibers, great attention is placed on the inclusion of agricultural wastes such as rice husk and walnut shell particles into polymeric composites by various researchers [24–26]. The convenience of their utilization in polymer composites lies in the fact that these biodegradable particles are obtained easily from agriculture wastes at zero cost while they can enhance the thermal, tribological and physicomechanical properties of the composites. Navin *et al* [27] studied the effect of rice husk on the properties of polyvinylchloride composites. Incorporation of rice husk increases the compressive strength and wear resistance properties. Nadir *et al* [28] investigated the influence of walnut shell on the physicomechanical properties of polypropylene composites. The investigation revealed that tensile modulus, bending modulus and water absorption of the composites significantly increased with increasing the walnut shell content. In another work, the inclusion of walnut shell particles was reported to increase the hardness of epoxy composites along with sustainable compressive and tensile properties by Vinay [29]. Shahryar and Hosseinzadeh [30] examined the mechanical and thermal properties of walnut shell powder filled polyurethane composites and observed that addition of 10 wt% walnut shell powder to polyurethane composites improves the hardness by 40%, tensile strength by 63% and the tensile modulus up to 34%. Furthermore, if ecofriendly materials are used in combination with polymers extracted from renewable recourses, such as starch, then this could result in a fully biodegradable composite [31]. Recognizing the above facts, the aim of this investigation is to study the effect of rice husk and walnut shell contents on the physical, mechanical, and thermal properties of corn starch based biodegradable composites

2. Materials and composites fabrication

2.1. Materials

The corn starch, glycerol and sodium hydroxide were obtained from Central Drug House (P) Ltd Delhi, India. The obtained corn starch contained about 12% of moisture content. Moreover, this corn starch was not thermoplastic therefore glycerol was added as a plasticizer to keep away the biocomposites from the development of pores and cracks [23]. The rice husk and walnut shell particles were collected from Tehri village of Uttarakhand, India. The particles that pass through 60 mesh sieve and retain on 100 mesh sieve were taken as reinforcement. The scanning electron microscope (SEM) images of the corn starch, walnut shell and rice husk particles are presented in figure 1.

Prior to being used in biocomposites, the rice husk and walnut shell particles were treated with sodium hydroxide solution for 24 h. After washing three times with distilled water, the particles were dried in an oven for 24 h at 60 °C.

2.2. Fabrication of biocomposites

The procedure used for the fabrication of biocomposites is described in figure 2. First of all, the corn starch and glycerol were mixed manually, hereafter named as corn starch resin and used as polymeric matrix. The compositional variations and nomenclature of the prepared biocomposites are presented in table 1. The rice husk and walnut shell particles in desired proportion were mixed for 5 min in the corn starch resin by using a shear-type mechanical mixer at 3000 rpm. The mixture was then placed into an iron mold of dimension $120 \times 60 \times 10$ mm^3 and heat cured at 100 °C of temperature in a compression-molding machine for 20 min

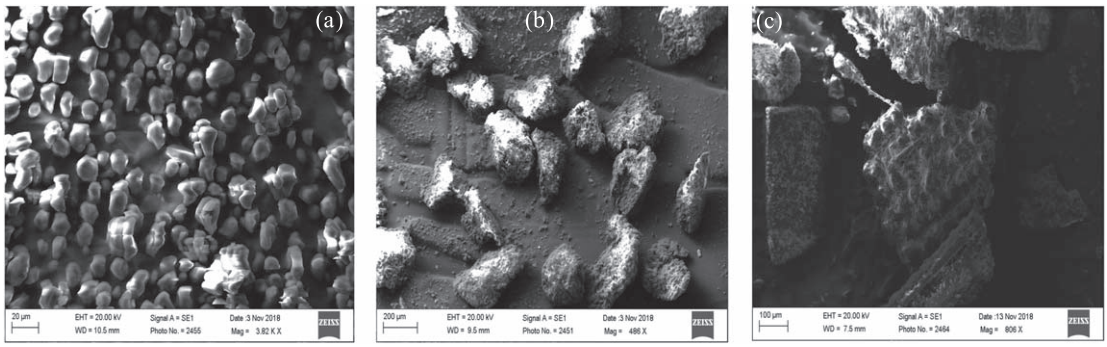

Figure 1. SEM micrographs of (a) Corn starch, (b) Walnut shell and (c) Rice husk.

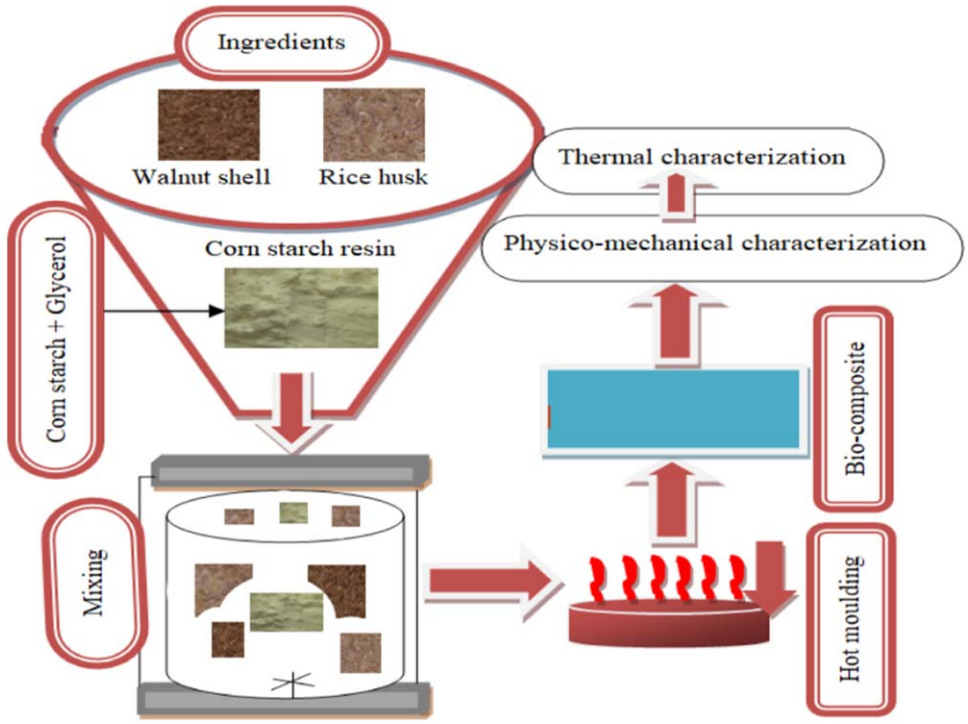

Figure 2. Schematic of biocomposite fabrication process.

Table 1. Designation and compositional variations.

Ingredients	Composition (wt%)					
	RBC-5	RBC-10	RBC-15	WBC-5	WBC-10	WBC-15
Corn starch resin	95	90	85	95	90	85
Rice husk	5	10	15	0	0	0
Walnut shell	0	0	0	5	10	15

RBC: Rice husk based biocomposite; WBC: Walnut shell based biocomposite.

under a pressure of 10 MPa. Finally, samples of appropriate sizes (figure 3) were cut and used for various characterizations.

2.3. Physical and mechanical characterization

Standard water displacement method was used for density measurement. The tensile, compressive and flexural tests were performed on flat biocomposite samples as per ASTM D3039 [32], ASTM D3410 [33] and ASTM

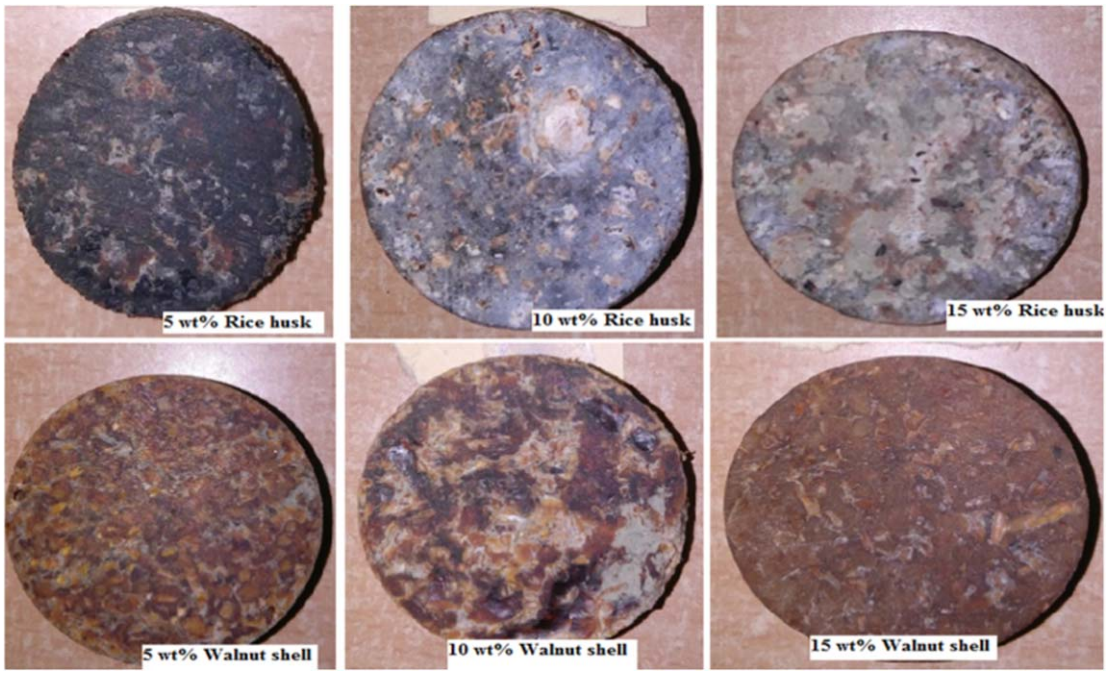

Figure 3. Specimen for water absorption test.

D790 [34] test standards respectively on Instron 1195 universal testing machine. Impact test was conducted according to ASTM D256 [35] with a using an impact tester machine IT 504 from Tinius Olsen whereas ASTM E384 [36] test standard was used for Vicker hardness measurement. Water absorption of the biocomposite specimen was measured as per ASTM D570-98 [37] by dipping in water for 24 h. The water absorption (%) was calculated from the following relation:

$$\text{Water absorption (\%)} = \frac{W_f - W_i}{W_i} \times 100 \tag{1}$$

Where, W_i is the weight of sample before dipping in water and W_f is the weight of the sample after dipping in water.

2.4. Biodegradability study

Soil burial method was used to study the biodegradability of the fabricated biocomposites. The specimens of dimensions 40 mm × 8 mm × 5 mm were buried under 20 cm of natural soil, located in the vicinity of university campus for seven weeks. Before start of testing, the specimens were dried at 60 °C for 24 h in an oven and weighed. Thereafter, specimens were weighed at a regular interval of one week. Before taking the final weight, the specimens were cleaned with ethanol and dried at 60 °C for 24 h. The biodegradability (%) of the biocomposite was determined with the help of following equation:

$$\text{Biodegradability (\%)} = \frac{M_i - M_f}{M_i} \times 100 \tag{2}$$

Where, M_i = weight of the specimen before testing, M_f = weight of the specimen after testing.

2.5. Thermal characterization

The thermogravimetric analysis (TGA) was performed on 50 mg of biocomposite sample in a TA-60WS type thermal analyzer supplied by Shimadzu scientific instrument, at a heating rate of 10 °C/min in the temperature ranges of 25 °C–500 °C under nitrogen (40 ml min^{-1} flow rate) atmosphere. The obtained results were analyzed as weight (%) with respect to temperature. Furthermore, to analyze the thermal stability of the biocomposites, oxidation index (OI) was computed by using the following equation [38]:

$$OI = 0.0696[AC] \tag{3}$$

Where, AC is the ash content of the biocomposite sample remains after TGA investigation.

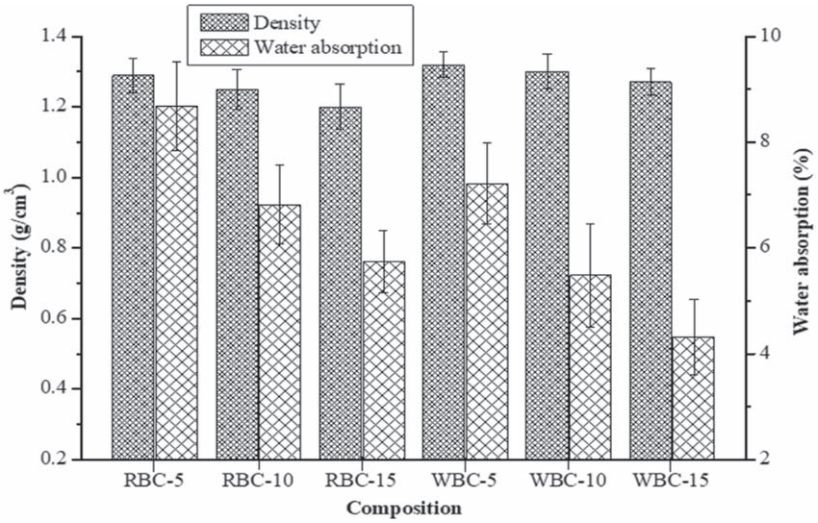

Figure 4. Density and water absorption of the biocomposites.

3. Result and discussion

3.1. Physical properties of the biocomposites

The results of the evaluated physical properties such as density and water absorption of the biocomposites are depicted in figure 4. the density of the biocomposites remains in the range of 1.20–1.29 g cm^{-3} and 1.27–1.32 g cm^{-3} for rice husk and walnut shell particles filled composites.

It was found that the increased content of rice husk or walnut shell in the biocomposite results in decreased density. This decrease in density can be related to the fact that the reinforced particles were lighter in comparison to corn starch resin. Further, it can be observed that the water absorption of the biocomposite decreases with the increase in rice husk and walnut shell content. This can be explained as follows. Due to the chemical similarity, a strong interfacial bonding will exist between the corn starch resin and rice husk and walnut shell reinforcement, which restrict the penetration of water/moisture [17, 39]. Moreover, the increased reinforcement will result in a more compact structure which helps reducing the mobility of the corn starch resin molecules and it also reduces water/moisture absorption [40, 41]. Water absorption of the biocomposites filled with the walnut shell was generally lower than the biocomposites filled with rice husk. This was mainly attributed to the presence of higher lignin content and lower hygroscopic materials (cellulose and hemicellulose) in walnut shell than rice husk. The hygroscopic material contains hydroxyl groups and has hydrophilic nature that can soak up water but lignin is hydrophobic and do not absorb water. The Lignin content of the rice husk (20%) is nearly 2.5 times lower to that of walnut shell (49.18%). Also the amount of hygroscopic materials in walnut shell (47.78%) is lower than that of rice husk (60%) [25, 28].

3.2. Biodegradation of the biocomposites

Biodegradation of the rice husk and walnut shell reinforced biocomposites was performed by burying specimens in microorganism-rich soil and the results are presented in figure 5. From this study, it was observed that the degradation rate of the biocomposites was decreased with an increase in rice husk and walnut shell content. Biocomposites with 5 wt% content (RBC-5/WBC-5) underwent a faster degradation than composites containing higher rice husk and walnut shell content. By the end of the seventh week, RBC-5/WBC-5 lost approximately 60 $\pm$ 1% of its initial weight, while all other biocomposites lost approximately 43 $\pm$ 4%. The reduced degradation rate with increased rice husk and walnut shell content may be attributed to the lower degradation rate of the rice husk and walnut shell compared to the corn starch resin.

3.3. Mechanical properties of the biocomposites

Results of the mechanical properties of the fabricated biocomposites are presented in figures 6 and 7. Results obtained from different mechanical testing displayed a continuous increase in evaluated properties, which was proportional to the amount of reinforcement. Thus, tensile strength (figure 6) for biocomposites reinforced with a 15 wt% of the walnut shell (WBC-15) and rice husk (RBC-15) content was 8.54 MPa and 10.70 MPa and it still remains 40%–67% higher than those of 5 wt% walnut shell (WBC-5) and rice husk (RBC-5) based biocomposites. It is well reported in the literature that pure starch is a brittle material [41]. The inclusion of

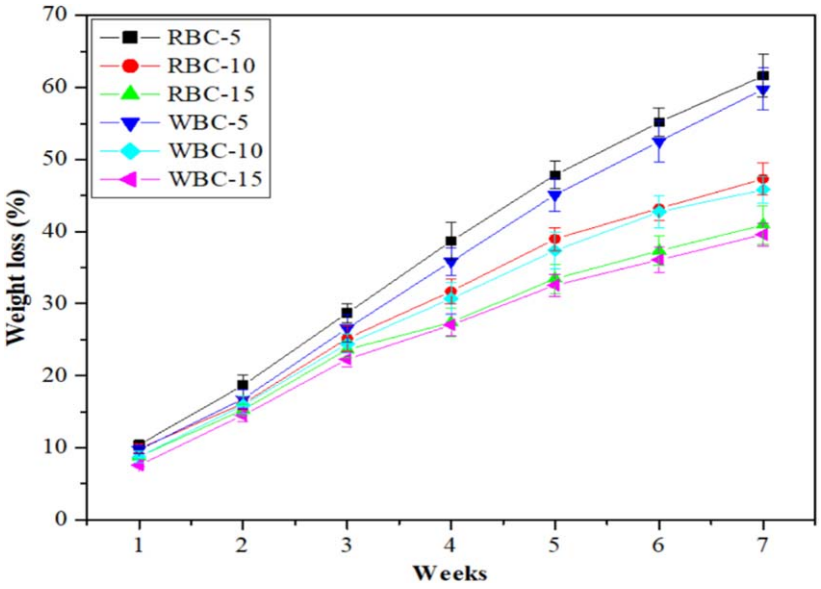

Figure 5. Biodegradability of the biocomposites.

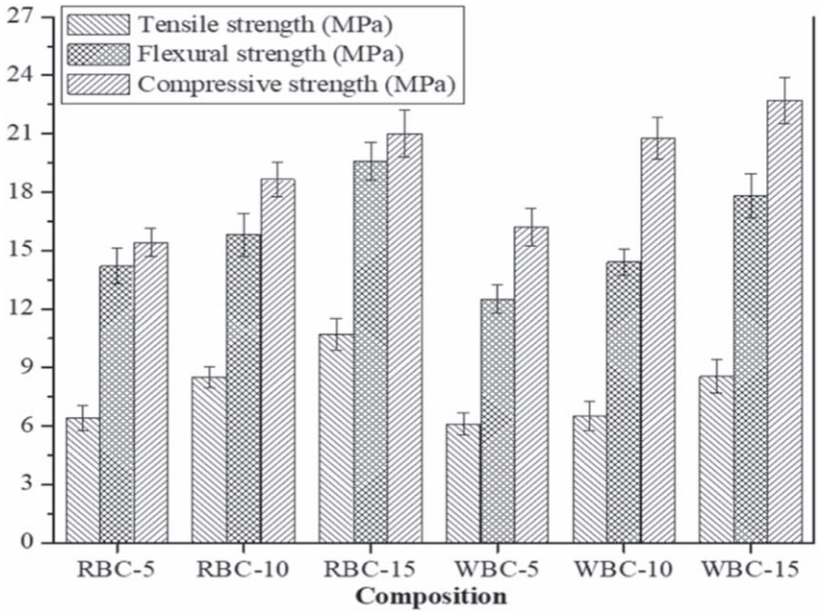

Figure 6. Tensile strength, flexural strength and compressive strength of the biocomposites.

natural fiber/particle in starch composite reduced its brittleness, and hence resulted in increased tensile strength [17, 43].

Similarly, the flexural strength and compressive strength (figure 6) of the biocomposites was improved from 12.50 to 19.60 MPa and from 15.40 to 22.7 MPa respectively, as the content of reinforcement (rice husk and walnut shell) increased from 5 wt% to 15 wt%. For WBC-15 biocomposite flexural strength and compressive strength increased by 42% and 40% whereas, for RBC-15 biocomposite, an improvement of 38% and 36% were registered compared to 5 wt% walnut shell (WBC-5) and rice husk (RBC-5) based biocomposites respectively. This increment may be due to the increase of incorporation of walnut shell and rice husk which increases the stress transfer between the reinforcement and corn starch resin interfaces [39, 44].

As can be found in figure 7, the hardness and impact energy of the biocomposites increases with increasing the amount of rice husk and walnut shell content from 5 to 15 wt% and decreasing the amount of corn starch resin from 95 to 85 wt%. The hardness and impact energy of the biocomposites lies in the range of 15.31–19.30 H_v and 0.316–0362 J for rice husk and 17–21.31 H_v and 0.278–0325 J for walnut shell based biocomposites

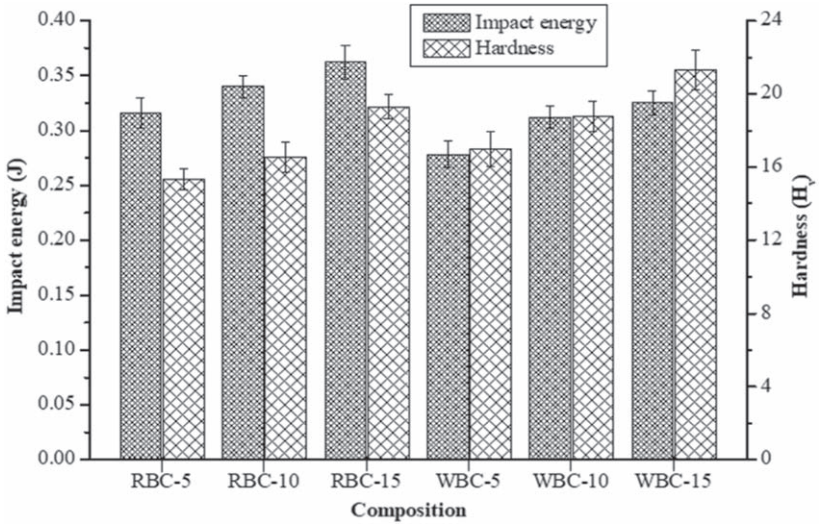

Figure 7. Impact energy and hardness of the biocomposites.

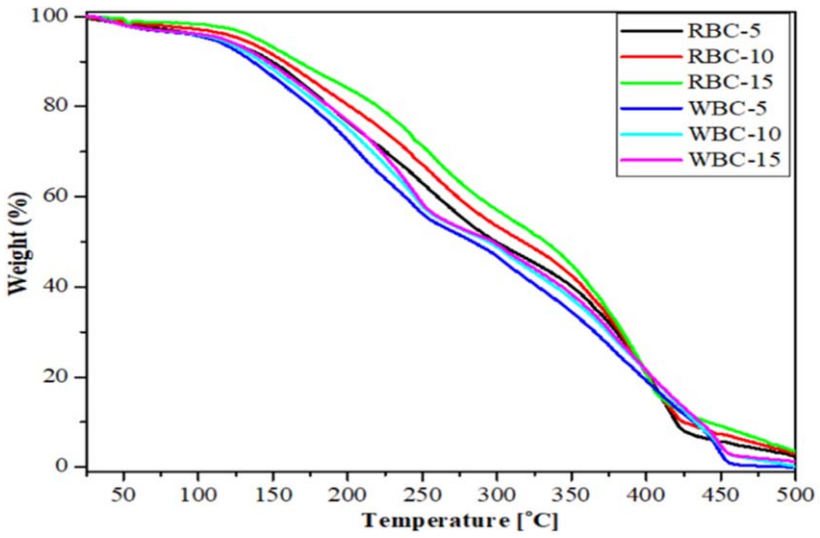

Figure 8. TGA spectrums of the biocomposites.

respectively. For 15 wt% rice husk based biocomposite (RBC-15) hardness increased by 26% and impact energy increased by 15% whereas for 15 wt% walnut shell based biocomposite (WBC-15), while an improvement of 17% and 25% were registered compared to 5 wt (RBC-5/WBC-5) reinforced biocomposites. This increase in hardness and impact energy may be due to the increased reinforcement which resulted in a highly compact structure. The compact structure resists the crack propagation/growth and hence resulting in increased mechanical properties of the composites [45].

3.4. Thermogravimetric analysis

The TGA spectrums of the evaluated biocomposites under oxygen atmosphere are presented in figure 8. The TGA spectrum of both rice husk and walnut shell based biocomposites exhibit two weight loss steps. In all biocomposites, the first weight loss occurs in the temperature range of 25 to 200 °C and related to the evaporation of water and glycerol [46]. The second weight loss occurs in the temperature range of 200 to 500 °C is due to the decomposition of the three major constituents (i.e. corn starch resin, walnut shell and rice husk) of the biocomposites. The thermal degradation of the rice husk, starch and walnut shell constituents begins above 200 °C and assigned to the degradation of hemicellulose, cellulose and lignin [47]. Starch was reported to decompose in between the temperature range of 250 °C–300 °C form levoglucose and some volatile products by molecular dehydration [48]. The path of the TGA curves corresponds to the decomposition of the starch

Table 2. TGA results of the biocomposites.

Biocomposite	Temperature at different weight loss (°C)			Ash content (AC)	Oxidation index (OI)
	T_5	T_{10}	T_{50}		
RBC-5	114	149	299	2.434	0.169
RBC-10	128	157	317	2.965	0.206
RBC-15	139	166	332	3.495	0.243
WBC-5	108	136	283	0.052	0.004
WBC-10	113	142	294	0.226	0.016
WBC-15	116	146	297	1.267	0.088

(250 °C–350 °C), hemicellulose (200 °C–300 °C), cellulose (300 °C–350 °C) and lignin (200 °C–500 °C) [17, 26, 47, 48].

One can see from table 2 that rice husk based biocomposites presented high ash content at the end of the TGA, around 2.5%–3.5% and may be related to its higher silica content [47]. Further, T_5, T_{10} and T_{50} (temperature corresponds to 5, 10 and 50% weight loss) and oxidation index (OI) of the biocomposites were determined and presented in table 2. One can see that the temperatures for 5, 10 and 50% weight loss increases noticeably with an increase in rice husk and walnut shell content. The rice husk and walnut shell raises the thermal stability of the biocomposites due to the higher thermal stability of cellulose and lignin. The ash content of the biocomposites also increased with the addition of rice husk and walnut shell content.

Furthermore, from table 2, it was found that the rice husk based biocomposites exhibits OI values lies in the range 0.169%–0.243% as compared to walnut shell based biocomposites having OI in the range of 0.004%–0.088%. These results confirmed that the addition of increased rice husk and walnut shell content enhanced the thermal stability of the corn starch based biocomposites, which was related to the good thermal stability of the cellulose and lignin [17, 47]. Moreover, the strong bonding between the reinforcement and corn starch resin also resulted in enhanced thermal stability as reported in literature [17].

4. Conclusions

Corn starch resin based biocomposites reinforced with different weight fraction (5–15 wt%) of agriculture waste (rice husk and walnut shell) have been fabricated and studied for physical, mechanical and thermal properties. The mechanical properties (tensile strength, impact energy, compressive strength, flexural strength and hardness) of the biocomposites found to increase with an increase in reinforcement. The rice husk and walnut shell reinforcement reduced the density, water absorption and improved the thermal stability of corn starch based biocomposites, especially when the reinforcement content reached 15 wt%. The degradation period of the biocomposites found to increase with the addition of rice husk and walnut shell content. Thus, based on this paper it has been concluded that agriculture waste reinforced corn starch resin based biocomposites could be utilized as an ecofriendly material in packaging and other short-life applications.

ORCID iDs

Tej Singh https://orcid.org/0000-0003-2316-4107
Brijesh Gangil https://orcid.org/0000-0002-5849-5881
Amar Patnaik https://orcid.org/0000-0001-9506-782X
Gusztáv Fekete https://orcid.org/0000-0002-6138-8382

References

[1] Hyun C K, Seongcheol M, Hyun K, Lindong Z, Abdullahil K and Jaehwan K 2016 Renewable smart materials *Smart Mater. Struct.* **25** 073001
[2] Suyi L and Wang K W 2017 Plant-inspired adaptive structures and materials for morphing and actuation: a review *Bioinsp. Biomim.* **12** 011001
[3] Sandeep K, Vinay K P, Mer K K S, Fekete G, Brijesh G and Singh T 2018 Influence of woven bast-leaf hybrid fiber on the physico-mechanical and sliding wear performance of epoxy based polymer composites *Mater. Res. Express* **5** 105705
[4] Singh T and Patnaik A 2015 Performance assessment of lapinus-aramid based brake pad hybrid phenolic composites in friction braking *Archives of Civil and Mechanical Engineering* **15** 151–61
[5] Singh T, Rathi M K, Patnaik A, Chauhan R, Ali S and Fekete G 2019 Application of waste tire rubber particles in non-asbestos organic brake friction composite materials *Mater. Res. Express* **6** 035703

[6] Banerjee A, Chatterjee K and Madras G 2014 Enzymatic degradation of polymers: a brief review *Mater. Sci. Technol.* **30** 567–73
[7] Tapan K D and Prusty S 2012 Review on conducting polymers and their applications *Polym.-Plast. Technol. Eng.* **51** 1487–500
[8] Fereshtehsadat M, Mohammadjavad E and Reza B 2018 Fabrication and characterization of a starch-based nanocomposite scaffold with highly porous and gradient structure for bone tissue engineering *Biomedical Physics & Engineering Express* **4** 055021
[9] Victor M C, Oleg A K and Valentine P A 2017 Conversion of plant biomass to furan derivatives and sustainable access to the new generation of polymers, functional materials and fuels *Russian Chemical Reviews* **86** 357
[10] Sanyang M L, Sapuan S M, Jawaid M, Ishak M R and Sahari J 2016 Development and characterization of sugar palm starch and poly (lactic acid) bilayer films *Carbohydrate Polymers* **146** 36–45
[11] Edhirej A, Sapuan S M, Jawaid M and Zahari N I 2017 Effect of various plasticizers and concentration on the physical, thermal, mechanical, and structural properties of cassava-starch-based films *Starch* **69** 1500366
[12] Yusof Y M, Shukur M F, Illias H A and Kadir M F Z 2014 Conductivity and electrical properties of corn starch-chitosan blend biopolymer electrolyte incorporated with ammonium iodide *Phys. Scr.* **89** 035701
[13] Jingyang G, Li Z, Qunyu G, Lei W and Erjuan Z 2018 A study on physicochemical properties and adsorption performance of modified porous maize starch *Mater. Res. Express* **5** 125303
[14] Jiun H L, Ghanbari T, Rahman W A W A and Majid R A 2018 Preparation and characterization of kenaf papers reinforced with tapioca starch: physicomechanical and morphological properties *Journal of Natural Fibers* **15** 191–203
[15] Khalil H P S A, Mohamad H C I C, Khairunnisa A R, Owolabi F A T, Asniza M, Samsul R, Fazita M R N and Paridah M T 2018 Development and characterization of bamboo fiber reinforced biopolymer films *Mater. Res. Express* **5** 085309
[16] Singh T, Gangil B, Patnaik A, Kumar S, Rishiraj A and Fekete G 2019 Physico-mechanical, thermal and dynamic mechanical behaviour of natural-synthetic fiber reinforced vinylester based homogenous and functionally graded composites *Mater. Res. Express* **6** 025704
[17] Peilei W, Chen F, Zhang H, Meng W, Sun Y and Liu C 2017 Large-scale preparation of jute fiber reinforced starch-based composites with high mechanical strength and optimized biodegradability *Starch* **69** 1700052
[18] Ramrirez M G L, Satyanarayna K G, Iwakiri S, Muniz G B, Tanobe V and Flores-Sahagund T S 2011 Study of the properties of biocomposites part I. cassava starch-green coir fibers from brazil *Carbohydrate Polymers* **86** 1712–22
[19] Ochi S 2006 Development of high strength biodegradable composites using Manila hemp fiber and starch-based biodegradable resin *Composites Part A: Applied Science and Manufacturing* **37** 1879–83
[20] Cheng W, Li F, Wang L, Li J, Guo A, Zhang C and Liu P 2015 Research on thermoplastic starch and different fibers reinforced biomass composites *RSC Advances* **5** 49824–30
[21] Daniele B, Bocchini S and Frache A 2016 Thermomechanical improvement of glycerol plasticized maize starch with high loading of cellulose, flax and talc fillers *Polymer International* **65** 955–62
[22] Gironès J, López J P, Mutjé P, Carvalho A J F, Curvelo A A S and Vilaseca F 2012 Natural fiber-reinforced thermoplastic starch composites obtained by melt processing *Compos. Sci. Technol.* **72** 858–63
[23] Guimarães J L, Wypych F, Saul C K, Ramos L P and Satyanarayana K G 2010 Studies of the processing and characterization of corn starch and its composites with banana and sugarcane fibers from brazil *Carbohydrate Polymers* **80** 130–8
[24] Aridi N A M, Sapuan S M, Zainudin E S and Al-Oqla F M 2016 Mechanical and morphological properties of injection-molded rice husk polypropylene composites *International Journal of Polymer Analysis and Characterization* **21** 305–13
[25] Arne S and Barrio A 2018 Fire retardancy of polypropylene composites reinforced with rice husks: from oxygen index measurements and cone calorimetry to large-scale single-burning-item tests *J. Appl. Polym. Sci.* **135** 46654
[26] Kamila S, Barczewski M, Górny R and Kloziński A 2018 Evaluation of highly filled epoxy composites modified with walnut shell waste filler *Polym. Bull.* **75** 2511–28
[27] Navin C, Fahim M, Sharma P and Bapat M N 2012 Influence of foaming agent on wear and mechanical properties of surface modified rice husk filled polyvinylchloride *Wear* **278-279** 83–6
[28] Nadir A, Kaymakci A and Ozdemir F 2013 Physical, mechanical, and thermal properties of polypropylene composites filled with walnut shell flour *Journal of Industrial and Engineering Chemistry* **19** 908–14
[29] Vinay K S 2015 Mechanical behavior of walnut (*Juglans* L) shell particles reinforced bio-composite *Science and Engineering of Composite Materials* **22** 383–90
[30] Shahryar P and Hosseinzadeh S 2018 Investigation on physico-mechanical, thermal and morphological of dipodal silane-modified walnut shell powder filled polyurethane green composites and their application for removal of heavy metal ions from water *Polym.-Plast. Technol. Eng.* **57** 1197–208
[31] Erika F, Kun D and Móczó J 2018 Thermoplastic starch/wood composites: effect of processing technology, interfacial interactions and particle characteristics. periodica polytechnica *Chem. Eng.* **62** 129–36
[32] ASTM D3039 2017 *Standard Test Method for Tensile Properties of Polymer Matrix Composite Materials* (West Conshohocken, PA: ASTM international)
[33] ASTM D3410 2016 *Standard test method for Compressive Properties of Polymer Matrix Composite Materials with Unsupported Gage Section by Shear Loading* (West Conshohocken, PA: ASTM international)
[34] ASTM D790 2017 *Standard Test Methods for Flexural Properties Of Unreinforced and Reinforced Plastics And Electrical Insulating Materials* (West Conshohocken, PA: ASTM international)
[35] ASTM D256 2018 *Standard Test Methods for Determining the Izod Pendulum Impact Resistance of Plastics* (West Conshohocken, PA: ASTM international)
[36] ASTM E384 2017 *Standard Test Method for Microindentation Hardness of Materials* (West Conshohocken, PA: ASTM international)
[37] ASTM D570-98 2018 *Standard Test Method for Water Absorption of Plastics* (West Conshohocken, PA: ASTM international)
[38] Singh T, Patnaik A and Gangil B 2016 Thermal stability analysis of nano particulate filled phenolic based friction composite materials *Journal of Industrial Textile* **45** 1335–49
[39] Ibrahim H, Farag M, Megahed H and Mehanny S 2014 Characteristics of starch-based biodegradable composites reinforced with date palm and flax fibers *Carbohydrate Polymers* **101** 11–9
[40] Hietala M, Mathew A P and Oksman K 2013 Bionanocomposites of thermoplastic starch and cellulose nanofibers manufactured using twin-screw extrusion *Eur. Polym. J.* **49** 950–6
[41] Anglès M N and Dufresne A 2000 Plasticized starch/tunicin whiskers nanocomposites. 1 *Structural analysis. Macromolecules* **33** 8344–53
[42] Oromiehie A R, lari T T and Rabiee A 2013 Physical and thermal mechanical properties of corn starch/LDPE composites *J. Appl. Polym. Sci.* **127** 1128–34
[43] Lu Y, Weng L and Cao X 2006 Morphological, thermal and mechanical properties of ramie crystallites-reinforced plasticized starch biocomposites *Carbohydrate Polymers* **63** 198–204

[44] Guleria A, Singha A S and Rana R K 2017 Preparation of starch based biocomposites reinforced with mercerized lignocellulosic fibers-evaluation of their thermal, morphological, mechanical and biodegradable properties *International Journal of Polymer Analysis and Characterization* **22** 595–609
[45] Kamarudin S H, Abdullah L C, Aung M M, Ratnam C T and Talib E R J 2018 A study of mechanical and morphological properties of PLA based biocomposites prepared with EJO vegetable oil based plasticiser and kenaf fibres *Mater. Res. Express* **5** 085314
[46] Mendes J F, Paschoalin R T, Carmona V B, Neto A R S, Marques A C P, Marconcini J M, Mattoso L H C, Medeiros E S and Oliveira J E 2016 Biodegradable polymer blends based on corn starch and thermoplastic chitosan processed by extrusion *Carbohydrate Polymers* **137** 452–8
[47] Kim H S, Kim S, Kim H J and Yang H S 2006 Thermal properties of bio-flour-filled polyolefin composites with different compatibilizing agent type and content *Thermochimica Acta* **451** 181–8
[48] Xia L, Wenyuan G, Qianqian J, Luqi H and Changxiao L 2011 Study on the morphology, crystalline structure, and thermal properties of Fritillaria ussuriensis maxim. starch acetates with different degrees of substitution *Starch* **63** 24–31

Science of Sintering, **51** (2019) 421-428

doi:https://doi.org/10.2298/SOS1904421K

UDK: 621.315.612; 622.785; 665.035.8

Sintering Effect on Electrical Properties and Morphology of Lead-Free $Na_{0.92}K_{0.08}NbO_3$ Ceramics

Gambheer Singh Kathait[1*)], N. S. Panwar[1], Prashant Thapliyal[1], Don Biswas[1], Vishal Rohilla[1], Surendra Singh[2]

[1]Deptt. of Instrumentation Engg.-USIC, H.N.B. Garhwal University, Srinagar Garhwal, Uttarakhand, India

[2]Department of Physics, H.N.B. Garhwal University, Srinagar Garhwal, Uttarakhand, India

Abstract:

Sodium potassium niobate (NKN) powders were synthesized by the solid-state reaction method. The NKN ceramics for composition $Na_{0.92}K_{0.08}NbO_3$ (NKN) were then fabricated by a two-step sintering technique. The effects of the two-step sintering on the properties of the ceramics were investigated. The pure phase NKN was achieved for all sintering temperatures of 1100, 1150, 1200 and 1250 ^oC. The observed change in the microstructure indicates that the grain size increases with the increasing sintering temperatures. Also, the two-step sintering technique produced a higher value of K/(K+Na) weight-% ratio and peak dielectric constant for sintering temperatures 1100, 1150 and 1200 ^oC. However, further increasing of the sintering temperatures at 1250 ^oC, reduces the K/(K+Na) weight-% ratio and the peak dielectric constant (εc).

Keywords*: Two-step sintering; K/(K+Na) weight-% ratio; Dielectric properties and Grain size.*

1. Introduction

Considering a wide range of applications in the area of sensors, actuators, and transducers related to all domains of science and engineering, ferroelectric materials are an important group of functional materials [1]. Perovskite (having ABO_3 structure) type ferroelectrics are the most typical displacive ferroelectrics, e.g., $BaTiO_3$, $KNbO_3$, $PbTiO_3$, $KTiO_3$, $PbZrO_3$, $LiNbO_3$, $LiTaO_3$, etc. [2,3]. The ABO_3 type compounds have excellent dielectric, ferroelectric, optical and piezoelectric properties, which have attracted considerable attention of researchers worldwide due to their broad range of technical applications [4-6]. In the ABO_3 type structure, the cations are based on the valence states and coordination number and occupy A or B sites. The A sites are generally occupied by the lower valency ions [7, 8] and the B sites are occupied by the high valency cations [7-10]. Materials that are composed of lead (Pb) in any form, are the most typical perovskites, such as $Pb(Mg_{1/3}Nb_{2/3})O_3$, $Pb(ZrTi)O_3$, $PbTiO_3$, and $Pb(Zn_{1/3}Nb_{2/3})O_3$–$PbTiO_3$, are the most widely used materials in industry [11-14]. From the previous studies, it is evident that the excellent dielectric properties of Pb based materials are related to the morphotropic phase boundary between orthorhombic, tetragonal or monoclinic phases [15-17]. However, considering the environmental and health concerns since lead (Pb) containing ceramics are toxic and evaporates during the sintering process, these ceramics need to be replaced. Therefore,

*) **Corresponding author:** gambhir11186@gmail.com

worldwide extensive research has been directed to achieve a lead-free piezoelectric material, which will result in less hazardous production methods and will be recyclable in nature. A solid solution of ferroelectric in nature $KNbO_3$ and anti-ferroelectric $NaNbO_3$ shows high piezoelectric and dielectric properties. The $Na_{0.5}K_{0.5}NbO_3$ (NKN) ceramics are one of the most versatile and promising candidate materials for lead-free piezoelectric ceramics because of its high piezoelectric, dielectric properties and Curie temperature (Tc) [18-21]. There are a number of approaches that have been used to obtain the $Na_{0.5}K_{0.5}NbO_3$ (NKN) powders [22-24]. The conventional mixed-oxide method has often been used to synthesize NKN powders. Apart from this method, many other chemical routes, such as the sol-gel process, hydrothermal and co-precipitate method, have been proposed for producing the fine NKN powders, but from the cost point of view, the raw materials of these methods are quite expensive. Further, it is proven that for many ceramics, the piezoelectric and dielectric properties are influenced by the grinding process and technique of sintering. Therefore, various techniques have been reported such as rapid-rate sintering, rate-controlled sintering, and two-step sintering [25-27]. Among these methods, the two-step sintering method is interesting because it can achieve a high ceramic density and produces small grains with a low rate of grain growth [25-27].

In the present work, the two-step sintering technique was applied to synthesize the NKN powder and ceramics, respectively. The characteristics of synthesized NKN ceramics were investigated. Also, for different sintering temperatures, the effect of the two-step sintering process on the ceramic properties was investigated.

2. Materials and Experimental Procedures

In the present study, $Na_{0.92}K_{0.08}NbO_3$ (NKN) ceramic powder was synthesized by the solid-state reaction method. The calculated molar ratio of inorganic mixtures, Na_2CO_3 (99.5 %, Sigma-Aldrich), K_2CO_3 (99.5 %, Sigma-Aldrich) and Nb_2O_5 (99.9 %, Sigma-Aldrich) was mixed by hand-grinding for 6 h. The stoichiometric amounts of K_2CO_3, Na_2CO_3 and Nb_2O_5 were weighed according to the chemical formula of $Na_{0.92}K_{0.08}NbO_3$ (NKN). The weighed oxides were mixed by manual grinding in acetone for 2 h (wet grinding) and without acetone for 4 h (dry grinding). The well-grinded powders were calcined at 900 ^oC for 4 h. After calcination, the obtained powders were taken for XRD analysis. Phase formation of the calcined powders was determined by XRD analysis, using X-Pert PANalytical diffractometer, having a fixed divergence$1/2^o$ slit, a Cu W/Si mirror, solar slit, and a 10 mm mask as incident optics and a parallel plate collimator, a solar slit and a proportional detector as diffracted beam optics. The calcined powders were pressed into disc shape pellets (samples) of 8 mm diameter. For the two-step sintering, the samples were sintered first at 1100, 1150, 1200 and 1250 ^oC for 4 h separately. The sintered pellets were ground again to form a fine powder. From the powder, disc shape pellets (samples) of 8 mm diameter were prepared again. These samples were again sintered at 1100, 1150, 1200 and 1250 ^oC for 4 h. The particle morphology was examined by scanning electron microscopy (SEM) using model EVO 18 Special Edition (Switzerland), manufactured by ZEISS. For the dielectric investigation, the silver paste was painted on both sides of the samples. Dielectric measurements were carried out by using an LCR meter (make: Fluke, model: PM6306) in conjunction with a furnace.

3. Results and Discussion

In the present work, the two-step sintering method was applied for fabrication of the NKN ceramics, i.e. the sample was first sintered at 1100, 1150, 1200 and 1250 ^oC for 4 h and again sintered at 1100, 1150, 1200 and 1250 ^oC for 4 h, followed by cooling to room

temperature. Crystallinity is determined by using an X-RAY diffractometer (XPERT-PRO) with a CuKα radiation source (λ=1.54059 Å), operated at a voltage of 45 kV and a current of 40 mA. The XRD patterns of the NKN ceramics sintered by the two-step sintering method are shown in Fig. 1. It can be observed from the figure, that the diffraction peaks are (0 1 2), (1 1 0), (0 2 4), (1 2 2), (3 0 0) and (2 2 0) within the 2θ range from 20° to 70°. The XRD results are consistent with the work done by Fisher et al. [28] who synthesized NKN by a solid-state technique. It is evident that all compositions showed pure perovskite phases with orthorhombic symmetry. No secondary phases could be found due to the application of sintering aids. Also, the diffraction angles had not changed, indicating that the lattice constant had changed very little [29].

Tab. I Lattice parameter of $Na_{0.92}K_{0.08}NbO_3$ ceramic for different sintering temperatures.

Sintering temperatures (°C)	a (Å)	c (Å)	a/c	**Structure phase**
T = 1100	7.8985	8.0085	1.0139	Orthorhombic
T = 1150	7.7766	8.0422	1.0341	Orthorhombic
T = 1200	7.7684	8.0450	1.0356	Orthorhombic
T = 1250	7.7582	8.0353	1.0357	Orthorhombic

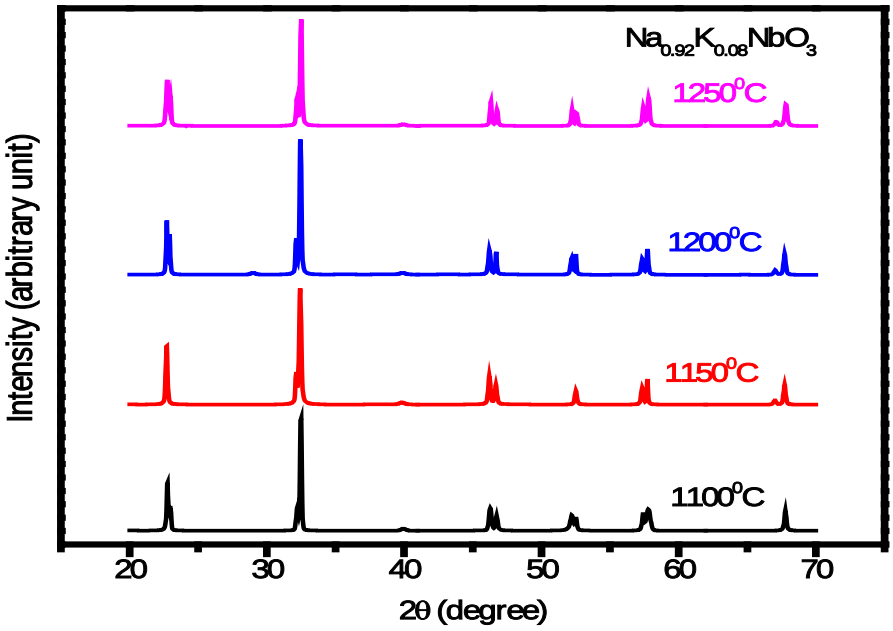

Fig. 1. XRD patterns of $Na_{0.92}$ $K_{0.08}NbO_3$ for different sintering temperatures.

Tab. I depicts that the c/a ratio is smaller than 1 (the c-axis lattice constant is smaller than the a-axis lattice constant). The analysis indicates that the crystalline structure is orthorhombic according to the JCPDF file No. 01-073-6542 at room temperature, for different sintering temperatures. Fig. 2 (a) indicates that c/a ratio and the grain size increases with sintering temperatures.

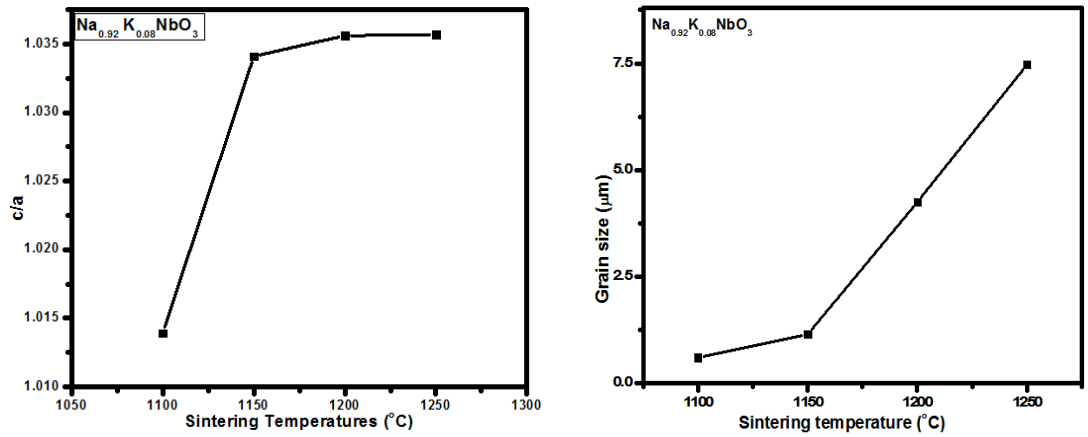

Fig. 2. Variation of (a) c/a and (b) grain size with sintering temperatures.

Morphology of $Na_{0.92}$ $K_{0.08}NbO_3$ ceramics with sintering temperature 1100, 1150, 1200 and 1250 ^oC are displayed in Fig. 3. With increasing sintering temperatures, a change in grain size was observed. The average grain size of the samples was in a range of ≃0.6μm to 7μm. Grain size increases with increasing the sintering temperature. At 1250 ^oC, it seems as if the grain melts, which results in the lowering of the dielectric constant at higher temperatures. This result suggests that the sintering temperatures have a strong effect on the microstructure of the NKN ceramics.

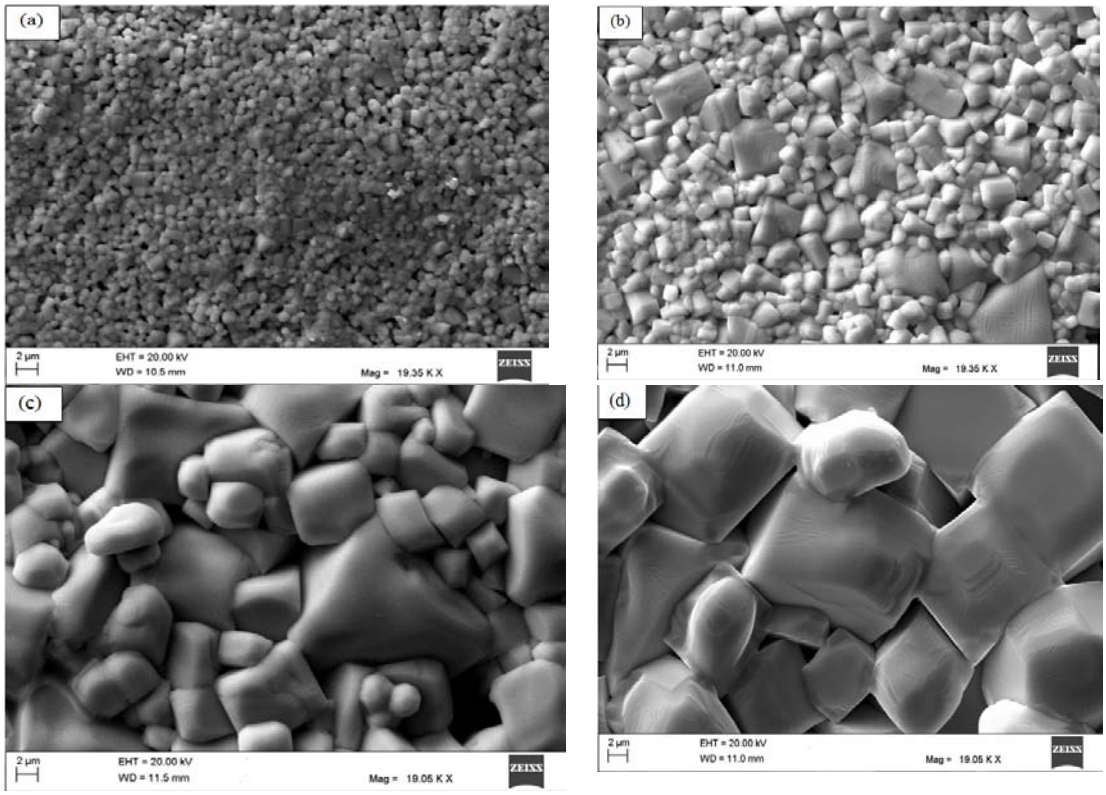

Fig. 3. Selected SEM micrographs of NKN ceramics fabricated by the two-step sintering with different sintering temperatures: (a) 1100^{o}C (b) 1150^{o}C (c) 1200^{o}C and (d) 1250^{o}C.

Tab. II SEM-EDAX quantitative analysis of $Na_{0.92}K_{0.08}NbO_3$ for sintering temperatures 1100, 1150, 1200 and 1250^oC.

Elements	**Sintering Temp. 1100 ^oC**		**Sintering Temp. 1150 ^oC**		**Sintering Temp. 1200 ^oC**		**Sintering Temp. 1250 ^oC**	
	Atomic%		Atomic%		Atomic%		Atomic%	
	Obs.	Cal.	Obs.	Cal.	Obs.	Cal.	Obs.	Cal.
O	66.86	60	63.97	60	65.77	60	66.29	60
Na	15.04	18.4	15.62	18.4	14.56	18.4	15.06	18.4
K	1.08	1.6	1.18	1.6	1.12	1.6	0.76	1.6
Nb	17.02	20	19.23	20	18.55	20	17.89	20
Escaping of Na & K	3.88		3.2		4.32		4.18	

Tab. II represents the SEM-EDAX quantitative analysis of $Na_{0.92}K_{0.08}NbO_3$ for different sintering temperatures. The K/(K+Na) weight-% ratio and peak dielectric constant (ϵ_c), increases with sintering temperature 1100, 1150 and 1200 ^oC. Further, the sintering of $Na_{0.92}K_{0.08}NbO_3$ ceramics at 1250 ^oC, as shown in Tab. III, results in lowering of both K/(K+Na) weight-% ratio and peak dielectric constant (ϵ_c).

Tab. III SEM-EDAX quantitative analysis of $Na_{0.92}K_{0.08}NbO_3$ for sintering temperatures 1100, 1150, 120 and 1250 ^oC. K/(K+Na) weight-% ratio and peak dielectric constant (ϵ_c) and Curie temperature (T_c).

Sintering temperatures (^oC)	**K/(K+Na) weight-% ratio**	**Peak dielectric constant**	**Curie temperature (^oC)**
T = 1100	10.884	1070.242	405
T = 1150	11.349	2613.234	405
T = 1200	11.583	3172.335	405
T = 1250	7.907	1459.098	400

As shown in Tab. III, the dielectric constant follows the K/(K+Na) weight-% ratio; however the transition temperature is nearly constant and it, seems independent of the sintering temperature. Fig. 4 indicates the variation of the dielectric constant for different sintering temperatures. Fig. 4 (a) and (b) indicate the value of dielectric constant and the dielectric loss tangent for different sintering temperatures and frequencies, respectively. Fig. 4(c) illustrates the dielectric constant at the room temperature and escaping of Na & K (%) of $Na_{0.92}K_{0.08}NbO_3$ ceramics for different sintering temperatures. From the Tab. III, it seems that the K/(K+Na) weight-% ratio has a great impact on the dielectric constant. A high value of the dielectric constant (ϵ_c= 3172.335), at Curie temperature, is investigated for a large K/(K+Na) weight-% ratio. Fig. 4(d) illustrate that at the room temperature, the dielectric constant and the grain size for ceramics sintered at 1150, 1200 and 1250 ^oC follow each other. With increasing the sintering temperature, pure NKN ceramics have the drawback of evaporation of alkali metal ions (K and Na) during sintering and exhibit inferior performance, as shown in Fig. 4 (a), in comparison with Pb based materials.

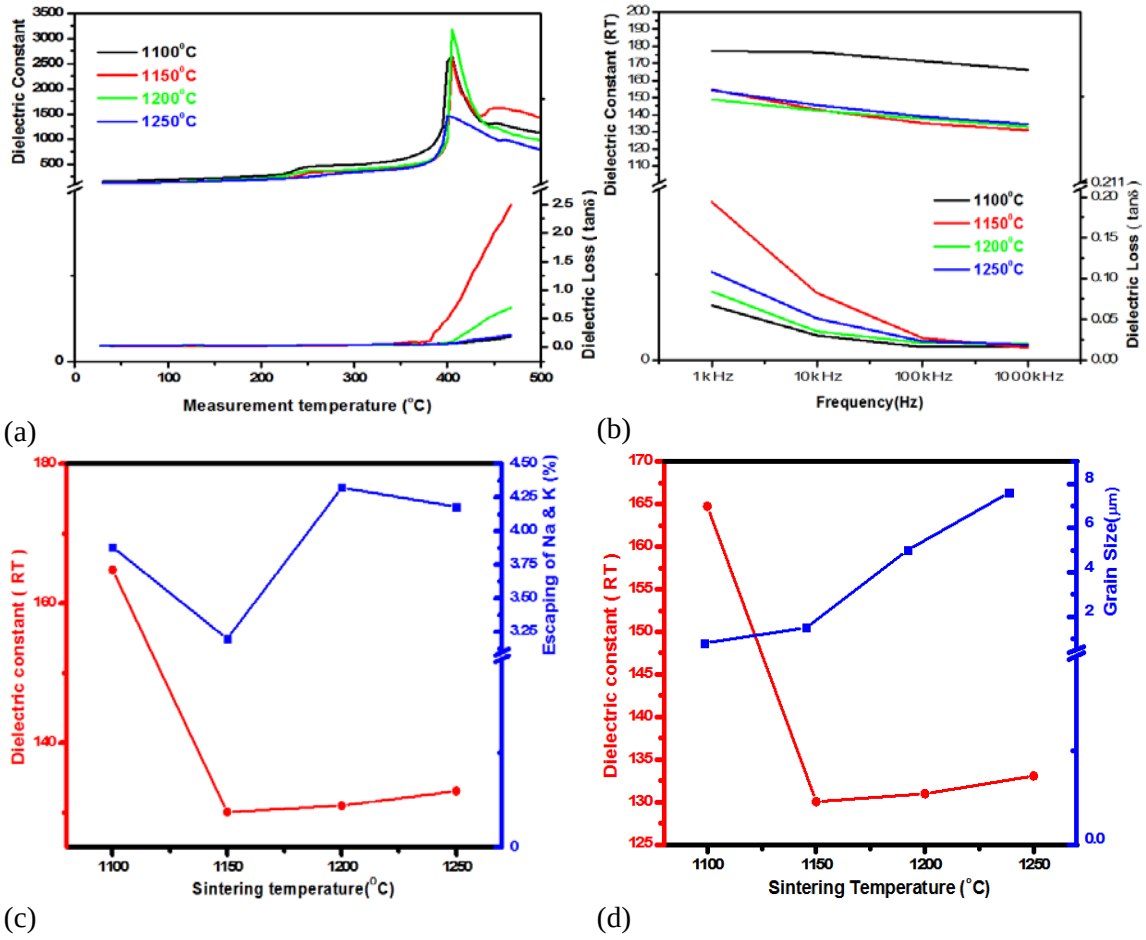

Fig. 4. (a) Dielectric constant and dielectric loss tangent versus measurement temperature of the sample; (b) dielectric constant and dielectric loss tangent versus frequency (the sample is at room temperature, RT); (c) dielectric constant and escaping of Na & K versus sintering temperature; and (d) dielectric constant and grain size versus sintering temperature. For the graphs (c) and (d), the sample is at room temperature and frequency is 1000 kHz.

4. Conclusion

$Na_{0.92}K_{0.08}NbO_3$ ceramics were synthesized by a two-step sintering process at different sintering temperatures and their dielectric properties and morphology were analyzed. The XRD pattern of NKN ceramics reveals the formation of a pure perovskite phase. The c/a ratio was found dependent on the grain size, and the grain size was found dependent on the sintering temperature. Analyzing the K/(K+Na) weight-% ratio, it was found that the dielectric property is highly dependent on the K/(K+Na) weight-% ratio. At a high sintering temperature (1250 °C), the low K/(K+Na) weight-% ratio, due to the evaporation of alkali metal ions (K and Na), lowers the dielectric constant.

Acknowledgments

The authors are thankful to the Department of Instrumentation Engineering-USIC, SOET, HNB Garhwal University, Srinagar (Garhwal), for providing laboratory facilities.

5. References

1. Setter, N. Piezoelectric Materials in Devices; EPFL Swiss Federal Institute of Technology: Lausanne, Switzerland, 2002.
2. H. Nagta, N. Chikoshi, T. Takenaka, Japanese Journal of Applied Physics, 38 (1999) 5497-5499.
3. Z. B. Vosika, V. V. Mitić, G. M. Lazović, Lj. Kocić, Science of Sintering, 49 (2017) 469-477.
4. G. A Samara, Ferroelectrics, 73 (1987)145-159.
5. Mathias, B.T., Phy Rev., 75 (1949)1771.
6. Y. Lu, D. Y. Jeong, Z. Y. Cheng, Q. M. Zhang, H. S. Luo, Z. W. Yin, and D. Viehland, Appl. Phys. Lett., 78 (2001) 109-11.
7. S. E. Park and T. R. Shrout, J. Appl. Phys., 82 (1997) 1804-11.
8. Mathias, B.T., Physical Review Journal Archive, 75 (1949)1771.
9. M, B.T., Remeika, Physical Review Journal Archive,82 (1951)727.
10. Wood, E.A., Act. Cryst.,04 (1955)353.
11. G. Shirane, R. Newnham, Phys. Rev., 96 (1954) 581.
12. B. Jaffe, W. R. Cook, and H. Jaffe, Piezoelectric Ceramics. Academic Press, New York, 1971.
13. Y. Lu, D. Y. Jeong, Z. Y. Cheng, Q. M. Zhang, H. S. Luo, Z. W. Yin, and D. Viehland, Appl. Phys. Lett., 78 (2001) 3109-11.
14. W. Ren, S. F. Liu, and B. K. Mukherjee, Appl. Phys. Lett., 80 (2002) 3174-6.
15. R. Guo, L. E. Cross, S. E. Park, B. Noheda, D. E. Cox, and G. Shirane, Phys. Rev. Lett., 84 (2000) 5423-6.
16. J. M. Kiat, Y. Uesu, B. Dkhil, M. Matsuda, C. Malibert, and G. Calvarin, Phys. Rev., 65 (2002) 064106.
17. K. Singh and D. Pandey, Phys. Rev., 67(2003) 064102-1–12.
18. G. Shirane, R. Newnham, and R. Pepinsky, Phys. Rev.,96 (1954) 581.
19. L. Egerton and D. M. Dillon, J. Am. Ceram. Soc., 42 (1959) 438.
20. R. E. Jaeger and L. Egerton, J. Am. Ceram. Soc., 45(1962) 209.
21. G. H. Haertling, J. Am. Ceram. Soc., 50 (1967) 329.
22. Y Saito., and H. Takao, J. Euro. Ceram. Soc.,27 (2007) 4085-4092.
23. C.-H. Lu, S.-Y. Lo, and H.-C. Lin. Mater. Lett.,34 (1998) 172-176.
24. C.-H. Lu, S.-Y. Lo, and Y. L. Wang. Mater. Lett.,55 (2002) 121-125.
25. X.-H.Wang, X.-Y. Deng, H. Zhou, L.-T. Li, and I.-W. Chen. J. Electroceram.,21 (2008) 230-233.
26. Narumon Lartcumfu, Chatchai Kruea-In, Nattaya Tawichai, And Gobwute Rujijanagul, Ferroelectrics, 456 (2013) 14-20,
27. S. E. Porozova, A. A. Gurov, M. N. Kachenuk, A. A. Smetkin, O. Yu. Kamenschikov, Science of Sintering,49 (2017) 99-105.
28. J. G. Fisher, D. Rout, K.-S. Moon, and S.-J. L. Kang. Mater. Chem. Phys., 120 (2010) 263-271.
29. Ruzhong Zuow, Jurgen Rodel, Renzheng Chen and Longtu Li, J. Am. Ceram. Soc., 89 (2006) 2010-2015.

Садржај: *Прах натријум калијум ниобата (НКН) је синтетисан реакцијом у чврстом стању. НКН керамике састава* $Na_{0.92}K_{0.08}NbO_3$ *су добијене након двостепеног синтеровања. Испитиван је утицај двостепеног синтеровања на својства керамике. Чиста фаза НКН је постигнута на свим температурама синтеровања 1100, 1150, 1200 и 1250* ^oC*. Промене уочене у микроструктури указују на раст зрна са порастом температуре синтеровања. Такође, двостепено синтеровање утиче на повећање*

тежинског односа K/(K+Na) и даје максимум диелетричне константе за температуре синтеровања 1100, 1150 и 1200 °C. Ипак, даљи раст температуре синтеровања од 1250 °C, смањује однос K/(K+Na) и диелектричну константу (єс).
***Кључне речи**: двостепено синтеровање, K/(K+Na) тежински однос, диелектрична својства, раст зрна.*

© 2018 Authors. Published by the International Institute for the Science of Sintering. This article is an open access article distributed under the terms and conditions of the Creative Commons — Attribution 4.0 International license (https://creativecommons.org/licenses/by/4.0/).

Taylor & Francis
Taylor & Francis Group

Phase Transitions
A Multinational Journal

ISSN: 0141-1594 (Print) 1029-0338 (Online) Journal homepage: http://www.tandfonline.com/loi/gpht20

Structural and dielectric anomaly in $Na_{1-x}K_xNbO_3$, at $x = 0.315$

Jyotsana Negi, Surendra Singh & N. S. Panwar

To cite this article: Jyotsana Negi, Surendra Singh & N. S. Panwar (2019): Structural and dielectric anomaly in $Na_{1-x}K_xNbO_3$, at $x=0.315$, Phase Transitions

To link to this article: https://doi.org/10.1080/01411594.2018.1563789

Published online: 03 Jan 2019.

Submit your article to this journal

View Crossmark data

Full Terms & Conditions of access and use can be found at
http://www.tandfonline.com/action/journalInformation?journalCode=gpht20

PHASE TRANSITIONS
https://doi.org/10.1080/01411594.2018.1563789

Taylor & Francis
Taylor & Francis Group

Check for updates

Structural and dielectric anomaly in $Na_{1-X}K_xNbO_3$, at $x = 0.315$

Jyotsana Negi[a], Surendra Singh[a] and N. S. Panwar[b]

[a]Department of Physics, HNB Garhwal University, Srinagar, India; [b]University Science Instrumentation Centre, HNB Garhwal University, Srinagar, India

ABSTRACT

Structural and dielectric properties of sodium-potassium niobate ($Na_{1-x}K_xNbO_3$) ($0.250 \leq x \leq 0.350$) ceramics, prepared by the solid-state reaction method were investigated. Observed dielectric properties show a strong compositional dependence, at all the measured temperatures (from room temperature to 150°C) and frequencies (from 1 to 1000 kHz). In the prepared compositions, the lowest values of dielectric permittivity, loss tangent and electrical conductivity were found, and an anomaly in the shifting pattern of X-ray diffraction (XRD) peaks and change in the slope of *a/c* vs. *x* plot were observed at $x = 0.315$. The observed structural and dielectric anomaly gives a morphotropic phase boundary-like indication, in $Na_{1-x}K_xNbO_3$ system, at $x = 0.315$.

ARTICLE HISTORY
Received 28 August 2018
Accepted 20 December 2018

KEYWORDS
Ferroelectrics; solid-state reaction

1. Introduction

ABO_3-type perovskite alkali metal niobates constitute an important group of oxides having technologically important ferroelectric and piezoelectric properties [1,2]. In the search of finding a suitable replacement of lead zirconium titanate (PZT), sodium-potassium niobate ($Na_{1-x}K_xNbO_3$) has attracted considerable attention [1]. Properties of the $Na_{1-x}K_xNbO_3$ system vary with varying composition (x), showing phase boundary at certain x, where the system shows anomalous behavior. Tennery and Hang [3] observed such phase boundary at $x = 0.475$, 0.325 and 0.175. Ahtee and Glazer [4] have reported three phase boundaries near $x = 0.18$, 0.32 and 0.50. Lingwal and Panwar [5] have observed the anomalous dielectric behavior for the compositions with $x = 0.1$, 0.3 and 0.5. Kandari et al have reported the dielectric and structural anomaly near $x = 0.175$ [6], 0.32 [7] and 0.475 [8] in this system. These phase boundaries attract considerable attention in the fashion of a particular phase boundary in $PbZr_{1-x}Ti_xO_3$ (PZT). In PZT, symmetry changes abruptly from rhombohedral to tetragonal, at $x = 0.48$, and the boundary remains approximately temperature independent, and is termed as morphotropic phase boundary (MPB) [9]. The MPB is explicitly different from the usual phase boundary, which may normally be temperature dependent. Piezoelectric properties of lead zirconium titanate (PZT) enhance in the vicinity of MPB. Among many alternatives, due to their relatively good ferroelectric properties, high Curie temperature (T_c), and high electromechanical coupling coefficient [10–12], sodium-potassium niobate ($Na_{1-x}K_xNbO_3$) based piezoelectric ceramics have possible potential to replace the lead-based ceramics. Therefore, it is natural to investigate such phase boundaries that show MPB-like behavior. Considerable studies have been carried out in the $Na_{1-x}K_xNbO_3$ system near $x = 0.5$ composition with various extra dopants to enhance piezoelectric properties, which is termed as polymorphic phase transition (PPT), where those extra dopants cause the change in the unit cell shape [13–16]. The piezoelectric constants of $Na_{1-x}K_xNbO_3$ ($x = 0.50$) and PZT ($x = 0.48$) are of the same order [9,10], and by appropriate doping, the value of the

CONTACT Jyotsana Negi jyotsana.jn42@gmail.com
© 2019 Informa UK Limited, trading as Taylor & Francis Group

piezoelectric coefficient may be significantly increased in both materials [13], which indicates the potential of $Na_{1-x}K_xNbO_3$ to replace PZT. NKN possessing three phase boundaries, near $x = 0.50$, 0.32, and 0.175, may be advantageous. Though the compositions near $x = 0.50$ have been extensively studied, a little attention has been paid for the compositions near $x = 0.30$ or 0.175. Baker et al. [17] determined the structure of perovskite $Na_{1-x}K_xNbO_3$, in the region of $0.24 < x < 0.36$ phase boundary by high resolution X-ray and neutron powder diffraction and found no significant structural change in this region, whereas Glazer and Ahtee found the transition from L to K phase at $x = 0.32$ [7]. Though no first order structural change with composition was observed, the anomalous physical and dielectric properties at these phase boundaries exhibit MPB-like behavior. Using neutron powder diffraction data Zhang et al. [18] observed increased octahedral strain in $Na_{1-x}K_xNbO_3$ ($x = 0.30$), when the material approached to rhombohedral-monoclinic phase boundary, similar to the behavior of PZT on approaching MPB.

Though there is controversy about the true nature of the MPB, even in the PZT [19–21], this technologically important behavior stimulates interest to investigate the electrical properties of ferro-ceramic solid solutions, near such compositions. To study the structural and dielectric behavior, solid solutions of sodium-potassium niobate ($Na_{1-x}K_xNbO_3$) were prepared with the solid-state reaction method, in the composition range $0.250 \leq x \leq 0.350$. The current compositions (x-values) were quite close to each other, much closer than those reported in previous works [8,22], so that composition showing anomalous behavior could be determined more precisely. The structure of the prepared samples was studied and determined using the X-ray diffraction (XRD) method. Dielectric properties of the prepared ceramic samples were measured in the frequency range from 1 to 1000 kHz, and temperature range from room temperature (RT) to 150°C. The observed anomaly in structural and dielectric behavior gives an indication of existence of MPB- like boundary, in $Na_{1-x}K_xNbO_3$ system, at $x = 0.315$.

2. Experimental procedure

Pellet samples of $Na_{1-x}K_xNbO_3$ ($0.250 \leq x \leq 0.350$) were prepared by the solid-state reaction method. Detail of the preparation and characterization procedure has been described in our previous communication [23]. Pellets with $x = 0.250$, 0.300, 0.310, 0.315, 0.320, 0.325, 0.330 and 0.350 were sintered, each composition for 4 h in the order of their melting points at 1170°C, 1165°C, 1160°C, 1156°C, 1152°C, 1150°C, 1148°C and 1145°C, respectively. The crystal structure of the sintered samples was examined using an X-ray diffractometer (PANalytical X'PERT PRO) with Cu K_α radiation (wavelength, $\lambda = 1.540598$ Å). Surface morphology, grain size and energy-dispersive X-ray analysis (EDAX) of the prepared pellets were studied using a scanning electron microscope (CARL ZEISS, MA15/EVO18). For dielectric measurements sintered pellets were electroded using air drying silver paste in parallel-plate capacitor configuration. Temperature, frequency and composition ($0.250 \leq x \leq 0.350$) dependences of dielectric permittivity (ε), loss tangent ($\tan \delta$) and electrical conductivity (σ) of the prepared samples are measured in the metal–insulator–metal configuration using an RCL meter (Fluke – PM6306); and a temperature controller having an accuracy of ± 1°C.

3. Results and discussion

Figure 1(a) presents the observed XRD patterns of the prepared $Na_{1-x}K_xNbO_3$ ($0.250 \leq x \leq 0.350$) pellet samples. Peak indexing was done with the help of Inorganic Crystal Structure Database (ICSD) [24]. The X-ray patterns of the prepared samples show polycrystalline behavior and were consistent with the ICSD (code 00-061-0310) data of $Na_{1-x}K_xNbO_3$, with peaks corresponding to (100), (010), (110), etc., showing monoclinic symmetry. For the prepared compositions ($0.250 \leq x \leq 0.350$), a gradual shifting of the prominent peaks was observed with varying x, Figure 1(b). For the compositions with $x \leq 0.315$, these peaks were observed to be shifted to higher angles, whereas for the compositions with $x > 0.315$, peaks shifting pattern was reversed, shifting to lower angle with increasing

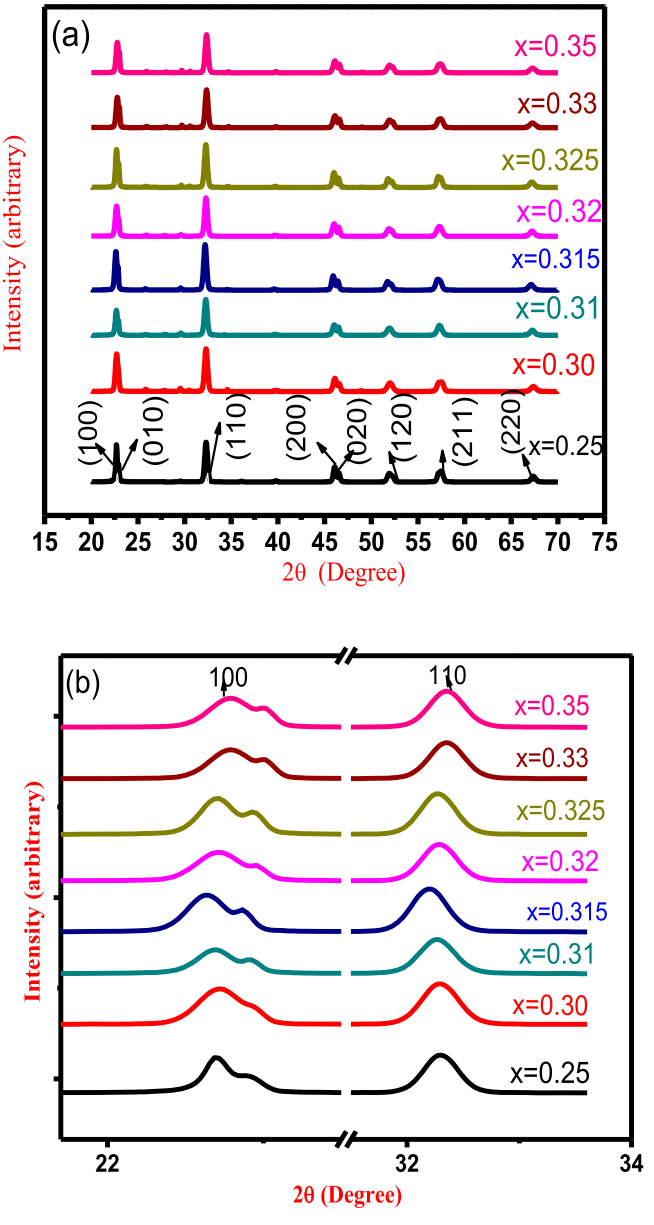

Figure 1. (a) XRD patterns for $Na_{1-x}K_xNbO_3$ ($0.250 \leq x \leq 0.350$) samples and (b) shifting of most intense peaks with composition (x).

x, indicating a break in the peak shifting pattern, at $x = 0.315$. A similar break in the peak shifting tendency was observed in $Na_{1-x}K_xNbO_3$, near the compositions with $x = 0.175$ and 0.475 [25,26]. Table 1 shows the lattice parameters of $Na_{1-x}K_xNbO_3$ for different x values. The cell parameters were refined by High Score Plus software [23,24]. The monoclinic Pm6 space group was chosen in these refinements. Values of calculated subcell parameters agree well with the reported results [3,27]. The observed variation of the a/c ratio with composition (x) is given in Figure 2. The slope of the a/c vs. x plot changes from positive to negative at the composition with $x = 0.315$, which confirms a structural anomaly at this composition. The observed energy-dispersive X-ray analysis (EDAX) results show significant escaping of alkali (Na and K) ions in the sintered pellets

Table 1. Lattice parameters of $Na_{1-x}K_xNbO_3$ for different x values.

Composition	Lattice parameters		
	a (Å)	b (Å)	c (Å)
$Na_{0.75}K_{0.25}NbO_3$	3.98	3.922	3.963
$Na_{0.70}K_{0.30}NbO_3$	3.97	3.913	3.949
	3.912	3.876	3.912 Ref. [3]
	3.915	3.8798	3.915 Ref. [27]
$Na_{0.69}K_{0.31}NbO_3$	3.976	3. 921	3.956
$Na_{0.685}K_{0.315}NbO_3$	3.967	3.915	3.952
$Na_{0.68}K_{0.32}NbO_3$	3.981	3.924	3.965
$Na_{0.675}K_{0.325}NbO_3$	3.981	3.924	3.965
$Na_{0.67}K_{0.33}NbO_3$	3.989	3.923	3.96
$Na_{0.65}K_{0.35}NbO_3$	3.984	3.923	3.959

with a lowest for the composition with $x = 0.325$ and the highest for $x = 0.310$, Table 2 and Figure 3. Variation of the grain size and density with composition is shown in Figure 4(a). The average grain sizes in the prepared pellets were observed to increase from 3.13 μm (for $x = 0.320$) and 5.4 μm (for $x = 0.250$); and the density increases 3.2 gm/cm^3 (for $x = 0.320$) and 3.8 g/cm^3 (for $x = 0.310$).

At room temperature (RT), the observed composition ($0.250 \leq x \leq 0.350$) dependence of the dielectric permittivity (ε) and loss tangent (tan δ) is shown in Figure 4(b) at different frequencies. The porosity and grain size greatly affect the dielectric properties of the samples [28]. The grain size dependent properties of ferroelectrics may be explained by the series dielectric mixing model [29], in which the decreasing dielectric permittivity with increasing grain size (>2 μm) can be understood in terms of the orientational average of the anisotropic dielectric constant of free single crystal. With this supposition the observed dielectric permittivity should decrease gradually with increasing grain size (>2 μm). The dielectric permittivity with porosity correction [30] is also shown in Figure 4 (c), which indicates that the dielectric permittivity of the prepared samples depends first of all on the composition and not on porosity or grain size. The correction of porosity was made in accordance with the guidelines presented in the paper [30]. The observed frequency dependence of dielectric

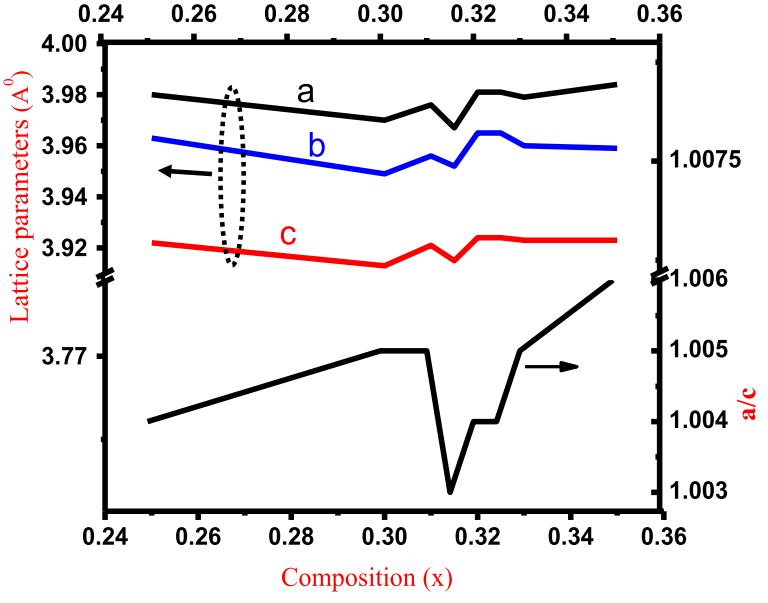

Figure 2. Variation of lattice parameters and *a/c* (ratio of lattice parameters, *a* and *c*) with composition (*x*) in $Na_{1-x}K_xNbO_3$ ($0.250 \leq x \leq 0.350$).

Table 2. EDAX results of $Na_{1-x}K_xNbO_3$ ($0.250 \leq x \leq 0.350$) samples.

	Atomic percentage							
	Observed				Calculated			
Material composition (x)	Na	K	Nb	O	Na	K	Nb	O
0.250	11.11	2.72	16.80	67.46	15	5	20	60
0.300	11.17	3.34	18.88	66.61	14	6	20	60
0.310	8.70	3.21	15.29	50.07	13.8	6.2	20	60
0.315	10.99	4.63	19.63	64.75	13.7	6.3	20	60
0.320	10.47	4.48	19.62	65.43	13.6	6.4	20	60
0.325	11.09	4.62	19.24	65.05	13.5	6.5	20	60
0.330	9.99	3.64	17.56	68.81	13.4	6.6	20	60
0.350	9.99	3.64	17.56	68.81	13.0	7.0	20	60

permittivity (ε) and tangent loss (tan δ) of the samples of different compositions, at RT, are given in Figure 5. Room temperature electrical conductivity (σ) of the prepared pellets for different compositions is given in Figure 6. Electrical conductivity being proportional to the dielectric permittivity shows similar variation as that of the dielectric constant. Generally, dielectric permittivity and loss tangent were observed to decrease and electrical conductivity increased with increasing frequency. These observations are in good agreement with the earlier reported results [10,22,31]. The dielectric dispersion and the corresponding circuit analogy for solid oxides show several relaxation modes. The decrease in the dielectric permittivity and loss can be attributed to the damping out of successive polarization modes with increasing frequency [32]. The observed dielectric behavior may be attributed to the polarization mechanism depending on the applied frequency, composition, grain size, grain boundary thickness, porosity, residual stress, thermal history of the dielectric and electrode interface effects [33].

To establish the significance of the composition dependence of the dielectric properties, measurements were carried out at different temperatures. For chosen frequency 1 MHz, the observed composition ($0.250 \leq x \leq 0.350$) dependence of ε, tan δ; and σ is shown in Figures 7 and 8, respectively, at different temperatures, far lower from the transition temperature. Dielectric permittivity, loss and electrical conductivity of all the prepared samples were generally found to increase with increasing temperature. Dielectric permittivity and electrical conductivity were also measured over a wide range of temperature (between RT and 500°C). Showing certain temperature dependent phase transitions

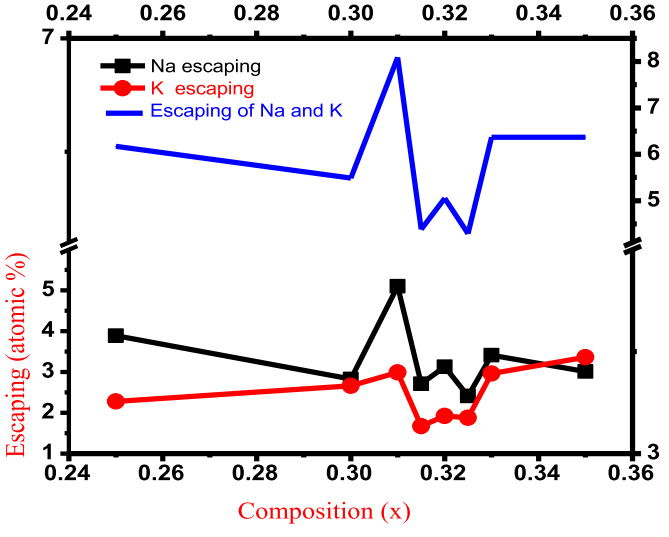

Figure 3. Variation of escaping of Na and K (atomic %) with composition (x), in $Na_{1-x}K_xNbO_3$ ($0.250 \leq x \leq 0.350$).

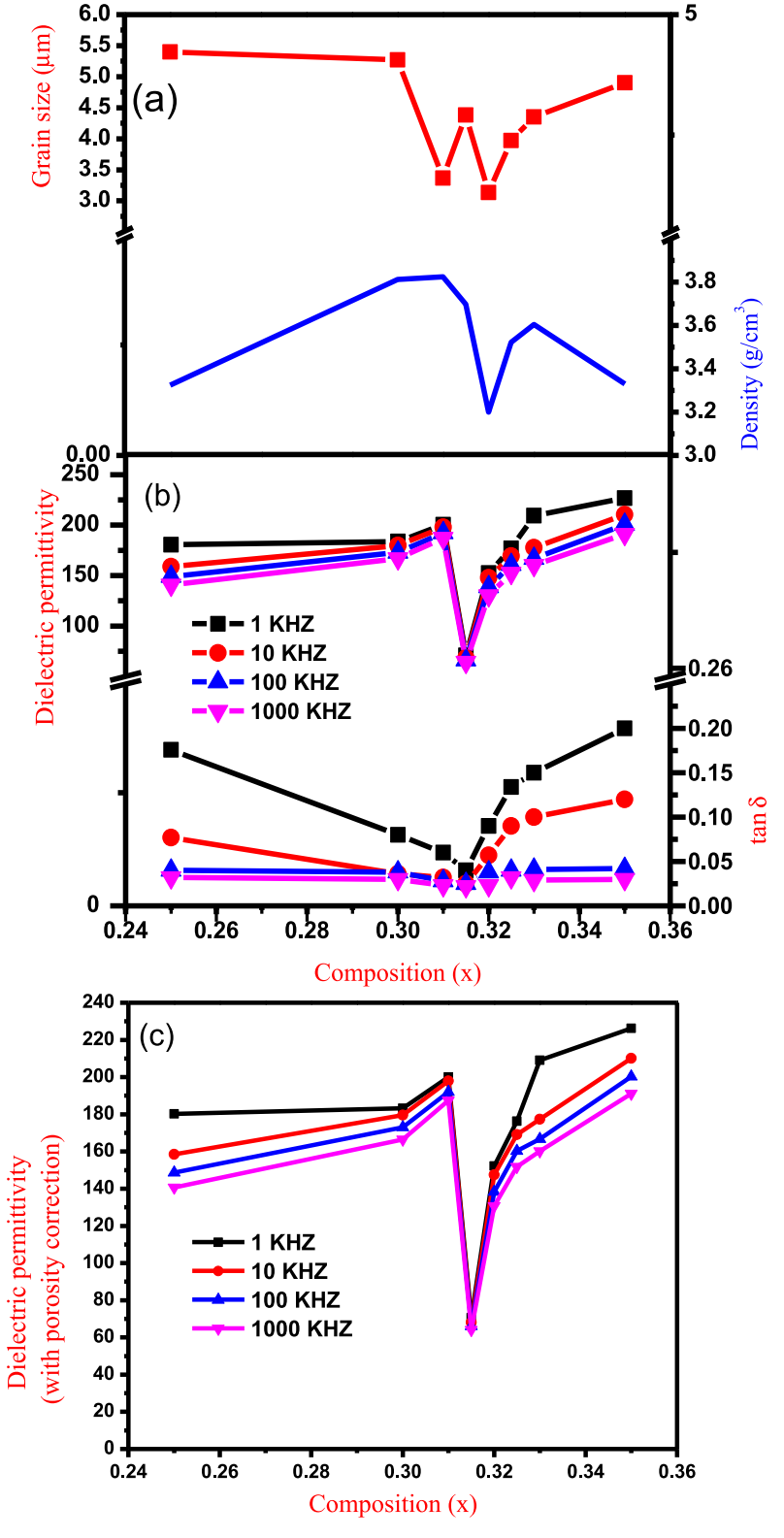

Figure 4. Composition variation of (a) grain size and density; (b) dielectric permittivity and tan δ; and (c) dielectric constant with porosity correction of $Na_{1-x}K_xNbO_3$ ($0.250 \leq x \leq 0.350$) at different frequencies and RT.

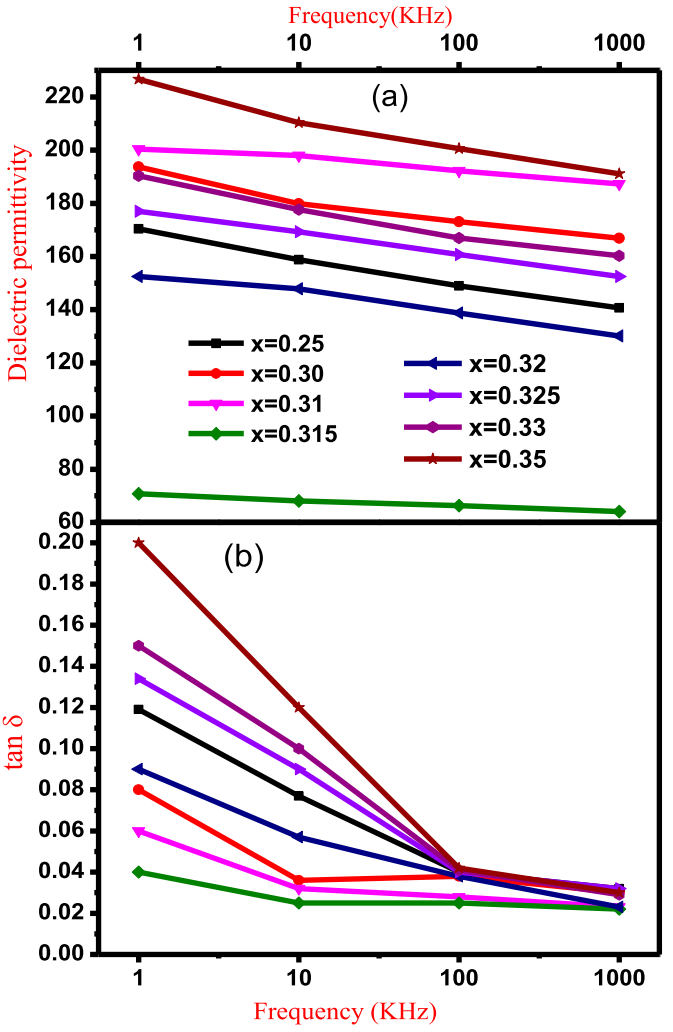

Figure 5. Frequency variation of (a) dielectric permittivity and (b) tan δ, in $Na_{1-x}K_xNbO_3$ ($0.250 \leq x \leq 0.350$).

values of ε and σ were found have local minima at all the measured temperatures for the composition with $x = 0.315$ among the prepared compositions. These results will be communicated separately.

Dielectric permittivity, loss tangent and electrical conductivity were observed minimum for $Na_{0.685}K_{0.315}NbO_3$, at different measured frequencies and temperatures, Figures 4–8, indicating that the dielectric behavior significantly depends on the composition of the $Na_{1-x}K_xNbO_3$ system. The effect of varying x could be understood in terms of the contribution of varying potential energy of the bonds with the neighboring oxygens by substitution of Na with K. These observations indicate that the dielectric behavior is dominantly driven by the composition rather than the porosity, grain size, temperature, or frequency, near $x = 0.315$. Raevskii et al. [5] have observed the composition (x) dependent electrical conductivity of $Na_{1-x}K_xNbO_3$, exhibiting minimum for the compositions near phase boundary. Other workers have also observed break in the X-ray peak shifting pattern near phase boundary [3,5,8].

Electrical behavior of ABO_3-type perovskites can explained on the basis of their n-type nature due to oxygen vacancies [8,22] and the effective polarization. In the n-type perovskites, with the increase in the A-site vacancies a lowest conductivity [5] and in the p-type ceramics a distinct conductivity

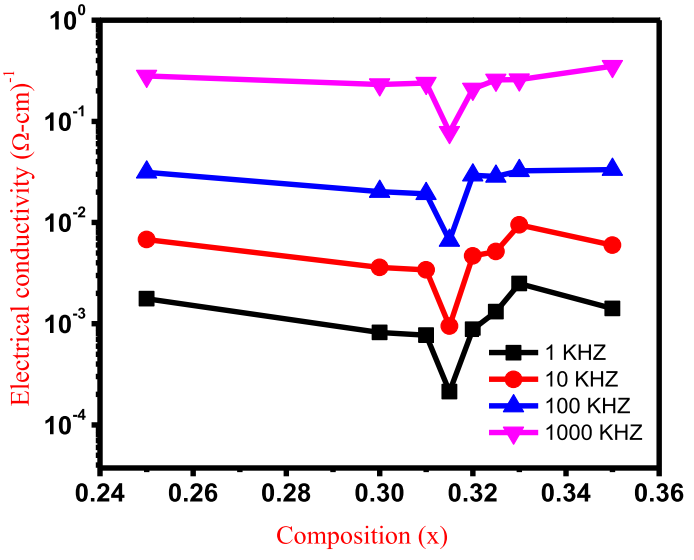

Figure 6. Variation of electrical conductivity of $Na_{1-x}K_xNbO_3$ ($0.250 \leq x \leq 0.350$) with composition (x) at different frequencies and RT.

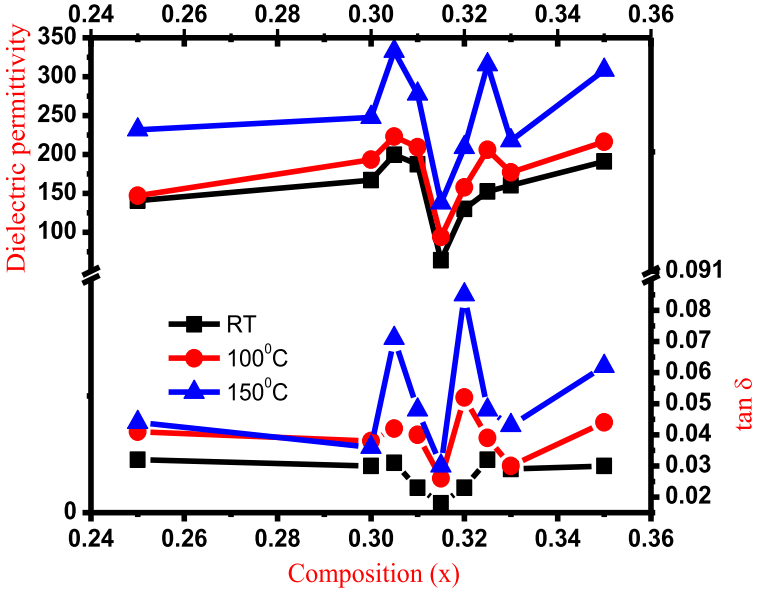

Figure 7. Variation of dielectric permittivity and tan δ with composition (x), in $Na_{1-x}K_xNbO_3$ ($0.250 \leq x \leq 0.350$) at different temperatures and 1 MHz.

maximum were observed [22,24] for the compositions near the phase boundary. In the currently presented $Na_{1-x}K_xNbO_3$ compositions, significant deficiency of alkali metal ions was observed, which agrees with other reported studies [8,34]. During sintering the intensification of diffusion processes significantly enhances the possibility of escape of highly volatile alkali metal ions from the lattice. However, A-site deficiency was found to have a maximum for the composition with $x = 0.310$ and a minimum for $x = 0.325$, Figure 3 and Table 2. Also neither the average grain size nor the relative density is extremal for the composition with $x = 0.315$, compared with other compositions. From the

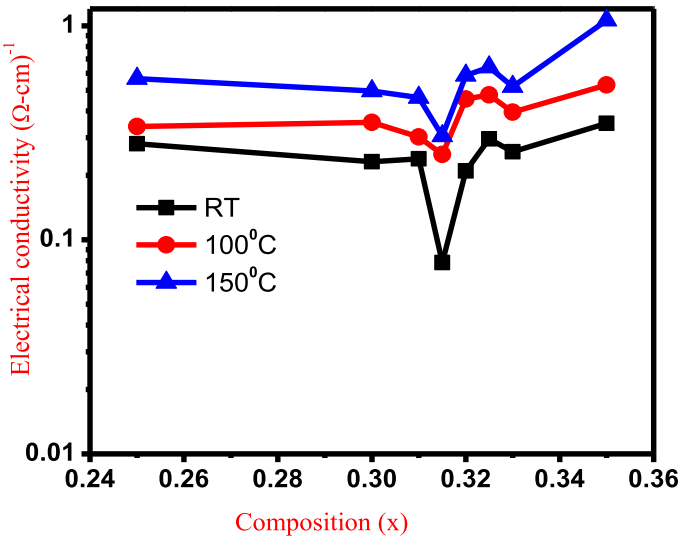

Figure 8. Variation of electrical conductivity (σ) with composition (x) in $Na_{1-x}K_xNbO_3$ ($0.250 \leq x \leq 0.350$) at different temperatures and 1 MHz.

X-ray measurements, a break in the most intense peaks shifting pattern and abrupt slope change in the lattice parameters and a/c vs. x plots indicate a structural anomaly at the composition $x = 0.315$, Figures 1 and 2. Dielectric permittivity, loss tangent and electrical conductivity were found to be a minimum for the composition with $x = 0.315$ among all the prepared samples for all the measured temperatures and frequencies, Figures 4–8. This indicates that the deficiency of the alkali ions, density of samples or grain size effects are not very effective but the structural property is more significantly responsible for the observed dielectric behavior of the prepared $Na_{1-x}K_xNbO_3$ compositions. The observed structural anomaly and the lowest values of dielectric permittivity, loss tangent and electrical conductivity indicated an MPB-like composition at $x = 0.315$ in the $Na_{1-x}K_xNbO_3$ system.

Disclosure statement

No potential conflict of interest was reported by the authors.

References

[1] Egerton L, Bieling CA. Isostatically hot-pressed sodium-potassium niobate transducer material for ultrasonic devices. Ceram Soc Bull. 1968;47:1151–1156.
[2] Samara GA. Effects of pressure on the dielectric properties and phase transitions of the alkali metal tantalates and niobates. Ferroelectrics. 1987;73:145–159.
[3] Tennery VJ, Hang KW. Thermal and X-ray diffraction studies of the $NaNbO_3$–$KNbO_3$ system. J Appl Phys. 1968;39:4749–4753.
[4] Egerton L, Dillon DM. Piezoelectric and dielectric properties of ceramics in the system potassium-sodium niobate. J Am Ceram Soc. 1959;42:438–442.
[5] Raevskii IP, Reznichenko LA, Prokopalo OI, et al. Phase- transition and electrical-properties of ferroelectric sodium niobate-based solid-solutions. Inorg Mater. 1979;15:686–688.
[6] Jaffe B, Jaffe H, Cook WR. Piezoelectric ceramics. London: Academic Press; 1971.
[7] Ahtee M, Glazer AM. Lattice parameters and tilted octahedra in sodium–potassium niobate solid solutions. Acta Crystallogr A: Cryst Phys, Diffr, Theor Gen Crystallogr. 1976;32:434–446.
[8] Lingwal V, Panwar NS. Morphotropic phase transitions in mixed sodium-potassium niobate system. Ferroelectrics. 2004;300:3–14.
[9] Jaffe B, Roth RS, Marzullo S. Properties of piezoelectric ceramics in the solid-solution series lead titanate-lead zirconate-lead oxide: Tin oxide and lead titanate-lead hafnate. J Res Natl Bur Stand (1934). 1955;55:239–253.

[10] Jaeger RE, Egerton L. Hot Pressing of potassium-sodium niobates. J Am Ceram Soc. 1962;45:209–213.
[11] Zhang MH, Wang K, Zhou JS, et al. Thermally stable piezoelectric properties of (K, Na)NbO3-based lead free perovskite with rhombohedral-tetragonal coexisting phase. Acta Mater. 2017;122:344–351.
[12] Yang D, Chai Q, Wei Q, et al. First-Principles Calculation of $K_{1-x}Na_xNbO_3$ solid solutions on electronic properties, structure, and phase transition. Phys. Chem. Chem. Phys. 2017;19:27368–27373.
[13] Saito Y, Takao H, Tani T, et al. Lead-free piezoceramics. Nature. 2004;432:84–87.
[14] Shrout TR, Zhang SJ. Lead-free piezoelectric ceramics: alternatives for PZT. J Electroceram. 2007;19:113–126.
[15] Zhang S, Xia R, Shrout TR. Modified $K_{0.5}Na_{0.5}NbO_3$ based lead-free piezoelectrics with broad temperature usage range. Appl Phys Lett. 2007;91:1–132913.
[16] Du H, Zhou W, Luo F, et al. Polymorphic phase transition dependence of piezoelectric properties in $(K_{0.5}Na_{0.5})NbO_3$–$(Bi_{0.5}K_{0.5})TiO_3$ lead-free ceramics. J Phys D. 2008;41:1–115413.
[17] Baker DW, Thomas PA, Zhang N, et al. Structural study of $K_xNa_{1-x}NbO_3$ (KNN) for compositions in the range x = 0.24–0.36. Acta Crystallogr B. 2009;65:22–28.
[18] Zhang N, Glazer AM, Baker D, et al. Structures of $K_{0.05}Na_{0.95}NbO_3$ (50–300 K) and $K_{0.30}Na_{0.70}NbO_3$ (100–200 K). Acta Crystallogr B. 2009;65:291–299.
[19] Noheda B, Cox DE, Shirane G. Stability of the monoclinic phase in the ferroelectric perovskite $PbZr_{1-x}Ti_xO$. Physical Review B. 2000;63:014103.
[20] Glazer AM, Thomas PA, Baba-Kishi KZ, et al. Influence of short-range and long-range order on the evolution of the morphotropic phase boundary in Pb(Zr1−xTix)O3. Phys Rev B. 2004;70:184123–184129.
[21] Ragini RR, Mishra SK, Pandey D. Room temperature structure of Pb ($Zr_xTi_{1-x}O_3$) around the morphotropic phase boundary region: A Rietveld study. J Appl Phys. 2002;92:3266–3274.
[22] Kandari AS, Lingwal V, Panwar NS. Morphotropic phase boundary in $Na_{1-x}K_xNbO_3$, near x = 0.32. Solid State Commun. 2010;150:74–77.
[23] Singh S, Negi J, Panwar NS. Dielectric properties of $Na_{1-x}K_xNbO_3$, near x = 0.5 morphotropic phase region. J Phys Chem Solids. 2018. doi:10.1016/j.jpcs.2018.08.018.
[24] Attia J, Bellaiche L, Gemeiner P, et al. Study of potassium-sodium-niobate alloys: A combined experimental and theoretical approach. J de Physique IV (Proceedings). 2005;128:55–60.
[25] Kandari AS, Lingwal V, Panwar NS. Morphotropic region in $Na_{1-x}K_xNbO_3$, between x = 0.17 and 0.18. Ferroelectrics. 2010;396:18–26.
[26] Kandari AS, Kandari K, Lingwal V, et al. Composition dependent dielectric anomaly in $Na_{1-x}K_xNbO_3$, at x = 0.475. Ferroelectrics. 2009;393:121–129.
[27] Tellier J, Malic B, Dkhil B, et al. Crystal structure and phase transition of sodium potassium niobate perovskites. Solid State Sci. 2009;11:320–324.
[28] Hollenstein E, Davis M, Damjanovic D, et al. Piezoelectric properties of Li-and Ta-modified $(K_{0.5}Na_{0.5})NbO_3$ ceramics. Appl Phys Lett. 2005;87(18):182905–1829051.
[29] Verkerk MJ, Middeluis BJ, Burggraaf AJ. Effect of grain boundaries on the conductivity of high purity ZrO2-Y2O3 ceramics. Solid State Ionics. 1982;6:159–170.
[30] Penn SJ, Alford NM, Templeton A, et al. Effect of porosity and grain size on the microwave dielectric properties of sintered alumina. J Am Ceram Soc. 1997;80:1885–1888.
[31] Haertling GH. Properties of hot-pressed ferroelectric alkali niobate ceramics. J Am Ceram Soc. 1967;50:329–330.
[32] Kandari AS, Bhandari A, Bourai AA, et al. Electrical properties of $Na_{1-x}K_xNbO_3$ ($0.28 \leq x \leq 0.40$). Ferroelectrics. 2009;386:139–151.
[33] Goodman G. Ceramic materials for electronics; processing, properties and applications, Buchanan RC, editor. New York, NY: Marcel Dekker Inc., 1991; p. 32.
[34] Tanaka J, Tsukioka M, Miyazawa Y, et al. The electrical conduction mechanism in the semiconducting sodium niobate. Solid State Commun. 1980;34:221–224.

MultiCraft

International Journal of Engineering, Science and Technology
Vol. 11, No. 3, 2019, pp. 40-48

INTERNATIONAL JOURNAL OF ENGINEERING, SCIENCE AND TECHNOLOGY

www.ijest-ng.com
www.ajol.info/index.php/ijest
© 2019 MultiCraft Limited. All rights reserved

Microcontroller based data acquisition system using error reduction technique

Don Biswas[1*], Kuldip Kumar[2], Vishal Rohilla[3], Gambheer Singh Kathait[4], Prashant Thapliyal[5], Arun Shekhar Bahuguna[6], Yogendra Pundir[7], Vinay Prasad tamta[8]

[1,3,4,5] Department of University Science Instrumentation Centre, Hemwati Nandan Bahuguna Garhwal University, Srinagar Garhwal, INDIA
[2,6,7]Department of Electronic and Communication Engineering, Hemwati Nandan Bahuguna Garhwal University, Srinagar Garhwal, INDIA
[8] Department of Information Technology, Hemwati Nandan Bahuguna Garhwal University, Srinagar Garhwal, INDIA

Abstract

The application of high-speed real-time data acquisition is becoming increasingly wide spread in industrial field, and its measurement accuracy is also increasing. In the present study, the development of a USB based data acquisition system is presented here, where a microcontroller based standalone embedded system is used as data collection and also field control device. The data acquisition system has been calibrated in terms of output voltage generated in signal conditioner. The USB device system also calibrated for the error in the output result. Here USB device has been programmed as Human Interface Device (HID) class, hence not requiring any kind of device specific driver. This data acquisition system is utilized to measure the flow of a channel. The flow of water is not acidic.

Keywords: USB, microcontroller, PIC, acquisition, data acquisition, programmer, digital.

DOI: http://dx.doi.org/10.4314/ijest.v11i3.5

1. Introduction

From industrial view point, the physical parameter flow is a very critical constant for certain locations like, different types of power plant, field plant, DM plant, bottling plant, etc. Flow can be measure in two ways; one is dependent upon the volume and the other is dependent upon weight. Solid may be measured in terms of either weight per unit time or mass per unit time. The solid quantity is measured in terms of volume very rarely. The liquid quantity is characterized with the measurement of volume rate or in weight rate. The Gas quantity is normally measured in volume rate. The flow rate can be measured using different sensors like DPT type instrument, turbine flow meter. It basically measures the pressure difference between two points. The pressure difference is calibrated in terms of flow measurement. The data acquisition system has been also calibrated according to that purpose. The whole system has been calibrated using different techniques. First, we send some sinusoidal signal and analyze the correlation characteristic of the measured voltage peak data, which includes mean value, variance, standard deviation, range, deviation etc., and then finds out the influence rules of software timing error on data acquisition and measurement accuracy (Monoranjan and Sarma, 2010).

The sine-wave signal of this closed-loop test system is constructed by the SCIENTECH (ST4060) single-channel signal source, KEYSIGHT (Infinii Vision DSO-X 2024A) oscilloscope, and data acquisition card. In the high-speed data acquisition, the repeatability and reproducibility error can be reduced. The faster, reliable, efficient data acquisition system has been introduced in the field of modern measuring instrument (Pandey and Arora, 2019). With the rapid development of various measuring instruments and equipment, the demand for accuracy, loss reduction and real-time of data acquisition measurement is also increasing (USB-IF, 2006; Song et al, 2011; Zhao et al, 2012; Niculescu et al., 2019). The popularity of Universal Serial Bus (USB) has been extended due to its inexpensive and easy-to-use nature. The short range (5m) communication medium has been used for the transfer of data from one device to another. In a regular PC (host), the communication device acts as a client (USB-IF,

2006). The USB was originally designed to connect PC with its peripherals (keyboard, mouse etc.). However, it has proven useful for many other applications, including measurement and automation (Liptak, 1985; Chang and Liu, 2003; Shao et al, 2010; Liu and Qi, 2012; Zhang et al, 2014; Biswas et al, 2016; Biswas and Bahuguna, 2017). A work has been conducted on a flow measurement system, from which data has been acquired and measured.

2. Methodology

The measured signal has acquired by De-Sauty bridge and Output of this bridge is going to the unit called instrumentation amplifier. Instrumentation amplifier is basically a difference amplifier, which amplifies the signals from De-Sauty Bridge. Now the 1st stage instrumentation amplifier output goes to the second stage amplifier which provides necessary amplification and zero, gain and span adjustment. Output of 2nd amplifier which is an AC signal, is applied to the next unit, which is called rectifier and filter network (Figure 1) (Biswas et al, 2016).

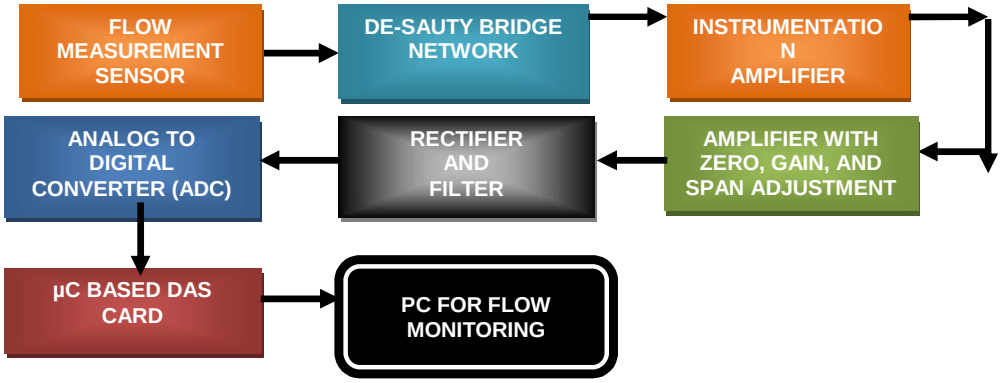

Figure 1: Water flow measurement system

The full wave rectifier output will pass through a filter network and ADC converter will convert the analog signal in the 8 bit digital signal. The USB based data acquisition system will acquire the data and collect it in the software which has been installed in the computer (Biswas and Bahuguna, 2017).

3. Sensor part

Flow may be of two types: viscous and turbulent. A restriction of known dimensions has been introduced in the case of variable head type flow meter sensor. This will increase a head loss or pressure drop at the restriction and will increase velocity in the flow. It may be used in a vertical line. The pressure drop across the obstruction will be the measurement or indication of the flow rate (Figure 2).

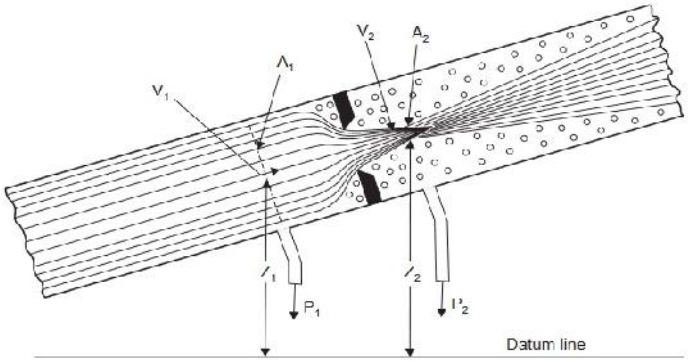

Figure 2: Detailed diagram of flow measuring system

The principle of the Head—type flow measurement is coming from the Bernoulli's theorem. The theorem states that in a flowing stream, the sum of the pressure head, the velocity head and the elevation head at one point is equal to their sum at another point in the direction of flow plus the loss due to friction between the two points. Velocity head is the pressure which is needed to increase the speed at which a liquid flows. Pressure head is the height of a liquid column that corresponds to a particular pressure exerted by the liquid column on the base of its container or pipeline (Liptak, 1985; Liptak, 2003; Liptak, 2006).

The position of upstream and downstream tap are shown by Section-1 is and Section-2 respectively. Here, the terms are described as T = Temperature, A = Area, ρ = Density, V = Stream velocity, P = Pressure and Z = Central line elevation respectively. If this elevation is quite small such that $Z_2 - Z_1$ is negligible, we may write the Bernoulli's equation for an incompressible ($\rho_1 = \rho_2$) frictionless and adaptive flow is written as

$$\frac{P_1}{\circ} + \frac{V_1^2}{2g} = \frac{P_2}{\circ} + \frac{V_2^2}{2g} \tag{1}$$

where, g = acceleration due to gravity, giving

$$P_1 - P_2 = \frac{V_2^2 \circ}{2g}(1 - (V_1/V_2)^2) \tag{2}$$

For Head- type of flow, the continuity equation is $Q = A_2V_2 = A_1V_1$

where, Q = volume flow rate in m^3/sec.

Combining Equations (1) and (2) and manipulating, one gets

$$Q = A_2V_2 = \frac{A_2}{\sqrt{(1-(A_2/A_1)^2}}(\sqrt{\frac{2g(P_1 - P_2)}{\circ}} = A_2M_{va}\sqrt{2gh}$$

$$M_{va} = \frac{1}{\sqrt{1-\left(\frac{A_2}{A_1}\right)^2}} = \text{Velocity approach factor}$$

where $h = (P_1 - P_2)/\rho$ = differential head

This is the equation for ideal volume flow rate (Liptak, 1985).

4. Circuit Diagram

The same DAS system has been utilized which is used and discussed in previous papers (Figure 3) (Biswas et al, 2016; Biswas and Bahuguna, 2017).

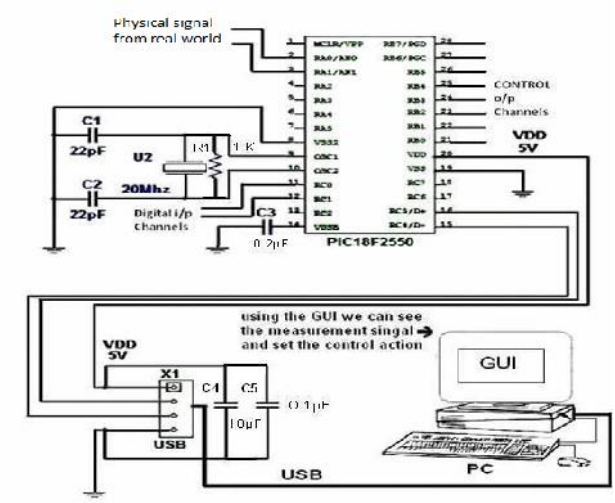

Figure 3: Circuit diagram of the measuring system

5. Results and Discussion

The flow measurement first calibrated in terms of voltage signal and the USB based data acquisition system also checks for any error or data loss. In order to increase the efficiency and accuracy of the data acquisition system, the repeatability and reliability of the measurement and control process has been checked and the timing error of the system software was also analyzed and studied. Sine-wave signal was widely used in many fields, such as computer, communication and industrial control etc. (Zhang et al, 2014). The system is used sine wave signal of different frequencies using function generator SCIENTECH (ST4060) and the output amplitude see as test signal and KEYSIGHT (infiniiVision DSO-X 2024A) digital oscilloscope applied to monitor the test signal. SCIENTECH (ST4060) single-channel function/arbitrary waveform generator, not only produced accurate, stable and low distortion output signal, but also outputted the highest 1 MHz sine-wave, meanwhile, it had seamless interconnect with KEYSIGHT series digital oscilloscope. At the same time, the system used DAS board to test signal through data acquisition system.

The DAS board was a multifunctional high-performance integrated interface board designed for industrial PC. The DAS board consists of a PIC 18F2550 series microcontroller (Manzanilla et al, 2009; Microchip, 2000). The board had 16-bit 16-channel/differential 8-way A/D input, 4-channel 16-bit independent D/A output, and its inbuilt A/D converter chip adopted high-performance, the maximum conversion rate was up to 50 kHz (Biswas and Bahuguna, 2017). The system adopted VB program to realize real-time programmable control of data acquisition card (Monoranjan and Sarma, 2009). Through the VB program timer control technique utilized to determine the sampling interval of data collection, the data acquisition of different test signals was carried out and the measuring precision of the collected datum were carried out. The overall test software frame and program interface were shown in Fig.4 and Fig.5. Figure 6 represents the flowchart of VB interface program to receive analog signal and digital signal (Michael, 2010; Li, 2017).

Setting SCIENTECH (ST4060) Single-channel function/arbitrary waveform generator to issue a working frequency of 50 Hz, the peak-to-peak value of 1V sine-signal, through the data acquisition card measured the peak-to-peak value of sine-wave signal, where the sampling timing was set to 100ms, 150ms, 200ms respectively (Zhao et al, 2012). Three types of timer interval were set to minimum value, carried out comparative test to data measurement accuracy, and each group of tests repeated five times, the results were as shown in Table 1.

Table 1: Peak voltage data acquisition at different sampling time (V)

Sampling Time	100ms	150ms	200ms
Visual Basic Timing Technique	0.9523 v	0.8752 v	0.7894 v
	0.9876 v	0.7853 v	0.7845 v
	0.95236 v	0.7845 v	0.8452 v
	0.89023 v	0.6578 v	0.7564 v

The system is more advantageous than the traditional serial communication system. The received data loss is very minimum and the system is more reliable and efficient. With the advancement of the USB system, the connecting output devices will work faster and efficiently (Pandey and Arora, 2019). Figures 7- 12, are shown for the purpose of calibration of that data acquisition system.

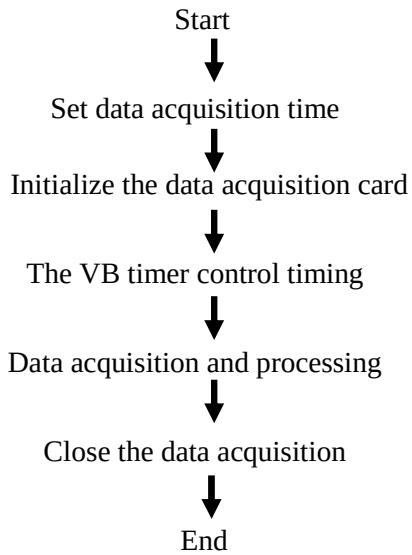

Figure 4: Program flow of data acquisition system

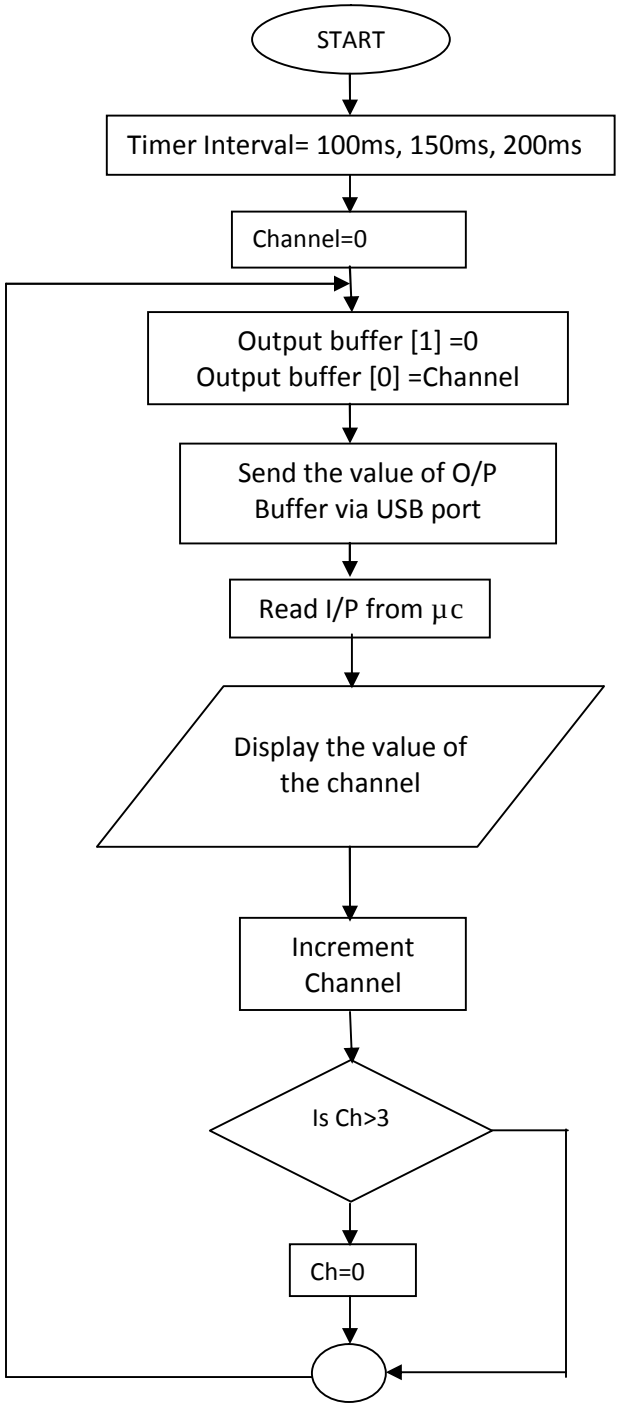

Figure 5: The Flowchart of VB program to receive analog and digital signal values

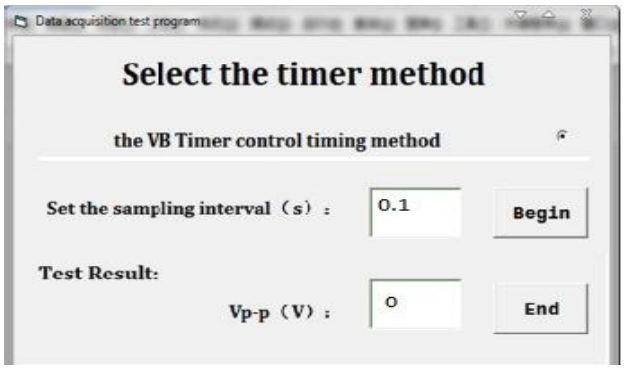

Figure 6: Test program interface

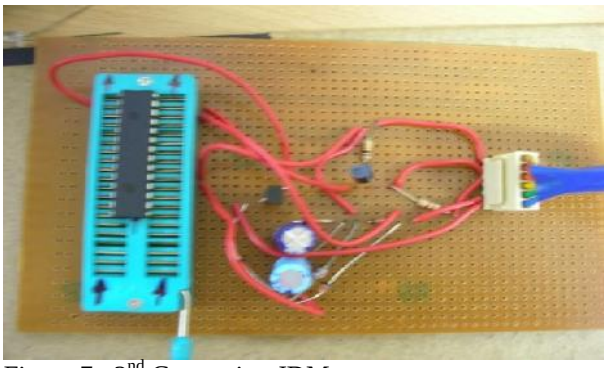

Figure 7: 2nd Generation JDM programmer

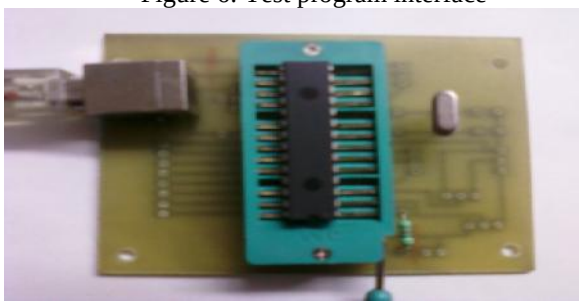

Figure 8: Microcontroller connected with USB

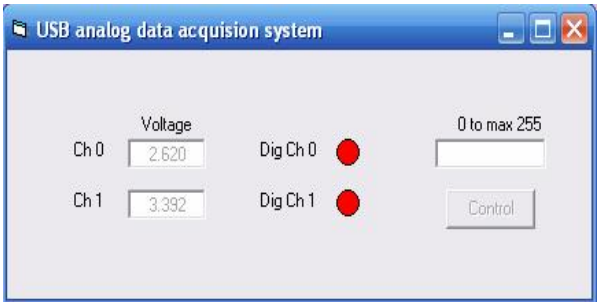

Figure 9: Analog data is being displayed and both digital channels are at logic '0'

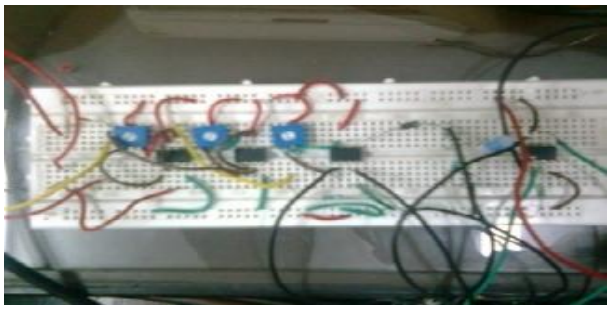

Figure 10. Circuit board

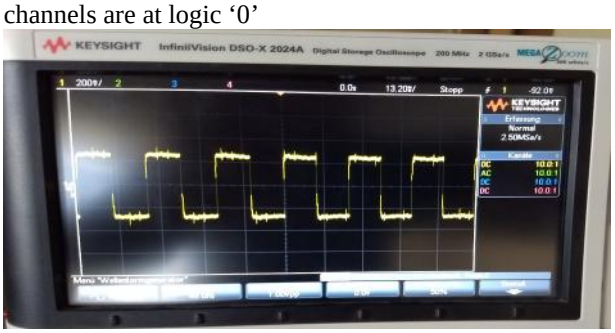

Figure 11: Square wave generated in CRO

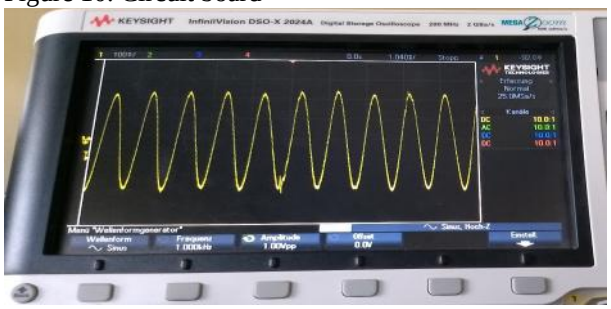

Figure 12: Microcontroller connected with USB and sinusoidal wave generated for calibration purpose

Repeatability error refers to the random error obtained from the same direction for multiple continuous measurement of the same input value in the whole measurement range and under the same working condition. The error has been measured and calculated. The mean value and Standard Deviation also calculated. The electronic flow measuring meters are used in many applications where the flow rate is vertical, and stream rate must be continuously monitored and checked. The data collected in a computer using a USB based data acquisition system (Ziad et al., 2006). The flow measuring meters have a limited range of operation. For turbine flow meters, the output DC voltage signal from the signal conditioner has been calibrated such that it will be proportional to the flow rate of the main stream. We calibrated the flow rate using this technology in a certain linear range to measure flow rate and draw a graph of flow verses voltage. The block diagram (Figure 13) demonstrates the whole process and the precision turbine flow meter shown in Figure 14 (Omega, 2000) is placed within that loop; the tank has a height (Omega, 2000). So, there is a

constant head pressure because of the water tank and the loop has 1/2-inch copper piping, 3/8-inch plastic flexible tubing, 3/8-inch brass flow straightening sections (18-diameters long) upstream and downstream of the flow meter, a 90-µm filter (Swagelok, Model SS-6TF-90) upstream of the flow straightening section and a ball valve upstream of the filter for adjusting the flow rate (Swagelok, 2000).

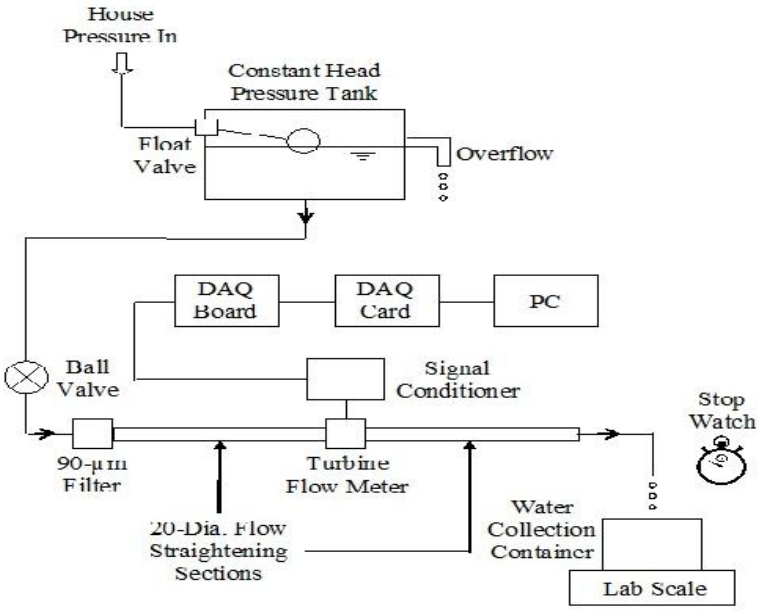

Figure 13: block diagram

The flow meter is attached to a signal conditioner (Model No. FLSC-61) and electrical voltage (12V DC) is connected to the signal conditioner with a power supply [FLSC-6, 2003]. A data acquisition card is set to acquire input data from the signal conditioner by opening the Visual Basic software on the personal computer [Michael, 2010]. The PC and DAS card already calibrated for measurement purpose and measure the flow of water by using the flow meter/signal conditioner voltage at the maximum mass flow rate achievable by the flow loop system, and the voltage at the minimum mass flow rate readable by the flow meter. We divide the range into ten equally-spaced nominal mass flow rate settings for the purpose of obtaining a mass flow rate calibration equation. We set the mass flow rate to one of the nominal values discussed above using the ball valve. The DAS card is installed in order to collect voltage data from the flow meter/signal conditioner [Ziad et al, 2006]. We measured the mass flow rate by hand five consecutive times while the DAS collects voltage data at a rate of one reading every 0.2 seconds as follows:

(i) A water collection container has been set on the measured scale (cm) and set zero scale level.
(ii) Placed the container under the stream of water exiting the flow meter and simultaneously start a digital stop watch.
(iii) Collected the water from the source for approximately 60 seconds.
(iv) After that withdraw the container from the water stream, and simultaneously stop the timer.

Measure the mass of liquid in the collection container using the measured scale and recorded it by hand.

According to the mass flow readings the calibration equation (may be the form of linear equation) for the flow meter will be found by plotting the mass flow rate readings versus the corresponding mean voltage readings, as shown below in Figure 15. The flow rate is linear (although not exactly) with respect to the voltage reading.

Figure 14: Turbine flow meter (FTB-9506)

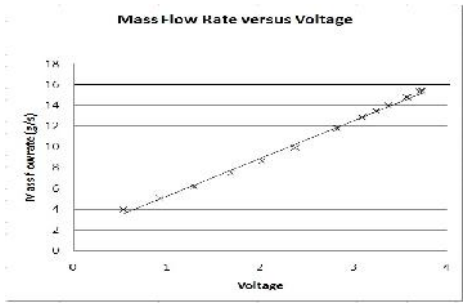

Figure 15: Variation of Mass flow rate with voltage

6. Conclusion

It has been observed that high speed data acquisition system have data loss also. Though using the error reduction technique we can optimize the error and collect the data accordingly. The advantage of this system is to reduce data loss error, while measuring any kind of physical parameter. The measured data, which is going through the USB acquisition system, so that, the serial communication is faster. The previous DAQ system is slow and too much data loss is taking place. The DAQ device may not be put at too much distance. They are not reliable according to the previously published papers. Taking the sine-wave as the test signal, from the sampling time length, the signal waveform analysis and the frequency three aspects, carries on the analysis to the measured voltage peak data correlation characteristic, including the mean value, variance, standard deviation, range, variation coefficient, deviation, kurtosis and so on.

References

Biswas D., Kathait G. S. and Rohilla V., 2016. To Design and Measure Physical Signal from a USB Based Data Acquisition System. *International Journal of Latest Technology in Engineering, Management & Applied Science*, Vol. 5, No.8, pp. 75-81.

Biswas D., and Bahuguna A., 2017. To Measure Physical Signal from Sensor and Control through Data Acquisition System. *International Journal of Advanced Research in Computer Science and Software Engineering*, Vol. 7, No. 5, pp. 377-388.

Chang F L, and Liu J., 2003. The application of multimedia timer in the fast data acquisition under the multi thread. *Computer application*, Vol. 23, No. 6, pp. 177- 178.

FLSC-6, 2003. Signal Conditioner, USA, Accessed 1 October 2018 <*http://www.omega.com/manuals/manualpdf/M2729.pdf*>

Liu H, and Qi Q. X., 2012. Design of a sine- wave measuring device based on STM32. *Modern Electronics Technique*, Vol. 17, No. 35, pp. 110-115.

Liptak G. B., 1985. *Process Instruments and Control Handbook*, 3rd Edition, McGraw Hill, New York, USA, pp. 1-1766.

Liptak G. B., 2003. *Instrument Engineers' Handbook*, 4th Edition, Taylor & Francis, London, New York, USA, pp. 1-46.

Li Y L., 2007. *Basic Visual programming*. China, Beijing, Tsinghua University press, 2nd Edition, pp. 96-320.

Liptak G. B., 2006. *Instrument Engineers' Handbook*, 4th Edition, Taylor & Francis, London, New York, USA, Vol. I & II, pp. 1-60 & 1-67.

Manzanilla G., Silva A., Barrera M., 2009. Temperature-Meter via USB Based on PIC 18F2550 for Solar Energy Concentrator System. *19th International Conference on Electrical, Communications, and Computers*, Cholula, Puebla, Mexico, pp. 1-7.

Michael H., 2010. *Microsoft Visual Basic 2010 Step by Step Theory and Applications, Microsoft Visual Basic 2010 Step by Step*, 1st Edition, Redmond, Washington, Microsoft Press store by Pearson, pp. 1-576. [Online]
https://www.microsoftpressstore.com/store/microsoft-visual-basic-2010-step-by-step-9780735645387

Microchip, 2000. Microcontroller chip PIC 18F2550 datasheet, Arizona, Accessed 1 October 2018 <*http://www.microchip.com*>

Monoranjan N. S. and Sarma K. C., 2009. Low cost PC based real time data logging system using PCs parallel port for slowly varying signals. *The journal of Assam Science Society*, Vol. 50, No. (1-2), pp. 36-41.

Monoranjan N. S. and Sarma. K. C., 2010. Design of PIC 12F675 microcontroller based data acquisition system for slowly varying signals. *The journal of Instrument Society of India*, Vol. 40, No. 1, pp 15-17.

Niculescu, Titu; Popescu, Florin Gabriel; Marcu, Marius; Slusariuc, Ioan Răzvan, 2019. Improving the quality of measurements in electrical processes using NI USB data acquisition systems. *Calitatea, suppl. Quality-Access to Success: Acces la Success*, Bucharest, Vol. 20, Iss. S1, pp. 293.

Omega, 2000. FTB-9506, Turbine Flow Meter, USA, Accessed 1 October 2018 <*http://www.omega.com/manuals/manualpdf/M2728.pdf*>

Pandey A.K., Arora S., 2019. Onboard Data Acquisition System to Monitor the Vehicle. *Advances in Intelligent Systems and Computing*, Springer, Singapore, Vol. 904. pp. 265-271.

Song P. F., Wang H. J., Zeng H., 2011. Research and design of high speed and deep storage data acquisition System. *Journal of instrumentation*, Vol. 4, No. 32, pp. 903-912.

Swagelok, 2000. Model SS-6TF-90 Filter, USA, Accessed 1 October 2018 *<https://www.swagelok.com/en/catalog/Product/Detail?part=SS-6TF-90>*

Shao Y. Y., Xu. X. D., Xuan G. T., 2010. Application of multimedia timer in real time data acquisition of construction machinery. *Computer and Information Technology*, Vol. 18, No. 2, pp. 16-18.

USB-IF, 2006. Universal Serial Bus, USA, Accessed 1 October 2018 *<http://www.usb.org/about>*

Zhao D. J., Jia J., Gao X. G., He X. L. and Li J P., 2012. High field asymmetric waveform ion mobility spectrum of sinusoidal waveform generation and ion separation characteristics. *Journal of Sensing Technology*, Vol. 7, No. 25, pp. 926-929.

Zhang H., Wang J. M., Cui K, et al., "A data transmission and time measurement system for bit commitment experiment. 19th *IEEE-NPSS. IEEE (Real Time Conference)*, Nara, Japan, pp. 1-2.

Ziad S., Alaa Al B. and Ismail Al K., 2006. A Novel Design of an Industrial Data Acquisition System. *2nd International Conference on Information & Communication Technologies*, Damascus, Syria, pp. 2589 – 2594.

Biographical notes

Don Biswas received M. Tech. in Instrumentation and Control Engineering from Calcutta University, India in 2010. He is working as Assistant Professor in the Department of Instrumentation Engineering, HNB Garhwal University. His research interests include Material engineering, Data acquisition System, etc.

Kuldip Kumar is working as Assistant Professor in the Department of Electronics and Communication Engineering, HNB Garhwal University. His research interests include Communication Engineering.

Vishal Rohilla is working as Assistant Professor in the Department of Instrumentation Engineering, HNB Garhwal University. His research interests include Material engineering, Instrumentation, Analytical Instruments, etc.

Gambheer Singh Kathait is working as Assistant Professor in the Department of Instrumentation Engineering, HNB Garhwal University. His research interests include Material engineering, etc.

Prashant Thapliyal is working as Assistant Professor in the Department of Instrumentation Engineering, HNB Garhwal University. His research interests include Material Science, etc.

Arun Shekhar Bahuguna is working as Assistant Professor in the Department of Electronics and Communication Engineering, HNB Garhwal University. His research interests include Communications, Antenna Systems, etc.

Yogendra Pundir is working as Assistant Professor in the Department of Electronics and Communication Engineering, HNB Garhwal University. His research interests include Communication Systems, etc.

Vinay Prasad tamta is working as Assistant Professor in the Department of Information Technology, HNB Garhwal University. His research interests include Information Technology, etc.

Received November 2019
Accepted May 2019
Final acceptance in revised form May 2019

Ferroelectrics

ISSN: 0015-0193 (Print) 1563-5112 (Online) Journal homepage: https://www.tandfonline.com/loi/gfer20

Influence of escaping of Na & K on physical properties in lead-free $Na_{0.92}K_{0.08}NbO_3$ ceramic

Gambheer Singh Kathait, Prashant Thapliyal, Don Biswas, Vishal Rohilla & Surendra Singh

To cite this article: Gambheer Singh Kathait, Prashant Thapliyal, Don Biswas, Vishal Rohilla & Surendra Singh (2019) Influence of escaping of Na & K on physical properties in lead-free $Na_{0.92}K_{0.08}NbO_3$ ceramic, Ferroelectrics, 551:1, 40-46, DOI: 10.1080/00150193.2019.1658026

To link to this article: https://doi.org/10.1080/00150193.2019.1658026

Published online: 03 Dec 2019.

Submit your article to this journal

View related articles

View Crossmark data

Full Terms & Conditions of access and use can be found at
https://www.tandfonline.com/action/journalInformation?journalCode=gfer20

FERROELECTRICS
2019, VOL. 551, 40–46
https://doi.org/10.1080/00150193.2019.1658026

Taylor & Francis
Taylor & Francis Group

Check for updates

Influence of escaping of Na & K on physical properties in lead-free $Na_{0.92}K_{0.08}NbO_3$ ceramic

Gambheer Singh Kathait[a], Prashant Thapliyal[a], Don Biswas[a], Vishal Rohilla[a], and Surendra Singh[b]

[a]Department of Instrumentation Engineering, USIC, H.N.B. Garhwal University, Srinagar Garhwal, Uttarakhand, India; [b]Department of Physics, H.N.B. Garhwal University, Srinagar Garhwal, Uttarakhand, India

ABSTRACT

Lead-free $Na_x K_{1-x}NbO_3$ (NKN) ceramic with $x = 0.08$ was prepared by a conventional solid-state reaction method to investigate the influence of the Escaping of Na & K on their physical properties. It has been found that the NKN ceramics with $x = 0.08$ exhibit pure perovskite (ABO_3) structure. The pure phase NKN was achieved for all sintering temperatures of 1100 °C, 1150 °C, 1200 °C and 1250 °C. Change in microstructure, indicates that the grain size increases with the increasing sintering temperatures. The dielectric constant was dependent of the Escaping of Na & K. From the analyses, we suggest that the high dielectric constant for the NKN ceramics near sintering temperature 1150 °C are closely related to their low escaping of Na & K and microstructures of uniformly distributed large grains rather than the widely believed morphotropic phase boundary effect of lattice parameter discontinuity.

ARTICLE HISTORY
Received 7 July 2018
Accepted 13 June 2019

KEYWORDS
Escaping of Na & K; sintering; dielectric constant and grain size

1. Introduction

Ferroelectricity is the phenomenon of spontaneous polarization. The spontaneous polarization (P_S) is the polarization which remains present in the ferroelectric material in the absence of the external electric field. With increasing temperature spontaneous polarization decreases rapidly on crossing the transition temperature. The most typical ABO_3 type displacive ferroelectrics are perovskite type (having $CaTiO_3$ structure), e.g. $BaTiO_3$, $KNbO_3$, $PbTiO_3$, $KTiO_3$, $PbZrO_3$, $LiNbO_3$, $LiTaO_3$, and so on [1, 2]. The Pb-based ceramics have been widely utilized in industrial applications for many years because of their excellent electrical properties [3–6]. However, since PbO is toxic and evaporates during the sintering process, PZT ceramics pose serious environmental problems. Therefore, extensive research has been directed at lead-free piezoelectric materials to replace Pb-based ceramics. Recently, significant progress has been reached in KNN-based ceramics, which showed that they may be promising candidates as lead-free piezoelectric materials [7–12]. Various approached have been used to obtain the NKN ceramics [13–15]. Interestingly, most of the recent investigations on KNN-based

CONTACT Gambheer Singh Kathait gambhir11186@gmail.com
Color versions of one or more of the figures in the article can be found online at www.tandfonline.com/gfer.
© 2019 Taylor & Francis Group, LLC

ceramics have been carried out based on the equal or nearly equal molar ratio of K to Na. The $Na_{0.5}K_{0.5}NbO_3$ (NKN) ceramic is a particularly promising candidate material for lead-free piezoelectric ceramics because of its high piezoelectric properties and Curie temperature (*Tc*) [16–19]. So far many research works have been carried out to improve sintering behavior of KNN-based compounds via doping [20–22] modification [23–25] Recent investigation on $(K_xNa_{1-x})_{0.97}Li_{0.03}Nb_{0.80}Ta_{0.20}O_3$ (KNLNT) ceramics showed that the speculated MPB associated with the K/Na ratio can hardly be observed and its influence on the high piezoelectric performance is very limited [26]. Insufficient density of KNN-based ceramics, possibility of compositional deviation of sintered ceramic from stoichiometry composition and formation of secondary phases due to volatilization of alkali elements during sintering [27, 28].

2. Experimental

In the present study, $Na_{0.92}$ $K_{0.08}NbO_3$ (NKN) ceramic powder was synthesized by solid state reaction method. Calculated molar ratio of inorganic mixtures, Na_2CO_3 (99.5%, Sigma-Aldrich), K_2CO_3 (99.5%, Sigma-Aldrich) and Nb_2O_5 (99.9%, Sigma-Aldrich) were mixed by hand-grinding for 6 h. The stoichiometric amounts of K_2CO_3, Na_2CO_3 and Nb_2O_5 were weighed according to the chemical formula of $Na_{0.92}$ $K_{0.08}NbO_3$ (NKN) and then the oxides were mixed by, manual grinding in acetone for 2 h (wet), 4 h (dry), and then calcinated at 900 °C for 4 h. After calcinations the obtained powder was taken for XRD analysis. Phase formation of the calcinated powders were determined by XRD analysis by a X-Pert PANalytical diffractometer using a fixed divergence 1/2° slit, a Cu W/Si mirror, a solar slit and a 10 mm mask as incident optics and a parallel plate collimator, a solar slit and a proportional detector as diffracted beam optics. The obtained powders were pressed into disc shape pellets, at a pressure of 2GPascal, with diameter 8 mm dia. piston. The samples were sintered at 1100 °C, 1150 °C, 1200 °C and 1250 °C for 4 h. The particle morphology was examined by scanning electron microscopy (SEM) using model EVO 18 Special Edition (Switzerland), manufactured by ZEISS. For the dielectric investigation, silver paste was painted on both sides of the samples. The coated pellets were dried for 2 h at room temperature (50 °C). Dielectric measurements were carried out using a LCR meter (make: Fluke, model: PM6306) in conjunction with a furnace.

3. Results and Discussion

In the present work, the conventional sintering method was applied for fabrication of the NKN ceramics, i.e. the sample were sintered at $T = 1100$ °C, 1150 °C, 1200 °C and 1250 °C for 4 h, followed by cooling to room temperature. Crystallinity are determined using a X-RAY diffractometer (XPERT-PRO) with a CuKα radiation source ($\lambda = 1.54059$ A^O), operated at a voltage of 45 kV and a current of 40 mA. The XRD patterns of the NKN ceramics sintered by conventional sintering method are shown in Figure 1. It can be observed from the figure that the diffraction peaks are (0 1 2), (1 1 0), (0 2 4), (1 2 2), (3 0 0) and (2 2 0) within the 2θ range from 20° to 70°. The XRD result is consistent with the work done by Fisher *et al.* [29] who synthesized NKN by a

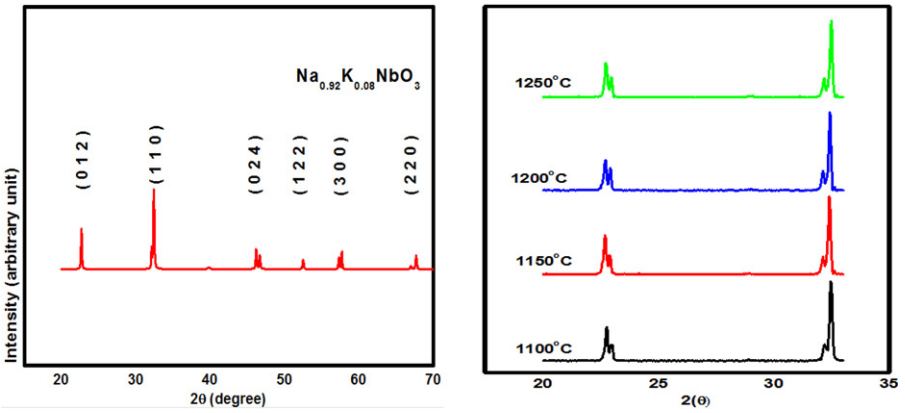

Figure 1. XRD patterns of $Na_{0.92}$ $K_{0.08}NbO_3$ for different sintering temperatures.

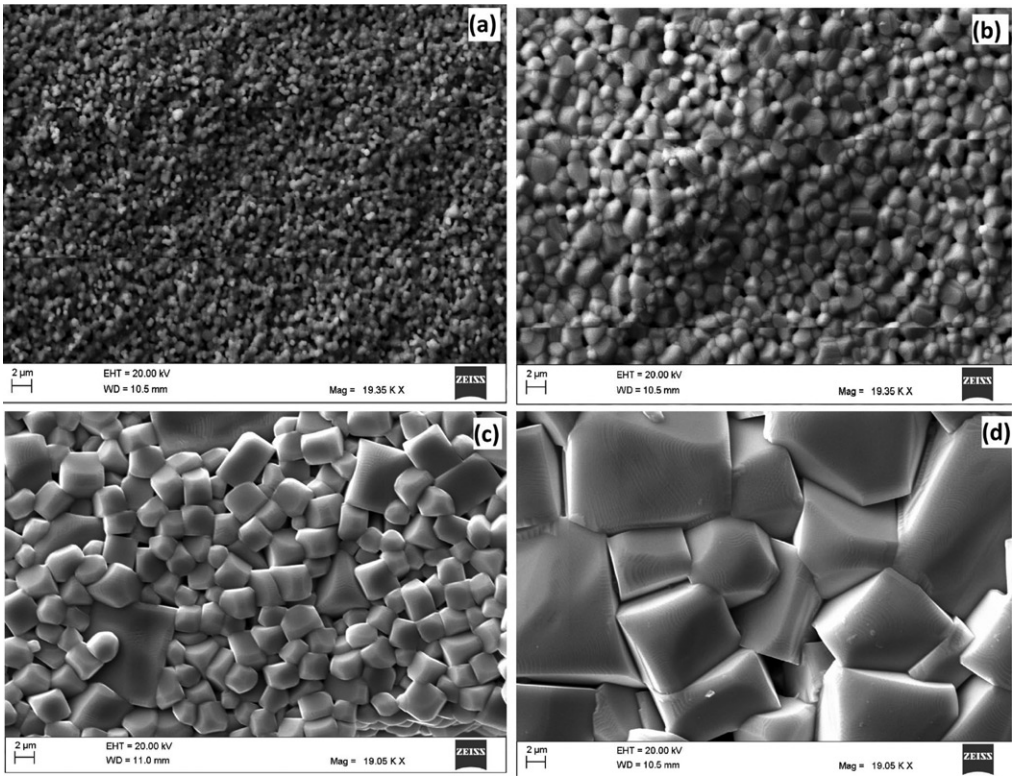

Figure 2. Selected SEM micrographs of NKN ceramics fabricated by different sintering temperatures (a) 1100 °C (b) 1150 °C (c) 1200 °C and (d) 1250 °C.

solid-state technique. The values of calculated sub cell parameters closely agree with the reported results [30, 31]. It is evident that all compositions showed pure perovskite phases with orthorhombic symmetry. No secondary phases could be found due to the application of sintering aids. Also, the diffraction angles had not changed, indicating that the lattice constant had changed very little [32]. The sintering temperature variation

Table 1. SEM-EDAX quantitative analysis of $Na_{0.92}K_{0.08}NbO_3$ for different sintering temperatures (T1 & *T2*): (a) 1100 °C, (b) 1150 °C, (c) 1200 °C and (d) 1250 °C.

	Sintering Temp. 1100°C		Sintering Temp. 1150°C		Sintering Temp. 1200°C		Sintering Temp. 1250°C	
	Atomic%		Atomic%		Atomic%		Atomic%	
Elements	Obs.	Cal.	Obs.	Cal.	Obs.	Cal.	Obs.	Cal.
O	66.43	60	65.77	60	65.08	60	65.26	60
Na	15.38	18.4	16.11	18.4	15.29	18.4	14.65	18.4
K	1.13	1.6	1.01	1.6	0.91	1.6	0.98	1.6
Nb	17.06	20	17.11	20	18.72	20	19.11	20
Escaping of Na & K	17.45%		14.4%		19%		21.85%	

Table 2. Escaping of Na & K (%) and dielectric constant (ϵ_c) for different sintering temperatures

Sintering temperatures (°C)	Escaping of Na & K (%)	ϵ_c	T_C (°C)
T = 1100	17.45	333.687	410
T = 1150	14.40	4181.565	415
T = 1200	19.00	1782.734	405
T = 1250	21.85	1773.639	400

had not a great effect on the phase shift on XRD pattern. The crystalline nature remains unaltered for the temperature variation (Figure 1).

Morphology of $Na_{0.92}K_{0.08}NbO_3$ is shown in Figure 2. With the increasing sintering temperatures from 1100 °C to 1250 °C, increase in grain size and microstructures of uniformly distributed large grains was observed. At 1150 °C the grain size was moderate and found around 1 µm. That results in intensified microstructure. It is worth noting that the grain sizes of NKN ceramics also show a clear bimodal distribution at 1150 °C, with many fine grains being located at the boundaries of coarse grains as shown in Figure 2(b). The average grain size of the samples was in a range ~0.45–7.436 µm. After 1150 °C, it seems as the grain size increases above 2 µm, this result in lowering of dielectric constant at higher temperatures. This result suggests that the sintering temperatures have too much effect on the microstructure and uniformly distributed large grains of the NKN ceramics.

Table 1 represents the SEM-EDAX quantitative analysis of $Na_{0.92}K_{0.08}NbO_3$ for different sintering temperatures. The observed atomic weight % shows escaping of Na and K with sintering temperatures 1100 °C, 1150 °C, 1200 °C and 1250 °C. Further sintering of $Na_{0.92}K_{0.08}NbO_3$ ceramics at 1150 °C, as shown in Table 2, results in lowering of both. At temperatures higher than 1150 °C a sharp increase in grain size of all temperatures occurs which is due to the loss of Na and K. Such behavior during sintering are in continuation of the nature of these materials [29–31].

Table 1 represents the SEM-EDAX quantitative analysis of $Na_{0.92}K_{0.08}NbO_3$ for different sintering temperatures. The low value of escaping of Na & K (%) at 1150 °C. Further increasing the sintering temperature increases the escaping of Na and K. This volatility of Na and K results in high value of peak dielectric constant (ϵ_c) at 1150 °C as shown in Table 2, at which the SEM results shows uniformly distributed large grains. Increasing the sintering temperature above 1150 °C results in high escaping of Na & K that decreases the peak dielectric constant (ϵ_c). Table 2 shows for temperatures higher than 1150 °C a sharp drop in dielectric constant for compositions with increasing sintering temperatures occurs, which is due to the loss of Na and K volatile elements resulting in reduction of the sample's mass. Appearance of such behavior during sintering of

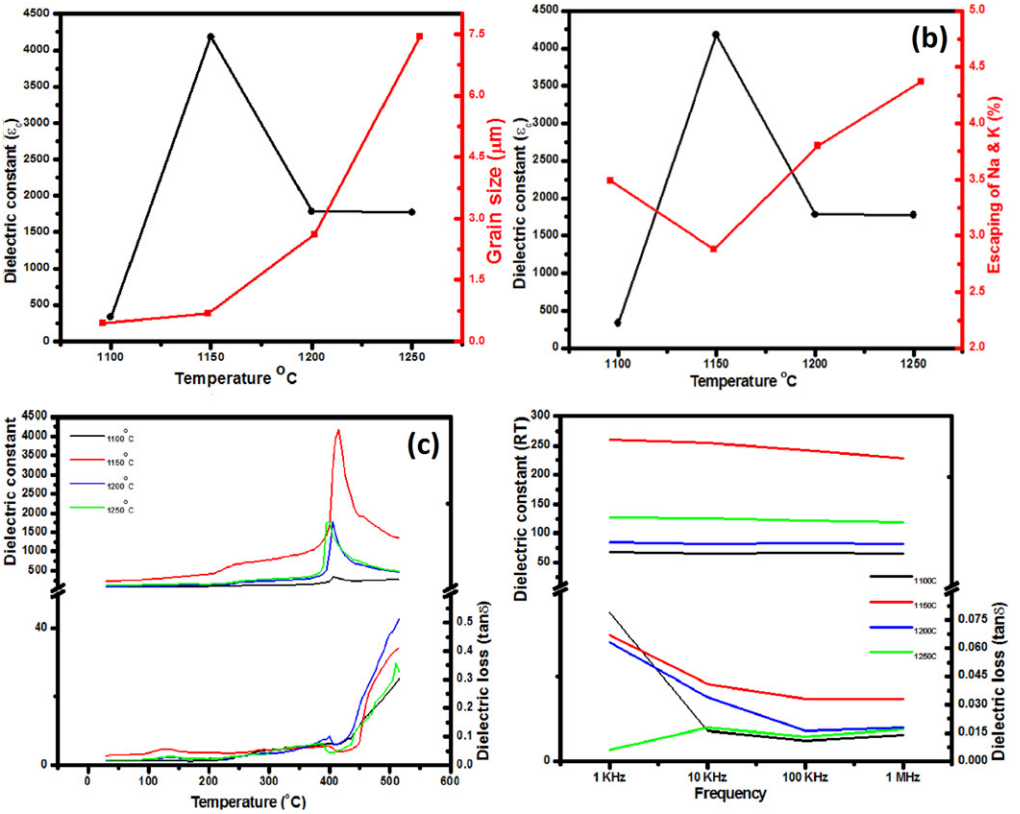

Figure 3. (a) Dielectric constant and grain size variation with different sintering temperature, (b) Dielectric constant and escaping of Na & K with different sintering temperature, Dielectric constant and dielectric loss with (c) temperature and (d) frequency.

NKN-based compounds results in difficulty and narrowness of proper sintering temperature range for these materials [33–35]. At higher temperatures, not only it is not possible to reach higher dielectric constant, but also there is risk of alkali elements loss. Transition temperature shifts slightly towards low temperature with increasing sintering temperature further 1150 °C.

Figure 3(a) indicate the peak dielectric constant and grain size dependence on sintering temperatures. After 1150 °C further sintering increases the grain size but reduces the peak dielectric constant. Figure 3(d) shows the frequency dependent dielectric constant and dielectric loss at room temperature. Dielectric constant remains constant throughout the frequency range for all sintering temperatures. Dielectric constant and dielectric loss at room temperature are higher at high frequency for sintering temperature 1150 °C.

4. Conclusions

The analysis shows the impact of different sintering temperatures on $Na_{0.92}K_{0.08}NbO_3$ ceramic. It is observed that with increasing sintering temperatures the grain size also increases. Also the volatility of Na and K is observed with increasing sintering temperatures that result in lowering of peak dielectric constant. At sintering temperature

1150 °C the grains are found uniformly distributed and low value of Escaping of Na & K results in high value of peak dielectric constant.

Acknowledgements

The authors are thankful to Prof. N. S. Panwar, Head, Department of Instrumentation Engineering-USIC, SOET, HNB Garhwal University, Srinagar (Garhwal), for his kind suggestion. Prof. N. S. Panwar is also thankfully acknowledged for providing laboratory facilities.

ORCID

Gambheer Singh Kathait http://orcid.org/0000-0002-2400-3391

References

[1] G. A. Samara, Effects of pressure on the dielectric properties and phase transitions of the alkali metal tantalates and niobates. *Ferroelectrics*. **73**(1), 145 (1987). DOI: 10.1080/00150198708227914.

[2] B. T. Mathias, J. P. Remeika, Dielectric properties of sodium and potassium niobates. *Phys. Rev*. **82**(5), 727 (1951). DOI: 10.1103/PhysRev.82.727.

[3] B. Jaffe, W. R. Cook, and H. Jaffe, *Piezoelectric Ceramics*, Vol. 3, ix, p 317. (Academic Press, New York, 1971).

[4] Y. Lu, D.-Y. Jeong, Z.-Y. Cheng, Q. M. Zhang, H.-S. Luo, Z.-W. Yin, and D. Viehland, Phase transitional behavior and piezoelectric properties of the orthorhombic phase of $Pb(Mg_{1/3}Nb_{2/3})O_3$–$PbTiO_3$ single crystals. *Appl. Phys. Lett*. **78**(20), 3109 (2001).

[5] W. Ren, S. F. Liu, and B. K. Mukherjee, Piezoelectric properties and phase transitions of/001S-oriented $Pb(Zn1/3Nb2/3)O_3$–$PbTiO_3$ single crystals. *Appl. Phys. Lett*. **80**(17), 3174 (2002). DOI: 10.1063/1.1474600.

[6] S. E. Park, and T. R. Shrout, Ultrahigh strain and piezoelectric behavior in relaxor based ferroelectric single crystals. *J. Appl. Phys*. **82**(4), 1804 (1997). DOI: 10.1063/1.365983.

[7] Y. Saito, H. Takao, T. Tani, T. Nonoyama, K. Takatori, T. Homma, T. Nagaya, and M. Nakamura, Lead-free piezoceramics. *Nature (London)*. **432**(7013), 84 (2004).

[8] Y. Guo, K. Kakimoto, and H. Ohsato, Phase transitional behavior and piezoelectric properties of $(Na_{0.5}K_{0.5})NbO_3$–$LiNbO_3$$(Na_{0.5}K_{0.5})NbO_3$–$LiNbO_3$ ceramics. *Appl. Phys. Lett*. **85**(18), 4121 (2004). DOI: 10.1063/1.1813636.

[9] M. Matsubara, K. Kikuta, and S. Hirano, Piezoelectric properties of (K0.5Na0.5)(Nb1 − xTax)O3 − K5.4CuTa10O29 ceramics. *J. Appl. Phys*. **97**(11), 114105 (2005). DOI: 10.1063/1.1926396.

[10] Y. Guo, K. Kakimoto, and H. Ohsato, $(Na_{0.5}K_{0.5})NbO_3$–$LiTaO_3$ lead-free piezoelectric ceramics. *Mater. Lett*. **59**(2–3), 241 (2005). DOI: 10.1016/j.matlet.2004.07.057.

[11] E. Hollenstein, M. Davis, D. Damjanovic, and N. Setter, Piezoelectric properties of Li- and Ta-modified (K0.5Na0.5)NbO3 ceramics. *Appl. Phys. Lett*. **87**(18), 182905 (2005). DOI: 10.1063/1.2123387.

[12] H.-Y. Park, C.-W. Ahn, H.-C. Song, J.-H. Lee, S. Nahm, K. Uchino, H.-G. Lee, and H.-J. Lee, Microstructure and piezoelectric properties of $0.95(Na_{0.5}K_{0.5})NbO_3$–$0.05BaTiO_3$ $0.95(Na_{0.5}K_{0.5})NbO_30.05BaTiO_3$ ceramics. *Appl. Phys. Lett*. **89**(6), 062906 (2006).

[13] Y. Saito, and H. Takao, Synthesis of polycrystalline plate like $KNbO_3$ particles by the topochemical micro-crystal conversion method and fabrication of grain-oriented $(K0.5Na0.5)NbO_3$ ceramics. *J. Euro. Ceram. Soc*. **27**(13–15), 4085 (2007). DOI: 10.1016/j.jeurceramsoc.2007.02.099.

[14] H. Lu, S.-Y. Lo, and H.-C. Lin, Hydrothermal synthesis of nonlinear optical potassium niobate ceramic powder. *Mater. Lett*. **34**(3–6), 172 (1998). DOI: 10.1016/S0167-577X(97)00170-5.

[15] C.-H. Lu, S.-Y. Lo, and Y. L. Wang, Glycothermal preparation of potassium niobate ceramic particles under supercritical condition. *Mater. Lett.* **55**(1–2), 121 (2002). DOI: 10.1016/S0167-577X(01)00633-4.

[16] G. Shirane, R. Newnham, and R. Pepinsky, Dielectric properties and phase transitions of NaNbO3 and (Na,K)NbO3. *Phys. Rev.* **96**(3), 581 (1954). DOI: 10.1103/PhysRev.96.581.

[17] L. Egerton, and D. M. Dillon, Piezoelectric and dielectric properties of ceramics in the system potassium-sodium niobate. *J. Am. Ceram. Soc.* **42**(9), 438 (1959). DOI: 10.1111/j.1151-2916.1959.tb12971.x.

[18] R. E. Jaeger, and L. Egerton, Hot pressing of potassium-sodium niobates. *J. Am. Ceram. Soc.* **45**(5), 209 (1962). DOI: 10.1111/j.1151-2916.1962.tb11127.x.

[19] G. H. Haertling, Properties of hot-pressed ferroelectric alkali niobate ceramics. *J. Am. Ceram. Soc.* **50**(6), 329 (1967). DOI: 10.1111/j.1151-2916.1967.tb15121.x.

[20] N. Klein, E. Hollenstein, D. Damjanovic, H. J. Trodahl, N. Setter, and M. Kuball, A study of the phase diagram of (K,Na,Li)NbO_3 determined by dielectric and piezoelectric measurements, and Raman spectroscopy. *J. Appl. Phys.* **102**(1), 014112 (2007).

[21] Y. Guo, K. Kakimoto, and H. Ohsato, Phase transitional behavior and piezoelectric properties of (Na0.5K0.5)NbO_3– $LiNbO_3$ ceramics. *Appl. Phys. Lett.* **85**(18), 4121 (2004). DOI: 10.1063/1.1813636.

[22] M. Matsubara, T. Yamaguchi, K. Kikuta, and S. I. Hirano, Effect of Li substitution on the piezoelectric properties of potassium sodium niobate ceramics. *Jpn. J. Appl. Phys.* **44**(8), 6136 (2005). DOI: 10.1143/JJAP.44.6136.

[23] Y. Guo, K. Kakimoto, and H. Ohsato, ($Na_{0.5}K_{0.5}$)NbO_3–$LiTaO_3$ lead-free piezoelectric ceramics. *Mater. Lett.* **59**(2–3), 241 (2005). DOI: 10.1016/j.matlet.2004.07.057.

[24] R. Wang, R.-J. Xie, K. Hanada, K. Matsusaki, H. Kawanaka, H. Bando, T. Sekiya, and M. Itoh, Enhanced piezoelectricity around the tetragonal/orthorhombic morphotropic phase boundary in (Na, K)NbO_3–$ATiO_3$ solid solutions. *J. Electroceram.* **21**(1–4), 263 (2008).

[25] Y. Saito, H. Takao, T. Tani, T. Nonoyama, K. Takatori, T. Homma, T. Nagaya, and M. Nakamura, Lead-free piezoceramics. *Nature* (London) **432**(7013), 84 (2004).

[26] L. Wu, J. L. Zhang, C. L. Wang, and J. C. Li, Influence of compositional ratio K/Na on physical properties in $K_xNa_{1-x}NbO_3$ ceramics. *J. Appl. Phys.* **103**(8), 084116 (2008). DOI: 10.1063/1.2907866.

[27] R. C. Chang, S.-Y. Chu, Y.-F. Lin, C.-S. Hong, P.-C. Kao, and C.-H. Lu, The effects of sintering temperature on the properties of ($Na_{0.5}K_{0.5}$)NbO_3-$CaTiO_3$ based lead-free ceramics. *Sens. Actuat. A.* **138**(2), 355 (2007).

[28] H. Birol, D. Damjanovic, and N. Setter, Preparation and characterization of ($K_{0.5}Na_{0.5}$)NbO_3 ceramics. *J. Eur. Ceram. Soc.* **26**(6), 861 (2006). DOI: 10.1016/j.jeurceramsoc.2004.11.022.

[29] J. G. Fisher, D. Rout, K.-S. Moon, and S.-J. L. Kang, High-temperature X-ray diffraction and Raman spectroscopy study of ($K_{0.5}Na_{0.5}$)NbO_3 ceramics sintered in oxidizing and reducing atmospheres. *Mater. Chem. Phys.* **120**(2–3), 263 (2010). DOI: 10.1016/j.matchemphys.2009.11.001.

[30] V. J. Tennery, K. W. Hang, and X. Thermal, Ray diffraction studies of the NaNbO3–KNbO3 system. *J. Appl. Phys.* **39**(10), 4749 (1968). DOI: 10.1063/1.1655833.

[31] C. N. W. Darlington, and H. D. Megaw, The low-temperature phase transition of sodium niobate and the structure of the low-temperature phase. *Acta Crystallogr. B Struct. Sci.* **B29**, 2171 (1973). DOI: 10.1107/S0567740873006308.

[32] R. Zuo, J. Rodel, R. Chen, and L. Li, Sintering and electrical properties of lead-free $Na_{0.5}K_{0.5}NbO_3$ piezoelectric ceramics. *J. Am. Ceram. Soc.* **89**(6), 2010 (2006). DOI: 10.1111/j.1551-2916.2006.00991.x.

[33] J. B. Lim, S. Zhang, J. H. Jeon, and T. R. Shrout, (K,Na)NbO_3-based ceramics for piezoelectric "hard" lead-free materials. *J. Am. Ceram. Soc.* **93**(5), 1218 (2010).

[34] M. Matsubara, T. Yamaguchi, K. Kikuta, and S. I. Hirano, Effect of Li substitution on the piezoelectric properties of potassium sodium niobate ceramics. *Jpn. J. Appl. Phys.* **44**(8), 6136 (2005). DOI: 10.1143/JJAP.44.6136.

Ceramics International 45 (2019) 13067–13071

Contents lists available at ScienceDirect

Ceramics International

journal homepage: www.elsevier.com/locate/ceramint

Temperature dependent dielectric properties of (na, K) NbO_3, near equimolar composition

Surendra Singh[a,*], Jyotsana Negi[a], N.S. Panwar[b]

[a] Department of Physics, H. N. B. Garhwal University, Srinagar, Garhwal, 246174, India
[b] University Science Instrumentation Centre, H. N. B. Garhwal University, Srinagar, Garhwal, 246174, India

ARTICLE INFO

Keywords:
Ferroelectrics
Solid state reaction
Dielectric constant
Electric conductivity

ABSTRACT

Pellet samples of $Na_{1-x}K_xNbO_3$ ($0.490 \leq x \leq 0.510$) were prepared using solid state reaction method with double sintering. Dielectric measurements were carried out on the prepared samples, from 30 to 500 °C, at 1 MHz. Dielectric constant and electrical conductivity were found minimum, for $x = 0.500$ among all the prepared compositions, at room temperature and at all the measured frequencies. Three distinguished phase transitions, at 200, 380 and 460 °C, were observed in dielectric measurements of the prepared compositions. The high temperature X-ray diffraction (HT- XRD) of the samples with $x = 0.500$, shows monoclinic phase between room temperature and 200 °C, tetragonal between 200 and 380 °C, tetragonal with increased lattice parameters, between 380 and 460 °C, and cubic phase beyond 460 °C. The tetragonal to tetragonal phase transition at 380 °C, and tetragonal to cubic at 460 °C was distinctly observed from dielectric and HT- XRD measurements in the present study.

1. Introduction

Perovskite sodium potassium niobate ($Na_{1-x}K_xNbO_3$), having cubic ABO_3 structure in high temperature paraelectric phase, is an interesting system due to its number of ferroelectric phases, with high spontaneous polarization at room temperature [1,2]. Ahtee et al. [3] studied the high-temperature phases of $NaNbO_3$–$KNbO_3$ solid solutions using high temperature XRD (HT –XRD). Nobre et al. [4,5] observed four phase transitions, from room temperature (RT) to 750 °C, in polycrystalline $Na_{0.85}Li_{0.15}NbO_3$ and $Na_{0.88}K_{0.15}NbO_3$. Dabin Lin et al. [6] observed tetragonal to tetragonal, and tetragonal to cubic phase transition temperature for ($Na_{0.89}K_{0.11}$) NbO_3 crystals, at 405 and 496 °C, respectively: and some workers [7–9] observed two phase transitions, near about 200 and 400 °C, in the dielectric measurements of sodium-potassium niobate (NKN) ceramics. The temperature dependent dielectric properties of the ABO_3 type perovskites have been associated with a significantly temperature dependent low frequency optical soft mode [10,11], which softens at the transition temperature (T_c), and is responsible for the anomalous dielectric behavior of these materials, at T_c. The phase transition in ferroelectrics is accompanied by anomalies in different physical quantities. Frequency of the soft mode tends to zero and the lattice displacement associated with it becomes unstable, leading to the phase transition, at T_c. A series of structural phase transitions in this system is associated with the tilting of the BO_6 octahedra [2]. However, the static tilting theory is the manifestation of the dynamic soft mode theory. NKN based ceramic and ceramics have significant potential to substitute the lead based oxides, in delay-lines and piezoelectric applications [12–16]. Promising piezoelectric properties in alkali niobates are believed to arise from the coexistence of thermodynamically equivalent phases at the morphotropic phase boundary (MPB) composition. At MPB, enhanced piezoelectric responses are found due to the ease of polarization rotation under the external electric field [17].

Jaffe et al. [18], Tennery and Hang [19], and Ahtee and Glazer [3] have presented phase diagram of $Na_{1-x}K_xNbO_3$ system showing different phase fields. In the compositional range $0.2 < x < 0.5$, above 400 °C, Ahtee and Glazer [3] have indicated the existence of a phase X, in the phase diagram, but suspected its existence in reality. Though beyond the phase X existence of cubic phase was evident, at higher temperatures [3].

Present study was focused on the temperature dependent dielectric properties of NKN composition with equimolar (Na, K) morphotropic composition. $Na_{1-x}K_xNbO_3$ ($0.490 \leq x \leq 0.510$) pellet samples were prepared by solid state reaction route using double sintering. Temperature dependence of dielectric constant and electric conductivity of the prepared samples was measured at 1 MHz and HT-XRD of the samples with $x = 0.500$ was carried out, in the temperature range from RT to 500 °C. Dielectric and structural evidence of the existence of

* Corresponding author.
E-mail address: jhinkwan.surendra@gmail.com (S. Singh).

https://doi.org/10.1016/j.ceramint.2019.03.238
Received 31 January 2019; Received in revised form 28 March 2019; Accepted 29 March 2019
Available online 30 March 2019
0272-8842/ © 2019 Elsevier Ltd and Techna Group S.r.l. All rights reserved.

the so called X phase has been reported.

2. Experimentation

The preparation method of $Na_{1-x}K_xNbO_3$ ($0.490 \le x \le 0.510$) ceramic pellets, their room temperature X-ray diffraction (XRD) patterns, surface morphology, density and low temperature dielectric properties have been described in a previous communication [20]. Presently, the dielectric constant (ε) and electric conductivity (σ) of the prepared samples were measured, in metal-insulator- metal (MIM) configuration, by RLC meter (Fluke, PM 6306), with increasing and decreasing temperature cycles, at 1 MHz. HT- XRD diffraction of the samples with x = 0.500 was carried out by an X-ray diffractometer (PANalytical, X'PERT PRO), in the temperature range from RT to 500 °C.

3. Results and discussion

3.1. Dielectric measurements

Variation of dielectric constant (ε) of different prepared compositions with increasing temperature has been shown in Fig. 1. For all the prepared compositions, dielectric constant was observed gradually increasing with increasing temperature, but with anomalously large values at around 200, 400 and 450 °C, indicating distinct phase transitions at these temperatures [21].

Near the first transition, around 200 °C, maximum peak value was observed for the composition with x = 0.495 (peak value 738, at 200 °C) and minimum peak value for x = 0.500 (peak value 253, at 210 °C). Dielectric constant shows the maximum peak value for the composition with x.

= 0.510 (peak value 5482, at 400 °C) and minimum for x = 0.500 (peak value 1552, at 405 °C). Around the third transition, at around 455 °C, the dielectric constant shows the maximum peak value for x = 0.505 (peak value 5499, at 460 °C) and minimum peak value for x = 0.500 (peak value 2290, at 460 °C). Among all the prepared compositions dielectric constant was observed minimum for x = 0.500 at all the measured temperatures, Fig. 1, showing MPB at this composition [20,22].

Fig. 2 shows the observed variation of dielectric constant (ε) of the prepared compositions with decreasing temperature. While decreasing temperature from 500 °C, the dielectric constant measurements show

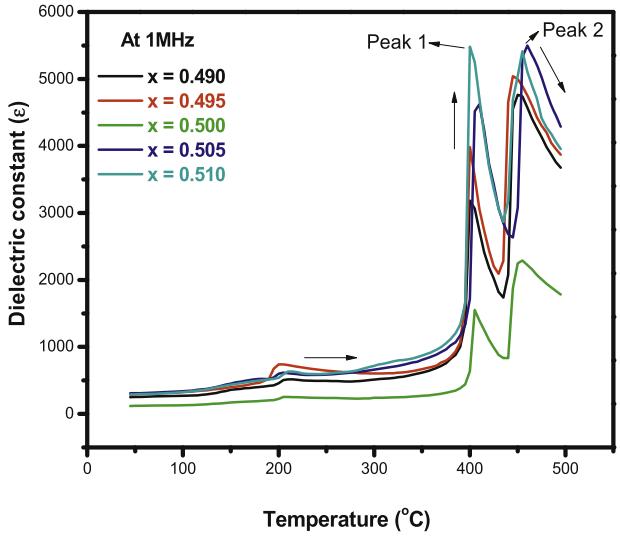

Fig. 1. Temperature variation (with increasing temperature) of dielectric constant (ε). of $Na_{1-x}K_xNbO_3$ ($0.490 \le x \le 0.510$) for different compositions (x), at 1 MHz.

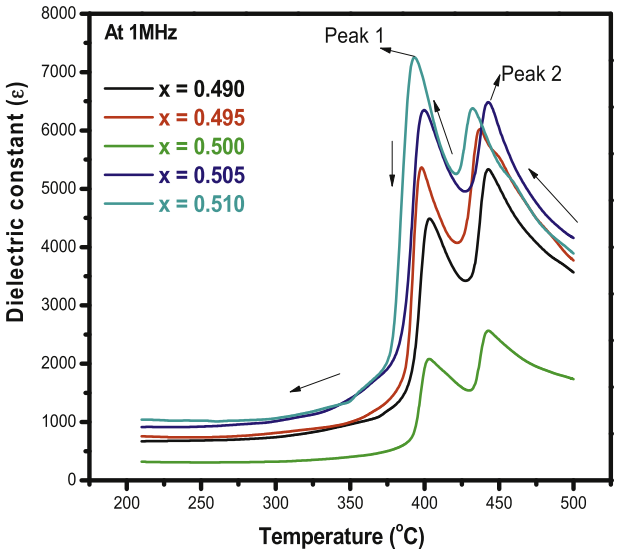

Fig. 2. Temperature variation (with decreasing temperature) of dielectric constant (ε) of $Na_{1-x}K_xNbO_3$ ($0.490 \le x \le 0.510$) for different compositions (x), at 1 MHz.

phase transitions varying from 430 to 440 °C, for x = 0.490 to 0.510. The maximum peak value was observed for x = 0.505 (peak value 6563, at 440 °C) and minimum peak value for x = 0.500 (peak value 2643, at 440 °C). With further decrease in temperature, the phase transitions were observed, at the temperatures varying between 385 and 400 °C, for all the prepared compositions with x = 0.490 to 0.510, Fig. 2. For the prepared samples, at this transition, the dielectric constant shows the maximum peak value for x = 0.510 (peak value 7335, at 385 °C) and minimum peak value for x = 0.500 (peak value 2184, at 400 °C). With decreasing temperature also the dielectric constant measurements show two distinguishable transitions, at around 400 and 440 °C. However, these transition temperatures were observed slightly shifted towards lower temperatures as compared to those observed with increasing temperature measurements. The dielectric constant was found minimum, for x = 0.500, in both the temperature cycles, at all the measured temperatures. Variation of dielectric constant with increasing and decreasing temperature cycle, for the samples with x = 0.500, is shown in Fig. 3.

With increasing and decreasing temperature, variation of electric conductivity (σ) of the prepared compositions has been shown in Figs. 4

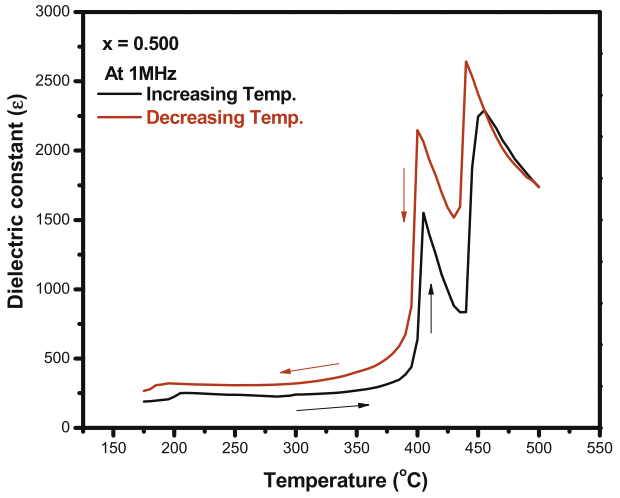

Fig. 3. Temperature variation of dielectric constant (ε) of $Na_{1-x}K_xNbO_3$ (x = 0.500), with. increasing and decreasing temperature, at 1 MHz.

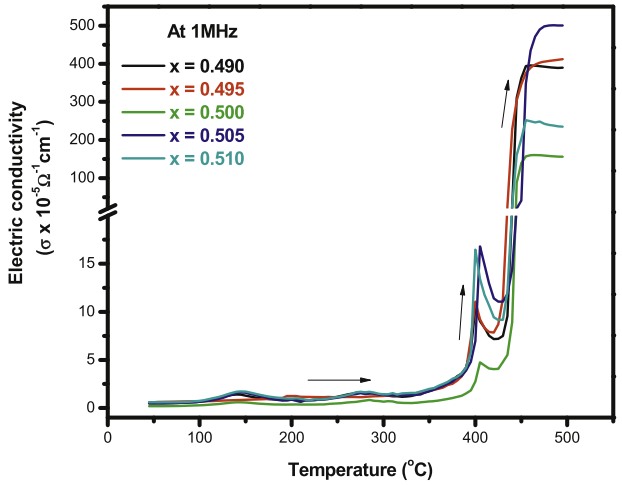

Fig. 4. Temperature variation of electric conductivity (σ) of $Na_{1-x}K_xNbO_3$ ($0.490 \leq x \leq 0.510$). for different compositions (x), at 1 MHz (with increasing temperature).

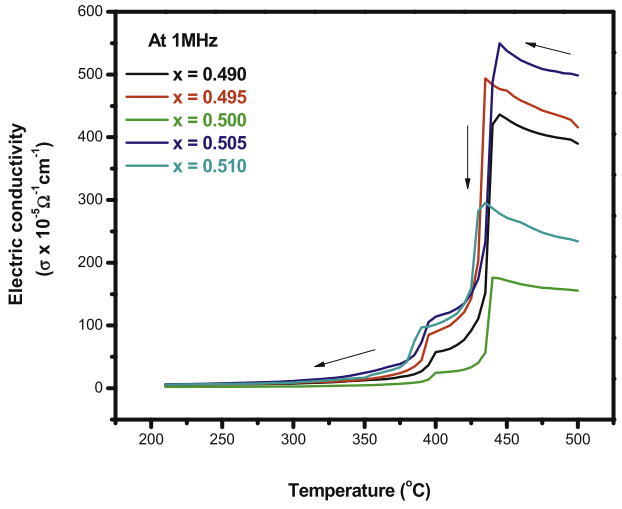

Fig. 5. Temperature variation of electric conductivity (σ) of $Na_{1-x}K_xNbO_3$ ($0.490 \leq x \leq 0.510$), for different compositions (x), at 1 MHz (with decreasing temperature).

and 5, respectively. The higher transition temperatures were observed varying from 400 to 405 °C, for x = 0.490 to 0.510. With the increasing temperature, electric conductivity shows the maximum peak value for x = 0.505 (peak value $16.81 \times 10^{-5}\,\Omega^{-1}cm^{-1}$, at 405 °C) and minimum peak value for x = 0.500 (peak value $4.10 \times 10^{-5}\,\Omega^{-1}cm^{-1}$, at 405 °C). With further increase in temperature electric conductivity shows transition temperatures ranging between 455 and 465 °C, for the prepared compositions, with maximum peak value for x = 0.505 (peak value $471.29 \times 10^{-5}\,\Omega^{-1}cm^{-1}$, at 465 °C) and minimum peak value for x = 0.500 (peak value $159.89 \times 10^{-5}\,\Omega^{-1}cm^{-1}$, at 455 °C), Fig. 4. The behavior of electric conductivity (σ) of the prepared compositions with decreasing temperature follows similar pattern as that for increasing temperature, with the transition temperatures varying between 435 and 445 °C, with maximum peak value for x = 0.505 (peak value $549.56 \times 10^{-5}\,\Omega^{-1}cm^{-1}$, at 445 °C) and minimum peak value for x = 0.500 (peak value $176.08 \times 10^{-5}\,\Omega^{-1}cm^{-1}$, at 445 °C), Fig. 5. With further decrease in temperature, another transition temperatures between 385 and 395 °C were observed for the prepared compositions, with maximum peak value for x = 0.505 (peak value $52.96 \times 10^{-5}\,\Omega^{-1}cm^{-1}$, at 390 °C) and minimum peak value for

Table 1
Transition temperatures observed from dielectric constant (ε), and electric conductivity (σ) measurements (with increasing temperature).

x value	Transition temperature (oC) from dielectric constant measurements		Transition temperature (oC) from electric conductivity (σ) measurements	
	peak 1	peak 2	peak 1	peak 2
0.490	400	455	400	460
0.495	400	445	400	460
0.500	405	455	405	455
0.505	410	460	405	465
0.510	400	455	400	455

x = 0.500 (peak value $24.70 \times 10^{-5}\,\Omega^{-1}cm^{-1}$, at 395 °C), Fig. 5. The electric conductivity measurement also shows two distinguishable transitions near 400 and 450 °C. Among all the prepared compositions the minimum electric conductivity observed for the composition x = 0.500, at all the measured temperatures, supports the existence of MPB, at this composition [20,22].

The higher temperature transitions observed from the peaks of dielectric constant and electric conductivity measurements, with increasing and decreasing temperatures, have been given in Tables 1 and 2, respectively. The electric conductivity peaks, at around 450 °C (peak 2), were found at slightly higher temperatures than those observed from the dielectric constant measurements, while the electric conductivity peaks at around 400 °C (peak 1), were found slightly lower than the dielectric constant peaks, for all the prepared samples. The difference in the transition temperature, observed from the electric conductivity and dielectric constant measurements may be due to the resultant effect of activation energy of surface terms [23], potential barrier heights at grain boundaries [24,25], and softening of the temperature dependent optical mode [10,11]. In the increasing temperature cycle value of dielectric constant at a temperature was observed lower than that observed in the decreasing temperature cycle, Figs. 1–3. In the decreasing temperature cycle all the peaks were observed slightly shifted towards lower temperature than those observed with increasing temperature. The observed variation in the dielectric constant, at a temperature, in the increasing and decreasing temperature cycle, is an indication of thermal hysteresis, which may be associated with the development of multi domain patterns caused by internal strain [26].

3.2. X-ray Diffractometer measurements

The observed HT- XRD patterns of the prepared samples, with x = 0.500, have been shown in Fig. 6. The room temperature XRD patterns of the prepared samples show polycrystalline behavior and were found in good agreement with the Inorganic Crystal Structure Database (ICSD)- (00-061-0315) data of $Na_{0.5}K_{0.5}NbO_3$, with peaks corresponding to (100), (110), (211), etc.

The observed XRD patterns of the prepared samples show

Table 2
Transition temperatures observed from dielectric constant (ε), and electric conductivity (σ) measurements (with decreasing temperature).

x value	Transition temperature (oC) from dielectric constant measurements		Transition temperature (oC) from electric conductivity (σ) measurements	
	Peak 2	Peak 1	peak 2	peak 1
0.490	440	400	445	395
0.495	435	395	435	390
0.500	440	400	445	395
0.505	440	400	445	390
0.510	430	390	435	385

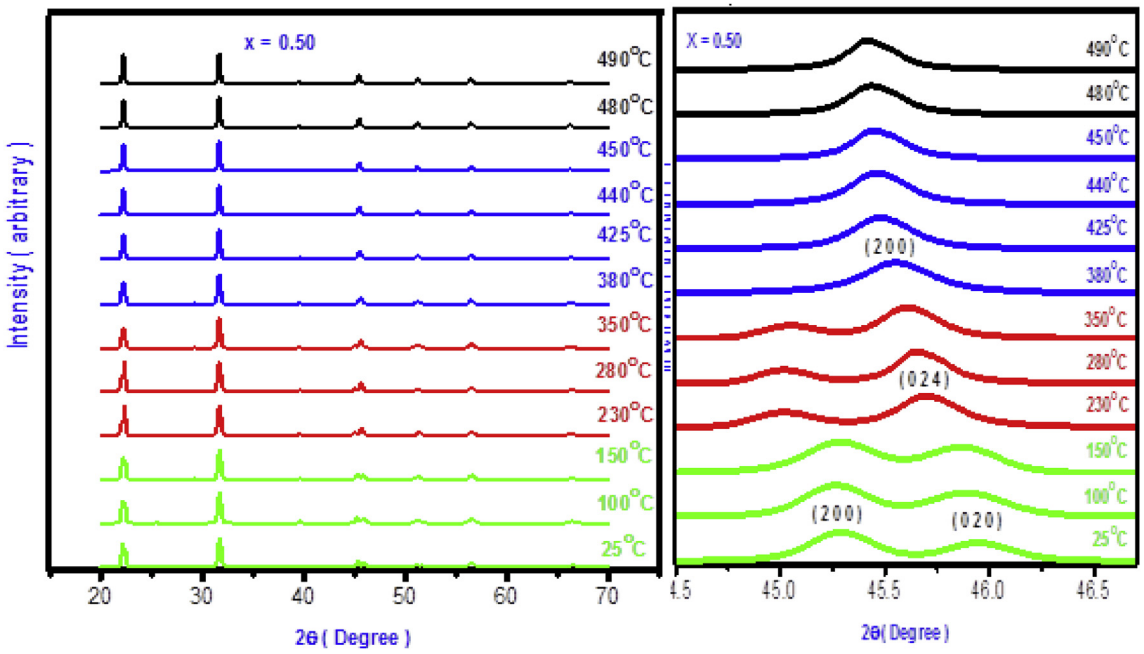

Fig. 6. Temperature variation of XRD patterns of Na_{1-x} K_xNbO_3 (x = 0.500).

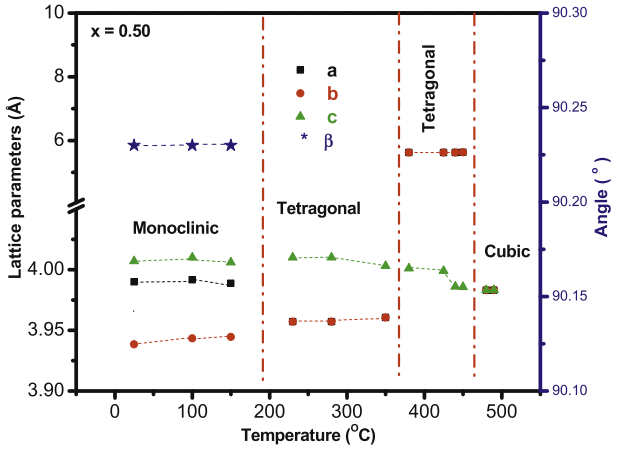

Fig. 7. Variation of lattice parameters with Temperature in Na_{1-x} K_xNbO_3 (x = 0.500).

monoclinic phase, between RT and around 200 °C, which is consistent with ICSD- (00-061-0317) and (00-061-0315) data, and in good agreement with the observations of reference [28]. Between 200 and 380 °C, it shows tetragonal phase, consistent with ICSD- (01-078-5547) data; between 380 and 460 °C, tetragonal phase, consistent with ICSD- (00-077-0037) data, and reference [4]; and above 460 °C, it shows cubic phase, compatible with ICSD- (00-060-0328) data, and consistent with reference [3].

In the HT- XRD patterns a continuous shifting of the most intense peaks (100), (010), (200), and (020) with temperature was observed in $Na_{1-x}K_xNbO_3$ (x = 0.500). Between RT to 200 °C, these peaks were observed shifting to higher angle with increasing temperature, above 200 °C these peaks shift towards lower angle with increasing temperature, and above 380 °C, peaks (100) and (200) vanished, and above 460 °C remaining peaks were observed slightly shifting towards lower angle, Fig. 6. The observed HT-XRD patterns clearly show the four distinguishable phases, with transitions at around 200, 380 and 460 °C. Observed temperature variation of lattice parameters and angle (β for monoclinic symmetry) has been shown in Fig. 7. The cell parameters were refined by High Score Plus software, using the Rietveld method [27], and the background was modeled using the Legendre polynom and the peaks' profiles were refined using a pseudo-Voigt function. The chosen space groups for these refinements were monoclinic Pm6, tetragonal P4mm, respectively [28]. Above 460 °C, the system shows cubic phase. Refined lattice parameters show the three abrupt changes as shown in Fig. 7. The observed diffraction patterns make it possible to distinguish the monoclinic, tetragonal, tetragonal and cubic symmetries.

The HT- XRD results of $Na_{1-x}K_xNbO_3$ (x = 0.500) pellets, show three phase transitions, monoclinic to tetragonal, tetragonal to tetragonal, and tetragonal to cubic at around 200, 380 and 460 °C, respectively. The observed HT- XRD results are in consistent with the transitions observed from the dielectric constant and electric conductivity measurements of $Na_{1-x}K_xNbO_3$ ($0.490 \leq x \leq 0.510$) pellets. Form these observations it is evident that the so called X phase exists as the tetragonal phase between 380 and 460 °C, in the measured compositions.

3.3. Conclusion

Among all the prepared $Na_{1-x}K_xNbO_3$ ($0.490 \leq x \leq 0.510$) compositions, dielectric constant and electric conductivity were found minimum for the samples with x = 0.500, at all the measured temperatures, which is a strong evidence of the existence of MPB at this composition. The HT- XRD results, observed for x = 0.500 composition, clearly indicate the existence of four distinct phases, viz., monoclinic, between RT and 200 °C; tetragonal, between 200 and 380 °C; tetragonal, between 380 and 460 °C; and cubic, above 460 °C, which is consistent with the dielectric and electric conductivity measurements.

References

[1] H.D. Megaw, The seven phases of sodium niobate, Ferroelectrics 7 (1974) 87–89.
[2] A.M. Glazer, K. Ishida, Cation displacements and octahedral tilts in $NaNbO_{[3]}$ Part I- Determination from x-ray difference reflections, Ferroelectrics 6 (1974) 219–1224.
[3] M. Ahtee, A.M. Glazer, High-temperature phases of sodium niobate- potassium niobate solid solutions, Ferroelectrics 12 (1976) 205–206.
[4] M.A.L. Nobre, S. Lanfredi, Impedance spectroscopy analysis of high- temperature phase transitions in sodium lithium niobate ceramics, J. Phys. Condens. Matter 12 (2000) 7833–7841.
[5] M.A.L. Nobre, S. Lanfredi, Phase transition in sodium lithium niobate polycrystal: an overview based on impedance spectroscopy, J. Phys. Chem. Solids 62 (2001) 1999–2006.

[6] D. Lin, Z. Li, F. Li, C. Cai, W. Liu, S. Zhang, Tetragonal- to- tetragonal phase transition in lead- free $(K_xNa_{1-x})NbO_3$ (x = 0.11 and 0.17) crystals, Crystals 4 (2014) 113–122.
[7] A.S. Kandari, A. Bhandari, A.A. Bourai, N.S. Panwar, Electrical properties of $Na_{1-x}K_xNbO_3$ ($0.28 \leq x \leq 0.40$), Ferroelectrics 386 (2009) 139–151.
[8] V. Lingwal, B.S. Semwal, N.S. Panwar, Relaxational behavior of mixed $NaNbO_{[3]}$-$KNbO_{[3]}$ system, Ferroelectrics 332 (2006) 219–225.
[9] Y. Zhen, J.F. Li, Normal sintering of (K, Na)$NbO_{[3]}$- based ceramics: influence of sintering temperature on densification, microstructure, and electrical properties, J. Am. Ceram. Soc. 89 (2006) 3669–3675.
[10] E. Pytte, Theory of perovskite ferroelectrics, Phys. Rev. B 5 (1972) 3758–3769.
[11] N.S. Panwar, T.C. Upadhyay, B.S. Semwal, Soft mode dynamics of perovskite type crystals, Pramana - J. Phys. 33 (1989) 603–616.
[12] L. Egerton, Dolores M. Dillon, Piezoelectric and dielectric properties of ceramics in the system potassium-sodium niobate, J. Amer. Soc. 42 (1959) 438–442.
[13] S.Y. Chu, W. Water, Y.D. Juang, J.T. Liaw, S.B. Dai, Piezoelectric and dielectric characteristics of lithium potassium niobate ceramic system, Ferroelectrics 297 (2003) 11–17.
[14] H. Zhang, Y. Zhu, P. Fan, M.A. Mawat, W. Ma, K. Liu, H. Liu, B. Xie, K. Wang, J. Koruza, Temperature-insensitive electric-field-induced strain and enhanced piezoelectric properties of < 001 > textured (K, Na)NbO3-based lead-free piezoceramics, Acta Mater. 156 (2018) 389–398.
[15] P. Fan, Y. Zhang, Qi Zhang, B. Xiea, Y. Zhua, M. Ali Mawat, W. Ma, K. Liu, J. Xiao, Haibo Zhang, Large strain with low hysteresis in Bi4Ti3O12 modified $Bi_{1/2}(Na_{[0.82]}K_{[0.18]})_{1/2}TiO_{[3]}$ lead-free Piezoceramics, J. Eur. Ceram. Soc. 38 (2018) 4404–4413.
[16] H. Zhang, P. Xu, E. Patterson, J. Zang, S. Jiang, J. Rödel, Preparation and enhanced electrical properties of grain-oriented $(Bi_{1/2}Na_{1/2})TiO_{[3]}$-based lead-free incipient piezoceramics, J. Eur. Ceram. Soc. 35 (9) (2015) 2501–2512.
[17] S.E. Park, T.R. Shrout, Ultrahigh strain and piezoelectric behavior in relaxor based ferroelectric single crystals, J. Appl. Phys. 82 (1997) 1804–1811.
[18] B. Jaffe, W.R. Cook, J.H. Jaffe, Piezoelectric Ceramics, Academic, New York, 1971.
[19] V.J. Tennery, K.W. Hang, Thermal and x-ray diffraction studies of the $NaNbO_{[3]}$–$KNbO_{[3]}$ system, J. Appl. Phys. 39 (1968) 4749–4753.
[20] S. Singh, J. Negi, N.S. Panwar, Dielectric properties of $Na_{1-x}K_xNbO_3$, near x = 0.5 morphotropic phase region, J. Phys. Chem. Solids 123 (2018) 311–317.
[21] G. Shirane, R. Newnham, R. Pepinsky, Dielectric properties and phase transitions of $NaNbO_{[3]}$ and (Na,K)$NbO_{[3]}$, Phys. Rev. 96 (1954) 581]–588.
[22] V. Lingwal, N.S. Panwar, Morphotropic Phase Transitions in Mixed Sodium-Potassium Niobate System Ferroelectrics 300 (2004), pp. 3–14.
[23] V.B. Kvaskov, Kh S. Valeev, A model of posistor effect in conducting barium titanate, Izv. Akad. Nauk SSSR, Ser. Fiz. 39 (1975) 1327–1331.
[24] W. Heywang, Barium titanate as barrier semiconductor, Solid State Electron. 3 (1961) 51–58.
[25] W. Heywang, Structural engineering of ferroelectrics, Ferroelectrics 49 (1983) 3–14.
[26] W. Merz, The dielectric behavior of $BaTiO_3$ single- domain crystals, Phys. Rev. 75 (1949) 687.
[27] J. Tellier, B. Malic, B. Dkhil, D. Jenko, J. Cilensek, M. Kosec, Crystal structure and phase transitions of sodium potassium niobate perovskites, Solid State Sci. 11 (2009) 320–324.
[28] J. Attia, L. Bellaiche, P. Gemeiner, B. Dkhil, B. Malic, Study of potassium- sodium-niobate alloys: a combined experimental and theoretical approach, J. Phys. IV France. 128 (2005) 55–60.

Ferroelectrics

ISSN: 0015-0193 (Print) 1563-5112 (Online) Journal homepage: https://www.tandfonline.com/loi/gfer20

Converse piezoelectric properties of K and Na-modified ($Na_{1-x}K_x$) NbO_3 lead free ceramics for x = 0.08 and 0.17

Don Biswas, Gambheer Singh Kathait, Prashant Thapliyal, Vishal Rohilla, Surendra Singh & Jyotsana Negi

To cite this article: Don Biswas, Gambheer Singh Kathait, Prashant Thapliyal, Vishal Rohilla, Surendra Singh & Jyotsana Negi (2019) Converse piezoelectric properties of K and Na-modified ($Na_{1-x}K_x$) NbO_3 lead free ceramics for x = 0.08 and 0.17, Ferroelectrics, 550:1, 228-232, DOI: 10.1080/00150193.2019.1652511

To link to this article: https://doi.org/10.1080/00150193.2019.1652511

Published online: 31 Oct 2019.

Submit your article to this journal

View related articles

View Crossmark data

Full Terms & Conditions of access and use can be found at
https://www.tandfonline.com/action/journalInformation?journalCode=gfer20

FERROELECTRICS
2019, VOL. 550, 228–232
https://doi.org/10.1080/00150193.2019.1652511

Taylor & Francis
Taylor & Francis Group

Check for updates

Converse piezoelectric properties of K and Na-modified ($Na_{1-x}K_x$) NbO_3 lead free ceramics for x = 0.08 and 0.17

Don Biswas[a], Gambheer Singh Kathait[a], Prashant Thapliyal[a], Vishal Rohilla[a], Surendra Singh[b], and Jyotsana Negi[b]

[a]USIC Department, HNB Garhwal University, Srinagar, Uttarakhand, India; [b]Department of Physics, HNB Garhwal University, Srinagar, Uttarakhand, India

ABSTRACT

The effect of potassium content on the structure and piezoelectric properties of the $Na_{1-x}K_xNbO_3$ (x = 0.08 and 0.17) (SPN) ceramics has been systematically studied. The pellets preparation and characterization have been reported earlier. The piezoelectric properties of the $Na_{1-x}K_xNbO_3$ (x = 0.08 and 0.17) were observed. The P-E loops, strain%, and the polarization current were observed. The value of d_{33}* increasing with the application of Electric field, the rate of increasing value of d_{33}* for x = 0.08 was faster than compared to x = 0.17. The value of d_{33}* for x = 0.08 and x = 0.17 are 144 (pm/V), 136 (pm/V) respectively at the applied field 44 kV/cm.

ARTICLE HISTORY
Received 6 September 2018
Accepted 13 June 2019

KEYWORDS
Ceramics; dielectric constant; piezoelectric; ferroelectrics

1. Introduction

The most widely used piezoelectric ceramics are lead oxide based ferroelectrics; especially PZT exhibits high piezoelectric properties close to a morphotropic phase boundary (MPB) between rhombohedral and tetragonal phases. Nevertheless, the famous PZT ceramics can contain up to 60% lead by weight. Due to the high toxicity of lead, there is significant interest in developing piezoelectric lead-free ceramics, with a particular interest in developing lead-free solid solution systems exhibiting a MPB, and due to co-existence of different phases at MPB, MPB cause instability to the polarization state which eases the rotation of the ferroelectric domains, hence material having MPB show high value of piezoelectric constant [1, 2]. Toxic lead-based ceramics have got our attention owing to the need for environmental protection, and rapid development of piezoelectric devices urgently calls for environment-friendly materials substituting for the widely used PZT system, among which lead-free alkali niobate ceramics based on ($Na_{1-x}K_xNbO_3$) (NKN) are the most promising since Saito et al. [3] reported that a high d_{33} (416 pC/N) constant has been obtained in the textured Li-modified NKN based ceramics with co-dopants of Ta and Sb. However, for the pure NKN system, the highest piezoelectric coefficient was not more than that 100 pC/N [4]. Morphotropic phase boundary (MPB) is considered as a critical factor for developing NKN-based piezoelectric materials with high performance [5]. It has also been studied that addition of K^+ to Na + site

CONTACT Don Biswas donusic06@gmail.com
Color versions of one or more of the figures in the article can be found online at www.tandfonline.com/gfer.
© 2019 Taylor & Francis Group, LLC

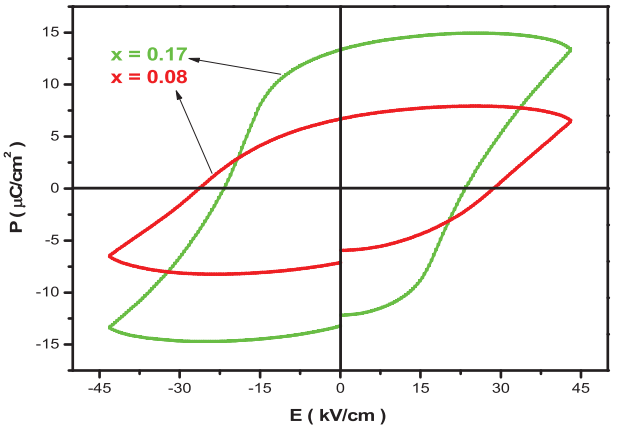

Figure 1. P-E hysteresis loops of the NKN ceramics sintered at 1230 °C temperature.

causes the negligible change in structure to but lower the transition temperature T_c [6–8] which improves its temperature stability, densification and leakage current, etc. there is a possibility that potassium volatilized more severe than that of sodium for the sample synthesized at 1080 °C. Ferroelectric materials having perovskite kind of structure, observed to have good piezoelectric property, that is, generation of mechanical stress (strain) in response of applied electric voltage (voltage). Many lead free ferroelectric materials have been studied till a date like NBT, KNN having good dielectric and piezoelectric properties and these properties are also enhanced through many processes, some of their properties get very close to PZT ceramic but none of them have good properties as PZT, more over their volatile nature is a big problem. For the $Na_{1-x}K_xNbO_3$ (x = 0.08 and 0.17) (SPN) ceramic compositions, dielectric and piezoelectric properties were obtained. In this study, we see the structure, microstructure, dielectric and piezoelectric properties of $Na_{1-x}K_xNbO_3$ ceramics for x = 0.08 and 0.17.

2. Experimental details

The raw materials used for preparing the composition, for the present study, were sodium carbonate (Na_2CO_3), potassium carbonate (K_2CO_3) and niobium pentoxide (Nb_2O_5) all of 99.99% pure. Sodium- potassium niobate pellet samples were prepared by conventional solid state reaction method. The preparation of pellets sample has been described in the previous communication [9]. Specimens were coated both sides using silver paste. Then they have been used for the measurement of piezoelectric properties at room temperature using the by aixACCT system GMBH.

3. Results and discussion

The characterization (XRD, SEM, EDAX, etc.) of the prepared samples has been described in previous communications [9].

Figure 1 represents the room-temperature P-E hysteresis loops observed for the $Na_{1-x}K_xNbO_3$ ceramics x = 0.08 and 0.017 specimens for the NKN pellets sintered at 1230 °C. The P-E hysteresis loops confirmed the ferroelectric nature of the prepared NKN

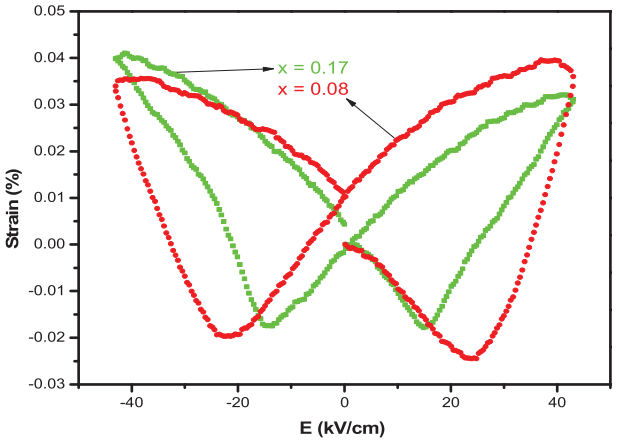

Figure 2. Field-induced strain loops of the NKN Ceramics sintered at 1230 °C temperature.

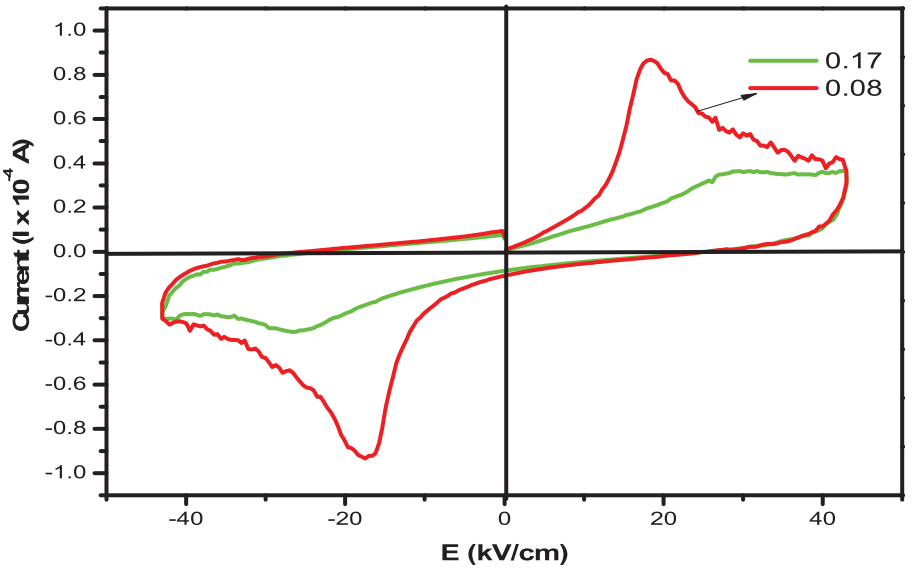

Figure 3. Electric field dependence of polarized current for the $Na_{1-x}K_xNbO_3$ ceramics (x = 0.08 and 0.17) sintered at 1230 °C.

pellet samples. The x = 0.08 specimen demonstrates a well-saturated hysteresis and fully developed shapes attained at around 44 kV/cm and at 1Hz, sintered at 1230 °C under atmospheric pressure. The P-E loops of all the $Na_{1-x}K_xNbO_3$ ceramics in Figure 2 exhibit good butterfly shapes, proving further their excellent piezoelectric properties. Figure 3 Electric field dependence of Polarized Current for the $Na_{1-x}K_xNbO_3$ ceramics (x = 0.08 and 0.17). The effective high-field converse piezoelectric coefficient d_{33}*, that is, the converse piezoelectric constant, can be calculated using the equation $d_{33}^* = S_{max}/E_{max}$ [10]. It can be seen in Table 1 that the $Na_{1-x}K_xNbO_3$ ceramics sintered at 1230 °C for 12 hours generally exhibit the good piezoelectric properties, in which we get the greater d_{33}* for x = 0.08 composition in higher Electric field range. According to the graph in Figure 2, the best value for the $Na_{1-x}K_xNbO_3$ ceramics (x = 0.08), d_{33}*, is 144.06 pm/V, at 44 kV/cm,

Table 1. Piezoelectric results of the $Na_{1-x}K_xNbO_3$ system.

Converse piezoelectric constant (pm/V)	Input hysteresis amplitude (v)	Converse piezoelectric constant (pm/V)	Input hysteresis amplitude (v)
d_{33}*	$Na_{1-x}K_xNbO_3$ (x = 0.17)	d_{33}*	$Na_{1-x}K_xNbO_3$ (x = 0.08)
133.91	5000	161.96	5000
137.84	4800	144.06	4800
133.87	4600	126.37	4600
140.33	4400	103.77	4400
132.96	4200	81.50	4200
134.50	4000	83.04	4000

The value of d_{33} at 5200 V= 176.73 pm/V (for x = 0.08).

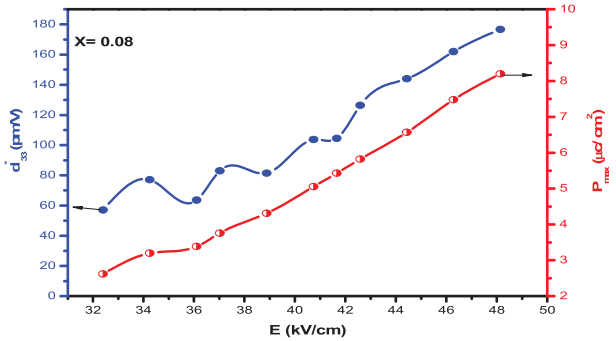

Figure 4. Electric field dependence of converse piezoelectric constant d_{33}* ceramics sintered at 1230 °C for x = 0.08.

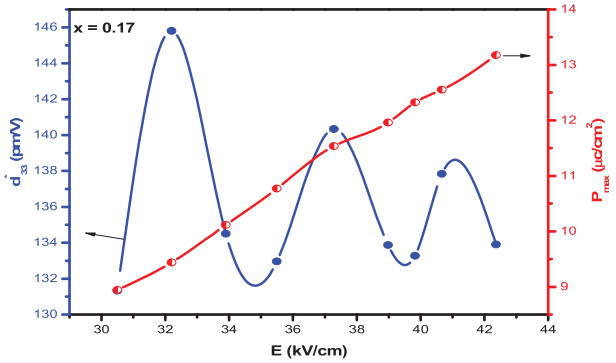

Figure 5. Electric field dependence of converse piezoelectric constant d_{33}* for the for the $Na_{1-x}K_xNbO_3$ $Na_{1-x}K_xNbO_3$ ceramics sintered at 1230 °C for x = 0.17.

respectively. The calculated coercive field from Figure 1 is 27.81 KV/cm for x = 0.08 composition and the value of coercive field for x = 0.17 was 21.34 KV/cm. Similarly, the calculated remanent polarization from Figure 1 is 5.3283 μC/cm^2 for x = 0.08 composition and the value of coercive field for x = 0.17 was 12.465 μC/cm^2. The calculated values show minimum leakage current [9], which can also be seen from the graph of P-E hysteresis loop (Figure 1, x = 0.08). The value of d_{33}* was increasing rapidly for x = 0.08 as compared to x = 0.17 in the higher Electric field range. The best value or the higher value is calculated for $Na_{1-x}K_xNbO_3$ ceramics for x = 0.08. For increasing the input hysteresis voltage by around 200 V, the piezoelectric constant is increasing by the rate 15 pm/V. So,

in higher voltage range the $Na_{1-x}K_xNbO_3$ ceramics for x = 0.08 showed good piezoelectric properties. The Figures 4 and 5 shows that the d_{33}* and the P_{max} were increasing for x = 0.08, but not stable for x = 0.17.

4. Conclusions

In the observed calculations, the $Na_{1-x}K_xNbO_3$ ceramics for x = 0.08 showed good converse piezoelectric constant. However, the samples are not denser enough because of K loss and porosity. It is observed that the dielectric constant is higher for $Na_{1-x}K_xNbO_3$ (x = 0.08) and lower for $Na_xK_{1-x}NbO_3$ (x = 0.17) with varying temperature condition as well as at room temperature. The dielectric loss is higher for the $Na_{1-x}K_xNbO_3$ (x = 0.17) sample and lower for $Na_{1-x}K_xNbO_3$ (x = 0.08) sample. So from the prepared samples, the composition $Na_{1-x}K_xNbO_3$ (x = 0.08) would have appreciable interest because of its good piezoelectric constant.

Acknowledgments

The authors are thankful to Prof. N. S. Panwar, HNB Garhwal University, Srinagar (Garhwal), for his kind suggestion. Prof. N. S. Panwar is also thankfully acknowledged for providing laboratory facilities.

ORCID

Don Biswas http://orcid.org/0000-0001-5130-087X

References

[1] Y. Tian, Y. Gong, and D. Meng *et al.*, Dielectric Dispersion, Diffuse Phase Transition, and Electrical Properties of BCT–BZT Ceramics Sintered at a Low-Temperature, *Journal of Elec Materi.* **44**, 2890 (2010). DOI: 10.1007/s11664-015-3727-3.

[2] S. Singh, J. Negi, and N. S. Panwar, Dielectric properties of $Na_{1-x}K_xNbO_3$, near x = 0.5 morphotropic phase region, *J. Phys. Chem. Solids* **123**, 311 (2018). DOI: 10.1016/j.jpcs.2018.08.018.

[3] Y. Saito et al., Lead-free piezoceramics, *Nature*. **42**, 84 (2004). DOI: 10.1038/nature03028.

[4] Y. P. Guo, K. Kakimoto, and H. Ohsato, Phase transitional behavior and piezoelectric properties of $(Na_{0.5}K_{0.5})NbO_3$–$LiNbO_3$ ceramics, *Appl. Phys. Lett.* **85** (18), 4121 (2004). DOI: 10.1063/1.1813636.

[5] P. Zhang, J. F. Li, K. Wang, and H. L. Zhang, Compositional dependence of piezoelectric properties in $Na_xK_{1-x}NbO_3$ lead-free ceramics prepared by spark plasma sintering, *J. Am. Ceram. Soc.* **89** (5), 1605 (2006). DOI: 10.1111/jace.13250.

[6] V. J. Tennery and K. W. Hang, Thermal and X-ray diffraction studies of the $NaNbO_3$–$KNbO_3$ system, *J. Appl. Phys.* **29**, 4749 (1968). DOI: 10.1063/1.1655833.

[7] G. Shirane, R. Newnham, and R. Pepinsky, Dielectric properties and phase yransitions of $NaNbO_3$ and (Na,K)NbO_3. *Phys. Rev.* **96** (3), 581 (1954). DOI: 10.1103/PhysRev.96.581.

[8] Y. C. Sheng *et al.*, Properties of (Na, K)NbO3 and (Li, Na, K)NbO3 ceramic mixed systems, *Ferroelectrics* **287**, 23 (2003). DOI: 10.1080/00150190390200767.

[9] D. Biswas *et al.*, Temperature dependence of dielectric properties of sodium potassium niobate ceramics for different values of x ($Na_{1-x}K_xNbO_3$), *Ferroelectrics* **526** (1), 168 (2018). DOI: 10.1080/00150193.2018.1456307.

[10] A. Jalalian *et al.*, Large piezoelectric coefficient and ferroelectric nanodomain switching in $Ba(Ti_{0.80}\ Zr_{0.20})O_3$-$0.5(Ba_{\ 0.70}Ca_{0.30})TiO_3$ nanofibers and thin films, *Appl. Phys. Lett.* **104** (10), 103112 (2014). DOI: 10.1063/1.4867013.

International Journal of Advanced Science and Technology
Vol. 28, No. 20, (2019), pp. 698 – 705

Temperature Dependence of Dielectric Conductivity in $KTa_xNb_{1-x}O_3$ System for $x \leq 0.5$

V. Lingwal[1], Binod Kumar Bhadri[2], A. S. Kandari[3], and N. S. Panwar[4]
[1]*Department of Physics, Pt. L.M.S. Government PG College Rishikesh, Dehradun, India*
[2]*Department of Higher Education, MHRD, New Delhi*
[3]*Department of Physics, Government PG College New Tehri, India*
[4] *University Science Instrumentation Center, HNB Garhwal University, Srinagar (Garhwal), India*

Abstract

Pellet samples of mixed potassium tantalate niobate ($KTa_xNb_{1-x}O_3$), for compositions x = 0, 0.1, 0.2, 0.3, 0.4 and 0.5 were prepared by solid-state reaction method. The calcined mixture was pressed at 0.2 GPa and sintered in a closed furnace to form 8 mm diameter pellets. Temperature variation of dielectric conductivity of the prepared samples has been studied in the frequency range from 0.1 KHz to 1 MHz. Dielectric conductivity has been observed increasing with increasing frequency and with increasing x values, for $x \leq 0.4$; for x = 0.5, conductivity decreases at 0.1, 1 and 10 KHz. At 100 and 1000 KHz conductivity decreases for x = 0.3, showing the MPT region. Anomalies have been observed near the transition temperatures of the samples in temperature-dielectric conductivity curves.

Keywords: *Conductivity, ferroelectrics, morphotropic region, perovskite, phase transition.*

I. INTRODUCTION

Potassium tantalate niobate, $KTa_xNb_{1-x}O_3$ (KTN), has received a great deal of attention as a ferroelectric material possessing the perovskite structure [1]. Because of its piezoelectric, pyroelectric, and electro- optic properties, the material is of interest for application in band filters, infrared detectors, and electro-optic modulators [1-2]. KTN has been proved a promising material which can compete with another well known ferroelectric material $Ba_{1-x}Sr_xTiO_3$ [3-5]. The Curie temperature and ferroelectric properties of KTN are composition dependent and can be varied by controlling the Ta : Nb ratio.

Dielectric measurements were first reported by Matthias et. al. [6] and Vousden [7] on the end members of KTN system, i.e., in $KNbO_3$ and $KTaO_3$ single crystals, and observed two transitions, at 224 and 434 ^oC, for $KNbO_3$, at 10 KHz. $KTaO_3$ remains in paraelectric phase up to very low temperature. Afterwards several investigators studied this system [8-28]. However, most of the studies were restricted to single crystal, and optical properties of the system. To make the material more applicable in different areas, studies should be carried out over a wide frequency and temperature range, and with varying composition. Temperature and frequency (from 0.1 KHz to 1 MHz) dependence of dielectric conductivity, of KTN system, for different x values have been investigated, in the present study.

ISSN: 2005-4238 IJAST

Copyright ⓒ 2019 SERSC

II. PREPARATION

In the present study the materials were prepared with conventional solid-state reaction method. The starting materials, used for preparing $KTa_xNb_{1-x}O_3$ system, were potassium carbonate (K_2CO_3), tantalum pentoxide (Ta_2O_5) and niobium pentoxide (Nb_2O_5). The purity of starting materials was better than 99.9%. The starting materials were initially dried at, 150 ^oC, to remove the absorbed moisture. K_2CO_3 is a hygroscopic material and hence due care was taken in its handling. Different compositions of $KTa_xNb_{1-x}O_3$ (x = 0 to 0.5), were prepared by weighing the starting materials in stoichiometric ratio. Each composition was manually dry mixed for 1 hour, with acetone for 1 hour and with methyl alcohol for another 1 hour using agate mullet mortar and pestle. The mixture was calcined in an alumina crucible, in ambient atmosphere, at 950 ^oC, for 4 hours, to remove carbonates present in the mixture. After cooling, in dry air, the calcined mixture was weighed to ensure complete carbonate removal from the mixture. The calcined mixture was fine ground for 1 hour and then pressed, at 0.2 GPa pressure, into pellets of 8 mm diameter, to increase the contact area to improve reaction rate. All the pellets were put in the furnace for sintering at the temperature below their melting points. The sintered pellets were electroded, with air drying silver paste, in metal-insulator- metal (MIM) configuration, for dielectric measurements.

III. DIELECTRIC CONDUCTIVITY

For studying the temperature, frequency and concentration dependence of dielectric properties measurement were made, run to run on the same sample and sample to sample for all samples prepared with the similar method, in the frequency range from 0.1 KHz to 1 MHz, and in temperature range from 50 to 450 ^0C. The observations were close to each other and the values were averaged. Capacitance and dissipation factor measurements were carried out in MIM configuration, using Fluke – PM6306 RCL meter. Dielectric constant (K) was calculated by the relation,

$K = C/C_o$; where C and C_o are the capacitances of the electrodes with and without dielectric, respectively; C_o is given by,

$C_o = (0.0885\ \pi r^2/d)$ pF; where r (cm) is the radius of the electrodes and d (cm) is distance between them. Dielectric conductivity (σ) was calculated by the relation,

$\sigma = \varepsilon_o \omega K \tan\delta$; where ε_o is the permittivity of free space, tan δ is the dissipation factor, and $\omega = 2\ \pi f$, where f is the applied frequency.

The observed x dependence of dielectric conductivity (σ) in $KTa_xNb_{1-x}O_3$ samples, for different frequencies, has been shown in Fig 1. Dielectric conductivity has been observed increasing with increasing frequency and with increasing x values, for $x \leq 0.4$; for x = 0.5, conductivity decreases at 0.1, 1 and 10 KHz. At 100 and 1000 KHz conductivity decreases for x = 0.3, showing the morphotropic phase transition (MPT) region.

Copyright ⓒ 2019 SERSC

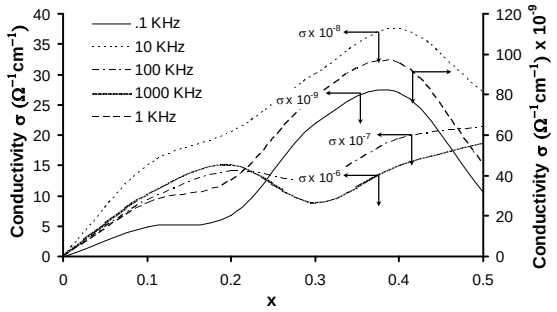

FIGURE 1. x dependence of dielectric conductivity, in $KTa_xNb_{1-x}O_3$, at different frequencies, and at room temperature

Temperature variation of dielectric conductivity, of $KNbO_3$ samples, at different frequencies has been shown in Fig. 2(a). It has been observed that, below the transition temperature, the dielectric conductivity increases with increasing temperature, showing semiconducting behavior and shows anomalous behavior near tetragonal- cubic transition, at all the observed frequencies. At 100 and 1000 KHz, with further increase in temperature, dielectric conductivity decreases, from 420 to the observed 470 ^{0}C. The decreasing nature of conductivity with increasing temperature shows positive temperature coefficient of resistivity (PTCR), in these samples. The magnitude of the dielectric conductivity is higher at higher frequencies, in this system. At 10 and 100 KHz, it was found of the order of 10^{-6} ($\Omega^{-1}cm^{-1}$), and at 1000 KHz, it was found of the order of 10^{-5} ($\Omega^{-1}cm^{-1}$). The observed temperature dependence of dielectric conductivity, in $KTa_xNb_{1-x}O_3$, for x = 0.1, between 150 and 400 ^{0}C, is shown in Fig. 2(b); and for x = 0.2, between 100 and 350 ^{0}C, is shown in Fig. 2(c). Similar results have been observed for these samples as that for $KNbO_3$. PTCR effect has been observed at both the transitions, for x = 0.1, i.e., orthorhombic- tetragonal (at 180 ^{o}C), and tetragonal-cubic (at 350 ^{o}C). Whereas this effect has been sharply observed only at 1000 KHz for x = 0.2. Here at tetragonal- cubic transition conductivity decreases from 300 to 330 ^{o}C, showing PTCR effect, and further increases with increasing temperature. Temperature dependence of dielectric conductivity, in $KTa_{0.3}Nb_{0.7}O_3$ samples, at 10, 100 and 1000 KHz, is shown in Fig. 2(d). The magnitude of the dielectric conductivity is higher at higher frequencies, in this composition. At 10 and 100 KHz, it was found of the order of 10^{-7} ($\Omega^{-1}cm^{-1}$); and at 1000 KHz, it was found of the order of 10^{-6} ($\Omega^{-1}cm^{-1}$), which is less than the previously observed compositions. PTCR effect has also been observed at tetragonal- cubic transition (210 ^{o}C) for these samples, at 1000 KHz.

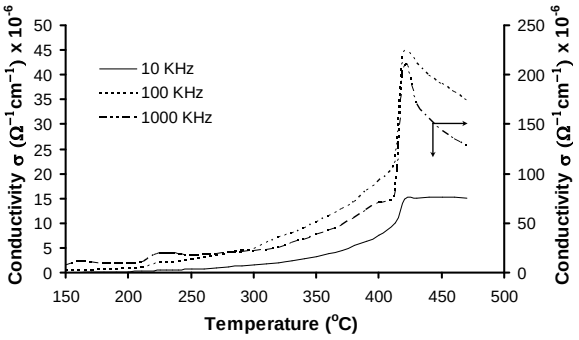

(a)

Copyright © 2019 SERSC

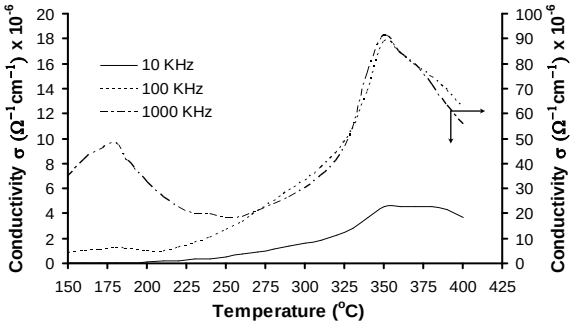

(b)

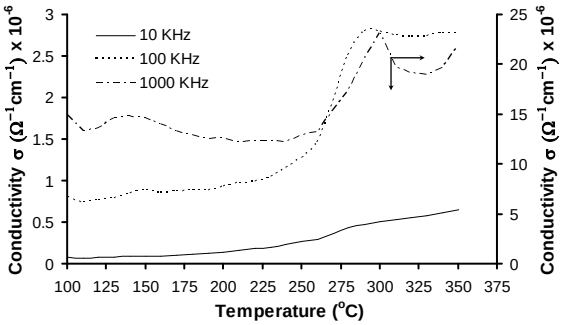

(c)

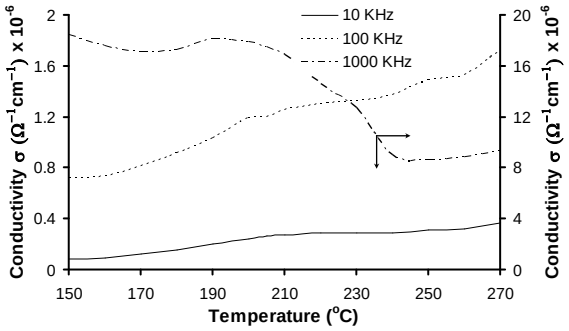

(d)

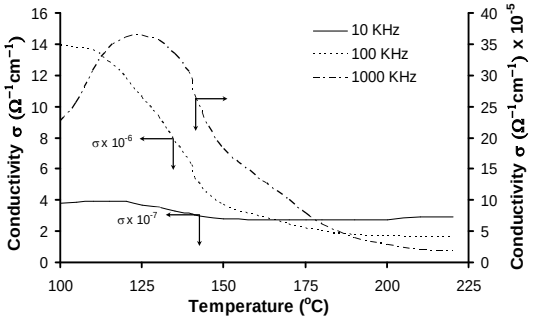

(e)

Copyright ⓒ 2019 SERSC

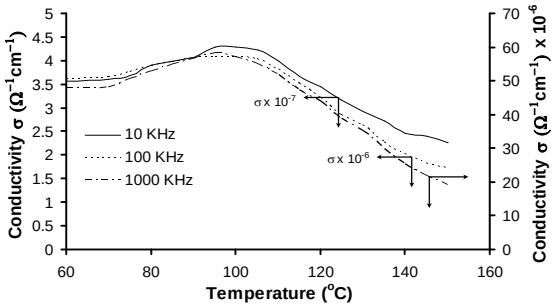

(f)

FIGURE 2. Temperature dependence of dielectric conductivity, in $KTa_xNb_{1-x}O_3$, at different frequencies for (a) x = 0, (b) x = 0.1, (c) x = 0.2, (d) x = 0.3, (e) x = 0.4 and (f) x = 0.5

Temperature dependence of the dielectric conductivity, for $KTa_{0.4}Nb_{0.6}O_3$ and $KTa_{0.5}Nb_{0.5}O_3$, at different frequencies is shown in Fig. 2 [(e) and (f)]. In both the compositions sharp PTCR effect has been observed at tetragonal-cubic transition, for all the observed frequency. Shifting of conductivity peaks on right side with increasing frequency in temperature versus conductivity curves show relaxation behavior of these samples.

The electrical conductivity is a measure of the conductance that a unit cube of the material offers to current flow in the given (dc) field. In an ac field, electrical conductivity and dielectric constant are related by dissipation factor, which measures the energy dissipation per cycle (usually in the form of heat) from the material. Also at particular x values the conductivity decreases, showing MPT regions. This is the most interesting region in the composition- property diagram of solid solution systems. MPT denotes the sharp structural transition in a solid solution on change in composition. The compositions of ferro- ceramic forming the morphotropic region (MR) are two- phase, and have extremal electro- physical properties, as a consequence of which they have acquired practical importance [29-30]. The little availability of systematic literature data on the pattern of change in electrical conductivity, as a function of composition, is due to its marked dependence on the quality of the ceramic. The ceramic obtained by the usual sintering procedure is porous. For solid solution of $KTa_xNb_{1-x}O_3$, the concentration dependence of electrical conductivity exhibits minima, the position of which closely agrees with that of the MR determined from results of the measurements of other properties, e.g., dielectric constant, loss tangent, and even XRD patterns, which shows break in tendency of the peak shifting [31].

In the ABO_3 type perovskite compounds two type of defects, *viz*., vacancies at A site, and vacancies at O site, contribute significantly to the electrical properties [30]. In the compositions near MR, it seems that during sintering of the samples the intensification of diffusion processes enhances significantly the possibility of escape of highly volatile alkali metal ions from the lattice. The A site vacancy concentration, in the compositions near MR, is higher than that in the specimens of other compositions. With this supposition, an increase in the number of V_A, which is acceptors [32], will enhance resistivity or decrease electrical conductivity. This can be explained on the fact that, the

Copyright ⓒ 2019 SERSC

electrons which are available in the conduction band for small value of conductivity, with increasing number of vacancies (i.e., acceptors), will be captured by these electrons and hence reducing the electrons in conduction band, and this results a decrease in conductivity. Since the V_A concentration in the specimens, similar in composition to MR is high, it must correspond to the electrical conductivity minima. This phenomenon is supported by the EDAX result, for $KTa_xNb_{1-x}O_3$ system, where significant decrease in the K, resulting significant increase in V_A, in these samples has been observed [31]. Similar results were obtained by Raevskii et al. [32] for different systems.

Also, like other oxide systems $KTa_xNb_{1-x}O_3$ has oxygen vacancies, and exhibits n- type properties [33]. Lowering of conductivity in MR region can be understood with the fact that, in n- type material, electrons will be available in the conduction band. With decreasing A site vacancies (which are acceptors) less number of the electrons will be captured and more electrons will be available in the conduction band, and that way it results an increase in conductivity for the compositions far from MR.

Wrobel et al. [34] have reported the results on the electrical properties in the MPT of ordinarily sintered Zr-Ti-Pb ceramics. All the specimens investigated had p- type conductivity. The concentration dependence of dielectric conductivity exhibited a distinct maximum corresponding to MPT, between rhombohedral and tetragonal ferroelectric phases. These results agree closely with the above given assumptions, because in the case of hole conductivity, an increase in V_A concentration, typical of compositions close to MR, must increase dielectric conductivity.

The observed increasing conductivity with temperature, in the present system, is similar to that in glasses, in which conduction is mainly attributed to the migration of mobile ions, such as Na^+, K^+, etc., under the influence of an applied electrical field. The current carriers are considered to be located in the potential wells and undergo thermal vibrations of magnitude proportional to the temperature. In the absence of an applied field the ions make random jumps according to the probability of surmounting the surrounding energy barriers but migrate preferentially in the direction of the applied field, which effectively lowers the energy barriers in the forward direction. The number of conducting ions, therefore, increases with both temperature and electric field.

In the prefect system oxygen vacancies could exist, which dominantly contribute to dielectric conductivity [35-36]. The oxygen vacancy binds one or two electrons creating F_1 or F_2 center. Empty vacancies and mono- electron states can be considered as the deep and shallow trap states or acceptor states. The F_2 state, which is able to give one electron to the conduction band, can be treated as donor. Therefore, the oxide system having oxygen vacancies can exhibit n-type properties [33]. In $KTa_xNb_{1-x}O_3$, a significant role is played not only by the presence of oxygen vacancies but also by their polarization produced by applied or measuring field. The effective polarization produced by polarizing field is composed of inertialess induced polarization, the inertial polarization of the space charge, and spontaneous polarization (in the ferroelectric state). The effective polarization determines the process of charge exchange with electrodes. It also determines the resultant current in the specimen circuit. The injected electrons can cause the transition of empty oxygen vacancies and F_1 centers localized inside the near- electrode layer to F_2 states. At sufficiently high temperature thermal generation of electrons from F_2 centers

Copyright ⓒ 2019 SERSC

and subsequent transition to F_1 states can induce some coupling. The polarization of ion space charge stimulates the process of charge carriers from electrodes. The injected charges screen this polarization and lead to unusual stability and behavior. The structural anomaly, as observed from the X- ray measurements [31], may also be held responsible for the minimum values of the dielectric conductivity of the composition with x = 0.3, among the prepared compositions.

PTCR effect observed in the present KTN samples is another interesting phenomenon. Goodman [37] observed that the PTCR behavior is closely related with the grain boundary. The PTCR behavior of the ceramics can be explained on the basis of Heywang model [38], which assumes that the acceptor type states of the grain boundaries create equivalent potential barriers associated with resistive depletion layers near the boundaries. The barrier heights depend on dielectric constant of bulk grains, as $T \rightarrow T_c$ (from high symmetry phase side), increasing dielectric constant leads to decrease in the barrier heights, which results exponential increase in conductivity. In the region $T < T_c$, grain boundary barrier heights are diminished due to the compensation of the grain boundary charge by spontaneous polarization [39], or due to the disappearance of localized states at the grain boundaries in orthogonal phase [40]. Near but below T_c, the diminishing barrier heights result high loss in the prepared samples, the loss is determined by the softening of the optical mode [41-42] rather than by the barrier heights. For the compositions with x = 0 and 0.1, at T_c dielectric loss was observed minimum, [31] which indicates that at this temperature barrier heights have not been fully diminished and they have dominating effect rather than the effect of optical mode softening [41-42] and the activation energy of surface terms, for these compositions. The dominating barriers might be allowing least current to pass through, which results lowest dielectric loss, at T_c. With increasing temperature, above T_c, activation energy of the surface terms increases and dielectric loss increases with temperature. Near but above T_c, dielectric constant decreases with increasing temperature [31], resulting increasing barrier heights, which leads to an increase in resistivity with the rise of temperature (PTCR behavior), until the activation energy becomes equal to or greater than the potential barrier. Beyond that temperature resistivity starts decreasing with further rise in temperature, as in the semiconductors.

REFERENCES

[1] P. Gunter and J.P. Huignard, *Photorefreactive Materials and Their Applications*, Topics in Applied Physics, **Vol. 61-62**, Berlin-Springer, (1988).
[2] A.J. Agranta, Top. Appl. Phys., **86**, 129 (2003).
[3] A.C. Carter, J.S. Horwitz, D,B. Chrisey, J.M. Pond, S.W. Kirchoefer and W. Chang, Intgr. Ferroelectrics, **17**, 273 (1997).
[4] V. Laur, G. Tanne, P. Laurent, A. Rousseau, M. Guilloux-Viry, and F. Huret, Ferroelectrics, **353**, 21 (2007).
[5] A. Rousseau, V. Laur, M. Guilloux-Viry, G. Tanne, F. Huret, S. Deputier, A. Perrin, F. Lalu and P. Laurent, Thin Solid Films, **515**, 2353 (2006).
[6] B.T. Matthias and J. Remeika, Phys. Rev., **82**, 727 (1951).
[7] P. Vousden, Acta Cryst., **4**, 373 (1951).
[8] S. Triebwasser, Phys. Rev., **114**, 63 (1959).
[9] G. Shirane and Y. Yamada, Phys. Rev., **177**, 2 (1969).
[10] A.H. Hewat, J. Phys. C, **6**, 1074 (1973).
[11] A. Reisman, S. Triebwasser and F. Holtzberg, J. Amer. Chem. Soc., **77**, 4228 (1955).

Copyright ⓒ 2019 SERSC

[12] M. Adachi and A. Kawabata, Japan. J Appl. Phys., **11**, 1855 (1972).
[13] J. Bursik, V. Zelezny, P. Vanek, J. Europ. Ceram. Soc., **25**, 2151 (2005).
[14] W. Piltai, J.G. Kim, J.H. Oh, C. Lee, D.W. Park and W.S. Ahn, J. Mater. Sci., **15**, 25 (2004).
[15] B.M. Nichols, B.H. Hoerman, J. -H Hwang, T.O. Mason and B.W. Wessels, J. Mater. Res., **18**, 106 (2003).
[16] M. Sepliarsky, S.R. Phillpot, M.G. Stachiotti and R.L. Migoni, J. Appl. Phys., **91**, 3165 (2002).
[17] P. Doussineau and A. Levelut, Europhys. Lett, **55**, 739 (2001).
[18] A. Onoe, A. Yoshida and K. Chikuma, Appl. Phys.Lett., **78**, 49 (2001).
[19] C.G. Duan, W.N. Mei, J. Liu and J.R. Hardy, J. Phys.: Condens. Matter, **13**, 8189 (2001).
[20] C.J. Lu and A.X. Kuang, J. Mater. Sci., **32**, 4421 (1997).
[21] G.K.L. Goh, H.Q. Han, C.P.K. Liew and C.S.S. Tay, J. Electrochem. Soc., **152**, C532 (2005).
[22] M.A. Gubbins, V. Casey and S.B. Newcomb, Thin Solid Films, **405**, 270 (2002).
[23] C. Wang, T. Wang and S. Zheng, Physica E, **14**, 242 (2002).
[24] G.K.L. Goh, C.G. Levi, J.H. Choi, and F.F. Lange, J. Cryst.Growth, **286**, 457 (2006).
[25] J.V. Mantese, N.W. Schubring, A.L. Micheli and A.B. Catalan, Appl. Phys. Lett., **67**, 721 (1995).
[26] W. Haas and R. Johannes, Appl. Optics, **6**, 2007 (1967).
[27] M.D. Fontana, E. Bouziane and G.E. Kugel, J. Phys.: Condens. Matter, **2**, 8681 (2001).
[28] S. Chattopadhyay, B.M. Nichols, J.H. Hwang, T.O. Mason and B.W. Wessels, J. Mater. Res., **17**, 275 (2002).
[29] E.G. Fesenko, *The Perovskite Family and Ferroelectricity*, Atomizdat, Moscow, (1972).
[30] B. Jaffe, W. Cook and H. Jaffe, *Piezoelectric Ceramics*, Mir Publishers, Moscow, (1974).
[31] Binod Kumar Bhadri, "Electrical properties of bulk $KTa_xNb_{1-x}O_3$ (x = 0 to 0.5) system", Ph.D. Thesis, HNB Garhwal University, 2013
[32] I. P. Raevskii, L. A. Reznichenko, O. I. Prokopalo and E.G. Fesenko, Izv. Akad. Nauk. SSSR, Neorg. Mater., **15**, 872 (1979).
[33] V.A. Bokov and I.E. Myl'nikova, Sov. Phys. Solid state, **3**, 613 (1961).
[34] Z. Wrobel and J. Handerek, Pr. Nauk. U. S1. Katowicach, **127**, 175 (1976).
[35] I. Prokopalo, Izv. Akad. Nauk. SSSR, **29** (1965) 1009.
[36] J. Handerek, A. Aleksandrowicz and M. Badurski, Acta Phyisa Polonica, **A56**, 769 (1979).
[37] G. Goodman, J. Am. Ceram. Soc., **46,** 48 (1963).
[38] W. Heywang, Solid State Electron., **3**, 51 (1961).
[39] W. Heywang, Ferroelectrics, **49**, 3 (1983).
[40] V.B. Kraskov and Kh. S. Valeev, Bull. Acad. Sci. USSR, Phys. Ser., **39**, 166 (1975).
[41] W. Cochran, Adv. Phys., **9**, 387 (1960).
[42] B.S. Semwal and N.S. Panwar, Bull. Mater. Sci., **15**, 237 (1992).

Copyright ⓒ 2019 SERSC

Available online at www.sciencedirect.com

jmr&t Journal of Materials Research and Technology

www.jmrt.com.br

Original Article

Natural-synthetic fiber reinforced homogeneous and functionally graded vinylester composites: Effect of bagasse-Kevlar hybridization on wear behavior

Tej Singh[a], *Brijesh Gangil*[b,*], *Bharat Singh*[c], *Shashi Kant Verma*[d], *Don Biswas*[e], *Gusztáv Fekete*[a]

[a] *Savaria Institute of Technology, Eötvös Loránd University, Szombathely 9700, Hungary*
[b] *Mechanical Engineering Department, H.N.B. Garhwal University, 246174, India*
[c] *Mechanical Engineering Department, Phonics Group of Institutions, Roorkee 247667, India*
[d] *Mechanical Engineering Department, I.E.T. B.U. Jhansi, 284127, India*
[e] *University Science Instrumentation Centre, H.N.B. Garhwal University, 246174, India*

ARTICLE INFO

Article history:
Received 24 June 2019
Accepted 25 September 2019
Available online 31 October 2019

Keywords:
Bagasse fiber
Kevlar fiber
Graded composites
Sliding wear
Microscopy

ABSTRACT

In this work, vinylester resin based and hybrid Kevlar-bagasse fiber reinforced homogeneous and graded composites were developed and evaluated for wear performance on a pin-on-disc machine. An orthogonal array (L_{16}) was applied to examine the influence of four tribological control factors i.e. fiber content, normal load, sliding distance and sliding velocity. The experimental results indicate that normal load emerges as the most important factor affecting the wear rate of vinylester based graded and homogeneous composites with a contribution ratio of 36.33% and 32.09% respectively. Furthermore, composites worn surfaces were analyzed using scanning electron microscopy and the possible wear mechanism was studied.

© 2019 The Authors. Published by Elsevier B.V. This is an open access article under the CC BY-NC-ND license (http://creativecommons.org/licenses/by-nc-nd/4.0/).

1. Introduction

Present age can be considered as composite age with a lot of work being done on this field and still a vast number of new areas are being worked on [1–3]. Nowadays, the engineering composites are designed as to arrange the transition in micro/nano structures in order to improve the overall execution of the component [4–8]. Functionally graded materials (FGM) comes under the heading of these cutting edge composites where a gradient in morphology/microstructure is deliberately being made to suit a particular application and to enhance the performance levels superior to their homogeneous counterparts [9,10]. The early concept of FGM was proposed in Japan in 1984 [11]. Since then, researchers start exploring the area of FGM because of the multi-fold poten-

* *Corresponding author.*
E-mail: brijesh.gangil@hnbgu.ac.in (B. Gangil).
https://doi.org/10.1016/j.jmrt.2019.09.071
2238-7854/© 2019 The Authors. Published by Elsevier B.V. This is an open access article under the CC BY-NC-ND license (http://creativecommons.org/licenses/by-nc-nd/4.0/).

Table 1 – Physical and mechanical properties of the selected materials.

Property	Bagasse fiber	Kevlar fiber	Vinylester resin
Density (g/cm^3)	1.25	1.44	1.05
Tensile strength (MPa)	290	2600	80
Tensile modulus (GPa)	17	82	3
Elongation (%)	6.3	2.4	5

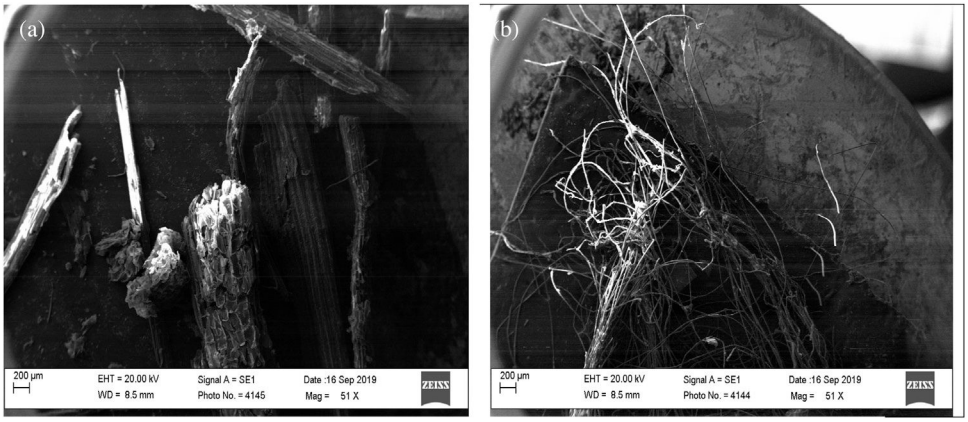

Fig. 1 – Scanning electron microscope images of (a) bagasse fiber and (b) Kevlar fiber.

tial of such materials in performance improvement. Since the last decade, material scientist had successfully developed various metal, ceramic and polymer based FGM to get the desired property gradient in the structure [12]. The functionally graded polymer composites having advantageous characteristics like high specific strength, high modulus, low weight, self-lubrication, low noise and ease in fabrication are a class of materials which is extensively used as components where friction and wear are critical issues [13,14]. Gangil et al. [15] studied the wear behaviour of fiber reinforced vinylester resin based FGM and homogeneous composites and found that FGM composites exhibit improved wear behaviour than homogeneous composites. Singh and Siddhartha [16] reported that the addition of glass fiber in polybutylene terephthalate graded composites contributed to escalated mechanical and thermo-mechanical properties in contrast with their homogeneous composites. Li et al. [17] successfully developed unidirectional continuous fiber reinforced polyethylene graded laminates and concluded that these graded composites exhibit 10–20% higher tensile strength compared to homogenous polyethylene composites. The influence of fiber hybridization (glass and carbon) on mechanical properties of graded epoxy composites was also investigated by Singh et al. [18]. They claimed that graded hybrid composite exhibits ~7-8% higher flexural modulus compared to classical hybrid composites.

Literature reveals that synthetic fibers such as glass, Kevlar, carbon and their combinations have been extensively used as reinforcement of polymeric graded composites. Generally, the synthetic fibers are incorporated with the main objective of improving the physico-mechanical and wear properties of the polymeric composites [19]. Apart from beneficial attributes these fibers are expansive, consumed higher energy, non-recyclable which may affect the final performance of the composite [20,21]. Recently, the increasing environmental awareness throughout the world has enforced the scientist to develop natural fiber reinforced polymer composites materials [22–25]. The natural fibers used in polymer composites offer various benefits such as environmental friendliness, light-weight, biodegradable, non-toxic, wide availability [26–29]. Despite the listed benefits, the natural fibers possess hydrophilic nature which leads to decline the physico-mechanical properties of the designed composites [30]. In this regard, hybridization of natural and synthetic fiber is reported to achieve higher performance properties, which would not be obtained with a single kind of reinforcement. Many studies have been conducted on the hybridization of natural-synthetic fiber such as bagasse-aramid by Anidha et al. [31], sugar palm-glass by Afzaluddin et al. [32], kenaf-glass by Ismail et al. [33] and curaua-aramid by Silva et al. [34] reported to improve the physico-mechanical, thermal and wear properties of the polymer composites.

Moreover one can expect that hybridization of synthetic fiber with natural fiber not only resulted in lower weight and cost with good physico-mechanical and wear properties but also reduces the environmental burden. However, there has been no systematic effort to evaluate the wear performance of an FGM containing synthetic and natural fibers in combination. Therefore, in current study, Kevlar and bagasse fibers reinforced vinylester based homogenous and graded composites were fabricated and evaluated for sliding wear performance.

2. Experimental details

2.1. *Materials and composite fabrication*

Vinylester resin, chopped bagasse and Kevlar fiber with an average size of 1–2 mm and 0.25 mm were taken as matrix

Table 2 – Detail of the composite composition and designation.

Composition (wt.%)	Designation								
	BK-0	BK-1	BK-2	BK-3	BK-4	BK-5	BK-6	BK-7	BK-8
Vinylester resin	100	95	90	85	80	95	90	85	80
Kevlar fiber	0	5	5	5	5	5	5	5	5
Bagasse fiber	0	0	5	10	15	0	5	10	15
Fabrication technique	Homogeneous					Graded			

Fig. 2 – Fabricated composites samples.

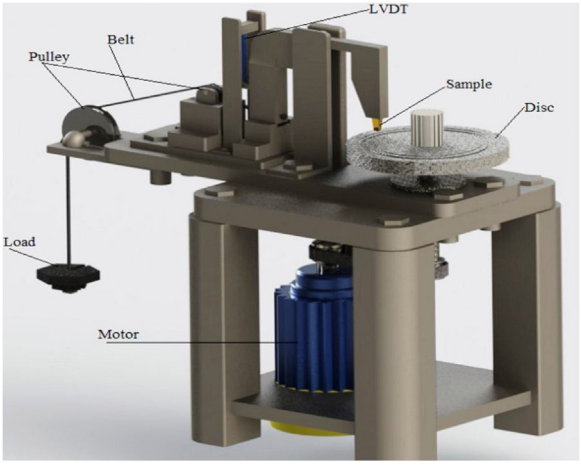

Fig. 3 – Scheme of pin-on-disc machine.

and reinforcing components. The ingredients were purchased from Dhanchan Industries Meerut, India. Chemically the bagasse fiber contains 37% cellulose, 22% lignin, 10% pectin and 21% hemicellulose [35]. The various properties of the selected ingredients are presented in Table 1, while the scanning electron microscope images of the selected bagasse and Kevlar fibers are presented in Fig. 1. Cobalt Naphthenate and ketone-peroxide in the ratio of 1.5:1 wt.% were used as accelerator and hardener. The fabrication of composite was initiated by mixing fiber in desired concentration with the resin, hardener and accelerator as presented in Table 2. Then after, the mixture was poured in glass tubes (Ø 10 mm, length = 110 mm). Gravity method is used for homogeneous composite, whereas vertical centrifugal casting technique is adopted for the fabrication of graded composites; where the known composition is taken in the glass tube and then rotated for 30 min at 1000 rpm. Then these specimens are kept further for curing at room temperature for 48 h and then taken out from the glass tube for wear tests. The developed composites are illustrated in Fig. 2.

2.2. *Sliding wear study*

The wear behaviour of the composites was analyzed as per ASTM G-99 test conditions. The wear tests were performed on a pin-on-disc machine (Fig. 3) equipped by DUCOM. The detailed schematic and working of the test rig is reported elsewhere [36]. A sequence of experiments were conducted with varying sliding velocities (1.5, 2.5, 3.5 and 4.5 m/s), normal load (10, 15, 20, 25 N), sliding distance (1, 2, 3, 4 km) and bagasse fiber loading (0, 5, 10, 15 wt.%) as given in Table 2. The material losses are measured by a precision electronic balance, while specific wear rate was determined as [37]:

$$\omega_s = \frac{\Delta w}{\partial \times t \times V_s \times \hbar_n} \quad (1)$$

Where, ω_s = specific wear rate (mm^3/Nm), Δw = sample weight loss (g), ∂ = density (g/mm^3), t = time (sec), V_s = sliding velocity (m/sec), $\hbar_n$ = applied load (N).

2.3. *Experiment design*

Taguchi method is a potent tool to analyze and optimize the impact of control factors on performance output. The Taguchi method contains following steps [38]:

Step I: Objective selection - The main characteristic of polymer composites is their wear performance. So, wear is selected as the main objective which has to be minimized.

Step II: Control factors and levels selection - Four control factors namely normal load, fiber loading, sliding speed and sliding distance with four levels each (Table 3) were utilized to study the wear behaviour of the composites.

Step III: Orthogonal array construction- The vital parts of the Taguchi method is the construction of orthogonal array. In the present work, an orthogonal array of L_{16} is taken as shown in Table 4.

Step IV: S/N ratio determination- In this step the obtained wear results were transformed into a signal to noise (S-N) ratio. Generally, higher-the-better, lower-the-better and nominal-

Table 3 – Levels of the control factor used in the experiment.

Controls factors	Levels				Units
	I	II	III	IV	
Sliding velocity (A)	1.5	2.5	3.5	4.5	m/s
Fiber content (B)	0	5	10	15	wt.%
Normal load (C)	10	15	20	25	N
Sliding distance (D)	1	2	3	4	km

Table 4 – Experimental design.

Test run	Control factors			
	A: Sliding velocity	B: Fiber content	C: Normal load	D: Sliding distance
1	1.5	0	10	1
2	1.5	5	15	2
3	1.5	10	20	3
4	1.5	15	25	4
5	2.5	0	15	3
6	2.5	5	10	4
7	2.5	10	25	1
8	2.5	15	20	2
9	3.5	0	20	4
10	3.5	5	25	3
11	3.5	10	10	2
12	3.5	15	15	1
13	4.5	0	25	2
14	4.5	5	20	1
15	4.5	10	15	4
16	4.5	15	10	3

the-better characteristics were used in the transformation. In current study, lower wear is desired hence, lower-the-better characteristics used for S-N ratio calculation [38]:

$$S-Nratio = -10\log\frac{1}{n}\left(\sum y^2\right) \quad (2)$$

Where y represents the W_s response and n denotes the number of experiments.

Step V: Contribution ratio (CR) determination- For effectiveness study, CR of each control factor was determined as [37]:

$$CR_i(\%) = \frac{(S-N)_{max,i} - (S-N)_{min,i}}{\sum_{i=1}^{j}\left[(S-N)_{max,i} - (S-N)_{min,i}\right]} \times 100 \quad (3)$$

Where, i = control factor, j = total number of control factors.

Step VI: Confirmation experiment- In the final step, a confirmation experiment is performed to validate the level of importance of the parameters taken during the analysis step.

3. Results and discussions

3.1. *Specific wear rate with respect to sliding velocity*

Plots of specific wear rate as a function of sliding velocity for neat vinylester and Kevlar-bagasse fiber based graded and homogeneous composites are illustrated in Fig. 4, while sliding distance (1 km) and normal load (10 N) remain fixed.

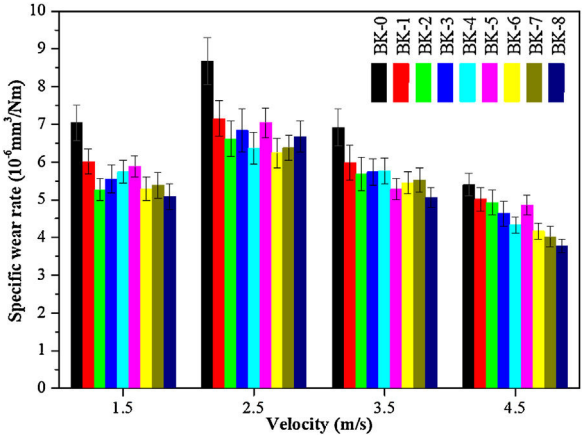

Fig. 4 – Specific wear rate as a function of sliding velocity.

The wear rate of the investigated composites (neat, homogeneous and graded) has been found to increase with rise in the sliding velocity to 2.5 m/s. Thereafter the wear rate decreased with further increase in sliding velocity from 2.5 to 4.5 m/s. The neat vinylester composite exhibits a higher wear rate to that of homogeneous and graded composites. The reduced wear for homogeneous and graded composites may be due to the self-lubricating nature and superior mechanical properties of the fibrous reinforcement [39]. From the graph, it is clear that, at higher sliding velocity, the graded composite with 15 wt.% bagasse fiber loading shows improved wear resistance as compared to the homogenous counterpart.

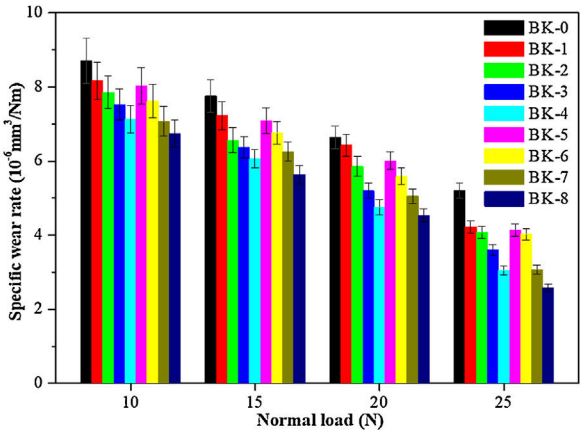

Fig. 5 – Specific wear rate as a function of normal load.

3.2. *Specific wear rate with respect to normal load*

Plots of specific wear rate as a function of normal load for neat vinylester and Kevlar-bagasse fiber based graded and homogeneous composites are illustrated in Fig. 5, while sliding distance (1 km) and sliding velocity (2.1 m/s) remain fixed.

As the load increases, the specific wear rate of graded/homogeneous composite decreases relative to the neat composite due to the more heat generation between the sliding surfaces. This may result in softening of the matrix and leads to the formation of a transfer film between two mating surfaces. This transfer film allows strong fiber-matrix bonding, which helps to reduce the interface de-bonding and also keeps the broken chopped fibers in the composite surface. This, in turn, prevents the early formation of third body abrasion [40]. Furthermore, due to the presence of Kevlar and bagasse fibers, the wear rate further decreases as they act as a blockade for the grooving and micro-ploughing mechanism of wear [41]. The graded composites show better wear resistance in contrast to their homogeneous counterpart for similar fiber loading and this is because better compaction and compatibility is achieved in case of graded composites due to centrifugal casting approach. Overall, 15 wt.% bagasse fiber reinforced graded composite exhibits a lower wear rate at higher velocity and load.

3.3. *Taguchi analysis of the composites*

Table 5 summarizes results of the Taguchi experimental design, presenting the specific wear rate of graded (W_{SG}) and homogeneous (W_{SH}) composites along with their respective S-N ratio. The overall means of the specific wear rate and the S-N ratio from all the experimental runs were $\sim 8.14 \times 10^{-6}$ mm^3/Nm and -18.10 dB for graded and $\sim 8.70 \times 10^{-6}$ mm^3/Nm and -18.66 dB for homogeneous composites respectively.

In addition, the lowest specific wear rate ($\sim 5.88 \times 10^{-6}$ mm^3/Nm) was found for test run 1 of graded composite and the highest specific wear rate ($\sim 12.34 \times 10^{-6}$ mm^3/Nm) for test run 13 of the homogeneous composite. Further, the S-N ratio response of wear rate for graded and homogeneous composites are provided in Table 6. From Table 6, one can easily infer that sliding velocity standout the most significant factor to influence the wear rate of the graded and homogeneous composites followed by fiber loading. However, the normal load and sliding distance are found to have less influence on the wear rate of the graded and homogeneous composites.

From Figs. 6 and 7, the optimum combination of control factors for the least wear rate of graded and homogeneous composites is determined as $A_1B_4C_1D_1$. The wear rates of homogeneous and graded composite material are shown in Table 5. From the test condition, it is obvious, that graded composite shows higher wear resistance than homogeneous composites. From this one can summarize that fabrication technique plays an important role in minimizing the wear. The contribution ratio of each control factor for wear rate of graded and homogeneous composites are determined and given in Fig. 8. The outcome demonstrates that normal load affects the wear rate of graded composites with a contribution ratio of 36.33% followed by fiber content, sliding velocity and sliding distance with a contribution ratio of 25.09%, 24.53% and 14.05% respectively. Normal load also has the strongest impact on the wear rate of homogeneous composites with a contribution ratio of 32.09% followed by sliding velocity, fiber content and sliding distance with a contribution ratio of 25%, 21.46% and 21.45%, respectively.

3.4. *Confirmation experiment*

For verifying the optimal condition for minimum specific wear rate obtained on the basis of Taguchi design, a confirmation test was conducted. The experiments were carried out under optimal conditions of control factors $A_1B_4C_1D_1$ to validate the reproducibility and feasibility of the Taguchi optimization. The predicted value of specific wear rate at optimal condition control factors i.e. $A_1B_4C_1D_1$ was calculated for graded and homogeneous composites using the following equations

$$\chi_G = \hbar + (A_1 - \hbar) + (B_4 - \hbar) + (C_1 - \hbar) + (D_1 - \hbar) \quad (4)$$

$$\chi_H = \lambda + (A_1 - \lambda) + (B_4 - \lambda) + (C_1 - \lambda) + (D_1 - \lambda) \quad (5)$$

Where, χ_G, $\hbar$ are the predicted average and overall experimental average of graded composite, χ_H, λ are the predicted average and overall experimental average of homogeneous composites respectively. The specific wear rate of graded composite by the predictive equation was found to be 5.40×10^{-6} mm^3/Nm and that for homogeneous composite is found to be 5.56×10^{-6} mm^3/Nm. The experimental results obtained are compared with the predicted results as shown in Table 7. An error of 2.96% and 3.42% for the specific wear rate has been observed for graded and homogeneous composites. This authenticates that the predicted values are reliable, consequently, Taguchi methodology can be said to be fit for predicting ideal control factors for wear minimization.

3.5. *Worn surface morphology*

For possible wear mechanism, the worn surfaces of the composites were investigated with the scanning electron microscope (SEM) and presented in Figs. 9–11. From SEM

Table 5 – Experimental results and corresponding S-N ratio.

Test run	W_{SG} 10^{-6} × (mm^3/Nm)	S-N ratio (db)	W_{SH} 10^{-6} × (mm^3/Nm)	S-N ratio (db)
1	5.880	−15.39	6.012	−15.58
2	6.716	−16.54	6.629	−16.43
3	8.260	−18.34	8.801	−18.89
4	8.605	−18.70	9.480	−19.54
5	10.18	−20.15	11.22	−21.00
6	8.370	−18.45	9.032	−19.12
7	7.512	−17.52	7.894	−17.95
8	7.026	−16.93	7.436	−17.43
9	8.602	−18.69	9.598	−19.64
10	8.684	−18.77	9.166	−19.24
11	8.354	−18.44	8.730	−18.82
12	8.211	−18.29	8.470	−18.56
13	11.40	−21.14	12.34	−21.83
14	9.076	−19.16	9.340	−19.41
15	7.046	−16.96	7.650	−17.67
16	6.365	−16.08	7.440	−17.43

Table 6 – S-N ratio response table for specific wear rate of graded and homogeneous composites.

	Level	Control factors			
		A	B	C	D
Average S-N ratio (dB) of graded composites	1	−17.24	−18.84	−17.09	−17.59
	2	−18.26	−18.23	−17.99	−18.26
	3	−18.55	−17.81	−18.28	−18.34
	4	−18.33	−17.50	−19.03	−18.20
Average S-N ratio (dB) of homogeneous composites	1	−17.61	−19.51	−17.74	−17.87
	2	−18.87	−18.55	−18.41	−18.63
	3	−19.07	−18.33	−18.84	−19.14
	4	−19.08	−18.24	−19.64	−18.99

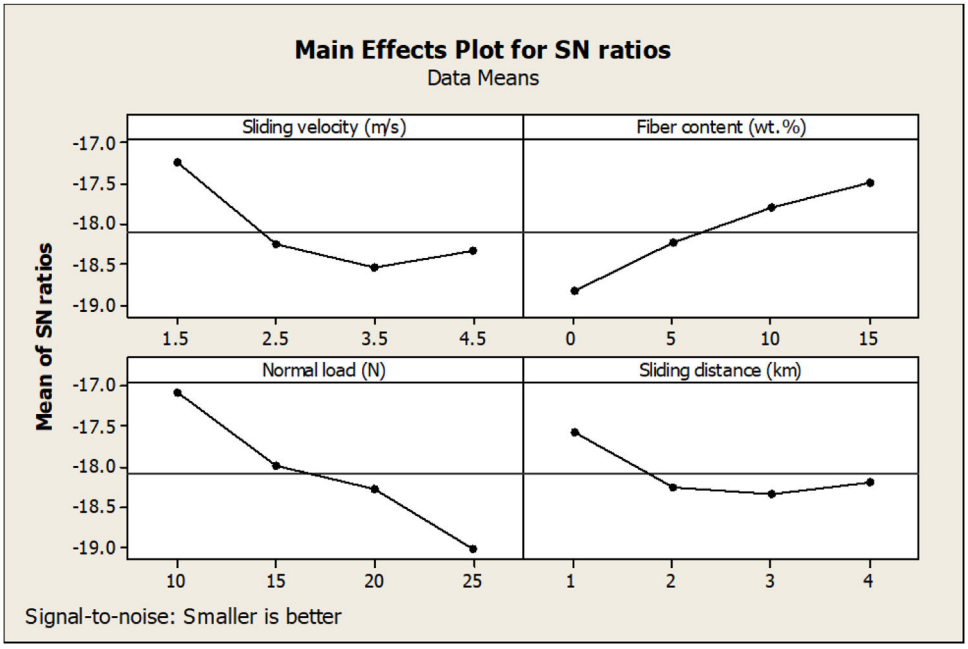

Fig. 6 – Main-effect plots for S-N ratio of specific wear rate of the graded composites.

observations it appears that composites (homogeneous or graded) under consideration exhibits various wear mechanism as per the operating conditions presented in Table 4. The wear behaviour of the composites varies with the fiber loading and operating conditions. The remarkable feature of the worn surfaces hybrid composites is a smooth topography. At lower sliding velocity, the worn surface was relatively smooth and wear rate increased with an increase

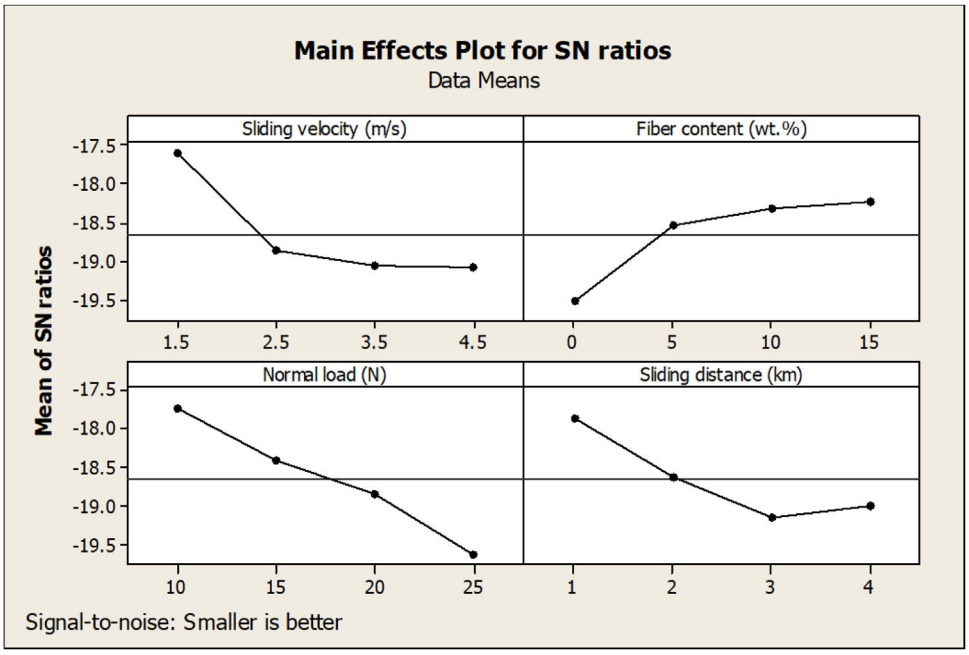

Fig. 7 – Main-effect plots for S-N ratio of specific wear rate of the homogeneous composites.

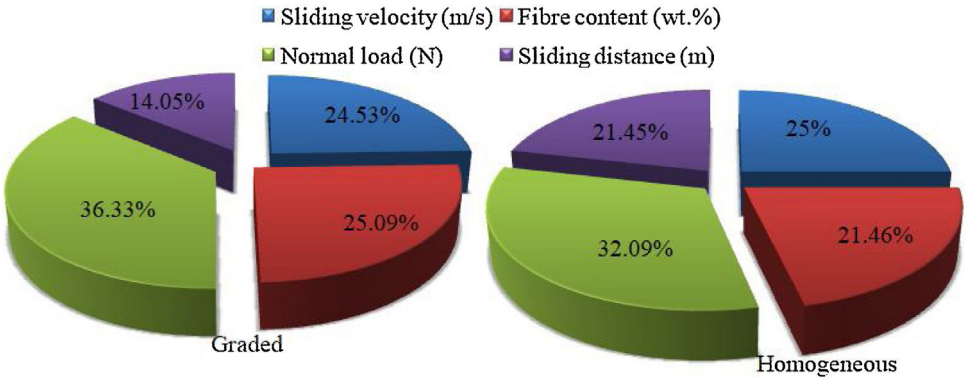

Fig. 8 – Contribution ratio of each control factor on specific wear rate of graded and homogeneous composites.

Table 7 – Outcomes of confirmation experiments.

	Optimum control factor		Error (%)
	Experimental	Predicted	
Graded	$A_1B_4C_1D_1$	$A_1B_4C_1D_1$	
Specific wear rate achieved $\times 10^{-6}$ mm^3/Nm	5.56	5.40	2.96
Homogeneous	$A_4B_1C_1D_1$	$A_4B_1C_1D_1$	
Specific wear rate achieved $\times 10^{-6}$ mm^3/Nm	5.75	5.56	3.42

in fiber loading and normal load. Fig. 9(a–d) of homogeneous and graded composite with ≤5 wt.% bagasse fiber loading, ≤15 N load, ≤2 km distance and 1.5 m/sec sliding velocity both exhibits almost similar wear rate which is in the range of ~5.88×10^{-6}–6.72×10^{-6} mm^3/Nm. This low wear rate of the composite at low sliding speed was due to this synergistic effect of bagasse and Kevlar fibers. Both homogeneous and graded composites show increased wear rate 9.48×10^{-6} mm^3/Nm and 8.61×10^{-6} mm^3/Nm respectively, As the bagasse fiber loading increases to 15 wt.%, normal load to 25 N, sliding distance to 4 km, as shown in Fig. 9(e, f).

In comparison with Fig. 9(a–d), it is clear that the worn surface of Fig. 9(e, f) for both homogeneous and graded composites exhibit higher wear rates with severe fiber breakage and surface damage. This severe fiber breakage and surface damage are due to frictional heat generated during sliding will leading to fiber-matrix debonding and hence increased wear rate [42]. The wear rate increased in both the

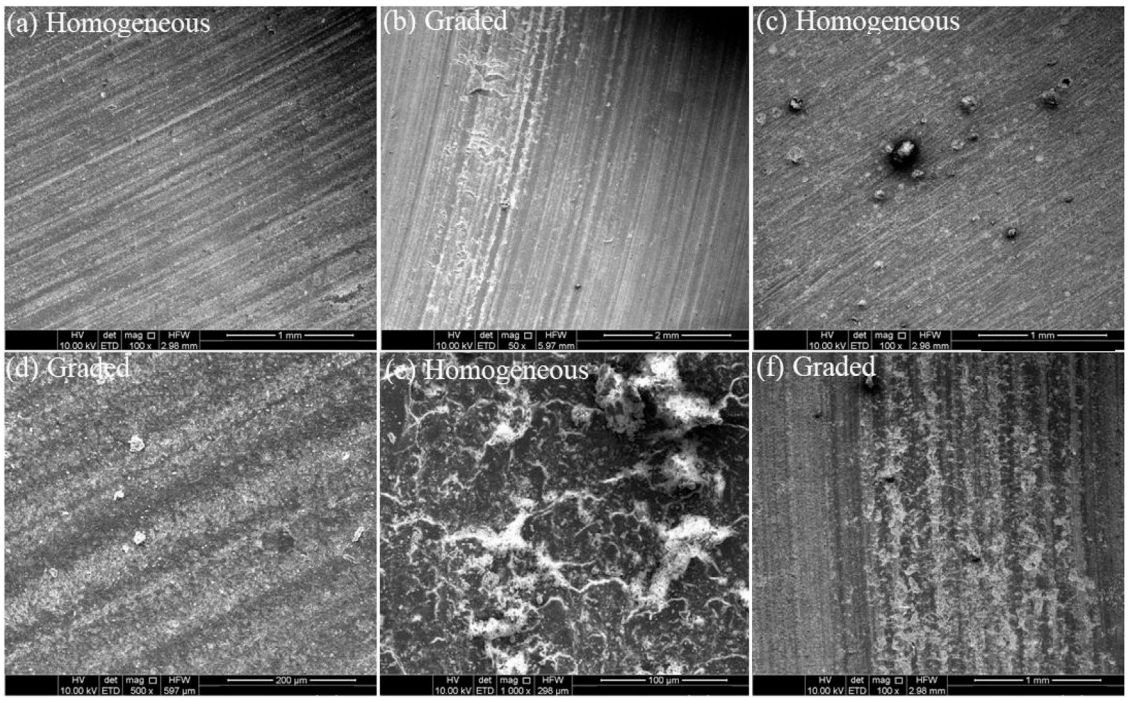

Fig. 9 – Worn surface morphology of homogeneous and graded composites.

graded and homogeneous composites and remain in the range of 8.37×10^{-6}–11.22×10^{-6} mm^3/Nm, as the sliding velocity increases to 2.5 m/s and sliding distance to 3–4 km (Table 4, Test run: 5–6). Their corresponding micrographs are shown in Fig. 10(a–d) reveals extensive matrix fragmentation and the manifestation of shallow furrows due to micro-ploughing in

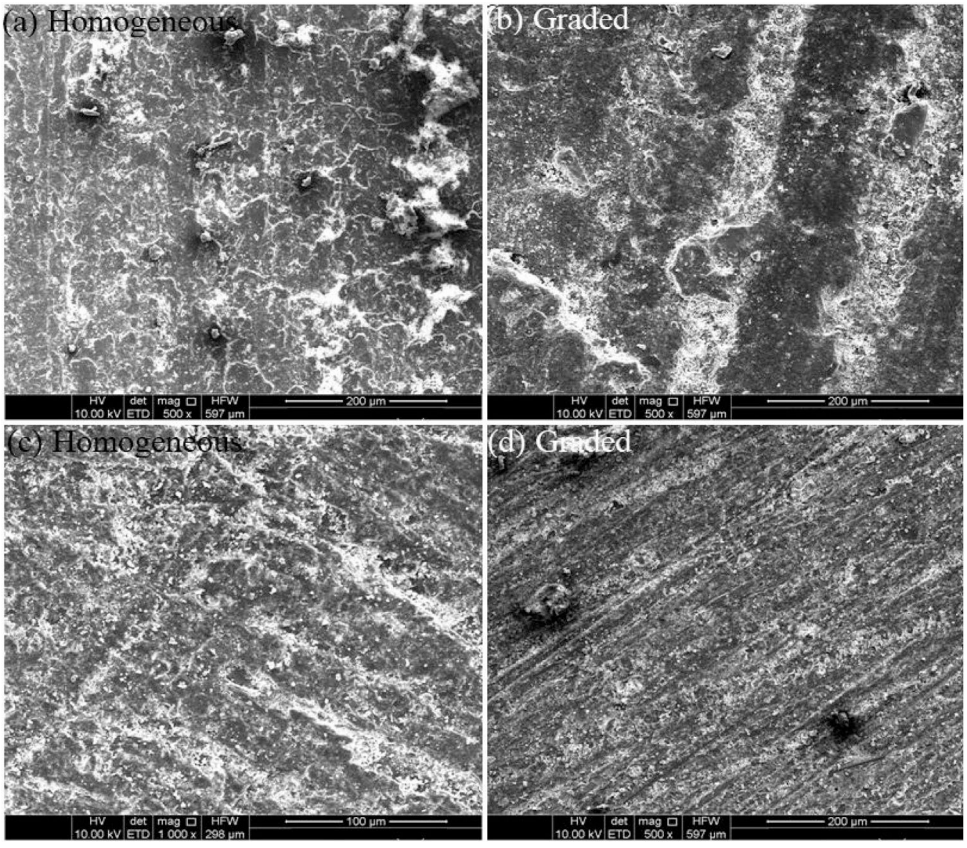

Fig. 10 – Worn surface morphology of homogeneous and graded composites.

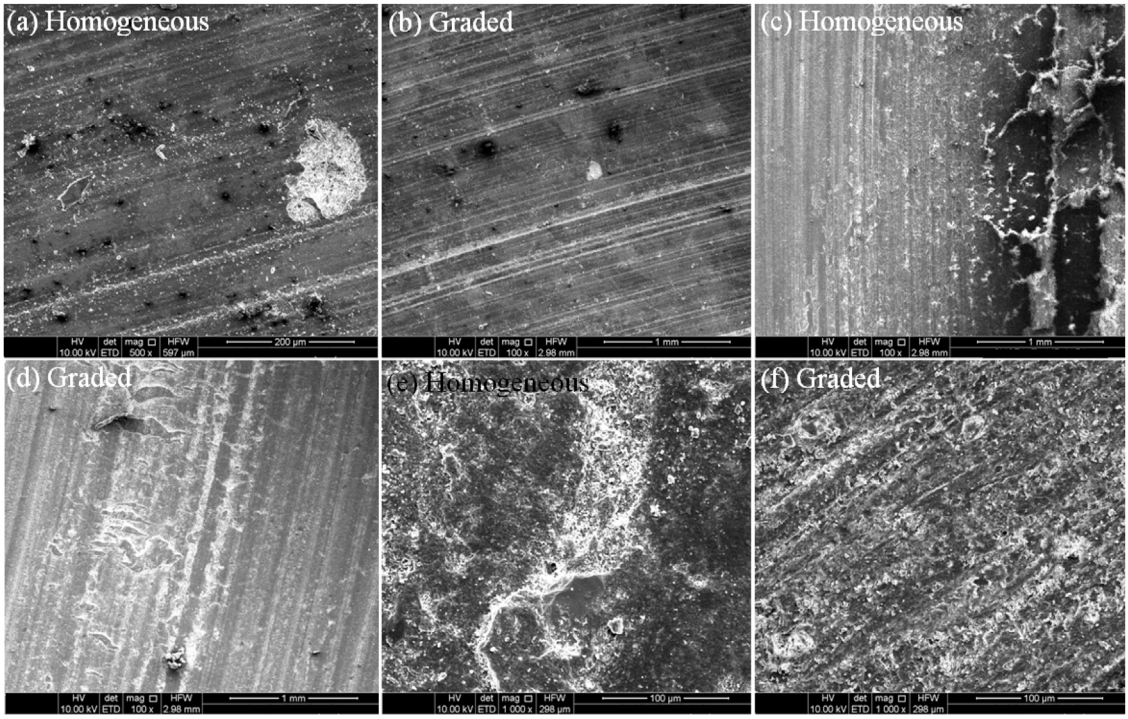

Fig. 11 – Worn surface morphology of homogeneous and graded composites.

the resin and micro-cutting of the fibers in both homogeneous and graded composites. This might be credited to the reduction of fiber-matrix adhesion with increased frictional heat resulted in higher wear rate due to peeling-off and pulverization of the fibers [43].

Fig. 11(a–d) shows the worn surface of ≤ 5 wt.% bagasse fiber reinforced composites tested under 20–25 N loads at 3.5 m/s of sliding speed and sliding distance of 3–4 km. The worn surfaces exhibit ploughed shear mark on the rubbing surface and fiber breakage and matrix wear debris accumulation of homogeneous and graded composites as shown in Fig. 11(a–d), (Table 4, Test run: 9–10) accounts for higher wear rate i.e. $\sim 9 \times 10^{-6}$ mm^3/N-m for both homogeneous and graded composites. Further, with an increase in sliding velocity to 4.5 m/s, bagasse fiber loading ≤ 5 wt.% and loads (≥20 N) wear rate increases tremendously for both homogeneous and graded composites and remains in between 9.076×10^{-6} and 12.34×10^{-6} mm^3/Nm. The distinct feature of the worn surface is the higher extent of fibers breakage or pulverization and debonding in the fiber-matrix adhesion. This may be attributed to the formation of large rough patches that appears on the worn surface as shown in Fig. 11(e, f). The protruding of fibers from shallow furrows drawn across the surface as a result of microploughing and extensive fibrillation of the fiber can also be seen. Also, delamination and thermo-fatigue failure of the matter from the surface of the composite is responsible for the highest wear rate.

4. Conclusions

In the present study, fixed Kevlar fiber (5 wt.%) and varying bagasse fiber (0, 5, 10, 15 wt.%) reinforced homogeneous and graded vinylester composites were designed, fabricated and evaluated for sliding wear behaviour. The specific wear rate of graded and homogeneous composites was first increased and then decreased with further increase in sliding velocity. Whereas, the specific wear rate shows a decreasing trend with an increased normal load. The minimum specific wear rate is shown by 15 wt.% bagasse fiber reinforced graded composite. The optimum combination of control factors to achieve minimum specific wear rate for homogeneous and graded composites is: 1.5 m/s sliding velocity (Factor A, Level 1), 15 wt.% bagasse fiber content (Factor B, Level 4), 10 N normal load (Factor C, Level 1) and 1 km sliding distance (Factor D, Level 1). The contribution of the normal load was the largest influence on the specific wear rate of graded and homogeneous composites with 36.33% and 32.09% respectively.

Conflict of interest

"The authors declare that they have no known competing financial interests or personal relationships that could have appeared to influence the work reported in this paper."

REFERENCES

[1] Ahmadian-Fard-Fini S, Ghanbari D, Salavati-Niasari M. Photoluminescence carbon dot as a sensor for detecting of *Pseudomonas aeruginosa* bacteria: hydrothermal synthesis of magnetic hollow $NiFe_2O_4$-carbon dots nanocomposite material. Composite B: Eng 2019;161:564–77.

[2] Ghanbari D, Salavati-Niasari M. Synthesis of urchin-like CdS-Fe_3O_4 nanocomposite and its application in flame

retardancy of magnetic cellulose acetate. J Ind Eng Chem 2015;24:284–92.
[3] Safajou H, Khojasteh H, Salavati-Niasari M, Mortazavi-Derazkola S. Enhanced photocatalytic degradation of dyes over graphene/Pd/TiO_2 nanocomposites: TiO_2 nanowires versus TiO_2 nanoparticles. J Colloid Interface Sci 2017;498:423–32.
[4] Ghanbari D, Salavati-Niasari M, Esmaeili-Zare M, Jamshidi P, Akhtarianfar F. Hydrothermal synthesis of CuS nanostructures and their application on preparation of ABS-based nanocomposite. J Ind Eng Chem 2014;20(5):3709–13.
[5] Jamshidi P, Ghanbari D, Salavati-Niasari M. Photocatalyst Al_2O_3-TiO_2: preparation of poly vinyl alcohol based nanocomposite by ultrasonic waves. J Mater Sci Mater Electron 2017;28(12):8950–9.
[6] Salavati-Niasari M, Davar F, Loghman-Estarki MR. Long chain polymer assisted synthesis of flower-like cadmium sulfide nanorods via hydrothermal process. J Alloys Compd 2009;481(1-2):776–80.
[7] Jamshidi P, Ghanbari D, Salavati-Niasari M. Sonochemical synthesis of $La(OH)_3$ nanoparticle and its influence on the flame retardancy of cellulose acetate nanocomposite. J Ind Eng Chem 2014;20(5):3507–12.
[8] Mahdiani M, Soofivand F, Ansari F, Salavati-Niasari M. Grafting of $CuFe_{12}O_{19}$ nanoparticles on CNT and graphene: Eco-friendly synthesis, characterization and photocatalytic activity. J Clean Prod 2018;176:1185–97.
[9] Sola A, Bellucci D, Cannillo V. Functionally graded materials for orthopedic applications - an update on design and manufacturing. Biotechnol Adv 2016;34:504–31.
[10] Oshkour AA, Pramanik S, Mehrali M, Yau YH, Tarlochan F, Osman NAA. Mechanical and physical behavior of newly developed functionally graded materials and composites of stainless steel 316L with calcium silicate and hydroxyapatite. J Mech Behav Biomed Mater 2015;49:321–31.
[11] Koizumi M, Niino M. Overview of FGM research in Japan. MRS Bull 1995;20:19–21.
[12] Udupa G, Rao SS, Gangadharan KV. Functionally graded composite materials: an overview. Procedia Mater Sci 2014;5:1291–9.
[13] Naebe M, Shirvanimoghaddam K. Functionally graded materials: a review of fabrication and properties. Appl Mater Today 2016;5:223–45.
[14] Almasi D, Sadeghi M, Lau WJ, Roozbahani F, Iqbal N. Functionally graded polymeric materials: a brif review of current fabrication methods and introduction of a novel fabrication method. Mater Sci Eng C 2016;64:102–7.
[15] Gangil B, Patnaik A, Kumar A, Kumar M. Investigations on mechanical and sliding wear behaviour of short fibre-reinforced vinylester-based homogenous and their functionally graded composites. Proc Inst Mech Eng Part L J Mater Des Appl 2012;226:300–15.
[16] Singh AK, Siddhartha. Mechanical and thermo-mechanical peculiarity of functionally graded materials-based glass fiber-filled polybutylene terephthalate composites. J Reinf Plast Compos 2018;37:410–26.
[17] Li L, Liu X, Zhou X, Hong J, Zhuang X, Yan X. Mechanical properties of unidirectional continuous fiber self-reinforced polyethylene graded laminates. Polym Compos 2015;36:128–37.
[18] Singh SB, Chawla H, Ranjitha B. Hybrid effect of functionally graded hybrid composites of glass-carbon fibers. Mech Adv Mater Struct 2019;26(14):1195–208.
[19] Liu Y, Ma Y, Lv X, Yu J, Zhuang J, Tong J. Mineral fibre reinforced friction composites: effect of rockwool fibre on mechanical and tribological behaviour. Mater Res Express 2018;5(9):095308.
[20] Reddy GR, Kumar MA, Karthikeyan N, Basha SM. Tamarind fruit fiber and glass fiber reinforced polyester composites. Mech Adv Mater Struct 2015;22:770–5.
[21] Singh T, Gangil B, Patnaik A, Biswas D, Fekete G. Agriculture waste reinforced cornstarch-based biocomposites: effect of rice husk/walnut shell on physicomechanical, biodegradable and thermal properties. Mater Res Express 2019;6(4):045702.
[22] Hamidon MH, Sultan MTH, Ariffin AH, Shah AUM. Effects of fibre treatment on mechanical properties of kenaf fibre reinforced composites: a review. J Mater Res Technol 2019;8(3):3327–37.
[23] Liu Y, Xie J, Wu N, Wang L, Ma Y, Tong J. Influence of silane treatment on the mechanical, tribological and morphological properties of corn stalk fiber reinforced polymer composites. Tribol Int 2019;131:398–405.
[24] Singh T, Tejyan S, Patnaik A, Singh V, Zsoldos I, Fekete G. Fabrication of waste bagasse fibre reinforced epoxy composites: study of physical, mechanical and erosion properties. Polym Compos 2019;40(9):3777–86.
[25] Fidelis MEA, Pereira TVC, Gomes OFM, Silva FA, Filho RDT. The effect of fiber morphology on the tensile strength of natural fibers. J Mater Res Technol 2013;2(2):149–57.
[26] Glória GO, Teles MCA, Neves ACC, Vieira CMF, Lopes FPD, Gomes MA, et al. Bending test in epoxy composites reinforced with continuous and aligned PALF fibers. J Mater Res Technol 2017;6(4):411–6.
[27] Singh T, Gangil B, Patnaik A, Kumar S, Rishiraj A, Fekete G. Physico-mechanical, thermal and dynamic mechanical behaviour of natural-synthetic fiber reinforced vinylester based homogenous and functionally graded composites. Mater Res Express 2019;6:025704.
[28] Liu Y, Wang L, Liu D, Ma Y, Tian Y, Tong J, et al. Evaluation of wear resistance of corn stalk fiber reinforced brake friction materials prepared by wet granulation. Wear 2019;432-433:102918.
[29] Oliveira CG, Margem FM, Monteiro SN, Lopes FPD. Comparison between tensile behavior of epoxy and polyester matrix composites reinforced with eucalyptus fibers. J Mater Res Technol 2017;6(4):406–10.
[30] Nascimento LFC, Monteiro SN, Louro LHL, Luz FS, Santos JL, Braga FO, et al. Charpy impact test of epoxy composites reinforced with untreated and mercerized mallow fibers. J Mater Res Technol 2018;7(4):520–7.
[31] Anidha S, Latha N, Muthukkumar M. Reinforcement of Aramid fiber with bagasse epoxy bio-degradable composite: investigations on mechanical properties and surface morphology. J Mater Res Technol 2019;8(3):3198–212.
[32] Afzaluddin A, Jawaid M, Salit MS, RidwanIshak M. Physical and mechanical properties of sugar palm/glass fiber reinforced thermoplastic polyurethane hybrid composites. J Mater Res Technol 2019;8(1):950–9.
[33] Ismail MF, Sultan MTH, Hamdan A, Shah AUM, Jawaid M. Low velocity impact behaviour and post-impact characteristics of kenaf/glass hybrid composites with various weight ratios. J Mater Res Technol 2019;8(3):2662–73.
[34] Silva AO, Monsores KGC, Oliveira SSA, Weber RP, Monteiro SN. Ballistic behavior of a hybrid composite reinforced with curaua and aramid fabric subjected to ultraviolet radiation. J Mater Res Technol 2018;7(4):584–91.
[35] Ramesh M, Palanikumar K, Reddy KH. Plant fibre based bio-composites: sustainable and renewable green materials. Renewable Sustainable Energy Rev 2017;79:558–84.
[36] Singh T, Chauhan R, Patnaik A, Gangil B, Nain R, Kumar A. Parametric study and optimization of multiwalled carbon nanotube filled friction composite materials using Taguchi method. Polym Compos 2018;39:E1109–17.
[37] Singh T, Patnaik A, Chauhan R, Chauhan P, Kumar N. Physico-mechanical and tribological properties of nanoclay

filled friction composite materials using Taguchi design of experiment approach. Polym Compos 2018;39:1575–81.
[38] Tejyan S, Singh T, Patnaik A, Fekete G, Gangil B. Physico-mechanical and erosive wear analysis of polyester fibre-based nonwoven fabric-reinforced polymer composites. J Ind Text 2019;49(4):447–64.
[39] Suresha B, Kumar KS, Seetharamu S, Kumaran PS. Friction and dry sliding wear behavior of carbon and glass fabric reinforced vinyl ester composites. Tribol Int 2010;43:602–9.
[40] Friedrich K, Liu Z, Hager AM. Recent advances in polymer composites' tribology. Wear 1995;190:139–44.
[41] Gong G, Yang H, Fu X. Tribological properties of kaolin filled UHMWPE composites in unlubricated sliding. Wear 2004;256:88–94.
[42] Zhao Q, Bahadur S. Investigation of the transition state in the wear of polyphenylene sulfide sliding against steel. Tribol Lett 2002;12:23–33.
[43] Basavarajappa S, Ellangovan S, Arun KV. Studies on dry sliding wear behaviour of graphite filled glass-epoxy composites. Mater Des 2009;30:2670–5.

Ferroelectrics

ISSN: 0015-0193 (Print) 1563-5112 (Online) Journal homepage: https://www.tandfonline.com/loi/gfer20

Converse piezoelectric properties of lead free $Ba_{1-x}Ca_xZr_{0.1}Ti_{0.9}O_3$ (x = 0.055) ceramics using double sintered method

Don Biswas, N. S. Panwar & Prolay Sharma

To cite this article: Don Biswas, N. S. Panwar & Prolay Sharma (2020) Converse piezoelectric properties of lead free $Ba_{1-x}Ca_xZr_{0.1}Ti_{0.9}O_3$ (x = 0.055) ceramics using double sintered method, Ferroelectrics, 568:1, 95-103, DOI: 10.1080/00150193.2020.1811032

To link to this article: https://doi.org/10.1080/00150193.2020.1811032

Published online: 03 Nov 2020.

Submit your article to this journal

Article views: 15

View related articles

View Crossmark data

Full Terms & Conditions of access and use can be found at
https://www.tandfonline.com/action/journalInformation?journalCode=gfer20

FERROELECTRICS
2020, VOL. 568, 95–103
https://doi.org/10.1080/00150193.2020.1811032

Taylor & Francis
Taylor & Francis Group

Check for updates

Converse piezoelectric properties of lead free $Ba_{1-x}Ca_xZr_{0.1}Ti_{0.9}O_3$ (x = 0.055) ceramics using double sintered method

Don Biswas[a], N. S. Panwar[a], and Prolay Sharma[b]

[a]University Science Instrumentation Centre, H.N.B. Garhwal University, Srinagar, India; [b]Instrumentation and Electronics Enginering, Jadavpur University, Kolkata, India

ABSTRACT

The influence of double sintering temperature on the phase structure, micro-structure and piezoelectric properties of $Ba_{1-x}Ca_xZr_{0.1}Ti_{0.9}O_3$ (x = 0.055) double sintered ceramics has been systematically studied. The pellet sample preparation and characterization have been reported in this paper. The converse piezoelectric properties of the $Ba_{1-x}Ca_xZr_{0.1}Ti_{0.9}O_3$ (x = 0.055) were observed. Depending upon the sintering temperature, the grain size and density of BCZT ceramics have been changed. The P-E loops, strain%, and the polarization current were measured. The value of d_{33} was decreasing with the application of an electric field in case of double sintered pellets. For sample x = 0.055, the value of d_{33}* at 1300, 1400 and 1450 °C temperature, was 173 (pm/V), 130 (pm/V), and 75 (pm/V), respectively, at applied field 29.33 kV/cm.

ARTICLE HISTORY
Received 7 October 2019
Accepted 31 March 2020

KEYWORDS
Ferroelectrics; piezoelectric constant; phase - structure; micro - structure

1. Introduction

Perovskite type materials possess spontaneous polarization. The ABO_3/Perovskite type materials are important due to the generation of spontaneous polarization. Spontaneous polarization means polarization in the absence of electrical field. The properties like dielectric and ferroelectric are very important due to its contribution to the field of sensors and transducers. Ferroelectric/ABO_3 materials have a good piezoelectric 'property,' i.e. generation of mechanical stress in the response of input voltage and vice versa. They may be a good replacement of PZT type material. Therefore, these ferroelectric/ABO_3 materials are largely used in various fields such as actuators, generators, sensors and transducers, etc. [1]. ABO_3 type materials such as lead zirconium titanate (PZT) have been extensively considered because of their high value of the dielectric and piezoelectric constant. It has been observed that PZT shows large d_{33} value due to the coexistence of two phases (rhombohedral and tetragonal) at MPB region [2–4]. The polarization state shows instability at MPB region, which eases the alteration of the ferroelectric domains; therefore causes the PZT system has high piezoelectric properties at MPB region [5]. Since PZT have the highest piezoelectric constant and important for many sensors but due to its toxic 'nature' some country prohibited it and going for

CONTACT Don Biswas donusic06@gmail.com
© 2020 Taylor & Francis Group, LLC

lead-free piezoelectric materials [6]. There are ABO_3 materials like $BaTiO_3$, NKN, KNN possess good dielectric and piezoelectric properties [7]. In these lead-free materials, Barium Calcium Zirconate Titanate (BCZT) shows high dielectric and piezoelectric properties which may be used to design different sensors like memory devices, ceramic capacitor etc. [8]. The lead-free BCZT has good piezoelectric properties reported by N. Buatip et al. [9]. N. Buatip observed that after sintering temperature 1300^0C, the piezoelectric properties has reduced. Tian et al. [10,11] reported regarding lead-free $(Ba_{1-x}Ca_xZr_{0.1}Ti_{0.9})$ O_3 $(0.00 \leq x \leq 0.20)$ piezoelectric ceramics designed by a solid-state method generated piezoelectric coefficient (d_{33}) of around 160– 600 pC/N.

Therefore, this study has a purpose of optimizing sintered pellets and electrical properties by variation of sintering temperature conditions and want to see the effect of that changes on phase structure, microstructure and piezoelectric properties of BCZT $(Ba_{0.935}Ca_{0.055}Zr_{0.1}Ti_{0.9}O_3)$ samples. In the present case, BCZT 'lead' free ceramics were studied in the double sintered conditions in the temperature range 1300 °C to 1450 °C for 6 hrs. The variation in sintering temperature was so chosen to understand the effect on grain size, microstructure and piezoelectric properties.

In this study, we prepared BCTZ pellet samples (x = 0.055) and see the effect of variation in sintering temperature and observe the changes in structure, microstructure and piezoelectric properties, among the prepared pellet samples.

2. Experimental details

Raw materials have been utilized for preparing the composition, for the current study, were Barium carbonate ($BaCO_3$), Calcium carbonate ($CaCO_3$), Zirconium oxide (ZrO_2) and Titanium oxide (TiO_2) all of 99.99% pure. BCZT Pellet samples were prepared using conventional solid-state reaction method with double sintering. The dissolved moisture has been removed from the prepared samples. The materials were dried in an oven, at 200 °C for 2 hours to remove the moisture. For x = 0.055 $(Ba_{1-x}Ca_xZr_{0.1}Ti_{0.9})$ O_3, the composition was made by weighing the materials in accurate stoichiometric ratio. The compositions were manually 'dry' mixed and ground for 4 hours and with methanol for another 2 hours. For the mixing purpose, 'agate' mullet mortar and pestle have been used. The mixed powder was taken into a furnace and calcined in the air at 1100 °C to remove carbonate. After reaching room temperature, they were taken out. They were weighed to check complete carbonate removal. After that the sintering process has been started. For that purpose, the pre-sintered mixture was taken into a pressing machine to make pellet samples. The powder or mixture was ground and pressed into that pressing machine having pressure 0.15 GPa. The pressing disk has 1 mm thickness and 8 mm diameter. Pellets of $Ba_{1-x}Ca_xZr_{0.1}Ti_{0.9}$ (x = 0.055) were double sintered, each composition for 6 (Average) hours, at 1300, 1400 and 1450 °C. The pellets were cooled first at room temperature, and when they were ready, they have been taken for measurement [11]. After first sintered, the pellets were taken for the second sintering process.

The crystal structure was recognized by X-ray diffraction (XRD) using CuKα1 radiation. The measured XRD pattern of the prepared $Ba_{1-x}Ca_xZr_{0.1}Ti_{0.9}$ powder sample (x = 0.055) is shown in Figure 1. X-Ray patterns of prepared $Ba_{1-x}Ca_xZr_{0.1}Ti_{0.9}$ pellet

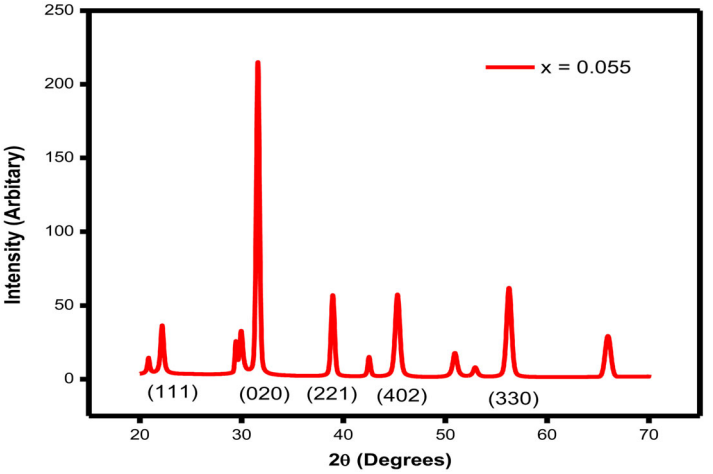

Figure 1. XRD patterns of $Ba_{1-x}Ca_xZr_{0.1}Ti_{0.9}$ (x = 0.055) powder sample at room temperature.

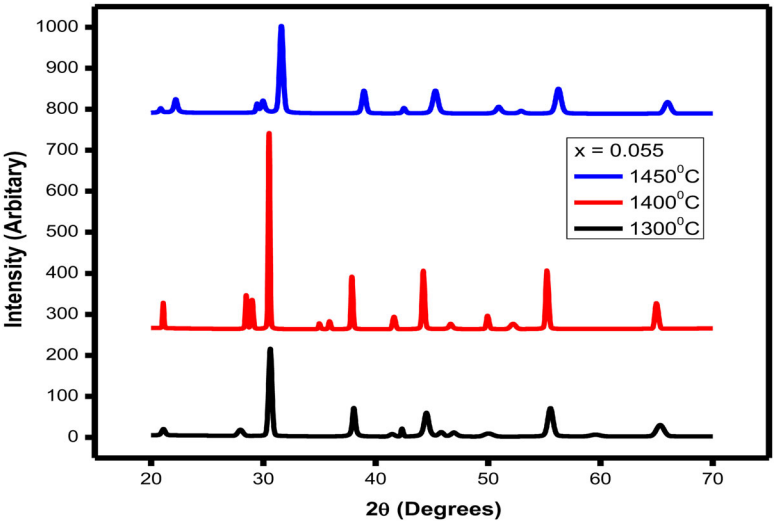

Figure 2. XRD patterns of $Ba_{1-x}Ca_xZr_{0.1}Ti_{0.9}$ (x = 0.055) pellet samples at different sintering temperature.

samples (double sintered) at 1300, 1400 and 1450 °C with the same composition (x = 0.055) of x is shown in Figure 2. XRD patterns of all prepared powder and pellet samples were measured at room temperature, with the help of Pan Analytical PW340 X-Ray diffractometer, having a wavelength 1.54060 A. The X-ray machine has been well-calibrated with standard samples.

SEM images of BCZT pellet samples were observed to study surface morphology and grain size. The model EVO 18 Special Edition (Made in Switzerland, manufactured by ZEISS) has been used to generate SEM images. From SEM images of prepared pellet samples, the average grain sizes were calculated between 0.70 and 2.6 μm.

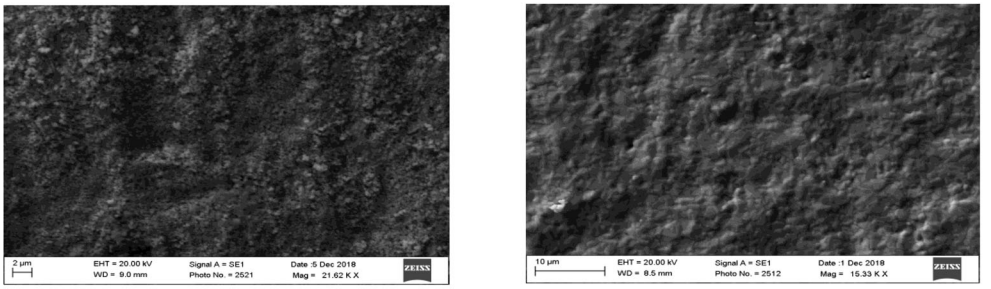

Figure 3. SEM images of $(Ba_{1-x}Ca_xZr_{1-y}Ti_y)\ O_3$ for $x = 0.055$ and $y = 0.9$, 1st sintered (left) and 2nd sintered (right), at 1300 °C temperature.

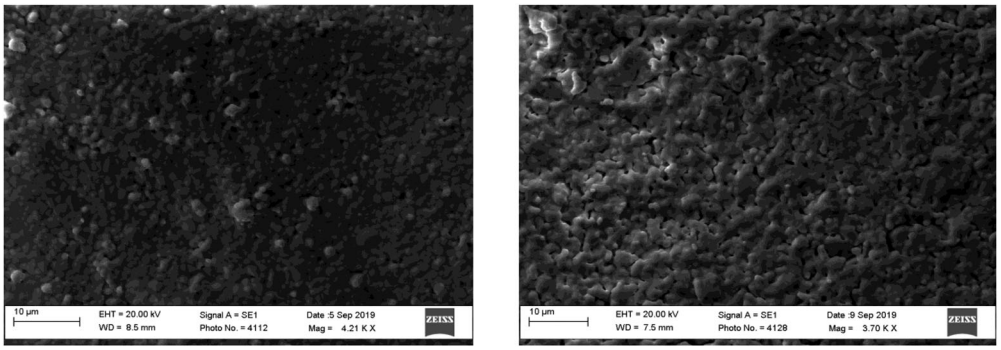

Figure 4. SEM images of $(Ba_{1-x}Ca_xZr_{1-y}Ti_y)\ O_3$ for $x = 0.055$ and $y = 0.9$, 1st sintered (left) and 2nd sintered (right), at 1400 °C temperature.

For measurement of the piezoelectric constant of prepared sintered pellets, specimens were coated both sides using a silver paste, in MIM (metal- insulator- metal) configuration. The prepared BCZT samples show an orthorhombic structure at room temperature. Converge piezoelectric constant 'd_{33}*' was measured using the aixACCT system GMBH. Then they have been used for the measurement of converse piezoelectric properties.

3. Results and discussion

Figure 1 shows XRD patterns of $Ba_{1-x}Ca_xZr_{0.1}Ti_{0.9}$ ($x = 0.055$) powder sample ceramics at room temperature. The sample shows a single perovskite structure, and no other phases were observed. The XRD patterns have 2θ angle scan range from 20–70°. The ceramic samples show polycrystalline behavior and were found in good consistency with Inorganic Crystal Structure Database (ICSD) - (00-056-1033) of BCZT ($x = 0.055$), with peaks corresponding to (111), (020), (221), etc. [12]. For double sintered samples, the XRD patterns for the same sample with different sintering temperature were similar i. e. Orthorhombic phase (ICSD file No.00-056-1033) (Figure 2). The lattice parameters were calculated by High Score Plus software ($a = 9.808$ A, $b = 5.652$ A, $c = 6.893$ A).

It was observed that sintering conditions at temperatures 1300, 1400 and 1450 °C have no effect on the phase structure of BCZT samples (Figure 2). Though it was seen that microstructures, together with grain size and density, are influenced by having different sintering temperature. Figures 3–5 shows the SEM images for the samples

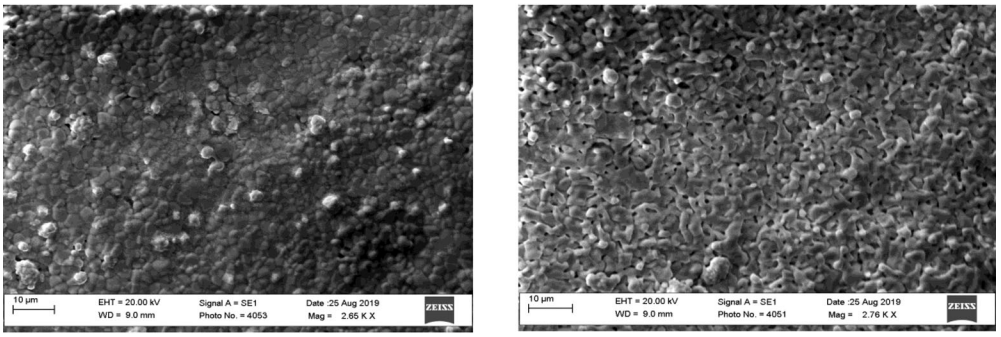

Figure 5. SEM images of $(Ba_{1-x}Ca_xZr_{1-y}Ti_y)$ O_3 for $x = 0.055$ and $y = 0.9$, 1st sintered (left) and 2nd sintered (right), at 1450 °C temperature.

Element	Weight%	Atomic %
O K	26.51	66.40
Ca K	3.05	3.05
Ti K	18.53	15.50
Zr L	-0.62	-0.27
Ba L	52.53	15.32
Total	100.00	

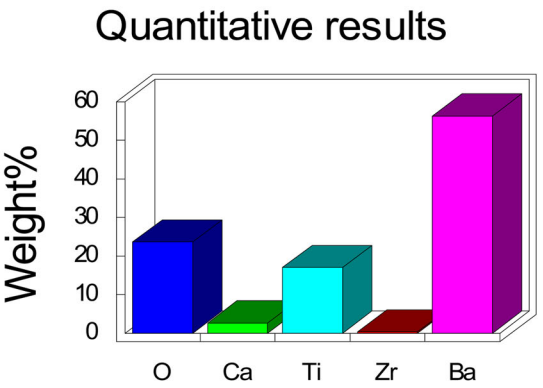

Figure 6. EDAX results of $(Ba_{1-x}Ca_xZr_{1-y}Ti_y)$ O_3 for $x = 0.055$, 2nd sintered at 1300° C temperature.

sintered at different temperature. It was seen from the SEM images, as the sintering temperature has been increased, the grain size or the grain boundary of the samples were increased. The atomic percentage of the present elements is shown in Figures 6–8. From the EDAX results, it has been seen that the barium percentage has been decreased as the sintering temperature has been increased. That means for higher sintering temperature the barium percentage decreased, and the oxygen percentage has been increased. For BCZT ceramics, an inhomogeneous increase in grain-size has been seen because of the variation in the sintering temperature from 1400 °C and 1450 °C for 6 hrs. The reason behind is longer dwelling time, and atoms were getting diffused into adjoining grains, at the grain boundary. It triggers the growth in grain size and increases the density of BCZT ceramics. [13–15]. The grain size and density of BCZT pellet samples show increasing trend when the sintering temperature (2 times) and dwelling time has been increased due to larger diffusion mechanisms that lead to good densification of lead-free ceramics.

P-E hysteresis loops of prepared BCZT pellet samples are shown in Figure 9. The measurement was taken at different applied 'voltages' but at the constant electrical field. The prepared samples were not poled, and measurements were taken at room temperature. From the measurement, the hysteresis loops show a typical ferroelectric nature of

Element	Weight %	Atomic %
O K	30.94	69.98
Ca K	4.12	3.72
Ti K	18.80	14.21
Zr L	-0.39	-0.16
Ba L	46.53	12.26
Total	100.00	

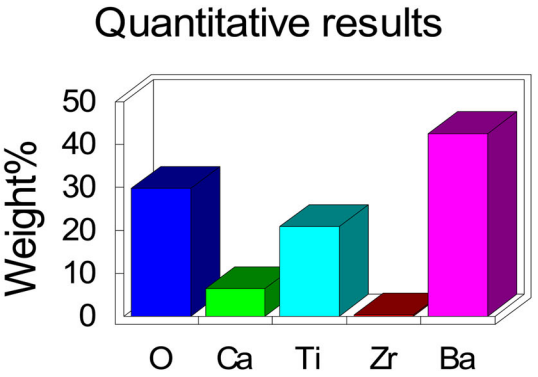

Figure 7. EDAX results of $(Ba_{1-x}Ca_xZr_{1-y}Ti_y)\ O_3$ for x = 0.055, 2nd sintered at 1400 °C temperature.

Element	Weight %	Atomic %
O K	29.75	67.11
Ca K	6.45	5.81
Ti K	20.95	15.78
Zr L	0.27	0.11
Ba L	42.58	11.19
Total	100.00	

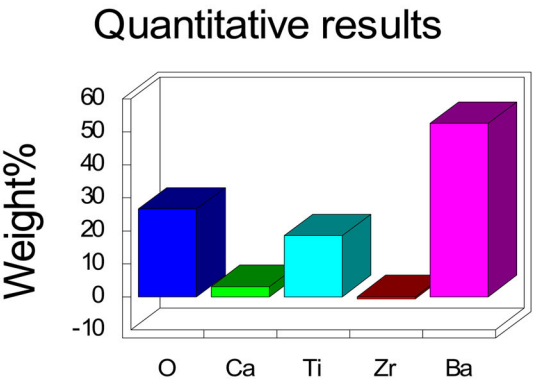

Figure 8. EDAX results of $(Ba_{1-x}Ca_xZr_{1-y}Ti_y)\ O_3$ for x = 0.055, 2nd sintered at 1450 °C temperature.

lead-free ceramics. From P-E hysteresis loops, the maximum value of remnant polarization (Pr) was 2.094 μC/cm^{2,} and the value of the cohesive field was 3.65 kV/cm (E_C), with sample x = 0.055, sintered at 1300^{0}C. A 'well saturated' loop is observed for BCZT ceramics sintered two times at a high-temperature range. From prepared pellet samples, well-saturated loops were observed because of 'high density' and 'low porosity'.

Figure 10 shows the current density loops for BCZT ceramic samples at different sintering temperatures. It has been seen that the current density has been decreased as the sintering temperature has been increased. The results were similar for P- E loops with the applied field. The maximum current density was seen for sample x = 0.055 sintered at 1300^{0}C, was 2.84×10^{-6} A.

Figure 11 shows P-E strain% loops for BCZT pellet samples at different sintering temperatures. The piezoelectric properties have been studied. They were measured at constant electric field 29.33(KV/cm). The variation of strain percentage with the electric field has been plotted in Figure 7. For x = 0.055, the effect of sintering temperature has been seen. For 1300^{0}C, the strain percentage was measured the maximum. As the sintering temperature has been increased, the strain percentage was decreasing. The maximum strain% was seen for sample x = 0.055 sintered at 1300^{0}C, was 173 pm/V (Table 1).

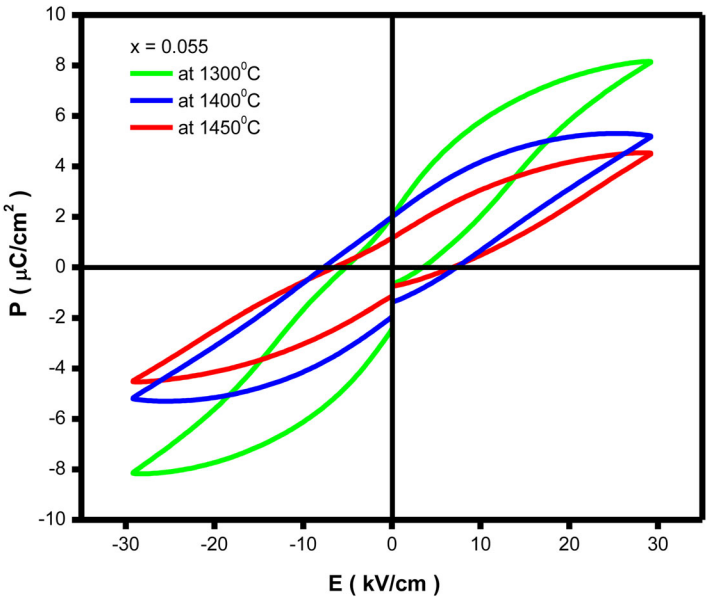

Figure 9. P- E loop of $(Ba_{1-x}Ca_xZr_{1-y}Ti_y)\ O_3$, for $x = 0.055$, double sintered, at different sintering temperature, at applied field 29.33 (kV/cm).

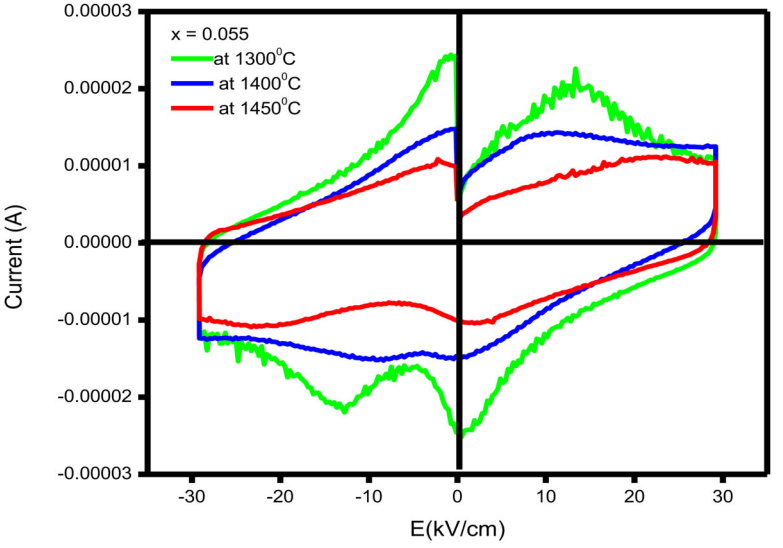

Figure 10. Current density results of $(Ba_{1-x}Ca_xZr_{1-y}Ti_y)\ O_3$, for $x = 0.055$, double sintered, at different sintering temperature, at applied field 29.33 (kV/cm).

4. Conclusion

From the above measurements, the value of converse Piezoelectric Constant has been decreased as the sintering temperature has been increased. This effect can be seen from the hysteresis (P- E Hysteresis loop) curve, as the sintering temperature has been increased the value of polarization has been decreased. From the microstructure

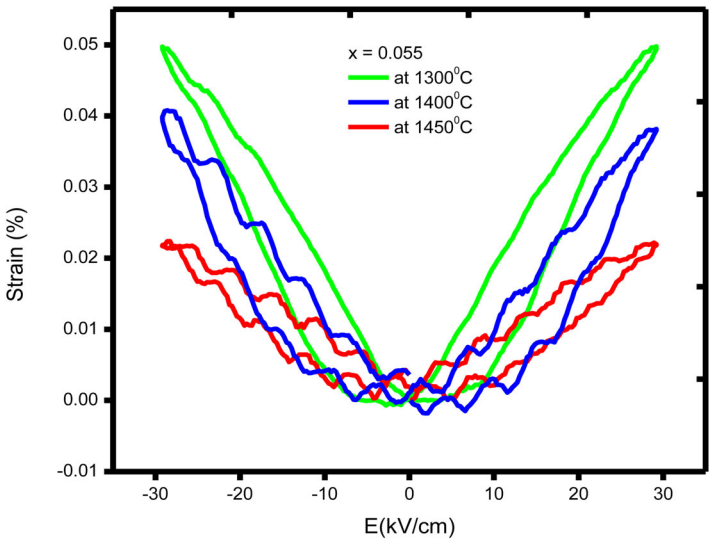

Figure 11. Strain (%) with change in the Electric field of $(Ba_{1-x}Ca_xZr_{1-y}Ti_y)\ O_3$, for $x = 0.055$, double sintered, at different sintering temperature, at applied field 29.33 (kV/cm).

Table 1. Converse Piezoelectric properties with a change in the sintering temperature of $(Ba_{1-x}Ca_xZr_{1-y}Ti_y)\ O_3$, for $x = 0.055$, double sintered, at applied field 29.33 (kV/cm).

X = 0.055	Sintering Temperature	Converse Piezoelectric Constant (d_{33}*) (pm/V)
	1300°C	173
	1400°C	130
	1450°C	75

viewpoint, grains have been increased as the sintering temperature increased. Therefore, the piezoelectric constant has been decreased in the case of double sintered pellet samples as the sintering temperature was increased.

ORCID

Don Biswas http://orcid.org/0000-0001-5130-087X

References

1. P. K. Panda, and B. Sahoo, PZT to lead free piezo ceramics: a review, *Ferroelectrics* **474** (1), 128 (2015). DOI: 10.1080/00150193.2015.997146.
2. P. Kantha *et al.*, Phase formation and electrical properties of BNLT–BZT lead-free piezoelectric ceramic system, *Curr. Appl. Phys.* **9** (2), 460 (2009). DOI: 10.1016/j.cap.2008.04.004.
3. D. Biswas *et al.*, Temperature dependence of dielectric properties of sodium potassium niobate ceramics for different values of x ($Na_{1-x}K_xNbO_3$), *Ferroelectrics* **526** (1), 168 (2018). DOI: 10.1080/00150193.2018.1456307.
4. V. Lingwal, and N. S. Panwar, Morphotropic phase transitions in mixed sodium-potassium niobate system, *Ferroelectrics* **300** (1), 3 (2004). DOI: 10.1080/00150190490442146.

5. Y. Tian *et al.*, Dielectric dispersion, diffuse phase transition, and electrical properties of BCT–BZT ceramics sintered at a low-temperature, *J. Electron. Mater.* **44** (8), 2890 (2015). DOI: 10.1007/s11664-015-3727-3.
6. E. Cross, Lead-free at last, *Nature* **432** (7013), 24 (2004). DOI: 10.1038/nature03142.
7. D. Biswas *et al.*, Converse piezoelectric properties of K and Na-modified $(Na_{1-x}K_x)$ NbO_3 lead free ceramics for x = 0.08 and 0.17, *Ferroelectrics* **550** (1), 228 (2019)., DOI: 10.1080/00150193.2019.1652511.
8. A. Frattini *et al.*, BCZT ceramics prepared from activated powders, *Proc. Mater. Sci.* **1**, 359 (2012)., DOI: 10.1016/j.mspro.2012.06.048.
9. N. Buatip *et al.*, Investigation on electrical properties of BCZT ferroelectric ceramics prepared at various sintering conditions, *Integr. Ferroelectr.* **187** (1), 45 (2018). DOI: 10.1080/10584587.2018.1445395.
10. M. E. Villafuerte-Castrejón *et al.*, Towards lead-free piezoceramics: facing a synthesis challenge, *Materials* **9** (1), 21 (2016). DOI: 10.3390/ma9010021.
11. Y. Tian *et al.*, Phase transition behavior and large piezoelectricity near the morphotropic phase boundary of lead-free $(Ba_{0.85}Ca_{0.15})(Zr_{0.1}Ti_{0.9})O_3$ ceramics, *J. Am. Ceram. Soc.* **96**, 496 (2012). DOI: 10.1111/jace.12049.
12. S. Sen, and R. Choudhay, Effect of doping Ca ions on structural and electrical properties of $Ba(Zr_{0.05}Ti_{0.95})O_3$ electroceramics, *J. Mater. Sci.: Mater. Electron.* **15** (10), 671 (2004). DOI: 10.1023/B:JMSE.0000038922.74021.d6.
13. P. Wang, Y. X. Li, and Y. Q. Lu, Enhanced piezoelectric properties of $(Ba_{0.85}Ca_{0.15})(Ti_{0.9}Zr_{0.1})O_3$ lead-free ceramics by optimizing calcination and sintering temperature, *J Eur. Ceram. Soc.* **31** (11), 2005 (2011). DOI: 10.1016/j.jeurceramsoc.2011.04.023.
14. J. Wu *et al.*, Sintering temperature-induced electrical properties of $(Ba_{0.90}Ca_{0.10})(Ti_{0.85}Zr_{0.15})O_3$ lead-free ceramics, *Mater. Res. Bull.* **47** (5), 1281 (2012). DOI: 10.1016/j.materresbull.2012.01.032.
15. J. Wu *et al.*, Effect of dwell time during sintering on piezoelectric properties of $(Ba_{0.85}Ca_{0.15})(Ti_{0.90}Zr_{0.10})O_3$ lead-free ceramics, *J. Alloys Compd.* **509** (41), L359 (2011)., DOI: 10.1016/j.jallcom.2011.08.024.

Materials Today: Proceedings 28 (2020) 28–31

Contents lists available at ScienceDirect

Materials Today: Proceedings

journal homepage: www.elsevier.com/locate/matpr

Structural and dielectric properties of Lead Magnesium Niobate and Ti-doped Lead Magnesium Niobate at room temperature

Sidharth Kashyap [a,*], S.C. Bhatt [a], Manish Uniyal [a], Gambheer Singh Kathait [b]

[a] Department of Physics, Hemvati Nandan Bahuguna Garhwal University, Srinagar Garhwal, Uttarakhand 246174, India
[b] Department of Instrumentation Engineering (USIC), Hemvati Nandan Bahuguna Garhwal University, Srinagar Garhwal, Uttarakhand 246174, India

ARTICLE INFO

Article history:
Received 11 December 2019
Accepted 2 January 2020
Available online 4 February 2020

Keywords:
Relaxor ferroelectrics
Perovskite
Sintering
Microstructure
Dielectric study

ABSTRACT

Lead based relaxor ferroelectric like Lead Magnesium Niobate and their binary solid solutions with Lead Titanate have great interest of research because of their significant and excellent dielectric, piezoelectric and electrostrictive properties. In the present work, the Lead Magnesium Niobate (PMN) and Lead Magnesium Niobate-Lead Titanate (0.75PMN-0.25PT) were prepared through solid state reaction method with double sintering process at 1200 °C for 6 hr. XRD data shows the pervoskite structure of the prepared sample. SEM report of PMN and 0.75PMN-0.25PT shows the different microstructure with dense grains. Dielectric study of PMN and 0.75PMN-0.25PT shows the effect of addition of PT content on electrical properties at room temperature.
© 2019 Elsevier Ltd. All rights reserved.
Selection and Peer-review under responsibility of the scientific committee of the International Conference on Advanced Materials and Nanotechnology.

1. Introduction

Lead Magnesium Niobate $Pb(Mg_{1/3}Nb_{2/3})O_3$ i.e. PMN is a complex $Pb(B',B'')O_3$ type perovskite compound known as relaxor ferroelectric material. The main characteristic of dielectric properties of PMN is the maximum of dielectric constant taking placed at negative temperature with diffuse phase transition [1,2]. It exhibits strong electrostrictive performance compared to other materials due to its high dielectric constant at low temperature. Because of the high dielectric constant, outstanding electrostrictive property and lower sintering temperature of PMN make it important for multilayer capacitors, actuators and electro-optic device applications [3,4].

The phase transition temperature and maximum of dielectric constant can be shifted towards the higher temperature range when $PbTiO_3$ is added to Lead Magnesium Niobate in proper stoichiometry. The temperature of maximum dielectric constant shifts up from −10 °C (~20000) in pure Lead Magnesium Niobate to 40 °C in 0.9PMN–0.1PT, under the application of electric field of frequency 100 Hz [5]. PMN-PT is a relaxor ferroelectric material which has been widely investigated due to their advantageous dielectric, piezoelectric and electrostrictive properties and widely used as multilayer capacitors, electrostrictive actuators, sensors and many other electronic and biomedical devices [6,7]. PMN-PT is a binary solid solution of relaxor ferroelectric Lead Magnesium Niobate and normal ferroelectric Lead Titanate (PT). These relaxor ferroelectrics have ABO_3 type crystal structure with mixed B-site. The properties of $(1-x)Pb(Mg_{1/3}Nb_{2/3})O_3$-$xPbTiO_3$ ceramics are changed as Ti concentration varies. A ceramic with low content of Ti behaves as a relaxor ferroelectric and with high amount of Ti the ceramic becomes a normal ferroelectric [8]. Hence the solid solution (1 − x)PMN-xPT possess different type of phase transition with different values of x. The dielectric property of the material is directly depending on the density of prepared sample. Densification of material is controlled by preparation and sintering process. Density of this type of PMN based perovskite will be increased when sintered in the temperature range 1200–1300 °C. It is difficult to prepare pure PMN-PT because of volatile nature of lead oxide. Therefore excess amount of MgO and PbO is added to starting reagent in stoichiometric proportion. It has been investigated that excess amount of MgO increase the dielectric and microstructural properties with reduced pyrochlore phase. The PMN-PT relaxor ferroelectric exhibit a morphotropic phase boundary (MPB) separating the rhombohedral and tetragonal phases. The MPB is located between x = 0.30 and 0.40 [9]. Compositions in the (1 − x)PMN-xPT with x greater than approximately 0.30 are piezoelectric [10,11].

On the basis of experimental results, it is found that, at the morphotropic phase boundary, the dielectric and piezoelectric proper-

* Corresponding author.
E-mail address: sid.kashyap1@gmail.com (S. Kashyap).

https://doi.org/10.1016/j.matpr.2020.01.032
2214-7853/© 2019 Elsevier Ltd. All rights reserved.
Selection and Peer-review under responsibility of the scientific committee of the International Conference on Advanced Materials and Nanotechnology.

ties are reached to maximum hence making the material significant for actuator and sensor applications [12,13].

2. Experimental

High purity oxides PbO, Nb_2O_5, MgO and TiO_2 were used as starting material in stoichiometric proportion. The Lead Magnesium Niobate and Lead Magnesium Niobate-Lead Titanate both were prepared by Solid State Reaction method as following.

2.1. Preparation of Lead Magnesium Niobate (PMN)

The Lead Magnesium Niobate i.e. PMN was prepared by two step solid state reaction method [14]. In the first step of reaction, powders of PbO and Nb_2O_5 were weighed in stoichiometric proportion and mixed by the agate mortar and pestle in ethanol medium for 2 h with 5% excess amount of PbO to compensate the loss of Lead at high temperature. The mixed sample was calcined at 820 °C for 3 h. The intermittent product $Pb_3Nb_2O_8$ was mixed with excess 2% MgO in stoichiometric proportion and calcined again at 800 °C for 3 h. The final product was pre-sintered at 900 °C for 6 h. The pre-sintered powder was pressed to prepare pellets of the sample without adding any binder. Prepared Pellets were sintered at 1150 °C for 6 h to get perovskite phase.

2.2. Preparation of Lead magnesium Niobate-Lead Titanate (0.75PMN-0.25PT)

The Lead Magnesium Niobate-Lead Titanate for x = 0.25 was prepared by columbite precursor method [15]. In this method, the stoichiometric amount of MgO and Nb_2O_5 were mixed in ethanol medium for 2 h and then calcined at 1110 °C for 5 h. The intermittent product $MgNb_2O_6$ was again mixed with PbO and TiO_2 in stoichiometric proportion. Extra 8% amount of PbO was also added because of its volatile nature at high temperature. The mixed powder was calcined at 920 °C for 2 h in closed alumina crucible. The prepared sample was pelletized without adding any binder and then sintered at 1200 °C for 6 h.

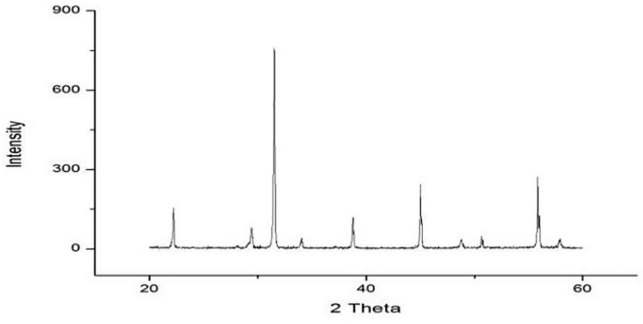

Fig. 1. XRD pattern of the Lead Magnesium Niobate calcined at 900 °C.

3. Characterization of samples

3.1. XRD analysis

X-ray diffraction method was used to identify the perovskite phases in the prepared sample. XRD patterns of Lead Magnesium Niobate and Lead Magnesium Niobate-Lead Titanate show that pyrochlore phase can be reduced by high temperature sintering process. Figs. 1 and 2 shows the XRD pattern of Lead Magnesium Niobate and Lead Magnesium Niobate-Lead Titanate. The diffraction intensity was measured from 20° to 80° at room temperature. From further phase study of PMN and (1 – x)PMN-xPT (for x = 0.25), it is clear that they exhibits cubic and rhombohedral (pseudocubic) crystal structure at room temperature respectively.

3.2. SEM analysis

SEM was used to study the grain size, crystalline size and surface morphology of the prepared sample. The scanning electron micrographs of the PMN and 0.75PMN-0.25PT heated at different temperatures are shown in the figures. The SEM images show that grains are arranged very close to each other. This compact form of grains is responsible for increase in density. Fig. 3(a) shows the grain size of ~1.5 μm with very small number of pores due to evaporation of lead from the sample. Fig. 3(b) shows the polygonal shaped grains with grain size between ~1.6 μm to greater than 2 μm. The average grain size and densities of prepared samples are given in the Table 1.

4. Dielectric study

The FLUKE PM6306 programmable Automatic RCL meter was used for precise measurements of resistance, capacitance and inductance. Variation in dielectric constant, electrical conductivity and tangent loss of PMN and 0.75PMN-0.25PT has been studied with different frequencies ranging from 1 KHz to 1 MHz at room temperature. It is investigated that the dielectric constant gradually decreases with increase in frequency. The decrease in dielec-

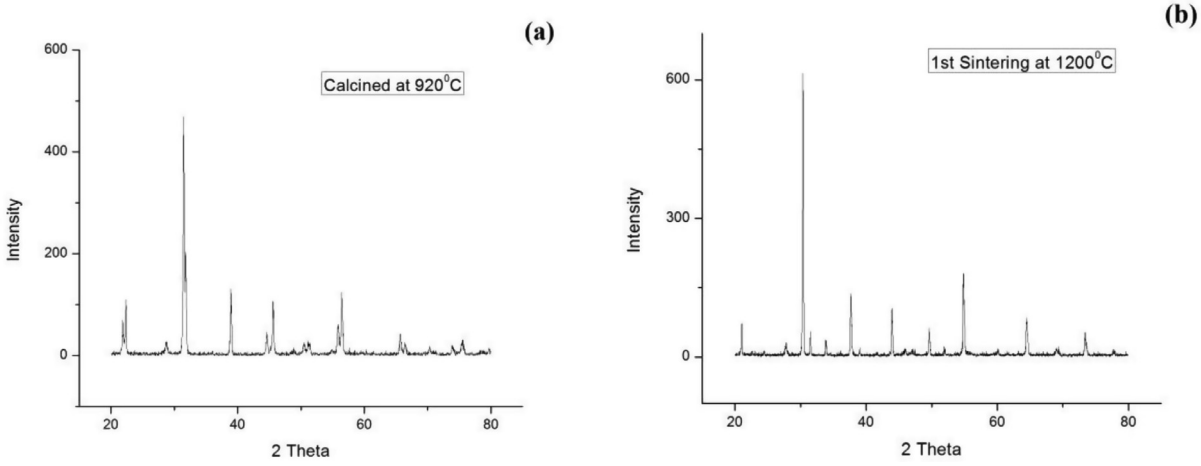

Fig. 2. XRD patterns of the 0.75PMN-0.25PT (a) calcined at 920 °C for 2 h and (b) sintered at 1200 °C for 6 h with reduced pyrochlore phases.

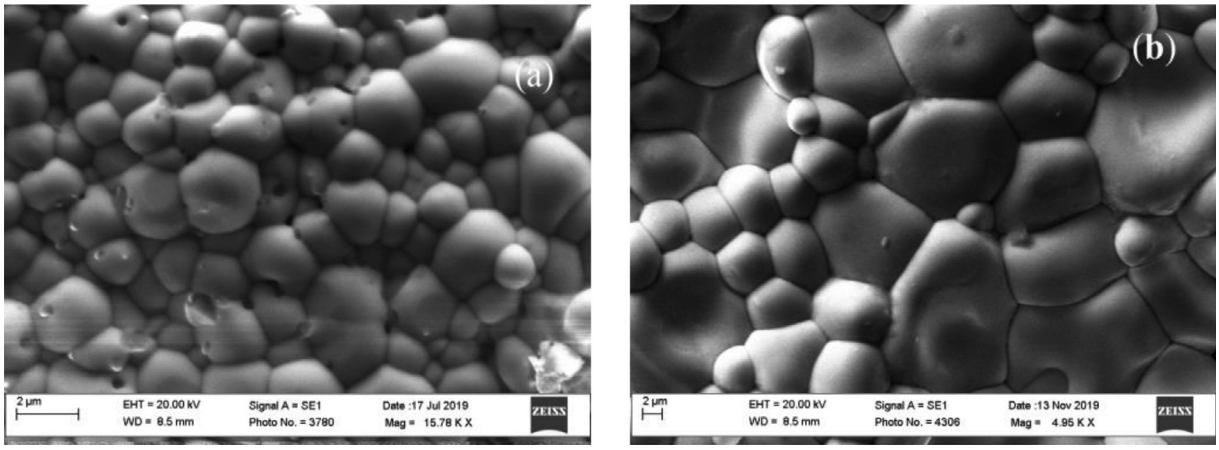

Fig. 3. SEM micrographs of (a) PMN and (b) 0.75PMN-0.25PT at sintering temperature 1150 °C and 1200 °C respectively.

Table 1
The average grain size and densities of PMN and 0.75PMN-0.25PT.

Sample	Sintering temperature	Density (gm/cm^{-3})	Average grain size (μm)
PMN	1150 °C	5.03	~1.5
0.75PMN-0.25PT	1200 °C	9.2	~2.5

Table 2
The values of dielectric constant, loss tangent and electrical conductivity of PMN with different frequencies at room temperature.

Sample	Frequency (KHz)	Dielectric Constant (ε_{RT})	Loss Tangent (tan δ)	Electrical Conductivity (ohm-cm)$^{-1}$
PMN	1	502.325	0.101	2.82×10^{-8}
	10	456.79	0.046	1.17×10^{-7}
	100	437.8628	0.024	5.84×10^{-7}
	1000	422.433	0.025	5.87×10^{-6}

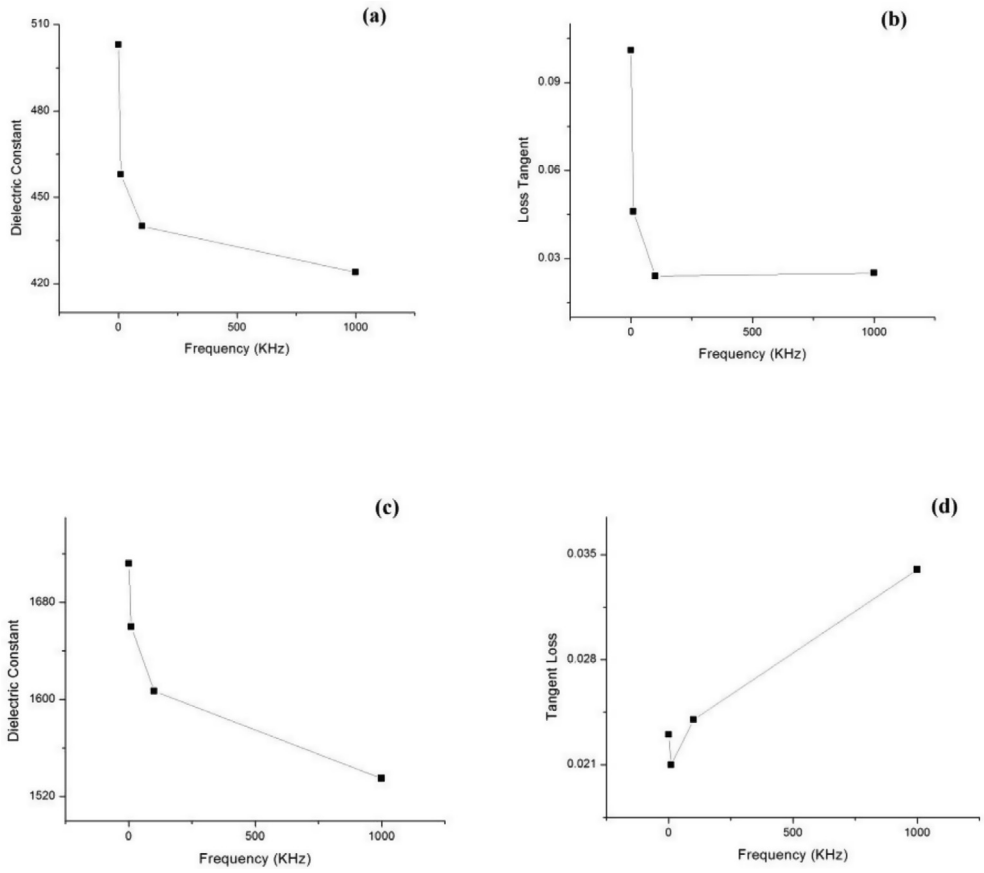

Fig. 4. Variation of dielectric constant and loss tangent as a function of frequency at room temperature for (a,b) PMN and (c,d) 0.75PMN-0.25PT samples respectively.

Table 3
The values of dielectric constant, loss tangent and electrical conductivity of 0.75PMN-0.25PT with different frequencies at room temperature.

Sample	Frequency (KHz)	Dielectric Constant (ε_{RT})	Loss Tangent (tan δ)	Electrical Conductivity (ohm-cm)$^{-1}$
0.75PMN-0.25PT	1	1712	0.023	2.19×10^{-8}
	10	1660	0.021	1.93×10^{-7}
	100	1607	0.024	2.14×10^{-6}
	1000	1535	0.034	2.89×10^{-5}

tric constant with increase in frequency may be due to disturbance in alignment of dipoles with alternating electric field [16]. The variation in dielectric constant, loss tangent and electrical conductivity of PMN and 0.75PMN-0.25PT at different frequencies are tabulated in Tables 2 and 3. Fig. 4 shows the frequency dependent nature of dielectric constant of PMN and 0.75PMN-0.25PT.

5. Conclusions

The relaxors PMN and 0.75PMN-0.25PT were prepared by solid state reaction method at different sintering and calcination temperature. From the XRD data, it is observed that both samples are in perovskite phase with small amount of pores due to volatile nature of Pb. SEM images show the formation of dens grains with well-defined compact boundaries. The dielectric study of PMN and 0.75PMN-0.25PT shows the frequency dependent nature of dielectric constant, and it is clear from the Tables 2 and 3, that the dielectric constant of PMN can be increased 4 or 5 times at room temperature by the stoichiometric addition of Ti content in PMN.

Declaration of Competing Interest

The authors declare that they have no known competing financial interests or personal relationships that could have appeared to influence the work reported in this paper.

Acknowledgements

Authors are thankful to Dept. of Instrumentation Engineering (USIC), Hemvati Nandan Bahuguna Garhwal University, Srinagar Garhwal, Uttarakhand for availing characterization and dielectric properties measurement facility.

References

[1] Y.H. Chen, K. Uchino, M. Shen, D. Viehland, J. Appl. Phys. 90 (3) (2001) 1455–1458.
[2] R. Yimnirun, S. Ananta, E. Meechoowas, S. Wongsaenmai, Phys. D: Appl. Phys. 36 (2003) 1615–1619.
[3] T.R. Shrout, J. Fielding Jr., Ultrason. Symp. (1990) 711.
[4] G.H. Haertling, J. Am. Ceram. Soc. 82 (1999) 797.
[5] R. Zhang, S. Peng, D. Xido, Y. Wang, B. Yang, J. Zhu, P. Yu, W. Zhang, Cryst. Res. Echol. 33 (5) (1998) 827–832.
[6] A.J. Moulson, J.M. Herbert, Electroceramics, second ed., Wiley, Chichester, 2003.
[7] K. Uchino, Ferroelectric Devices, Marcel Dekker, New York, 2000.
[8] J. Huang, N.D. Chateen, J.J. Fitzgerald, Chem. Mater. 10 (1998) 3848–3855.
[9] A. Benayad, G. Sebald, B. Guiffard, L. Lebrun, D. Guyomar, E. Pleska, J. Phys. IV Proc. 126 (2005) 53–57.
[10] S.W. Choi, T.R. Shrout, S.J. Jang, A.S. Bhalla, Ferroelectrics 100 (1989) 29–38.
[11] C. Noblanc, P. Deljurie, Gaucher, G. Calvarin, Silicates Industriels 227–23 (1) (1993) 11–12.
[12] J.F. Tressler, T.R. Howarth, Proc 2nd IEEE Int Symp, 2 (2000) 561.
[13] H.L.W. Chen, P.K.L. Ng, C.L. Choy, Appl. Phys. Lett. 74 (1999) 3029.
[14] W.D. Kingry, Introduction to Ceramics, 2nd ed., Wiley, New York, 1960.
[15] S.L. Swartz, T.R. Shrout, Mater. Res. Bull. 17 (1982) 1245–1250.
[16] A.N. Tarale, S. Premkumar, V.R. Reddy, Ferroelectrics 516 (2017) 8–17.

Ferroelectrics

ISSN: 0015-0193 (Print) 1563-5112 (Online) Journal homepage: https://www.tandfonline.com/loi/gfer20

Piezoelectric properties of $Na_{1-x}K_xNbO_3$, near x = 0.500 morphotropic phase region

Surendra Singh & N. S. Panwar

To cite this article: Surendra Singh & N. S. Panwar (2020) Piezoelectric properties of $Na_{1-x}K_xNbO_3$, near x = 0.500 morphotropic phase region, Ferroelectrics, 558:1, 240-245

To link to this article: https://doi.org/10.1080/00150193.2020.1735907

Published online: 04 May 2020.

Submit your article to this journal

View related articles

View Crossmark data

Full Terms & Conditions of access and use can be found at
https://www.tandfonline.com/action/journalInformation?journalCode=gfer20

FERROELECTRICS
2020, VOL. 558, 240–245
https://doi.org/10.1080/00150193.2020.1735907

Taylor & Francis
Taylor & Francis Group

Check for updates

Piezoelectric properties of $Na_{1-x}K_xNbO_3$, near x = 0.500 morphotropic phase region

Surendra Singh[a] and N. S. Panwar[b]

[a]Department of Physics, H.N.B. Garhwal University, Srinagar, Garhwal, India; [b]University Science Instrumentation Centre, H.N.B. Garhwal University, Srinagar, Garhwal, India

ABSTRACT

Sodium-potassium niobate ($Na_{1-x}K_xNbO_3$) ceramic pellets were prepared, near equimolar Na- K composition, by solid state reaction method with double sintering. Remnant polarization, coercive field, polarization current and converse piezoelectric coefficient (d^*_{33}) of the prepared samples were measured. The observed properties exhibit strong composition dependence- a morphotropic phase transition type behavior, showing extremal piezoelectric properties for potential lead free transducer applications, at the composition with x = 0.500.

ARTICLE HISTORY
Received 24 June 2019
Accepted 5 January 2020

KEYWORDS
Ferroelectric; perovskite; remnant polarization; converse piezoelectric coefficient (d^*_{33};); morphotropic phase transition

1. Introduction

In the search of lead- free transducer materials perovskite sodium potassium niobate (NKN) system has been quite attractive [1]. This system exhibits a series of phase transitions, between 600 and −200 °C [2–5]. At room temperature this system shows orthorhombic structure with a small perovskite subcell but the perovskite units of monoclinic symmetry [6]. Ceramics of these materials require long sintering periods for sufficient densification. $Pb(Zr,Ti)O_3$ (PZT) ceramics show enhanced piezoelectric properties near morphotropic phase boundary (MPB) composition [7–8]. From the structural and dielectric measurements it has been observed that $Na_{1-x}K_xNbO_3$ (x = 0 to 1) (NKN) ceramics also show morphotropic phase boundaries near the compositions with x = 0.175 [9], 0.32 [10], 0.475 [11], and 0.500 [2, 12–13], indicating the technologically potential extremal electro- physical properties, at these compositions.

In the present study $Na_{1-x}K_xNbO_3$ $(0.490 \leq x \leq 0.510)$ ceramic samples were prepared by solid state reaction route using double sintering, near equimolar (Na, K) morphotropic phase boundary. Composition variation of remnant polarization, coercive field, converse piezoelectric coefficient (d^*_{33}) and polarization current was measured in the prepared samples.

The preparation method of pellets, their observed X-ray diffraction (XRD) patterns, surface morphology, density, etc. have been described in a previous communication [13]. For piezoelectric measurements sintered pellets were electroded, in parallel capacitor configuration, with silver coating deposited by dc magnetron sputtering of a silver

CONTACT Surendra Singh jhinkwan.surendra@gmail.com.
© 2020 Taylor & Francis Group, LLC

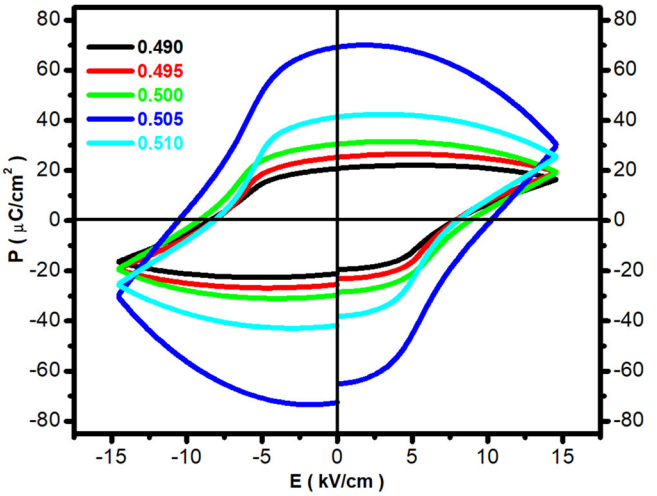

Figure 1. P-E loop for different compositions (x) of $Na_{1-x}K_xNbO_3$, at applied field 14 kV/cm.

target. Polarization and piezoelectric parameters were measured using a ferroelectric- (PE loop tracer) and piezo- meter (AixACCT Systems, GmbH).

2. Results and discussion

The observed polarization- electric field (P-E) hysteresis loops at room temperature, for unpoled NKN samples ($0.490 \leq x \leq 0.510$) under an applied electric field of 14 kV/cm and 1 Hz, have been shown in Figure 1. All the samples show a normal hysteresis loop confirming ferroelectric nature of all the prepared NKN ceramics. The observed large value of polarization and converse piezoelectric coefficient, as applications of small field, was found comparable with modified NKN ceramics [14]. The observed strain (%) versus electric field behaviors for NKN ceramics, measured at 1 Hz and room temperature, are shown in Figure 2. The S (%)-E loops show the largest strain for $x = 0.500$ among the prepared samples, at the applied field of 14 kV/cm.

Figure 3 shows variation of remnant polarization (P_r) and coercive field (E_c) of the prepared samples with composition (x). The P_r value of the ceramics for $x = 0.510$ is found to be 33.81 μC/cm^2, which increases up to 67.13 μC/cm^2, for $x = 0.505$, and further, P_r decreases with decreasing x, in the measured range. This could be related to the morphotropic phase transition, near the composition with $x = 0.500$, due to increased distortion in the cell (13). The E_c value is also found increased from 7.60 to 9.86 kV/cm, as x decreases from 0.510 to 0.505, which further decreases with decrease in x. This may be attributed to the presence of internal bias field, and can be asserted from the asymmetric shape and horizontal off-set of coercive field, which essentially increases the E_c value. E_c may also increase due to increased distortion in the cell by decreasing the volume of switchable domains [15]. Shape of the P-E hysteresis loop depends on the microstructure, stress, defects, and processing conditions [16]. It has been reportedly observed that the piezoelectric properties not only depend on the preparation conditions, but also on the type of the manufacturing company and the grain size of the starting materials [17].

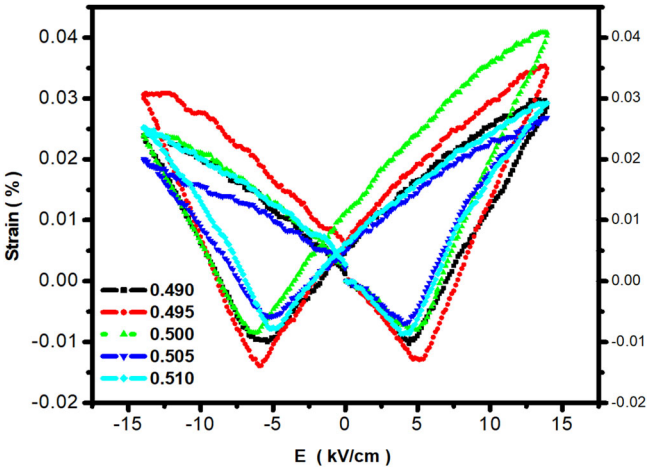

Figure 2. Variation of strain (%) with electric field, in $Na_{1-x}K_xNbO_3$ ($0.490 \leq x \leq 0.510$), at applied field 14 kV/cm.

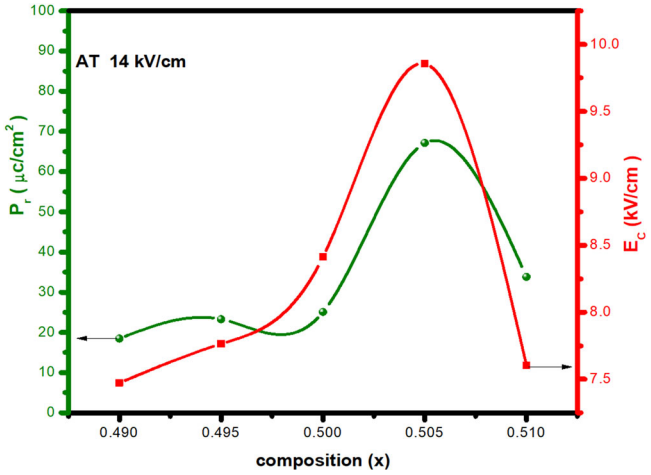

Figure 3. Variation of remnant polarization (P_r) and coercive field (E_c) with composition x, in $Na_{1-x}K_xNbO_3$ ($0.490 \leq x \leq 0.510$).

The converse piezoelectric coefficient (d^*_{33}) was calculated as the ratio of the maximum strain to the maximum field in the cycle, S_{max}/E_{max} [18]. Figure 4 shows the variation of converse piezoelectric constant (d^*_{33}) of NKN ceramics with x, at room temperature. For the composition with $x = 0.510$ value of d^*_{33} was observed 270.36 pm/V, which decreases to 241.55 pm/V for $x = 0.505$, and abruptly increases to 352.52 pm/V for $x = 0.500$, and thereafter decreases with decreasing x. The polarization current, Figures 5 and 6, also follows the nature as followed by remnant polarization (P_r) and coercive field (E_c). The anomalous change in these piezoelectric properties, at $x = 0.500$, may be associated with the structural transition with composition, near the morphotropic phase boundary.

Hysteresis loops and piezoelectric properties significantly depend on crystal structure, grain size and density of ceramics [19–20]. In the ferroelectric ceramics grain boundary

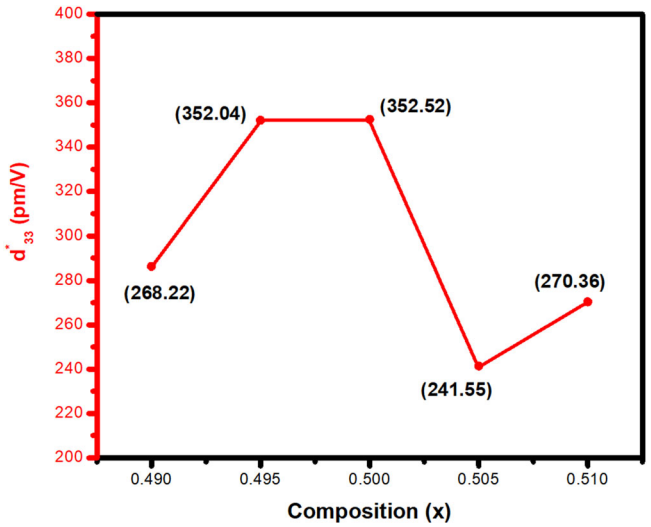

Figure 4. Variation of the converse piezoelectric coefficient (d^*_{33}) with composition x, in $Na_{1-x}K_xNbO_3$ ($0.490 \leq x \leq 0.510$).

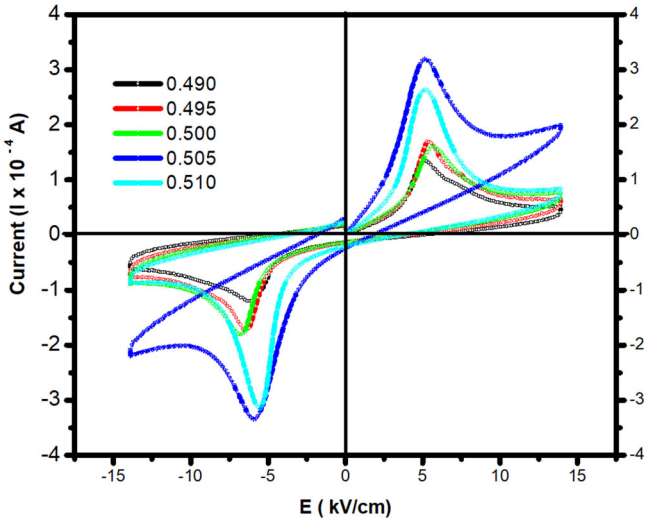

Figure 5. Variation of polarization current with electric field, in $Na_{1-x}K_xNbO_3$ ($0.490 \leq x \leq 0.510$), at 14 kV/cm.

is a low permittivity region and therefore, at the grain boundary, the polarization may be quite low. Also the space charges in grain boundary exclude polarization charge on grain surface, which may result in polarization discontinuity on grain surface to form depolarization field, and polarization decreases. With increasing grain size number of grain boundaries decreases, which results increase in remnant polarization with increasing grain size [19]. The processing affects grain boundary properties and microstructure of a ceramic. The grain boundary resistivity affects the space-charge accumulation and thus the size- effect response is masked in the ferroelectric grains [20–28]. The observed varying piezoelectric properties may be attributed to the control of the grain boundary

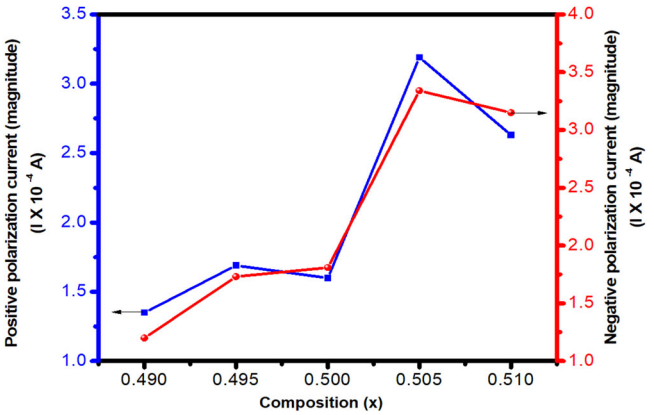

Figure 6. Variation of polarization current with composition (x) in $Na_{1-x}K_xNbO_3$ ($0.490 \leq x \leq 0.510$), at 14 kV/cm.

resistivity and the grain size, in the present preparation procedure. The reported and present observations show that preparation process, composition and structure greatly influence the piezoelectric properties of the ceramics. A composition dependent structural anomaly seems effectively significant for the observed piezoelectric properties, near morphotropic phase region.

References

[1] Y. Saito *et al.*, Lead-free piezoceramics, *Nature* **432** (7013), 84 (2004). DOI: 10.1038/nature03028.

[2] L. Egerton, and D. M. Dillon, Piezoelectric and dielectric properties of ceramics in the system potassium-sodium niobate, *J. Am. Ceram. Soc.* **42** (9), 438 (1959). DOI: 10.1111/j.1151-2916.1959.tb12971.x.

[3] G. Shirane, R. Newnham, and R. Pepinsky, Dielectric properties and phase transitions of $NaNbO_3$ and (Na, K) NbO_3, *Phys. Rev.* **96** (3), 581 (1954). DOI: 10.1103/PhysRev.96.581.

[4] V. J. Tennery, and K. W. Hang, Thermal and X-ray diffraction studies of the $NaNbO_3$–$KNbO_3$ system, *J. Appl. Phys.* **39** (10), 4749 (1968). DOI: 10.1063/1.1655833.

[5] V. J. Tennery, Dielectric properties and phase transitions of ferroelectric sodium-strontium niobates, *J. American Ceramic Society* **49** (7), 376 (1966). DOI: 10.1111/j.1151-2916.1966.tb13288.x.

[6] P. Voudsen, A study of the unit-cell dimensions and symmetry of certain ferroelectric compounds of niobium and tantalum at room temperature, *Acta Crystal.* **4**, 373 (1951).

[7] B. Jaffe, W. R. Cook, and J. H. Jaffe, *Piezoelectric Ceramics* (Academic, NewYork, 1971).

[8] J. Rodel *et al.*, Perspective on the development of lead-free piezoceramics, *J. Am. Ceram. Soc.* **92** (6), 1153 (2009). DOI: 10.1111/j.1551-2916.2009.03061.x.

[9] A. S. Kandari, V. Lingwal, and N. S. Panwar, Morphotropic region in $Na_{1-x}K_xNbO_3$, between x = 0.17 and 0.18, *Ferroelectrics* **396** (1), 18 (2010). DOI: 10.1080/00150191003791683.

[10] A. S. Kandari, V. Lingwal, and N. S. Panwar, Morphotropic phase boundary in $Na_{1-x}K_xNbO_3$, near x = 0.32, *Solid State Commun.* **150** (1-2), 74 (2010). DOI: 10.1016/j.ssc.2009.10.002.

[11] A. S. Kandari *et al.*, Composition dependent dielectric anomaly in $Na_{1-x}K_xNbO_3$, at x = 0.475, *Ferroelectrics* **393** (1), 121 (2009). DOI: 10.1080/00150190903413190.

[12] V. Lingwal, and N. S. Panwar, Morphotropic phase transitions in mixed sodium-potassium niobate system, *Ferroelectrics* **300** (1), 3 (2004). DOI: 10.1080/00150190490442146.
[13] S. Singh, J. Negi, and N. S. Panwar, Dielectric properties of $Na_{1-x}K_xNbO_3$, near x = 0.5 morphotropic phase region, *J. Phys. Chem. Solids* **123**, 311 (2018). DOI: 10.1016/j.jpcs.2018.08.018.
[14] E. Hollenstein *et al.*, Piezoelectric properties of Li- and Ta-modified $(K_{0.5}Na_{0.5})NbO_3$ ceramics, *Appl. Phys. Lett.* **87** (18), 182905 (2005). DOI: 10.1063/1.2123387.
[15] S. Mitra, A. R. Kulkarni, and O. Prakash, Diffuse phase transition and electrical properties of lead-free piezoelectric (Li_xNa_{1-x}) NbO_3 $(0.04 \leq x \leq 0.20)$ ceramics near morphotropic phase boundary, *J. Appl. Phys.* **114** (6), 064106 (2013). DOI: 10.1063/1.4817815.
[16] D. Damjanovic, Ferroelectric, dielectric and piezoelectric properties of ferroelectric thin films and ceramics, *Rep. Prog. Phys.* **61** (9), 1267 (1998). DOI: 10.1088/0034-4885/61/9/002.
[17] H. S. Nalwa, *Handbook of Nanostructured Materials and Nanotechnology* (Academic Press, New York, 1999).
[18] J. Hao *et al.*, Phase transitions, relaxor behavior, and large strain response in $LiNbO_3$-modified $Bi_{0.5}(Na_{0.80}K_{0.20})_{0.5}TiO_3$ lead-free piezoceramics, *J. Appl. Phys.* **114** (4), 044103 (2013). DOI: 10.1063/1.4816047.
[19] V. R. Mudinepalli *et al.*, Effect of grain size on dielectric and ferroelectric properties of nanostructured $Ba_{0.8}Sr_{0.2}TiO_3$ ceramics, *J. Adv. Ceram.* **4** (1), 46 (2015). DOI: 10.1007/s40145-015-0130-8.
[20] Z. Y. Shen, and J. F. Li, Enhancement of piezoelectric constant d_{33} in $BaTiO_3$ ceramics due to nano-domain structure, *J. Ceram. Soc. Japan* **118** (1382), 940 (2010). DOI: 10.2109/jcersj2.118.940.
[21] G. H. Haertling, Hot-pressed lead zirconate-lead titanate ceramics containing bismuth, *Am. Ceram. Soc. Bull.* **43**, 875 (1964).
[22] A. H. Webster, and T. B. Weston, The grain-size dependence of the electromechanical properties in lead zirconate-titanate ceramics, *J. Can. Ceram. Soc.* **37**, 51 (1968).
[23] H. T. Martirena, and J. C. Burfoot, Grain-size effects on properties of some ferroelectric ceramics, *J. Phys. C: Solid State Phys.* **7** (17), 3182 (1974). DOI: 10.1088/0022-3719/7/17/024.
[24] Z. Surowiak, M. F. Kupriyanov, and D. Czekaj, Properties of nanocrystalline ferroelectric PZT ceramic, *J. Eur. Ceram. Soc.* **21** (10-11), 1377 (2001). DOI: 10.1016/S0955-2219(01)00022-X.
[25] P. Zheng *et al.*, Grain-size effects on dielectric and piezoelectric properties of poled $BaTiO_3$ ceramics, *Acta Mater.* **60** (13-14), 5022 (2012). DOI: 10.1016/j.actamat.2012.06.015.
[26] Y. Huan *et al.*, Grain size effects on piezoelectric properties and domain structure of $BaTiO_3$ ceramics prepared by two-step sintering, *J. Am. Ceram. Soc.* **96** (11), 3369 (2013). DOI: 10.1111/jace.12601.
[27] J. L. Zhang *et al.*, Strong piezoelectricity exhibited by large-grained $BaTiO_3$ ceramics, *Appl. Phys. Lett.* **104** (22), 222909 (2014). DOI: 10.1063/1.4881597.
[28] T. Hoshina, Size effect of barium titanate: fine particles and ceramics, *J. Ceram. Soc. Japan* **121** (1410), 156 (2013). DOI: 10.2109/jcersj2.121.156.

Applied Innovative Research
Vol. 2, September 2020, pp. 226-230

Estimation of some essential, non essential toxic and toxic elements in some Indian black tea sold in market by 'ICP-MS' and their risk assessment.

Vishal Rohilla[a*], Don Biswas[a], Prashant Thapliyal[a], Gambheer Singh Kathait[a] & Surendra Singh[b]

[a] Department of Instrumentation Engineering-USIC, H N B Garhwal University, Srinagar (Garhwal) - 246 174, India

[b] Department of Physics, H N B Garhwal University, Srinagar (Garhwal) – 246 174, India

Received 7 September 2020

Tea *'Camellia sinensis'* is the most consumed non essential, non alcoholic liquid in the world. Black Tea finds its place in Indian culture as well as a part of diet of Indian population. Tea is known for its relaxing effect and therapeutic use as it contains bioactive *polyphenols, amino acids, caffeine, theophylline* and volatile organic compounds. Significant research efforts have been carried out on Tea for its health benefits. However, some ill effects also have been reported. Present work has been carried out to determine the essential, non essential toxic and toxic elements namely Iron (Fe), Copper (Cu), Cobalt (Co), Chromium (Cr), Aluminum (Al), Arsenic (As) and Lead (Pb); health risks associated with them among adult population. For this, the twelve well known and most selling (most consumed) Tea brands available in local Indian market were selected and analyzed by sophisticated instrument ICP-MS.

Keywords: ICP-MS; Tea; Trace elements; Aluminum; Black Tea; Alzheimer's; Dementia

Introduction

Tea with botanical name *'Camellia sinensis'* is the most consumed non essential, non alcoholic liquid in the world. It is now the part of routine habits and diet of the people, while looking in the prospect of Indian population. They consume it without knowing its health benefits or adverse effects. It is now become an integral part of culture also, one can observe that Tea being offered as the welcome drink on the arrival of guests in any Indian family home. This formal use of Tea in Indian culture was come in the period of colonial rule[1]. Use of Tea was different in ancient time, about 5000 years back Chinese people find its use as a traditional medicine. Indian people were known about the medicinal values of it which can be found in *Ayurveda* known as *Rasayanas*[2,3]. Researchers in past had put their efforts to determine the health benefits of Tea and found out that it contains bioactive *polyphenols, amino acids, caffeine, theophylline* and volatile organic compounds[4,5]. Due to its rich bioactive and anti oxidant contents, it prevents aging effects; anticancer activity; prevents cardiovascular diseases and cure several skin disorders[3]. Besides the organic contents, it contains inorganic elements too out of which some are trace elements those considered as essential, some are non essential elements which upon accumulation in body produce disease and highly toxic elements that produce permanent tissue damage or unwanted growth of tissues[6]. In present work, we have determined four essential trace elements Iron (Fe), Copper (Cu), Cobalt (Co) and Chromium (Cr); one non essential harmful Aluminum (Al) and toxic Arsenic (As) and Lead (Pb). Occurrence of them in Tea must be known so that, the daily intake can be estimated and controlled. For this the twelve well known and most selling (most consuming ≥ 1 million people) Tea brands available in local Indian market were selected and analyzed by sophisticated instrument ICP-MS. and the health risks associated with them were assessed.

Materials and Methods

Sample preparation

For analysis, analytical reagent grade Nitric Acid [HNO_3] and deionized MilliQ water having resistivity ≥ 18.2 MΩ were used. Glassware were avoided during whole analysis, all the utensils and materials were first washed with deionized MilliQ water and left soaked for 20 h. in 5% v/v Nitric Acid [HNO_3]. Prior to use they were rinsed with deionized MilliQ water five times.

*Corresponding author (E-mail: mail.vishal.pd@gmail.com)

Twelve different Black Tea pickings' of most selling brands were purchased from local grocery shops. Which were in packing of 100 gm to 250 gm weight. Samples were digested by single acid [Nitric Acid] method for organic and food items on hot water bath.

Tea samples, each of 500mg were poured into 30ml capacity PTPFE vials with cap, 10 mL of concentrated Nitric Acid was added and all samples were left for 20 h with loose caps. Semitransparent color of the solution was observed after 20 h. Further samples were then placed in hot water bath at temperature $90^0 \pm 2^0$C, approximately after 4 h. All samples were turned into colorless transparent solution. Samples were then left to get cooled to room temperature and filtered with Whatman filter paper of 42 grade, 1 mL of aliquot from each filtered sample is then diluted in 100 mL of 2% v/v Nitric Acid.

Instrument and calibration

ICP-MS instrument model Perkin Elmer NexIon-300x was used and calibrated with stocked standard solution, Perkin Elmer Pure Plus Multi-element Calibration Standard part No. N9300233: Fe, Cu, Co, Cr, Al, As and Pb all elements were in 10 µg/mL. Operating parameters of instrument were: RF Power 1500W; Plasma gas flow 18 L/min; Auxiliary gas flow 1.2 L/min; Integral Time 15s; Sweeps 20; Reading 1; Replicates 3; Scanning Mode Peak hopping, Method Quantitative; Calibration Type External ; Measurement Time 15 min.

Method validation

Method was validated by measuring the trueness, recovery, precision, repeatability, Limit of Detection and Limit of Quantification for each element to be detected.

Instrument was calibrated with different solution of concentration of elements in increasing order; regression line was obtained with a high coefficient of correlation 0.991. Trueness, precision of measured value was verified by measuring the known concentration value solution for each element ten times on consecutive three days. Experiment was repeated ten times again for each element, deliberate addition of known concentration of elements and percentage recovery was observed for increasing concentration. LOD and LOQ were calculated as 3* σ and 10* σ of ten measurements on blank solution. Values of percentage recovery, LOD and LOQ for each element are listed in Table 1.

Results

Table 2 shows the results of analysis. Concentration of elements is presented here in µg kg^{-1}. Brand names samples are avoided here. Different naming is done from sample S1 to S12. Results indicate that most abundant is Aluminum highest concentration 538832.7 µg kg^{-1} is present in sample S4 and lowest 125995.3 µg kg^{-1} in sample S2; least abundant is Arsenic, highest concentration 9.1 µg kg^{-1} is present in sample S11 and lowest in sample S2 below the detection limit of instrument 0.01 µg kg^{-1}.

Risk Assessment

While assessing the risks, it has assumed that most of the adult Indian population including men [average body weight 67.4 kg] and women [average body weight 64.9 kg] consumes three cups of Tea daily.

Table 1 — Values of LOD, LOQ and percentage recovery, for each element.

Element	LOD [µg kg^{-1}]	LOQ [µg kg^{-1}]	Precision % [coefficient of variation]	Average recovery % in 4 concentrations
Fe (Iron)	10.0	33.33	12	114 ±15
Cu (Copper)	0.10	0.3288	4	94±8
Co (Cobalt)	0.70	2.331	10	85±3
Cr (Chromium)	0.01	0.056	15	88±4
Al (Aluminum)	0.48	1.7088	14	110±8
As (Arsenic)	0.01	0.06	5	93±3
Pb (Lead)	10	3.58	4	108±7

Table 2 — Concentration of elements measured µg kg^{-1}; * below detection limit of instrument.

Element	S1	S2	S3	S4	S5	S6	S7	S8	S9	S10	S11	S12
Al	135875.4	125995.3	363703.6	538832.7	474916.5	312894.3	351526.5	281787.8	343456.4	468271.6	178788.2	451832.8
Cr	0.858	N. D.*	8.567	6	1.23	3.313	2.24	4.3	3	5.36	13.4	4.61
Fe	55732.4	45506.7	35013.6	36372.5	21786.5	81345.7	74564.8	67513.8	88556.3	22025.7	20243.8	15743.8
Co	331.2	190.3	450.2	210.6	223.4	128.6	119.5	495.5	110.32	213.5	187.5	147.6
Cu	13147.4	21025.6	21448.2	11347.5	17245.6	13266.4	15678.3	17725.6	43484.3	25683.6	29745.5	27893.7
As	0.46	N. D.*	0.01	0.41	3.6	1.87	1.56	4.97	2.31	2.3	9.1	3.17
Pb	2.41	2.02	3.1	7.46	2.13	8.23	2.11	9.3	4.42	4.32	2.3	3.63

First, on early morning (Bed Tea), second with the breakfast and third in the evening (evening Tea). Each cup (75 ml) of Tea is made by boiling approximately 500 mg of Tea with water. Table 3 represents elements that have maximum occurrence in any tea brand. Daily intake has been calculated, according to assumption.

Discussion

Iron (Fe)

Iron is important one out of the essential trace elements, it has significant role in biological systems of humans as an ingredient of *Haem* proteins that performs the function of oxygen transport. Types of *Haem* proteins are *haemoglobin, myoglobin*, and the *cytochromes.* Iron is a constituent of some enzymes also, that play a major role in oxygen and food metabolism like *succinic dehydrogenase, mitochondrial NADH-dehydrogenase* and *xanthine oxidase.* Iron occurs as naturally in all food items. Sometimes doctors prescribe an additional intake of Iron in some clinical conditions. Significant loss of Iron during menstrual period occurs in females hence, more Iron is required than males. Provisional Maximum Tolerable Daily Intake [PMTDI] of iron is specified as 0.8 mg per kg body weight[7]. The maximum daily intake of Iron detected in Tea sample is 132.83 µg hence it is well below the PMTDI.

Copper (Cu)

Copper is an essential trace element that helps in formation of blood hemoglobin, melanin which plays important biological role in staying healthy body and skin . It helps in proper functioning of thyroid gland as well as it neutralize free radicals through its antioxidant property. Some other forms of Copper like *Sulfate* and *Nitrites* act as pro-oxidant that may cause Alzheimer's disease[8]. According to Guidelines[9] PMTDI of Copper is specified as 0.5 mg. per kg. body weight. The maximum daily intake of Copper detected in Tea samples is 65.23 µg hence it is below the PMTDI.

Table 3 — Estimated daily consumption.

Element	Maximum concentration[µg kg^{-1}]	Sample name	Daily int [µg]
Al	538832.7	S4	808.2
Cr	13.4	S11	0.02
Fe	88556.3	S9	132.8
Co	495.5	S8	0.74
Cu	43484.3	S9	65.23
As	9.1	S11	0.01
Pb	9.3	S8	0.01

Cobalt (Co)

Cobalt is another essential trace element that is being consumed through diet. Vegetables and water are the main source. It is one of the constituent of vitamin B12 [Cobalamin] and certain enzymes. It has been reported that cobalt keeps nervous system and blood cells healthy. Some researchers have reported that Cobalt [ii] compounds show carcinogenic activity[10]. Provisional Maximum Tolerable Daily Intake [PMTDI] of cobalt is specified as 0.1 to 1 mg. per kg of body weight[11]. The maximum Daily intake of Cobalt detected in Tea samples is 0.74 µg hence it is well below the PMTDI.

Chromium (Cr)

It has been proven that Chromium plays a significant role in regulation of carbohydrate and lipid metabolism as well as insulin activity[12]. Hence, it is an essential trace element, reduce the risk of diabetes and promote healthy cardiac activity. However, higher level of Chromium intake through respiration have been reported as carcinogen[13]. Provisional Maximum Tolerable Daily Intake [PMTDI] of Chromium is specified as 0.1 mg. per kg of body weight[14]. The maximum Daily intake of Chromium detected in Tea samples is 0.02 µg^{-1} hence it is well below the PMTDI.

Aluminum (Al)

Aluminum is non essential for humans. It forms hydroxides that shows a very little solubility and hence shows speciation in body. Several epidemiological studies have shown an increased risk of various mental disorders, including Alzheimer's disease, associated with increased aluminum intake[15, 16]. Patients with renal disorders are at higher risk of aluminum toxicity. Provisional Maximum Tolerable Daily Intake [PMTDI] of aaluminum is specified as 7.0 mg. per kg of body weight[17]. The maximum Daily intake of Aluminum detected in Tea samples is 808.25 µg hence it is well below the PMTDI.

Arsenic (As)

Arsenic occurs naturally and has been reported to have tendency to enter into food system via plants, animals and most prominently via fish. Arsenic has found its main use in pesticides and electronic components. Most of the organic arsenic gets excreted through body. This is the inorganic arsenic that causes

toxicity since it inactivates more than 200 enzymes that causes cellular activity, DNA repair and synthesis[18]. Provisional Maximum Tolerable Daily Intake [PMTDI] of Arsenic is specified as 0.015 mg. per kg of body weight[19]. The maximum Daily intake of Arsenic detected in Tea samples is 0.01 µg hence it is well below the PMTDI.

Lead (Pb)

Researcher have reported that, Lead is highly toxic and carcinogen as it has tendency to replace other essential elements like Calcium, Phosphorous and Iron etc. that are bound to protein molecules. It also inhibits the activity of *Haem* proteins and enzymes that cause a severe damage to the DNA, tissues and organs[20]. Provisional Maximum Tolerable Daily Intake [PMTDI] of Lead is specified as 0.025 mg. per kg. body weight[21]. The maximum Daily intake of Lead detected in Tea samples is 0.01 µg hence it is well below the PMTDI.

Conclusions

Results have been shown that Tea can be a rich source of essential trace elements. It also contains high levels of non essential toxic Aluminum. Researchers have been shown that Aluminum has a tendency of accumulation in bone, kidney and spinal cord that also increases with aging[22-24]. Recent researches have been shown that, the rate of occurrence of Alzheimer disease and metal toxicity increase rigorously with increasing age[23-24]. An unusual case of *myelopathy* due to aluminum toxicity has been reported[25], authors have diagnosed a 28 year old man suffering from gradual weakness of his limbs and motor ability due to exceptionally high aluminum level in his blood. Both young leaves and older leaves of Tea plant are being utilized to make black tea and green. Researchers have been shown that both types of leaves contain high level of Aluminum[26]. However, the concentration of aluminum estimated during our work does not show an enormous high amount but found in significantly high amount. It can be stated that the regular consumption of more than 3 cups of Tea may significantly increase the accumulation level of Aluminum in body, hence may contribute to consequences of this accumulation. Similar type of inference was observed during literature review, one research group in their review, based on survey of functional foods consumption including tea and coffee, have been reported that Tea consumption was highest in Finland population among the four countries namely Finland, United States, Belgium and Japan[27]. When we put our attention to the situation on Alzheimer's and Dementia in these countries we observed that death rate due to said diseases was highest in Finland among these countries in relation with the population in year 2014[28]. In remaining three countries number of patients suffering from Alzheimer's and Dementia shows increase in trend[29-31]. So, there is a need to assess biologically the intake of Aluminum via Tea and other food items and its contribution to accumulated Aluminum and the health risks associated. Our study has shown the presence of trace elements within the safe limits. But it is evident that the certain chemical forms of detected trace elements including Aluminum and others may cause toxicity. So total elemental determination may not be adequate hence more intense research efforts are required.

Acknowledgement

Researchers of our group are thankful to H N B Garhwal University, Srinagar Garhwal and Dean School of Engineering, Prof. N S Panwar for his significant motivation and providing the access to instrument ICP-MS and facilities.

References

1 Teabox (2017). An overview: Tea Industry in India accessed on 24 June 2019. https://Tea101.Teabox.com/brief-history-indian-Tea-industry.
2 Narender K Jain, Maqsood Siddiqi and John Weisburger, CAB International, p. 9 (2006).
3 Parmar Namita, Rawat Mukesh and Kumar J. Vijay Camellia Sinensis, *Global J Pharmacol,* 6 (2) (2012) 52.
4 Tariq M, Naveed A & Ali K Barkat, *J Med Plants Res,* 4 (19) (2010) 2028.
5 Cabrera C, Gimenez R & Lopez M C, *J Agri Food Chem,* 51 (15) (2003) 4427.
6 Watrak Sandra, et al., *KOSMOS*, 65 (4) (2016) 563.
7 WHO International Programme on Chemical Safety, IPCS Inchem home,WHO food additives series 571 Iron accessed on 30 June 2019. http://www.inchem.org/documents/jecfa/jecmono/v18je18.htm.
8 Osredkar J & Sustar N *J Clinic Toxicol,* S3:001, (2011).
9 WHO International Programme on Chemical Safety, IPCS Inchem home, WHO food additives series 17 551 Copper, accessed on 1 July 2019. http://www.inchem.org/documents/jecfa/jecmono/v17je31.htm.
10 Bhattacharya P T, Misra Satya Ranjan & Hussain Mohsina, *Scientifica Cairo*, 5464373 (2016). doi: 10.1155/2016/5464373.
11 D J Snodin, *Human Exper Toxicolo,* 34 (12) (2015) 1258.
12 Vincent J B, *Acc Chem Res*, 33 (7) (2000) 503.

13 Costa Max & Klein Catherine B, *Rev Toxicolo*, 36 (2) (2006) 155-163.
14 Kogan S, Zeng Q, Ash N & Greenes R A, *Proc AMIA Symp*, (2001) 329.
15 Martyn C N, *et al., Lancet* (1) (1989) 59.
16 Forbes W F, Lessard S & Gentleman J F, *Can J Aging*, 14 (1995) 642–656.
17 WHO International Programme on Chemical Safety, IPCS Inchem home, WHO food additives series 24 657 Aluminum accessed on 3 July 2019. http://www.inchem.org/documents/jecfa/jecmono/v024je07.htm.
18 Johnstone R M, Sulfhydryl agents: arsenicals, In: Hochster RM, Quastel JH [eds], Metabolic Inhibitors: A Comprehensive Treatise, Academic Press, New York, 2 (1963) 99.
19 WHO International Programme on Chemical Safety, IPCS Inchem home, WHO food additives series 24 658 Arsenic accessed on 4 July 2019. http://www.inchem.org/documents/jecfa/jecmono/v024je08.htm.
20 Godwin Hilary Arnold, The biological chemistry of lead Current Opinion in Chemical Biology, 5 (2) (2001) 223.
21 WHO. International Programme on Chemical Safety, IPCS Inchem home, WHO food additives series 21 622 Lead, accessed on 5 July 2019. http://www.inchem.org/documents/jecfa/jecmono/v21je16.htm.
22 Lukiw Walter J, *et al*., *J Alzheimers Dis Parkinsonism*, 8 (6) (2018) 457, DOI: 10.4172/2161-0460.1000457.
23 Vas C J *et al*. *Int Psychogeriatr*, 13 (4) (2001) 439.
24 Mathuranath P S, *et al*., *Neurol India*, 60 (6) (2012) 625. doi: 10.4103/0028-3886.105198.
25 Verma R & Sarkar S, *Neurol India*, 67 (3) (2019) 866.
26 Chenery E M, *Plant and Soil*, 6 (1955) 174.
27 Ozen Asli E, Pons Antoni & Tur Josep A, Nutrition Reviews, 70 (8) (2012) 472. doi:10.1111/j.1753-4887.2012.00492.x.
28 Official Statistics of Finland (OSF): Causes of death [e-publication]. ISSN=1799-5078. 2016, 3. Deaths from dementia and Alzheimer's disease are increasing. Helsinki: Statistics Finland [referred: 17.10.2019]. http://www.stat.fi/til/ ksyyt/2016/ksyyt_2016_2017-12-29_kat_003_en.html.
29 2019 Alzheimer's Disease Facts and Figures, accessed on 23 September 2019. https://www.alz.org/media/Documents/alzheimers-facts-and-figures-2019-r.pdf.
30 Alzheimer's association (2019) Alzheimer's and Dementia Resources Alzheimer's and Dementia in Japan accessed on 23 September 2019. https://www.alz.org/jp/dementia-alzheimers-japan.asp.
31 Belgium 2013: The prevalence of dementia in Europe accessed on 23 September 2019. https://www.alzheimer-europe.org/Policy-in-Practice2/Country-comparisons/2013-The-prevalence-of-dementia-in-Europe/Belgium.

IJEP 40 (11) : 1154-1163 (2020)

Seasonal And Morphological Analysis Of Airborne PM_{10} And $PM_{2.5}$ In Srinagar Garhwal (Himalaya Region)

Alok Sagar Gautam[1], R. S. Negi[2]*, Sanjeev Kumar[1], Don Biswas[3] and Santosh Rawat[2]

1. *Hemvati Nandan Bahuguna Garhwal University, Department of Physics, Birla Campus, Srinagar, Garhwal - 246 174*
2. *Hemvati Nandan Bahuguna Garhwal University, Department of Rural Technology, Chauras Campus, Srinagar, Garhwal - 246 174*
3. *Hemvati Nandan Bahuguna Garhwal University, Department of USIC, Chauras Campus, Srinagar, Garhwal - 246 174*

**Corresponding author, Email : rsnegi64@rediffmail.com; sk8190179@gmail.com*

To understand the morphology and chemical constituent of ambient air in Srinagar, Garhwal valley, an experiment was carried out in the Department of Physics, Chauras campus, Hemwati Nandan Bahuguna Garhwal University. The particulate matter (PMs) were collected by using fine particulate dust sampler (APM 550 and APM 460 NL, Envirotech, New Delhi) and analysed by using SEM and EDAX technique (CARL ZEISS, MA15/EVO18). The average mass concentration of PM_{10} is recorded as 107.4 ± 16.3 $\mu g/m^3$, whereas the average mass concentration of $PM_{2.5}$ is recorded as 88.48 ± 14.74 $\mu g/m^3$ which are much higher than the standard value prescribed by WHO and NAAQS. The reason behind such a huge concentration is identified as massive construction of building, stone crusher factory and exponential growth in vehicles, forest fire and other anthropogenic activities in the surrounding area. The SEM analysis suggest that silicon (Si), oxygen (O), sodium (Na), aluminium (Al) are dominantly present in form of silica (SiO_2), aluminosilicate (Si-Al rich), sea spray, mineral dust and gold (Au), zinc (Zn) and barium (Ba) may be present due to natural ores in surrounding hills in all seasons. But in the case of the post-monsoon season, nearly 25% of $PM_{2.5}$ consists of carbon particles, which is more likely to be coming from soot particle emission from biomass burning.

KEYWORDS

SEM, EDAX, Forest fire, Anthropogenic activities, Particulate matter ($PM_{2.5}$ and PM_{10})

1. INTRODUCTION

The particles in the atmosphere are a complex mixture of organic and inorganic species that play a very crucial role in cloud formation, distribution of solar radiation and cloud droplet nucleating ability, acidification, dry deposition and precipitation that support life in planet [1,2,3]. The sources of such atmospheric particles are mainly natural as well as anthropogenic. Activities, such as dust, sea spray, volcanic emission, industrial power plant and combustion of solid fuel for domestic use and exponential growth of vehicles. Almeida and Colbeck suggest that the airborne particulate matter (PM) is a complex mixture of various chemical varieties [4,5]. Loading of such particulate matters (PMs) particles in valley configuration along with metrological parameters and their chemical characteristics are mentioned by Gautam [6]. Generally, the aerosol can be reached in high altitude areas by valley breeze activity on the central Himalayan region [7]. The particles having a aerodynamic diameter less than 10 μm (PM_{10}) are called inhalable particles and below 2.5 μm ($PM_{2.5}$) are called respirable particles which are highly penetrable and can be reached to alveoli in human lungs [8]. The dispersion of PM_{10} and $PM_{2.5}$ is a worldwide issue that governs ambient air quality, visibility, various health issues such as respiratory and cardiovascular diseases [9]. Therefore, it is very important to understand their chemical composition and size distribution of ambient air at Alaknanda valley. The scanning electron microscope with energy dispersed X-ray analysis (SEM/EDAX) is often used by researchers to identify the chemical composition of airborne particles particulate matters (PMs) in ambient air. Scanning electron microscope with energy dispersed X-ray analysis (SEM/EDAX) allows us to collect some essential information of element composition particle density and morphology and also their possible originating sources of sample air at observation site [10].

To determine the possible sources of particulate matters (PMs) it is very essential to analyse their elemen-

© 2020 - Kalpana Corporation

Table 1. *Charecteristics of the observation site*

Location of sampling station	Zonal actvities	Majour sources of PMs
Departemnt of Physics, Chauras campus, HNBGU, Sringar	Hydro power plant (330 MW)	Waste burning
	Chemistry laboratory	Transport activity
	Construction of national highway (NH-58)	Spray and paint shop
	Agricultural and solid wood burning	Stone crusher
	Hotel and restaurant	-

tal composition as compared to their bulk elemental composition analysis [11]. In this research paper, we tried to analyze and characterize the possible sources of particulate matters (PMs), their variability, air mass back trajectory alongwith metrology and topology of Alaknanda valley in the central Himalayan region of Uttrakhand state of India.

2. MATERIAL AND METHOD

2.1 Study area

Alaknanda valley (Srinagar) located at (30.22 N, 78.78 E) at the bank of Alaknanda river at the elevation of 560 m. It is located about 356 km and 153 km from Delhi and Dehradun and connected by National Highway (NH-58). The Srinagar is the largest town in the entire Garhwal region and it is home of 21,000 in habitants as per census in 2011 and also it is the administrative division of northern Indian state of Uttrakhand. The climate of Srinagar is sub-tropical (average annual rainfall 1000-1500 mL) and average temperature varies in the range of 2-40^{0}C in winters and summers [12]. The observation site is surrounded by the vegetation dominantly covered by Chir pines *(Pinus roxhburghi),* Shecham *(Dalbergia sissoo)* and Oks *(Querussemi carpifolia)* at different elevation and inclination [13]. There are no major industries except some stone crushers, bakeries, hotels and restaurants; however, Seilaqui and Haridwar industrial areas are situated in the area of 100 km and 70 km, respectively. The sampling site is 50 m away from the road with moderate traffic and in the 500 m, chemistry lab and solid-state research lab are located. The Alaknanda river experience maximum suspended load due to southwest monsoon precipitation and melting of a glacier during monsoon season and left massive sand deposition at its river banks (nearest sand deposition site is located about 700 m). There is a hydro-electric power plant of capacity 330 MW on the Alaknanda river within the range of 5 km from the sampling site (Table 1) [14].

2.2 Sampling and analysis

2.1.1 Sample collection: The observations of PM_{10} and $PM_{2.5}$ were carried out at 10 m below ground level at Department of Physics, Hemvati Nandan Bahuguna Garhwal University (HNBGU), Srinagar, Pauri Garhwal, using fine particulate dust sampler (APM 550 and APM 460 NL, Envirotech, New Delhi). The instrument was set at constant flow rate of 1 m^3/hr over a period of the 24 hr. To collect the samples of particulate matters (PMs), we used quartz filter paper (PM_{10}) and glass fibre filters paper ($PM_{2.5}$) during the entire observation period (1 January 2017 to 31 December 2017) once in a week [3]. To remove moisture from filter paper, samples were kept in the desiccators for 24 hr and then stored in the air tight box to minimise the atmospheric influence.

2.1.3 Sample analysis: The desiccated sample's filter papers were weighed using electronic microbalance (Model GR202, A and D Company Ltd., Japan) with 0.01 mg resolution. The convergence of particles was resolved by the difference between their weights before and after sampling [1]. The samples were analyzed by SEM/EDAX at University Science and Instrument Centre (USIC), HNBGU, Chauras campus. The scanning electron microscope (SEM) analysis of prepared samples was done by the CARL ZEISS, MA15/EVO18 having dispersed energy of the X-ray system with an accelerating voltage of 20-30 kV.

3. RESULT AND DISCUSSION

The analysis process of collected samples' was performed from 1 January 2017 to 31 December 2017. We have investigated the morphological, chemical properties through loading of sample dust. Now we consider only one sample from each season - 9 January 2017, 17 April 2017, 21 August 2017 and 20 November 2017 as a proxy of winter, pre-monsoon, monsoon and post-monsoon, respectively for the analysis.

3.1 Meteorological parameters and PMs

Background meteorological parameters play potential role in the variation of PMs in the troposphere and govern the process like aerosol loading, wet deposition, etc. The temperature, humidity, wind speed, wind direction and total rainfall alongwith monthly mass concentration of PM_{10} and $PM_{2.5}$ are represented in figure

© 2020 - Kalpana Corporation

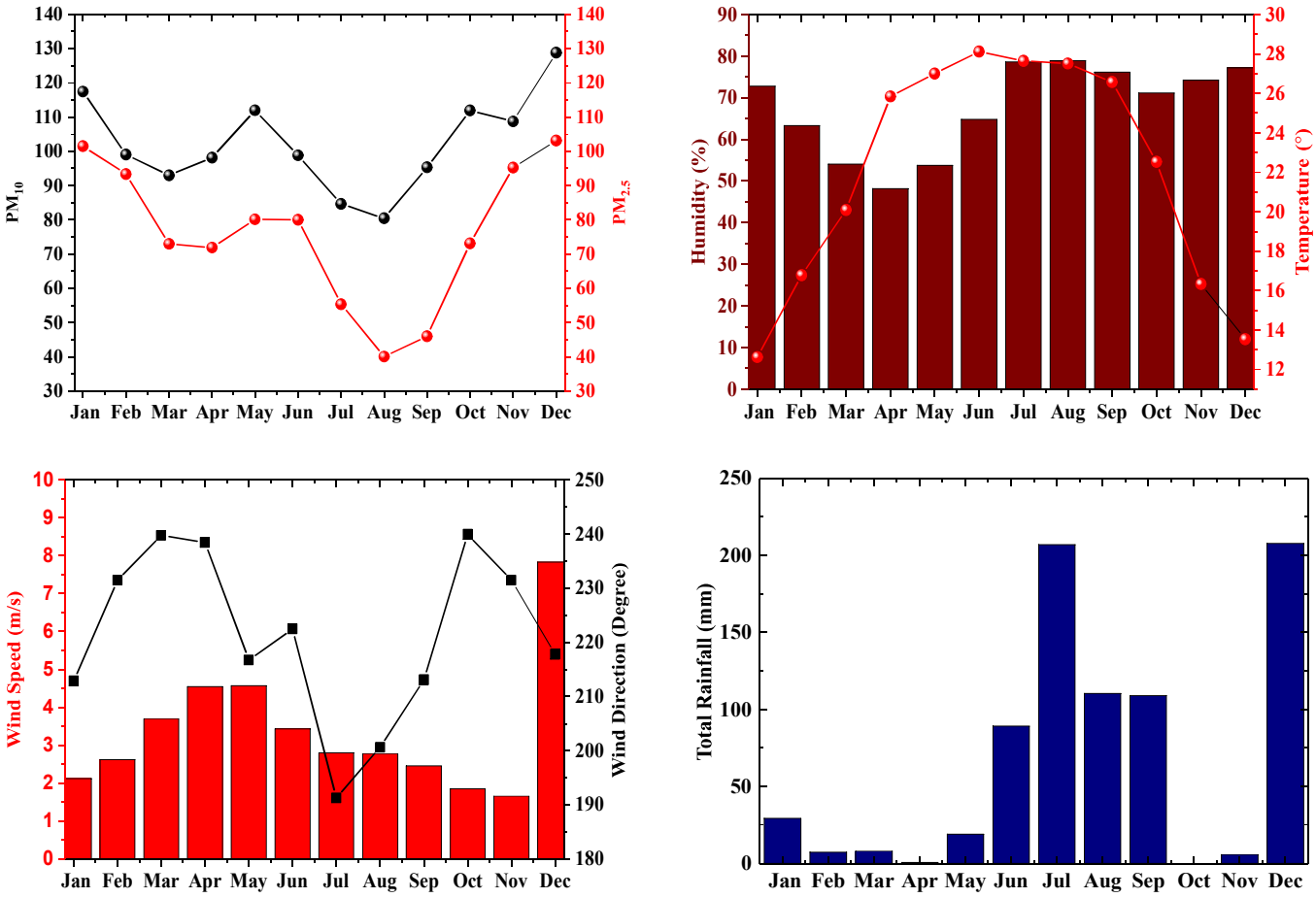

Figure 1. *Monthly variation of PM_{10} and $PM_{2.5}$ alongwith background meteorological conditions at a monitoring site*

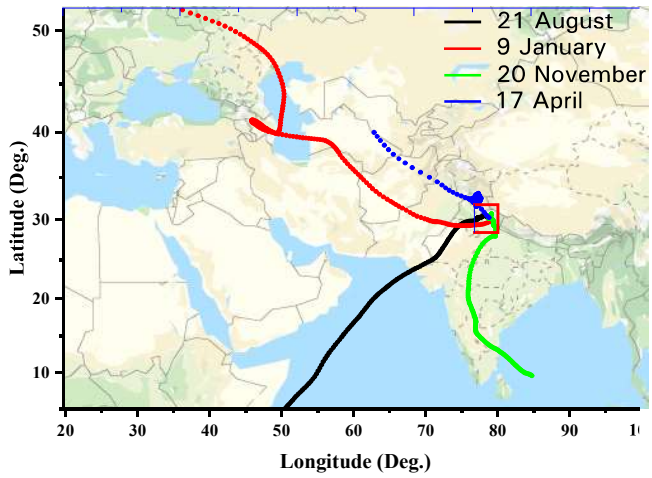

Figure 2. *HYSPLIT air mass back trajectory*

1. The temperature shows an inverted bell shape trend, in which temperature began increasing to a maximum value in June (28.11°C) and further shows drastic decrease in temperature by December (13.53°C). But the minimum monthly temperature of 12.6°C was reported in January. The monthly variation of humidity vs temperature showed an inverse relationship with each other. The maximum humidity was recorded in August (78.94%), however minimum humidity is obtained in April (48.19%). Wind speed became maximum in April and minimum in November. A rapid increase in the wind speed observed in December, which seems to be linked to western disturbance activities alongwith an increase in precipitation. Wind direction showed widespread variability throughout the year probably due to topography of the observation location.

The amount of precipitations affects the mass concentration of PMs, in June, July, August and September 2017. Observations show a highest rainfall of 207.7 mm in December. Wet scavenging induced a low concentrations of PM_{10} (80.43 $\mu g/m^3$) and $PM_{2.5}$ (40.0943 $\mu g/m^3$) in the month of August. The maximum monthly mass concentration of PM_{10} (128.79 $\mu g/m^3$) and $PM_{2.5}$ (103.15 $\mu g/m^3$) were reported in December 2017 attributed to long-range transport mechanism alongwith massive wood burning activities at the surrounding area [15,16]. The effect of long-range transport was also investigated using HYSPLIT air back mass trajectory analysis to understand the point of origin of pollutants (Figure 2).

© 2020 - Kalpana Corporation

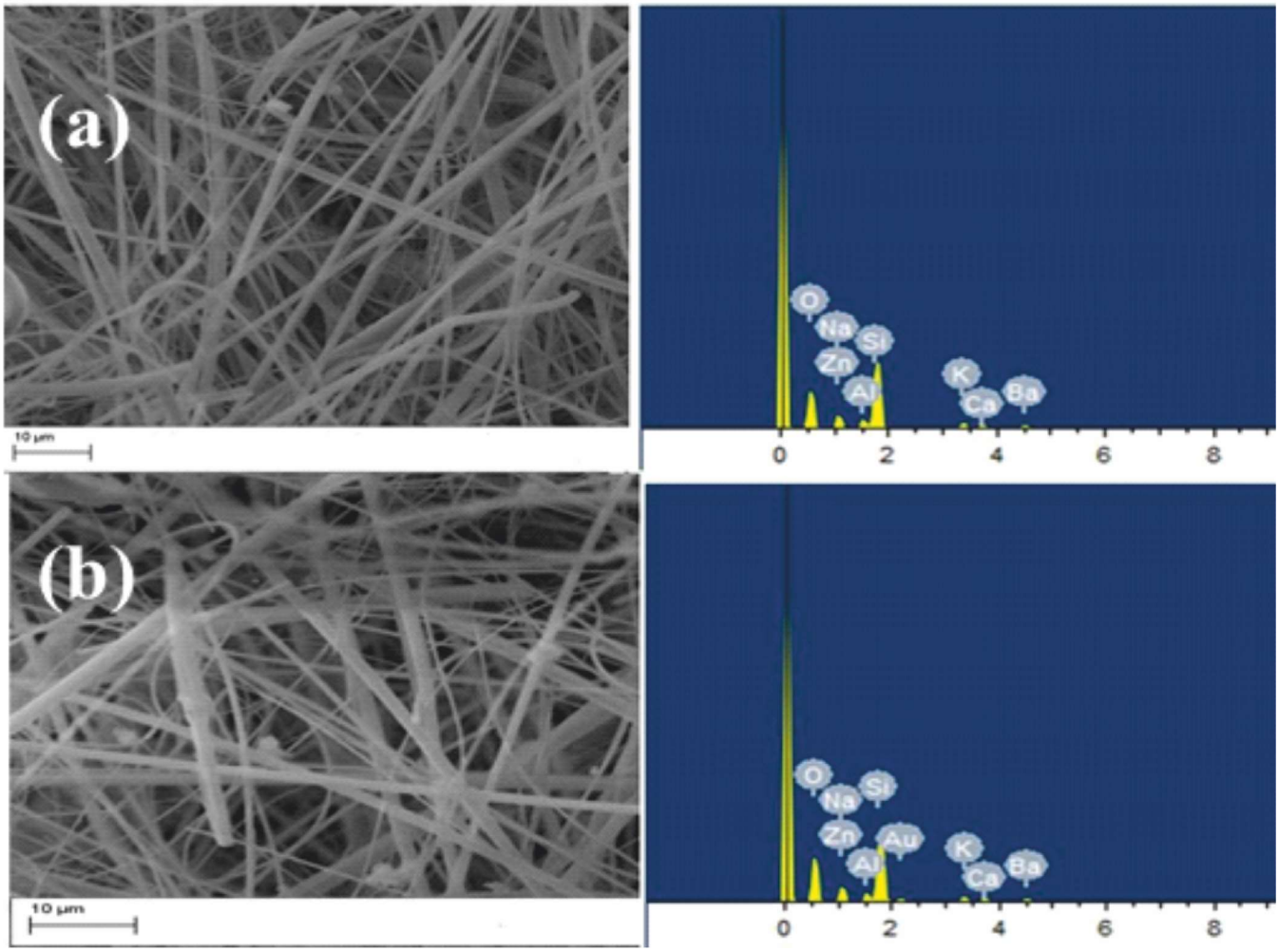

Figure 3. *SEM and EDAX micrographs of (a) PM_{10} and (b) $PM_{2.5}$ in winter season*

3.2 SEM and EDAX analysis

3.2.1 Morphology of PM_{10} and $PM_{2.5}$ in the winter season: The SEM micrographs and EDAX spectra of PM_{10} and $PM_{2.5}$ during the winter season are represented by figure 3. The EDAX spectra of PM_{10} and $PM_{2.5}$ indicates the presence of the following elements in PM_{10} as O (51.41%)> Si (26.84%)> Na (6.67%)> Ba (4.96%) > Zn(2.97%)> Al (2.94%)> K (2.59%)> Ca (1.62%) whereas $PM_{2.5}$ shows almost similar tendency with slight variation of mass concentrations such as O (52.30%)> Si (24.30%)> Na (6.59%)> Ba (4.18%) > Au (3.26%)> Zn (3.06%)> Al (2.71%)> K (2.29%) (Figure 4a and 5a). In winter season, oxygen (O), silicon (Si) and sodium (Na) were highly abundant and contributed upto 84.92% in PM_{10} and 83.19% in $PM_{2.5}$, respectively. From the analysis it is confirmed that the contribution of silica (SiO_2), felsic silicates (Si and Al-rich), mineral dust are present in the sample [17]. The fine details of various types of silicates are well classified and documented by their observation at Agra, India [18].

3.2.2 Morphology of PM_{10} and $PM_{2.5}$ in the pre-monsoon season: Figure 6 represents the SEM micrographs (10 μm resolution) and EDAX spectra of PM_{10} and $PM_{2.5}$ in the pre-monsoon season. The EDAX spectra of PM_{10} and $PM_{2.5}$ of sampled air indicate the presence of O, Si, Na, Zn, Ba, K, Al, Au and O, Si, Na, Ba, Zn, Al, Au, K elements, respectively. On the basis SEM analysis, the tendency of occurrence of elemental mass composition in PM_{10} and $PM_{2.5}$ are O (50.54%)>Si (25.88%)> Na (6.44%)> Zn (4.30%)> Ba (4.17%)> K (2.63%)> Al (2.35%)>Au (2.35%) and O (53.15%) > Si (24.58%)> Na (6.61%)> Ba (4.13%)> Zn (3.02%)> Al (2.77%)> Au (2.38%)> K (2.33%), respectively (Figure 4b and 5b). Oxygen (O), silicon (Si) and sodium (Na) are highly abundant and contributed upto 82.86% in PM_{10} and 84.34% in $PM_{2.5}$ of the entire mass. The presence of O, Si, Na, Al may be due to contributions of silica (SiO_2), felsic silicates (Si and Al-rich), whereas Si-Na mixture may be due to sea salt

© 2020 - Kalpana Corporation

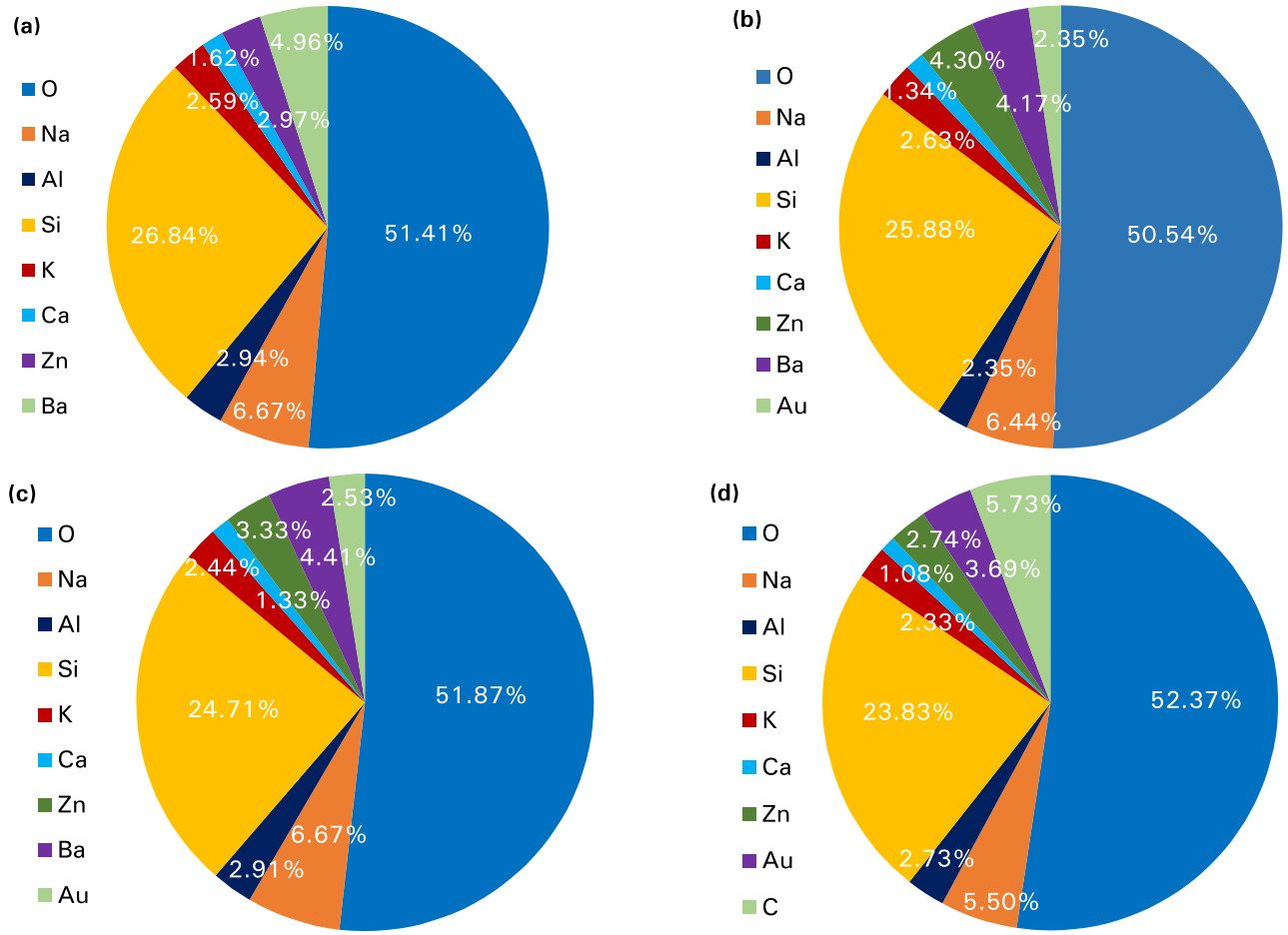

Figure 4. *Elemental compositions of PM_{10} in different seasons*

and mineral dust compounds [17]. Sources of these elements are likely from various natural activities such as dust storm, conversion from other compounds in the atmosphere as well as anthropogenic activities such as construction works, transportation and other energy production activities [11]. The trend of elemental composition is similar in both PMs. The presence of Au, Zn, Ba may be due to natural mineral deposition in Srinagar valley, Garhwal Himalaya.

3.2.3 Morphology of PM_{10} and $PM_{2.5}$ in monsoon: Figure 7 represents the SEM micrographs and EDAX spectra of PM_{10} and $PM_{2.5}$ at the monitoring site in Srinagar valley. EDAX spectra of PM_{10} and $PM_{2.5}$ sample air indicates the presence of O, Na, Si, Al, Ca, Zn, Ba and K and O, Na, Al, Si, Ca, K, Zn, Ba elements as an airborne particle. On the basis of analysis, we observed the following tendency of occurrence of elements in PM_{10} and $PM_{2.5}$ as O (51.87%) > Si (24.71%) > Na (6.67%) > Ba (4.49%) > Zn (2.95%) > Al (2.4%) > K (2.44%) and O (52.60%) > Si (24.80%) > Na (6.53%) > Ba (4.49%) > Zn (2.95%) > K (2.65%) > Al (2.4%) > Au (2.33%), respectively (Figure 4c and 5c). Oxygen (O), silicon (Si) and sodium (Na) were highly abundant and contributed upto 83.25% and 83.93% of PM_{10} and $PM_{2.5}$ of the entire mass of PMs, respectably. From the analysis, it is confirmed that the origin of the elements are from silica, felsic silicates (Si and Al-rich), sea spay, natural ore and mineral compounds [17]. The presence of Ca probably indicates the contribution of $CaCO_3$ in the calcite phase originated due to the local transportation, construction and natural dust by stone crusher in both PMs ($\leq 50\ \mu m$). Au is dominantly present in winter, pre-monsoon and monsoon due to gold depositions in the surrounding hills [13].

3.2.4 SEM and EDAX of PM_{10} and $PM_{2.5}$ in post-monsoon : Figure 8 represents the SEM micrographs and EDAX spectra of PM_{10} and $PM_{2.5}$ of collected sample at the monitoring site. The EDAX spectra of PM_{10} and $PM_{2.5}$ indicates the presence of O, Na, Si, Al, Ca, Zn, Ba, K and O, Na, Al, Si, Ca, K, Zn, Ba elements as airborne particle. On the basis of analysis, we observed the following tendency of occurrence of elements in PM_{10} and $PM_{2.5}$ as (52.37%) > Si (23.83%) > C (5.73%) > Na (5.5%) > Zn (2.74%) > K (2.33%) > Al (2.73%) > Ca (1.08%) and O (47.86%) > C (24.17%) > Si

© 2020 - Kalpana Corporation

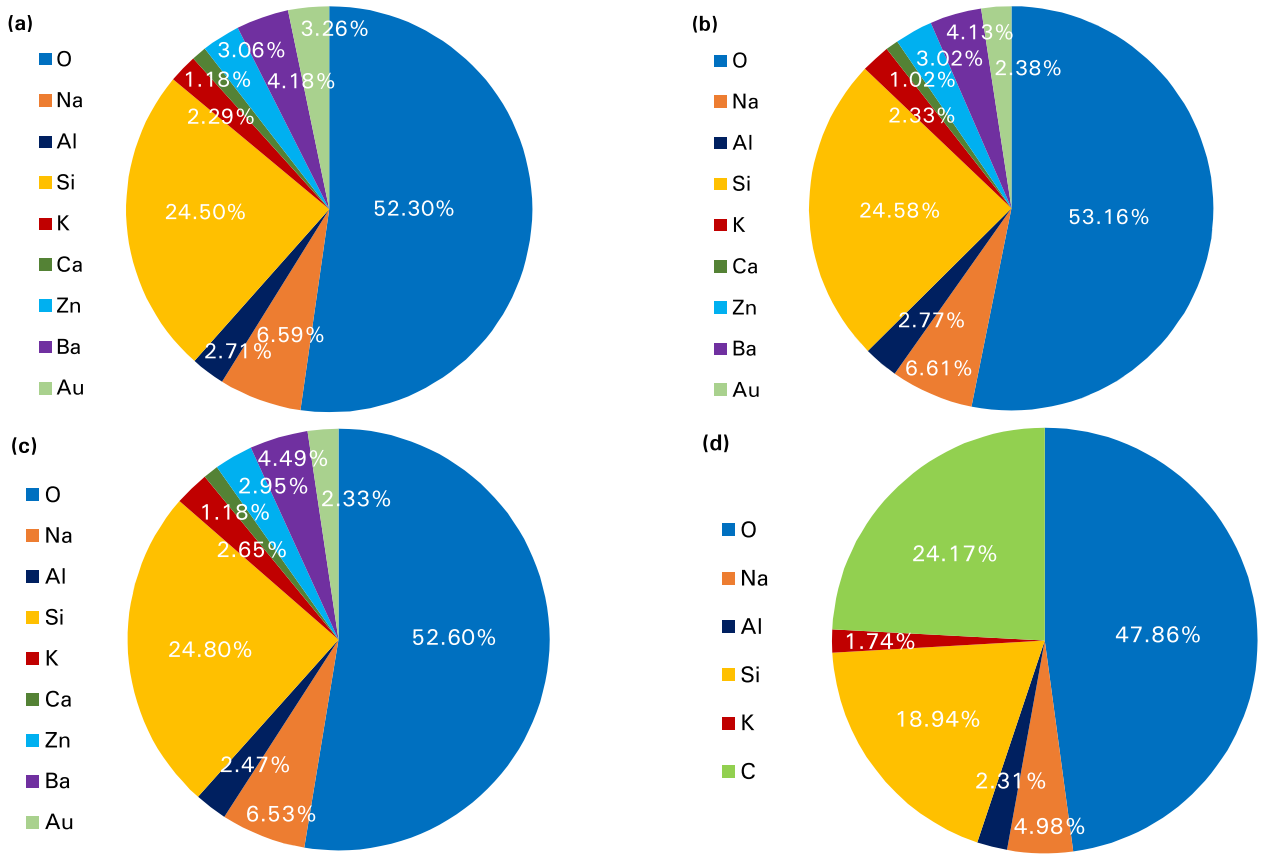

Figure 5. *Elemental compositions of $PM_{2.5}$ in different seasons*

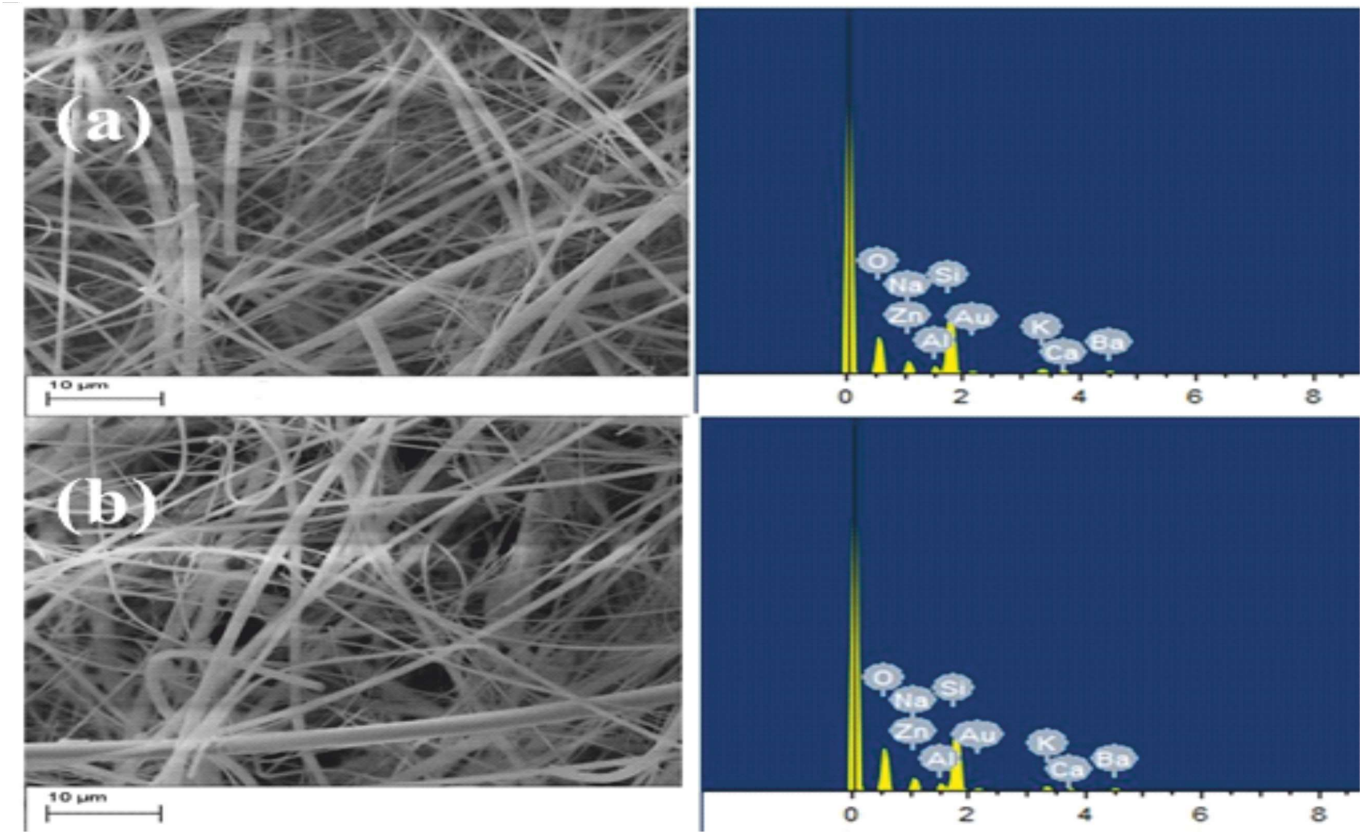

Figure 6. *SEM micrographs and EDAX spectra of (a) PM_{10} and (b) $PM_{2.5}$ in pre-monsoon season*

© 2020 - Kalpana Corporation

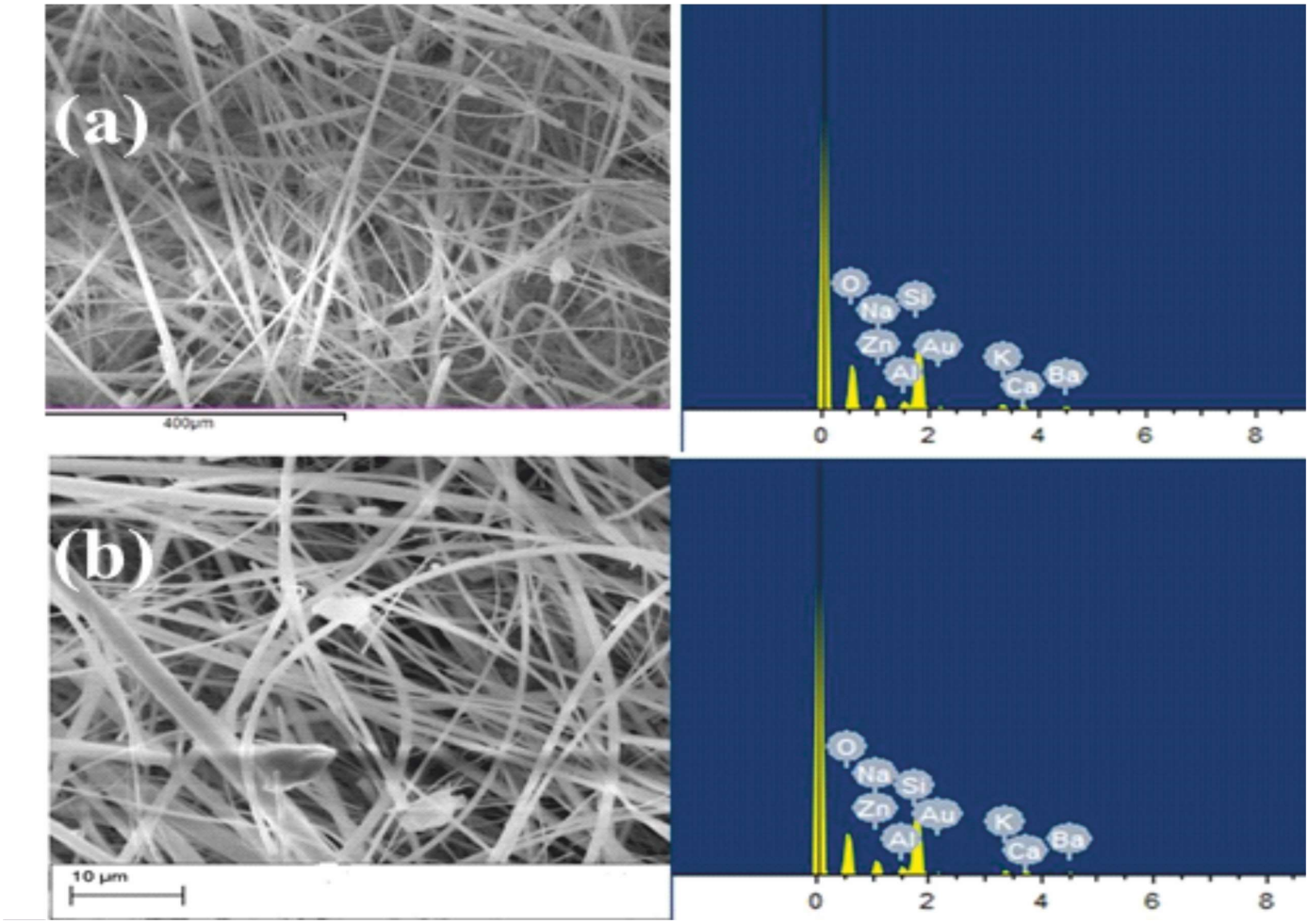

Figure 7. *SEM micrograph and EDAX spectra of PM_{10} and $PM_{2.5}$ in monsoon season*

(18.94%) > Na (4.98%) > Al (2.31%) > K (1.74%), respectively (Figure 4d and 5d). In PM_{10}, oxygen (O), silicon (Si) and carbon (C) were highly abundant and contributed upto 81.93% of total elemental composition due to the presence of silicon oxide (SiO_2) or quartz type composition. Quartz is a principal constituent of different rocks and usually generated from cutting of rocks for road construction, wood/coal burning process, etc., [18,19]. The presence of Si-Al, Ca, K and Zn are due to the occurrence of the following compounds like aluminosilicate, sea spray, flyash, etc. But in case of $PM_{2.5}$, carbon (24.17%), O, Si are dominantly present whereas Na, Al and K are present in minor quantity. This results illustrate the presence of soot particles, mineral dust clay mainly originated from anthropogenic activities such as construction, transportation, conversion process during combustion in the typical particle dimension \ size range (1-2 μm) [11].

3.3 Mass concentrations of PM_{10} and $PM_{2.5}$

The time series of average mass concentrations of PM_{10} and $PM_{2.5}$ are presented in figure 9. The mass concentration of PM_{10} and $PM_{2.5}$ indicate several peaks during observation, the highest peak was reported on 30 Dec 2017 as well as secondary peaks were obtained on 12 December 2017, 13 November 2017 and 10 January 2017. Due to solid wood, agricultural waste burning, cooking and warming activities in post-monsoon and winter. But high mass concentration in pre-monsoon season may be due to wildfire, high traffic, construction of NH-58 and by other anthropogenic activities in surrounding areas. The time series also indicate a drastic fall during monsoon season, the lowest value of PM_{10} and $PM_{2.5}$ was observed on 13 August 2017 of 80 $\mu g/m^3$ and 45.2 $\mu g/m^3$, respectively. The average mass concentration of PM_{10}, was reported as 107.4 ± 16.3 $\mu g/m^3$ and $PM_{2.5}$ was recorded as 88.48 ± 14.74 $\mu g/m^3$. This result indicates that the concentration of particulate matters are much higher than permissible limits prescribed by WHO (PM_{10} - 20 $\mu g/m^3$, $PM_{2.5}$ - 10 $\mu g/m^3$) and NAAQS (PM_{10} - 60 $\mu g/m^3$, $PM_{2.5}$ - 40 $\mu g/m^3$) [20,21].

© 2020 - Kalpana Corporation

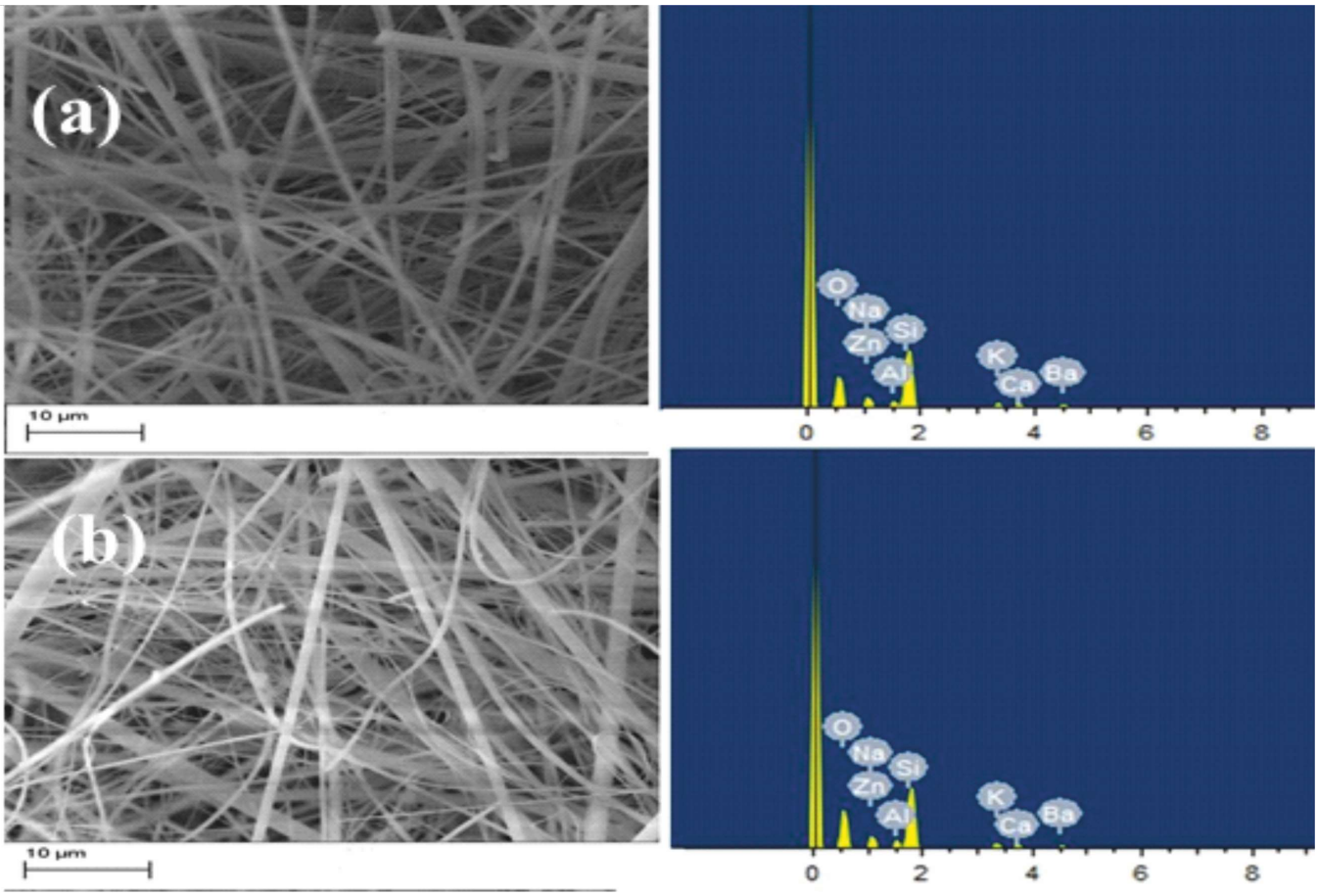

Figure 8. *SEM micrograph and EDAX spectra of PM_{10} and $PM_{2.5}$ in post-monsoon season*

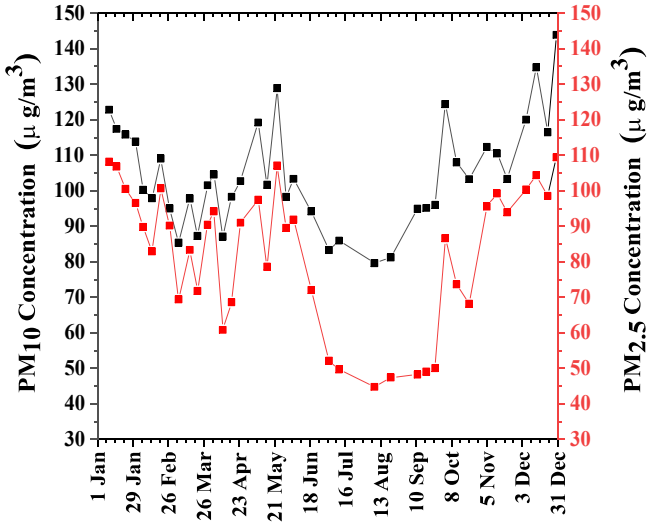

Figure 9. *Time series of mass concentration of PM_{10} and $PM_{2.5}$ at the monitoring site*

3.4 Air mass back trajectory analysis

The air mass back trajectory analysis helps to find out the apparent source of the pollutants [22]. In this study, we have analyzed the 7 days air back mass trajectory at 1000 m from ground level with the help of National Oceanic and Atmospheric Administration (NOAA) Air Resources Laboratory (ARL) Hybrid Single-Particle Lagrangian Integrated Trajectory (HYSPLIT) model. Further, visualization software (origin) has been used to plot the above results (Figure 2). In winter season (9 January 2017) the air mass was originating from the west part of Russia, at longitude 30° N and latitude 55° E and travels through Syria, Turkmenistan, Afghanistan, the western part of Pakistan via Punjab to Srinagar. In the case of pre-monsoon (17 April 2017) the air mass is originating in the longitude 60 - 65° N and latitude 40 - 45° E, from the border of Uzbekistan and Turkmenistan and travels through the western part of Afghanistan via Punjab. In the monsoon the air mass is originating from the longitude 50° N and latitude 20° E of Somalia through the Arabian sea, the air mass travels over western Gujarat, Rajasthan via Haryana to study site. Now on the basis of visualization of figure 2, we conclude that in the case of monsoon (21 August 2017), the air mass is mainly originating from Bay of Bengal, between the longitude (70 - 90° N) and latitude (5 -10° E) and travels through the Indian continent over the Tamil Nadu, Karnataka, Maharashtra,

© 2020 - Kalpana Corporation

via Madhya Pradesh, Utter Pradesh to Srinagar valley.

4. CONCLUSION

A study was carried out to investigate and understand the presence of particulate matter (PMs) by using SEM and EDAX technique in ambient air of Srinagar valley (Garhwal Himalayan region) of Uttarakhand, India. During the observation period, the following conclusions are drawn from the experiment. The SEM micrographs technique indicates that size, shape and morphology of $PM_{2.5}$ and PM_{10} are different from each other. The EDAX spectra of $PM_{2.5}$ and PM_{10} conclude that the chemical composition of particulate matters are slightly different and contain different elements in their respective groups. Silicon, oxygen and aluminium are dominantly present in the form of silica (SiO_2), aluminosilicate phase (Si and Al-rich) in particulate matter (PMs) and originated from massive construction of NH-58, stone crusher factory located near the observation site. In the case of winter, carbon is highly abundant upto 24.17% and 5.73% in $PM_{2.5}$ and PM_{10} of the entire mass of elements maybe due to transportation, agricultural waste burning and other anthropogenic activities in the surrounding areas near observation site. The average mass concentration of particulate matter (PMs) is beyond the permissible limit of WHO and NAAQS. The presence of elements like Au, Zn and Ba is due to natural ores and mineral in and around the site.

ACKNOWLEDGEMENT

The authors would like to express their sincere gratitude to the Science and Engineering Research Board (SERB), Department of Science and Technology (DST) project entitled "Formation Mechanism and Characteristics of Aerosols in Different Season and its Impact on Cloud formation - Processes and Climate at Himalayan region Uttarakhand (SERB DST No: SB/EMEQ-043/2014 dated 08 March 2016) for their financial support for the research.

REFERENCES

1. Bisht, D. S., *et al.* 2015. Carbonaceous aerosols and pollutants over Delhi urban environment: Temporal evolution, source apportionment and radiative forcing. *Sci. Total Env.,* 521(522):431–445.
2. Datta, A., *et al.* 2010. Variation of ambient SO_2 over Delhi. *J. Atmos. Chem.,* 65:127-143. DOI: 10.1007/s10874-011-9185-2.
3. Kulshrestha, A., *et al.* 2009. Chemical characterization of water soluble aerosols in different residential environments of semi-arid region of India. *J. Atmos. Chem.,* 62:121-138.
4. D'Almeida, G.A., P. Koepke and E.P. Shettle. 1991. Atmospheric aerosols: Global climatology and radiative characteristics. A. Deepak Publishing, Hampton, USA.
5. Colbeck, I. and M. Lazaridis. 2010. Aerosols and environmental pollution. *Die Naturewissenschaften.,* 97(2):117-131.
6. Gautam, A.S., *et al.* 2018. Chemical characteristics of atmospheric aerosol at Alaknanda valley (Srinagar) in the central Himalaya region. *Int. J. Env. Res.,* 12(5): 681–691.
7. Gautam, R., *et al*. 2011. Accumulation of aerosols over the Indo-Gangetic plains and southern slopes of the Himalayas: Distribution, properties and radiative effects during the 2009 pre-monsoon season. *Atmos. Chem. Phys.,* 11:12841-12863.
8. Heyder, J. 1986. Single-particle deposition in human airways. **In** Physical and chemical characterization of individual airborne particles. **Ed** K.R. Spurny. pp.73-85.
9. Chen, Y., *et al.* 2006. Microanalysis of ambient particles from Lexington, KY, by electron microscopy. *Atmos. Env.,* 40 (4): 651-663.
10. Cong, Z., *et al*. 2010. Elemental and individual particle analysis of atmospheric aerosols from the high Himalayas. *Env. Monit. Assess.,*160:323-335.
11. Li, W., *et al.* 2010. Size, composition and mixing state of individual aerosol particles in a south China coastal city. *J. Env. Sci.,* 22 (4):561-569.
12. FSI. 2017. State of Forest Report 2009. Forest Survey of India, Ministry of Environment and Forests, Govt. of India, Dehradun. pp 159-162.
13. MSME. 2012. Brief industrial profile/Pauri Garhwal/ micro, small and medium enterprises development institute Kambangal, Kaladhungi road, Haldwani, Nainital, Uttarakhnad.
14. Bahuguna, Y.M., J. Sharma and S. Gairola. 2011. Phytodiversity in the submergence area of the Srinagar hydroelectric power project in Garhwal Himalaya, Uttarakhand. *Int. J. Env. Sci.,* 1(7):1448-1458.
15. Tiwari, S., A.S. Gautam and U.C. Dumka. 2016. Assessment of $PM_{2.5}$ and PM_{10} over Guwahati in Brahmaputra river valley: Temporal evolution, source apportionment and meteorological dependence. *Atmos. Poll. Res.,* xxx:1-16.
16. Ramos, A. C., *et al.* 2009. Characterization of atmospheric aerosols by SEM in rural area in the western part of Mexixoandits relation with different pollution sources. *Atmos. Env.,* 43: 6159-6167.
17. Moreno, T., *et al.* 2003. The geology of ambient aerosols: Characterizing urban and rural/coastal silicate $PM_{10\text{-}2.5}$ and $PM_{2.5}$ using high volume cascade

© 2020 - Kalpana Corporation

collection and scanning electron microscopy. *Atmos. Env.,* 37:4265-4276.
18. Pipal, A.S., A. Kulshrestha and A. Taneja. 2011. Characterization and morphological analysis of airborne $PM_{2.5}$ and PM_{10} in Agra located in north central India*. Atmos. Env.,* 45:3621-3630.
19. Xie, K., *et al.* 2004. Chemical characterization of individual particles (PM_{10}) from ambient air in Guiyang city, China. *Sci. Total Env.,* 343:261-272.
20. WHO. 2005. Air quality guidelines for particulate matter, ozone, nitrogen dioxide and sulphur dioxide. World Health Organizations, Geneva, Switzerland.
21. NAAQS. 2012. Review of the national ambient air quality. Available at : http://www.cpcb.nic.in/National-Ambient-Air-Quality-Standards.php.
22. Sen, A., *et al.* 2017. Variation in particulate matter over Indo Gangetic Plains and Indo-Himalayan Range during four field campaigns in winter monsoon and summer monsoon : Role of pollution pathways. *Atmos. Env.,* 154:200-224.

© 2020 - Kalpana Corporation

Science of Sintering, **52** (2020) 97-107

doi:https://doi.org/10.2298/SOS2001097K

UDK: 546.824; 666.3.019; 665.7.035.8

Effect of Modified Two-step Sintering Approaches on Potassium Tantalum Niobate–Barium Titanate (KTN-BT) Ceramics and Their Dielectric and Piezoelectric Properties

Gambheer Singh Kathait[1*)], M. K. Panda[2], N. S. Panwar[3]

[1,3]Department of Instrumentation Engineering-USIC, SOET, HNBGU Srinagar Garhwal, Uttarakhand, India.

[2]Department of Electrical Engineering, GBPIET, Pauri Garhwal, Uttarakhand, India.

Abstract:

The Potassium Tantalum Niobate-Barium Titanate (KTN–BT) solid solution system ceramics with the composition $0.02K(Ta_{0.5}Nb_{0.5})O_3-0.98BaTiO_3$ were prepared by a two-step sintering mechanism, for different sintering durations. Crystalline and microstructure analyses of the prepared samples were performed. Dielectric and piezoelectric properties were also investigated. Moreover, apparent piezoelectric constant d_{33} was measured using the slope of strain vs. electric field curves for these ceramics. It was observed that the high values of density, electrical conductivity, relative dielectric permittivity (ε_r = 3615.983), piezoelectric coefficient (d_{33} = 315 pm/V) and remnant polarization (P_r = 9.53 $\mu C/cm^2$) were obtained for ceramics prepared through a new variation of the conventional two-step sintering method. Finally, the relationship between sintering mechanism, microstructure and piezoelectricity was discussed for the $0.02K(Ta_{0.5}Nb_{0.5})O_3-0.98BaTiO_3$ ceramics.

Keywords*: Barium titanate; Two-step sintering; Dielectric constant; Piezoelectric property; Microstructure analysis.*

1. Introduction

The $Pb(Zr,Ti)O_3$ based (PZT-based) ferroelectrics have ABO_3 type structure. These ferroelectrics have excellent electrical and dielectric properties. These ceramics have been widely utilized in practical applications for many years. The data on the harmful effect of Pb on health and the environment have been known for a longer period. Hence, there is an increasing demand for environment-friendly lead-free ferroelectric materials for different dielectric and piezoelectric device applications [1-7]. Recently, lead-free ferroelectrics have become highly attractive materials providing a solution to conventional Pb based ferroelectrics [8]. However, compared with PZT ceramics [9] their ferroelectric related properties are very poor, and therefore, it is difficult to use them to replace PZT ceramics.

Ferroelectric materials such as barium titanate ($BaTiO_3$) are of interest in the context of ceramic capacitors and piezoelectric transducers. These materials typically exhibit several phase transformations. For these ceramics, above the Curie point, the crystal symmetry becomes insufficient for piezoelectricity. $BaTiO_3$ is a famous material that was historically widely used as a piezoelectric material before the discovery of PZT. High d_{33} values (350

*) **Corresponding author:** gambhir11186@gmail.com

pCN^{-1}, 460 pCN^{-1} and 788 pCN^{-1}, respectively) were reported in the previous years for the $BaTiO_3$ ceramics [10-12].

Potassium Niobate ($KNbO_3$, KN) ceramics have attracted considerable attention as a candidate material for lead-free piezoelectric applications. The single-crystal $KNbO_3$ (KN) has large piezoelectricity and a high Curie point [13, 14]. However, because of the poor sinterability of $KNbO_3$ ceramics by conventional firing in the air, there are few reports on the electrical properties of $KNbO_3$ ceramics [15-18]. Wainer and Wentworth, in a survey-type study, reported that at room temperature, $BaTiO_3$ ceramics containing 10 % $KNbO_3$ shows a dielectric constant about the same as that of $BaTiO_3$ ceramics [19]. Recently, however, chemically modified $KNbO_3$ and Sodium Niobate ($NaNbO_3$) solid solution ceramics have been reported as new lead-free piezoelectrics with a new morphotropic phase boundary (MPB) and piezoelectric properties similar to those of PZT ceramics [20, 21].

Barium Titanate ($BaTiO_3$, BT) and Potassium Niobate ($KNbO_3$, KN) are ferroelectric oxides having the perovskite structure. A unique feature of this pair of oxides is that $KNbO_3$ is the only known ferroelectric material that shows the same phase symmetries and the same sequence of transitions as $BaTiO_3$. The temperatures corresponding to the cubic-tetragonal, tetragonal-orthorhombic and orthorhombic-rhombohedral transitions are 120, 5 and -90 ^oC for $BaTiO_3$ and 435, 225 and -10 ^oC for $KNbO_3$ [22]. It was reported that a unique ceramic system with a "wide-band MPB region" exists between tetragonal and orthorhombic ferroelectric phases for the Potassium Niobate-Barium Titanate (KN-BT) system [23]. Previous investigations reported that at room temperature, the 0.5BT-0.5KN solid solution ceramics had artificial MPB, i.e., pseudo-MPB [23]. The previously reported phase diagrams for the KN-BT solid solution system showed the paraelectric phase formation at room temperature [24]. The high piezoelectric properties for a BT/KN composite have been attributed to the interfaces between tetragonal BT grains and orthorhombic KN grains [25, 26]. The dielectric constant of 0.8KN/0.2BT ceramics increased as BT grain size increased. This was attributed to the dielectric property of BT grains [27]. There have been a lot of reports on grain size effect for BT ceramics such as the dielectric constant increases as grain size increases for grain size < 1 μm [28-33].

BT and potassium niobate ($KNbO_3$, KN) (BT–KN) nanocomplex ceramics were also prepared by the solvothermal method [34], and it was reported that the ceramics exhibited good ferroelectric property [35]. Further, from the previous results it is proven that for many ceramics, the piezoelectric and dielectric properties are highly influenced by the technique of sintering. Therefore, worldwide various techniques have been reported for the preparation of ceramics, such as rapid-rate sintering, rate-controlled sintering, and two-step sintering [36, 37]. Among these methods, the two-step sintering method is interesting because it can achieve a high ceramic density and produces small grains [36, 37]. It is evident that the sintering density is influenced by the sintering time and also the duration of mechanical activation [38].

In this study, to clarify the role of sintering duration on microstructure, dielectric properties and piezoelectric properties in the case of the two-step sintering method, a new approach of the method was applied and compared to the conventional two-step sintering method. For the objective, the $0.02K(Ta_{0.5}Nb_{0.5})O_3–0.98BaTiO_3$ ceramics with different sintering duration were prepared by a conventional and modified two-step sintering method and the correlation of obtained microstructures with dielectric and piezoelectric properties were done. A particular attention was paid to the relationship between duration of sintering and the piezoelectric properties.

2. Materials and Experimental Procedures

In order to obtain fine-grained and dense $0.02K(Ta_{0.5}Nb_{0.5})O_3–0.98BaTiO_3$ ceramics, a two-step sintering method reported for BT ceramics by Karaki et al. was used [18]. Barium

Carbonate ($BaCO_3$), Titanium Dioxide (TiO_2), Potassium Carbonate (K_2CO_3),Tantalum Pentaoxide (Ta_2O_5) and Niobium Pentaoxide (Nb_2O_5) were taken to form the composition $0.02K(Ta_{0.5}Nb_{0.5})O_3–0.98BaTiO_3$. The conventional solid-state reaction method was used to prepare the ceramics. Reagent grade Barium Carbonate ($BaCO_3$), Titanium Dioxide (TiO_2), Potassium Carbonate (K_2CO_3), Tantalum Pentaoxide (Ta_2O_5) and Niobium Pentaoxide (Nb_2O_5) of high purity (≥ 99.0 %) were used as starting materials. The raw material was dried at 150 ^oC for one hour, weighed in stoichiometric proportions. After weighing the material, manual grinding in acetone for 2 h (wet) and 4 h (dry) was carried out. The ground powder was calcinated at 1000^oC for 6 h in an alumina crucible. The calcinated powder was ground for half an hour. Pellets of 8 mm diameter were prepared at a pressure of 0.25 GPa and sintered at 1240 ^oC by a two-step sintering method. These pellets were prepared by three approaches. First (TS 1) and second (TS 2) approaches are conventional two-step sintering methods for 6 h and 12 h respectively. For the third (TS 3) approach second sintering was done according to the program shown in Fig. 1. The temperature was set at 1200 °C for 10 h and then changed to 1240 ^oC for 2 h. The $0.02K(Ta_{0.5}Nb_{0.5})O_3–0.98BaTiO_3$ ceramics with various microstructures were prepared. Sintered pellets were taken for XRD, SEM, LCR and Piezo analysis.

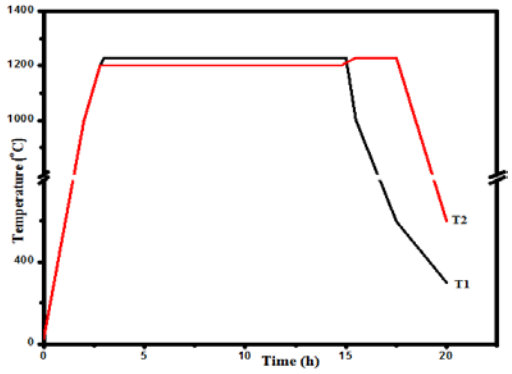

Fig. 1. A schematic diagram of the two-step sintering program for TS 3 approach for the $0.02K(Ta_{0.5}Nb_{0.5})O_3–0.98BaTiO_3$ ceramics.

The crystalline orientation was measured by X-ray diffraction (XRD), on an X-Pert PANalytical diffractometer, model PW40, using a fixed divergence1/2^o slit, a Cu W/Si mirror, a solar slit, and a 10 mm mask as incident optics and a parallel plate collimator, a solar slit and a proportional detector as diffracted beam optics. The X-RAY diffractometer with a CuKα radiation source (λ=1.54059 Å) was operated at a voltage of 45 kV and a current of 40 mA. The XRD results indicate that only pure perovskite structure exists for all $0.02K(Ta_{0.5}Nb_{0.5})O_3–0.98BaTiO_3$ samples, obtained with different sintering durations. Both the faces of sintered pellets were coated with silver paste for electrical connection. The coated pellets were dried for 1 h at room temperature (25 ^oC). A computer-controlled system, including LCR meter (Fluke, PM6306) was used to measure dielectric constant, dielectric loss and thermal conductivity for different temperature and frequency. The LCR meter was used in conjunction with a furnace. By using the LCR meter software dielectric constant and dielectric loss was measured with temperature variation, for the frequency region of 1 kHz to 1 MHz. The particle morphology and element atomic % of the ceramic were examined by scanning electron microscopy with EDAX (SEM-EDAX) using model EVO 18 Special Edition (Switzerland), manufactured by ZEISS. The silver-coated pellets were taken for piezoelectric coefficient d_{33} measurement and strain analysis using a Piezo Loop Tracer, model aixPES manufactured by aixACT systems GamH. For 1Hz frequency, the electric field was varied from low to high voltage and corresponding d_{33} and strain were measured.

3. Results and Discussion

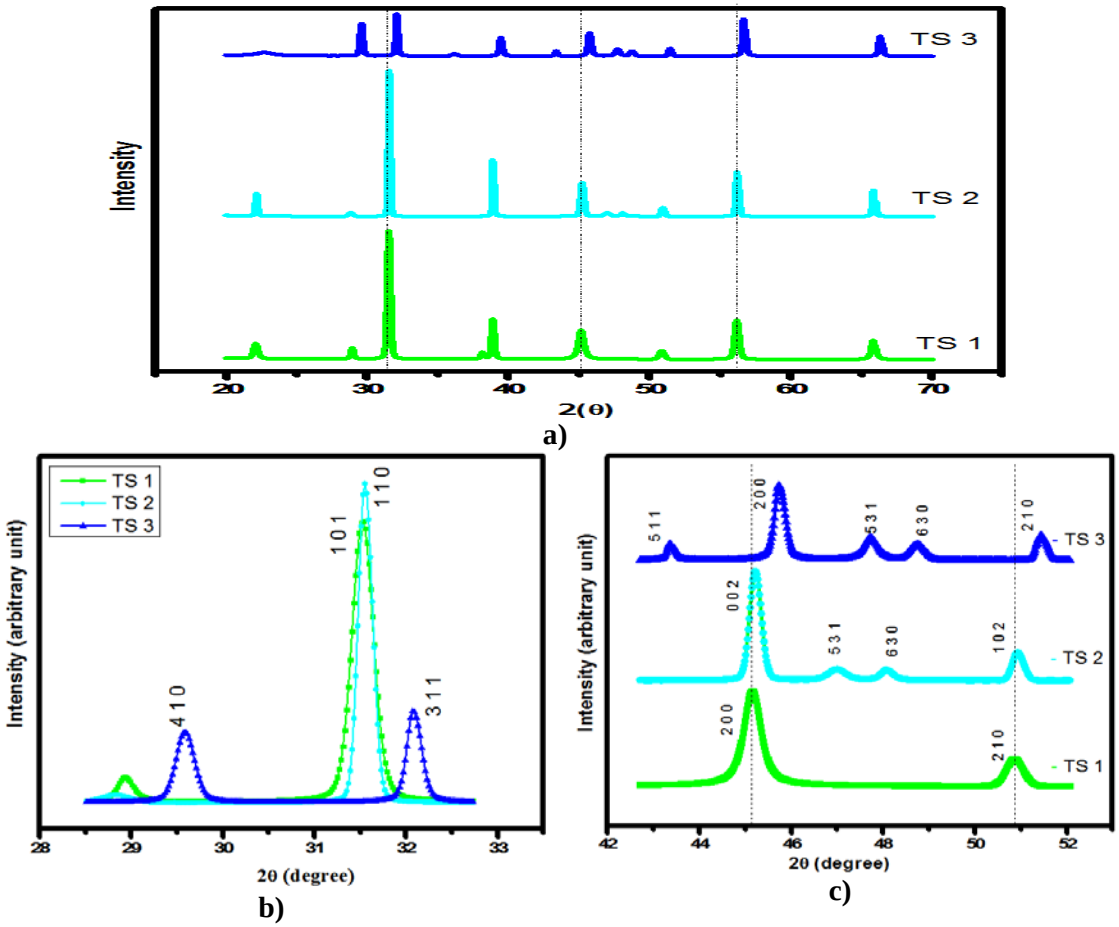

Fig. 2. (a),(b) and (c) XRD patterns of $0.02K(Ta_{0.5}Nb_{0.5})O_3–0.98BaTiO_3$ ceramics for different two-step sintering approaches TS 1, TS 2 and TS 3.

In the present work, the two-step sintering method was applied for fabrication of the $0.02K(Ta_{0.5}Nb_{0.5})O_3–0.98BaTiO_3$ ceramics, i.e. the samples were sintered at 1240 ^oC for 6 h, 12 h and 1200 ^oC for 10 h with1240 ^oC for 2 h, followed by cooling to room temperature. The XRD patterns of all obtained $0.02K(Ta_{0.5}Nb_{0.5})O_3–0.98BaTiO_3$ samples are shown in Fig. 2(a), (b) and (c). It can be observed from Fig. 2(a) that the diffraction peaks are within the 2θ range from 20^o to 70^o. The XRD result is consistent with the work done by S. Wada et al. [23] who synthesized KN-BT by a solid-state technique. The values of calculated sub-cell parameters closely agree with the reported results [23, 24]. The ceramic with sintering temperature 1240 ^oC shows (1 0 1)/(1 1 0) peak splitting around 2θ = 31.5^o, confirming the tetragonal symmetry as shown in Fig. 2(b). From Fig. 2(c) it is evident that the change in the sintering approach, from TS 1 to TS 2 and finally to TS 3, causes the shift of the (2 0 0/0 0 2) peak towards higher diffraction angles. The crystalline structure was found tetragonal with perovskite phases for all samples with secondary phases for samples prepared by TS 2 and TS 3 approaches. For the ceramics prepared by TS 1 approach, the lattice constants have not changed significantly to that of $BaTiO_3$ according to JCPDF file reference code 01-074-4540.

TS 2 approach also contributes to a pure tetragonal symmetry as per JCPDF file reference code 01-074-1958. However, between 46^o and 48^o, two new peaks were observed, which becomes significantly noticeable in TS 3.The TS 3 approaches also results in a

tetragonal phase as per JCPDF file reference code 01-075-1169. Few new significant peaks were observed at around 29.5°, 47.5° and 48.5° as shown in Fig. 2(b) and 2(c), that correspond to (4 1 0), (5 3 1) and (6 3 0) respectively as per JCPDF file reference code 00-043-0631. The new peak was corresponds to the secondary phase due to deformation such as melting of grains. In Fig. 2(b) the peaks (101/110) got split into peaks (4 1 0) and (3 1 1) at 29.59 ° and 32.07 ° respectively. The lattice constant and c/a ratio were calculated using Rietveld method through HighScore Plus software. The decrease of c/a ratio ratios resulted in the effective enhancement of the density for TS 1and TS 3. For TS 2 method also lower c/a ratio was obtained, but the interfaces might be diffused between KN and BT grains that decreased the dielectric and piezoelectric properties. For TS 3 method large grain size resulted in small grain boundaries. The small grain boundaries caused less energy loss through the grain boundaries that resulted in enhanced properties. Another origin of dielectric and piezoelectric enhancement for the $0.02K(Ta_{0.5}Nb_{0.5})O_3–0.98BaTiO_3$ ceramics can be considered as distorted interface region between BT-rich tetragonal and KN-rich orthorhombic grains [25]. The average grain size was measured using the SEM for ceramic prepared by TS 1, TS 2 and TS 3 method.

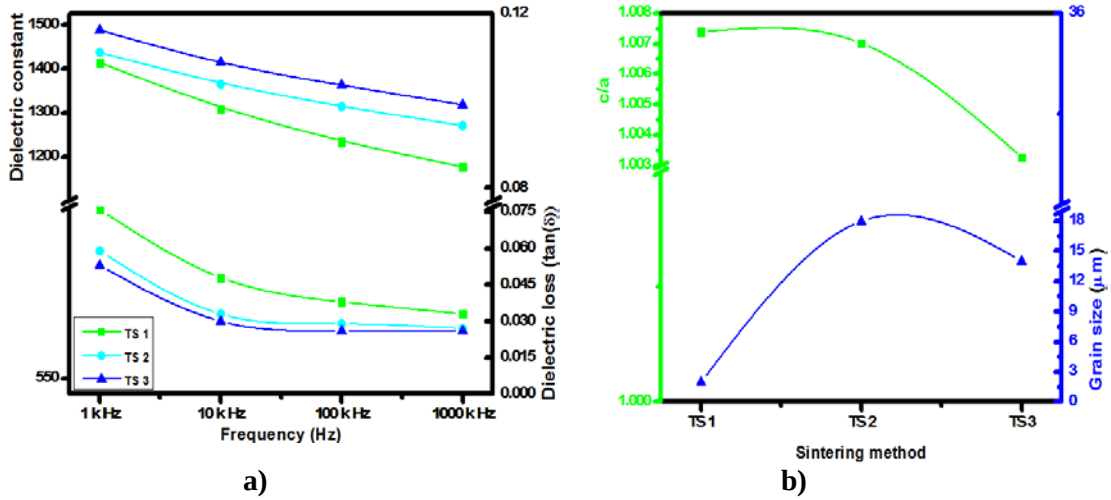

Fig. 3. (a) Dielectric constant and dielectric loss (at room temperature) variation with frequency and (b) c/a ratio and grain size measured for TS 1, TS 2 and TS 3 sintering methods

Fig. 3 (a) indicates that the ceramics prepared by TS 1, TS2 and TS 3 methods have a similar dielectric response for low to high frequency variations. The TS 3 approach results in an optimized dielectric constant and low loss at high frequency. The TS 3 method of two-step sintering leads to a smaller c/a ratio and a larger grain size as shown in Fig. 3(b). The secondary phase resulted in the shift of X-ray diffraction peak (2 0 0/0 0 2) towards higher diffraction angles. The right shifting of the intensity peak in XRD patterns may be due to a smaller c/a ratio and distorted interface region for TS 3 method. The interfaces might be diffused between KN and BT grains, which can be understood with the SEM image.

The cross-sectional morphology of $0.02K(Ta_{0.5}Nb_{0.5})O_3–0.98BaTiO_3$ ceramics sintered with TS 1, TS 2 and TS 3 approaches are shown in Fig. 4(a), (b) and (c). With the increase in sintering duration from 6 h to 12 h, an increase in the grain size and the microstructures of uniformly distributed large grains was observed. For ceramics prepared by TS 1 approach, small grains with grain size around 2 μm were found as shown in Fig. 4(a). Increasing the two-step sintering duration from 6 h to 12 h, large grains with grain size around 18μm were observed as shown in Fig. 4(b). The melting of a few grains was also observed in the microstructure. For the TS 3 approach of sintering, an average grain size (~14 μm) with a

more uniform microstructure was found. The average grain size of the samples for the TS 3 approach was in a range of ~12-15 μm. Fig. 5(a) indicates an increase of dielectric constant in the case when the average grain size reaches the value of ~ 14 μm. Enhancement of the dielectric properties with enlargement of the average grain size is in accordance with the previous results [27]. This result suggests that the modified two-step sintering approach TS 3 has a significant effect on the microstructure and uniformly distributed large grains of the KTN-BT ceramics. For the TS 2 sintering approach, the grain size increases above 18μm as shown in Fig. 4(b), also it seems as the grains are melting. That results in an abnormal microstructure. Also, it was revealed that both $BaTiO_3$ and $CaZrO_3$ can induce abnormal grain growth behavior in KNN ceramics [39, 40]. The addition of KTN caused abnormal grain growth. Compared with pure NKN ceramics, the addition of KTN promoted grain growth, but not as considerably as NKN. It is suggested that the rapid grain growth in the case of KTN is due to the low melting point (1050 ^{o}C) of KTN. For the same reason, abnormal grain growth inhibited sintering to some extent. During the sintering of the samples at 1240 °C for 12 h or more, large amounts of liquid phase seems to be formed, which lead to the exaggerated grain growth and melt behavior. However, the weight loss of samples is largely owing to the evaporation of alkali oxides.

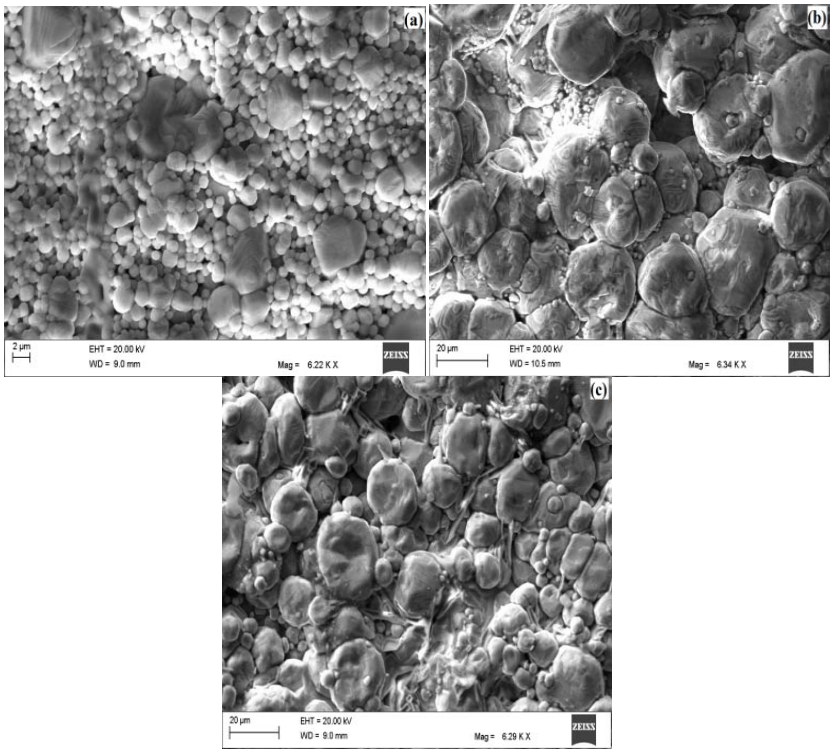

Fig. 4. Selected SEM micrographs of $0.02K(Ta_{0.5}Nb_{0.5})O_3–0.98BaTiO_3$ fabricated by different two-step sintering approaches (a) TS 1 (b) TS 2 and (c) TS 3.

Samples prepared by TS 3 approach were found most dense, among the prepared compositions. The variation of the grain size and density with different sintering approaches are shown in Fig. 5(a). The density of prepared samples is 3.82, 4.22 and 4.393 g/cm^3 for sintering approach TS 1, TS 2 and TS 3 respectively. The density and porosity greatly affect the dielectric properties of the samples [41, 42]. During sintering, the process of grain growth and densification requires material transport, which may occur via various phenomena such as surface diffusion, grain boundary diffusion, lattice diffusion, viscous flow and evaporation [43]. The SEM result shows the melting behavior of grains that may be correlated with the

grain boundary diffusion and a low melting point of KTN may result in the viscous flow. Also as the sintering duration increases the evaporation of alkali ion takes place, which is evident from the SEM-EDAX results. Fig. 5 (b) indicates the value of dielectric constant and the dielectric loss tangent for different two-step sintering approaches. It is evident from the previous results that the two-stage sintering was used to activate different sintering mechanisms in different temperature ranges and to increase grain growth and enhance the densification mechanism. Improvement in microstructure and density was observed using this method. Yu Huan et al. [44] reported similar observations for two-stage sintered BT ceramics. The dielectric constant and losses significantly change with the variation of sintering duration. As shown in Fig. 5(b) dielectric constant and loss tangent were found maximum for TS 3 method.

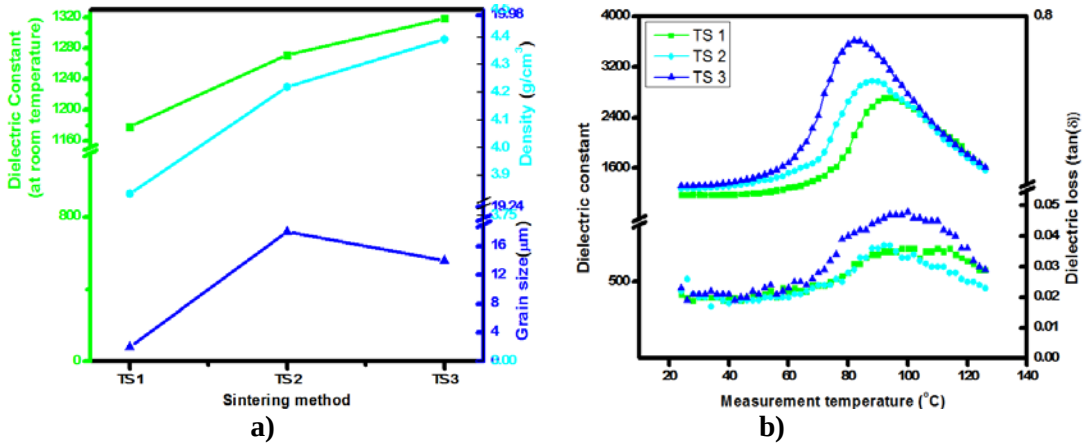

Fig. 5. (a) Dielectric constant at room temperature, density and grain size variation with different sintering methods (b) Variation of dielectric constant (ε) and dielectric loss (tanδ) with temperature.

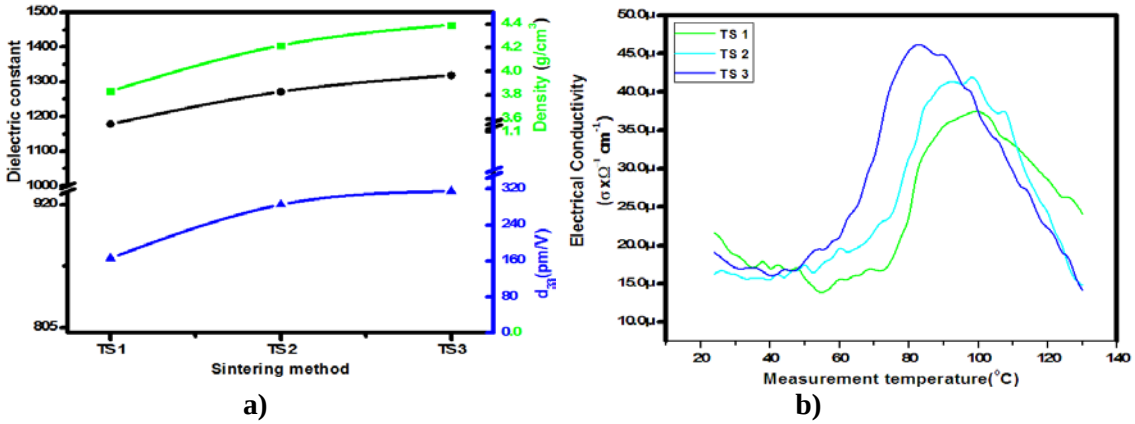

Fig. 6. (a) Dielectric constant, density and d_{33} measured at room temperature versus applied sintering approach (b) Electrical conductivity for different sintering approach versus temperature.

It has been observed that the alkali ion escaping is significantly higher than oxygen escaping (Table I). Due to the excess of the vacancies at A-site, with respect to that at O site, p-type conduction is expected to be present in the $0.02K(Ta_{0.5}Nb_{0.5})O_3–0.98BaTiO_3$. If the escaping of the alkali ions is more pronounced, a larger number of 'holes' will be available for conduction. According to that, with an increase in the A-site vacancy concentration in the

samples obtained by TS 2 and TS 3 approaches (Table I) a distinct conductivity maximum was observed, as shown in Fig. 6(b). Also, the electrical conductivity follows the dielectric and piezoelectric patterns with measurement temperatures for ceramics prepared by TS 1, TS 2 and TS 3 approach. As shown in table-1, it is evident that the atomic escaping of Potassium and Oxygen vacancy follows the pattern of grain size for different sintering approaches and these results are in support of previous results [45].

Tab. I SEM-EDAX quantitative analysis of $0.02K(Ta_{0.5}Nb_{0.5})O_3–0.98BaTiO_3$ for different two-step sintering approaches TS 1, TS 2 and TS 3.

	Two-step sintering for 6h (TS 1)		**Two-step sintering for 12h (TS 2)**		**Modified Two-step sintering for 12h (TS 3)**	
Element	**Weight %**	**Atomic %**	**Weight%**	**Atomic %**	**Weight%**	**Atomic%**
O	25.17	66.98	22.53	63.24	24.59	65.81
K	0.26	0.29	0.00	0.00	0.07	0.08
Ta	3.54	0.83	1.75	0.43	1.47	0.35
Nb	1.05	0.48	0.00	0.00	0.02	0.01
Ba	53.17	16.48	56.87	18.60	55.42	17.28
Ti	16.80	14.93	19.13	17.93	18.43	16.47

At room temperature, the bipolar strain-electric field (S–E) and polarization–electric field (P–E) curves were measured for $0.02K(Ta_{0.5}Nb_{0.5})O_3–0.98BaTiO_3$ ceramics. The electric field was varied at frequency of 1 Hz for S-E and P-E response as shown in Fig. 6(a) and (b), respectively. Furthermore, the remnant polarization (P_r), the maximum polarization (P_{max}), the coercive field (E_c), the maximum strain (S_{max}), and the normalized strain coefficient ($d_{33}=S_{max}/E_{max}$) values are also listed in Table II.

Tab. II Parameters obtained from dielectric, ferroelectric and piezoelectric study of $0.02K(Ta_{0.5}Nb_{0.5})O_3–0.98BaTiO_3$ ceramics.

S. No.	**Sintering Method**	**Sintering Duration**	**T_c (^oC)**	**P_r ($\mu C/cm^2$)**	**S_{max} (%)**	**E_c (kV/cm)**	**d_{33} (pm/V)**
1	Two-step (TS 1)	6 h	94	4.85	0.017	4.88	166
2	Two-step (TS 2)	12 h	88	6.25	0.022	5.25	285
3	Two-step (TS 3)	10 h +2 h	84	9.53	0.031	6.18	315

It is observed that a large strain seems to exist for the sintering method TS 3. Slight asymmetry is observed in the (S-E) loops at TS 3 as shown in Fig. 7(a), which may be due to the internal field induced by the presence of defects caused by the malleable nature of KTN and vacancy due to escaping of alkali ion [46]. However, the addition of a stable ferroelectric end-member BT in the KTN solid solution should result in increased domain stability. It can be seen from the Table II that the P_r and E_c increase considerably, as the amount of BT increases for two-step sintering method TS 2, compared to the values obtained in the TS 1 approach. P_r and E_c further increase with the TS 3 approach as shown in Fig. 7(b), irrespective of the amount of BT. It shows that all the P–E loops are well saturated, as shown in Fig. 7(b).

The bipolar strain-electric field (S–E) loops also showed a normal butterfly shape with increased negative strain. It can be seen that low-field piezoelectric properties exhibited a strong dependence on the sintering approach applied in $0.02K(Ta_{0.5}Nb_{0.5})O_3–0.98BaTiO_3$ ceramics rather than grain size and amount of BT.

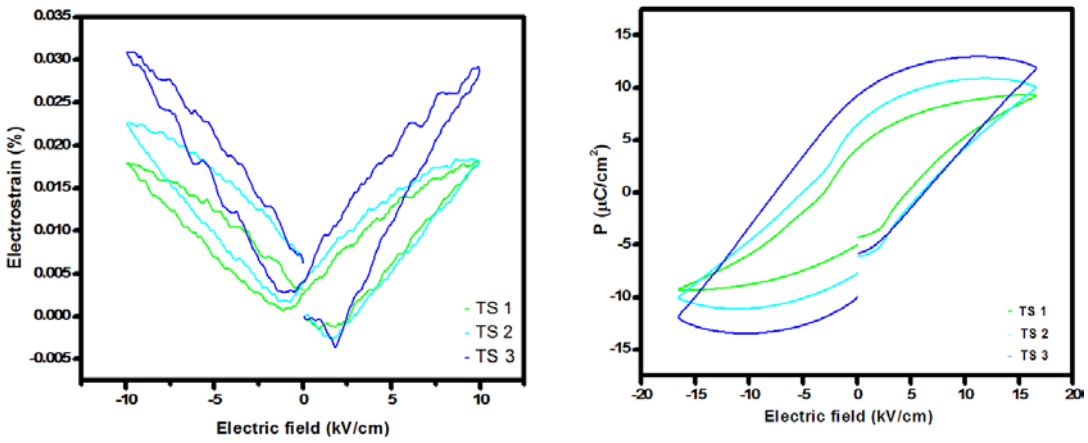

Fig. 7. (a) S-E (strain-electric field) curves and (b) Polarization–electric field hysteresis loops of the $0.02K(Ta_{0.5}Nb_{0.5})O_3–0.98BaTiO_3$ ceramics for different two-sintering approaches.

4. Conclusion

The $0.02K(Ta_{0.5}Nb_{0.5})O_3–0.98BaTiO_3$ lead-free piezoelectric ceramic was prepared by the conventional solid-state reaction method through two-step sintering approaches for different durations. The ceramic exhibited a fine grain growth with relatively uniform particle size. A typical ferroelectric nature has been observed for prepared samples. The high volatility of K results in p-type conduction that enhances the electrical conductivity, dielectric and piezoelectric properties. For the first time, for ceramics sintered at 1240 ^oC with a modified two-step sintering TS 3 approach, the excellent value of piezoelectric coefficient d_{33} = 315 pm/V and saturation polarization P_{sat} = 11.86 μC/cm^2 were found and it is close to the theoretical value. Large value of remnant polarization P_r = 9.53 μC/cm^2 with coercive field E_c = 6.18 kV/cm has been achieved. The strain-electric field measurements revealed the sprout shape nature with a maximum remnant strain of 0.031 %.

Acknowledgments

The authors are thankful to the Department of Instrumentation Engineering-USIC, SOET, HNB Garhwal University, Srinagar (Garhwal), for providing laboratory facilities.

5. References

1. G. Li, Z. Chen, X. Sun, L. Liu, L. Fang, B. Elouadi, Mater. Res. Bull., 65 (2015) 260.
2. Z. Chen, G. Li, X. Sun, L. Liu, L. Fang, Ceram. Int., 41 (2015) 11057.
3. S. Zheng, E. Odendo, L. Liu, D. Shi, Y. Huang, L. Fan, J. Chen, L. Fang, B. Elouadi, J. Appl. Phys., 113 (2013) 094102.
4. J.M. Deng, X.J. Sun, S.S. Liu, L.J. Liu, T.X. Yan, L. Fang, B. Elouadi, J. Adv. Dielectr., 06 (2016) 1650009.
5. L.J. Liu, M.X. Wu, Y.M. Huang, L. Fang, H.Q. Fan, Mater. Res. Bull., 46 (2011) 1467.
6. C. Li, H. Xiang, J. Chen, L. Fang, Ceram. Int., 42 (2016) 11453-11458.

7. C. Li, X. Wei, L. Fang, H. Yan, Michael J. Reecec, Ceram. Int., 41 (2015) 9923-9930.
8. Setter, N. Piezoelectric Materials in Devices; EPFL Swiss Federal Institute of Technology: Lausanne, Switzerland, 2002.
9. B. Jaffe, W. R. Cook, Jr., and H. Jaffe: Piezoelectric Ceramics, Academic Press, New York, 1971.
10. Takahashi H, Numamoto Y, Tani J, Matsuta K, Qiu J and Tsurekawa S, Japan. J. Appl. Phys., 45 (2006) L30
11. Karaki T, Yan K, Miyamoto T and Adachi M, Japan. J. Appl. Phys., 46 2007 L97
12. Wada S, Takeda K, Muraishi T, Kakemoto H, Tsurumi T and Kimura T, Japan J. Appl. Phys., 46 (2007) 7039.
13. K. Nakamura, T. Tokiwa, and Y. Kawamura: J. Appl. Phys. 91 (2002) 9272.
14. S. Wada, A. Seike, and T. Tsurumi: Jpn. J. Appl. Phys. 40 (2001) 5690.
15. B. Jaffe, W. R. Cook, and H. Jaffe: Piezoelectric Ceramics, Academic Press, New York, 1971.
16. S. Tashiro, H. Nagamatsu, and K. Nagata: Jpn. J. Appl. Phys. 41 (2002) 7113.
17. M. Uniyal, K. Singh, S. Bhatt, R. P. Pant, D. K. Suri, and B. S. Semwal: Int. J. Pure Appl. Phys. 41 (2003) 305.
18. P. Dubernet and J. Ravez: Ferroelectrics 211 (1998) 51.
19. Eugene Wainer and Chandler Wentworth, Niobate and Tantalate Dielectrics, J . Am. Ceram. Soc., 5 (1952) 207-14
20. Y. Saito, H. Takao, T. Tani, T. Nonoyama, K. Takatori, T. Homma, T. Nagata, and M. Nakamura, Nature, 432 (2004) 84.
21. Y. Guo, K. Kakimoto, and H. Ohsato, Appl. Phys. Lett., 85 (2004) 4121.
22. Franco Jona and G. Shirane, Ferroelectric Crystals. Perganion Press, Inc., New York, 1962.
23. S. Wada, M. Nitta, N. Kumada, D. Tanaka, M. Furukawa, S. Ohno, C. Moriyoshi, and Y. Kuroiwa, Jpn. J. Appl. Phys., 47 (2008) 7678-7684.
24. R. J. Bratton and T. Y. Tien, Phase Transitions in the System BaTi03-KNb03, J. Am. Ceram. Soc., 50 (1967) 90-93.
25. S.Wada, S. Shimizu, P. Plupan, N. Kumada, D. Tanaka, M, Furukawa, C. Moriyoshi and Y. Kuroiwa, Jou. of the Cer. Soc. of Japan, 118 (2010) 691-695.
26. S. Wada, M. Nitta, N. Kumada, D. Tanaka, M. Furukawa, C. Moriyoshi and Y. Kuroiwa, Key Eng. Mater. (2009) in press.
27. Kenta Yamashita, Ichiro Fujii, Kouichi Nakashima, Nobuhiro Kumada, Yoshihiro Kuroiwa, Tetsuhiro Takahashi, Takeo Tsukada and Satoshi Wada, Key Engineering Materials**,** 566 (2013) 34-37.
28. Y. Kigoshi, S. Hatta, T. Teranishi, T. Hoshina, H.Takeda, O. Sakurai and T. Tsurumi, Key Eng. Mater., 445 (2010) 27-30.
29. X. Wang, R. Chen, Z. Gui, L. Li, Materials Science and Engineering, B99 (2003) 199-202.
30. M. H. Fray, Z. Xu, P. Han and D.A. Payne, Ferroelectrics, 206 (1998) 337.
31. A. Polotai, A. Ragulya and C. Randoll, Ferroelectrics, 288 (2003) 93.
32. Y. Park, Y.H. Kim, H.G. Kim, Materials Letters, 28 (1996) 101-106
33. G. Arlt, D. Hennings and G. De With, Jpn. J. Appl. Phys., 58 (1985) 1619.
34. S.Wada, S. Shimizu, K.Yamashita, I. Fujii, K. Nakashima, N. Kumada, Y. Kuroiwa, Y. Fujikawa, D. Tanaka, M. Furukawa, Jap. Jou. of App. Physics, 50 (2011) 09NC08.
35. I. Fujii, S. Shimizu, K. Yamashita, K. Nakashima, N. Kumada, C. Moriyoshi, Y. Kuroiwa, Y. Fujikawa, D. Tanaka, M. Furukawa, S. Wada, Appl. Phy. Lett., 99 (2011) 202902.
36. X.-H.Wang, X.-Y. Deng, H. Zhou, L.T. Li, and I.W. Chen, J. Electroceram., 21 (2008) 230-233.

37. S. E. Porozova, A. A. Gurov, M. N. Kachenuk, A. A. Smetkin, O. Yu. Kamenschikov, Science of Sintering, 49 (2017) 99-105.
38. V. V. Petrovic, H. Milosevic, V. B. Pavlovic, Science of Sintering, 45 (2013) 133-139.
39. K.Wang, F. Z. Yao, W. Jo, D. Gobeljic, V.V. Shvartsman, D.C. Lupascu, J.F. Li, J. Rödel, Adv. Funct. Mater. 23 (2013) 4079-4086.
40. H.Y. Park, C.W. Ahn, H.C. Song, J.H. Lee, S. Nahm, K. Uchino, H.G. Lee, H.J. Lee, Appl. Phys. Lett., 2006 89 062906.
41. Q. Xu, X.F. Zhang, H.X. Liu, W. Chen, M. Chen, B.H. Kim, Mater. Des., 32 (2011) 1200-1204.
42. Satoshi Wada1, Momoyo Nitta1, Nobuhiro Kumada1, Daisuke Tanaka, Masahito Furukawa, Chikako Moriyoshi and Yoshihiro Kuroiwa, Key Engineering Materials, 422 (2010) 34-37.
43. B. Malic, J. Koruza, J. Hrescak, J. Bernard, K. Wang, J.G. Fisher, A. Bencan, Materials 8 (2015) 8117-8146.
44. Yu Huan, Xiaohui Wang, Jian Fang, and Longtu Li, J. Am. Ceram. Soc., 96 (2013) 3369-3371.
45. Venkata Raman, Mudinepalli, Leng Feng, Wen-Chin Lin, B. S. Murty, Journal of Advanced Ceramic, 4 (2015) 46-53.
46. Zheng.J.X, Liu.Y.J, Peng.F.J, Liu.X, Gong.Q.Y, Zhou.S.K, Huang.H.D, Thin Solid Films, 548 (2013) 118-124.

Сажетак: *Чврсти раствор калијум тантал ниобат-баријум титанатне керамике (KTN–BT) састава* $0.02K(Ta_{0.5}Nb_{0.5})O_3{-}0.98BaTiO_3$ *је припремљен двостепеним синтеровањем, са различитим временима задржавања. Фазни састав и микроструктурна анализа су урађене на припремљеним узорцима. Диелектрична и пиезоелектрична својства су такође испитивана. Привидна пиезоелектрична константа* d_{33} *је измерена из нагиба криве напрезање у функцији електричног поља. Добијене су високе вредности густине, електричне проводљивости, релативне диелектричне пермитивности (*ε_r *= 3615.983), пиезоелектричног коефицијента (*d_{33} *= 315 pm/V) и заостале поларизације (*P_r *= 9.53 μC/cm*^{2}*) за керамику припремљену употребом нових варијација конвенционалног двостепеног синтеровања. Коначно, обрађене су релације између механизма синтеровања, микроструктуре и пиезоелектричности за* $0.02K(Ta_{0.5}Nb_{0.5})O_3{-}0.98BaTiO_3$*керамику.*

Кључне речи*: баријум-титанат, двостепено синтеровање, диелектрична костанта, пиезоелектрична својства, микроструктурна анализа.*

© 2020 Authors. Published by association for ETRAN Society. This article is an open access article distributed under the terms and conditions of the Creative Commons — Attribution 4.0 International license (https://creativecommons.org/licenses/by/4.0/).

Ferroelectrics

ISSN: 0015-0193 (Print) 1563-5112 (Online) Journal homepage: https://www.tandfonline.com/loi/gfer20

Electrical properties of, $Na_{1-0.315}K_{0.315}Nb_{1-y}Ta_yO_3$ ($0 \le y \le 0.05$) system

Jyotsana Negi, Surendra Singh & N. S. Panwar

To cite this article: Jyotsana Negi, Surendra Singh & N. S. Panwar (2020) Electrical properties of, $Na_{1-0.315}K_{0.315}Nb_{1-y}Ta_yO_3$ ($0 \le y \le 0.05$) system, Ferroelectrics, 558:1, 117-127, DOI: 10.1080/00150193.2020.1735896

To link to this article: https://doi.org/10.1080/00150193.2020.1735896

Published online: 04 May 2020.

Submit your article to this journal

Article views: 5

View related articles

View Crossmark data

Full Terms & Conditions of access and use can be found at
https://www.tandfonline.com/action/journalInformation?journalCode=gfer20

FERROELECTRICS
2020, VOL. 558, 117–127
https://doi.org/10.1080/00150193.2020.1735896

Taylor & Francis
Taylor & Francis Group

Check for updates

Electrical properties of, $Na_{1-0.315}K_{0.315}Nb_{1-y}Ta_yO_3$ $(0 \leq y \leq 0.05)$ system

Jyotsana Negi[a], Surendra Singh[a], and N. S. Panwar[a]

[a]Department of Physics, HNB Garhwal University, Srinagar, Garhwal, India; [b]University Science Instrumentation Centre, HNB Garhwal University, Srinagar, Garhwal, India

ABSTRACT

$Na_{0.685}K_{0.315}Nb_{1-y}Ta_y\ O_3$ (where $y = 0$, 0.01, 0.02, 0.03, 0.04, 0.05) based ceramics were synthesized by the conventional solid-state reaction process. The effects of (Ta) – doping on the phase structure and electrical properties of ($NKNTaO_3$) were observed. The cell parameters were refined by High Score Plus software, using Rietveld method, The monoclinic Pm(6) space group was chosen in these refinements. X-ray diffraction analysis shows that the crystal structure of the ceramics, without and with Ta-doping possessed monoclinic symmetry. Among the prepared compositions, a break in the XRD peaks shifting tendency was observed at $y = 0.03$, and also maximum dielectric permittivity, loss tangent and electrical conductivity observed at the composition with $y = 0.03$.

ARTICLE HISTORY
Received 26 July 2019
Accepted 3 November 2019

KEYWORDS
XRD; dielectric permittivity; loss tangent; electrical conductivity

1. Introduction

The Sodium Potassium Niobate (NKN) based ceramics are considered as one of the promising lead-free candidates for its high-piezoelectric properties comparable to PZT-based ceramics [1–3]. Lead-based piezoelectric ceramics such as $Pb(Zr, Ti)O_3$ (PZT) have been widely used in sensors, transducers, actuators, and other important devices for decades. Because of the toxicity of lead, lead-free piezoceramics have received increasing attention from the view point of environment in recent years. Sodium Potassium niobate (NKN) ceramics have begun to attract much attention because Ta and Li substitution for a K, Na or Nb site improved the dielectric and piezoelectric properties of NKN ceramics [4–6]. The more general system (K, Na, Li) (Nb, Ta, Sb)O_3 seems to be a big breakthrough made by Saito et al.[1], who obtained high d_{33} (416 pC/N) in textured NKN-based ceramics as a promising candidate for lead-free piezoelectric ceramics. According to Ahtee & Glazer (1976) [7], the boundary at $x = 0.5$ is from monoclinic symmetry (Pm) on the Na-rich side. Hrešcak et al. reported that even the choice of the Nb_2O_5 precursor (orthorhombic or monoclinic polymorph) can influence the homogeneity of the NKN solid solution [8].This issue is particularly pronounced in complex solid solutions, where in pursuit of a higher piezoelectric coefficient d_{33}, compositions on phase boundaries are constructed by introducing additional elements as substituent's on A- and B-sites of the NKN perovskite lattice [9–11]. It was found that

CONTACT Jyotsana Negi jyotsana.jn42@gmail.com
© 2020 Taylor & Francis Group, LLC

the inhomogeneous distribution of the A-site (K, Na) and B site (Nb, Ta) cations is correlated [12] In the case of the Li- and Ta-modified in NKN (NKLNT) solid solution. The authors demonstrated that the inhomogeneity of the cations in the pre calcination steps actually determines the compositional fluctuation in the sintered ceramics and results in inferior dielectric, ferroelectric, and piezoelectric properties. The use of pre-reacted $(Nb,Ta)_2O_5$ solid solution [12] or individual perovskite components [13] in the initial mixture have been suggested as efficient methods to achieve compositionally well-homogenized ceramics, but these modifications also require several additional processing steps.

In previous communication [14] we observed structural anomaly and lowest values of dielectric permittivity, loss tangent and electrical conductivity, indicated an MPB-like composition, at $x = 0.315$, in $Na_{1-x}K_xNbO_3$ system. In present work, tantalum (Ta) were doped in $Na_{0.685}K_{0.315}Nb_{1-y}O_3$ $(0 \leq y \leq 0.05)$ ceramics by forming a new solid solution to get better electrical properties. Present compositions (x values) were closure to the previously reported work. The effects of additives on the structural behavior and electrical properties have been studied.

2. Material preparation and characterization

2.1. Preparation

Pellet samples of $Na_{0.685}K_{0.315}Nb_{1-y}Ta_yO_3$ $(0 \leq y \leq 0.05)$ were prepared by solid-state reaction method, using the powders of Na_2CO_3, K_2CO_3, Nb_2O_5, and Ta_2O_5 (all with purity $\geq$ 99.9%, from MERK, Germany). At first the raw powders were separately dried, at 200 °C for 2 h, to remove the absorbed moisture and weighed in stoichiometric ratio. The weighed powders were dry mixed and ground for 4 h, and then wet mixed with acetone and ground for 2 h, using agate mullet mortar and pestle. The mixture was calcined in an alumina crucible, in ambient atmosphere, at 900 °C, for 4 h, to remove the present carbon dioxide. When the furnace was switched off and cooled to room temperature the calcined mixture was weighed to ensure the complete carbon dioxide removal from the mixture. The calcined mixture was further ground for half an hour and then pressed into pellets of 8 mm diameter and about 2 mm thickness, using 0.4 GPa uniaxial pressure. These pellets, with $y = 0$, 0.01, 0.02, 0.03, 0.04 and 0.05 were sintered, each composition for 4 h in the order of their melting points, at 1170, 1165, 1160, 1156, and 1152 °C, respectively, in a high temperature muffle furnace. The crystal structure of the sintered samples was examined using an X-ray diffractometer (PANalytical X'PERT PRO) with Cu K_α radiation (wavelength, $\lambda = 1.540598$ Å). Surface morphology, grain size and energy dispersive X-ray analysis (EDAX) of the prepared pellets were studied using a scanning electron microscope (CARL ZEISS, MA15/EVO18). For dielectric measurements sintered pellets were electroded, using air drying silver paste, in parallel- plate capacitor configuration. Temperature, frequency and composition $(0 \leq y \leq 0.05)$ dependences of dielectric permittivity (ε), loss tangent (tan δ) and electrical conductivity (σ) of the prepared samples are measured in metal-insulator-metal (MIM) configuration, using an RCL meter (Fluke–PM6306); and a temperature controller having an ±1 °C accuracy.

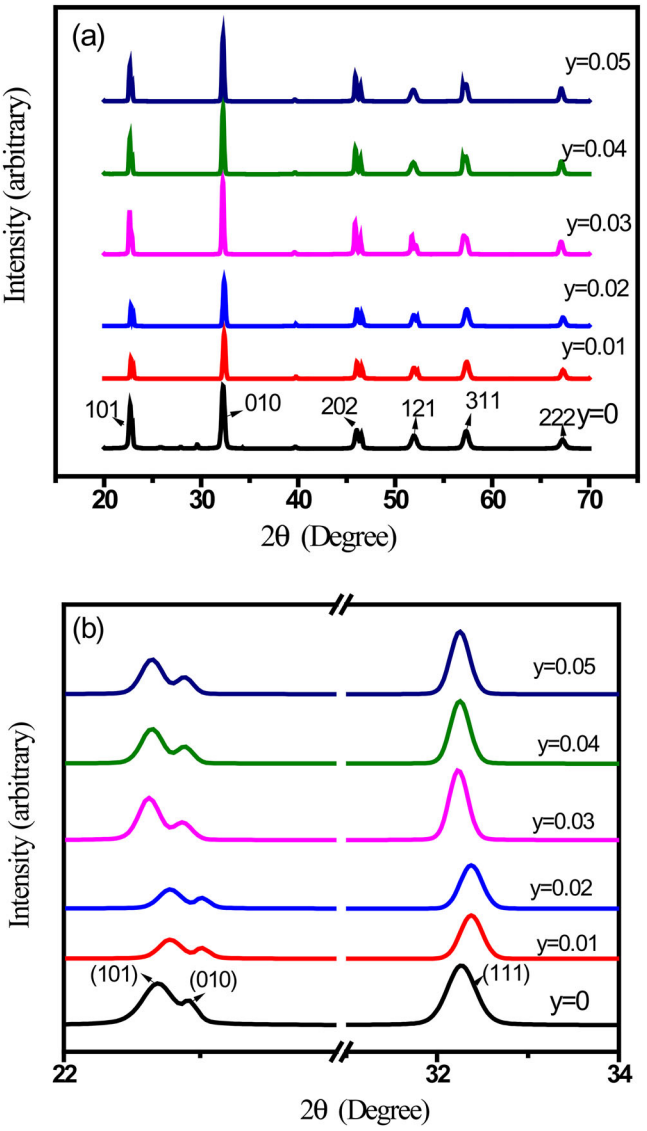

Figure 1. (a) XRD patterns for $Na_{0.685}K_{0.315}Nb_{1-y}Ta_yO_3$ $(0 \leq y \leq 0.05)$ samples, (b) shifting of most intense peaks with composition (y).

3. Results and discussion

3.1. XRD pattern

Figure 1a presents the observed XRD patterns of the prepared $Na_{0.685}K_{0.315}Nb_{1-y}Ta_yO_3$ $(0 \leq y \leq 0.05)$ pellet samples. Peak indexing was done with the help of Inorganic Crystal Structure Database (ICSD) [15]. The X-ray patterns of the prepared samples show polycrystalline behavior and were consistent with the ICSD (code 00-078-5546) data of $Na_{1-x}K_xNbO_3$, for $y = 0$, 1, 2, 3, 4 and 5%, with peaks corresponding to (100), (010), (202), (121) etc., showing monoclinic symmetry. For the prepared compositions

Table 1. Lattice parameters of $Na_{0.685}K_{0.315}Nb_{1-y}Ta_yO_3$ for different y values.

Lattice parameters composition (y)	a (Å)	b (Å)	c (Å)
$Na_{1-0.315}K_{0.315}Nb_{1-0}Ta_0O_3$	3.967	3.915	3.952 [14]
$Na_{1-0.315}K_{0.315}Nb_{1-0.01}Ta_{0.01}O_3$	3.97	3.928	3.966
$Na_{1-0.315}K_{0.315}Nb_{1-0.02}Ta_{0.02}O_3$	3.978	3.962	3.970
$Na_{1-0.315}K_{0.315}Nb_{1-0.03}Ta_{0.03}O_3$	3.999	3.998	3.996
$Na_{1-0.315}K_{0.315}Nb_{1-0.04}Ta_{0.04}O_3$	3.912	3.976	3.959
$Na_{1-0.315}K_{0.315}Nb_{1-0.05}Ta_{0.05}O_3$	3.9	3.92	3.91

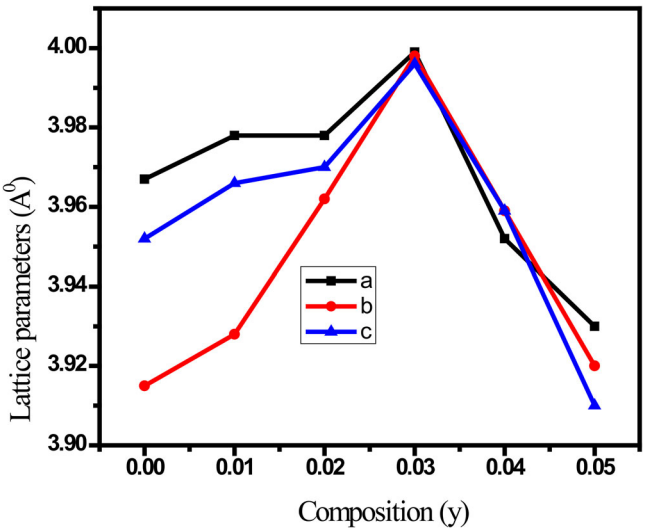

Figure 2. Variation of lattice parameters with, composition (y), in $Na_{0.685}K_{0.315}Nb_{1-y}Ta_yO_3$ ($0 \leq y \leq 0.05$).

$Na_{1-0.315}K_{0.315}Nb_{1-y}Ta_yO_3$ ($0 \leq y \leq 0.05$), a gradual shifting of the prominent peaks was observed with increasing tantalum concentration (y value) in Figure 1b. For the compositions with $y \leq 0.03$, these peaks were observed to be shifted to higher angles, whereas for the compositions with $y > 0.03$, peaks shifting pattern was reversed, shifting to higher angle with increasing y, indicating a break in the peak shifting pattern, at $y = 0.03$. A similar break in the peak shifting tendency was observed, in $Na_{1-x}K_xNbO_3$, near the compositions with $x = 0.32$, 0.475 and 0.175 [16–18]. Table 1 shows the lattice parameters of $Na_{1-x}K_xNb_{1-y}Ta_yO_3$ for y value. The cell parameters were refined by High Score Plus software [14, 19]. The monoclinic Pm (6) space group was chosen in these refinements. Values of calculated subcell parameters agree well with the reported results [14, 20]. The observed subcell parameters variation with composition (y) is given in Figure 2, resulting in increases in the lattice parameters a, b and c. These changes in the lattice parameters of the KNTN [21] crystals may be due to the volume of the lattice cell increased with the decrease in x and y. The cation radius of the tantalum r(Ta^{5+}) is slightly smaller than that of the niobium r(Nb^{5+}), while the volume of the as-grown crystals increase with decrease of Nb concentration (as Table 1 shown). Thus the main reason for the increase in the volume was the fact that the cation radius of potassium r(K+) is larger than that of sodium r(Na+).

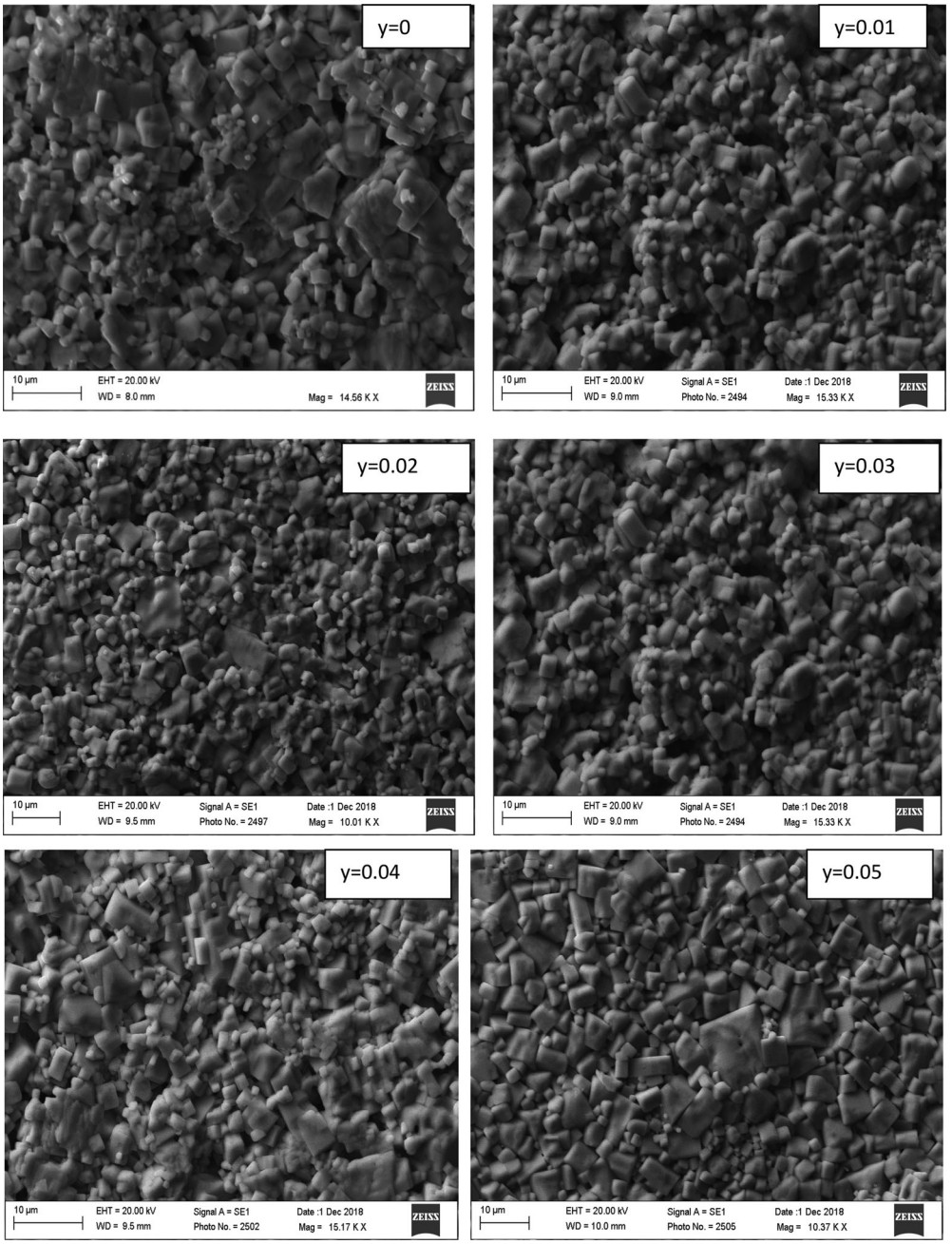

Figure 3. SEM photographs of $Na_{0.685}K_{0.315}Nb_{1-y}Ta_yO_3$ $(0 \leq y \leq 0.05)$ samples.

4. SEM and Energy Dispersive X-ray Analysis (EDAX)

Surface morphology of the prepared samples was studied by scanning electron microscope (SEM) using (CARL ZEISS, MA15/EVO18). Figure 3 shows the scanning electron micrographs of the prepared samples. The observed EDAX results of the prepared $Na_{0.685}K_{0.315}Nb_{1-y}Ta_yO_3$ $(0 \leq y \leq 0.05)$ samples have been given in Table 2.

Table 2. EDAX results of $Na_{0.685}K_{0.315}Nb_{1-y}Ta_yO_3$ ($0 \leq y \leq 0.05$).

	Atomic percentage									
	Observed					Calculated				
Material composition (y)	Na	K	Nb	Ta	O	Na	K	Nb	Ta	O
0	10.99	4.63	19.63	0	64.75	13.7	6.3	20	0	60
0.01	12.44	2.81	15.96	0.62	67.41	13.7	6.3	19.8	0.2	60
0.02	12.51	3.05	16.32	0.71	66.41	13.7	6.3	19.6	0.4	60
0.03	8.84	4.72	18.22	0.75	67.70	13.7	6.3	19.4	0.6	60
0.04	12.36	3.20	16.98	0.81	66.15	13.7	6.3	19.2	0.8	60
0.05	9.66	4.43	18.49	0.9	67.64	13.7	6.3	19	1	60

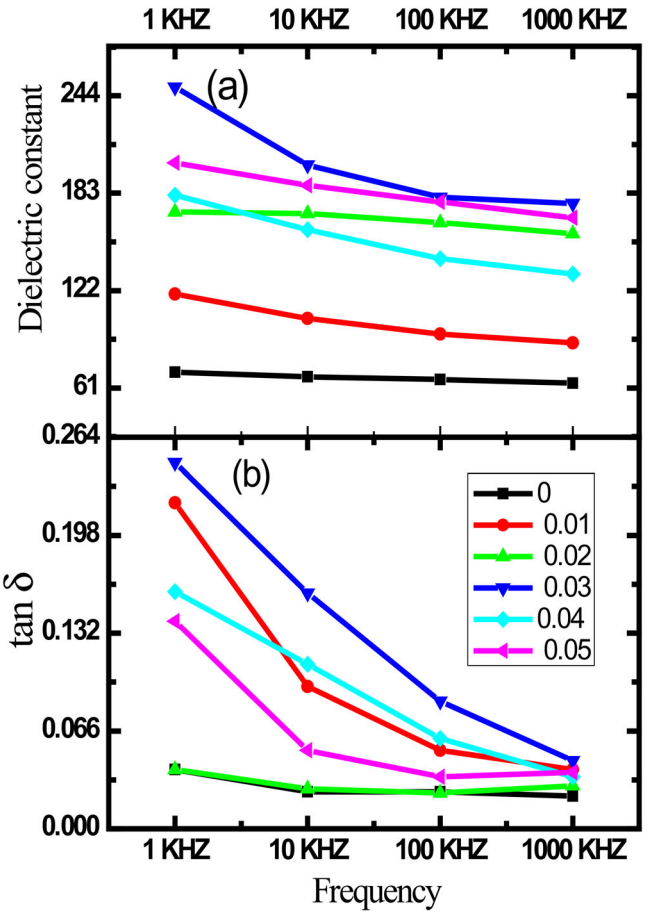

Figure 4. Frequency variation of (a) dielectric permittivity, and (b) tan δ, In $Na_{1-0.315}K_{0.315}Nb_{1-y}Ta_yO_3$ ($0 \leq y \leq 0.05$) with composition (y).

The EDAX results of the presently prepared $Na_{0.685}K_{0.315}Nb_{1-y}Ta_yO_3$ ($0 \leq y \leq 0.05$) compositions show significant escaping of alkali ions. The alkali ion escaping was observed significantly higher than oxygen escaping which is given in Table 2. Due to the excess of the vacancies at A-site than that at O-site, p-type conduction is envisaged in the present $Na_{0.685}K_{0.315}Nb_{1-y}Ta_yO_3$ ($0 \leq y \leq 0.05$) compositions. The A-site vacancy

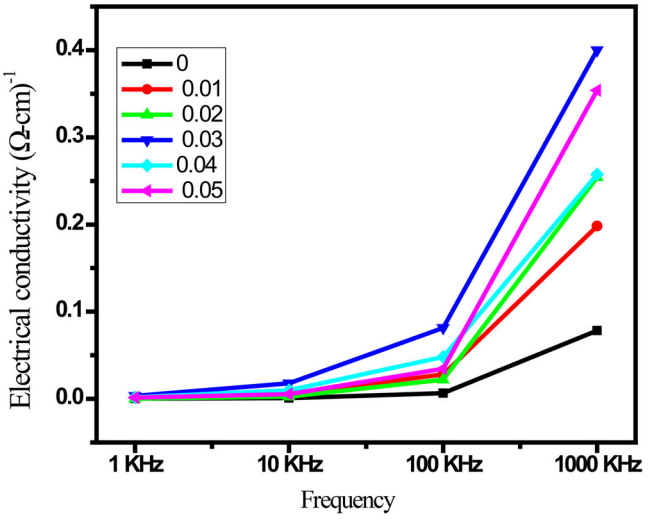

Figure 5. Variation of electrical conductivity (σ) with frequency, $Na_{0.685}K_{0.315}Nb_{1-y}Ta_yO$ in ($0 \leq y \leq 0.05$).

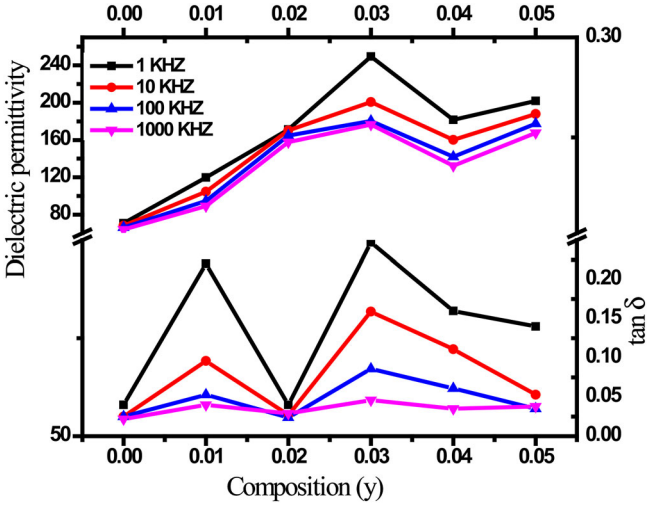

Figure 6. Variation of dielectric permittivity and tan δ of $Na_{0.685}K_{0.315}Nb_{1-y}Ta_yO_3$ ($0 \leq y \leq 0.05$) with composition (y), at different frequencies and RT.

attracts electron and acts as acceptor, and due to the electron deficiency the A-site vacancy behaves as 'hole' in the lattice.

5. Dielectric properties

The observed composition ($0 \leq y \leq 5\%$) dependence of dielectric permittivity (ε), loss tangent (tan δ) and electrical conductivity (σ) of $Na_{0.685}K_{0.315}Nb_{1-y}Ta_yO_3$ ceramics, at room temperature (RT) and different frequencies has been given in Figures 4 and 5. For all the prepared compositions, generally, ε and tan δ were observed decreasing and σ increasing, with increasing frequency.

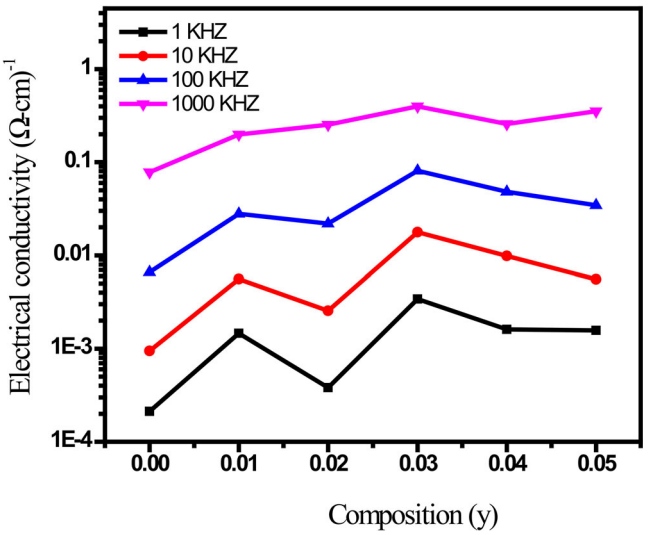

Figure 7. Variation of electrical conductivity of $Na_{0.685}K_{0.315}Nb_{1-y}Ta_yO_3$ $(0 \leq y \leq 0.05)$ with composition (y), at different frequencies and RT.

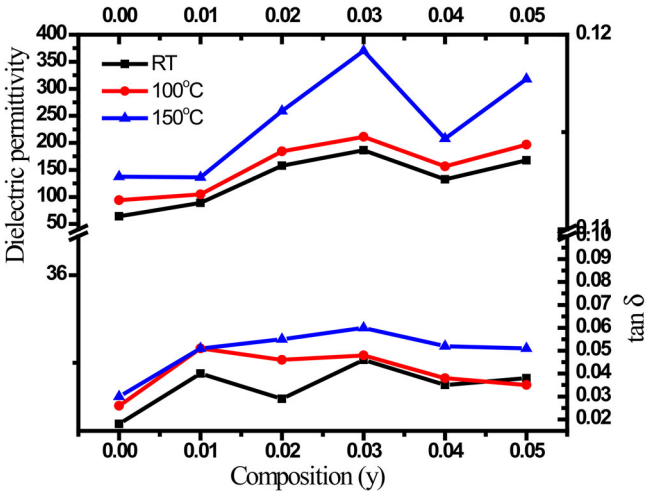

Figure 8. Variation of dielectrical constant and tan δ of $Na_{0.685}K_{0.315}Nb_{1-y}Ta_yO_3$ $(0 \leq y \leq 0.05)$ with composition (y), at different temperature.

These observations are in good agreement with the earlier reported results [22–24]. The observed composition dependence of ε and σ, for different frequencies at RT, has been shown in Figures 6 and 7. At all the applied frequencies, a remarkable maximum in ε and σ, at the composition with $y = 0.03$, indicates a morphotropic transition. Raevskii et al. [25] observed composition dependence of dielectric conductivity and explained the morphotropic-phase-boundary (MPB), for the compositions displaying extremal value of electrical conductivity at MPB. At 1 MHz the observed composition $Na_{0.685}K_{0.315}Nb_{1-y}Ta_yO_3$ $(0 \leq y \leq 0.05)$, dependence of ε and σ, at different temperatures, has been shown in Figures 8 and 9. With increasing temperature, in the measured

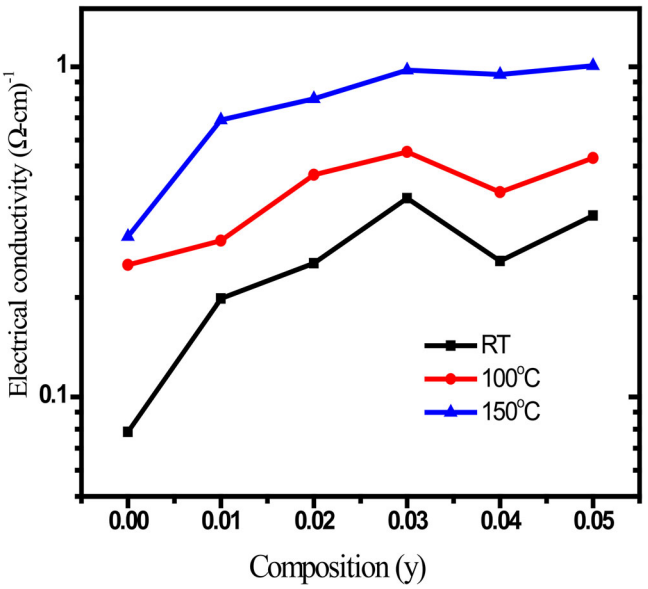

Figure 9. Variation of electrical conductivity of $Na_{0.685}K_{0.315}Nb_{1-y}Ta_yO_3$ $(0 \leq y \leq 0.05)$ with composition (y), at different temperature.

range, ε and σ of all the prepared samples were found increasing. For all the measured temperatures, ε and σ increase with y for the compositions with $y \leq 0.03$. At the composition with $y = 0.03$, ε and σ have maximum value, and thereafter, ε and σ were observed decreasing with increasing y. indicates an MPB behavior, for the prepared ceramics with $y = 0.03$.

Observed composition dependence of electrical conductivity and explained the MPB, for the compositions exhibiting maxima, in $Na_{0.685}K_{0.315}Nb_{1-y}Ta_yO_3$. The composition dependent structural anomaly and the escape of alkali ions may be held responsible for the observed dielectric behavior of $Na_{0.685}K_{0.315}Nb_{1-y}Ta_yO_3$ $(0 \leq y \leq 0.05)$ system. Because of the increased presence of non-ferroelectric low permittivity grain boundaries dielectric permittivity, generally, decreases with decreasing grain size [26]. The loss decreases due to the reduction in the number of grain boundaries with increasing grain size. Moreover, the interplay of porosity, grain size, liquid phase presence, ordering, etc. may be held responsible for the observed dielectric behavior in these perovskite ceramics.

The ABO_3 perovskites may have two major defects, *viz*, A-site, and O-site vacancies [27], and there is no concrete evidence of vacancies [27–29] reported at B-site. Electrical properties are significantly affected by the presence of these vacancies with isovalent substitution of Ta at Na/K site, at room temperature, resulting increased effective polarization and thereby increases in conductivity, in general, however, near MPB it is observed markedly high. In these oxides the conduction process may be explained on the basis of the majority of acceptor or donor concentration. Due to the deficiency of electron the A-site vacancy contributes 'hole', and due to the excess of electrons the O-site vacancy contributes extra electrons for conduction in the solid. In that way if there are only A-site vacancies, the solid should show p-type behavior, or if there are only O-site vacancies it should behave as n-type. Majority of A- or O-site

vacancies decides the majority of charge carriers, and thereby the p- or n-type nature of the conduction. The alkali ions escaping were observed significantly higher than oxygen escaping [16]. Due to the excess of the vacancies at A-site after Ta doping, than that at O-site, p-type conduction is envisaged in the present $Na_{0.685}K_{0.315}Nb_{1-y}Ta_yO_3$ compositions. Due to the high escaping of the alkali ions more number of 'holes' will be available for conduction, resulting higher conductivity in the compositions with $y = 0.03$, than other compositions. The p-type conductivity is reportedly observed in many oxides [30], where 'superoxidation' excess of A-site vacancies over the O-site vacancies, is more probable. In the p-type ceramics, with increased A-site vacancy concentration, for the compositions near MPB, a distinct conductivity maximum has been reported [18, 25]. Presently, with a decrease in A-site vacancy concentration for the composition, near MPB with $y = 0.03$, a distinct conductivity maximum was observed, which agrees with the above given supposition. For the composition near MPB, it seems that during sintering of the samples the intensification of diffusion processes remarkably reduces the possibility of escape of highly volatile alkali metal ions from the lattice. The properties of ceramics depend on the preparation process, and are subject to systematic and statistical fluctuations in the samples of a given batch. These fluctuations may be due to inhomogeneity in microchemistry, mechanical differences in the forming process, chemical modification and varying shrinkage at the time of sintering.

The reported and present observations indicates that the deficiency of the alkali ions, density of samples or grain size effects are not very effective but the structural property is more significantly responsible for the observed dielectric behavior of the prepared $Na_{0.685}K_{0.315}Nb_{1-y}Ta_yO_3$ ($0 \leq y \leq 0.05$) compositions. The observed structural anomaly and maximum values of dielectric permittivity, loss tangent and electrical conductivity, indicated an MPB composition, at $y = 0.03$, in $Na_{0.685}K_{0.315}Nb_{1-y}Ta_yO_3$ ($0 \leq y \leq 0.05$) system.

References

[1] Y. Saito *et al.*, Lead-free piezoceramics, *Nature* **432** (7013), 84 (2004).

[2] T. R. Shrout, and S. J. Zhang, Lead-free piezoelectric ceramics, *J. Electroceram.* **19**, 111 (2007).

[3] M. Matsubara, K. Kikuta, and S. Hirano, Piezoelectric properties of (K0.5Na0.5)(Nb1 − xTax)O3 − K5.4CuTa10O29 ceramics, *J. Appl. Phys.* **97** (11), 114105 (2005). DOI: 10.1063/1.1926396.

[4] Y. P. Guo, K. Kakimoto, and H. Ohsato, Phase transitional behavior and piezoelectric properties of (Na0.5K0.5)NbO3–LiNbO3 ceramics, *Appl. Phys. Lett.* **85** (18), 4121 (2004). DOI: 10.1063/1.1813636.

[5] M. Matsubara *et al.*, Effect of Li Substitution on the Piezoelectric Properties of Potassium Sodium Niobate Ceramics, *Jpn. J. Appl. Phys.* **44**, 6136–6142 (2005).

[6] Y. P. Guo, K. Kakimoto, and H. Ohsato, Na0.5K0.5)NbO3–LiTaO3 lead-free piezoelectric ceramics, *Mater. Lett.* **59** (2-3), 241 (2005).

[7] M. Ahtee, and A. M. Glazer, Lattice parameters and tilted octahedra in sodium–potassium niobate solid solutions, *Acta Cryst. A* **32** (3), 434 (1976). DOI: 10.1107/S0567739476000983.

[8] J. Hrešcak *et al.*, The influence of different niobium pentoxide precursors on the solid-state synthesis of potassium sodium niobate, *Eur. Ceram. Soc.* **33**, 3065 (2013). DOI: 10.1016/j.jeurceramsoc.2013.07.006.

[9] V. G. Hill, L. L. Y. Chang, and R. I. Harker, Subsolidus stability relations in the system $KTaO_3$-$KNbO_2$, *J. Am. Ceram. Soc.* **51** (12), 723 (1968). DOI: 10.1111/j.1151-2916.1968.tb15938.x.
[10] D. Jenko *et al.*, Electron microscopy studies of potassium sodium niobate ceramics, *Microsc. Microanal.* **11** (6), 572 (2005). DOI: 10.1017/S1431927605050683.
[11] L. Ramajo *et al.*, Influence of B-site compositional homogeneity on properties of $(K_{0.44}Na_{0.52}Li_{0.04})(Nb_{0.86}Ta_{0.10}Sb_{0.04})O_3$-based piezoelectric ceramics, *Eur. Ceram. Soc.* **34** (10), 2249 (2014).
[12] Y. Wang *et al.*, Compositional inhomogeneity in Li- and Ta-modified (K, Na)NbO_3 Ceramics, *J. Am. Ceram. Soc.* **90** (11), 3485 (2007).
[13] N. M. Hagh, B. Jadidian, and A. Safari, Property-processing relationship in lead-free (K,Na,Li) NbO_3-solid solution system, *J. Electroceram.* **18**, 339 (2007). DOI: 10.1007/s10832-007-9171-x.
[14] J. Negi, S. Singh, and N. S. Panwar, Structural and dielectric anomaly in $Na_{1-X}K_xNbO_3$, at x = 0.315, *Phase Transit* **92** (2), 149 (2019). DOI: 10.1080/01411594.2018.1563789.
[15] J. Tellier *et al.*, Crystal structure and phase transitions of sodium potassium niobate perovskites, *Solid State Sci.* **11** (2), 320 (2009). DOI: 10.1016/j.solidstatesciences.2008.07.011.
[16] A. S. Kandari, V. Lingwal, and N. S. Panwar, Morphotropic phase boundary in, near, *Solid State Commun.* **150** (1-2), 74 (2010). DOI: 10.1016/j.ssc.2009.10.002.
[17] A. S. Kandari *et al.*, Composition dependent dielectric anomaly in $Na_{1-x}K_xNbO_3$, at x = 0.475, *Ferroelectric* **393** (1), 121 (2009).
[18] A. S. Kandari, V. Lingwal, and N. S. Panwar, Morphotropic region in $Na_{1-x}K_xNbO_3$, Between x = 0.17 and 0.18, *Ferroelectric* **396** (1), 18 (2010). DOI: 10.1080/00150191003791683.
[19] J. Attia *et al.*, Study of potassium-sodium-niobate alloys, *J. Phys. IV France.* **128**, 55 (2005).
[20] V. J. Tennery and K. W. Hang, *J. App. Phys.* **39**, 4749 (1968). DOI: 10.1063/1.1655833.
[21] T. Hao *et al.*, Origin of giant piezoelectric effect in lead-free $K_{1-x}Na_xTa_{1-y}Nb_yO_3$ single crystals, *Z. Sci. Rep.* **6**, 25637 (2016). DOI: 10.1038/srep25637.(2016).
[22] R. E. Jaeger, and L. Egerton, Hot pressing of potassium-sodium niobates, *J. Am. Ceram. Soc.* **45** (5), 209 (1962). DOI: 10.1111/j.1151-2916.1962.tb11127.x.
[23] S. Narayana Murty, K. Umakantham, and A. Bhanumathi, Ferroelectric behaviour of lanthanum doped (NaK)NbO 3 ceramics, *Ferroelectric* **82** (1), 141 (1988). DOI: 10.1080/00150198808201348.
[24] G. H. Haertling, Properties of hot-pressed ferroelectric alkali niobate ceramics, *J. Am. Ceram. Soc.* **50** (6), 329 (1967). DOI: 10.1111/j.1151-2916.1967.tb15121.x.
[25] I. P. Raevskii, L. A. Reznichenko, O. I. Prokopalo, Izv. Akad. Nauk SSSR, **15**, 872 (1979).
[26] M. H. Frey *et al.*, The role of interfaces on an apparent grain size effect on the dielectric properties for ferroelectric barium titanate ceramics, *Ferroelectric* **206** (1), 337 (1998). DOI: 10.1080/00150199808009168.
[27] B. Jaffe, W. R. Cook, and J. H. Jaffe, *Piezoelectric Ceramics* (Academic, New York, 1971).
[28] V. Lingwal, and N. S. Panwar, Morphotropic phase transitions in mixed sodium-potassium niobate system, *Ferroelectric* **300** (1), 3 (2004). DOI: 10.1080/00150190490442146.
[29] E. V. Bursyan, *Nonlinear Crystal-Barium Titanate* (Nauka Press, Moskva 1974).
[30] J. Z. Rudolph, *Naturforsch* **14a**, 727 (1959).

Ferroelectrics

ISSN: 0015-0193 (Print) 1563-5112 (Online) Journal homepage: https://www.tandfonline.com/loi/gfer20

Two-step sintering affecting the escaping of Na and K and its impact on dielectric properties and morphology of lead-free $Na_{0.92}K_{0.08}NbO_3$ ceramics

Gambheer Singh Kathait & N. S. Panwar

To cite this article: Gambheer Singh Kathait & N. S. Panwar (2020) Two-step sintering affecting the escaping of Na and K and its impact on dielectric properties and morphology of lead-free $Na_{0.92}K_{0.08}NbO_3$ ceramics, Ferroelectrics, 554:1, 187-196, DOI: 10.1080/00150193.2019.1684760

To link to this article: https://doi.org/10.1080/00150193.2019.1684760

Published online: 25 Feb 2020.

Submit your article to this journal

View related articles

View Crossmark data

Full Terms & Conditions of access and use can be found at
https://www.tandfonline.com/action/journalInformation?journalCode=gfer20

FERROELECTRICS
2020, VOL. 554, 187–196
https://doi.org/10.1080/00150193.2019.1684760

Taylor & Francis
Taylor & Francis Group

Check for updates

Two-step sintering affecting the escaping of Na and K and its impact on dielectric properties and morphology of lead-free $Na_{0.92}K_{0.08}NbO_3$ ceramics

Gambheer Singh Kathait and N. S. Panwar

Department of Instrumentation Engineering-USIC, H.N.B. Garhwal University, Srinagar, India

ABSTRACT

Lead-free $Na_xK_{1-x}NbO_3$ (NKN) ceramics with $x = 0.08$ were prepared by a conventional solid-state reaction method. A two-step sintering technique was used for the sintering of ceramics. In this study, the influence of escaping of Na and K on the physical properties of prepared samples is investigated. It has been observed that the NKN ceramics with sintering temperature 1150 °C, 1200 °C and 1250 °C exhibit quite different microstructures from those with single sintering temperature. The lattice parameter discontinuity previously reported at $x = 0.475$ has not been confirmed. The permittivity, piezoelectric constant d_{33}, show broad peaks at the sintering temperature 1200 °C, where permittivity and d_{33} are maximum and dependent on the escaping of Na and K. Further, all the ceramics sintered at 1200 °C have the high permittivity ($\epsilon_c = 3175$) and piezoelectric values ($d_{33} = 192$ pm/V). From the analyses, we suggest that the high permittivity and piezoelectric properties for the NKN ceramics near 1200 °C are closely related to their escaping of Na and K and microstructures of well-faceted and uniformly distributed large grains rather than the widely believed morphotropic phase boundary effect of lattice parameter discontinuity.

ARTICLE HISTORY
Received 24 June 2019
Accepted 9 September 2019

KEYWORDS
Two-step sintering; microstructure; grain size; escaping of Na and K; dielectric properties

1. Introduction

The perovskite (ABO_3)-type compounds have attracted considerable attention due to their wide range of technological importance. The ABO_3-type ferroelectrics are typical displacive ferroelectrics that possess excellent dielectric, piezoelectric and optoelectronic properties [1]. Materials composed of lead (Pb) such as $Pb(ZrTi)O_3$, $Pb(Mg_{1/3}Nb_{2/3})O_3$, $PbTiO_3$, and $Pb(Zn_{1/3}Nb_{2/3})O3–PbTiO3$ in either ceramic or crystal form, because of their high dielectric, piezoelectric and optical properties are widely applied in the industry [2–5]. However, due to the toxicity of lead oxide to health and the environment, it is restricted to many applications. Recently, extensive research has been made to replace lead (Pb)-based compounds with lead-free alternatives. Significant progress in NKN-based ceramics showed that they may be promising candidates as lead-free piezoelectric materials [6–11]. In recent time, investigations carried out on NKN ceramics are mostly based on the equal or nearly equal molar ratio of K to Na. It was reported that NKN

CONTACT Gambheer Singh Kathait gambhir11186@gmail.com
© 2020 Taylor & Francis Group, LLC

ceramics with an equal molar ratio of Na and K, prepared by the conventional solid-state reaction method exhibit a kp peak and the d_{33} value of 80 pC/N [12]. To obtain good piezoelectric properties in the NKN-based ceramics, the equal molar ratio of K/Na has been widely accepted worldwide.

Dai *et al.* [13] have already shown the influence of the Na/K ratio on electrical properties and phase structures of $Na_{1-x}K_xNbO_3$ compositions with $x = 0.46$–0.52, prepared by conventional solid-state reaction method, and investigated that a typical morphotropic phase boundary exists, at $x = 0.52$–0.525. In the reported works, to understand the detailed influence of the escaping of Na and K on the phase structure and electrical behavior, the K composition interval between neighboring samples have been either too large [14–17] or too small [6, 13, 18, 19]. The dielectric and piezoelectric properties of many ceramics are also influenced by the techniques of grinding and sintering. Therefore, various techniques have been reported such as rapid-rate sintering, rate-controlled sintering, and two-step sintering [20, 21]. Among these methods, because of the high ceramic density, the two-step sintering method is interesting [20, 21]. Considering the importance of further design and development of new NKN-based lead-free piezoelectric ceramics, we reexamined the two-step sintering and alkali compositional influence on the physical properties in NKN ceramics in this work. Microstructures, crystalline structures, phase transitions, and dielectric and piezoelectric properties were investigated.

2. Experimental

In this study, $Na_{0.92}K_{0.08}NbO_3$ (NKN) ceramic powder was synthesized by the conventional solid-state reaction method. The calculated molar ratio of inorganic mixtures, Na_2CO_3 (99.5%, Sigma-Aldrich), K_2CO_3 (99.5%, Sigma-Aldrich) and Nb_2O_5 (99.9%, Sigma-Aldrich), was mixed by hand-grinding for 6 h. The stoichiometric amounts of K_2CO_3, Na_2CO_3, and Nb_2O_5 were weighed according to the chemical formula of $Na_{0.92}K_{0.08}NbO_3$ (NKN) and then the oxides were mixed by, manual grinding in acetone for 2 h (wet grinding), 4 h (dry grinding). The well-grinded powder is then calcinated at 925 °C for 4 h in a closed alumina crucible. After calcination the obtained powder was grounded for 1 h and taken for XRD analysis. Phase formation of the calcinated powders was determined by XRD analysis by an X-Pert PANalytical diffractometer using a fixed divergence1/2° slit, a Cu W/Si mirror and a solar slit as incident optics and a parallel plate collimator and proportional detector as diffracted beam optics. The obtained powders were pressed into disc shape pellets, at a pressure of 2-GPa, with diameter 8 mm Dia. piston. The samples were sintered at 1150 °C, 1200 °C and 1250 °C for 4 h. The sintered pellets were crushed and again pellets were made and sintering was done again. The particle morphology was examined by scanning electron microscopy (SEM) using model EVO 18 Special Edition (Switzerland), manufactured by ZEISS. For the dielectric investigation, the silver paste was painted on both sides of the samples in metal–insulator–metal (MIM) configuration. The coated pellets were dried for 2 h at temperature 50 °C. Dielectric constant (ε), loss tangent ($\tan\delta$) and electric conductivity (σ) of the prepared samples were measured, in MIM configuration, by RLC

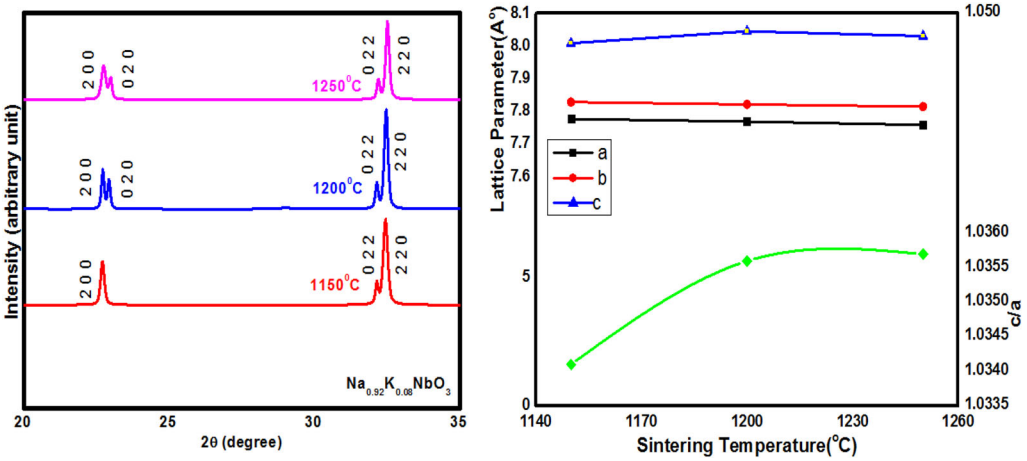

Figure 1. (a) XRD patterns of $Na_{0.92}$ $K_{0.08}NbO_3$. (b) Variation of lattice parameters, and *c*/*a* ratio for sintering temperature 1150 °C, 1200 °C and 1250 °C.

meter (Fluke, PM 6306), in the frequency range from 1 kHz to 1 MHz, at different temperatures, in conjunction with a furnace.

3. Results and discussion

In this study, the two-step sintering method was applied for fabrication of the NKN ceramics, i.e. the samples were sintered at 1150 °C, 1200 °C and 1250 °C for 4 h twice, followed by cooling to room temperature. Crystallinity is determined using an X-ray diffractometer (XPERT-PRO) with a CuKα radiation source ($\lambda = 1.54059$ Å), operated at a voltage of 45 kV and a current of 40 mA. The XRD patterns of the NKN ceramics sintered by the two-step sintering method are shown in Figure 1(a). It can be observed from Figure 1(a) that the diffraction peaks are (2 0 0), (0 2 0), (0 2 2) and (2 2 0) within the 2θ range from 20° to 35°. The XRD result is consistent with the work done by Fisher *et al.* [22] who synthesized NKN by a solid-state technique. The values of calculated subcell parameters closely agree with the reported results [6, 15–23]. The ceramic with sintering temperature 1200 °C shows (2 0 0)/(0 2 0) peak splitting around $2\theta = 22.5°$, confirming the orthorhombic symmetry. It is evident that the (0 2 0) peak is missing for sintering temperature 1150 °C, and the crystalline structure was found monoclinic, while other ceramics sintered at 1200 °C and 1250 °C showed pure perovskite phases with orthorhombic symmetry according to the JCPDF file reference code 01-073-6542. Secondary phases could not be found due to the application of sintering aids. Also, the lattice constant has not changed significantly which resulted in a negligible change in diffraction angles [24]. The sintering temperature variation had a great effect on the phase shift on the XRD pattern. The crystalline nature altered for the temperature variation. For the prepared composition for different sintering temperatures, generally, $a < c$, and slop of the plot of *c*/*a* ratio with temperatures was found positive as the structural anomaly is shown in Figure 1(b).

The cross-sectional morphology of modified NKN ceramics sintered at 1150 °C, 1200 °C and 1250 °C is shown in Figure 2. With the increasing sintering temperature

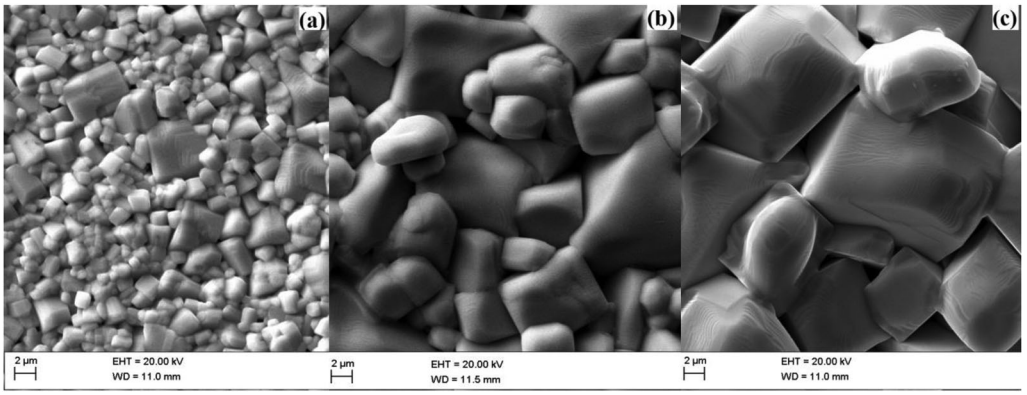

Figure 2. Selected SEM micrographs of NKN ceramics fabricated by different sintering temperatures (a) 1150 °C (b) 1200 °C and (c) 1250 °C.

from 1150 °C to 1250 °C, an increase in the grain size and the microstructures of uniformly distributed large grains was observed. At 1150 °C the grain size was moderate and found around 1 µm. That results in the intensified microstructure. It is worth noting that the grain sizes of NKN ceramics also show a clear bimodal distribution at 1150 °C, with many fine grains being located at the boundaries of coarse grains as shown in Figure 2(a). The average grain size of the samples was in a range of ∼1.5–9.5 µm at 1200 °C. Figure 2(b) clearly indicates as the grain size increases around 6.5 µm, it results in an increase of dielectric constant at higher temperatures. This result suggests that the sintering temperatures have a significant effect on the microstructure and uniformly distributed large grains of the NKN ceramics. Above 1250 °C the grain size increases above 9.5 µm as shown in Figure 2(c), also it seems as the grains are melting. That results in an abnormal microstructure. Sintering temperatures variation of density of the prepared samples is shown in Figure 3. The variation of the average grain size with sintering temperatures is shown in Figure 2(a). The average grain size was found the maximum (3.15 µm) for sintering temperatures 1200 °C, and minimum (1 µm) for sintering temperatures 1150 °C, among the prepared samples. Density of prepared samples are 3.447 g/cc, 3.536 g/cc and 3.094 g/cc for sintering temperature 1150 °C, 1200 °C and 1250 °C, respectively. The density and porosity greatly affect the dielectric properties of the samples [25, 26]. Samples with sintering temperatures 1200 °C were found most dense, among the prepared compositions (Figure 2(b)). During sintering, the process of grain growth and densification requires material transport, which may occur via various phenomena such as surface diffusion, grain boundary diffusion, lattice diffusion, viscous flow and evaporation [27]. It is evident from the previous results that the two-stage sintering was used to activate different sintering mechanisms in different temperature ranges and to increase grain growth and enhance the densification mechanism. But no improvement in density and microstructure was observed using this method. Chen *et al.* [28] reported similar observations for two-stage sintered NKN ceramics. It is reported that surface diffusion is the dominating sintering mechanism, in the NKN ceramics [27].

Table 1 represents the SEM–EDAX quantitative analysis of $Na_{0.92}K_{0.08}NbO_3$ for different sintering temperatures. The observed atomic weight% shows escaping of Na and

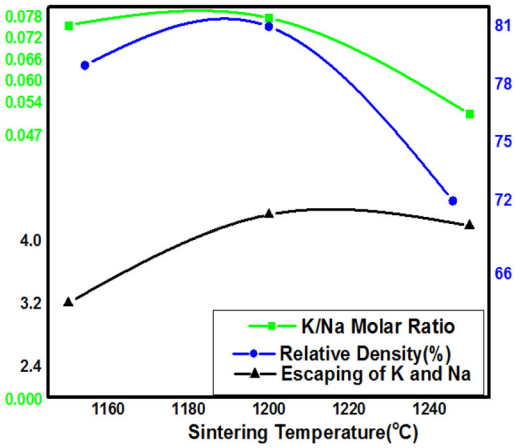

Figure 3. K/Na molar ratio, escaping of K and Na and relative density with sintering temperature.

Table 1. EDAX results of $Na_{0.92}K_{0.08}NbO_3$ system.

	Sintering temp. 1150 °C Atomic%		Sintering temp. 1200 °C Atomic%		Sintering temp. 1250 °C Atomic%	
Elements	Obs.	Cal.	Obs.	Cal.	Obs.	Cal.
O	63.97	60	65.77	60	66.29	60
Na	15.62	18.4	14.56	18.4	15.06	18.4
K	1.18	1.6	1.12	1.6	0.76	1.6
Nb	19.23	20	18.55	20	17.89	20
Escaping of Na & K	3.2		4.32		4.18	

K with sintering temperatures 1150 °C, 1200 °C and 1250 °C. At temperatures higher than 1200 °C a sharp increase in grain size for all temperatures was observed which results in a lowering of density and also high loss of Na and K was found. Such behavior during sintering is in continuation of the nature of these materials [15, 23].

The observed sintering temperature dependence of dielectric constant (ε), loss tangent ($\tan\delta$) and electric conductivity (σ) of $Na_{0.92}K_{0.08}NbO_3$ ceramics, at room temperature (RT) and different frequencies, have been given in Figure 4(a,b). For composition sintered at 1200 °C, generally, ε, $\tan\delta$ and σ were observed increasing with increasing frequency. These observations are in good agreement with the earlier reported results [29–31]. Again, for all the applied frequencies, a remarkable maximum in ε, $\tan\delta$, and σ, at the sintering temperature 1200 °C, indicates a strong morphotropic transition driven by the sintering temperature rather than frequency or composition. The ferroelectric properties of ceramics significantly depend on the preparation process and are subject to systematic and statistical variation in the samples. These variations may be due to inhomogeneity in microstructure, mechanical differences in the manufacturing process and varying shrinkage at the time of sintering.

The ABO_3 perovskites may have two major defects, *viz.*, A-site and O-site vacancies [2], and there is no proven evidence of vacancies reported at B site. Ferroelectric properties are majorly affected by the presence of these vacancies [2, 32–35]. In these oxides, the conduction process may be explained on the basis of the majority of acceptor or donor concentration. Due to the deficiency of electron, the A-site vacancy contributes 'hole', and due to the

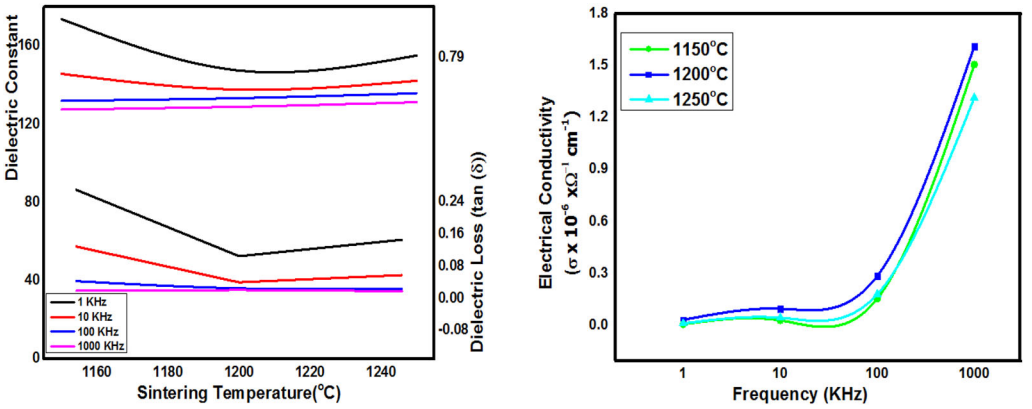

Figure 4. (a) Variation of dielectric constant (ε) and dielectric loss (tanδ) with different sintering temperature, in $Na_{0.92}K_{0.08}NbO_3$, at room temperature. (b) Variation of electric conductivity (σ) with frequency for different sintering temperatures, in $Na_{0.92}K_{0.08}NbO_3$, at room temperature.

excess of electrons, the O site vacancy contributes extra electrons for conduction in the solid. The majority of A or O site vacancies decide the majority of charge carriers, and thereby the p- or n-type nature of the conduction. The EDAX results of the presently prepared $Na_{0.92}K_{0.08}NbO_3$ compositions show significant escaping of alkali ions, with a maximum for the sintering temperature with 1200 °C (Table 1, Figure 5). Due to the excess of the vacancies at A-site than that at O-site, p-type conduction is investigated for sintering temperature 1200 °C, in the present $Na_{0.92}K_{0.08}NbO_3$ composition. Due to the high escaping of the alkali ions, more number of 'holes' will be available for conduction, resulting in higher conductivity in the composition with sintering temperature 1200 °C, than other sintering temperatures as shown in Figure 4(b).

Figure 3 shows K/Na molar ratio, escaping of K and Na and relative density with sintering temperatures. It is evident that the relative density is influenced by the escaping of K and Na.

The dielectric constant of the ceramics generally increases with increasing density [15, 36]. In this study, density as in Figure 3 and dielectric constant is shown in Figure 6(a) were found maximum, for sintering temperature 1200 °C, that are relevant with previously reported results. As shown in Figure 6(b), the temperature increases the dielectric constant and dielectric loss increases for all variations of sintering temperatures.

Table 2 shows the morphotropic, dielectric and piezoelectric parameters analyzed for the $Na_{0.92}K_{0.08}NbO_3$ ceramics. All the properties are in well support to each other and clearly depicts the impact of morphotropic and escaping of Na and K.

Figure 7 shows the *P*–*E* hysteresis loops of the $Na_{0.92}K_{0.08}NbO_3$ ceramics for the sintering temperature from 1150 °C to 1250 °C. It shows that all the *P*–*E* loops are well saturated. Remnant polarization P_r produces slight fluctuation as the sintering temperature varies, and the value of P_r settles into the 15–17 μC/cm^2 range. The sample sintered at 1200 °C shows the highest $P_r = 16.93$ μC/cm^2, which is distinct from the P_r of other sintering temperatures.

The S–E (strain–electric field) curves of the sintered $Na_{0.92}K_{0.08}NbO_3$ ceramics evaluated at 1 Hz at different sintering temperatures are shown in Figure 7(b). The S–E

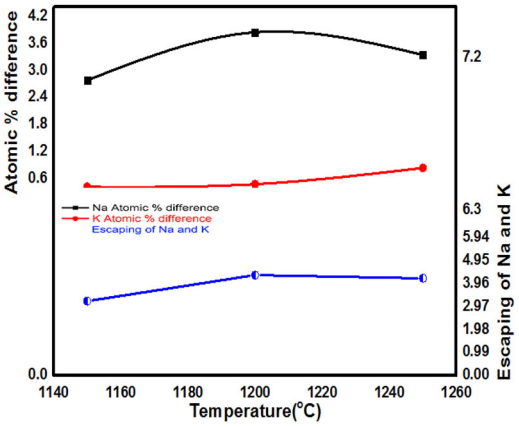

Figure 5. Variation of escaping of Na and K (atomic%) with sintering temperature, in $Na_{0.92}K_{0.08}NbO_3$.

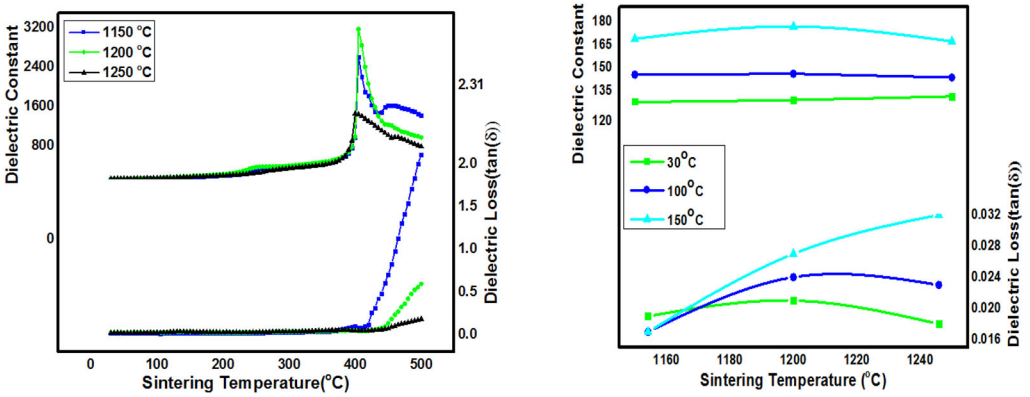

Figure 6. (a) Variation of dielectric constant (ε) and dielectric loss (tanδ) with sintering temperatures. (b) ε and tanδ with various sintering temperatures.

Table 2. Morphotropic, dielectric and piezoelectric parameter for $Na_{0.92}K_{0.08}NbO_3$ ceramics.

S. no.	Sintering temperature (°C)	Average grain size (μm)	Density (g/cc)	Escaping of Na and K	ε_C	d_{33} (pm/V)	P_r (μC/cm^2)
1	1150	1.2	3.447	3.20	2540	188	15.52
2	1200	6.5	3.530	4.32	3175	192	16.93
3	1250	9.5	3.094	4.18	1550	120	9.50

curves exhibit a typical ferroelectric butterfly curve behavior. In Figure 8(a), it should be noted that the piezoelectric constant d_{33}, which is defined as the maximal strain divided by the applied electric field, evaluated for the NKN ceramics with the composition ratio of $Na_{0.92}K_{0.08}NbO_3$ is 192 pm/V at sintering temperature 1200 °C.

We undertake detailed investigations to clarify the mechanism of the increase in d_{33}. Dielectric and piezoelectric behaviors had an almost similar tendency, i.e., dielectric and piezoelectric maximum at sintering temperature 1200 °C, where the escaping of Na and K is maximum. This suggested that the enhancement of dielectric and piezoelectric properties was originated from the same enhancement mechanism [26]. Figure 8(b) shows a proportional relation between escaping of Na and K, electrical conductivity and

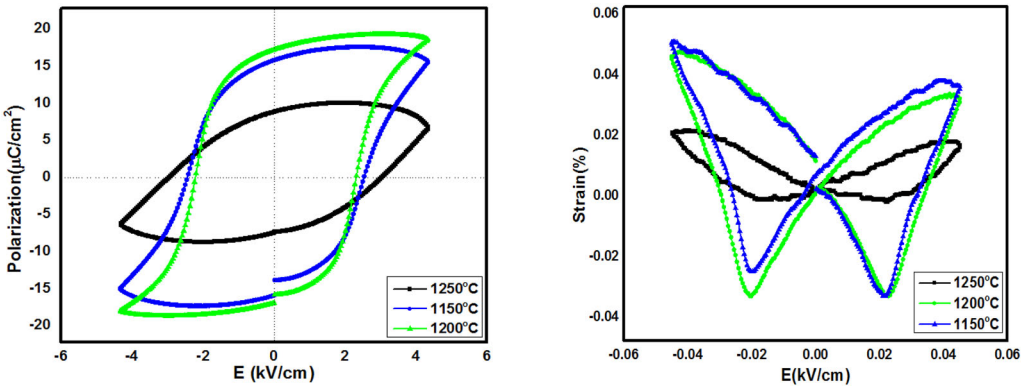

Figure 7. (a) Polarization–electric field hysteresis loops of the $Na_{0.92}K_{0.08}NbO_3$ ceramics sintered at different temperatures. (b) S–E (strain–electric field) curves of the $Na_{0.92}K_{0.08}NbO_3$ ceramics sintered at different temperatures.

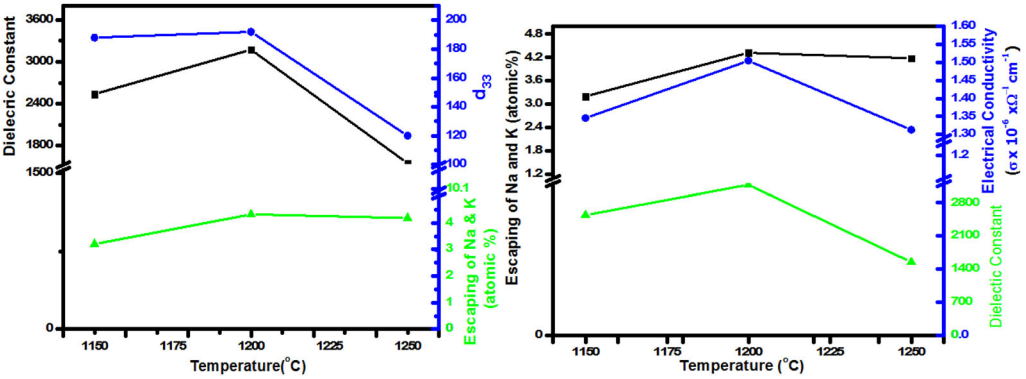

Figure 8. Dielectric constant, escaping of Na & K and (a) d_{33}, (b) electrical conductivity for different sintering temperatures.

dielectric constant at all sintering temperatures. The escaping of alkali elements closely follow the electrical conductivity of the ceramics for all sintering temperatures and affect the dielectric behavior.

4. Conclusions

The $Na_{0.92}K_{0.08}NbO_3$ lead-free piezoelectric ceramic was prepared by the conventional solid-state reaction method. The powder exhibited a fine grain with relatively uniform particle size. Typical ferroelectric nature has been observed for the prepared sample. The high volatility of Na and K results in p-type conduction that enhances the electrical conductivity, dielectric and piezoelectric value. For the first time, for ceramics sintered at 1200 °C, the excellent value of piezoelectric constant $d_{33} = 192$ pm/V and saturation polarization $P_{sat} = 18.36$ μC/cm^2 were found and it is near to the theoretical value. Large value of remnant polarization $P_r = 16.93$ μC/cm^2 with coercive field $E_c = 2.38$ kV/cm has achieved. The strain–electric field measurements revealed the "sprout" shape nature with a maximum remnant strain of 0.05%.

References

[1] G. A. Samara, Effects of pressure on the dielectric properties and phase transitions of the alkali metal tantalates and niobates, *Ferroelectrics* **73** (1), 145 (1987). DOI: 10.1080/00150198708227914.

[2] B. Jaffe, W. R. Cook, and H. Jaffe, *Piezoelectric Ceramics*, v. 3, ix edition (New York: Academic Press, 1971).

[3] Y. Lu *et al.*, Phase transitional behavior and piezoelectric properties of the orthorhombic phase of $Pb(Mg_{1/3}Nb_{2/3})O_3$–$PbTiO_3$ single crystals. *Appl. Phys. Lett.* **78** (20), 3109 (2001). DOI: 10.1063/1.1372360.

[4] W. Ren, S. F. Liu, and B. K. Mukherjee, Piezoelectric properties and phase transitions of 001S-oriented $Pb(Zn_{1/3}Nb_{2/3})O_3$–$PbTiO_3$ single crystals. *Appl. Phys. Lett.* **80** (17), 3174 (2002). DOI: 10.1063/1.1474600.

[5] S. E. Park, and T. R. Shrout, Ultrahigh strain and piezoelectric behavior in relaxor based ferroelectric single crystals. *J. Appl. Phys.* **82** (4), 1804 (1997). DOI: 10.1063/1.365983.

[6] Y. Saito *et al.*, Lead-free piezoceramics. *Nature (London)* **432** (7013), 84 (2004). DOI: 10.1038/nature03028.

[7] Y. Guo, K. Kakimoto, and H. Ohsato, Phase transitional behavior and piezoelectric properties of $(Na_{0.5}K_{0.5})NbO_3$–$LiNbO_3(Na_{0.5}K_{0.5})NbO_3$–$LiNbO_3$ ceramics. *Appl. Phys. Lett.* **85** (18), 4121 (2004). DOI: 10.1063/1.1813636.

[8] M. Matsubara, K. Kikuta, and S. Hirano, Piezoelectric properties of $(K_{0.5}Na_{0.5})(Nb_{1-x}Ta_x)O_3-K_{5.4}CuTa_{10}O_{29}$ ceramics. *J. Appl. Phys.* **97** (11), 114105 (2005). DOI: 10.1063/1.1926396.

[9] Y. Guo, K. Kakimoto, and H. Ohsato, $(Na_{0.5}K_{0.5})NbO_3$–$LiTaO_3$ lead-free piezoelectric ceramics. *Mater. Lett.* **59** (2–3), 241 (2005). DOI: 10.1016/j.matlet.2004.07.057.

[10] E. Hollenstein *et al.*, Piezoelectric properties of Li- and Ta-modified $(K_{0.5}Na_{0.5})NbO_3$ ceramics. *Appl. Phys. Lett.* **87** (18), 182905 (2005). DOI: 10.1063/1.2123387.

[11] H. Y. Park *et al.*, Microstructure and piezoelectric properties of $0.95(Na_{0.5}K_{0.5})NbO_3$–$0.05BaTiO_30.95$ $(Na_{0.5}K_{0.5})$ $NbO_30.05BaTiO_3$ ceramics. *Appl. Phys. Lett.* **89** (6), 062906 (2006). DOI: 10.1063/1.2335816.

[12] L. Egerton, and D. M. Dillon, Piezoelectric and dielectric properties of ceramics in the system potassium-sodium niobate. *J. Am. Ceram. Soc.* **42** (9), 438 (1959). DOI: 10.1111/j.1151-2916.1959.tb12971.x.

[13] Y. J. Dai, X. W. Zhang, and K. P. Chen, Morphotropic phase boundary and electrical properties of $K_{1-x}Na_xNbO_3$ lead-free ceramics. *Appl. Phys. Lett.* **94** (4), 042905 (2009). DOI: 10.1063/1.3076105.

[14] L. Wu *et al.*, Influence of compositional ratio K/Na on physical properties in $(K_xNa_{1-x})NbO_3$ ceramics. *J. Appl. Phys.* **103** (8), 084116 (2008). DOI: 10.1063/1.2907866.

[15] V. J. Tennery, and K. W. Hang, Thermal and x-ray diffraction studies of the $NaNbO_3$-$KNbO_3$ system. *J. Appl. Phys.* **39** (10), 4749 (1968). DOI: 10.1063/1.1655833.

[16] R. E. Jaeger, and L. Egerton, Hot pressing of potassium-sodium niobates. *J. Am. Ceram. Soc.* **45** (5), 209 (1962). DOI: 10.1111/j.1151-2916.1962.tb11127.x.

[17] B. P. Zhang *et al.*, Compositional dependence of piezoelectric properties in $Na_xK_{1-x}NbO_3$ lead-free ceramics prepared by spark plasma sintering. *J. Am. Ceram. Soc.* **89** (5), 1605 (2006). DOI: 10.1111/j.1551-2916.2006.00960.x.

[18] D. W. Baker *et al.*, Structural study of $K_xNa_{1-x}NbO_3$ (KNN) for compositions in the range $x = 0.24$–0.36. *Acta Crystallogr. B: Struct. Sci.* **B65**, 22 (2009). DOI: 10.1107/S0108768108037361.

[19] N. Zhang *et al.*, Structures of $K_{0.05}Na_{0.95}NbO_3$ (50–300 K) and $K_{0.30}Na_{0.70}NbO_3$ (100–200 K). *Acta Crystallogr. B: Struct. Sci.* **B65**, 291 (2009). DOI: 10.1107/S0108768109011057.

[20] X.-H. Wang *et al.*, Bulk dense nanocrystalline BaTiO3 ceramics prepared by novel pressureless two-step sintering method. *J. Electroceram.* **21** (1–4), 230 (2008). DOI: 10.1007/s10832-007-9143-1.

[21] N. Lartcumfu *et al.*, Fabrication of sodium potassium niobate ceramics by two step sintering assisted molten salts synthesis. *Ferroelectrics* **456** (1), 14 (2013). DOI: 10.1080/00150193.2013.846171.

[22] J. G. Fisher *et al.*, High-temperature X-ray diffraction and Raman spectroscopy study of $(K_{0.5}Na_{0.5})NbO_3$ ceramics sintered in oxidizing and reducing atmospheres. *Mater. Chem. Phys.* **120**, 263 (2010). DOI: 10.1016/j.matchemphys.2009.11.001.

[23] C. N. W. Darlington, and H. D. Megaw, The low-temperature phase transition of sodium niobate and the structure of the low-temperature phase. *Acta Crystallogr. B: Struct. Sci.* **B29**, 2171 (1973). DOI: 10.1107/S0567740873006308.

[24] R. Zuo *et al.*, Sintering and electrical properties of lead-free $Na_{0.5}K_{0.5}NbO_3$ piezoelectric ceramics. *J. Am. Ceram. Soc.* **89** (6), 2010 (2006). DOI: 10.1111/j.1551-2916.2006.00991.x.

[25] Q. Xu *et al.*, Effect of sintering temperature on dielectric properties of $Ba_{0.6}Sr_{0.4}TiO_3$–MgO composite ceramics prepared from fine constituent powders. *Mater. Des.* **32** (3), 1200 (2011). DOI: 10.1016/j.matdes.2010.10.018.

[26] S. Wada *et al.*, Phase diagram and microstructure analysis of barium titanate–potassium niobate system piezoelectric ceramics. *KEM* **421–422**, 34 (2009). DOI: 10.4028/www.scientific.net/KEM.421-422.34.

[27] B. Malic *et al.*, Sintering of lead-free piezoelectric sodium potassium niobate ceramics. *Materials* **8**, 8117 (2015). DOI: 10.3390/ma8125449.

[28] I. W. Chen, and X. H. Wang, Sintering dense nanocrystalline ceramics without final-stage grain growth. *Nature* **404** (6774), 168 (2000). DOI: 10.1038/35004548.

[29] S. Narayana Murty, K. Umakantham, and A. Bhanumathi, Ferroelectric behavior of Lanthanum doped (NaK)NbO_3 ceramics. *Ferroelectrics* **82** (1), 141 (1988). DOI: 10.1080/00150198808201348.

[30] L. E. Cross, Electric double hysteresis in $(K_xNa_{1-x})NbO_3$ single crystals. *Nature* **181** (4603), 178 (1958). DOI: 10.1038/181178a0.

[31] G. H. Haertling, Properties of hot-pressed ferroelectric alkali niobate ceramics. *J. Am. Ceram. Soc.* **50** (6), 329 (1967). DOI: 10.1111/j.1151-2916.1967.tb15121.x.

[32] A. S. Kandari, V. Lingwal, and N. S. Panwar, Morphotropic region in $Na_{1-x}K_xNbO_3$, between $x = 0.17$ and 0.18. *Ferroelectrics* **396** (1), 18 (2010). DOI: 10.1080/00150191003791683.

[33] V. Lingwal, and N. S. Panwar, Morphotropic phase transitions in mixed sodium-potassium niobate system. *Ferroelectrics* **300** (1), 3 (2004). DOI: 10.1080/00150190490442146.

[34] E. V. Bursyan, *Nonlinear Crystal-Barium Titanate* (Moskva: Nauka Press, 1974).

[35] S. Singh, J. Negi, and N. S. Panwar, Dielectric properties of $Na_{1-x}K_xNbO_3$, near $x = 0.5$ morphotropic phase region. *J. Phys. Chem. Solids* **123**, 311 (2018). DOI: 10.1016/j.jpcs.2018.08.018.

[36] H. Chen *et al.*, The size effect of $Ba_{0.6}Sr_{0.4}TiO_3$, thin films on the ferroelectric properties. *Appl. Surf. Sci.* **252** (12), 4171 (2006). DOI: 10.1016/j.apsusc.2005.06.027.

Journal of Physics and Chemistry of Solids 146 (2020) 109583

Contents lists available at ScienceDirect

Journal of Physics and Chemistry of Solids

journal homepage: http://www.elsevier.com/locate/jpcs

Temperature-dependent dielectric and structural properties of Li-doped (Na, K) NbO_3 near the morphotropic phase region

Surendra Singh [a,*], N.S. Panwar [b]

[a] Department of Physics, H. N. B. Garhwal University, Srinagar Garhwal, India
[b] University Science Instrumentation Centre, H. N. B. Garhwal University, Srinagar Garhwal, 246174, India

ARTICLE INFO

Keywords:
Ferroelectrics
Solid-state reaction
Dielectric constant
High temperature X-ray diffraction

ABSTRACT

In this study, pellet samples of $(Na_{0.5}K_{0.5})_{1-y}Li_yNbO_3$, (NKLN) $y \leq 0.06$, were prepared using a conventional solid-state reaction method with double sintering. The temperature-dependent dielectric constant and high-temperature X-ray diffraction characteristics of the prepared compositions were observed. Four consistent distinct phases were determined according to the observations as follows. For the compositions where $y \leq 0.02$, the phases exhibited monoclinic symmetry between room temperature and about 200 °C, tetragonal between about 200 °C and 400 °C, tetragonal with different symmetry between about 400 °C and 460 °C (the so-called X phase), and cubic symmetry above about 460 °C. For the compositions with higher Li concentrations (y) between $0.03 \leq y \leq 0.06$, the X phase was not observed and two distinct phase transitions were observed from monoclinic to tetragonal at around 200 °C, and from tetragonal to cubic at around 460 °C.

1. Introduction

The ABO_3 perovskite structure is important because of its capacity to adjust to mismatches in the equilibrium bond lengths between and within the A and B sites, as well as to both cation and anion vacancies, cooperative orbital ordering or atomic displacements, cation ordering, and the formation of intergrowth structures. This capacity allows the tuning of interesting physical properties. Sodium potassium niobate ($Na_{1-x}K_xNbO_3$, NKN) has a cubic ABO_3 structure in the high-temperature paraelectric phase and it is an interesting system because of its numerous ferroelectric phases with high spontaneous polarization at room temperature [1,2]. The solid solutions of NKN have attracted significant attention because of their electromechanical properties and potential technological applications [3–6]. In the phase diagram obtained for the NKN system, Ahtee and Glazer [7] indicated the existence of the X phase above 400 °C in the compositional range from $0.2 < x < 0.5$, but they doubted its existence in reality. Beyond the X phase, the occurrence of the cubic phase was evident at higher temperatures [7]. Nobre and Lanfredi [8,9] observed four phase transitions from room temperature (RT) to 750 °C in $Na_{0.85}Li_{0.15}NbO_3$ [8] and $Na_{0.88}Li_{0.12}NbO_3$ [9]. Lin et al. [10] observed high-temperature phase transitions in $(Na_{0.89}K_{0.11})NbO_3$ crystals at 405 °C and 496 °C, and two phase transitions near about 200 °C and 400 °C have been reported based on dielectric measurements in NKN ceramics [11–13]. Dielectric and high-temperature X-ray diffraction (HT-XRD) measurements indicate the existence of four distinct phases in the equimolar (Na, K)NbO_3, i.e., monoclinic between RT and 200 °C, tetragonal between 200 °C and 380 °C, tetragonal between 380 °C and 460 °C, and cubic above 460 °C [14]. However, many studies failed to detect any phases such as the X phase in the equimolar (Na, K)NbO_3 system modified using various dopants [15–20].

NKN ceramics have considerable potential for replacing lead-based piezoelectric materials and they have attracted much attention because of their combination of reasonable piezoelectric properties and high Curie temperatures ($T_C > 400$ °C) [3–6]. However, it is very difficult to obtain dense and well sintered NKN ceramics using ordinary sintering processes because of the high volatility of alkali metal oxides at high temperatures. Thus, many modifiers have been added to NKN to form new solid solutions to improve the densification and dielectric properties of NKN ceramics.

The temperature-dependent low frequency optical soft mode is responsible for the temperature-dependent dielectric properties of ABO_3 type perovskites [21,22]. The low lying temperature-dependent optical mode softens at the transition temperature (T_c) and it is responsible for the anomalous dielectric behavior of these materials at T_c. The frequency of the soft mode tends to zero and the associated lattice

* Corresponding author.
E-mail address: jhinkwan.surendra@gmail.com (S. Singh).

https://doi.org/10.1016/j.jpcs.2020.109583
Received 18 September 2019; Received in revised form 27 May 2020; Accepted 27 May 2020
Available online 18 June 2020
0022-3697/© 2020 Elsevier Ltd. All rights reserved.

Raw materials (K_2CO_3, Na_2CO_3, Li_2CO_3, and Nb_2O_5) with purity greater than 99.9% weighed precisely according to the required stoichiometric ratios.

↓

Stoichiometric wet mixture ground for 2 h and then ground dry for 4 h.

↓

Ground power calcined at 950°C for 4 h, before pressing at 0.4 GPa into pellets with a diameter of 8 mm and thickness of ~ 2–3 mm.

↓

Sintering temperatures of NKLN compositions selected according to their melting points [23] and pellets with each composition sintered for 4 h.

↓

Some sintered pellets crushed, ground finely, and pressed into pellets, before further sintering each for 4 h.

↓

Sintered pellets used as electrodes in metal–insulator–metal (MIM) configuration to obtain dielectric measurements.

Scheme 1. Preparation steps for $(Na_{0.5}K_{0.5})_{1-y}Li_yNbO_3$, (NKLN) $y \leq 0.06$.

displacement becomes unstable, thereby leading to the phase transition at T_c. A series of structural phase transitions in this system are associated with tilting of the BO_6 octahedra [2]. However, the static tilting theory is a manifestation of the dynamic soft mode theory. The observed anomalies in different physical quantities are associated with the structural phase transition of perovskites near T_c [21,22].

The present study was conducted to determine the temperature-dependent dielectric and structural properties of lithium (Li) doped equimolar (Na, K)NbO_3 morphotropic compositions. Pellet samples of $(Na_{0.5}K_{0.5})_{1-y}Li_yNbO_3$ (NKLN), where $y \leq 0.06$, were prepared by a solid-

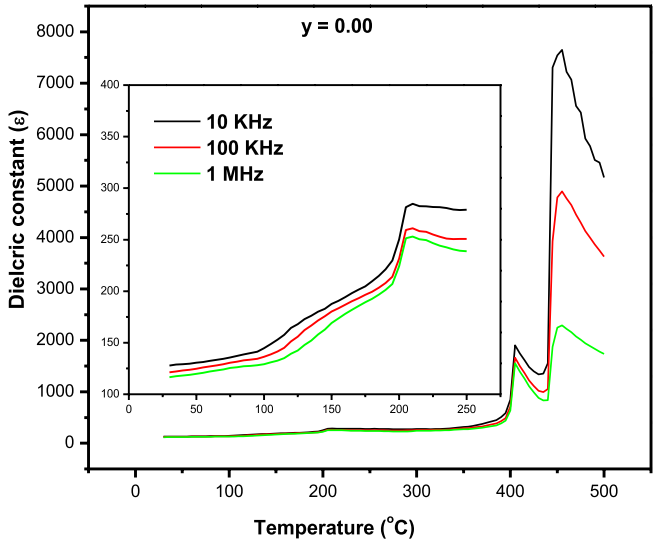

Fig. 1. Temperature-dependent variations in dielectric constant (ε) for $(Na_{0.5}K_{0.5})_{1-y}Li_yNbO_3$, where y = 0.00, at different frequencies.

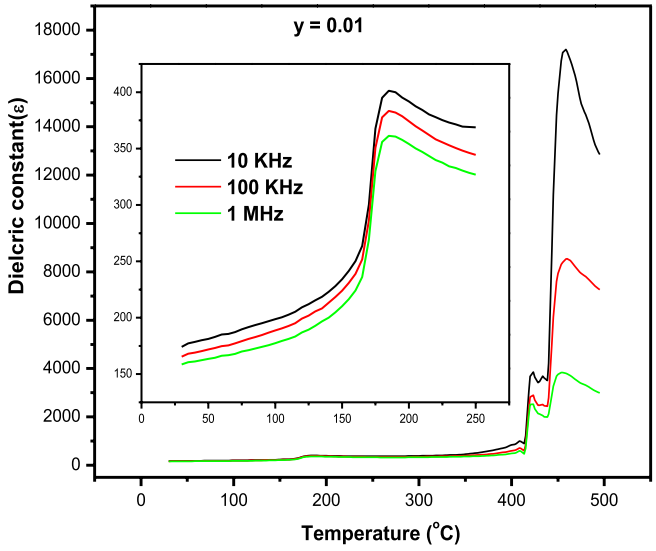

Fig. 2. Temperature-dependent variations in dielectric constant (ε) for $(Na_{0.5}K_{0.5})_{1-y}Li_yNbO_3$, where y = 0.01, at different frequencies.

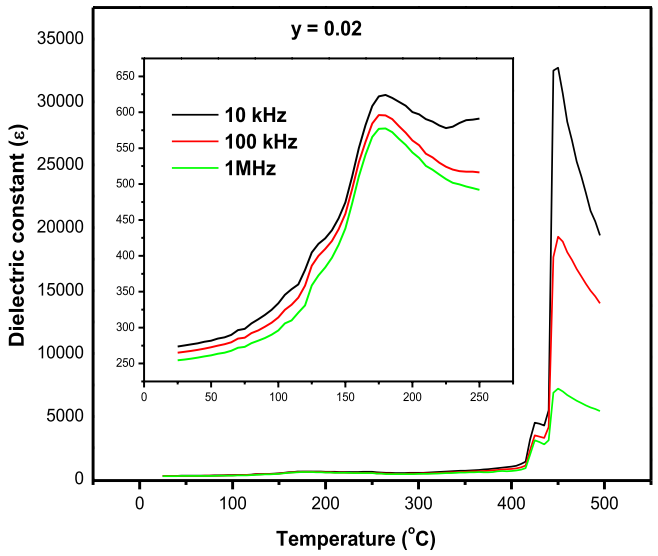

Fig. 3. Temperature-dependent variations in dielectric constant (ε) for $(Na_{0.5}K_{0.5})_{1-y}Li_yNbO_3$, where y = 0.02, at different frequencies.

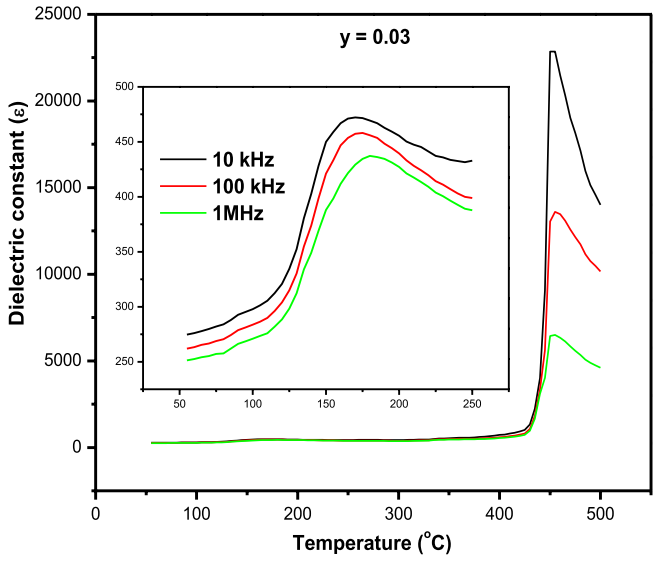

Fig. 4. Temperature-dependent variations in dielectric constant (ε) for $(Na_{0.5}K_{0.5})_{1-y}Li_yNbO_3$, where y = 0.03, at different frequencies.

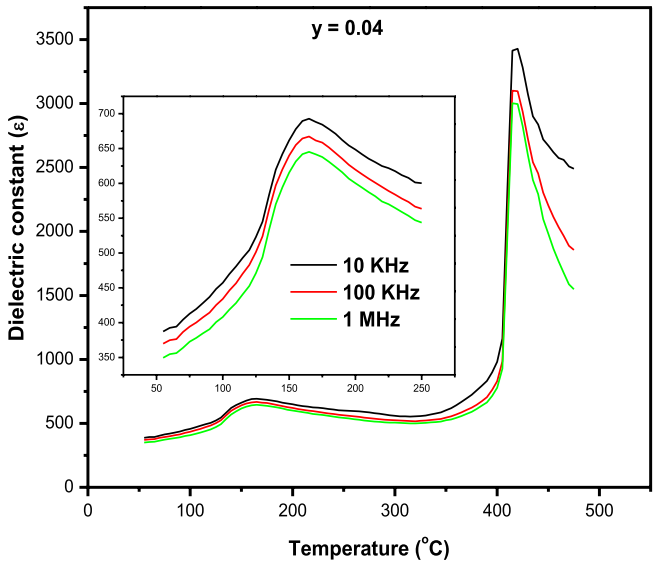

Fig. 5. Temperature-dependent variations in dielectric constant (ε) for $(Na_{0.5}K_{0.5})_{1-y}Li_yNbO_3$, where y = 0.03, at different frequencies.

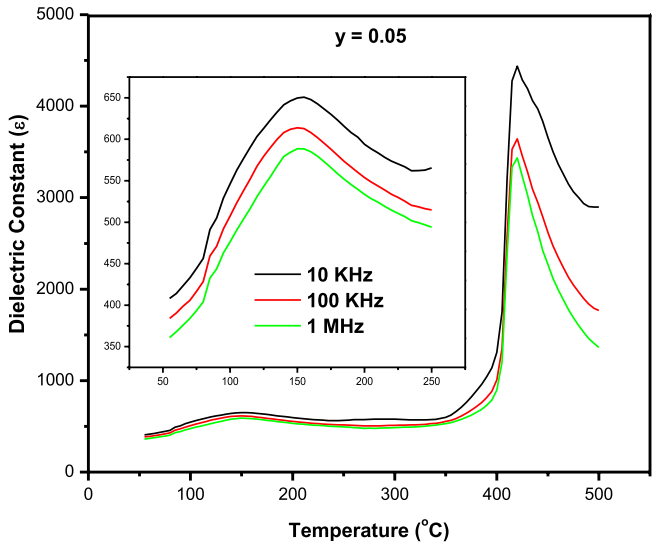

Fig. 6. Temperature-dependent variations in dielectric constant (ε) for $(Na_{0.5}K_{0.5})_{1-y}Li_yNbO_3$, where y = 0.05, at different frequencies.

state reaction route using double sintering. The dielectric constants were measured for the prepared samples in the frequency range between 10 kHz and 1 MHz, and in the temperature range from RT to 500 °C. HT-XRD measurements were acquired for the prepared samples in the temperature range from RT to 500 °C.

2. Experimental

Ceramic pellets of NKLN where $y \leq 0.06$ were prepared using the conventional solid-state reaction method. The raw materials comprising K_2CO_3, Na_2CO_3, Li_2CO_3, and Nb_2O_5 with purity greater than 99.9% (from Merck KGaA, Germany) were dried at 200 °C for 2 h to remove moisture and weighed in stoichiometric ratios. The method used to prepare the different compositions was similar to that described in a previous study [23]. A schematic figure illustrating the preparation of the materials is shown in Scheme 1.

HT-XRD measurements were obtained for all of the prepared compositions with an X-ray diffractometer (PANalytical, X'PERT PRO) using Cu-$K_{\alpha 1}$ radiation at a wavelength of 1.5405980 Å in a wide 2θ range ($20° < 2\theta < 70°$) and at a scanning rate of 6°/min. The sintered pellets were used to prepare electrodes with air dryable conducting silver paste in a metal–insulator–metal (MIM) configuration to obtain dielectric measurements. The dielectric constant (ε) was measured for each prepared sample in a MIM configuration using an RCL meter (Fluke, PM6306) in the frequency range from 10 kHz to 1 MHz and the temperature range from RT to 500 °C.

3. Results and discussion

3.1. Dielectric measurements

The variations in the dielectric constant (ε) determined for the different prepared compositions according to the temperature are shown in Figs. 1–7. For all of the prepared compositions, the dielectric constant gradually increased as the temperature increased, but anomalously large values were obtained at around 200 °C, 400 °C, and 450 °C for the

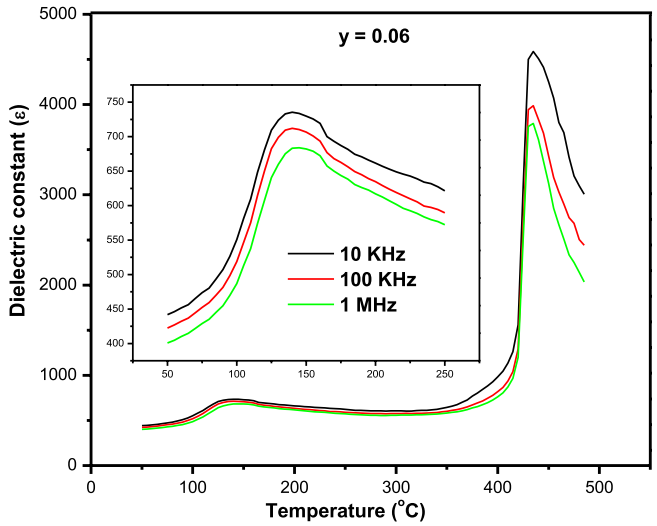

Fig. 7. Temperature-dependent variations in dielectric constant (ε) for $(Na_{0.5}K_{0.5})_{1-y}Li_yNbO_3$, where y = 0.06, at different frequencies.

compositions where y ≤ 0.02, thereby indicating that phase transitions occurred at these three temperatures [5]. For the compositions where 0.03 ≤ y ≤ 0.06, anomalously large dielectric constant values were only observed at around 200 °C and 450 °C but not around 400 °C, thereby indicating that phase transitions only occurred at these two temperatures. Thus, the temperature-dependent dielectric measurements are presented only for the compositions where y ≤ 0.06. Furthermore, for the compositions where y ≥ 0.03, the temperature-dependent dielectric measurements indicated the occurrence of only two transitions (at around 200 °C and 450 °C), so the HT-XRD results are only presented for the compositions where y ≤ 0.05 in this study.

For the compositions where y ≤ 0.02, three transitions occurred around 200 °C, 400 °C, and 460 °C according to the dielectric measurements (Figs. 1–3). As the Li concentration increased, the transition near 200 °C shifted toward a lower temperature for all of the prepared compositions. In addition, the transition peak at around 400 °C shifted toward a higher temperatures for the compositions where y ≤ 0.02. As the Li (0.03 ≤ y) concentration increased further, the peak at around 400 °C shifted to a higher temperature and it merged with the peak at around 460 °C for the compositions where y ≥ 0.03. At Li concentrations where y ≥ 0.03, the dielectric measurements only indicated two peaks with transitions at around 200 °C and 460 °C. At higher concentrations, the solubility of Li in the A sites of NKN became difficult due to the different crystallization patterns of $LiNbO_3$ and (Na, K) NbO_3 [15], which may explain the observed shifts in the transition temperatures (Figs. 4–7). Both NKN and $LiNbO_3$ have basic NbO_6 octahedral structure units but different structures [15]. NKN has a mixed structure comprising distorted small-cell perovskite ($KNbO_3$) [24] and distorted multiple-cell perovskite ($NaNbO_3$) [25]. However, $LiNbO_3$ has a lithium niobate structure, which can be described as a heavily distorted perovskite or an ordered phase derived from the corundum structure [15]. The different distortions of the perovskite cells with basic components comprising $NaNbO_3$, $KNbO_3$, and $LiNbO_3$, as well as their differing proportions in the prepared ceramics may explain the observed shifts in the transition temperature(s). At lower concentrations, Li mainly replaced Na and K in the A sites of the ABO_3 perovskite structure (i.e., forming a solid solution), thereby leading to a linear shift in the transition temperature(s) (Figs. 4–7).

3.2. HT-XRD measurements

The HT-XRD patterns obtained for the prepared samples where y ≤ 0.05 are shown in Figs. 8–12. The HT-XRD patterns obtained for the prepared samples indicated polycrystalline behavior. The XRD patterns for all of the prepared samples indicated a monoclinic phase between RT and around 200 °C, which was consistent with Inorganic Crystal Structure Database (ICSD) data (00-061-0317 and 00-061-0315). Between 200 °C and 380 °C, the results indicated the occurrence of a tetragonal phase, which was consistent with ICSD data (01-078-5547). For the compositions where y ≤ 0.02, tetragonal symmetry was indicated between 380 °C and 460 °C, which was consistent with ICSD data (00-077-0037) and a previous study [10] (Figs. 8 and 9). Above 460 °C, all of the compositions exhibited cubic symmetry, which was compatible with ICSD data (00-060-0328) (Figs. 8–12).

The HT-XRD patterns indicated continuous shifts of the intense peaks at (200), (002), (221), and (112) as the temperature changed for NKLN, where 0.01 ≤ y ≤ 0.02 (Figs. 8 and 9). Between RT and 200 °C, these peaks shifted to a higher angle as the temperature increased. Between 200 °C and 380 °C, the peaks shifted toward lower angles as the temperature increased and the heights of the peaks also changed, where the smaller peaks became larger and vice versa. Above 380 °C, the peak at (221) vanished, and the remaining peaks shifted slightly toward lower

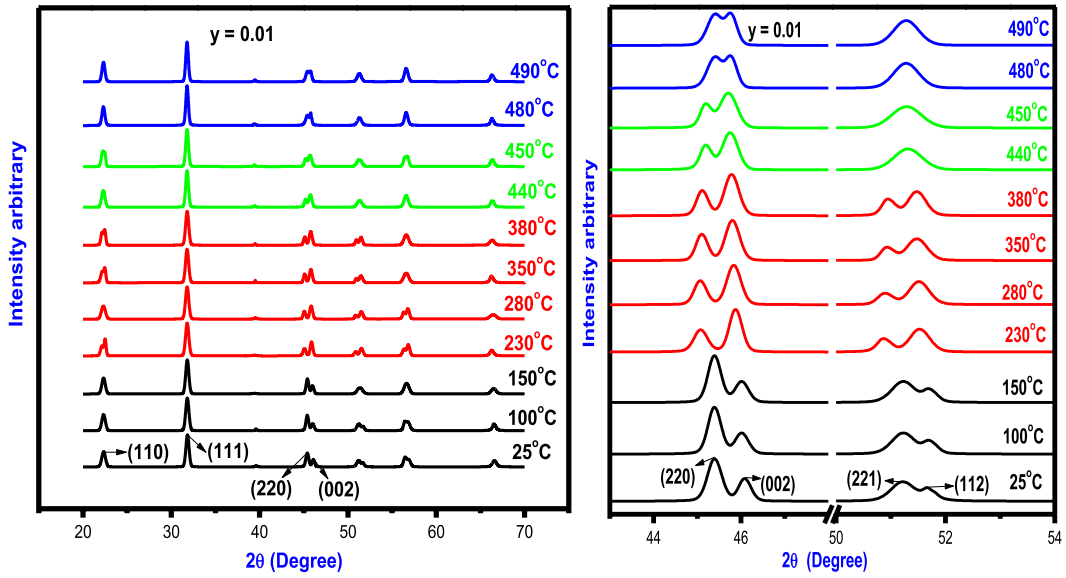

Fig. 8. High temperature-XRD patterns obtained for $(Na_{0.5}K_{0.5})_{1-y}Li_yNbO_3$, where y = 0.01.

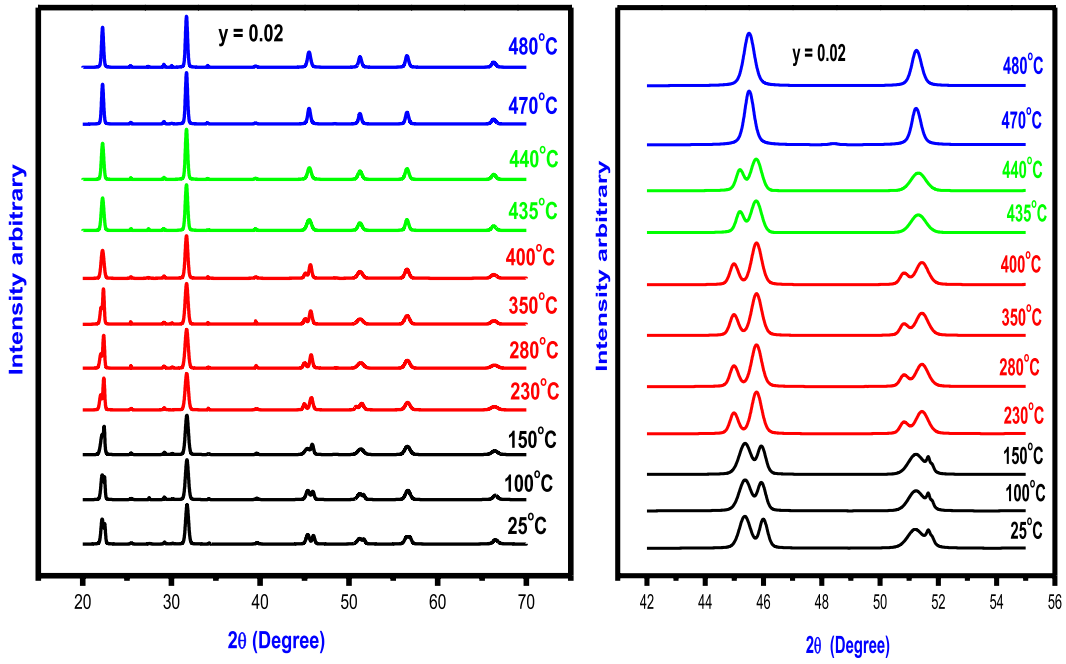

Fig. 9. High temperature-XRD patterns obtained for $(Na_{0.5}K_{0.5})_{1-y}Li_yNbO_3$, where y = 0.02.

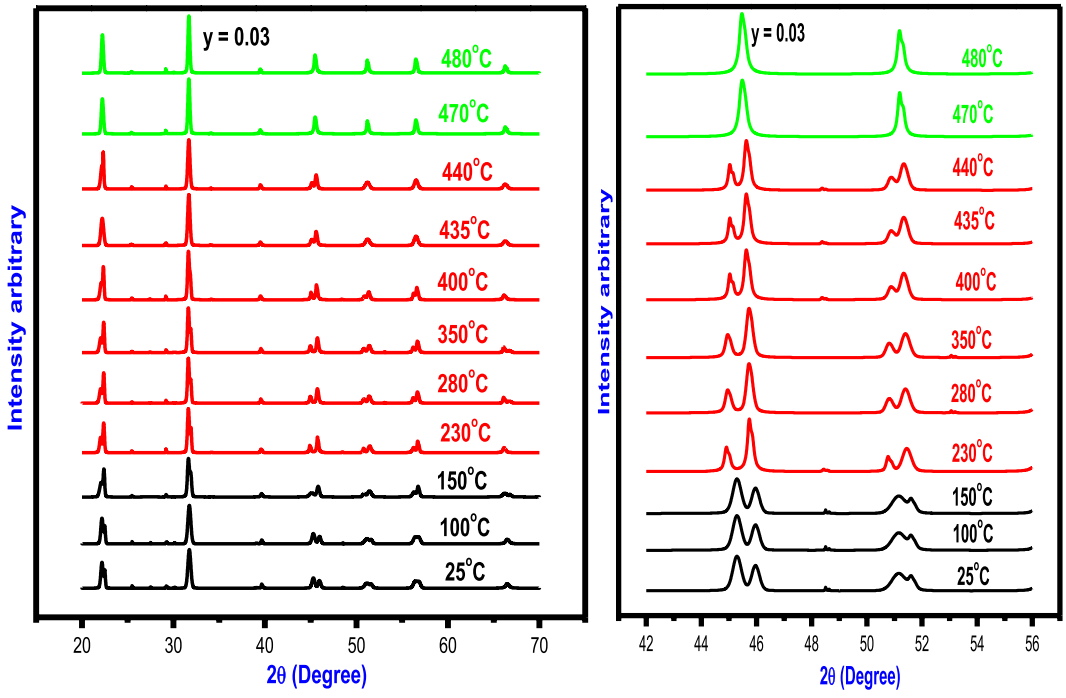

Fig. 10. High temperature-XRD patterns obtained for $(Na_{0.5}K_{0.5})_{1-y}Li_yNbO_3$, where y = 0.03.

angles above 460 °C.

In the HT-XRD patterns obtained for NKLN, where $0.03 \leq y \leq 0.05$, the intense peaks at (200), (002), (221), (220), and (112) shifted continuously as the temperature increased (Figs. 10–12). Between RT and 200 °C, the peaks shifted toward higher angles as the temperature increased. Between 200 °C and 460 °C, the peaks shift toward lower angles as the temperature increased and the peak height also changed, where the smaller peaks became larger and vice versa. Above 460 °C, the peak at (220) vanished and the remaining peaks shifted slightly toward lower angles. The observed HT-XRD patterns clearly indicated four distinct phases in NKLN where $y \leq 0.02$, with transitions at around 200 °C, 380 °C, and 460 °C. However, for the compositions where $0.03 \leq y \leq 0.05$, the observed HT-XRD patterns clearly indicated only three distinct phases, with transitions at around 200 °C and 460 °C.

The cell parameters were refined by utilizing High Score Plus software, where the background was modeled using the Legendre polynomial and the pseudo-Voigt function with the Rietveld method [26]. The space groups selected for these refinements were monoclinic Pm6 and tetragonal P4mm, respectively [27]. For all of the prepared NKLN compositions where $y \leq 0.05$, the observed temperature-dependent

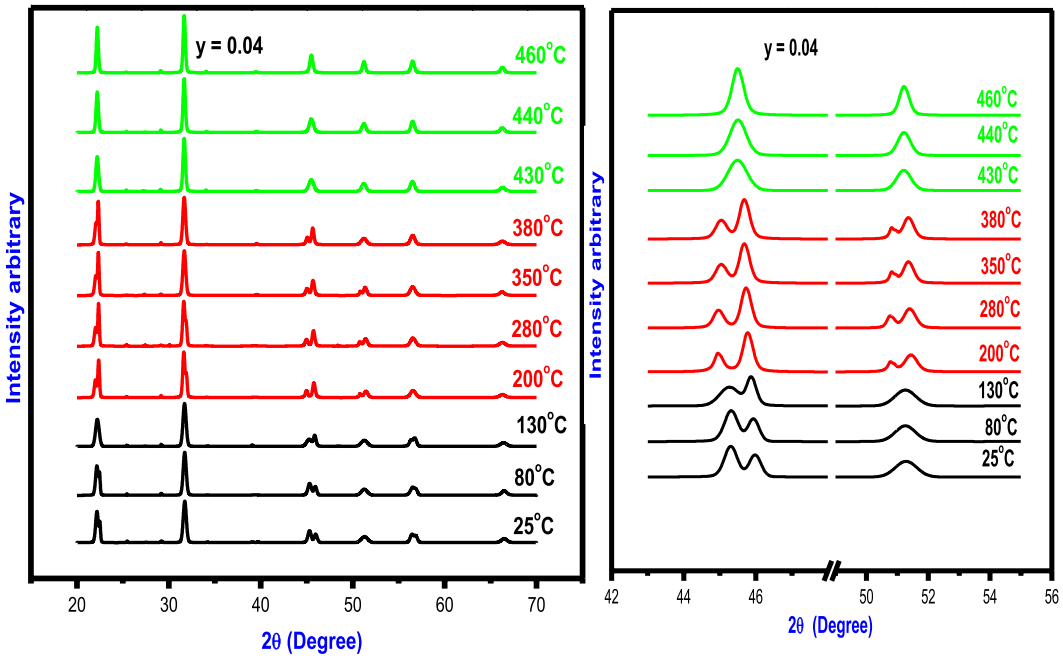

Fig. 11. High temperature-XRD patterns obtained for $(Na_{0.5}K_{0.5})_{1-y}Li_yNbO_3$, where y = 0.04.

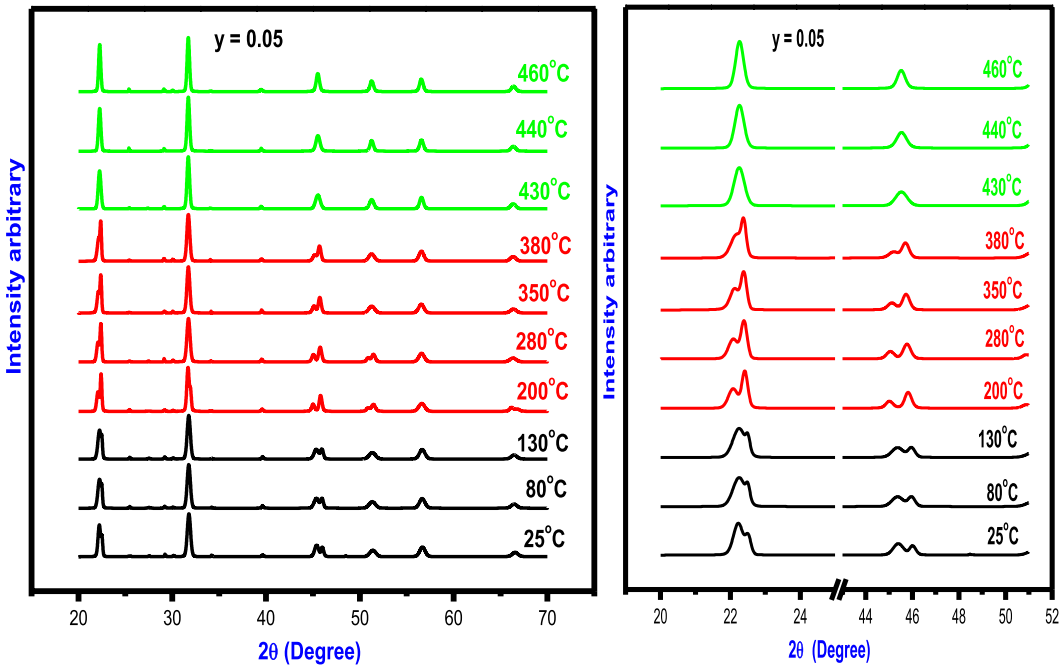

Fig. 12. High temperature-XRD patterns obtained for $(Na_{0.5}K_{0.5})_{1-y}Li_yNbO_3$, where y = 0.05.

variations in the lattice parameters and angle (β for monoclinic symmetry) are shown in Figs. 13–17. For the compositions where $0.01 \leq y \leq 0.02$, the observed lattice parameters allowed the monoclinic, tetragonal, tetragonal, and cubic symmetries to be distinguished. By contrast, for the compositions where $0.03 \leq y \leq 0.05$, the observed lattice parameters allowed the monoclinic, tetragonal and cubic symmetries to be distinguished (Figs. 15–17).

The HT-XRD results obtained for the NKLN pellets indicated the occurrence of three phase transitions comprising monoclinic to tetragonal, tetragonal to tetragonal, and tetragonal to cubic at around 200 °C, 380 °C, and 460 °C, respectively, for the compositions where $0.01 \leq y \leq 0.02$, whereas two phase transitions from monoclinic to tetragonal at around 200 °C and tetragonal to cubic at around 460 °C were distinguished for the compositions where $0.03 \leq y \leq 0.05$. The HT-XRD results were consistent with the transitions determined based on the dielectric constant measurements for the prepared compositions.

The transition temperatures determined for all the individual compositions of the NKLN system prepared in this study ($y \leq 0.05$) based on the dielectric constant measurements and HT-XRD results were independent of the frequencies, and the same transition temperatures were observed at all the measured frequencies for a given composition. For the composition where y = 0.03, the dielectric constant peak shifted and

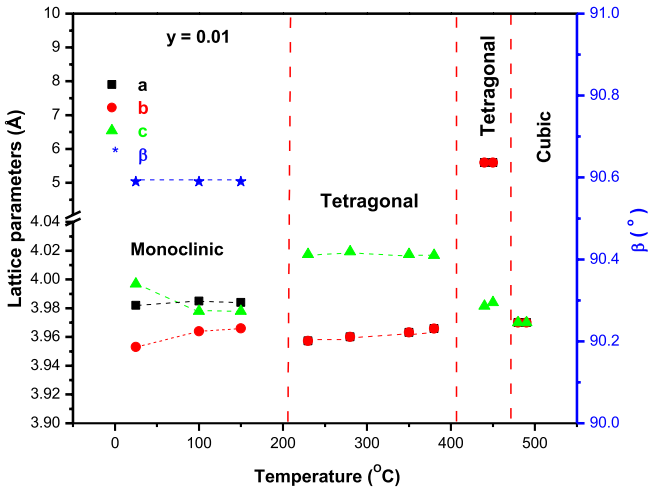

Fig. 13. Temperature-dependent variations in the lattice parameters for $(Na_{0.5}K_{0.5})_{1-y}Li_yNbO_3$, where y = 0.01.

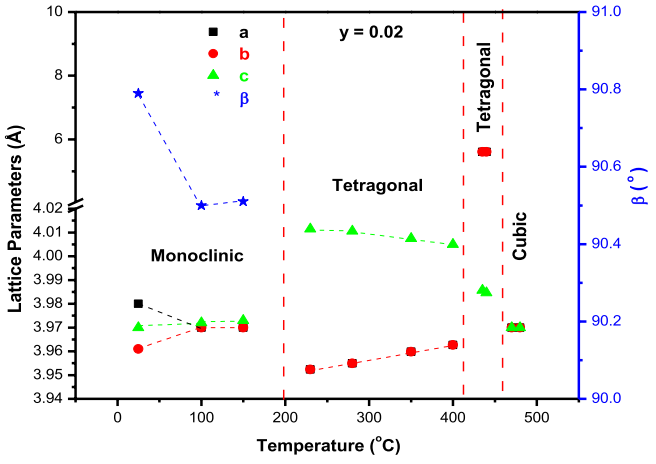

Fig. 14. Temperature-dependent variations in the lattice parameters for $(Na_{0.5}K_{0.5})_{1-y}Li_yNbO_3$, where y = 0.02.

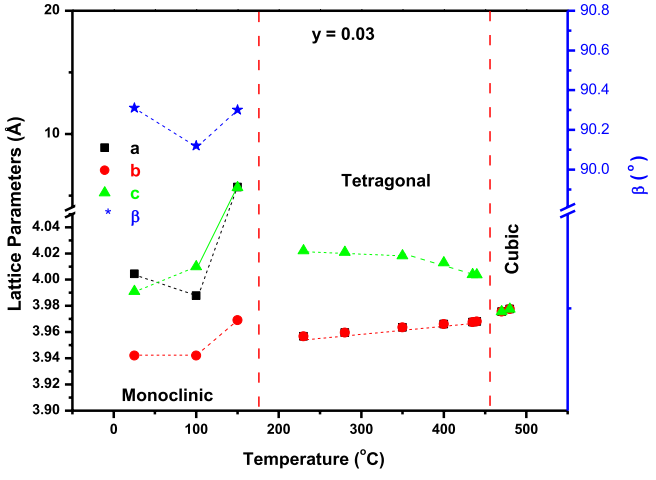

Fig. 15. Temperature-dependent variations in the lattice parameters for $(Na_{0.5}K_{0.5})_{1-y}Li_yNbO_3$, where y = 0.03.

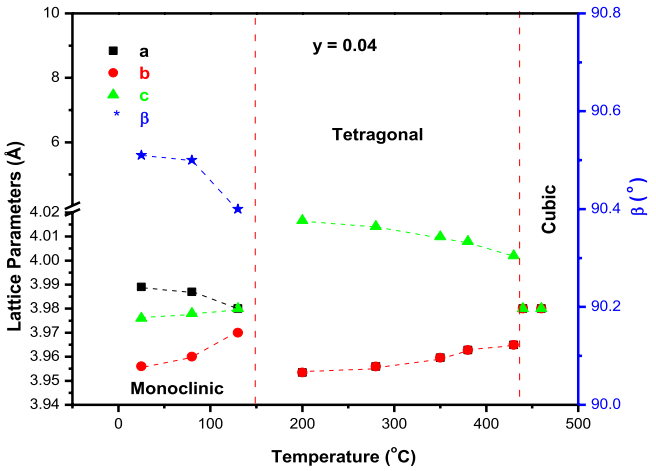

Fig. 16. Temperature-dependent variations in the lattice parameters for $(Na_{0.5}K_{0.5})_{1-y}Li_yNbO_3$, where y = 0.04.

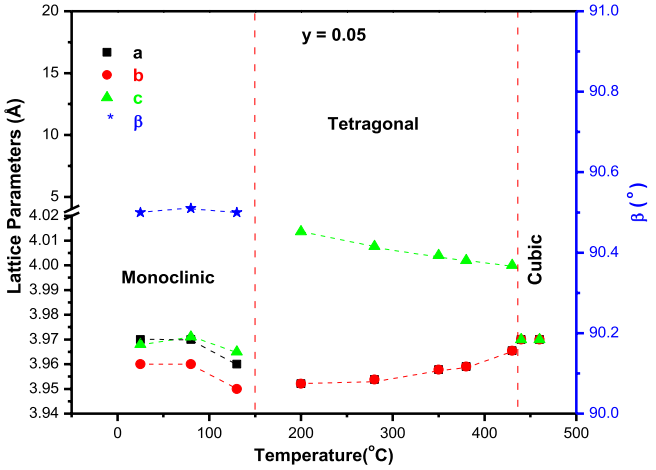

Fig. 17. Temperature-dependent variations in the lattice parameters for $(Na_{0.5}K_{0.5})_{1-y}Li_yNbO_3$, where y = 0.05.

broadened with the frequency at the transition temperature (Fig. 4), thereby indicating the relaxor type behavior of this composition [28]. However, relaxor type behavior was not observed for all of other compositions [11].

4. Conclusions

In the present study, the results showed that for NKLN with compositions where $y \leq 0.02$, the dielectric constant increased as the temperature increased and anomalous behavior was detected at the transition temperatures, i.e., from monoclinic to tetragonal at about 200 °C, tetragonal to tetragonal at about 380 °C, and tetragonal to cubic at about 460 °C. By contrast, for the compositions where $0.03 \leq y \leq 0.06$, the phase transitions occurred from monoclinic to tetragonal at about 200 °C and tetragonal to cubic at about 460 °C. As the Li concentration (y) increased, the transition temperature at around 200 °C shifted to a lower temperature and that at about 380 °C shifted to a higher temperature for all of the measured compositions. For the compositions where the Li concentration $y \leq 2$ (mole) %, a tetragonal to tetragonal transition was determined, which could not be detected for the compositions where $y \geq 3$ (mole) % Li, and only three phases were detected for the compositions where $0.03 \leq y \leq 0.06$, i.e., monoclinic from RT to about 200 °C, tetragonal from about 200 °C to 460 °C, and cubic

symmetry above about 460 °C (Figs. 15–17). The temperature-dependent dielectric constant measurements were consistent with the HT-XRD results obtained for the prepared compositions. These transitions may be associated with the temperature-dependent softening of the low lying optical phonon mode. The variations in the transition temperature(s) with the doping concentration may be due to the changes in the mass and force constant in the lattice [21,22]. As the temperature tends to T_c, the soft mode frequency tends to zero and the lattice undergoes a structural phase transition, thereby explaining the anomalous dielectric properties.

CRediT authorship contribution statement

Surendra Singh: Conceptualization, Formal analysis, Writing - original draft, Writing - review & editing. **N.S. Panwar:** Conceptualization, Formal analysis, Writing - original draft, Writing - review & editing.

Appendix A. Supplementary data

Supplementary data to this article can be found online at https://doi.org/10.1016/j.jpcs.2020.109583.

References

[1] H.D. Megaw, The seven phases of sodium niobate, Ferroelectrics 7 (1974) 87–89.
[2] A.M. Glazer, K. Ishida, Cation displacements and octahedral tilts in $NaNbO_3$ Part I-Determination from X-ray difference reflections, Ferroelectrics 6 (1974) 219–224.
[3] D.W. Baker, P.A. Thomas, N. Zhang, A.M. Glazer, A comprehensive study of the phase diagram of $K_xNa_{1-x}NbO_3$, Appl. Phys. Lett. 95 (2009), 091903.
[4] L. Wu, J.L. Zhang, C.L. Wang, J.C. Li, Influence of compositional ratio K/Na on physical properties in $(K_xNa_{1-x})NbO_3$ ceramics, J. Appl. Phys. 103 (2008), 084116.
[5] G. Shirane, R. Newnham, R. Pepinsky, Dielectric properties and phase transitions of $NaNbO_3$ and $(Na,K)NbO_3$, Phys. Rev. 96 (1954) 581–588.
[6] G.H. Haertling, Properties of hot-pressed ferroelectric alkali niobate ceramics, J. Am. Ceram. Soc. 329 (1967) 10–13.
[7] M. Ahtee, A.M. Glazer, High-temperature phases of sodium niobate- potassium niobate solid solutions, Ferroelectrics 12 (1976) 205–206.
[8] M.A.L. Nobre, S. Lanfredi, Impedance spectroscopy analysis of high-temperature phase transitions in sodium lithium niobate ceramics, J. Phys. Condens. Matter 12 (2000) 7833–7841.
[9] M.A.L. Nobre, S. Lanfredi, Phase transition in sodium lithium niobate polycrystal: an overview based on impedance spectroscopy, J. Phys. Chem. Solid. 62 (2001) 1999–2006.
[10] D. Lin, Z. Li, F. Li, C. Cai, W. Liu, S. Zhang, Tetragonal-to-tetragonal phase transition in lead-free $(K_xNa_{1-x})NbO_3$ (x = 0.11 and 0.17) crystals, Crystals 4 (2014) 113–122.
[11] A.S. Kandari, A. Bhandari, A.A. Bourai, N.S. Panwar, Electrical properties of $Na_{1-x}K_xNbO_3$ ($0.28 \leq x \leq 0.40$), Ferroelectrics 386 (2009) 139–151.
[12] V. Lingwal, B.S. Semwal, N.S. Panwar, Relaxational behavior of mixed $NaNbO_3$-$KNbO_3$ system, Ferroelectrics 332 (2006) 219–225.
[13] Y. Zhen, J.F. Li, Normal sintering of (K, Na)NbO_3- based ceramics: influence of sintering temperature on densification, microstructure, and electrical properties, J. Am. Ceram. Soc. 89 (2006) 3669–3675.
[14] S. Singh, J. Negi, N.S. Panwar, Temperature dependent dielectric properties of (Na, K) NbO_3, near equimolar composition, Ceram. Int. 45 (2019) 13067–13071.
[15] Y. Guo, K. ichi Kakimoto, H. Ohsato, Phase transitional behavior and piezoelectric properties of $(Na_{0.5}K_{0.5})NbO_3$–$LiNbO_3$ ceramics, Appl. Phys. Lett. 85 (2004) 18.
[16] E. Hollenstein, M. Davis, D. Damjanovic, N. Setter, Piezoelectric properties of Li- and Ta-modified $(K_{0.5}Na_{0.5})NbO_3$ ceramics, Appl. Phys. Lett. 87 (2005) 182905.
[17] P. Zhao, B.P. Zhang, J.F. Li, Enhancing piezoelectric d_{33} coefficient in Li/Ta-codoped lead-free (Na, K)NbO_3 ceramics by compensating Na and K at a fixed ratio, Appl. Phys. Lett. 91 (2007) 172901.
[18] G.Z. Zang, J.F. Wang, H.C. Chen, W.B. Su, C.M. Wang, P. Qi, B.Q. Ming, J. Du, L. M. Zheng, S. Zhang, T.R. Shrout, Perovskite $(Na_{0.5}K_{0.5})_{1-x}(LiSb)_xNb_{1-x}O_3$ lead-free piezoceramics, Appl. Phys. Lett. 88 (2006) 212908.
[19] J.G. Wu, D.Q. Xiao, Y.Y. Wang, J.G. Zhu, P. Yu, Effects of K content on the dielectric, piezoelectric, and ferroelectric properties of $0.95(K_xNa_{1-x})NbO_3$-$0.05LiSbO_3$ lead- free ceramics, J. Appl. Phys. 103 (2008) 24102.
[20] K. Yan, X. Ren, Multi-phase transition behaviour and large electrostrain in lead-free (K, Na, Li)NbO_3 ceramics, J. Phys. D Appl. Phys. 47 (2014), 015309.
[21] E. Pytte, Theory of perovskite ferroelectrics, Phys. Rev. B5 (1972) 3758–3769.
[22] N.S. Panwar, T.C. Upadhyay, B.S. Semwal, Soft mode dynamics of perovskite type crystals, Pramana - J. Phys. 33 (1989) 603–616.
[23] S. Singh, J. Negi, N.S. Panwar, Dielectric properties of $Na_{1-x}K_xNbO_3$, near x = 0.5 morphotropic phase region, J. Phys. Chem. Solid. 123 (2018) 311–317.
[24] M.L. Keith, R. Roy, Structural relations among double oxides of trivalent elements, Am. Mineral. 39 (1954) 1.
[25] H.D. Megaw, Crystal structure of double oxides of the perovskite type, Proc. Phys. Soc. 58 (1946) 133.
[26] J. Tellier, B. Malic, B. Dkhil, D. Jenko, J. Cilensek, M. Kosec, Crystal structure and phase transitions of sodium potassium niobate perovskites, Solid State Sci. 11 (2009) 320–324.
[27] J. Attia, L. Bellaiche, P. Gemeiner, B. Dkhil, B. Malic, Study of potassium- sodium-niobate alloys: a combined experimental and theoretical approach, J. Phys. IV France 128 (2005) 55–60.
[28] G. Goodman, R.C. Buchanan, T.G. Reynolds III, in: Relva C. Buchanan (Ed.), Ceramic Materials for Electronics; Processing, Properties, and Application, Marcel Dekker Inc., New York, 1991, p. 32.

Ferroelectrics

ISSN: 0015-0193 (Print) 1563-5112 (Online) Journal homepage: https://www.tandfonline.com/loi/gfer20

Preparation of potassium tantalum niobate–barium titanate (KTN-BT) solid solution system ceramics and their piezoelectric properties

Gambheer Singh Kathait, M. K. Panda & N. S. Panwar

To cite this article: Gambheer Singh Kathait, M. K. Panda & N. S. Panwar (2020) Preparation of potassium tantalum niobate–barium titanate (KTN-BT) solid solution system ceramics and their piezoelectric properties, Ferroelectrics, 555:1, 109-117, DOI: 10.1080/00150193.2019.1691388

To link to this article: https://doi.org/10.1080/00150193.2019.1691388

Published online: 26 Feb 2020.

Submit your article to this journal

Article views: 2

View related articles

View Crossmark data

Full Terms & Conditions of access and use can be found at
https://www.tandfonline.com/action/journalInformation?journalCode=gfer20

FERROELECTRICS
2020, VOL. 555, 109–117
https://doi.org/10.1080/00150193.2019.1691388

Taylor & Francis
Taylor & Francis Group

Check for updates

Preparation of potassium tantalum niobate–barium titanate (KTN-BT) solid solution system ceramics and their piezoelectric properties

Gambheer Singh Kathait[a], M. K. Panda[b], and N. S. Panwar[a]

[a]Department of Instrumentation Engineering, USIC, H.N.B. Garhwal University, Srinagar Garhwal, Garhwal, Uttarakhand, India; [b]Department of Electrical Engineering, GBPIET, Pauri Garhwal, Uttarakhand, India

ABSTRACT

Potassium tantalum niobate ($KTa_{1-y}Nb_yO_3$, KTN)-barium titanate ($BaTiO_3$, BT) solid solution system 0.02[KTN]-0.98[BT] ceramics with various microstructures were prepared by modified two-step sintering method, and their dielectric and piezoelectric properties were observed. For $0.02K(Ta_{0.5}Nb_{0.5})O_3$-$0.98BaTiO_3$ ceramics ferroelectric tetragonal crystalline structure was found for sintering temperature1230, 1240, 1250, 1260, and 1270 °C. A large grain growth was observed for the BT grains of the samples. By observing the strain vs. electric field curves slope apparent piezoelectric constant d_{33}* was investigated. The piezoelectricity d_{33} is found in proportional to escaping weight % of potassium at increasing sintering temperatures. Enhanced piezoelectric constant d_{33}* of value 391 pm/V was found for sintering temperature 1240 °C.

ARTICLE HISTORY
Received 7 July 2019
Accepted 3 November 2019

KEYWORDS
Barium titanate; grain growth; potassium tantalum niobate; dielectric constant; piezoelectric property; microstructure analysis

1. Introduction

Ferroelectric materials such as barium titanate ($BaTiO_3$, BT) are of interest in the context of ceramic capacitors and piezoelectric transducers. These materials typically exhibit several phase transformations; above the Curie point, the crystal symmetry becomes insufficient for piezoelectricity. Pure BT has lower piezoelectric sensitivity than lead titanate zirconate or lead zirconium titanate ($Pb(Zr,Ti)O_3$, PZT). However, doped BT can exhibit competitive piezoelectricity with the benefit of being lead free. Addition of dopants shifts the phase transformation temperatures; in particular, the Curie point is shifted to a lower temperature. Although this is a drawback for high temperature applications, the increased ambient temperature properties could be beneficial for applications of piezoelectric materials where service temperature is moderate. Extensive studies have been performed on the piezoelectric and dielectric properties of BT based ceramics. The data on the harmful effect of Pb on health and the environment have been known for a longer period. Hence, there is an increasing demand for environment-friendly lead-free ferroelectric materials. However, as compared with lead-based ceramics such as PZT ($PbZr_xTi_{1-x}O_3$), PMN-PT ($PbMg_{1/3}Nb_{2/3}O_3$-$PbTiO_3$) and PZnN-PZT

CONTACT Gambheer Singh Kathait gambhir11186@gmail.com
© 2020 Taylor & Francis Group, LLC

($PbZn_{1/3}Nb_{2/3}O_3$-PZT) [1], their dielectric and piezoelectric properties are not so good to replace lead-based ceramics. Across the globe researchers have attempted to optimize the ferroelectric properties of lead-free ferroelectrics such as bismuth layer-structure ferroelectrics, barium titanate ($BaTiO_3$, BT) and potassium niobate ($KNbO_3$, KN); however, less improvement was observed in the properties [1–4]. Recently, lead-free piezoelectrics with modified potassium niobate ($KNbO_3$, KN) and sodium niobate ($NaNbO_3$, NN) ceramics have been investigated with a new morphotropic phase boundary (MPB) and high piezoelectric properties [5, 6]. Some researchers already studied solid solution ceramics between BT and KN [7–9]. Bratton and Tien reported a phase diagram for BT-KN system, in which for a BT-rich phase, Curie temperature (TC) decreased to below room temperature with increasing KN content, while for a KN-rich phase, TC also decreased to below room temperature with increasing BT content [8]. Irle and Blacknik reported a different phase diagram, in which for a BT-rich phase, TC decreased to below room temperature with increasing KN content, while for a KN-rich phase, the successive phase transition behaviors were identical to those of pure KN [9]. Recently a unique ceramic system was observed with a wide-band MPB region between tetragonal and orthorhombic phases for the Potassium Niobate-Barium Titanate (KN-BT) ceramic system [9]. BaTiO3 and $KNbO_3$ crystals are typical lead-free ferroelectrics and there have been a number of reports on their domain engineering [10–13]. TEM observation indicated the existence of three phases in one grain, i.e., tetragonal, rhombohedral and the interface between the two phases, while the XRD analysis confirmed the monoclinic phase for the MPB composition. The MPB composition of PZT has monoclinic origin with a distorted interface region. The distorted interface region might be the reason for optimized piezoelectricity in PZT. Ishibashi and Iwata suggested that the absence of energy barrier between tetragonal and rhombohedral phases in the MPB region caused field-induced phase transition [14, 15]. Fu and Cohen applied the first principle calculation and confirmed that by an external field polarization rotation mechanism was originated that resulted in an ultrahigh electromechanical response [16, 17]. In this study, to clarify the role of two-step sintering temperature on piezoelectricity, a relationship between sintering temperature and escaping of alkali ions and the piezoelectric property was investigated using the $0.02K(Ta_{0.5}Nb_{0.5})O_3$-$0.98BaTiO_3$ ceramics. For the objective, various sintering temperature was applied to the $0.02K(Ta_{0.5}Nb_{0.5})O_3$-$0.98BaTiO_3$ ceramics by a modified two-step sintering method, and the ceramic microstructures were analyzed by a scanning electron microscopy (SEM). Also, the dielectric and apparent piezoelectric constant d_{33}^* was measured. The relationship between density and piezoelectricity was discussed for $0.02K(Ta_{0.5}Nb_{0.5})O_3$-$0.98BaTiO_3$ ceramics.

2. Experimental procedure

A slight modification was made in the conventional two-step sintering method reported for BT ceramics by Karaki et al., to prepare fine-grained and dense ceramics for the $0.02K(Ta_{0.5}Nb_{0.5})O_3$-$0.98BaTiO_3$ ceramics [18]. Barium Carbonate ($BaCO_3$), Titanium Dioxide (TiO_2), Potassium Carbonate (K_2CO_3),Tantalum Pentaoxide (Ta_2O_5), and Niobium Pentaoxide(Nb_2O_5) were taken in the molar ratio $0.02[K(Ta_{0.5}Nb_{0.5})O_3$-

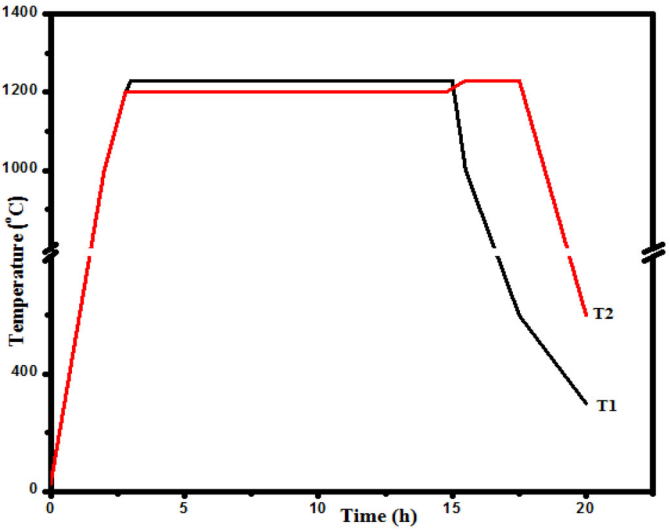

Figure 1. A schematic two-step sintering program for the $0.02[KT_{0.5}N_{0.5}]$-0.98BT ceramics.

$0.98[BaTiO_3]]$. Conventional solid state reaction method was used to prepare the ceramic. Reagent grade Barium Carbonate ($BaCO_3$), Titanium Dioxide (TiO_2), Potassium Carbonate (K_2CO_3), Tantalum Pentaoxide (Ta_2O_5) and Niobium Pentaoxide (Nb_2O_5) of high purity 99.0% were used as starting materials. The raw material was dried at 200°C for two hours to remove moisture and then weighed in stoichiometric proportions. Manual grinding in acetone for 2 h (wet) and 4 h (dry) was carried out. The ground powder was calcinated at 1000°C for 6 h in an alumina crucible. The calcinated powder was manually ground for half an hour. Very thin pellets were prepared at a hydrostatic pressure of 0.2GPascal, with diameter 8 mm dia piston. Pellets were prepared by two-step sintering method with different temperature program. These pellets were sintered at temperature 1230, 1240, 1250, 1260, and 1270 °C for 12 h in first sintering (T1). Sintered pellets were crushed into powder and again pellets were prepared at a pressure of 0.2GPascal, with diameter 8 mm dia piston. Second sintering (T2) was done according to program as shown in Figure 1. For the second sintering (T2) the temperature was set at 1200 °C for 11 h and then changed to 1230, 1240, 1250, 1260, and 1270 °C, for 2.5 h and the $0.02[KT_{0.5}N_{0.5}]$-0.98BT ceramics with various microstructures were prepared. This process of sintering is applied for different sintering temperatures for composition $0.02[KT_{0.5}N_{0.5}]$-0.98BT. Sintered pellets were taken for XRD analysis. XRD analysis was obtained for intensity *versus* angle (2Θ, in the range between 20 and 70).

The crystalline structure was measured by X-ray diffraction (XRD), on an X-Pert PANalytical diffractometer using a fixed divergence1/2° slit, a Cu W/Si mirror and a 10 mm mask as incident optics and a parallel plate collimator and a proportional detector as diffracted beam optics. Only pure perovskite structure exists for all $0.02K(Ta_{0.5}Nb_{0.5})O_3$-$0.98BaTiO_3$ ceramics with different sintering temperatures. Sintered pellet was coated with high-quality silver paste on both sides. The silver-coated pellets were dried for 2 h at room temperature. A computer-controlled system, with LCR meter (make: Fluke, model: PM6306) was used to measure temperature and frequency

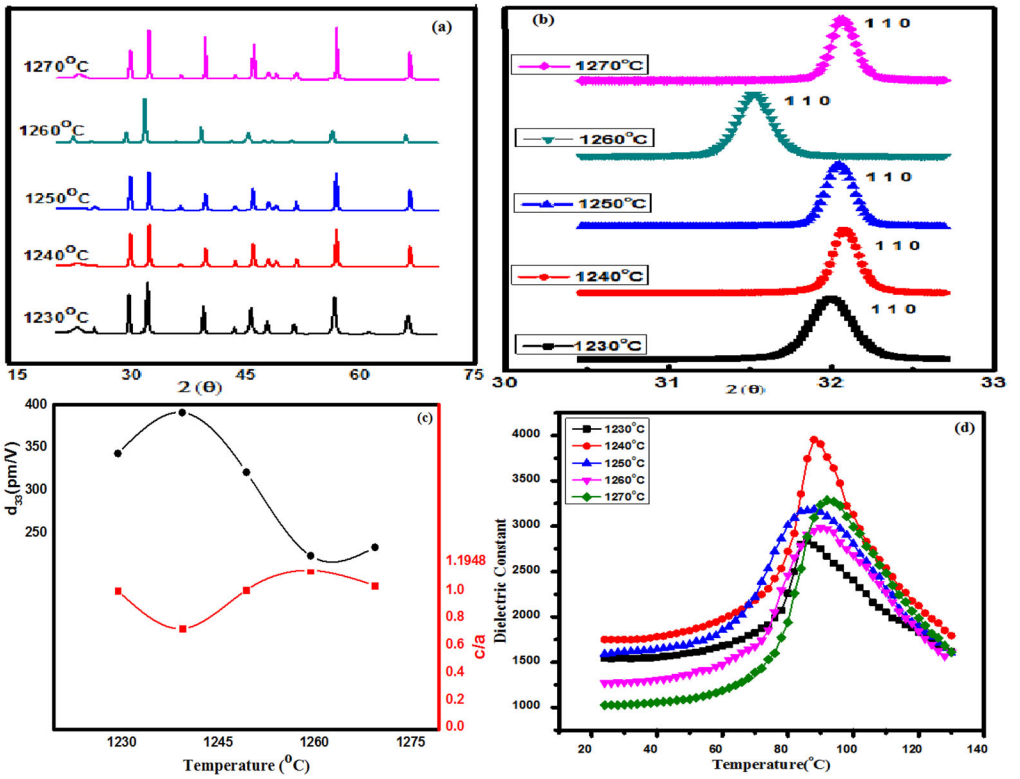

Figure 2. (a) XRD pattern, (b) Phase shift, (c) d_{33}* *vs.* c/a, and (d)Dielectric Constant for sintering temperatures 1230,1240,1250,1260, and 1270 °C.

dependence of dielectric properties. Both low frequency (1 KHz) and high frequency (1 MHz) dielectric measurement were performed using this LCR meter. The microstructure was examined by scanning electron microscopy (SEM) using model EVO 18 Special Edition (Switzerland), manufactured by ZEISS. The silver-coated pellets were taken for apparent piezoelectric coefficient d_{33}* measurement and strain analysis using a Piezo Loop Tracer, model aixPES manufactured by aixACT systems GamH.

3. Results and discussion

The crystallinity of the prepared ceramics was determined using an X-RAY diffractometer (XPERT-PRO) with a Cu Kα radiation source ($\lambda = 1.54059$ Å), operated at a voltage of 45kV and a current of 40 mA. The XRD patterns of $0.02[KT_{0.5}N_{0.5}]$-0.98BT for sintering temperatures 1230, 1240, 1250, 1260, and 1270 °C are shown in Figure 2(a). As depicted in Figure 2(a) the $\theta/2\theta$ X-ray diagram shows that the prepared 0.02KT0.5N0.5-0.98BT ceramics are crystalline in perovskite phase. The patterns for sintering temperature 1230, 1240, 1250, 1260, and 1270 °C crystalline in nature and well oriented. The crystal structure exhibits tetragonal symmetry for all samples that are under observation. In all of them a single phase perovskite solid solutions, is observed. In Figure 2(b) the slope of the plot changes from negative to positive at the sintering temperature 1240 °C,

Table 1. Lattice parameter of $0.02[KT_{0.5}N_{0.5}]$-0.98BT ceramics, for sintering temperature1230, 1240, 1250, 1260, and 1270 °C

Temp (°C)	a	c	c/a
1230	3.9768	4.0157	1.009781734
1240	7.6045	5.5784	0.733565652
1250	3.9686	4.0273	1.01479111
1260	4.0224	4.6562	1.157567621
1270	3.9447	4.1263	1.046036454

which indicates structural anomaly at this sintering temperature, a MPT type behavior [19].

The XRD analysis shows the possibility of distorted interface region between BT and KTN. Figure 2(b) shows shifting pattern of (1 1 0) with sintering temperature, the result are supported by the d_{33*} pattern Figure 2(c) and dielectric analysis Figure 2(d). The Curie temperature gets shifted to high temperature with increasing sintering temperatures Figure 2(d). However, between 46° and 48°, two new peaks were observed, which becomes significantly noticeable for sintering temperature 1240°C.

Table 1 shows the c/a pattern with increasing sintering temperature. The results are supported by the enhanced and varied pattern of d_{33}* value as sown in Figure 2(c).

Figure 3 shows SEM micrographs of the $0.02[KT_{0.5}N_{0.5}]$-0.98BT ceramics prepared at 1230 °C (Figure 3(a)), 1240 °C (Figure 3(b)), 1250 °C (Figure 3(c)), 1260 °C (Figure 3(d)), and 1270 °C (Figure 3(e)). An uniform grain growth was observed for the BT grains of the samples, which was consistent with a previous study [20]. Fig. 3(a),(b) and (c) shows better uniformity of microstructures for sintering temperature 1230 °C, 1240 °C, and 1250 °C. As the sintering temperature is increased the KN-rich nano-grains became liquid at higher temperatures [14], which results in a slightly melt microstructure as shown in Fig. 3(c) and (d). That results in an abnormal microstructure. The melting behavior of grains that may be correlated with the grain boundary diffusion and a low melting point of KTN may result in the viscous flow. The grain size is $\sim 4\,\mu$m, $6\,\mu$m, $9\,\mu$m, $13\,\mu$m and $18\,\mu$m for 1230 °C, 1240 °C, 1250 °C, 1260 °C and 1270 °C.

Table 2 indicates the atomic weight % observed and calculated in samples sintered at various sintering temperatures. From the SEM-EDAX analysis it is observed that escaping of Potassium is maximum for sintering temperature 1240 °C. The piezoelectricity d_{33}* is found in proportional to escaping weight % of Potassium at increasing sintering temperatures. It seems for the ceramics sintered at 1240 °C, enhanced diffusion processes significantly increase the escaping of alkali ions. The A-site vacancy concentration, for the ceramics sintered at 1240 °C, is higher than that in the ceramics of other sintering temperatures. The A-site vacancy attracts electron and acts as acceptor, and due to the electron deficiency, the A-site vacancy behaves as 'hole' in the lattice. Due to the less escaping of the alkali ions very low number of holes will be present for conduction for the composition sintered at 1240 °C. It seems that during sintering of the samples the intensification of diffusion processes remarkably reduces the possibility of escape of highly volatile alkali metal ions from the lattice. This volatility of potassium (K) results in a high value of peak dielectric constant (ϵ_c) at 1240 °C as shown in Fig. 4(a), at which the SEM results show uniformly distributed large grains. Increasing the sintering temperature above 1240 °C results in the low escaping of K that decreases the peak

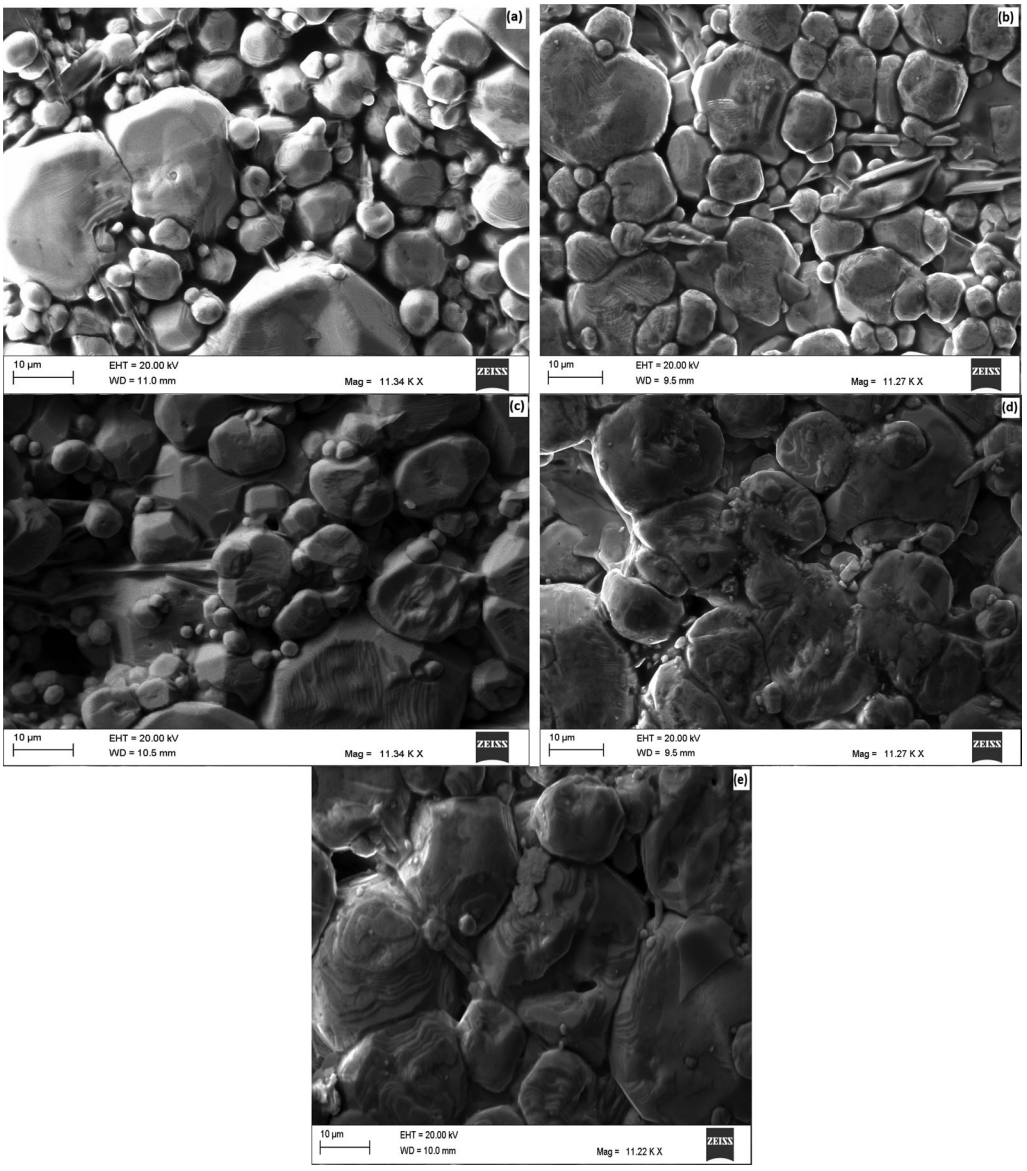

Figure 3. SEM micrographs of the $0.02[KT_{0.5}N_{0.5}]$-0.98BT ceramics prepared by two-step sintering.

dielectric constant (ϵ_c). The reduction in K content results in a decrease of d_{33}^* and dielectric constant which was consistent with a previous study [7].

Figure 4(a) shows the Dielectric constant and dielectric loss behavior with increasing sintering temperatures measured at room temperature. The maximum value of dielectric constant 1749, was found for 1240 °C at room temperature and 3955 at curie temperature Figure 2(d). Figure 4(b) depicts that the dielectric constant and dielectric loss gets saturated at high frequency (MHz).

The S-E (strain-electric field) relationship of the $0.02K(Ta_{0.5}Nb_{0.5})O_3$-$0.98BaTiO_3$ ceramics observed at 1 Hz at different sintering temperatures are shown in Fig. 5(a). The

Table 2. SEM-EDAX quantitative analysis of $0.02[K(Ta_{0.5}Nb_{0.5})O_3\text{-}0.98[BaTiO_3]$. for different sintering temperatures (T1& T2): (a) 1230 °C, (b) 1240 °C, (c) 1250 °C, (d) 1260 °C, and (e) 1270 °C

	Sintering temp. 1230 °C Atomic %		Sintering temp. 1240 °C Atomic %		Sintering temp. 1250 °C Atomic %		Sintering temp. 1260 °C Atomic %		Sintering temp. 1270 °C Atomic %	
Elements	Obs.	Cal.	Obs.	Cal.	Obs.	Cal.	Obs.	Cal.	Obs.	Cal.
Oxygen (O)	69.92	60	65.38	60	69.25	60	66.94	60	65.19	60
Potassium (K)	0.13	0.4	0.08	0.4	0.12	0.4	0.17	0.4	0.2	0.4
Tantalum (Ta)	1.07	0.2	0.7	0.2	0.84	0.2	0.88	0.2	0.56	0.2
Niobium (Nb)	1.02	0.2	0.64	0.2	0.17	0.2	0.98	0.2	0.57	0.2
Barium (Ba)	14.36	19.6	16.85	19.6	15.28	19.6	16.56	19.6	17.33	19.6
Titanium (Ti)	13.5	19.6	16.36	19.6	14.34	19.6	14.46	19.6	16.15	19.6
Escaping of K	67.50%		80%		70%		57.50%		50%	

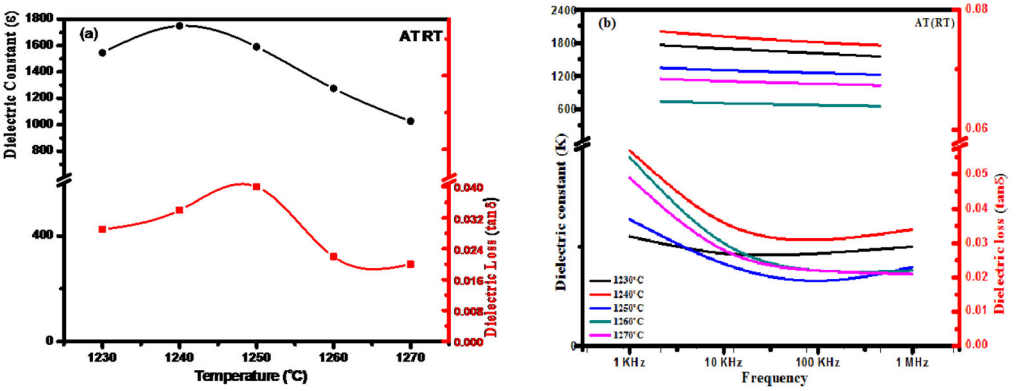

Figure 4. Dielectric Constant and Loss (tan(δ)) with Sintering temperatures 4(a) and Frequency 4(b).

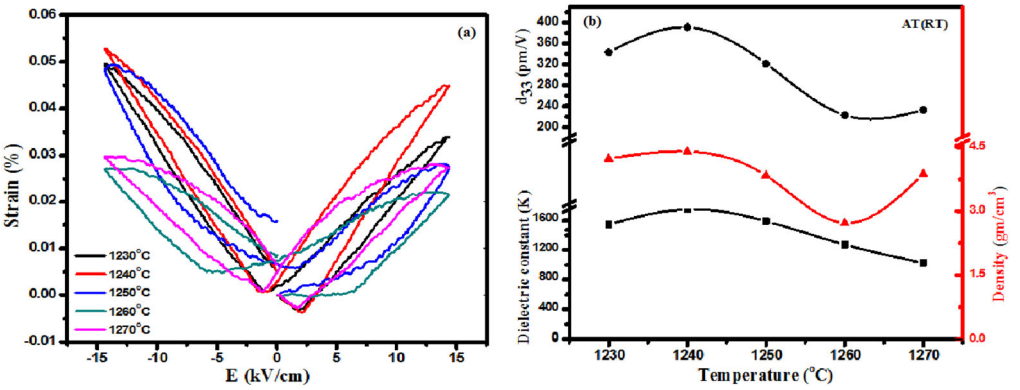

Figure 5. (a) P-E curves measured at 1 Hz and (b) Dielectric Constant d_{33*} and density at room temperature for the sintered KTN-BT microstructured ceramics.

S-E relationships reveal a typical ferroelectric butterfly behavior. The maximal strain divided by the applied electric field called apparent piezoelectric constant d_{33}*, estimated for the KTN-BT ceramics with the composition ratio of $0.02[K(Ta_{0.5}Nb_{0.5})O_3\text{-}0.98[BaTiO_3]$ is 391 pm/V at sintering temperature 1240 °C. These d_{33}* values are higher than that of the sintered $BaTO_3$ ceramics (d_{33}*=162 pm/V [18]) and for the KN/

BT complex (KN/BT = 0.25, d_{33}*=318pm/V [18]). We assume that an increase in the dielectric strain is related to the increase in the dielectric constant of the KN/BT complexes. We undertake detailed investigations to clarify the mechanism of the increase in d_{33}. Figure 5(b) shows a proportional relation between dielectric constant, d_{33}* and density at all sintering temperatures. All values are at maximum at 1240 °C. In Figure 5(b), it should be noted that the dielectric and piezoelectric behaviors had almost similar tendency, i.e., dielectric and apparent d_{33} maximum at 0.02[K(Ta0.5Nb0.5)O_3-0.98[$BaTiO_3$]. ceramics. This suggested that the enhancement of dielectric and piezoelectric properties behaviors had almost similar tendency. This suggested that the enhancement of dielectric and piezoelectric properties was originated from the same enhancement mechanism [21].

4. Conclusions

The X-ray diagram shows that the prepared 0.02[$KT_{0.5}N_{0.5}$]-0.98BT ceramics are crystalline in perovskite phase. The pattern for sintering temperatures 1230, 1240, 1250, 1260, and 1270 °C are crystalline in nature and well oriented. SEM analysis indicates that the microstructure of the ceramics with sintering temperature 1240 °C has large grain with dense microstructure. From the SEM-EDX analysis, the volatility of K content increases of d_{33}* and dielectric constant which was consistent with a previous study. The Dielectric and apparent piezoelectric constant d_{33}* were observed maximum for sintering temperature1240 °C for the 0.02K($Ta_{0.5}Nb_{0.5}$)O_3-0.98$BaTiO_3$ ceramics, and it was confirmed that the results are effective for enhancement of dielectric and piezoelectric properties.

Acknowledgments

The authors are thankful to Department of Instrumentation Engineering-USIC, SOET, HNB Garhwal University, Srinagar (Garhwal), for providing laboratory and analytical facilities.

References

[1] Demartin Maeder M. and Damjanovic D., Piezoelectric Materials in Devices, (N. Setter, Lausanne), EPFL, 2002, p. 389.
[2] Jona F. and Shirane G., Ferroelectric Crystals (Dover, New York), 1993, p. 108.
[3] B. Jaffe, W. R. Cook, Jr., and H. Jaffe, Piezoelectric Ceramics (Academic Press, New York), 1971, p. 135.
[4] Y. Zu: Ferroelectric Materials and their Applications, (North-Holland, Amsterdam), 1991, p. 101.
[5] Bratton R. J. and Tien T. Y., *J. Am. Ceram. Soc.*, 50 (1967) 90. DOI: 10.1111/j.1151-2916.1967.tb15046.x.
[6] Guo Y., Kakimoto K. and Ohsato H., *Appl. Phys. Lett.*, 85 (2004) 4121. DOI: 10.1063/1.1813636.
[7] Wada S., Suzuki S., Noma T., Suzuki T., Osada M., Kakihana M., Park S. E., Cross L. E., and Shrout T. R., *Jpn. J. Appl. Phys.* 38 (1999) 5505. DOI: 10.1143/JJAP.38.5505.
[8] Irle E. and Blacknik R., *Thermochim. Acta*, 185 (1991) 355. DOI: 10.1016/0040-6031(91)80056-O.

[9] Wada S., Nitta M., Kumada N., Tanaka D., Furukawa M., Ohno S., Moriyoshi C. and Kuroiwa Y., *Jpn. J. Appl. Phys*., 47 (2008) 7678. DOI: 10.1143/JJAP.47.7678.
[10] Wada S., Muraoka K., Kakemoto H., Tsurumi T., and Kumagai H., *Jpn. J. Appl. Phys*., 43 (2004) 6692. DOI: 10.1143/JJAP.43.6692.
[11] Wada S., Yako K., Kakemoto H., Erhart J., and Tsurumi T., *Key Eng. Mater*., 269 (2004) 19. DOI: 10.4028/www.scientific.net/KEM.269.19.
[12] Park S.-E., Wada S., Cross L. E., and Shrout T. R., *J. Appl. Phys*. 86 (1999) 2746. DOI: 10.1063/1.371120.
[13] Wada S., Tsurumi T., *British Ceramic Transactions*, 103 (2004) 93. DOI: 10.1179/096797804225012747.
[14] Wada Satoshi, Shimizu Shigehito, Pulpan Petr, Kumada Nobuhiro, Tanaka Daisuke, Furukawa Masahito, Moriyoshi Chikako And Kuroiwa Yoshihiro, *Journal of the Ceramic Society of Japan*, 118 (2010) 691. DOI: 10.2109/jcersj2.118.691.
[15] Ishibashi Y. and Iwata M., *Jpn. J. Appl. Phys*., 37 (1998) L985. DOI: 10.1143/JJAP.37.L985.
[16] Karaki T., Yan K., Miyamoto T., and Adachi M., *Jpn. J. Appl. Phys*., 46 (2007) L97. DOI: 10.1143/JJAP.46.L97.
[17] Fu H. and Cohen R. E., *Nature*, 403 (2000) 281. DOI: 10.1038/35002022.
[18] Ueno S., Kawashima H., Nakashima K., Kumada N., Magome E. et al., *J. Appl. Phys*., 114 (2013) 074103[1]. DOI: 10.1063/1.4818960.
[19] Klein Naama, Hollenstein Evelyn, Damjanovic Dragan, Trodahl H. J., Setter Nava, and Kuball Martin, *J. Appl. Phys*., 102 (2007) 014112. DOI: 10.1063/1.2752799.
[20] Shimizu, S., Kumada N., Nakashima K., Fuji I., Tanaka D., Uchikoshi T., Sakka Y. and Wada S., *Key Eng. Mater*.. 485 (2011) 89.
[21] Wada Satoshi, Nitta Momoyo, Kumada Nobuhiro, Tanaka Daisuke, Furukawa Masahito, Moriyoshi Chikako and Kuroiwa Yoshihiro, Key Engineering Materials (Trans Tech Publications, Switzerland). 421 (2010) p. 34.

Indian Journal of Pure & Applied Physics
Vol. 58, November 2020, pp. 783-786

Electrical Properties of lead free ceremics $Na_{1-X}K_xNbO_3$, at x=0.305.

Jyotsana Negi[a], Surendra Singh[a] & N S Panwar[b*]

[a]Department of Physics, HNB Garhwal University, Srinagar (Garhwal)-246 174, India

[b]University Science Instrumentation Centre, HNB Garhwal University, Srinagar (Garhwal)-246 174, India

Received 17 September 2018; accepted 18 September 2020

By solid state reaction method, ceramic pellets of $Na_{0.695}K_{0.305}NbO_3$ have been prepared. X-ray- diffraction, Piezo properties, scanning electron microscope, and temperature dependence of dielectric constant and loss tangent of the prepared samples have been studied. It has been observed that, at the transition temperature, dielectric constant peak shifts to lower temperature, and the dielectric constant and loss tangent peak heights decrease, with increasing frequency, and show three structural phase transitions.

Keywords: Ferroelectrics, solid state reaction, dielectric constant, dielectric conductivity.

1 Introduction

Lead-based ferroelectric and piezoelectric materials, such as $PbTiO_3$-$PbZrO_3$ (PZT), are most widely used in acoustic transducers, actuators, and other electromechanical fields because of their electromechanical and high piezoelectric properties[1]. However, despite the toxic nature of PbO (which comprises 60–70 wt% of ceramic) it is most commonly used in PZT-based materials, therefore an urgent demand is to find lead-free materials to replace Pb-based ceramics in future. One of the most excellent candidates is sodium potassium niobate, (Na, K)NbO_3 (NKN), based solid solutions due to the high piezoelectric response, good ferroelectric properties, and especially high Curie temperature. Guo *et al.* [2] prepared the (1-x)KNN-x$LiNbO_3$ ceramics, exhibiting excellent piezoelectric properties, d_{33} ~ 235 pC/N, kt ~ 48%, and T_C ~ 460 °C, which is in the vicinity of the morphotropic phase boundary (MPB) of $(K_{0.5}Na_{0.5})NbO_3$ and $LiNbO_3$ binary solid solution system. In addition, some modified NKN ceramics prepared by conventional solid-state sintering method have been investigated[3-6].

The low dielectric constant of perovskite $Na_{1-x}K_xNbO_3$ ceramics, coupled with fine structure and improved piezoelectric activity, especially near the equimolar composition of Na and K, make these materials desirable for transducer and certain solid ultrasonic delay line applications, which require the use of thin-section transducers[7]. Dielectric measurements were first reported, by Matthias and Remeika[8] on end members of $Na_{1-x}K_xNbO_3$ system, *i.e.*, on $NaNbO_3$ and $KNbO_3$, single crystals and observed three transitions at 80, 370 and 480°C for $NaNbO_3$; and two transitions, at 224 and 434°C, for $KNbO_3$, at 10 KHz. Afterwards several investigators studied this system[9-11]. However, these studies were restricted to low range single frequencies.

The aim of our work is to study the crystal structure, dielectric properties of (NaK)NbO_3 system.

2 Experimental Details

Pellet samples of $Na_{1-x}K_xNbO_3$ ($0.250 \leq x \leq 0.350$) were prepared by solid-state reaction method, using the powders of Na_2CO_3, K_2CO_3, Nb_2O_5 (all with purity ≥ 99.9%, from MERK, Germany). At first the raw powders were separately dried, at 200 °C for 2 hours, to remove the absorbed moisture and weighed in stoichiometric ratio. The weighed powders were dry mixed and ground for 4 hours, and then wet mixed with acetone and ground for 2 hours, using a gate mullet mortar and pestle. The mixture was calcined in an alumina crucible, in ambient atmosphere, at 900 °C, for 4 hours, to remove the present carbon dioxide. When the furnace was switched off and cooled to room temperature the calcined mixture was weighed to ensure the complete carbon dioxide removal from the mixture. The calcined mixture was further ground for half an hour and then pressed into pellets of 8 mm diameter and about 2 mm thickness, using 0.4 GPa uniaxial pressure. These pellets, with

*Corresponding author: (Email: jyotsana.jn42@gmail.com)

x = 0.250, 0.300, 0.310, 0.315, 0.320, 0.325, 0.330 and 0.350, were sintered, each composition for 4 hours in the order of their melting points, at 1170, 1165, 1160, 1156, 1152, 1150, 1148 and 1145 ^{o}C, respectively, in a high temperature muffle furnace. The crystal structures of the sintered samples were examined using an X-ray diffractometer (PANalytical X'PERT PRO) with Cu K_{α} radiation (wavelength, λ = 1.540598 Å)[10]. X-ray diffraction (XRD) patterns of all the prepared samples were taken with 2Θ in the range from 20 to 70^{o}, at ambient temperature. Surface morphology, grain size and energy dispersive X-ray analyses (EDAX) of the prepared pellets were studied using a scanning electron microscope (CARL ZEISS, MA15/EVO18)[11]. Measurement of Polarization characteristics and piezoelectric parameters of the prepared samples, using a ferroelectric- (PE loop tracer) and piezo- meter (AixACCT Systems, GmbH). For dielectric measurements sintered pellets were electroded, using air drying silver paste, in parallel-plate capacitor configuration. Temperature, frequency and composition ($0.250 \leq x \leq 0.350$) dependence of dielectric constant (K), loss tangent (tan δ) and dielectric conductivity (σ) of the prepared samples were measured in MIM configuration, in the 1 to 1000 KHz frequency range, using an RCL meter (Fluke– PM6306); and the temperature ranging from RT to 150 ^{o}C, using a temperature controller having an accuracy of ±1 ^{o}C.

3 Results and Discussion

Figure 1 presents the observed XRD patterns of the prepared $Na_{1-x}K_xNbO_3$ (0.305) pellet samples. Peak indexing was done with the help of Ceramic Inorganic Data Cards[12]. The X-ray patterns show polycrystalline behavior of the prepared samples and were consistent with reference with the Inorganic Crystal Structure Database (ICSD) (code 00-061-0310) data of $(Na,K)NbO_3$ with peaks corresponding to (100), (110), (200), *etc*.

The cell parameters were refined by High Score Plus software, using the Rietveld method[13], and the background was modeled using the Legendre polynom and the peaks' profiles were refined by a pseudo-Voigt function. The monoclinic Pm6 space group was chosen in these refinements. Values of calculated subcell parameters are a = 3.963, b=3.901, c= 3.937 and β angle is 90.35 is closely agree with the reported results[14, 15], Fig. 2 shows the scanning electron micrographs (SEM) of the prepared samples. The density and porosity greatly affect the dielectric properties of the samples[16].

The observed energy dispersive X-ray analysis (EDAX) results, show significant escaping of alkali (Na and K) ions in the sintered pellets,

The observed polarization- electric field (P-E) hysteresis loops at room temperature, for unpoled NKN samples under an applied electric field of 22 kV/cm and 1 Hz, have been shown in Fig. 3. and the strain (%) at RT, under an applied electric field of 22kV/cm and 1Hz, have been shown in Fig. 4. All the

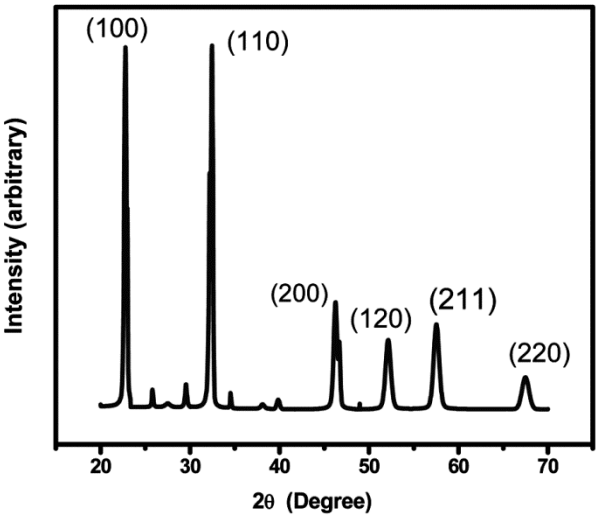

Fig. 1 — XRD patterns for $Na_{0.695}K_{0.305}NbO_3$ samples

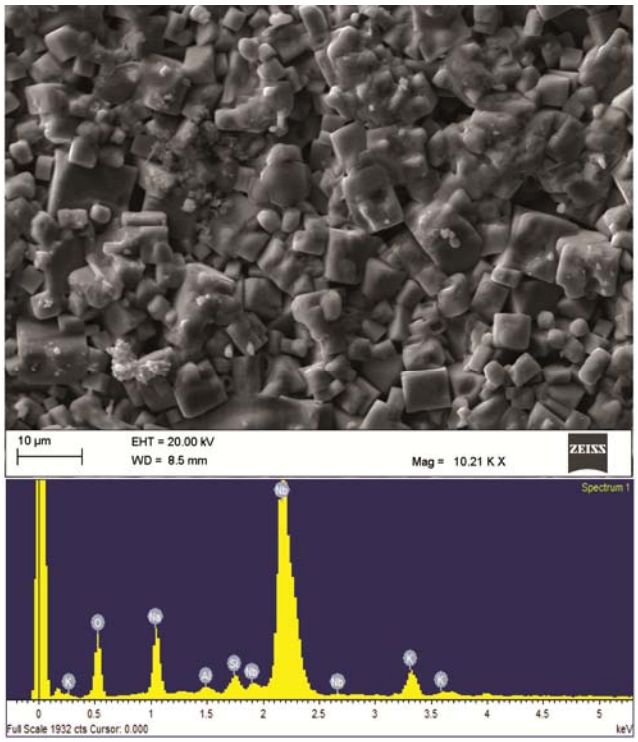

Fig. 2 — SEM photographs and EDAX of $Na_{1-x}K_xNbO_3$ sample

samples show a normal hysteresis loop confirming ferroelectric nature of all the prepared NKN ceramics. Shape of the P-E hysteresis loop depends on the microstructure, stress, defects, and processing conditions [17]. It has been reportedly observed that the ferro- and piezo- electric properties not only depend on the preparation conditions, but also on the type of the manufacturing company and the grain size of the starting materials[18,19].

The temperature dependence of dielectric constant for different frequency has been shown in Fig. 5. , at 10, 100 and 1000 kHz, respectively. Three structural phase transitions, at about 180, 400 and 458 °C have been observed. Between these temperatures $K_xNa_{1-x}NbO_3$ is in monoclinic, tetragonal, rombhohedral and cubic phase, as observed in the previously reported studies [20-23]. Similar behavior is observed for the loss tangent, as shown in Fig. 6. The temperature dependence of conductivity for composition has been shown in Fig. 7, at 10, 100 and 1000 kHz, respectively. The figures show that the conductivity of the $K_xNa_{1-x}NbO_3$ system increases with the increase of temperature. It is also observed that the conductivity increases with increasing concentration of K in the mixed system.

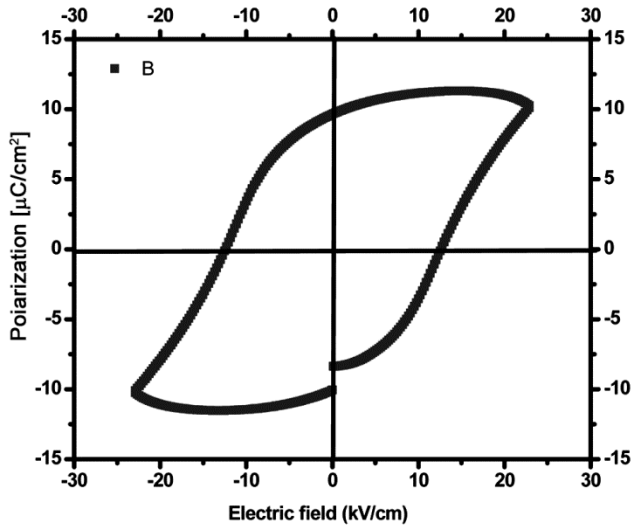

Fig. 3 — P-E loop for different composition(s) of $Na_{1-x}K_xNbO_3$, at applied field 22 kV/cm.

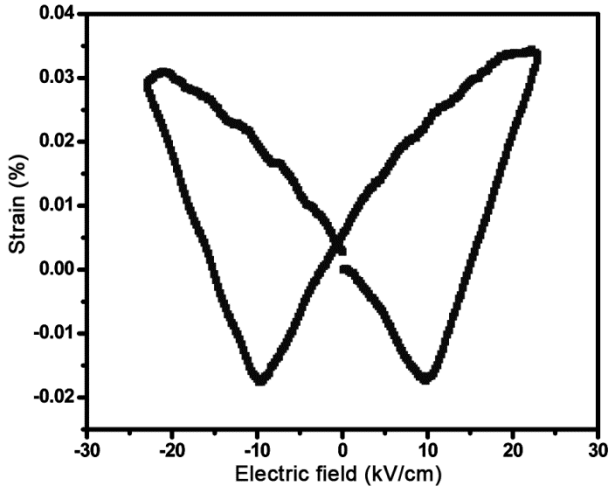

Fig. 4 — Variation of strain (%) with electric field, in $Na_{1-x}K_xNbO_3$,at applied field 22 kV/cm.

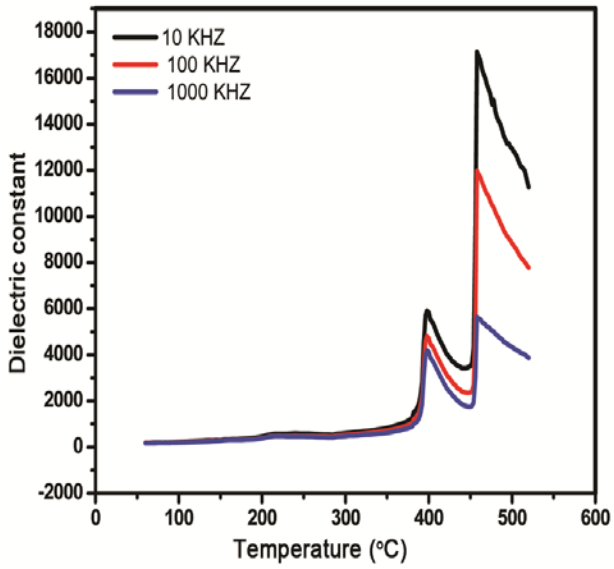

Fig. 5 — Temperature variation of dielectric constant (K) of $Na_{1-x}K_xNbO_3$, for different frequency.

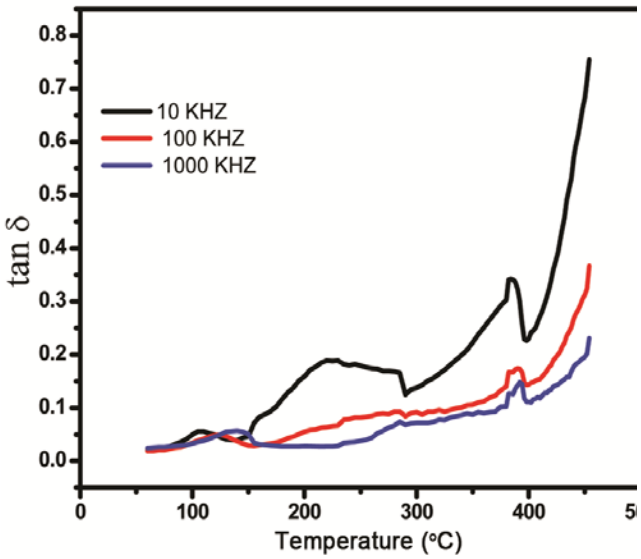

Fig. 6 — Temperature variation of dielectric loss (tan δ) of $Na_{1-x}K_xNbO_3$, for different frequency.

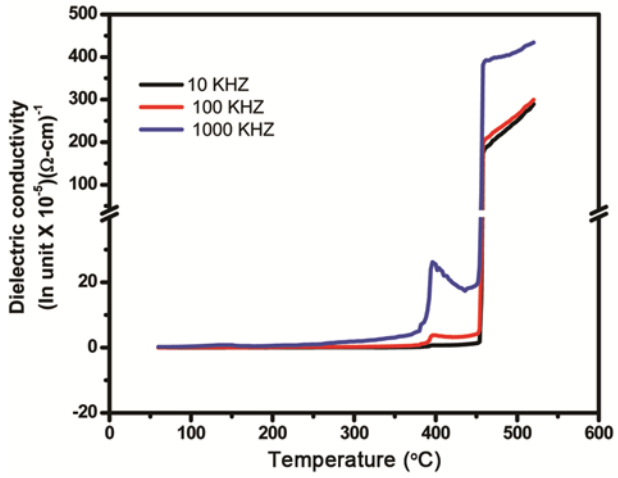

Fig. 7 — Temperature variation of dielectric conductivity (σ) of $Na_{1-x}K_xNbO_3$, for different frequency.

References

1 Chen K X, Yang G S, Wang D F & Li J B, *J Appl Phys*, 4 (2007) 101.

2 Guo Y P, Kakimoto K & Ohsato H, *Appl Phys Lett*, 85 (2004) 4121.

3 Meng H Q, Yang Y, Wang Y P, Wan D D, Li Q & Cheng Y, *Ferroelectrics*, 404 (2010) 105.

4 Matsubara M, Yamaguchi T, Sakamoto W, Kikuta K, Yogo T & Hirano S, *J Am Ceram Soc*, 88 (2005) 1190.

5 Rubio-Marcos F, Ochoa P & Fernandez J F, *J Eur Ceram Soc*, 27 (2007) 3589.

6 Rubio-Marcos F, Marchet P, Merle-Méjean T & Fernandez J F, *Mater Chem Phys*, 123 (2010) 91.

7 Egerton L & Bieling C A, *Ceram Bull*, 47 (1968) 1151.

8 Matthias B T & Remeika J, *Phy Rev*, 82 (1951) 727.

9 Shirane G, Newnham R & Pepinsky R, *Phys Rev*, 96 (1954) 581.

10 Negi J, Singh S & Panwar N S, *Phase Trans*, 92 (2019) 149.

11 Negi J, Singh S & Panwar N S, *Ferroelectric*, 558 (2020) 117.

12 Tellier J, Malic B, Dkhil B, Jenko D, Cilensek J & Kosec M, *Solid State Sci*, 11 (2009) 320.

13 Attia J, Bellaiche L, Gemeiner P, Dkhil B & Malic B, *J Phys IV France*, 128 (2005).

14 Tennery V J & Hang K W, *J Appl Phys*, 39 (1968) 4749.

15 Darlington C N W & Megaw H D, *Acta Cryst*, B29 (1973) 2171.

16 Hollenstein E, Davis M, Damjanovic D & Setter N, *Appl Phys Lett*, 87 (2005) 182905.

17 Kandari A S, Kandari K, Lingwal V, Bourai A A & Panwar N S, *Ferroelectrics*, 393 (2009) 121.

18 Jaeger R E & Egerton L, *J Am Ceram Soc*, 45 (1962) 209.

19 Saito Y, Takao H, Tani T, Nonoyama T, Takatori K, Homma T, Nagaya T & Nakamura M, *Lett Nat*, 432 (2004) 84.

20 Shirane G, Newniham R & Pepinsky R, *Phys Rev*, 96 (1954) 581.

21 Mathias B T & Remeika J, *Phys Rev*, 82 (1951) 727.

22 Hellwege K H & Hellwege A M, *Numerical Data and Function Relationship in Science and Technology, New Series, Springer- Verlag,* New York, 16 (1981) 45.

23 Cochran W, *Phys Rev Lett*, 3 (1959) 412.

Ferroelectrics

ISSN: (Print) (Online) Journal homepage: https://www.tandfonline.com/loi/gfer20

Dielectric properties of $Na_{1-x}K_xNbO_3$ (NKN) ($0.160 \leq x \leq 0.200$) ceramics synthesized by double sintered method

Don Biswas , Prolay Sharma & N. S. Panwar

To cite this article: Don Biswas , Prolay Sharma & N. S. Panwar (2021) Dielectric properties of $Na_{1-x}K_xNbO_3$ (NKN) ($0.160 \leq x \leq 0.200$) ceramics synthesized by double sintered method, Ferroelectrics, 571:1, 214-229

To link to this article: https://doi.org/10.1080/00150193.2020.1853757

Published online: 09 Feb 2021.

Submit your article to this journal

View related articles

View Crossmark data

Full Terms & Conditions of access and use can be found at
https://www.tandfonline.com/action/journalInformation?journalCode=gfer20

FERROELECTRICS
2021, VOL. 571, 214–229
https://doi.org/10.1080/00150193.2020.1853757

Taylor & Francis
Taylor & Francis Group

Check for updates

Dielectric properties of $Na_{1-x}K_xNbO_3$ (NKN) ($0.160 \leq x \leq 0.200$) ceramics synthesized by double sintered method

Don Biswas[a], Prolay Sharma[b], and N. S. Panwar[a]

[a]University Science Instrumentation Centre, H.N.B. Garhwal University, Srinagar, India; [b]Instrumentation and Electronics Engineering, Jadavpur University, Kolkata, India

ABSTRACT

In this study, pellet samples of $Na_{1-x}K_xNbO_3$ (NKN) ($0.160 \leq x \leq 0.200$) were prepared using the solid- state reaction method with double sintering. Electric conductivity (σ), loss tangent (tan δ), and dielectric constant (ε) were observed for all the prepared compositions from room temperature (RT) to 480 °C, at 10, 100, and 1000 KHz. For the prepared compositions ($0.160 \leq x \leq 0.200$), XRD patterns were observed at room temperature. For the pellet samples ($0.160 \leq x \leq 0.200$), escaping of Na and K were found minimum for the compositions with $x = 0.175$. The EDAX confirms 'p- type' conductivity in $Na_{1-x}K_xNbO_3$ ceramics. Further, the conductivity was found minimum due to less 'A- site' vacancy concentration, near MR region. The electrical conductivity (σ) and dielectric constant (ε) were found minimum for $x = 0.175$, among the prepared compositions.

ARTICLE HISTORY
Received 6 July 2020
Accepted 7 October 2020

KEYWORDS
Ceramics; dielectric constant; ferroelectrics; phase transitions

1. Introduction

Lead based ferroelectric materials like PZT (Lead zirconate titanate) are very important due to their large value of the piezoelectric and dielectric constant [1, 2]. Their physical properties are greatly altered in the morphotropic phase region (MPB) due to the occurrence of change in their internal structure [3]. In morphotropic phase region (MR), the crystal structure of the material changes abruptly and the physical properties are extremal [4]. In this MPB system, physical behaviors are anomalous, and were found composition dependent. The Perovskite ABO_3 type compounds are acknowledged due to their various applications in the modern sensors and transducers. One is NKN (Na, K) NbO_3 (Sodium- potassium niobate) based system, which is lead free ABO_3 type ferroelectrics, has large piezoelectric properties and can be used in large piezo- and ferro- electric devices [5–7]. $KNbO_3$ is a ferroelectric material at room temperature, whereas $NaNbO_3$, an antiferroelectric, at room temperature and becomes ferroelectric below 200 °C [8–10]. If we add a very little quantity of $KNbO_3$ with $NaNbO_3$, the physical properties of $NaNbO_3$, altered to a great extent. So, variation in physical properties may be created in Sodium-potassium niobate $Na_{1-x}K_xNbO_3$ system, for all possible values of x (from 0 to 1) [11, 12].

The lead free $NaNbO_3$, is important due to its property called anti- ferroelectric, and becomes ferroelectric, due to some change in their physical structure. Researchers found

CONTACT Don Biswas donusic06@gmail.com
© 2021 Taylor & Francis Group, LLC

that it behaves like ferroelectric with T_C= 480 °C [13–15]. For a particular chemical composition ratio of Na & K, the physical properties are extremal because of the unexpected change in lattice parameters, is typically called morphotropic phase region [2].

In this MPB system, physical behaviors are anomalous, and were found composition dependent. The electrical properties were found anomalous near the mixture of composition of $KNbO_3$-$NaNbO_3$ [16]. Raevskii et al. explained the behavior near MPT region in $Na_{1-x}K_xNbO_3$, based on the concentration dependence theory of electrical conductivity [17], produces lower value at these concentrations. Kandari et al. reported the well known MPB region(s) [18–20], in $Na_{1-x}K_xNbO_3$, at the compositions with x = 0.17, 0.32, and 0.475. Kandari et al. observed the electrical properties with different Na/K ratio and the structural properties of $Na_{1-x}K_xNbO_3$, at the compositions with x = 0.17 to 0.18, found a typical MPB exists, at x = 0.175 [20]. Tennery et al. [21] found three different MPB regions, on the findings of lattice parameters, at x = 0.17, 0.325, and 0.475. In solid solution systems, from the existing composition- property diagram, near the morphotropic phase boundary, ferro-composition has a two- or more phases with extremal electro-physical properties [22–26]. Surendra et al. [27] explained that with change in composition, MPB produces anomalous dielectric and structural properties [28–32], in a solid solution. Ye-Jing Dai et al. observed with a different ratio of Na/K on electrical properties and phase structures of $Na_{1-x}K_xNbO_3$ compositions, prepared by the conventional solid-state reaction method, with x = 0.46 to 0.52 [33]. Ye-Jing Dai et al. investigated a distinctive MPB exists, at x = 0.52–0.525. The Li modified composition ($Na_{0.5}K_{0.5}$) NbO_3 also showed good piezoelectric properties among lead free piezoelectric ceramics [23].

Kandari et al. found p-type conductivity in $Na_{1-x}K_xNbO_3$ and high conductivity, near MPB region [20]. But it is highly suspicious due to insufficient EDAX results. Also from the RT XRD results, the structures of the prepared compositions were not monoclinic. The present study was focused on the physical properties of $Na_{1-x}K_xNbO_3$ ($0.160 \leq x \leq 0.200$), near MPB region. The ceramic pellet samples were prepared by solid state reaction method using two-stage sintering process. For the prepared compositions of $Na_{1-x}K_xNbO_3$ ($0.160 \leq x \leq 0.200$), dielectric properties, x-ray diffraction patterns, and EDAX results have been observed near MPB region. In the present results, low conductivity was found at x = 0.175, due to MPB characteristics.

2. Experimental details

The ceramic pellets were prepared using solid- state reaction method ($0.160 \leq x \leq 0.200$) and have been described in details in a previous communication [34, 35]. To prepare the compositions, raw materials of sodium carbonate (Na_2CO_3), potassium carbonate (K_2CO_3), and niobium pentoxide (Nb_2O_5) has been taken. All the above said materials are 99.99% pure. The materials were taken for drying purpose, at 200 °C for 2 hours, and weighing in the proper stoichiometric ratio to prepare the compositions of $Na_{1-x}K_xNbO_3$, ($0.160 \leq x \leq 0.200$).

To prepare the compositions of $Na_{1-x}K_xNbO_3$, ($0.160 \leq x \leq 0.200$), raw materials were taken, manually mixed and grind for 4 hours. The mixture was added with acetone liquid and grind for extra 2 hours with the help of agate mullet mortar and pestle. Then

the mixed powder was taken for calcination, at 900 °C for 4 hours. The calcined powder was cooled down to room temperature.

To prepare pellet samples of $Na_{1-x}K_xNbO_3$, they were ground and pressed into the disk of 8 mm diameters and generally have 1–2 mm thickness at 0.2 GPa pressure. The pellet samples of $Na_{1-x}K_xNbO_3$ ($0.160 \leq x \leq 0.200$) were sintered for 4 hrs, and range of the temperature has been selected between 1130 °C and 1136 °C, with decrease order of x (K content). Again the pellet samples were crushed and were prepared again, according to the previous condition. The pellet samples were taken out when it cooled down to room temperature.

Scanning Electron Microscopy is used to view the microstructure and grain size of the prepared pellet samples, with model EVO 18 Special Edition (Switzerland) manufactured by CARL ZEISS. EDAX measurement of the prepared pellet samples were observed with the same instrument. The average size of grains was found between 6 and 9 μm range [36, 37].

For all the prepared compositions ($0.160 \leq x \leq 0.200$), room temperature XRD were observed. For this purpose, the X- ray diffractometer (PANalytical, X'PERT PRO) has been used, with Cu$K_{\alpha 1}$ radiation of wavelength 1.5405980 Å radiation. The 2θ angle has been selected from 20° to 70°.

For all the prepared compositions ($0.160 \leq x \leq 0.200$), dielectric constant (ε), loss tangent (tan δ), and electric conductivity (σ) were observed, systematically. First, they were electroded, with both side have conducting paste of silver, in metal-insulator-metal (MIM) configuration, by RLC meter (Fluke, PM 6306), with increasing temperature cycles, at 10, 100, and 1000 KHz.

3. Results and discussion

3.1. XRD results

For the prepared compositions of $Na_{1-x}K_xNbO_3$ ($0.160 \leq x \leq 0.200$), X-ray diffraction patterns were observed. The powder X-ray diffraction patterns of $N_{1-x}K_xNbO_3$ ($0.160 \leq x \leq 0.200$) are shown in Fig. 1(I) and (II).

From the observed room temperature XRD patterns, powder samples of $N_{1-x}K_xNbO_3$ confirms polycrystalline nature and were observed in good consistency with the Inorganic Crystal Structure Database (ICSD) (code 01-074-2025) record of $Na_{1-x}K_xNbO_3$, with peaks corresponding to (020), (022), (004), and (024), etc.

For the prepared compositions of $Na_{1-x}K_xNbO_3$ ($0.160 \leq x \leq 0.200$), a continuous shifting has been observed, in the most intense peaks (020), (022), (004), and (024), with the increment in the value of potassium concentration (x). From the observed XRD patterns of $Na_{1-x}K_xNbO_3$ ($0.160 \leq x \leq 0.200$), intense peaks were observed shifting to higher angle with increasing x, except for the composition with $x = 0.175$, where peaks were shifted to lower angle, appearing with an anomalous behavior and a break in the peak shifting tendency, is given in Fig. 2. Kandari et al. observed similar phenomena in $Na_{1-x}K_xNbO_3$, near MR with $x = 0.475$ [20].

For the prepared compositions of $Na_{1-x}K_xNbO_3$ ($0.160 \leq x \leq 0.200$), slop of the lattice variables with composition (x) is given in Fig. 3. Normally, $a < c$, and the variation of the slop was observed positive; except with compositions ($0.170 \leq x \leq 0.180$), where $a > c$, and the variation of the plot was observed negative, suggesting a structural anomaly in this MR region.

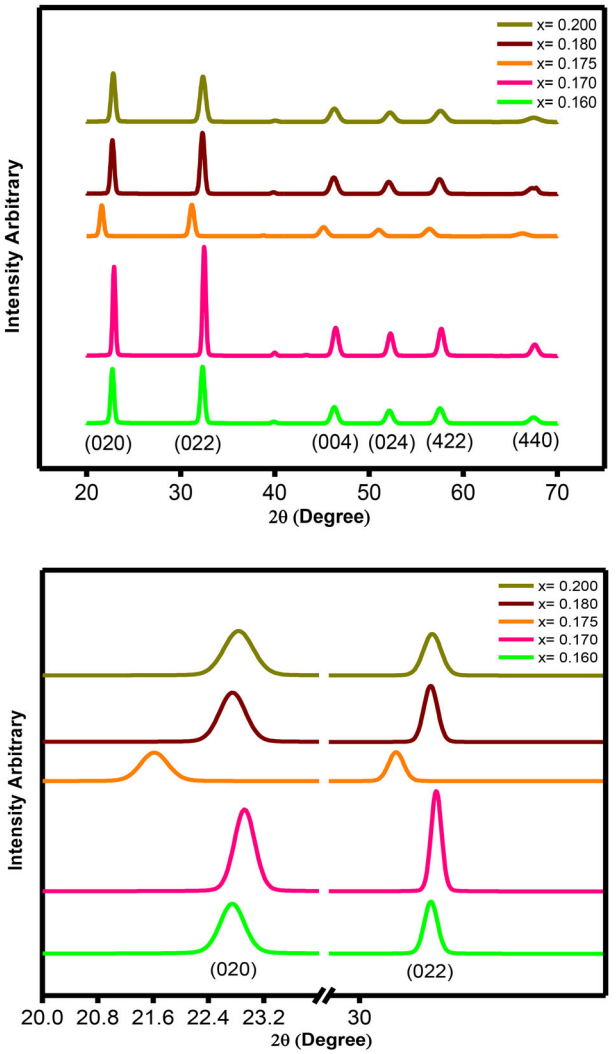

Figure 1. (I) XRD patterns of $Na_{1-x}K_xNbO_3$ system, with x ($0.160 \leq x \leq 0.200$). (II) Expanded XRD patterns of $Na_{1-x}K_xNbO_3$ system, with x ($0.160 \leq x \leq 0.200$).

For the prepared compositions of $Na_{1-x}K_xNbO_3$ ($0.160 \leq x \leq 0.200$), the cell variables were calculated Rietveld method using (High Score Plus) software, and Legendre polynom was used for background modeling and the "peaks" profiles were manipulated using a pseudo-Voigt function [38, 39]. For the above refinements of XRD data, monoclinic Pm6 was selected as space groups [40].

3.2. Dielectric results

For the prepared compositions of $Na_{1-x}K_xNbO_3$ ($0.160 \leq x \leq 0.200$), dielectric constant (ε) and electric conductivity (σ) with composition (x), at 1 MHz, has been given in Fig. 3(I) and (II), respectively. The variation of dielectric constant (ε), loss tangent (tan δ) and Electric conductivity (σ) with compositions, at different temperatures and 1 MHz

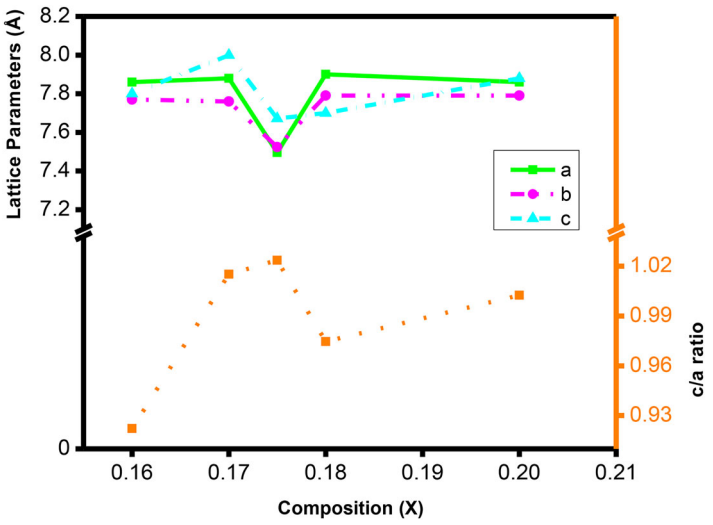

Figure 2. Variation of c/a (ratio of lattice parameters, c and a) with composition (x), in $Na_{1-x}K_xNbO_3$ ($0.160 \leq x \leq 0.200$).

frequency, has been given in Figs. 4–6. Similarly, the variation of dielectric parameters with compositions (x), at different frequencies and room temperature, is given in Figs. 7–9.

For the prepared compositions of $Na_{1-x}K_xNbO_3$ ($0.160 \leq x \leq 0.200$), dielectric constant were found increasing, with increasing potassium concentration (x value), except with value $x = 0.175$. An irregular decrease in the value ($x = 0.175$) of dielectric parameters were measured. The measured dielectric constant was going downwards after $x = 0.170$ and for the composition $x = 0.175$, it was found minimum. After $x > 0.175$, gradual changes in the dielectric properties were visible with increasing x. In Figs. 4–9, a physically a composition driven dielectric anomaly was found, at $x = 0.175$, at all measured range of frequency and room temperature.

Same phenomena have been occurred with the value of electrical conductivity and shows similar variation as seen in the case of dielectric constant. Normally, ε and tan δ were measured decreasing and σ increasing with change in increasing order of frequency. Moreover, these outcomes are in fine consistency with the previous reported publications [12, 36, 37, 41].

The capacitor shows low reactance at high frequencies for a sinusoidal signal, due to that conduction loss decreases in the resistor, appearing minimum loss with increasing frequency. For $x = 0.175$, dielectric parameters were found minimum, due to an anomalous decrease in the values of electric conductivity (σ), loss tangent (tan δ), and dielectric constant (ε), which is composition dependent rather than frequency and temperature, indicates MPT region, among the prepared compositions. The MPT i.e., morphotropic phase transition was explained by Raevskii et al. [17], which is based on composition dependence of electrical conductivity, which produces minimum value at these concentrations, in $Na_{1-x}K_xNbO_3$ solid solutions. So, a physically compositional dependence of dielectric anomalous behavior was found with variation in the composition, at $x = 0.175$, at all measured frequencies and room temperature, is given in Figs. 4–9. The decrease in the dielectric parameters, like dielectric permittivity and loss may

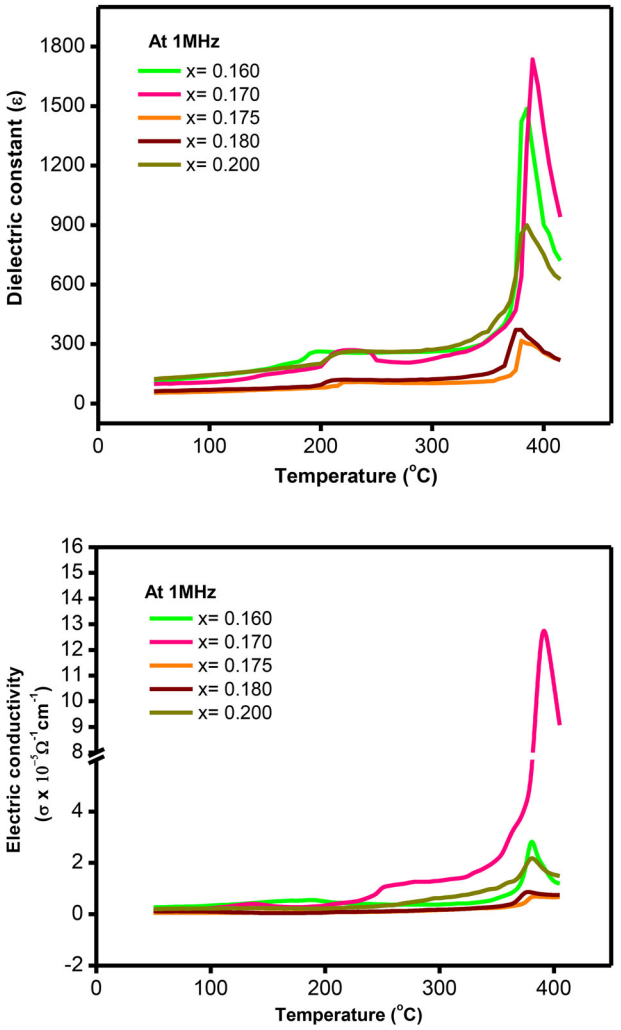

Figure 3. (I) Temperature dependent dielectric properties of $Na_{1-x}K_xNbO_3$ system ($0.160 \leq x \leq 0.200$), at 1 MHz. (II) Temperature dependent electrical conductivity of $Na_{1-x}K_xNbO_3$ system ($0.160 \leq x \leq 0.200$), at 1 MHz.

be associated to the damping out of successive polarization modes with increasing frequency [42]. Moreover, the factors like grain size, composition, interplay of porosity, grain boundary thickness, applied frequency, liquid phase presence, residual stress, and thermal hysteresis can influence the observed behavior in dielectric properties [43]. The increasing grain size of the material, physically tells about decrease in loss, due to the reduced no. of grain boundaries.

For the prepared composition ($x = 0.17$), the increasing and deceasing order of dielectric properties was carried out with variation in temperature, and is given in Fig. 10. The dielectric property with increasing and decreasing temperature was measured for $x = 0.17$. Mason et at observed the decreasing order measurement was about 500 times greater than increasing order measurement [44]. For the above said composition, therefore, repeated measurements have been done with the sample again and again to confirm

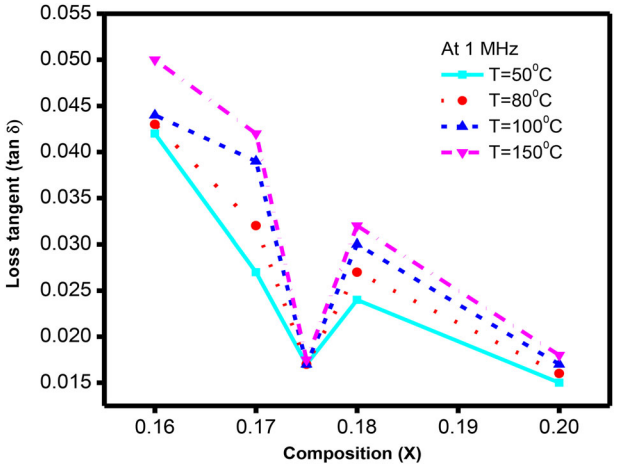

Figure 4. Variation of loss tangent (tan δ) with composition (x), in $Na_{1-x}K_xNbO_3$ ($0.160 \leq x \leq 0.200$), at different temperatures.

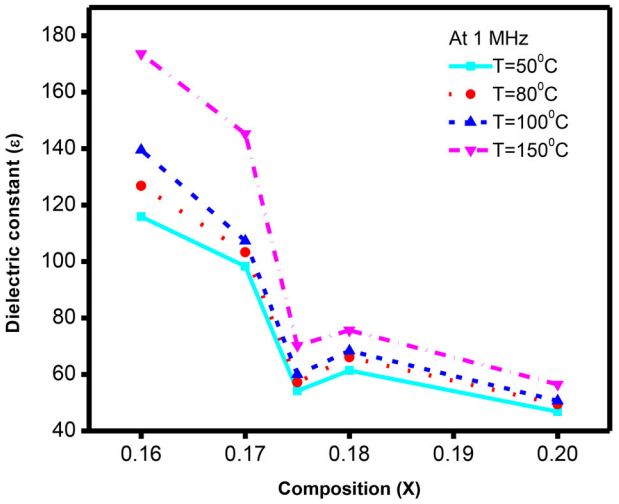

Figure 5. Variation of dielectric constant (ε) with composition (x), in $Na_{1-x}K_xNbO_3$ ($0.160 \leq x \leq 0.200$), at different temperatures.

the above phenomena. The shifting in Curie temperature of increasing and decreasing dielectric measurement (Fig. 10) can be explained, due to large thermal hysteresis present in this system. The results may be similar for other compositions. The structural properties may vary from sample to sample as shown by electrical evidence [45].

3.3. SEM results

The microstructures of $Na_{1-x}K_xNbO_3$ ($0.160 \leq x \leq 0.200$) ceramic pellet samples have been observed with the help of EVO 18 special edition Scanning Electron Microscope (SEM) made by ZEISS. The SEM images of $Na_{1-x}K_xNbO_3$ (NKN) ($0.160 \leq x \leq 0.200$) ceramics are shown in Figs. 11–15. They were found homogeneous, uniform, and fine-

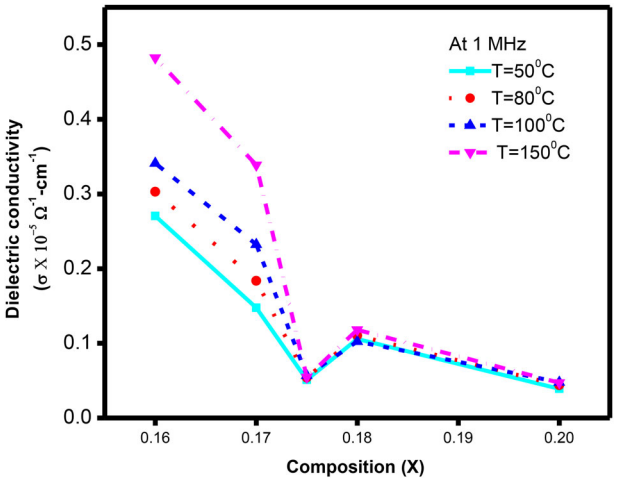

Figure 6. Variation of dielectric conductivity (σ) with composition (x), in $Na_{1-x}K_xNbO_3$ ($0.160 \leq x \leq 0.200$), at different temperatures.

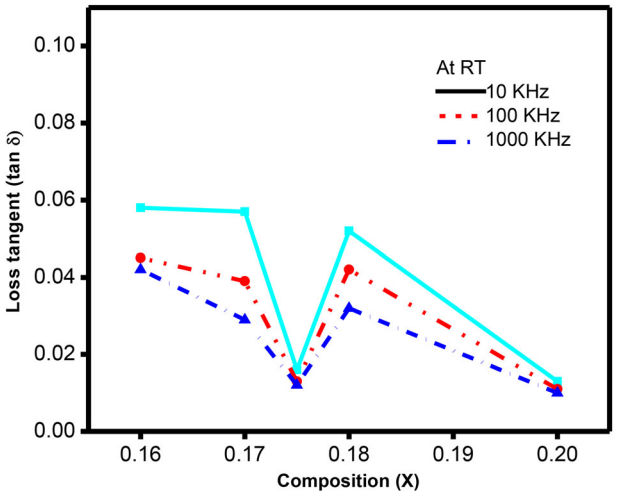

Figure 7. Variation of loss tangent (tan δ) with composition (x), in $Na_{1-x}K_xNbO_3$ ($0.160 \leq x \leq 0.200$), at different frequencies.

grained. During sintering process, the mechanism of grain growth and densification needs material transport, that may appear via grain boundary diffusion, surface diffusion, lattice diffusion, evaporation, and viscous flow [46]. In all the prepared compositions, grain sizes are average and show inhomogeneity or uniformity at $x = 0.17$, which can support the decreasing of interfacial energy of ceramics. An inhomogeneous grain size was observed for the sample $x = 0.175$ and after $x > 0.175$ their homogeneity enhances. The "double" sintering process is applied to trigger different sintering processes in different temperature ranges, and to slow up grain growth and improve the densification process. However, no enhancement in microstructure has been observed using this two- step sintering process. Chen et al. [47] observed similar interpretations for the double sintered $Na_{1-x}K_xNbO_3$ ceramics.

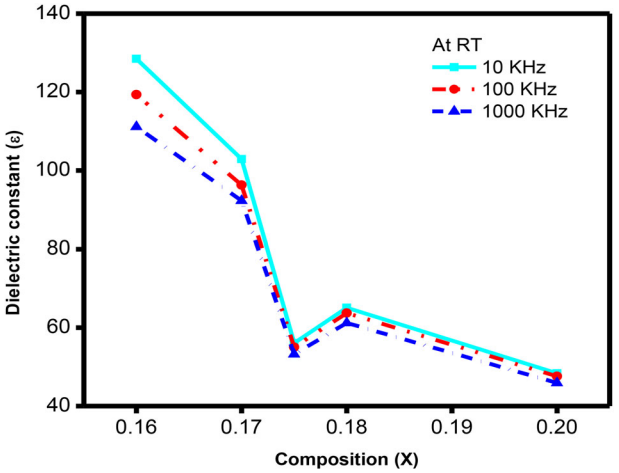

Figure 8. Variation of dielectric constant (ε) with composition (x), in $Na_{1-x}K_xNbO_3$ ($0.160 \leq x \leq 0.200$), at different frequencies.

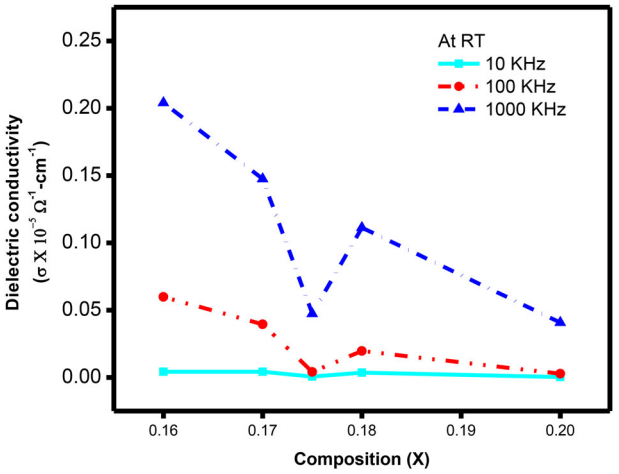

Figure 9. Variation of dielectric conductivity (σ) with composition (x), in $Na_{1-x}K_xNbO_3$ ($0.160 \leq x \leq 0.200$), at different frequencies.

For the prepared compositions of $Na_{1-x}K_xNbO_3$ ($0.160 \leq x \leq 0.200$), EDAX analysis was observed. A considerable escaping amount of alkali (Na and K) ions were found in "double sintered" pellets and for the composition $x = 0.175$, showing the minimum escaping of alkali (Na and K) ions. From the EDAX analysis, for the compositions ($0.160 \leq x \leq 0.200$), Sodium (Na) escaping was measured larger than that of K. For $x = 0.175$, minimum escaping was observed of alkali (Na and K) ions, among the prepared compositions. The percentage of escaping of sodium was always higher than potassium. By making variations in the stoichiometric ratio, a considerable affect was observed in the grain size, morphology and density of the sintered $Na_{1-x}K_xNbO_3$ pellet samples [37].

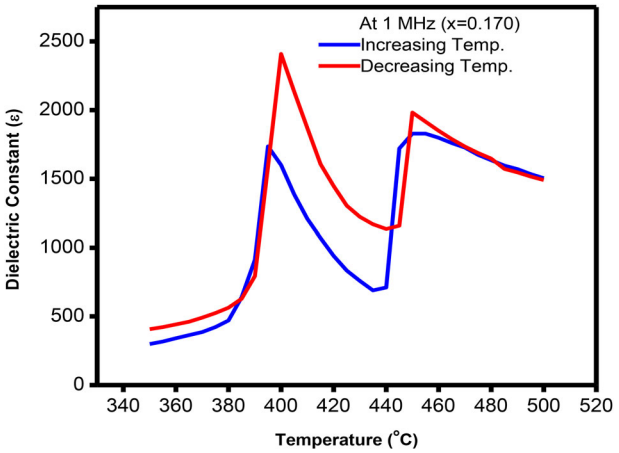

Figure 10. Temperature dependent dielectric constant of $Na_{1-x}K_xNbO_3$ system, at $x = 0.170$, for increasing and decreasing order of temperature.

In the $Na_{1-x}K_xNbO_3$ ceramics, surface diffusion is found more dominating sintering process; resulting extreme grain growth, during the start of sintering, due to low activation energy of surface diffusion and due to that fact grain coarsening has been introduced. That was reduction of the total surface area through increase of the average size of the particles or grains. So, that is called the grain coarsening. Now, grain growth here once again the driving force is basically changing surface area. Not the surface energy term, but the surface area. Here, it is surface energy and surface area both are changing. So, this is also another possibility, but in principle, this is not so feasible because once these larger particles are there, the sintering itself becomes difficult and it may not reduce its pores so easily. So, until now less one goes to a very high temperature. So, once that coarsening takes place, the pore removal becomes quite difficult and resulting poor densification [48, 49]. One method is to find the defects present in $Na_{1-x}K_xNbO_3$ ceramics, which tells about the path of diffusion. These defects are thermodynamic species and creation of defects lowers the free energy of the system. During sintering process, the material grain growth, free surfaces, reaction of grain boundaries and lattice atoms changes and can alter the contribution of different mechanisms. Every diffusing element/species whether it is volatile or non- volatile, are basically ions of different charges, with different diffusion rates. So, different diffusing elements/species or ions can have different vapor pressures, diffusion paths and different diffusion rates, and their effective effect greatly alter the properties of density and grain size of the prepared compositions.

There are two types of defects were found in the ABO_3 type perovskite compounds, viz., vacancies reported at A site, and O-site [24]. The vacancies are effectively responsible to show the variation in electrical properties [18–20, 24, 31, 50]. The oxygen vacancies not only played a major significant role in changing the properties of electrical behavior, but the spontaneous polarization produced by the applied field is also equally responsible for the variation of electrical properties. With variation or increasing in K at the Na site, in $NaNbO_3$, which have antiferroelectric nature at room

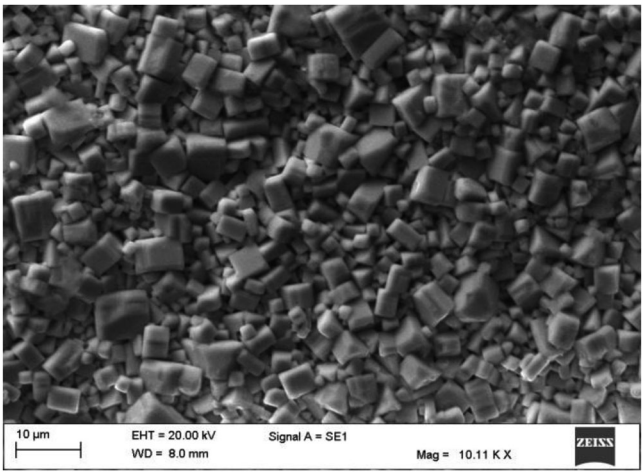

Figure 11. SEM images of $Na_{1-x}K_xNbO_3$ for $x = 0.160$.

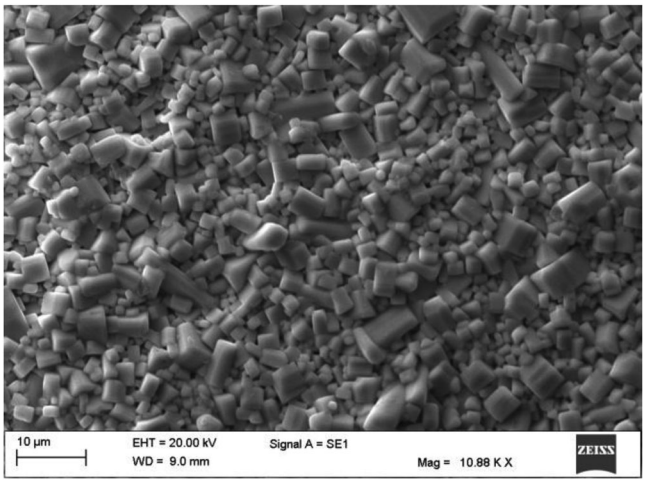

Figure 12. SEM images of $Na_{1-x}K_xNbO_3$ for $x = 0.170$.

temperature, converts itself into ferroelectric nature, contributing to effective polarization, which results better conductivity, normally, though, it is seen very minimum near the MPB region. The conduction process in these oxides may be understood with the behavior of the majority of acceptor or donor concentration. In ABO_3 type perovskite compounds, if deficiency of electron has been occurred at A-site, it donates "hole" and if excess electron has been found at O-site, it donates additional electrons for conduction in solids. In the same manner, if vacancies found only at A-site, the solid may behave as p-type, or if there are only O-site vacancies it should work as the n-type. The majority of A- or O-site vacancies will be the more responsible factor, to determine whether it is p- or n-type in nature. For prepared ceramics $Na_{1-x}K_xNbO_3$ compositions, EDAX results show considerable escaping of alkali (Na and K) ions, with the lowest value for the composition $x = 0.175$, is given in Table 1.

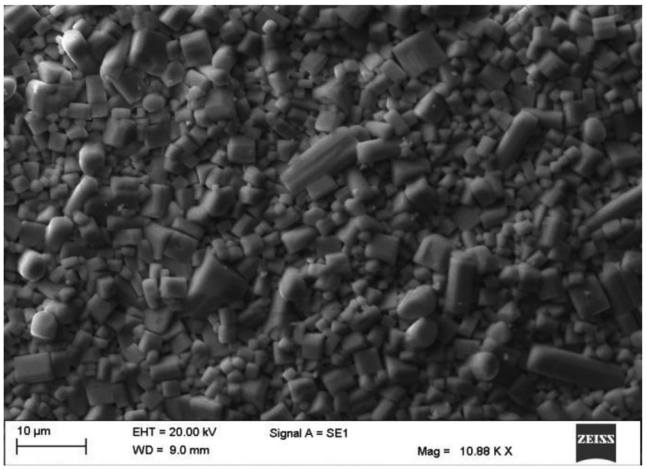

Figure 13. SEM images of $Na_{1-x}K_xNbO_3$ for $x = 0.175$.

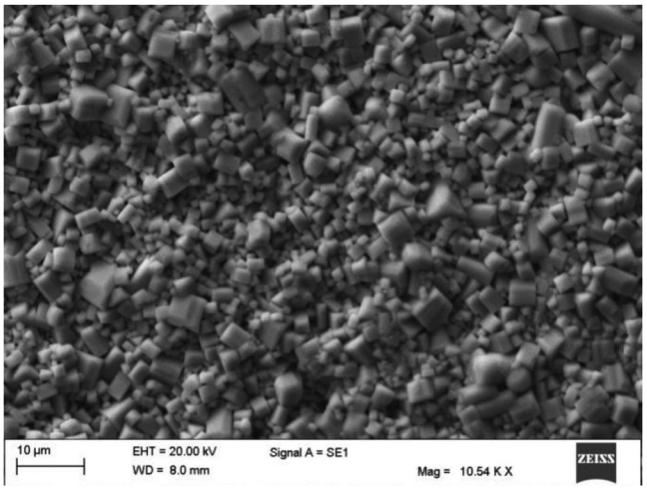

Figure 14. SEM images of $Na_{1-x}K_xNbO_3$ for $x = 0.180$.

The oxygen escaping was observed lower compared with the escaping of alkali (Na and K) ions. So, if A-site has more vacancies than that at O-site, and on the basis of this fact, the present $Na_{1-x}K_xNbO_3$ compositions have P-type nature in conduction. The electrons are attracted by the "A-site" vacancy and works as acceptor and because of electron deficiency; the "A-site" vacancy works as "hole" in the cell. For $x = 0.175$, the escaping of alkali ions were found minimum, so that, very small no of "holes" has been generated at "A-site" and that triggers decreased conductivity, among the prepared compositions. Many researchers reported regarding the p-type conductivity in many solids viz., Pb (Ti, Zr) O_3, ZrO_2, etc. [27, 51], where "superoxidation," i.e., "A-site" has more vacancies than that at "O"-site, is further viable. For p-type conductivity, lowest escaping of the highly volatile alkali ions produces minimum number of "holes" for conduction, showing lower conductivity, near MR with $x = 0.175$,

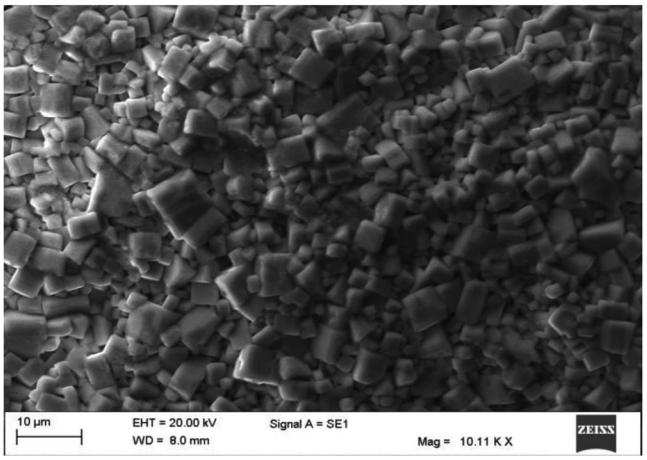

Figure 15. SEM images of $Na_{1-x}K_xNbO_3$ for $x = 0.200$.

Table 1. EDAX results of the $Na_{1-x}K_xNbO_3$ system.

	Atomic % (Measured)				Atomic % (Calculated)				Atomic % (Escaping)	
x value	Na	K	Nb	O	Na	K	Nb	O	Na	K
0.160	14.09	1.17	17.93	66.81	16.8	3.2	20	60	2.71	2.03
0.170	13.95	1.73	18.32	66.00	16.6	3.4	20	60	2.65	1.67
0.175	14.19	2.07	18.89	72.34	16.5	3.5	20	60	2.31	1.43
0.180	13.79	1.57	18.52	65.94	16.4	3.6	20	60	2.61	2.03
0.200	12.54	2.12	18.79	66.55	16.0	4.0	20	60	3.46	1.88

among the prepared compositions. Surendra et al. reported similar observation, near MR with $x = 0.500$ [27].

Kandari et al. found p-type conductivity in $Na_{1-x}K_xNbO_3$ due to more "A-site" vacancy concentration [20]. Moreover, compositions near MPB have distinct high conductivity were observed. In the present study, the compositions were double sintered with temperature increasing rate 6°/min and compositions near MPB have low conductivity were observed. In the present case, with less "A"-site vacancy concentration, with compositions near MR ($x = 0.175$) have low conductivity was measured, which are in good agreement with the above described phenomena.

With the compositions near MR, during sintering mechanism, it shows that the intensification of diffusion processes distinctively decreases the possibility of escape of highly volatile alkali metal ions. From the observations, electrical properties of the prepared pellet samples of $Na_{1-x}K_xNbO_3$ were greatly influenced by the structural change, preparation process and composition.

4. Conclusions

In the MPB region, for all the prepared compositions of $Na_{1-x}K_xNbO_3$ ($0.160 \leq x \leq 0.200$), dielectric constant, loss tangent, and electric conductivity were observed the lowest for the sample with $x = 0.175$, at all the considered frequencies, which indicates the presence of MPB at this composition. Also from the SEM results,

the composition x = 0.175, has low escaping of Na and K, which showed the lower conductivity from the other composition.

References

[1] N. Nagta, and T. Chikoshiand, Ferroelectric properties of bismuth layer-structured compound $Sr_xBi_{4-x}Ti_{3-x}Ta_xO_{12}$ ($0 \leqq x \leqq 2$), *J. Appl. Phys. Part I* **38**, 5497 (1999).

[2] M. Suzuki *et al.*, $Bi_{3-x}M_xTiTaO_9$ M = La or Nd) ceramics with high mechanical quality factor Q_m. *Jpn. J. Appl. Phys.* **42** (Part 1, No. 9B), 6090 (2003). DOI: 10.1143/JJAP.42.6090.

[3] Y. Ishibashi, Theory of the morphotropic phase boundary, *Ferroelectrics* **264** (1), 197 (2001). DOI: 10.1080/00150190108008570.

[4] R. Guo *et al.*, Origin of the high piezoelectric response in PbZr1-xTixO3, *Phys. Rev. Lett.* **84** (23), 5423 (2000)., DOI: 10.1103/PhysRevLett.84.5423.

[5] Y. Saito *et al.*, Lead-free piezoceramics, *Nature* **432** (7013), 84 (2004)., DOI: 10.1038/nature03028.

[6] M. Dawber, K. M. Rabe, and J. F. Scott, Physics of thin-film ferroelectric oxides, *Rev. Mod. Phys.* **77** (4), 1083 (2005). DOI: 10.1103/RevModPhys.77.1083.

[7] L. Wang, K. Yao, and W. Ren, Piezoelectric $K_{0.5}Na_{0.5}NbO_3$ thick films derived from polyvinylpyrrolidone-modified chemical solution deposition, *Appl. Phys. Lett.* **93** (9), 092903 (2008). DOI: 10.1063/1.2978160.

[8] G. Shirane, R. Newnham, and R. Pepinsky, Dielectric properties and phase transitions of $NaNbO_3$ and (Na, K) NbO_3, *Phys. Rev.* **96** (3), 581 (1954). DOI: 10.1103/PhysRev.96.581.

[9] L. E. Cross and B. J. Nicholson, The optical and electrical properties of single crystals of sodium niobate, *Philos. Mag.* **46** (376), 453 (1955). DOI: 10.1080/14786440508520582.

[10] R. H. Dungan and R. D. Golding, Metastable ferroelectric sodium niobate, *J. Am. Ceram. Soc.* **47** (2), 73 (1964). DOI: 10.1111/j.1151-2916.1964.tb15658.x.

[11] M. Ahtee and A. W. Hewat, Structural phase transitions in sodium-potassium niobate solid solutions by neutron powder diffraction, *Acta Cryst. A.* **34** (2), 309 (1978). DOI: 10.1107/S056773947800056X.

[12] M. Ahtee and A. M. Glazer, Lattice parameters and tilted octahedra in sodium-potassium niobate solid solutions, *Acta Cryst. A.* **32** (3), 434 (1976). DOI: 10.1107/S0567739476000983.

[13] B. T. Mathias, New ferroelectric crystals. *Phys. Rev.* **75**, 1771 (1949).

[14] B. T. Matthias, and J. P. Remeika, Dielectric properties of sodium and potassium niobates, *Phys. Rev.* **82** (5), 727 (1951). DOI: 10.1103/PhysRev.82.727.

[15] E. A. Wood, Polymorphism in potassium niobate, sodium niobate and other ABO_3 compounds, *Acta Cryst.* **4** (4), 353 (1951). DOI: 10.1107/S0365110X51001112.

[16] L. Wu *et al.*, Influence of compositional ratio K/Na on physical properties in $(K_xNa_{1-x})NbO_3$ ceramics, *J. Appl. Phys.* **103** (8), 084116 (2008). DOI: 10.1063/1.2907866.

[17] I. P. Raevskii, L. A. Reznichenko, and O. I. Prokopalo, Phase-transition and electrical-properties of ferroelectric sodium niobate-based solid-solutions, *Izv. Akad. Nauk SSSR* **15**, 872 (1979).

[18] A. S. Kandari, V. Lingwal, and N. S. Panwar, Morphotropic phase boundary in $Na_{1-x}K_xNbO_3$ near, x = 0.32, *Solid State Commun.* **150** (1-2), 74 (2010). DOI: 10.1016/j.ssc.2009.10.002.

[19] A. S. Kandari *et al.*, Composition dependent dielectric anomaly in $Na_{1-x}K_xNbO_3$, at x = 0.475, *Ferroelectrics* **393** (1), 121 (2009). DOI: 10.1080/00150190903413190.

[20] A. S. Kandari, V. Lingwal, and N. S. Panwar, Morphotropic region in $Na_{1-x}K_xNbO_3$, between x= 0.17 and 0.18, *Ferroelectrics* **396** (1), 18 (2010). DOI: 10.1080/00150191003791683.

[21] V. J. Tennery and K. W. Hang, Thermal and X-ray diffraction studies of the $NaNbO_3$-$KNbO_3$ system, *J. Appl. Phys.* **39** (10), 4749 (1968). DOI: 10.1063/1.1655833.

[22] A. M. Glazer *et al.*, Influence of shortrange and long-range order on the evolution of the morphotropic phase boundary in $Pb(Zr_{1-x}Ti_x)O_3$, *Phys. Rev. B.* **70** (18), 184123 (2004). DOI: 10.1103/PhysRevB.70.184123.

[23] K. Kakimoto *et al.*, Raman scattering study of piezoelectric $(Na_{0.5}K_{0.5})NbO_3$-$LiNbO_3$ ceramics, *Jpn. J. Appl. Phys.* **44** (9B), 7064 (2005). DOI: 10.1143/JJAP.44.7064.

[24] B. Jaffe, W. R. Cook, and J. H. Jaffe, *Piezoelectric Ceramics* (Academic, New York, NY, 1971).

[25] Y. Ishibashi and M. Iwata, A theory of morphotropic phase boundary in solid-solution systems of perovskite-type oxide ferroelectrics, *Jpn. J. Appl. Phys.* **38** (Part 1, No. 2A), 800 (1999). DOI: 10.1143/JJAP.38.800.

[26] N. Klein *et al.*, A study of the phase diagram of (K, Na, Li) NbO_3 determined by dielectric and piezoelectric measurements, and Raman spectroscopy, *J. Appl. Phys.* **102** (1), 014112 (2007). DOI: 10.1063/1.2752799.

[27] S. Singh, J. Negi, and N. S. Panwar, Dielectric properties of $Na_{1-x}K_xNbO_3$, near x = 0.5 morphotropic phase region, *J. Phys. Chem. Solids* **123**, 311 (2018). DOI: 10.1016/j.jpcs.2018.08.018.

[28] S. E. Park and T. R. Shrout, Ultrahigh strain and piezoelectric behavior in relaxor based ferroelectric single crystals, *J. Appl. Phys.* **82** (4), 1804 (1997). DOI: 10.1063/1.365983.

[29] B. Noheda, Structure and high-piezoelectricity in lead oxide solid solutions, *Curr. Opin. Solid State Mater. Sci.* **6** (1), 27 (2002). DOI: 10.1016/S1359-0286(02)00015-3.

[30] Y. Guo, K. I. Kakimoto, and H. Ohsato, Phase transitional behavior and piezoelectric properties of $(Na_{0.5}K_{0.5})NbO_3$ –$LiNbO_3$ ceramics, *Appl. Phys. Lett.* **85** (18), 4121 (2004). DOI: 10.1063/1.1813636.

[31] V. Lingwal, and N. S. Panwar, Morphotropic phase transitions in mixed sodium-potassium niobate system, *Ferroelectrics* **300** (1), 3 (2004). DOI: 10.1080/00150190490442146.

[32] S. Y. Chu *et al.*, Properties of (Na, K) NbO_3 and (Li, Na, K) NbO_3 ceramic mixed systems, *Ferroelectrics* **287** (1), 23 (2003). DOI: 10.1080/00150190390200767.

[33] Y. J. Dai, X. W. Zhang, and K. P. Chen, Morphotropic phase boundary and electrical properties of $K_{1-x}Na_xNbO_3$ lead-free ceramics, *Appl. Phys. Lett.* **94** (4), 042905 (2009). DOI: 10.1063/1.3076105.

[34] D. Biswas *et al.*, Temperature dependence of dielectric properties of sodium potassium niobate ceramics for different values of x ($Na_{1-x}K_xNbO_3$), *Ferroelectrics* **526** (1), 168 (2018). DOI: 10.1080/00150193.2018.1456307.

[35] D. Biswas *et al.*, Converse piezoelectric properties of K and Na-modified $(Na_{1-x}K_x)$ NbO_3 lead free ceramics for x = 0.08 and 0.17, *Ferroelectrics* **550** (1), 228 (2019). DOI: 10.1080/00150193.2019.1652511.

[36] R. E. Jaeger, and L. Egerton, Hot Pressing of potassium-sodium niobates, *J. Am. Ceram. Soc.* **45** (5), 209 (1962). DOI: 10.1111/j.1151-2916.1962.tb11127.x.

[37] G. H. Heartling, Properties of hot-pressed ferroelectric alkali niobate ceramics, *J. Am. Ceram. Soc.* **50**, 329 (1967).

[38] J. Tellier *et al.*, Crystal structure and phase transitions of sodium potassium niobate perovskites, *Solid State Sci.* **11** (2), 320 (2009). DOI: 10.1016/j.solidstatesciences.2008.07.011.

[39] L. V. Azaroff, *Elements of X-Ray Crystallography* (McGraw Hill Book Company, New York, NY, 1968).

[40] J. Attia *et al.*, Study of potassium-sodium-niobate alloys: a combined experimental and theoretical approach, *J. Phys. IV France.* **128**, 55 (2005). DOI: 10.1051/jp4:2005128009.

[41] L. E. Cross, Electric double hysteresis in (KxNa1-x) NbO_3 single crystals, *Nature* **181** (4603), 178 (1958). DOI: 10.1038/181178a0.

[42] A. S. Kandari *et al.*, Electrical properties of $Na_{1-x}K_xNbO_3$ ($0.28 \leq x \leq 0.40$), *Ferroelectrics* **386** (1), 139 (2009)., DOI: 10.1080/00150190902961900.

[43] G. Goodman, *Ceramic Materials for Electronics; Processing, Properties and Applications*, edited by R. C. Buchanan (Marcel Dekker Inc, New York, NY, 1991).

[44] W. P. Mason and B. T. Matthias, Theoretical model for explaining the ferroelectric effect in barium titanate, *Phys. Rev.* **74** (11), 1622 (1948). DOI: 10.1103/PhysRev.74.1622.

[45] J. M. Walter, The dielectric behavior of $BaTiO_3$ single-domain crystals, *Phys. Rev.* **75**, 687 (1948).
[46] B. Malic *et al.*, Sintering of lead-free piezoelectric sodium potassium niobate ceramics, *Materials (Basel).* **8** (12), 8117 (2015). DOI: 10.3390/ma8125449.
[47] I. W. Chen and X. H. Wang, Sintering dense nanocrystalline ceramics without final-stage grain growth, *Nature* **404** (6774), 168 (2000). DOI: 10.1038/35004548.
[48] J. Koruza and B. Malic, Initial stage sintering mechanism of $NaNbO_3$ and implications regarding the densification of alkaline niobates, *J. Eur. Ceram. Soc.* **34** (8), 1971 (2014). DOI: 10.1016/j.jeurceramsoc.2014.01.035.
[49] R. M. German and Z. A. Munir, Surface-area reduction during isothermal sintering, *J. Am. Ceram. Soc.* **59** (9-10), 379 (1976). DOI: 10.1111/j.1151-2916.1976.tb09500.x.
[50] E. V. Bursyan, *Nonlinear Crystal-Barium Titanate* (Nauka Press, Moskva, 1974).
[51] J. Z. Rudolph, About the conduction mechanism of oxidic semiconductors at high temperatures, *Naturforsch* **14a**, 727 (1959).

Journal of Physics and Chemistry of Solids 151 (2021) 109853

Contents lists available at ScienceDirect

Journal of Physics and Chemistry of Solids

journal homepage: http://www.elsevier.com/locate/jpcs

Structural and electrical properties of lead-free $Na_{0.685}K_{0.315}Nb_{1-y}Ta_yO_3$ ($0 \leq y \leq 0.05$) ceramics

Jyotsana Negi [a,*], N.S. Panwar [b]

[a] Department of Physics, HNB Garhwal University, Srinagar, Garhwal, 246174, India
[b] University Science Instrumentation Centre, HNB Garhwal University, Srinagar, Garhwal, 246174, India

ARTICLE INFO

Keywords:
NKN
Phase structure
Electrical properties

ABSTRACT

Piezoceramic $Na_{0.685}K_{0.315}Nb_{1-y}Ta_yO_3$ (NKNT) (where $y \leq 0.05$) samples were prepared via a solid-state reaction using double sintering. The effects of Ta-doping on the phase structure and electrical properties of the NKNT ceramics were investigated. The temperature dependence of the dielectric constant, loss tangent, and dielectric conductivity of the prepared samples was measured from RT to 500 °C at 10 kHz and 1 MHz. High temperature X-ray diffraction (HT- XRD) measurements were carried out on the prepared samples between RT and ~200 °C, 200 and 380 °C, 380 and 460 °C, and above 460 °C, which showed monoclinic, tetragonal, tetragonal, and cubic phases, respectively. In $Na_{0.685}K_{0.315}Nb_{1-y}Ta_yO_3$, all the transition peaks were observed to gradually shift towards lower temperatures upon increasing the Ta concentration at $y \leq 0.05$ in the temperature range from RT to 500 °C.

1. Introduction

Lead-free ferroelectric ($Na_{1-x}K_xNbO_3$)-based materials are widely used due to their excellent electromechanical properties, high acoustic vibration speeds, high Curie temperature ($T_C = 420$ °C), and low density [1].

Moreover, it is also interesting to understand the nature of ion diffusion in these materials. Many oxide glasses consisting of different glass formers (B_2O_3, P_2O_5, etc.), a metal oxide (M_2O; M = Ag, Li, Na, and K), and a doping salt (MX; X = I, Cl, Br, and F) have been investigated [2]. KNN-based ceramics exhibit good piezoelectric properties. Saito et al. have reported the huge piezoelectric effect in Li, Ta, Sb co-doped KNN ceramics, which show a high piezoelectric coefficient (d33 = 416 pC/N) [3].

K0.5Na0.5NbO3 (KNN) has cubic symmetry in the Pm3 m space group at >690 K and tetragonal symmetry (P4mm) in the temperature range of 470–690 K [4]. When KNN is cooled below 470 K, the tetragonal phase transforms into an orthorhombic phase (Amm2), which in turn transforms at ~110 K into a rhombohedral phase (R3m) [5].

Ahtee and Glazer [6] have reported the phase diagram of the $Na_{1-x}K_xNbO_3$ system, which shows diverse phase-fields. In the phase diagram, the compositional range ($0.2 < x < 0.5$) at temperatures above 400 °C established the presence of phase X [6]. Though beyond phase X the occurrence of the cubic phase was evident at higher temperatures [3]. Present dielectric and structure measurements support the existence of the X phase. In a previous communication [7], a morphotropic-like phase boundary was observed in $Na_{1-x}K_xNbO_3$ near x = 0.315 and after that the electric properties due to Ta-doping [8] were observed. Furthermore, the variations in the dielectric and structural properties with temperature were measured.

The present study is focused on the temperature-dependent dielectric properties of NKTN-based materials. Ta ($0 \leq y \leq 0.05$) was doped in $Na_{0.685}K_{0.315}Nb_{1-y}Ta_yO_3$ ceramics [7,8] by forming a new solid solution to obtain improved electrical and structural properties. The phase transition behavior were observed using high-temperature X-ray diffraction analysis of the system.

2. Experimental

Ceramic pellets of $Na_{0.685}K_{0.315}Nb_{1-y}Ta_yO_3$ ($0 \leq y \leq 0.05$) were blended via a solid-state reaction method using the crude powders of Na_2CO_3, K_2CO_3, Nb_2O_5, Ta_2O_5 (99.9%, MERCK, Germany). The preparation of $Na_{0.685}K_{0.315}Nb_{1-y}Ta_yO_3$ ($0 \leq y \leq 0.05$) ceramic pellets has been described in an earlier publication [7,8]. High-temperature X-ray diffraction (HT- XRD) spectra were recorded to analyze the phase transition behavior of the ceramic pellets at different temperatures.

* Corresponding author.
E-mail address: jyotsana.jn42@gmail.com (J. Negi).

https://doi.org/10.1016/j.jpcs.2020.109853
Received 12 April 2020; Received in revised form 12 November 2020; Accepted 13 November 2020
Available online 21 November 2020
0022-3697/© 2020 Elsevier Ltd. All rights reserved.

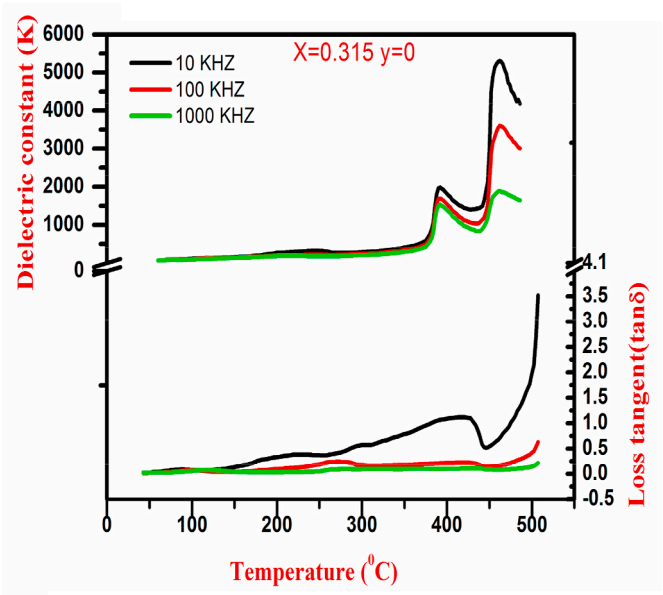

Fig. 1. Temperature variation of the dielectric constant and tangent loss observed for $Na_{0.685}K_{0.315}Nb_{1-y}Ta_yO_3$ (y = 0.00) at different frequencies.

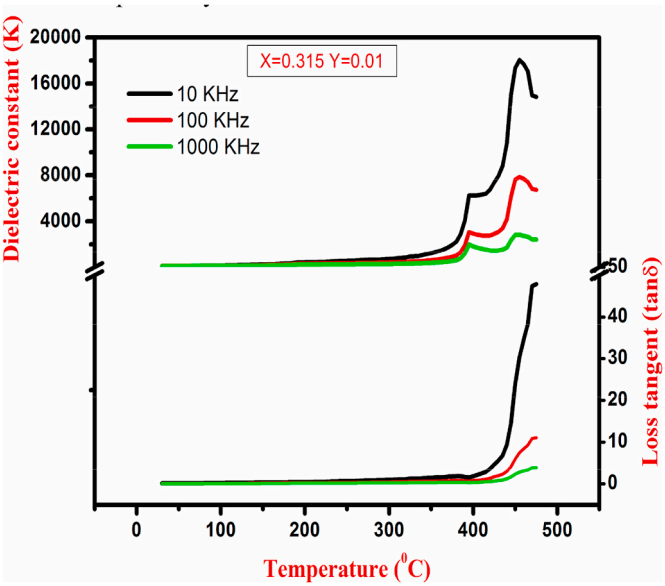

Fig. 2. Temperature variation of the dielectric constant and tangent loss observed for $Na_{0.685}K_{0.315}Nb_{1-y}Ta_yO_3$ (y = 0.01) at different frequencies.

X-ray diffraction measurements were carried out using Cu $K_{\alpha 1}$ radiation ($\lambda = 1.5405980$ Å) on a X-ray diffractometer (PANalytical, X'PERT PRO) at a glancing incident angle over a 2θ range of 20–70° at an scanning rate of 6°/min. For our dielectric measurements the sintered pellets were used as the electrode utilizing air drying silver paste in a parallel-plate capacitor configuration. The temperature, frequency, and composition ($0 < y < 0.05$) dependences of dielectric permittivity (K), loss tangent (tan δ), and electrical conductivity (σ) of the prepared samples were measured in a metal-insulator-metal (MIM) configuration using an RCL meter (Fluke–PM6306) in the frequency range from 10 KHz to 1 MHz from RT to 500 °C.

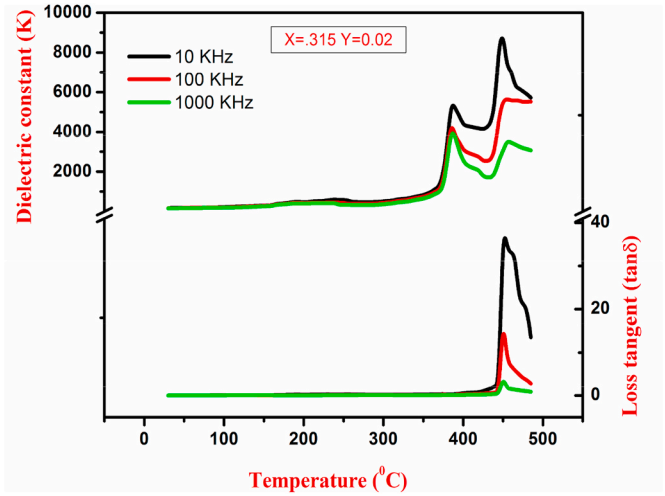

Fig. 3. Temperature variation of the dielectric constant and tangent loss observed for $Na_{0.685}K_{0.315}Nb_{1-y}Ta_yO_3$ (y = 0.02) at different frequencies.

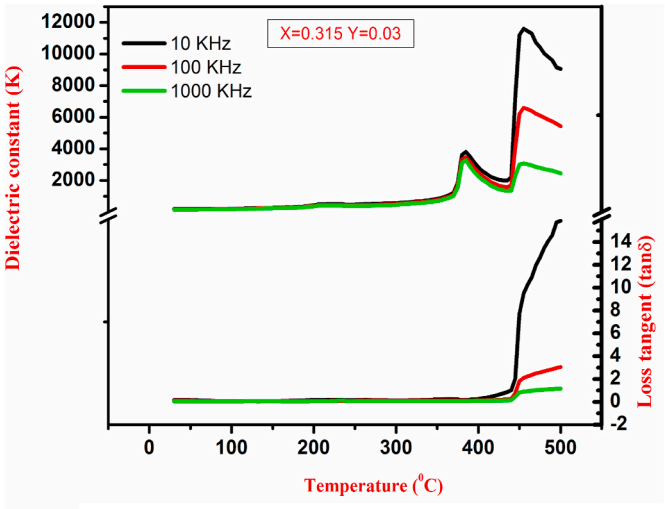

Fig. 4. Temperature variation of the dielectric constant and tangent loss observed for $Na_{0.685}K_{0.315}Nb_{1-y}Ta_yO_3$ (y = 0.03) at different frequencies.

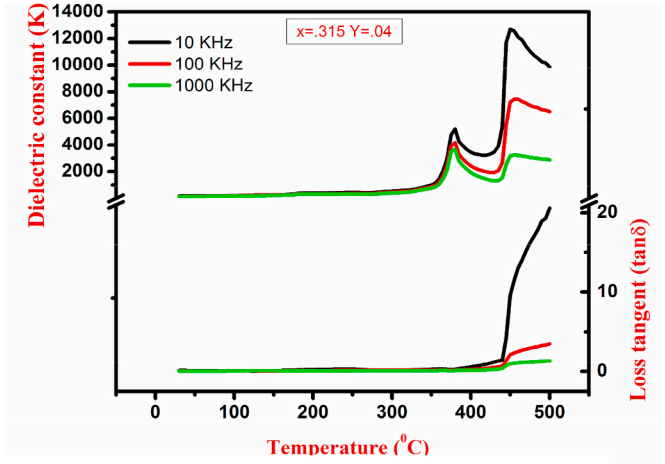

Fig. 5. Temperature variation of the dielectric constant and tangent loss observed for $Na_{0.685}K_{0.315}Nb_{1-y}Ta_yO_3$ (y = 0.04) at different frequencies.

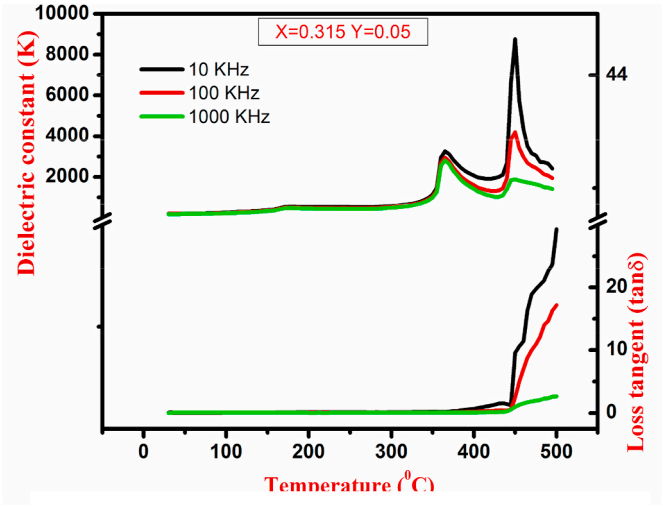

Fig. 6. Temperature variation of the dielectric constant and tangent loss observed for $Na_{0.685}K_{0.315}Nb_{1-y}Ta_yO_3$ (y = 0.05) at different frequencies.

3. Results and discussion

3.1. Dielectric measurements

The dielectric constant (K) and tangent loss (tan δ) of the different frequencies and temperatures at different doping concentrations are shown in Figs. 1–6. The data shows that the K and tan δ curves shift downward upon increasing the frequency from 10 kHz to 1000 kHz for all the prepared samples. We have also observed enormous anomalous peaks near the probe temperature at 200, 380, and 450 °C for all the deliberate frequencies, as shown in Figs. 1–6. The downward shift in the K and tan δ curves or reducing peak strength at a particular temperature can be attributed to the damping out of successive relaxation modes in the lattice [9]. While the anomalous peak in the dielectric constant curve near the probe temperature at 200, 380, and 460 °C indicate the distinct phase transitions of the materials [10]. These peaks signify that the phase transition of each sample composition highly depends on the temperature and its phase change from monoclinic to tetragonal, tetragonal to tetragonal, and tetragonal to cubic occurs at transition temperatures of 200, 380, and 460 °C respectively.

From the above measurements, we have optimized the value of the frequency and concentration (x). Consequently, we analyzed the behavior of the dielectric constant and electrical conductivity of the piezoceramics materials at different temperatures and compositions (y ≤ 0.05) and a fixed frequency (f = 1000 kHz) and x value (0.315). Fig. 7 shows the dielectric constant (K) of $Na_{0.685}K_{0.315}Nb_{1-y}Ta_yO_3$ as a function of temperature for different compositions (y = 0–0.05) at a fixed frequency (1000 kHz) and x value (0.315). After normalization of Fig. 7, we observed that the peak at the three transition temperatures (200, 380, and 460 °C) were shifted towards lower temperatures upon increasing the weight percentage of y (Ta-doping at the B-site in the composition) from 0 to 0.05. From Fig. 7, it was observed that upon increasing the value of y from 0 to 0.05, the first transition temperature was shifted from 205 to 175 °C, the second transition temperature was shifted from the 395 to 360 °C, and the third temperature was shifted from 465 to 445 °C. An appropriate reason for the shifting of the peak observed for the dielectric constant with temperature will be discussed below. The temperature-dependent dielectric conductivity of the $Na_{0.685}K_{0.315}Nb_{1-y}Ta_yO_3$ composition with different doping concentrations of Ta on the B-site (0 = y ≤ 0.05) at a fixed frequency (1000 kHz) and x value (0.315) was measured, as shown in Fig. 8. We observed two intense anomalous peaks (Fig. 8) for all of the prepared samples. However, both peaks (peak 1 and peak 2) were shifted toward lower temperatures upon increasing the weight percentage of y from 0 to 0.05. These shifts in the conductivity peaks with temperature signify that the electric phase of the composition changes from a ferro-to para-electric phase transition [12–14]. The phase transition phenomena is consistent in the XRD analysis (Figs. 9–14) and will be discussed below. We have observed two intense peaks in the dielectric constant and conductivity analyses (Figs. 7 and 8) at a particular temperature (the same for both the cases), which is known as the transition temperature (T_c) and was also shifted to lower temperature upon increasing the doping concentration of Ta on the B-site (0 ≤ y ≤ 0.05) in the composition. According to the literature, perovskite-type composite materials show anomalous behavior at T_c because the frequency of the soft mode in the perovskite material tends to zero at T_c and the lattice displacement associated with

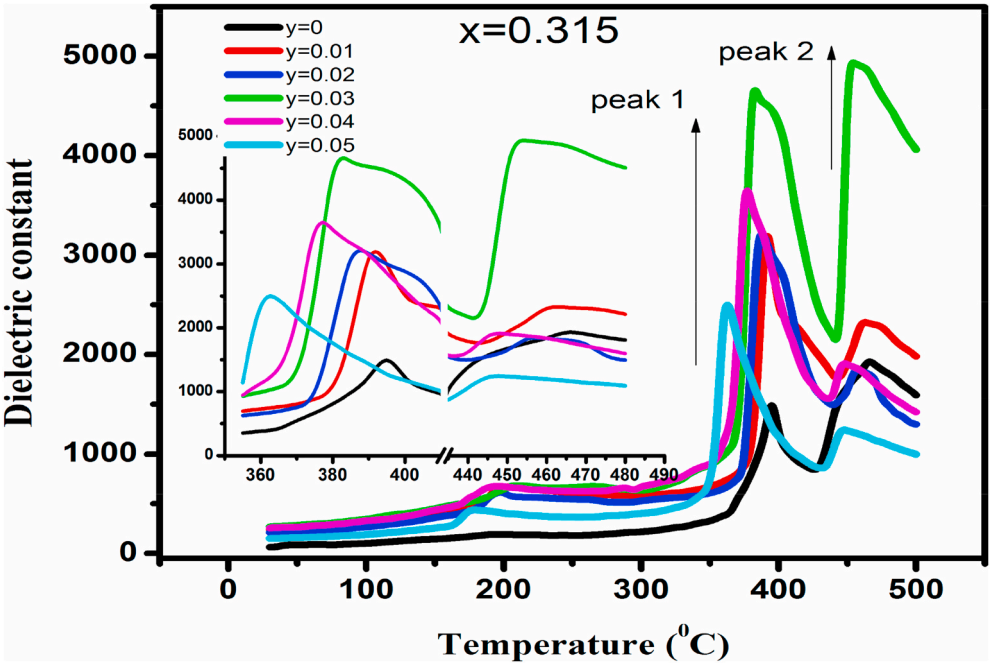

Fig. 7. Temperature variation of the dielectric constant (K) observed for $Na_{0.685}K_{0.315}Nb_{1-y}Ta_yO_3$ (0 ≤ y ≤ 0.05) at different compositions (y) and 1 MHz.

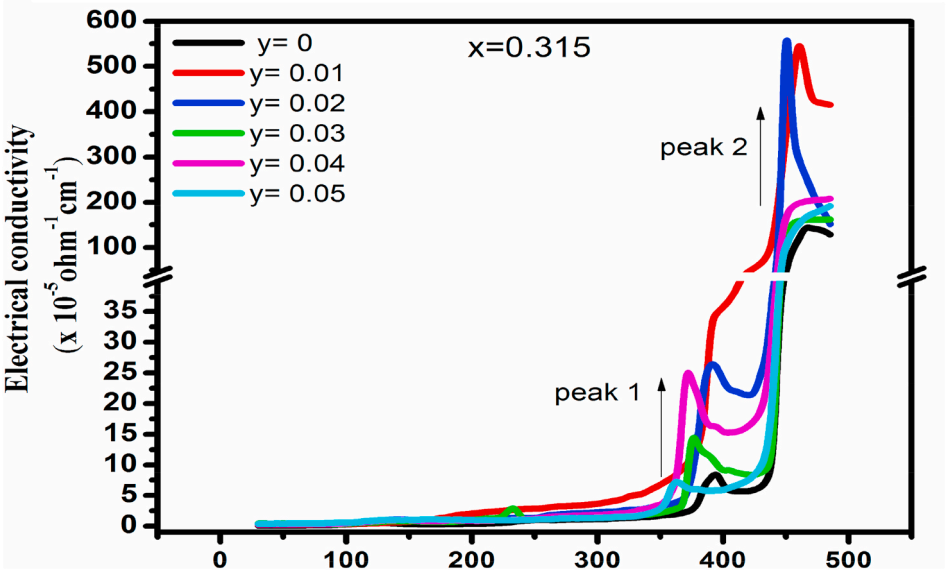

Fig. 8. Temperature variation of the dielectric conductivity (σ) observed for $Na_{0.685}K_{0.315}Nb_{1-y}Ta_yO_3$ ($0 \leq y \leq 0.05$) at different compositions (y) and 1 MHz.

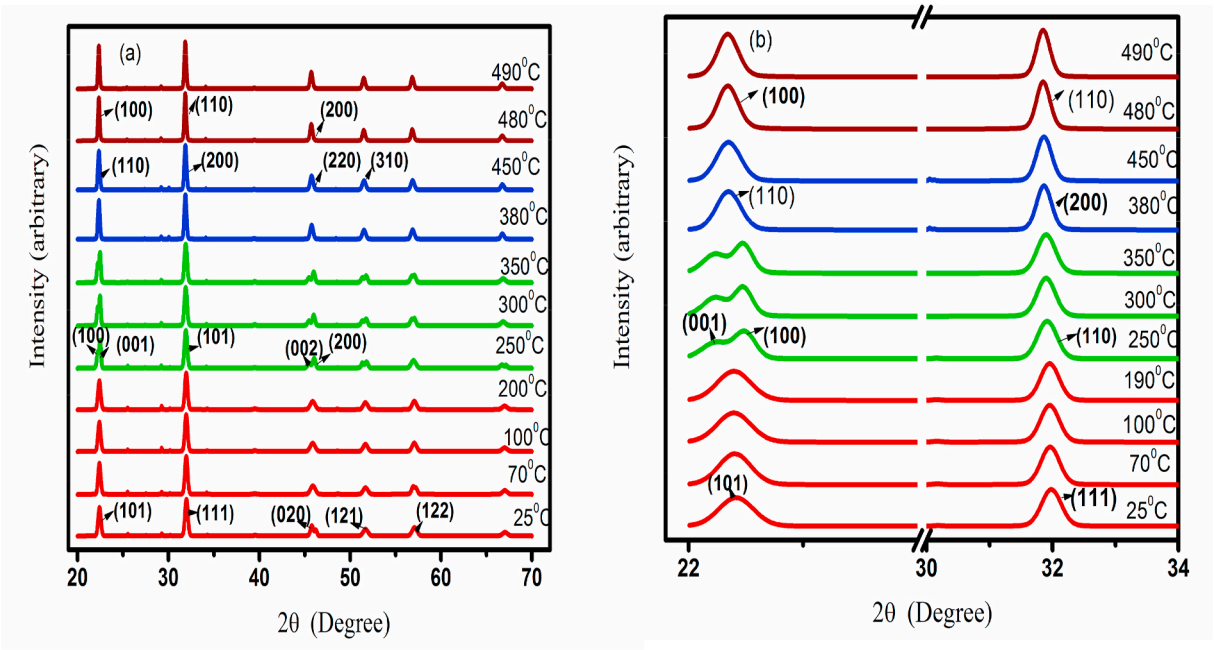

Fig. 9. (a) XRD patterns obtained for $Na_{0.685}K_{0.315}Nb_{1-y}Ta_yO_3$ (y = 0) and (b) the shifts observed for the most intense peaks.

it becomes unstable leading to a phase transition. In addition, increasing the Ta-doping concentration at the B-site ($0 \leq y \leq 0.05$) can modify the structure, grain boundary barrier height, and activation energy of the $Na_{0.685}K_{0.315}Nb_{1-y}Ta_yO_3$ composition resulting in the observed shift.

3.2. X-ray diffraction analysis

Figs. 9–11 show the HT-XRD spectra obtained for $Na_{0.685}K_{0.315}Nb_{1-y}Ta_yO_3$ pellets prepared using a weight percentage of y = 0, 0.02, and 0.05, respectively. The measured XRD peaks have been indexed using Inorganic Crystal Structure Database (ICSD)-(01-078-5546), (01-078-5547), (00-077-0037), and (00-060-0328). The HT- XRD spectra of the prepared samples exhibit polycrystalline behavior. Fig. 9(a) shows the HT- XRD patterns display a continuous shift in the most intense peaks with temperature in $Na_{0.685}K_{0.315}Nb_{1-y}Ta_yO_3$ (y = 0). From RT to 200 °C, the more intense peaks corresponding to (101) and (111) were observed to shift to higher angles upon increasing the temperature. Above 200 °C, the most intense peaks corresponding to (001), (100) and (110) shift toward lower angles with increasing temperature. At 380 °C, the peaks at (001) and (100) vanish and above 480 °C the observed peaks corresponding to (100) and (110) are slightly shifted towards higher angles, as shown in Fig. 9(b). The observed HT-XRD patterns demonstrate four distinguishable phases with transitions at 200, 380, and 460 °C. The observed temperature variation in the lattice parameters (a, b, and c) and β angle (for monoclinic symmetry) is shown in Fig. 10. The cell parameters were refined using High Score Plus software, in which the background was modeled using the Legendre polynomial and the pseudo-Voigt function with the Rietveld method [29].

In the HT- XRD patterns obtained for $Na_{0.685}K_{0.315}Nb_{0.98}Ta_{0.02}O_3$, a continuous shift in the most intense peaks corresponding to (100), (111),

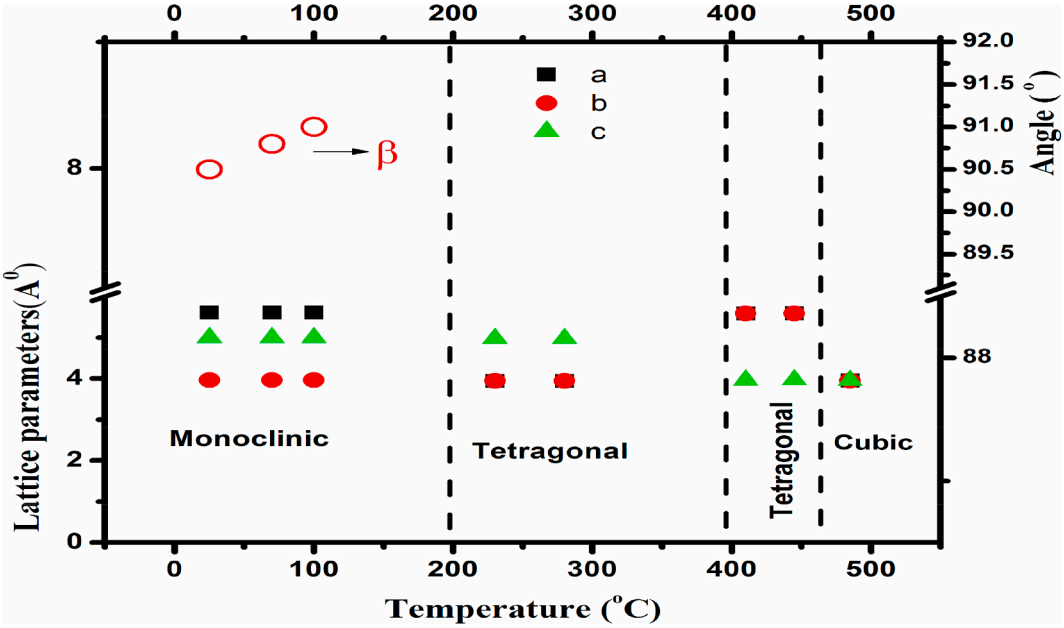

Fig. 10. Temperature variation of the lattice parameters observed for $Na_{0.685}K_{0.315}Nb_{1-y}Ta_yO_3$ (y = 0).

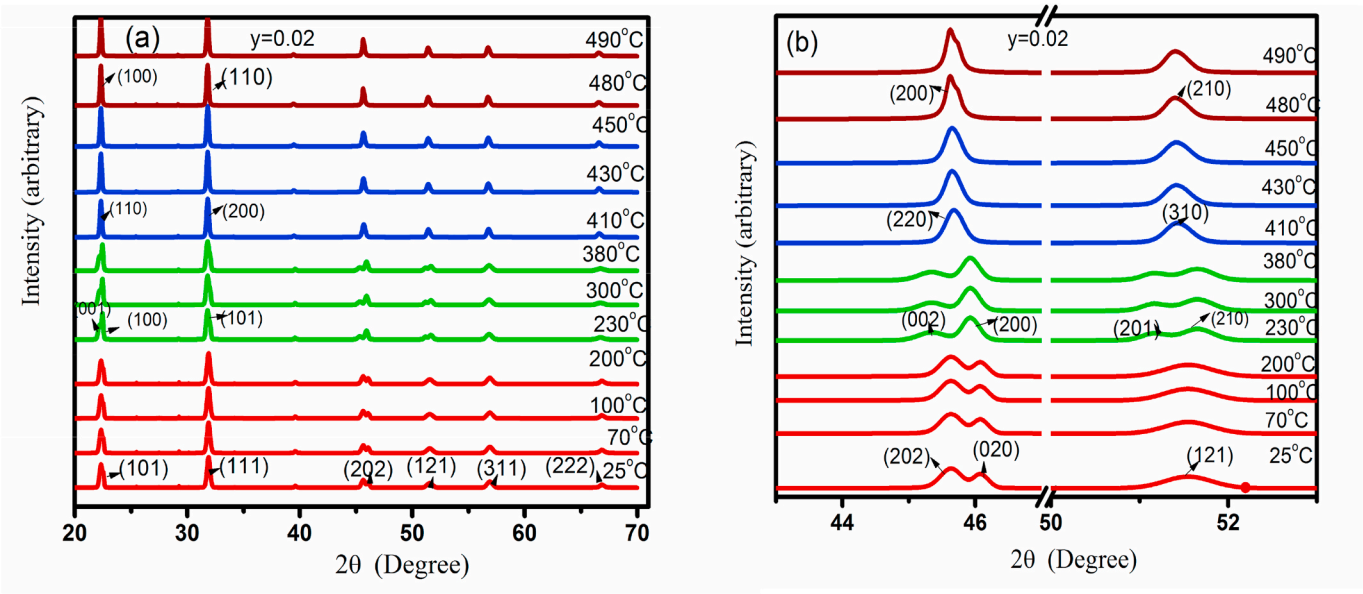

Fig. 11. (a) XRD patterns obtained for $Na_{0.685}K_{0.315}Nb_{1-y}Ta_yO_3$ (y = 0.02) and (b) the shifts observed for the most intense peaks.

(202), (121), (311), etc., with temperature was observed (Fig. 11). Between RT and 200 °C, these peaks were observed to shift to higher angles upon increasing the temperature, between 200 and 380 °C, the (202) and (020) peaks were inverted, between 380 and 460 °C, the (202) and (020) peaks vanished, and above 460 °C the remaining peaks were observed to slightly shift towards higher angles. The lattice parameters calculated from these data are presented in Fig. 12.

The HT-XRD patterns observed for $Na_{0.685}K_{0.315}Nb_{1-y}Ta_yO_3$ (y = 0.05) are shown in Fig. 13. A continuous shift in the most intense peaks corresponding to (100), (111), (202), (121), (311), etc., with temperature was observed. Between RT and 200 °C, these peaks were observed to shift to higher angles upon increasing the temperature, between about 200 and 380 °C the (202) and (020) peaks were inverted, between 380 and 460 °C the peaks for (202) and (020) vanish, and above 460 °C the remaining peaks were observed to slightly shift toward higher angles with increasing temperature. The observed HT-XRD patterns clearly indicate four distinct phases in NKTN where $y \leq 0.05$ with transitions at 200, 380, and 460 °C. The variation in the lattice parameters with temperature is shown in Fig. 14.

The HT-XRD patterns and dielectric measurements demonstrate four distinguishable phases with transitions at 200, 380, and 460 °C in Ta-doped $Na_{0.685}K_{0.315}NbO_3$. Between RT and 200 °C a monoclinic phase was observed, between 200 and 380 °C was tetragonal, between 380 and 460 °C was tetragonal, and above 460 °C, the system exhibits a cubic phase. The HT-XRD results were consistent with the transitions determined based on the dielectric constant measurements obtained for the prepared compositions. Ahart et al. [30] found that a phase boundary region can present in a pure material under pressure at low temperature and consequently the polarization can easily rotate between different symmetries. In order to obtain a compression in the lattice constant, they

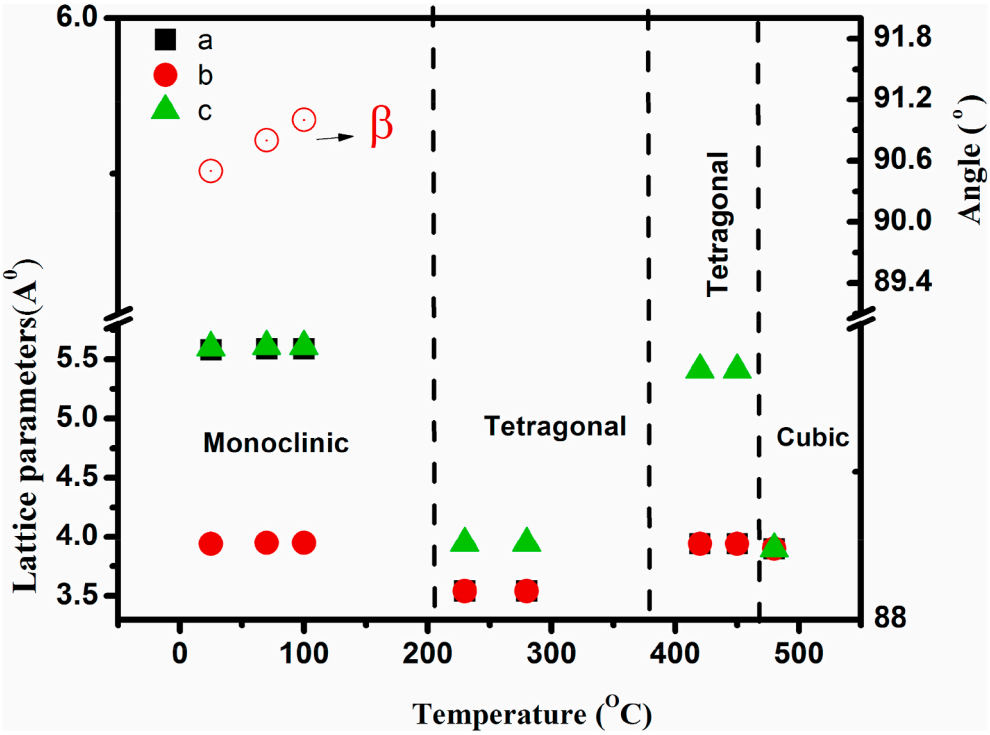

Fig. 12. Temperature variation of the lattice parameters observed for $Na_{0.685}K_{0.315}Nb_{1-y}Ta_yO_3$ (y = 0.02).

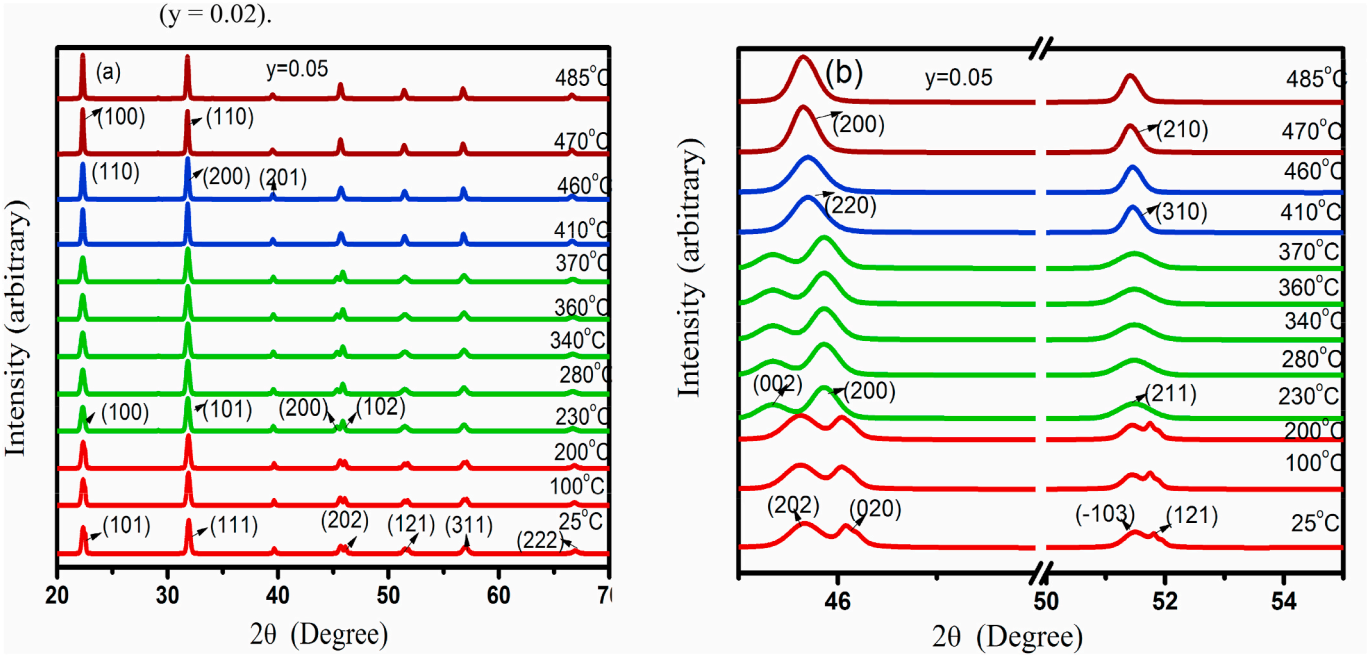

Fig. 13. (a) XRD patterns obtained for $Na_{0.685}K_{0.315}Nb_{1-y}Ta_yO_3$ (y = 0.05) and (b) the shifts observed for the most intense peaks with composition (y) at higher temperature.

applied chemical pressure by substituting a smaller atom with similar polarizability for Pb in the A site in $PbTiO_3$.We found this mechanism is also suitable for the NKN system. Trace impurities (tungsten and cobalt) were introduced into NKN by prolonging the milling time. The ionic radiuses of tungsten and cobalt are smaller than that of niobium, which leads to a decrease in the lattice constant and also makes the phase transition temperature shift to low temperature [31].

4. Conclusions

In the present study, a dielectric loss was observed with increasing temperature in all the NKTN compositions where $y \leq 0.05$ and at a given temperature it has been observed to decrease at higher frequencies. The dielectric loss can be represented by the circuit analog of the resistance in parallel with a capacitor [19]. At higher temperatures, the leakage current through the resistor will increase and thus increase the dielectric

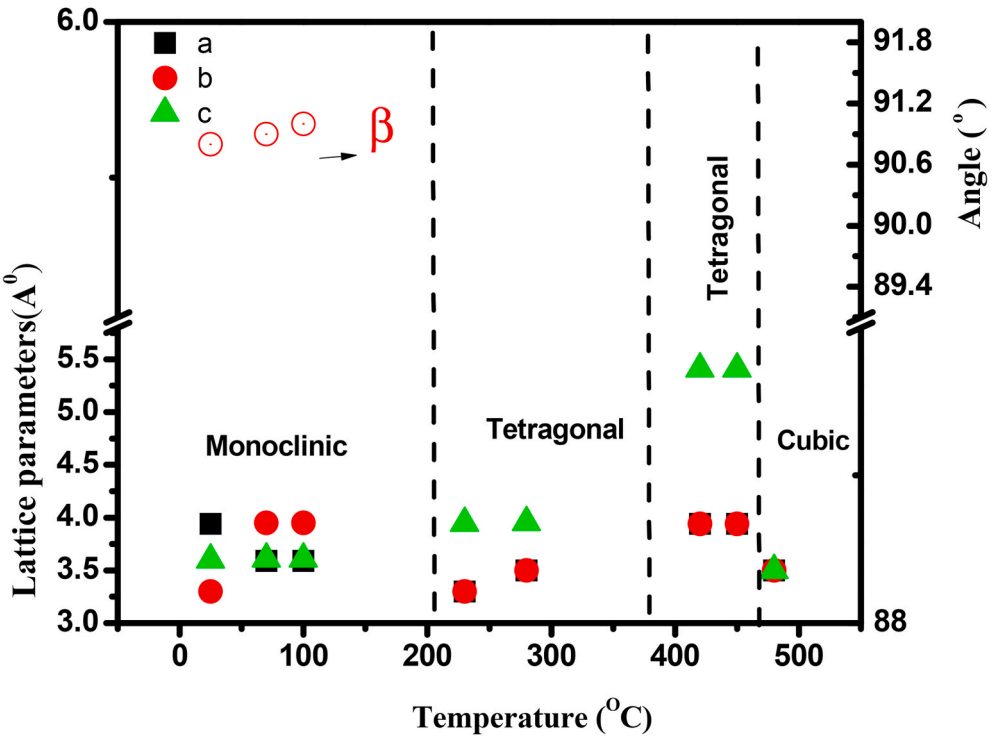

Fig. 14. Temperature variation of the lattice parameters observed for $Na_{0.685}K_{0.315}Nb_{1-y}Ta_yO_3$ (y = 0.05).

loss and for a higher frequency, the capacitor offers low reactance path to the sinusoidal signal, which minimizes the conduction losses in the resistor, and consequently, decreasing the loss with increasing frequency. The effects of Ta substitution on the phase structure and electric properties of the $Na_{0.685}K_{0.315}NbO_3$ ceramic were investigated. It was found that the anomalously large value of the dielectric constant at 200, 380, and 460 °C, indicates the distinct phase transitions at these temperatures, whereas upon doping of Ta at the B-site, the first transition temperature was observed to gradually decrease with increasing y, from 205 to 175 °C, for the prepared compositions. Concomitantly, the value of the second transition temperature gradually decreases from 395 to 360 °C, and the third from 465 to 445 °C upon increasing the Ta content, $y \leq 0.05$. The HT-XRD patterns and dielectric measurements demonstrate the four distinguishable phases with transitions at 200, 380, and 460 °C in Ta-doped $Na_{0.685}K_{0.315}NbO_3$. Between RT and 200 °C, this indicated a monoclinic phase; between 200 and 380 °C, a tetragonal phase; between 380 and 460 °C, a tetragonal phase; and above 460 °C, the system exhibits a cubic phase. Overall, the obtained results indicate that NKN-type ceramics can be good candidates for lead-free electronic applications.

Declaration of competing interest

The authors declare that they have no known competing financial interests or personal relationships that could have appeared to influence the work reported in this paper.

Appendix A. Supplementary data

Supplementary data to this article can be found online at https://doi.org/10.1016/j.jpcs.2020.109853.

References

[1] Priya, S. Nahm, Lead-free Piezoelectrics, Springer, New York, 2012.
[2] E.M. Masoud, M. Khairy, M.A. Mousa, J. Alloys Compd. 569 (2013) 150–155.
[3] Y. Saito, H. Takao, T. Tani, T. Nonoyama, K. Takatori, T. Homma, T. Nagaya, M. Nakamura, Nature 432 (2004) 84–87.
[4] L. Liu, M. Knapp, H. Ehrenberg, L. Fang, L.A. Schmitt, H. Fuess, M. Hoelzeld, M. Hinterstein, J. Appl. Cryst. 49 (2016) 574–584.
[5] J. Tellier, B. Malic, B. Dkhil, D. Jenko, J. Cilensek, M. Kosec, Solid State Sci. 11 (2009) 320–324.
[6] M. Ahtee, A.M. Glazer, Acta Cryst A32 (1976) 434–446.
[7] J. Negi, S. Singh, N.S. Panwar, Phase Trans. 92 (2019) 149–158.
[8] J. Negi, S. Singh, N.S. Panwar, Ferroelectrics 558 (2020) 117–127.
[9] R.C. Buchanan, M. Dekker, Inc., Ceramic Materials for Electronics: Processing, Properties, and Applications, second ed., 1991, p. 532. New York.
[10] G. Shirane, R. Newnham, R. Pepinsky, Phys. Rev. 96 (1954) 581–588.
[12] M.H. Francombe, B. Lewis, J Electronic Contrl 2 (1957) 387–403.
[13] M.P. Ivliev, I.P. Raevskii, L.A. Reznichenko, S.I. Raevskaya and V.P. Sakhnenho, 45 (2003) 1984-1989.
[14] S.Y. Chu, W. Water, Y.D. Juang, J.T. Liaw, Ferroelectrics 287 (2003) 23–33.
19 T. Sakudo, J. Phys. Soc. Jpn. 15 (1960) 2112–2113.
[29] J. Tellier, B. Malic, B. Dkhil, D. Jenko, J. Cilensek, M. Kosec, Solid State Sci. 11 (2009) 320–324.
[30] M. Ahart, M. Somayazulu, R.E. Cohen, P. Ganesh, P. Dera, H. Mao, Nature 451 (2008) 545–548.
[31] L. Liu, Y. Huang, Y. Li, L. Fang, H. Dammak, H. Fan, M.P. Thi, Mater. Lett. 68 (2012) 300–302.

Ceramics International 47 (2021) 12066–12071

Contents lists available at ScienceDirect

Ceramics International

journal homepage: www.elsevier.com/locate/ceramint

Annealing temperature-dependent structural and electrical properties of $(Ta_2O_5)_{1-x}$ - $(TiO_2)_x$ thin films, $x \leq 0.11$

Prashant Thapliyal [a,b,*], Alok S. Kandari [c], Vijendra Lingwal [d], N.S. Panwar [a], G. Mohan Rao [b]

[a] Department of Instrumentation Engineering, H.N.B. Garhwal University, Srinagar Garhwal, Uttarakhand, India
[b] Department of Instrumentation and Applied Physics, Indian Institute of Science, Bangalore, India
[c] Department of Physics, Govt. PG College New Tehri, Uttarakhand, India
[d] Department of Physics, Pt. L.M.S. Govt. PG College Rishikesh, Dehradun, Uttarakhand, India

ARTICLE INFO

Keywords:
Sputtering
Annealing temperature
Dielectric constant
Leakage current

ABSTRACT

$(Ta_2O_5)_{1-x}$- $(TiO_2)_x$ (TTO_x) thin films, with x = 0, 0.03, 0.06, 0.08, and 0.11, were deposited using magnetron direct current (DC) sputtering method onto the P/boron-silicon (1 0 0) substrates by varying areas of Tantalum and Titanium metallic targets, in oxygen environment at ambient temperature. The as-deposited thin films were annealed at temperatures ranging from 500 to 800 °C. Generally, the formation of the Ta_2O_5 structure was observed from the X-ray diffraction measurements of the annealed films. The capacitance of prepared metal–oxide– semiconductor (MOS) structures of Ag/TTO_x/p-Si was measured at 1 MHz. The dielectric constant of the deposited films was observed altering with varying composition and annealing temperature, showing the highest value 71, at 1 MHz, for the TTO_x films, x = 0.06, annealed at 700 °C. With increasing annealing temperature, from 700 to 800 °C, the leakage current density was observed, generally decreasing, from 10^{-5} to 10^{-8} A cm^{-2}, for the prepared compositions. Among the prepared compositions, films with x = 0.06, annealed at 800 °C, having the observed value of dielectric constant 48, at 1 MHz; and the leakage current density 2.7 × 10^{-8} A cm^{-2}, at the electric field of 3.5 × 10^5 V cm^{-1}, show preferred potential as a dielectric for high-density silicon memory devices.

1. Introduction

Interest in searching for high dielectric constant (K) materials for memory elements to miniaturize electronic gadgets has increased by manifold in the last few decades. For this purpose, many high-K metal oxides, e.g., titanium oxide (TiO_2), tantalum pentoxide (Ta_2O_5), etc. [1–4], have been examined. These materials can substitute the elemental silicon-based dielectrics, such as SiO_2, SiO_xN_y, etc. Ta_2O_5 is used frequently as a gate dielectric due to its high dielectric constant and compatibility with silicon devices and the existing process infrastructure for manufacturing memory devices [5]. The dielectric characteristics have been reportedly improved when other metal oxides were added to Ta_2O_5 [6]. Electrical properties of Ta_2O_5 have been found to improve by adding TiO_2 or Y_2O_3 [7,8], which has been associated with the compensation of oxygen vacancies in Ta_2O_5 by the added material. The relative permittivity (K) of Ta_2O_5 films was considerably enhanced with a small fraction of TiO_2 and annealing [7,9]. With the doping of 8% (mole) TiO_2, the K of bulk Ta_2O_5 was observed to drastically increased [9], from 35 to 126. Gan et al. [10] observed the maximum value of dielectric constant 55 for the sputter-deposited annealed films using $(TiO_2)_{0.08}$- $(Ta_2O_5)_{0.92}$ ceramic target. With high dielectric constant, low leakage current requirements must also have to be fulfilled in dynamic random access memory (DRAM) capacitors for better performance [11]. With annealing, Ta_2O_5 thin films' leakage current has been reportedly found to improve [12–17]. The optimization of high dielectric constant and low leakage current density together has technical potentiality for DRAM applications. In the present study, TTO_x thin films of different compositions were deposited by sputtering the varying areas of tantalum and titanium metal targets in oxygen. Presently, the observed structural, compositional, and electrical characteristics of the deposited thin films have been reported. The feasibility of the potential composition for memory devices, in terms of high dielectric constant and low leakage current density, has been analyzed.

* Corresponding author. Department of Instrumentation Engineering, H.N.B. Garhwal University, Srinagar Garhwal, Uttarakhand, India.
E-mail address: pra.thapli1986@gmail.com (P. Thapliyal).

https://doi.org/10.1016/j.ceramint.2021.01.050
Received 4 December 2020; Received in revised form 4 January 2021; Accepted 5 January 2021
Available online 8 January 2021
0272-8842/© 2021 Elsevier Ltd and Techna Group S.r.l. All rights reserved.

2. Experimental

Thin TTO_x films were deposited on the (1 0 0) p-type silicon substrates. At first, the silicon substrates were rinsed by deionized water and kept for ultrasonication for 5 min in the solution of acetone and deionized water to eliminate surface impurities. To remove the oxide layer from the surface, the substrates were dipped into 1: 20 hydrogen fluoride (HF) solution and rinsed sufficiently by the deionized water and ultrasonication before placing them into the vacuum chamber. Along with a solid Ta target, Ti and Ta targets, both radially cut into an identical star shape, were arranged in the Ta (solid target) - Ti (radially cut star shape) - Ta (radially cut star shape) sequence to form a target assembly for sputtering. Each target had purity 99.99%, 2-inch diameter, and 1 mm thickness. Initially, the depositions were done by arranging the star-shaped Ti target over the identical star-shaped Ta target, such that the similar star-shaped Ta target fully masked the star-shaped Ti target. In this arrangement, only the Ta faces were exposed for sputtering. When sputtered in the ambient oxygen, only tantalum oxide films were expected with this arrangement. Then, for each deposition, the Ti target was exposed gradually with the increasing area for sputtering to form TTO_x compositions. Pirani and penning gauges were connected to the sputtering system to measure the pressure in the different ranges. The thin film preparation method and experimental details for the different measurements have been described elsewhere [18].

In the present study, X-ray diffraction (XRD) measurements were carried out in a range of $20° \leq 2\theta \leq 65°$, at a scanning rate of 3°/minute. The SEM-EDS and XPS measurements show formation of TTO_x compositions (with x = 0, 0.03, 0.06, 0.08, and 0.11), for different relative sputtering areas of the metal targets. The energy of the electron beam used was 20 keV, in SEM-EDS measurements. X-ray photoelectron spectroscopy (XPS) measurements were performed using Kratos Axis Ultra DLD, monochromatic Al *Kα* radiation 1486.6 eV, with a resolution of 0.1 eV. The as-deposited thin films were used for XPS measurements, before depositing silver (Ag) conducting contacts onto the films for electrical measurements. The deposited films' thickness was measured about 280 ± 10 nm. $Ag/TTO_x/p\text{-}Si$ MOS capacitors were fabricated by sputter-depositing of silver, as the top electrode by using a shadowing mask (with circular openings of 0.5 mm diameter), and on the back side of p-Si substrate, as the bottom electrode without any mask. The leakage current density was measured with Ferroelectric P-E loop tracer with piezometer (aixACCT Systems GmbH, aixPES).

3. Results and discussion

The obtained XRD results of the prepared film samples have been shown in Fig. 1. The prepared films of all the compositions annealed at and above 700 °C show orthorhombic Ta_2O_5 structure, Fig. 1. The observed diffraction peaks, corresponding to (0 0 1), (2 0 0), (2 0 1), (0 0 2), (3 1 0), and (2 0 2) planes, were found matching with Inorganic Crystal Structure Database (ICSD)- (01-089-2843) data and reported results [19–21] for orthorhombic Ta_2O_5. Titanium could not be detected in the XRD measurements due to its low amount in these samples. However, some presence of crystalline TiO_2 was suspected in the prepared film samples. For $x \leq 0.03$, crystal structure formation was observed in TTO_x thin films, annealed at and above 600 °C, whereas films with $x \geq 0.06$ exhibit crystal structure on annealing at and above 700 °C, Fig. 1. The observed XRD patterns of the deposited films of a select composition, with x = 0.06, have been shown in Fig. 2.

The observed energy dispersive spectrum of the as-deposited $TTO_{0.06}$ films, with distinct characteristic Ta, Ti, and O peaks, has been shown in Fig. 3.

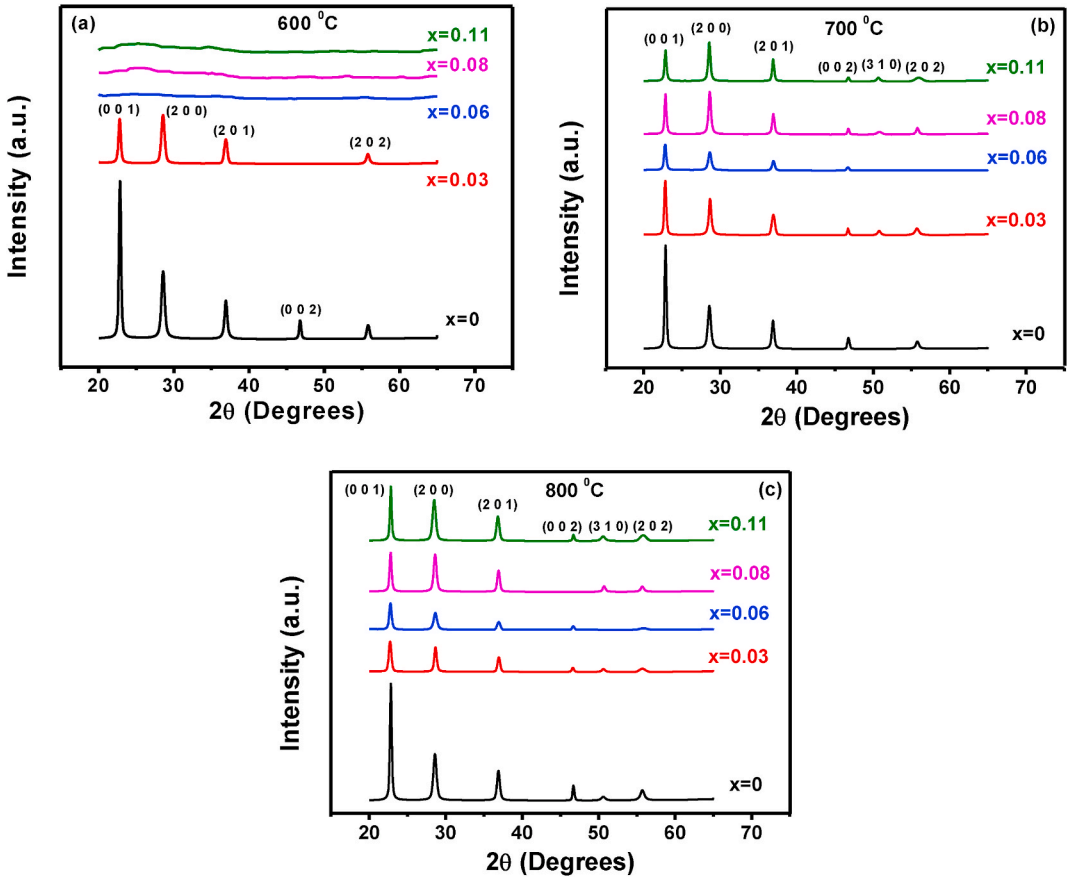

Fig. 1. XRD patterns of TTO_x, ($0 \leq x \leq 0.11$), thin films annealed at (a) 600, (b) 700, and (c) 800 °C.

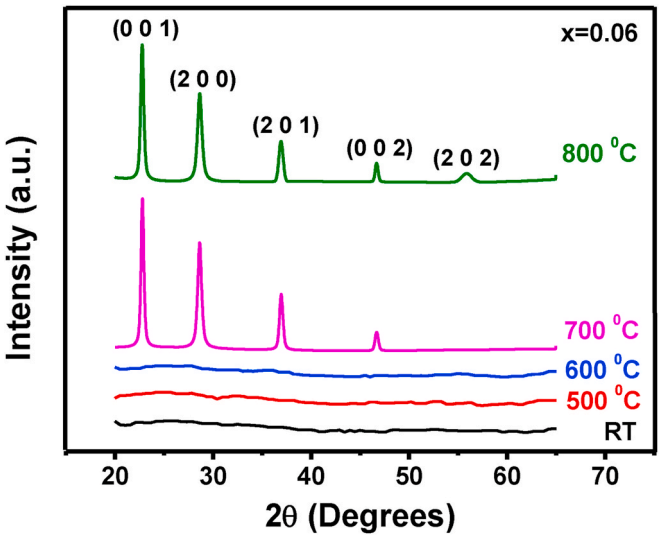

Fig. 2. XRD patterns of annealed $TTO_{0.06}$ thin films.

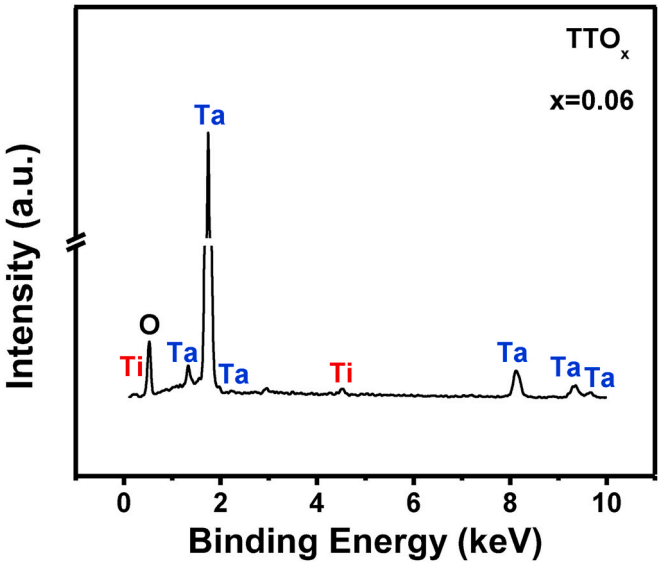

Fig. 3. EDS spectrum of $TTO_{0.06}$ thin films.

The composition (x) of the prepared TTO_x films, determined using the atomic percentage data obtained from EDS measurements, is summarized in Table 1. The XPS measurement results, Figs. 4 and 5, were found consistent with the EDS results.

The XPS survey spectra of the deposited films show Ta 4f and Ta 4d characteristic peaks, at about 25–29 eV and 230–240 eV, respectively, Fig. 4. The characteristic Ti 2p peak, at about 458–467 eV, and distinct O 1s peak, at about 530 eV were observed.

For the deposited TTO_x films, the XPS narrow spectra show the core level binding energy of Ta 4f in the 29- 25 eV range, with two peaks corresponding to Ta $4f_{5/2}$ and Ta $4f_{7/2}$, Fig. 5(a). For the composition x = 0.03, the binding energy of Ta $4f_{5/2}$ and Ta $4f_{7/2}$ were found at 28.7 and 26.8 eV, respectively, indicating the fully oxidized state of tantalum [22]. Ta $4f_{5/2}$ and Ta $4f_{7/2}$ peaks were observed separated by 1.9 eV, which agrees with the reported results [21,23,24]. The characteristic peaks of Ta $4f_{5/2}$ and Ta $4f_{7/2}$ were found at 27.6 and 25.8 eV, respectively, for the films with x = 0.11, showing the shifting of 1.1 and 1.0 eV, in the binding energy of Ta $4f_{5/2}$ and Ta $4f_{7/2}$, respectively, than that for x = 0.03.

XPS narrow spectra of Ti 2p of the TTO_x films with compositions x = 0, 0.03, 0.06 and 0.11, have been shown in Fig. 5(b). For the composition x = 0, the region around the 466.0 eV shows the complex background of Ta $4p_{1/2}$, which is close to Ti $2p_{1/2}$. Generally, Ti $2p_{3/2}$ peak's binding energy ranges from 458.6 to 459.2 eV for Ti^{4+} in TiO_2 [25]. The core-level binding energy of Ti $2p_{1/2}$ and Ti $2p_{3/2}$ were found at 466.6 and 459.2 eV, respectively, for TTO_x films with x = 0.03. It was noticed that the Ti $2p_{1/2}$ and Ti $2p_{3/2}$ peaks were separated by 7.4 eV. The shifting in the binding energy of Ti $2p_{3/2}$ was observed from 459.2 to 458.2 eV for TTO_x films with a change in x from 0.03 to 0.11. The binding energy of Ti $2p_{3/2}$ was shifted by 1.0 eV. The Ti $2p_{1/2}$ and Ti $2p_{3/2}$ peaks were found at 464.1 and 458.2 eV, respectively, in the films with x = 0.11, suggesting a spin-orbit splitting of 5.9 eV, which is closer to the oxidation state of Ti^{4+} (5.5 eV) [21,25].

In the XPS narrow spectra, the characteristic peak of O 1s was observed in the binding energy range 529.9–530.9 eV, with no considerable shift in binding energy with the composition (x) in TTO_x films, Fig. 5(c), which is consistent with the reported results [22], No metallic states were found in the observed spectra, indicating that the tantalum (Ta) and titanium (Ti) atoms were fully oxidized, and TTO_x compositions were formed in the deposited films. The observed XPS narrow spectra of Ta 4f, Ti 2p and O 1s were fitted with OriginPro 8.5 software.

TTO_x thin films were deposited onto semiconductor (Si) and were annealed at different temperatures, from 500 to 800 °C. Onto the annealed TTO_x films, metal (Ag) was deposited to form MOS structure. The capacitance-voltage (C–V) characteristics were studied at 1 MHz, under the reciprocating applied DC voltage (between +10 and −10 V), with a 50 mV oscillating signal. Fig. 6 shows the observed C–V characteristics of $TTO_{0.06}$, assisted MOS structures. The inversion, depletion, and accumulation regions, showing their charge status, were observed in the C–V characteristics [18,21]. The low hysteresis of C–V curves indicates low trap densities. In the observed C–V characteristics, the presence of positive fixed oxide charge ($+Q_f$) at the interface of silicon and deposited film may be held responsible for shifting towards more negative bias [26]. The value of the dielectric constant (K) was measured using relation [27].

$$K = (C\ d) / A\ \varepsilon_o, \quad (1)$$

where C (F) is the measured capacitance of oxide film in the accumulation region of C–V characteristics, d (meter) the thickness of prepared film, A ($meter^2$) is the area of the prepared capacitor, ε_o is the permittivity of free space (8.854×10^{-12} F/m).

The highest capacitance (441 pF) was found, for Ag/$TTO_{0.06}$/Si capacitors, films annealed at 700 °C, at 1 MHz, among the prepared compositions, Fig. 6. The dielectric constant of the deposited TTO_x films, annealed at 700 °C, was found 48, 39, 71, 59 and 47 for the compositions with x = 0, 0.03, 0.06, 0.08 and 0.11, respectively. At 1 MHz, presently obtained maximum value of dielectric constant 71, for x = 0.06, is better than that reported earlier [10,28], for the films prepared from the sputtering of ceramic TTO_x target with x = 0.08.

In the present study, K was observed, generally improving with increasing x (≤ 0.06), which may be explained with the following supposition. Like many other oxides, the deep double donor oxygen vacancies [29] in Ta_2O_5 may produce two free electrons. With the doping of TiO_2 in Ta_2O_5, the Ta^{5+} sites are substituted by Ti^{4+} ions, and the oxygen vacancies are compensated in the deposited films [8,30]. The

Table 1
x calculated from EDS results of deposited TTO_x films.

S. No.	x	Ti (atomic %)	Ta (atomic %)	O (atomic %)
1.	0	–	36.81	63.19
2.	0.03	0.40	36.73	62.88
3.	0.06	0.87	38.81	60.32
4.	0.08	1.24	38.51	60.26
5.	0.11	1.65	35.46	62.89

deep double vacancy converts into a single donor complex, which may produce a single electron and forms the 'Ti - oxygen vacancy -' when a relatively small quantity of Ti is added into Ta_2O_5 [31,32]. A single donor is usually shallower than a double donor. The increased number of single donors produced in the crystal lattice contributes to the charge storage, enhancing the dielectric constant, presently up to x = 0.06. For the sufficient quantity of Ti ions, electrically inactive 'Ti - oxygen vacancy - Ti' complexes form, by two Ti single acceptors and an oxygen vacancy. Now, less charge may appear in the crystal lattice due to the formation of electrically inactive complexes; thus, the dielectric constant reduces with a further increase of x (>0.06).

The value of K of Ag/TTO_x/Si capacitors, at room temperature (RT), was observed increasing, up to 700 °C, and decreased with further increasing annealing temperature, Fig. 7. With increasing annealing temperature, improved crystallization of the prepared films may be one reason for this enhancement, up to 700 °C. However, the dielectric constant measured at room temperature was found maximum for TTO_x, x = 0, annealed at 600 °C, compared to the other compositions (x), which may be due to the early formation of the crystal structure. At higher annealing temperatures (≥700 °C), oxygen leaves from the oxide film volume and diffuses to the interface of film and substrate, forming a low-K interfacial SiO_2 layer with the semiconducting substrate, may result in the reduced value of the dielectric constant of the prepared MOS system [33].

The observed room temperature leakage current density (J) variation of Ag/TTO_x/Si, assisted MOS structures, for different compositions (x ≤ 0.11), annealed at different temperatures, at the applied electric field, E = 3.5×10^5 V cm^{-1} (corresponding to applied 10 V), has been shown in Fig. 8. For all the prepared compositions, generally, the leakage current density gradually decreased with increasing annealing temperature, up to 700 °C. In comparison, with further annealing at 800 °C, the leakage current was found drastically reduced by an order of ~3. With increasing annealing temperature, the improved crystallization, reduced oxygen vacancies, bond defects, and film stress [34] may be held responsible for the decreased leakage current, generally, for annealing temperature up to 700 °C, in the present observations. The drastic decrease in the leakage current of the films annealed at 800 °C may be attributed to the formation of the additional oxide layer (SiO_2) and improved quality of Si- oxide interface, resulting in higher barrier height at the interface [35]. Formation of low dielectric constant SiO_2 layer at the film- Si interface reduces the effective capacitance of the MOS structure, which may be attributed to the observed decrease in the dielectric constant of prepared structures, annealed at 800 °C, Fig. 7.

The J-E plots of the Ag/TTO_x/Si MOS structures, for x = 0 to 0.11, films annealed at 800 °C, have been shown in Fig. 9. At the electric field of 1×10^5 V cm^{-1} (corresponding to applied 3 V), the leakage current density of Ag/TTO_x/Si capacitors, for x = 0, was obtained 2×10^{-8} A cm^{-2}; with the addition of titanium the leakage current density was observed decreased to 4.2×10^{-9} A cm^{-2}, for the composition with x = 0.03; and was found increased to 9.2×10^{-9} A cm^{-2}, for x = 0.11. These results are better, even at twice the electric field, than reported by Chandra Sekhar et al. [21].

Among the prepared compositions, the leakage current density was found minimum, for x = 0.03, annealed at 800 °C, Fig. 9; however, the dielectric constant was found 23 for this composition, at RT, Fig. 7. Though the leakage current density was found the lowest, for x = 0.03, the dielectric constant was also found considerably low, 23, for the films annealed at 800 °C. Whereas, for x = 0.06, the dielectric constant was found the highest, 71 and 48, and leakage current density 3.4×10^{-5} A cm^{-2} and 2.7×10^{-8} A cm^{-2}, at an applied electric field of 3.5×10^5 V cm^{-1}, for the films annealed at 700 and 800 °C, respectively. Consideration of the values of leakage current and dielectric constant may be decisive for a suitable choice of the composition of the compatible dielectric for silicon memory devices. The leakage current density was found slightly higher for the films with x = 0.06, but the dielectric constant was more than twice that for x = 0.03. These observations indicate that the composition with x = 0.06, annealed at 800 °C, may be a preferred choice for memory devices among the prepared compositions.

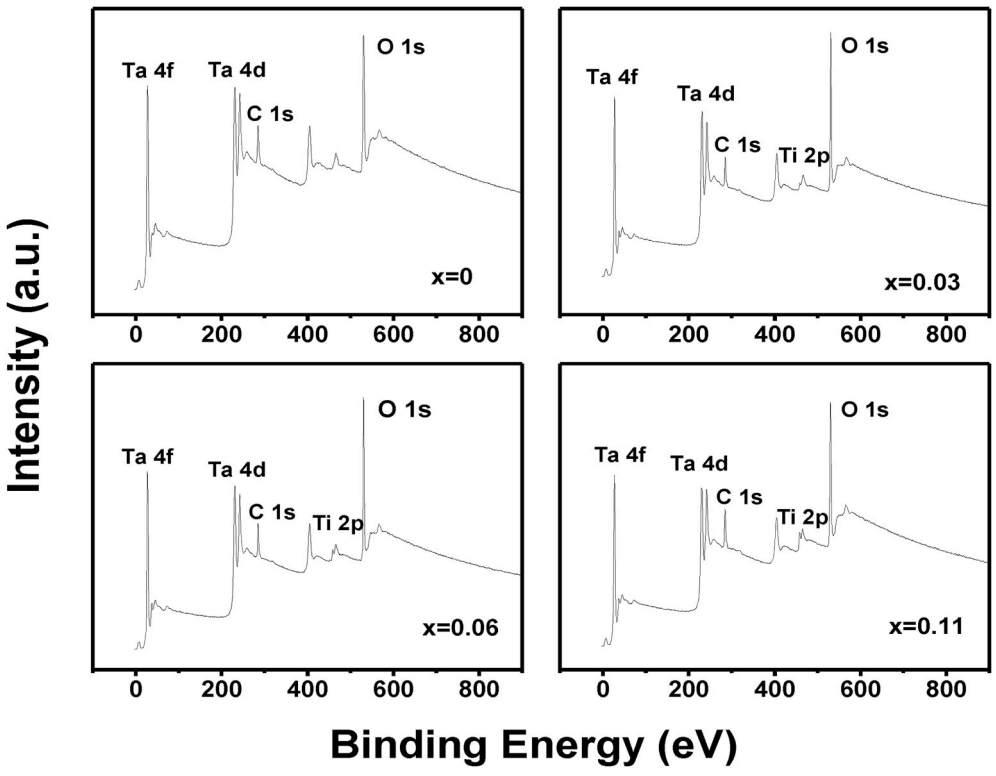

Fig. 4. XPS survey spectrum of TTO_x films for different compositions (x).

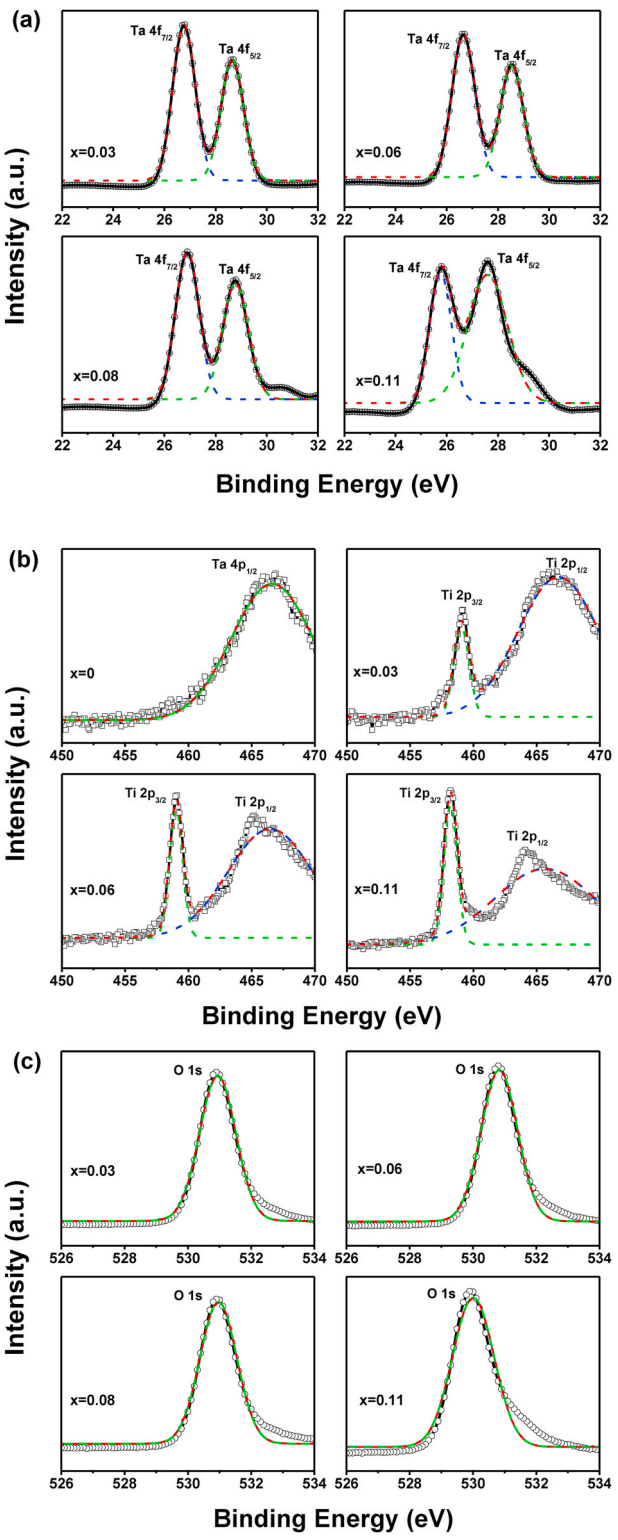

Fig. 5. XPS narrow scan spectra of TTO_x films for different compositions (x), for (a) Ta 4f, (b) Ti 2p, and (c) O 1s.

4. Conclusions

TTO_x films with x = 0, 0.03, 0.06, 0.08, and 0.11 were sputter-deposited by varying the relative sputtering areas of the Ta and Ti metal targets. Films deposited at RT were annealed at 500, 600, 700, and 800 °C. The formation of an orthorhombic Ta_2O_5 structure was confirmed by X-ray diffraction results. The structure and electrical properties of the deposited thin films were found enormously depending on the annealing temperature. With an increase in annealing temperature (≤700 °C), the dielectric constant of the prepared Ag/TTO_x/Si structures at RT was observed increasing, which may be attributed to the enhanced crystal structure of the deposited films. With further annealing at 800 °C, the formation of a low-K SiO_2 interfacial layer with the silicon substrate may be attributed to the observed decrease in the dielectric constant of the structure. Among the prepared compositions, the maximum dielectric constant was found 71, for the films with x = 0.06, annealed at 700 °C, which is higher than the sputter-deposited films using ceramic $(TiO_2)_x$-$(Ta_2O_5)_{1-x}$ targets, with x = 0.08. For all the prepared compositions, the leakage current density was observed, generally decreasing with increasing annealing temperature (≤700 °C), which may be attributed to the improved crystallization, reduced oxygen vacancies, bond defects, and film stress. For the films annealed at 800 °C, the leakage current density was observed drastically decreased to the order of 10^{-8} A cm^{-2}, which may be due to the formation of an oxide layer and improved quality of Si- oxide interface. A trade-off between the observed dielectric constant and leakage current density of the prepared compositions indicates that TTO_x films, with x = 0.06, annealed at 800 °C, shows a preferred choice of a compatible dielectric for the silicon memory devices.

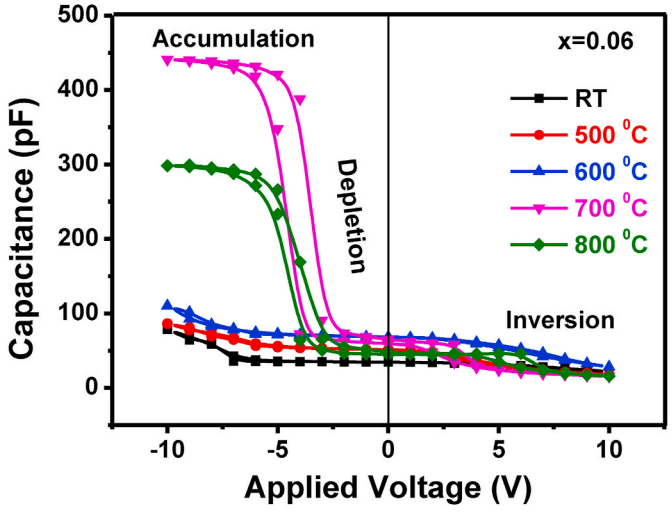

Fig. 6. Capacitance - voltage characteristics of Ag/$TTO_{0.06}$/Si capacitors at different annealing temperatures.

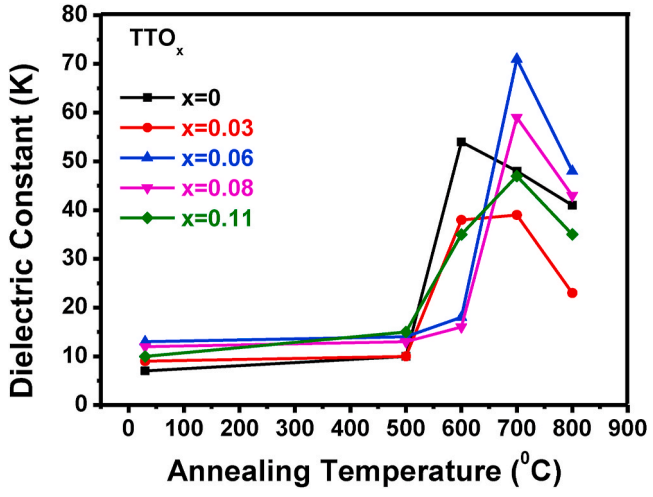

Fig. 7. Annealing temperature variation of the dielectric constant of TTO_x films for different compositions (0 ≤ x ≤ 0.11).

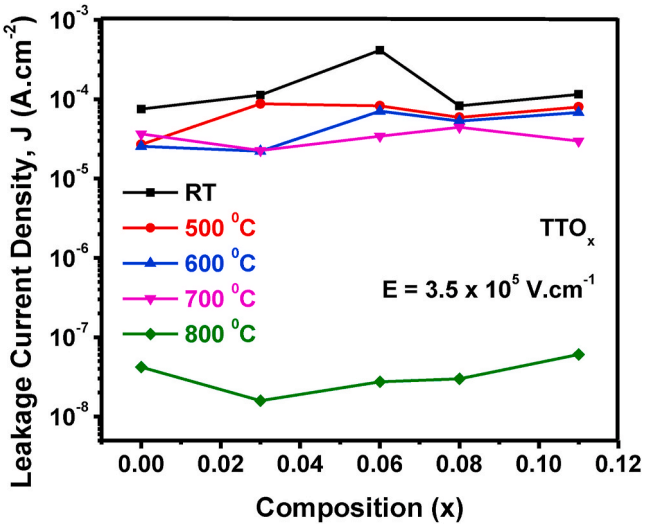

Fig. 8. The plot of leakage current density versus composition, at RT, for Ag/TTO_x/Si capacitors, at applied electric field 3.5×10^5 V cm^{-1}, films annealed at different temperatures.

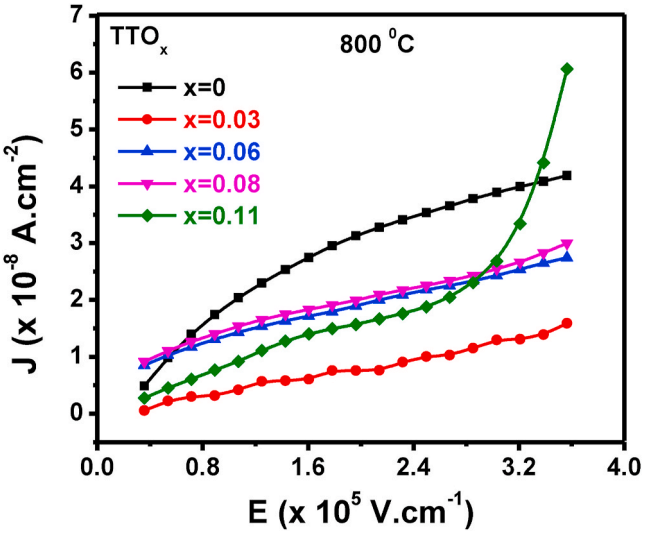

Fig. 9. The J-E plot of TTO_x, ($0 \leq x \leq 0.11$) films, annealed at 800 °C.

Declaration of competing interest

The authors declare that they have no known competing financial interests or personal relationships that could have appeared to influence the work reported in this paper.

References

[1] M. Kadoshima, M. Hiratani, Y. Shimamoto, K. Torii, H. Miki, S. Kimura, T. Nabatame, Rutile-type TiO_2 thin film for high-k gate insulator, Thin Solid Films 424 (2003) 224–228.

[2] S. Ramanathan, C.M. Park, P.C. McIntyre, Electrical properties of thin film zirconia grown by ultraviolet ozone oxidation, J. Appl. Phys. 91 (2002) 4521–4527.

[3] A. Callegari, E. Cartier, M. Gribelyuk, H.F.O. Schmidt, T. Zabel, Physical and electrical characterization of hafnium oxide and hafnium silicate sputtered films, J. Appl. Phys. 90 (2001) 6466–6475.

[4] G.B. Alers, D.J. Werder, Y. Chabal, H.C. Lu, E.P. Gusev, E. Garfunkel, T. Gustafsson, R. Urdahl, Intermixing at the tantalum oxide/silicon interface in gate dielectric structures, Appl. Phys. Lett. 73 (1998) 1517–1519.

[5] H. Shinriki, M. Nakata, UV-O_3 and dry-O_2: two-step annealed chemical vapor-deposited Ta_2O_5 films for storage dielectrics of 64-Mb DRAM's, IEEE Trans. Electron. Dev. 38 (1991) 455–462.

[6] L. Manchanda, M.D. Morris, M.L. Green, R.B. van Dover, F. Klemens, T.W. Sorsch, P.J. Silverman, G. Wilk, B. Busch, S. Aravamudhan, Multi-component high- K gate dielectrics for the silicon industry, Microelectron. Eng. 59 (2001) 351–359.

[7] D.H. Triyoso, R.I. Hegde, S. Zollner, M.E. Ramon, S. Kalpat, R. Gregory, X.D. Wang, J. Jiang, M. Raymond, R. Rai, D. Werho, D. Roan, B.E. White Jr., P.J. Tobin, Impact of titanium addition on film characteristics of HfO_2 gate dielectrics deposited by atomic layer deposition, J. Appl. Phys. 98 (2005), 054104–054104-8.

[8] K.M.A. Salam, H. Fukuda, S. Nomura, Effects of additive elements on improvement of the dielectric properties of Ta_2O_5 films formed by metalorganic decomposition, J. Appl. Phys. 93 (2003) 1169–1175.

[9] R.F. Cava, W.F. Peck Jr., J.J. Krajewski, Enhancement of the dielectric constant of Ta_2O_5 through substitution with TiO_2, Nature 377 (1995) 215–217.

[10] J.-Y. Gan, Y.C. Chang, T.B. Wu, Dielectric property of $(TiO_2)_x$- $(Ta_2O_5)_{1-x}$thin films, Appl. Phys. Lett. 72 (1998) 332–334.

[11] T. Hori, Gate Dielectrics and MOS ULSIs, vol. 34, Springer, New York, 1997, p. 9 [(chapter 1)].

[12] G.D. Wilk, R.M. Wallace, J.M. Anthony, High-k gate dielectrics: current status and materials properties considerations, J. Appl. Phys. 89 (2001) 5243–5275.

[13] E. Atanassova, T. Dimitrova, in: H.S. Nalwa (Ed.), Handbook of Surface and Interfaces of Materials, vol. 4, Academic Press, San Diego, USA, 2001, p. 439.

[14] C. Isobe, M. Saitoh, Effect of ozone annealing on the dielectric properties of tantalum oxide thin films grown by chemical vapor deposition, Appl. Phys. Lett. 56 (1990) 907–909.

[15] K. Shimizu, M. Katayama, H. Funaki, E. Arai, M. Nakata, Y. Ohji, R. Imura, Stoichiometry measurement and electric characteristics of thin-film Ta_2O_5 insulator for ultra-large-scale integration, J. Appl. Phys. 74 (1993) 375–380.

[16] S. Kamiyama, H. Suzuki, H. Watanabe, A. Sakai, H. Kimura, J. Mizuki, Ultrathin tantalum oxide capacitor process using oxygen-plasma annealing, J. Electrochem. Soc. 141 (1994) 1246–1251.

[17] Y. Matsui, K. Torii, M. Hirayama, Y. Fujisaki, S. Iijima, Y. Ohji, Reduction of current leakage in chemical-vapor deposited Ta_2O_5 thin-films by oxygen-radical annealing, IEEE Electron. Device Lett. 17 (1996) 431–433.

[18] Prashant Thapliyal, Alok S. Kandari, Vijendra Lingwal, N.S. Panwar, G. Mohan Rao, Post deposition annealing dependent structural and C-V characteristics of $(Ta_2O_5)_{0.965}$-$(TiO_2)_{0.035}$ thin films, Mater. Today: Proceedings (2020), https://doi.org/10.1016/j.matpr.2020.09.297.

[19] T.J. Bright, J.I. Watjen, Z.M. Zhang, C. Muratore, A.A. Voevodin, D.I. Koukis, D. B. Tanner, D.J. Arenas, Infrared optical properties of amorphous and nanocrystalline Ta_2O_5 thin films, J. Appl. Phys. 114 (2013), 083515-083515-10.

[20] W. Miao, M.M. Zhu, Z.C. Li, Z.J. Zhang, Optical and electric properties of aligned-growing Ta_2O_5 nanorods, Mater. Trans. 49 (2008) 2288–2291.

[21] M. Chandra Sekhar, N. Nanda Kumar Reddy, V.K. Verma, S. Uthanna, Structural, optical and electrical properties of DC reactive magnetron sputtered $(Ta_2O_5)_{1-x}(TiO_2)_x$ thin films, Ceram. Int. 42 (2016), 18870-18870-9.

[22] P. Shang, S. Xiong, L. Li, D. Tian, W. Ai, Investigation on thermal stability of Ta_2O_5, TiO_2 and Al_2O_3 coatings for application at high temperature, Appl. Surf. Sci. 285P (2013) 713–720.

[23] E. Atanassova, D. Spassov, X-ray photoelectron spectroscopy of thermal thin Ta_2O_5 films on Si, Appl. Surf. Sci. 135 (1998) 71–82.

[24] S.V. Jagadeesh Chandra, S. Uthanna, G. Mohan Rao, Effect of substrate temperature on the structural, optical and electrical properties of dc magnetron sputtered tantalum oxide films, Appl. Surf. Sci. 254 (2008) 1953–1960.

[25] J. Moulder, W. Stickle, P. Sobol, K. Bomben, Handbook of X-Ray Photoelectron Spectroscopy, Physical Electronics, Inc., Norwalk, 1995.

[26] S.M. Sze, Physics of Semiconductor Devices, second ed., Wiley, New York, 1981.

[27] Vijendra Lingwal, N.S. Panwar, Morphotropic phase transitions in mixed sodium-potassium niobate system, Ferroelectrics 300 (2004) 3–14.

[28] Aradhana Bhandari, Dielectric Properties of TiO_2 ($\leq$ 10% Mole) Mixed Ta_2O_5, Ph. D. Thesis, H.N.B. Garhwal University, Srinagar (Garhwal), 2013.

[29] R. Ramprasad, First principles study of oxygen vacancy migration in tantalum pentoxide, J. Appl. Phys. 95 (2004) 954–957.

[30] H. Fujikawa, Y. Taga, Effects of additive elements on electrical properties of tantalum oxide films, J. Appl. Phys. 75 (1994) 2538–2544.

[31] W.S. Lau, L.L. Leong, T. Han, N.P. Sandler, Detection of oxygen vacancy defect states in capacitors with ultrathin Ta_2O_5films by zero-bias thermally stimulated current spectroscopy, Appl. Phys. Lett. 83 (2003) 2835–2837.

[32] W.S. Lau, T. Han, General theory of acceptor-oxygen-vacancy complex single donor in high-dielectric-constant metallic oxide insulators, Appl. Phys. Lett. 86 (2005), 152107-152107-3.

[33] Chyuan Haur Kao, Pei Lun Lai, Hsin Yuan Wang, The comparison between Ta_2O_5 and Ti-doped Ta_2O_5 dielectrics, Surf. Coating. Technol. 231 (2013) 512–516.

[34] E. Atanassova, M. Kalitzova, G. Zollo, A. Paskaleva, A. Peeva, M. Georgieva, G. Vitali, High temperature-induced crystallization in tantalum pentoxide layers and its influence on the electrical properties, Thin Solid Films 426 (2003) 191–199.

[35] T. Dimitrova, K. Arshak, E. Atanassova, Crystallization effects in oxygen annealed Ta_2O_5 thin films on Si, Thin Solid Films 381 (2001) 31–38.

RESEARCH ARTICLE Indian Journal of Agricultural Research, Volume 55 Issue 2: 181-186 (April 2021)

Estimation of Heavy Metals in Some Indian Black Tea Leaves by Inductively Coupled Plasma Mass Spectrometer (ICP-MS) and Associated Health Risks

Vishal Rohilla, Gambheer Singh Kathait, Don Biswas, Prashant Thapliyal, Bharti Ruhela[1] **10.18805/IJARe.A-5429**

ABSTRACT

Background: Some of the heavy metals are considered beneficial, if intake of them is within permissible trace amount and some other are highly toxic even in trace amount. So, heavy metals intake is one of the major concerns. Heavy metals enter into body via air, water, food, clothing and some of them gets accumulate in body organs this leads to many disorders and causes life threatening diseases including cancer. All of our food comes from plants directly or indirectly. Tea the highly consuming beverage after water comes from the leaves of plant/shrub *Camellia Sinensis*.

Methods: Aim of the present work is to determine the elements present in Tea brew (Chai, boiling the Tea leaves in water) made from black Tea leaves of major brands available in local Indian market, more specifically heavy metals Cobalt (Co), Arsenic (As), Silver (Ag), Cadmium (Cd), Indium (In), mercury (Hg) and Lead (Pb). Total eleven samples were investigated with the instrument Perkin Elmer NexIon-300x Inductively Coupled Plasma Mass Spectrometer (ICP-MS).

Result: Results have shown that Cobalt, Arsenic, Cadmium, Indium and Lead were present in all samples. Cobalt concentration varies from lowest 71.9 µg/kg to highest 214.3 µg/kg; Arsenic concentration varies from lowest 1.2 µg/kg to highest 53.7 µg/kg; Cadmium concentration varies from lowest 15.4 µg/kg to highest 75.03 µg/kg; Indium concentration varies from lowest 0.054 µg/kg to highest 0.70 µg/kg; Lead concentration varies from lowest 61.0 µg/kg to highest 2404.3 µg/kg. Mercury was present in two samples only in S9 and S11 with concentration 6.2 µg/kg and 1.4 µg/kg respectively; Out of eleven samples only seven samples have shown the presence of Silver its concentration varies from lowest 10.3 µg/kg to highest 193.0 µg/kg; Samples S2, S7, S8 and S10 were shown the absence of Silver and Mercury; Lead was found to be most abundant with concentration 2404.3 µg/kg and Indium was found to be least abundant with concentration 0.054 µg/kg.

Key words: Carcinogen, Heavy metals, ICP-MS, Indian black tea.

INTRODUCTION

Heavy metals intake is one of the major concerns in human health perspective these days. Idris *et al*. (2013) and Dabanović *et al*. (2016) have proposed the definition of heavy metals as "Heavy metals have the relative atomic weight greater than element Sodium (Na) and density of the elements greater than 5 g cm^{-3}", Moreover, all these metals have an atomic number greater than 20 Rajeswari *et al*. (2014) proposed that, the determination of heavy metals depends on the atomic number, atomic weight, density and position in the periodic table. Very low content of highly toxic heavy metals such as Arsenic, Cadmium, Lead and Mercury, may cause undesirable effects, because of the accumulation effect according to study conducted by Olivier *et al*. (2009) showed that the rate of excretion of heavy metals by the kidneys is very low. Heavy metals enter into body via air, water, food and clothing. All of our food comes directly or indirectly from plants. Environmental exposure to heavy metal pollution is due to increased industrial activities, burning of MSW, vehicular exhaust, irrigation with industrial effluents, fertilizers, chemical waste and different type of dye colors. Most of these organic and inorganic pollutants found in top layer of the soil, Prasad and Hitinayake (2012). It is evident from the study conducted by G.K. Saikia *et al*. (2014), that several types of pests and insects affect the Tea crop and as a preventive measure farmers use different types of insecticides and pesticides. Manju Mahurpawar (2015) in her study she had proposed that, heavy metals in gaseous state can spread many miles away from the sources by wind. Since, Tea is most consuming nonalcoholic beverage in India and the production of tea has become stagnant, Indian tea brands import it from rest of the tea producing countries Sabi Gogoi *et al*. (2016). Anil Kumar Singh (2018) and Tanmoy Karak, *et al*. (2011) had presented the review on the elemental contents in Tea and Tea infusion and their detection method. So, the aim of the present work

Department of Instrumentation Engineering- USIC, H.N.B. Garhwal University, Srinagar Garhwal, Pauri-246 174, Uttarakhand, India.
[1]Indermani Shiksha Niketen, Pilani-333 031, Rajasthan, India.

Corresponding Author: Vishal Rohilla, Department of Instrumentation Engineering- USIC, H.N.B. Garhwal University, Srinagar Garhwal, Pauri-246 174, Uttarakhand, India.
Email: mail.vishal.pd@gmail.com

How to cite this article: Rohilla, V., Kathait, G.S., Biswas, D., Thapliyal, P., Ruhela, B. (2021). Estimation of Heavy Metals in Some Indian Black Tea Leaves by Inductively Coupled Plasma Mass Spectrometer (ICP-MS) and Associated Health Risks. Indian Journal of Agricultural Research. 55(2): 181-186. DOI: 10.18805/IJARe.A-5429.

Submitted: 16-10-2019 **Accepted:** 16-01-2020 **Online:** 22-08-2020

is to determine how much the elements present in Tea brew (Chai, boiling the Tea leaves in water) made from black Tea leaves of major brands available in local Indian market (more than 1 Million consumers), more specifically heavy metals Cobalt (Co), Arsenic (As), Silver (Ag), Cadmium (Cd), Indium (In), mercury (Hg) and Lead (Pb) by most accurate and sensitive analytical technique "*Inductively Coupled Plasma Mass Spectroscopy*" (ICP-MS).

MATERIALS AND METHODS

Materials

Black Tea of different companies and different brands were bought from a local market store that is being consumed by more than 1 million peoples. Total eleven types of Tea bought were in different packages of different weight ranging 100 gm and 250 gm.

Prior to analysis to avoid any contamination of previously present heavy metals all glassware and plastic ware were soaked in 2% HNO_3 solution for 24 h and boiled for 1 h and washed 3 times with 2% HNO_3 solution.

Sample Preparation

Samples were prepared in the same manner in which the Tea brew (Chai) is made in India. *i.e* boiling the Tea leaves in water rigorously for 2-3 times, so that the experimental brew become same as the real composition that people take in Tea brew. Tea packets were opened just before making the Tea brew. Tea brew were prepared by boiling 500 mg of Tea leaves from each packet in 50 ml of 5% HNO_3 solution, taken in platinum coated stain less steel vessel for five minutes on induction cooking plate operating at 1000 W power, the solution reduced to 15 ml. HNO_3 used was of AR grade and water was distilled deionized Millipore water ($\dot{\rho}$ = 18.2 M&Ω). The reduced solution is then directly filtered into 15 ml vials of high density polyethylene (HDPE) with the help of funnels of same HDPE material and Filter paper (Watman No. 42). Solution is then diluted in 2% HNO_3 in the ratio of ten is to one and analyzed in Perkin Elmer Nexlon-300x Inductively Coupled Plasma Mass Spectrometer (ICP-MS).

Instrument and method

Instrument used was Perkin Elmer Nexlon-300x Inductively Coupled Plasma Mass Spectrometer (ICP-MS). The Instrument operating conditions were as follows:

RF power/ W	1500 W
Plasma gas flow	18 L/min
Auxiliary gas flow	1.2 L/min
Integral time	15 s
Sweeps	20
Reading	1
Replicates	3
Scanning mode	Peak hopping
Method	Total quant
Calibration type	External
Measurement time per sample	15 min (approx.)

All the Tea samples were diluted in 2% HNO_3 solution made by distilled deionized Millipore water. 1 ml of each sample is mixed in 10 ml of 2% HNO_3. Instrument was calibrated using external standard 200 µg/L mix of 13 elements in 1% HNO_3 obtained from Perkin Elmer. Three replicates of measurement were done for each sample and statically computed average of readings is presented in Table 1. Semiquantitative method (Total Quant) of analysis is chosen because of it is easy, rapid and accurate. Its accuracy has been reported as it has relative percentage error within 10% and reproducibility (relative standard deviation lower than 5%) at concentrations equal to or greater than 10 times the detection limit (DL) by Antonio *et al*. (2003).

RESULTS AND DISCUSSION

Table 1 is representing the results. Different nomenclature S1, S2 and so on has been adopted for tea names and their brands to avoid any conflict. Average of three measurements at three different times is presented along with standard deviation in measured values. Results have shown that, Cobalt, Arsenic, Cadmium, Indium and Lead were present in all samples. Cobalt concentration varies from lowest 71.9 µg/kg in sample S2 to highest 214.3 µg/kg in sample S8; Arsenic concentration varies from lowest 1.2 µg/kg in sample S2 to highest 53.7 µg/kg in sample S9; Cadmium concentration varies from lowest 15.4 µg/kg in sample S2 to highest 75.03 µg/kg in sample S1; Indium concentration varies from lowest 0.054 µg/kg in sample S9 to highest 0.70 µg/kg in sample S2; Lead concentration varies from lowest 61 µg/kg in sample S6 to highest 2404.3 µg/kg in sample S1. Mercury concentration was detected in two samples only in S9 and S11 with concentration 6.237 µg/kg and 1.386 µg/kg respectively, for all other samples S1-S8 and S10 it was found below the detection limit of instrument; Similarly, the Silver was found below the detection limit of instrument in samples S2, S7,S8 and S10 other seven samples have shown the Silver concentration varies from lowest 10.3 µg/kg in sample S5 to highest 193µg/kg in sample S9; Lead was found to be most abundant with concentration 2404.3 µg/kg and Indium was found to be least abundant with concentration 0.054 µg/kg.

Daily intake of heavy metals via Tea is calculated on the fact that, an adult Indian population consumes three cups of tea daily. Results are presented in Table 2.

Cobalt (Co)

Cobalt has properties similar to those of Iron and Nickel. Cobalt is one of the constituent of vitamin B12 or Cyanocobalamin, Pratt (1972). Vitamin B12 is essential for good health in animals and humans, Strachan (2010) and *ATSDR* (2004). Effects of Cobalt on health have been discussed by Paustenbach (2013) and Unice K.M. (2014). When Cobalt combined with Tungsten it causes cancer, *IARC* (2006) and Wild *et al*. (2009). General public comes in exposure to cobalt through food and drinks, Manju Mahurpawar (2015). Highest concentration of cobalt was

Table 1: Concentration of elements in samples values and deviation.

Element	S1	S2	S3	S4	S5	S6	S7	S8	S9	S10	S11
Co	213.4±10.1	71.9±3.2	205.7±6.4	84.7±5.2	122.95±7.5	97.5±7.8	117.7±9.5	214. 3±7.1	97.1±12.8	182.6±16.1	111.7±10.8
As	39.8±2.1	1.2±0.5	23.1±3.1	8.6±1.2	15.9±1.5	6.2±1.3	14.8±2.8	42.1±2.4	53.7±5.3	33.1±7.0	21.4±3.1
Ag	152.9±3.5	BDL	22. 5±1.2	44.5±3.4	10.3±1.9	18.1±2.3	BDL	BDL	193.0±6.8	BDL	58.2±1.8
Cd	75.03±4.0	15.4± 1.5	40.5±2.6	16.6±2.0	30.2±2.1	34.1±4.2	38.3±2.4	43.3±2.8	42.8±3.5	53.3±6.3	42.0±3.4
In	5.6±1.5	0.70±0.2	0.21±0.3	0.24±0.9	0.12±0.03	0.32±0.5	0.12±0.9	0.3±0.6	0.054±0.02	0.17± 0.1	0.077± 0.02
Hg	BDL	BDL	BDL	BDL	BDL	BDL	BDL	BDL	6.2±1.7	BDL	1.4±0.13
Pb	2404.3±18.1	168.3±11.2	485.4±12.0	235.5±9.1	856.2±4.5	61.0±5.0	220.1±2.3	733.6± 6.4	912.8±12.5	403.0±9.3	486± 4.8

(in micro gram per Kilogram); BDL below detection limit of instrument.

Table 2: Calculated daily intake of elements via three cups of tea.

Element	Maximum concentration (µg/kg)	Daily intake (µg/kg)
Co	214.3	0.32
As	53.7	0.08
Ag	193	0.29
Cd	75.03	0.11
In	5.6	0.008
Hg	6.2	0.009
Pb	2404.3	3.60

found 214.3 µg/kg. Calculated daily intake via tea 32.0 µg/kg is found below the permissible maximum daily intake.

Arsenic (As)

Arsenic is also a natural semi metal having properties like metals. Arsenic can be found in trace amount in water, rocks, soil. Arsenic generally exists in combination with other elements like oxygen and sulfur, Nrashant Singh, *et al*. (2007) and Aronson (1994). It has been reported that exposure to arsenic in trace amount produces serious health effects like skin cancer, arteriosclerosis, heart disease, chronic lung disease, reproductive system disorder, Nrashant Singh, *et al*. (2007). High arsenic level in drinking water can affect the visual perception of children, Siripitayakunkit *et al.* (2000) and Siripitayakunkit et.al (2000). In West Bengal (India), the arsenic concentration in ground water highly used as drinking water is about 60 to 3700 µg/l, Acharyya (2002). Risk of Arsenic exposure gets increased when peoples use crops that irrigated with arsenic effected water. Highest concentration of Arsenic was found 53.7 µg/kg. Calculated daily intake via tea 0.08 µg/kg is found below the permissible maximum daily intake.

Silver (Ag)

Silver is one of the ornamental metals semiprecious and rare. Naturally exists in trace amount in water, rocks, soil. It occurs mainly in compound form Silver nitrate, Silver Chloride, Silver Sulfide and Silver Oxide. It finds its use in making jewelry, electronic industry, dental fillings and some pesticides. Silver compounds can turn the skin and other body parts in gray or blue gray color called *Argyria*. Exposure to higher level of silver compounds may cause breathing problems, lung and throat irritation and stomach pain, *ATSDR* (1990). At the nano size scale Silver is harmful Thabet *et al*. (2010). To study this Zebrafish has been chosen as model and it has been found that high dose slows down the development of embryo and several other abnormalities may develop, Fako *et al*. (2009). Highest concentration of Silver was found 193.0 µg/kg. Calculated daily intake via tea 0.29 µg/kg is found below the permissible maximum daily intake.

Cadmium (Cd)

Cadmium is highly toxic and carcinogenic for humans, IARC (1979). Naturally exist in trace amount in water, rocks, soil. Cadmium readily react with Sulfur and Chlorine these

compounds easily soluble in water. It has been used extensively in electronics industry most common uses are different types of solders due to low melting point, pigments, batteries, in phosphor materials of CRT screens and many more, Hiscock (1983) and Tolcin (2015). Toxicity and effect of Cadmium on human health and plants has been studied extensively by many authors, Prodan (1932). Cadmium reacts with Calcium inside body, this reduces the Calcium level and bones become weak, Dartmouth, *et al*.. Accumulation of Cadmium leads to pancreatic cancer, prostate cancer, kidney and various other types of cancers Vladimir Djordjevic, *et al*. (2017) and David Wallace (2017). Highest concentration of Cadmium was found 75.03 µg/kg. Calculated daily intake via tea 0.11 µg/kg is found below the permissible maximum daily intake.

Indium (In)

Indium is soft and silvery metal it is relatively rare metal. Mostly found with in Zinc, Copper and Iron ores. Naturally it occurs in trace amount in water, rocks, soil. Indium tends to be enriched in Sulûde minerals and in Tin oxide, Smith *et al*. (1978) and Wood *et al* (2006). Indium found its use in alloys as it decreases the melting point, different types of solders, electronic components like transistors, LEDs, Indium Tin Oxide ITO is used for making different type of transparent coating, Jorgenson (2005) and Nakamura, *et al*. (1994). Prolonged exposure to Indium produces interstitial pneumonia, lung damage, liver damage, Homma *et al* (2003) and Chonan *et al*. (2007). Highest concentration of Indium was found 5.6 µg/kg. Calculated daily intake via tea 0.008 µg/kg is found below the permissible maximum daily intake.

Mercury (Hg)

Mercury is a shiny metal due to its liquid state at room temperature it is called as liquid silver. It exists naturally in trace amount in water, rocks, soil. Mercury found in three different forms elemental (or metallic) Mercury, inorganic Mercury compounds (Sulfides, Oxides *etc*.) and organic Mercury compounds (methylmercury, phenylmercuric acetate). Mercury found its use in thermometers, fluorescent light bulbs, fertilizers, pesticides and various industrial activities, Thomas W. Clarkson (1997). When living organisms exposed to elemental or inorganic Mercury they convert it into organic Mercury, which is highly toxic, Farhana Zahir, *et al*. (2005). Mercury causes numerous disorders in humans several studies in past and recent showed this. Mercury affects the nervous system of fetus according to study foetus being more susceptible to methylmercury toxicity, Snyder (1971). In adults it causes Alzheimer's and Parkinson's diseases, Olivieri *et al*. (2002). High dose of mercury can cause lungs, lever to damage, eyesight may loss, immune system modulation *etc*., Tan and Parkin (2000) and Apaydın *et al*. (2016). Highest concentration of Mercury was found 6.2 µg/kg. Calculated daily intake via tea 0.009 µg/kg is found below the permissible maximum daily intake.

Lead (Pb)

Lead is soft, bluish grey metal it occurs naturally in earth crust. Due to human activities it can be found in varying amount all over the environment water, rocks and soil. Lead is an abundant metal mainly found in the form of lead sulfide, lead sulfate and lead carbonate. It founds its extensive use in batteries, paints, gasoline, various types of solders, radiation shielding and many more, Robert, Ziegfeld (1964) and Adrian Demayo, *et al*. (1982). There is no such level of lead that appears to be necessary or beneficial to the body and no "safe" level of exposure to lead has been found, Gagan Flora *et al*. (2012). Exposure to Lead affects the nervous system, Hematopoietic System, Renal dysfunction, Cardiovascular, reproductive system and bone, Kalia Flora (2005) and Guidotti *et al*. (2008). Highest concentration of Lead was found 2404.3 µg/kg. Calculated daily intake via tea 3.06 µg/kg is found below the permissible maximum daily intake.

CONCLUSION

All the samples appears to be different from each other in terms of presence of heavy metals, this may be due to the different region of cultivation, difference in the way of handling and processing. Also, the different regions of India have different levels of pollution of heavy metals in air, water, rocks and soil. High levels of concentration of highly toxic Mercury and Lead have been found in some samples so there is a need strict legal guideline for quality control and routine monitoring. The concentration of all heavy metal and their daily intake is well below the permissible daily intake but the retention of them in body may cause serious problems in later life span. Peoples who drink more than three or four cups of Tea regularly are at higher risk of getting exposure to heavy metal contents of Tea. This may lead to adverse effects on their health and organs. Further, by identifying the origin of Tea and by measuring the heavy metals in Tea leaves and other plants with reference to our experiment it can be conclude that the heavy metal pollutants are present in the environment of that region. The way in which Tea is cultivated, harvested, handled and processed needs to be reviewed.

ACKNOWLEDGEMENT

Authors are thankful to Prof. N.S. Panwar, Dean, School of Engineering and Technology, H.N.B. Garhwal University, Srinagar Garhwal. For his kind guidance, motivation and support during the work carried out.

REFERENCES

Acharyya, S.K. (2002). Arsenic contamination in ground water affecting major part of the southern West Bangal and parts of Western Chhattisgarh: Source and mobilization process. Curr. Sci. 82: 740-744.

Adrian Demayo, Margaret, C. Taylor, Kenneth W. Taylor, Peter, V. Hodson and Paul B. Hammond (1982). Toxic effects of lead and lead compounds on human health, aquatic life, wildlife plants and livestock. C R C Critical Reviews in Environmental Control. 12(4): 257-305.

Anil Kumar Singh and Sunil Kumar Pathak (2018). Potassium in tea [*Camellia sinensis* (L.) O. Kuntze] cultivation from soil to cup quality-A review. Agricultural Reviews. 39(1): 40-47.

Antonio Moreda, Pin eiroa andrew Fisherb, Steve J. Hill (2003). The classification of Tea according to region of origin using pattern recognition techniques and trace metal data. Journal of Food Composition and Analysis. 16(2): 195-211.

Apaydın, F.G., Baş, H., Kalender, S., Kalender, Y. (2016). Subacute effects of low dose lead nitrate and mercury chloride exposure on kidney of rats. Environ. Toxicol. Pharmacol. 41: 219-224.

Aronson, S.N. (1994). Arsenic and old myths. R. I. Med. 77: 233-234.

Agency for Toxicological Substances and Disease Registry (*ATSDR*) (1990). Toxic Substances Portal: Silver, Public Health Statement for Silver, *CAS#:* 7440-22-4.

Agency for Toxicological Substances and Disease Registry (*ATSDR*) (2004). Toxicological profile for cobalt. U.S. Department of Health and Human Services, Public Health Service.

Chonan, T., Taguchi, O. and Omae, K. (2007). Interstitial pulmonary disorders in indium-processing workers. European Respiratory Journal. 29: 317-324.

Dabanović, V., Šoškić, M., Đurović, D. and Mugoša, B. (2016). Investigation of heavy metals content in selected Tea brands marketed in podgorica, montenegro. Int. J. Pharm. Sci. Res. 7(12): 4798-04.

Dartmouth;Toxic Metals Research Program, Center for Environmental Health Sciences. Hanover, NH. *<http://toxnet.nlm.nih.gov/cgibin/sis/search/f?/temp/"'vgmfsK:2>.*

David, R. Wallace (2017). Expanding the Role of Cadmium in Pancreatic Cancer. EC Pharmacology and Toxicology ECO. 19-21.

Fako, V.E., Furgeson, D.Y. (2009). Zebraûsh as a correlative and predictive model for assessing biomaterial nanotoxicity; Adv. Drug. Deliv. Rev. 61: 478-86.

Farhana Zahir, Shamim J. Rizwi, Soghra K. Haq, Rizwan H. Khan (2005). Low dose mercury toxicity and human healt. Environ. Toxicol. Pharmacol. Sep. 20(2): 351-60.

Gagan Flora, Deepesh Gupta, Archana Tiwari. (2012). Toxicity of lead: A review with recent updates. Interdiscip Toxicol. 5(2): 47-58.

Guidotti, T.L., McNamara, J., Moses, M.S. (2008). The interpretation of trace element analysis in body fluids. Indian J. Med. Res. 128: 524-532.

Homma, T., Ueno, T., Sekizawa, K., Tanaka, A. and Hirata, M. (2003). Interstitial pneumonia developed in a worker dealing with particles containing indium-tin oxide. Journal of Occupational Health. 45: 137-139.

Hiscock, S.A. (1983). Trends in the Uses of Cadmium (1970-1979); Ecotoxicolgy and Env. Safety. 7: 25-32.

Idris, M.A., Kolo, B.G., Garba, S.T., Waziri, I. (2013). Pharmaceutical industrial effluent: heavy metal contamination of surface water in Minna, Niger State, Nigeria. Bull. Environ. Pharm. Life Sci. 2(3): 40-44.

International Agency for Research on Cancer (IARC), Working Group on the Evaluation of Carcinogenic Risk to Humans. (2006). Cobalt in hard metals and cobalt sulfate, gallium arsenide, indium phosphide and vanadium pentoxide.

International Agency for Research on Cancer, IARC (1979). Monographs on the Evaluation of the Carcinogenic Risk of Chemicals to Humans; IARC, Lyon, pp. 1: 20-27.

Jorgenson, J.D., George, M.W. (2005). Indium. Open-File Report 2004-1300.Reston, VA: *U.S.* Geological Survey. Retrieved from http://minerals.usgs/gov/minerals/pubs/commodity/indium/.

Kalia, K., Flora, S.J. (2005). Strategies for safe and effective therapeutic measures for chronic arsenic and lead poisoning. J. Occup Health. 47: 1-21.

Manju Mahurpawar (2015). Effects of heavy metals on human health; Int. Jou. of res. Granthaalayah; Social Issues and Environmental Problems.

Nrashant Singh, Deepak Kumar, Anand P. Sahu (2007). Arsenic in the environment: Effects on human health and possible prevention. Journal of Environmental Biology April. 28(2): 359-365.

Nakamura, S., Mukai, T., Senoh, M. (1994). Candela-class high-brightness In-GaN/AlGaN double-heterostructure blue-light-emitting diodes. Appl. Phys. Lett. 64: 1687-1689.

Olivier Barbier, Grégory Jacquillet, Michel Tauc, Marc Cougno, Philippe Poujeol, (2009). Effect of Heavy Metals on and Handling by, the Kidney. Nephron Physiol. 99: 105-110.

Olivieri, G., Novakovic, M., Savaskan, E., Meier, F., Baysang, G., Brockhaus, M., Muller-Spahn, F. (2002). The effects of estradiol on SHSY5Y neuroblastoma cells during heavy metal induced oxidative stress, neurotoxicity and beta-amyloid secretion. Neuroscience. 113(4): 849-855.

Pratt, J.M. (1972). Inorganic chemistry of vitamin B12; Inorganic chemistry of vitamin. pp.ix+347 pp.

Paustenbach, D.J. Tvermoes, B.E., Unice, K.M. (2013). A review of the health hazards posed by cobalt. Crit. Rev. Toxicol. 43(4): 316-362.

Prasad Dharmasena and G. Hitinayake (2012). Yield damage functions for tea sector in Sri Lanka and India: An Empirical estimation. Agric. Sci. Digest. 32 (2): 133-136, 201.

Prodan, L. (1932). Cadmium Poisoning: The history of cadmium poisoning and uses of cadmium. Journal of Industrial Hygiene. 14: 132-55 ref.58.

Rajeswari, T.R. and Sailaja, N. (2014). Impact of heavy metals on environmental pollution. Journal of Chemical and Pharmaceutical Sciences. 3:175-181.

Robert, L., Ziegfeld, B.S. (1964). Importance and Uses of Lead. Archives of Environmental Health, An International Journal. Vol. 8, Iss. 2.

Sabi Gogoi, Gaurav Mishra and A.K. Deka (2016). Soil nutrient dynamics in tea agroforestry ecosystem of Golaghat district of Assam, India. Agric. Sci. Digest. 36 (3): 185-19.

Saikia, G.K., Barbora, A.C. and Deka, M.K. (2014). Pest, disease and weed incidence and crop yield as influenced by organic culture in tea [*Camellia sinensis* (L.) o. kuntze]: Agric. Sci. Digest. 34(2): 119-122.

Strachan S. (2010). Trace elements. Curr Anaesth Crit Care. 21 (1): 44-48.

Siripitayakunkit, U., Lue, S., Choprapawan, C. (2000): Possible effects of arsenic on Visual Perception and Visual-motor Integration of children in Thailand. 4th International conference on Arsenic exposure and Health effects, San Diego, CA, June 18-22, p. 22.

Siripitayakunkit, U., A. Thonghong, M. Pradipasen, T. Vorapongsathron (2000). Growth of children with different arsenic accumulation, Thailand. 4th International conference on Arsenic exposure and Health effects, San Diego, CA, June 18-22. p. 150.

Smith, I.C., Carson, B.L., Hoffmeister, F. (1978). Trace metals in the environment. Volume 5: Indium. Ann Arbor, MI: Ann Arbor Science.

Snyder, R.D. (1971): Congenital mercury poisoning. New Engl. J. Med. 71. 284: 1014-1016.

Tanmoy Karak, Ranjit Kumar Paul, Funso Raphael Kutu, Aradhana Mehra, Puja Khare, Amrit Kumar Dutta, Krishnamoni Bora, Romesh Kumar Boruah (2011): Comparative Assessment of Copper, Iron and Zinc Contents in Selected Indian (Assam) and South African (Thohoyandou) Tea (*Camellia sinensis* L.) Samples and Their Infusion: A Quest or Health Risks to Consumer, Biol. Trace Elem. Res DOI 10.1007/s12011-016-0783-3.

Thabet M. Tolaymat, Amro M. El Badawy, Ash Genaidy, Kirk G. Scheckel, Todd P. Luxton, Makram Suidan (2010). An evidence-based environmental perspective of manufactured silver nanoparticle in syntheses and applications: A systematic review and critical appraisal of peer-reviewed scientific papers. Science of the Total Environment. 408: 999-1006.

Tolcin, A.M. (2015). Mineral year book: cadmium. US geological Survey.

Thomas W. Clarkson (1997). The Toxicology of Mercury. Critical Reviews in Clinical Laboratory Sciences. 34(4): 369-403.

Tan, M., Parkin, J. (2000). Route of decomposition of thiomersal (thimerosal); Int. J. Pharmaceutics. 208: 23-34.

Vladimir Djordjevic, Djordje Knezevic, David R. Wallace, Slavko Matic, Nemanja Zaric, Ivana Pavlovic, Zeljko Radojkovic, Marko Bogdanovic, Sanja Jovanovic, Slavenko Ostojic, Mirko Kerkez (2017). Cadmium and human pancreatic cancer-Is there a connection? ; Pancreatology Volume 17, Issue 3, Supplement, July Pages S10.

Wild, P.. Bourgkard, E., Paris, C. (2009). Lung cancer and exposure to metals: the epidemiological evidence. Methods Mol. Biol. 472: 139-16.

Wood, S.A., Samson, I.M. (2006). The aqueous geochemistry of gallium, germanium, indium and scandium. Ore. Geol. Rev. 28(1): 57-102.

CuO Nanoparticles Decorated MIP-Based Electrode for Sensitive Determination of Gallic Acid in Green Tea

Debangana Das, Don Biswas, Ajanto Kumar Hazarika, Santanu Sabhapondit, Runu Banerjee Roy, Bipan Tudu, and Rajib Bandyopadhyay

***Abstract*—The present work elucidates a method for the economic development of a reproducible electrode for sensitive determination and prediction of the amount of gallic acid (GA) in green tea (GT) by molecularly imprinted polymer (MIP) technology. The electrode material has been synthesized by co-polymerization of itaconic acid and ethylene glycol dimethacrylate (EGDMA) followed by implantation of copper oxide nanoparticles (CuO NPs). The electrode demonstrated two wide linear ranges, i.e., 1 μM – 100 μM and 100 μM to 900 μM with a low detection limit of 12.6 nM. The practical applicability of the electrode has been validated by quantifying the amount of GA in GT samples. Principal component analysis (PCA) has been performed and class separability index (SI) of 31.27 has been obtained. To explore the predictive ability of the electrode, partial least square regression (PLSR) and principal component regression (PCR) models have been developed. This has been done by correlating the differential pulse voltammetry (DPV) signals from the electrode and the corresponding high performance liquid chromatography (HPLC) data. While with PLSR, average prediction accuracy of 88.97 % is obtained with root mean square error of calibration (RMSEC) as low as 1.35, PCR results in an average prediction accuracy of 87.24 % with RMSEC being 1.38.**

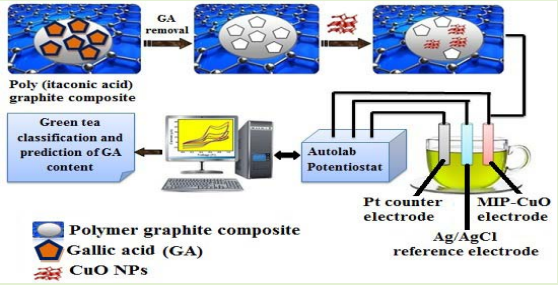

***Index Terms*—CuO nanoparticles, gallic acid, green tea, molecularly imprinted polymer, regression models.**

I. Introduction

GREEN tea has a unique role in shaping the modern tea industry due to its befittingly illustrious history of production and consumption. Out of innumerable compounds present in GT, some of the important chemical constituents are listed in Table S1. Amongst them, GA (3,4,5- trihydroxybenzoic acid) has been identified to be the main free phenolic acid present in GT [1]. The chemical structure of GA is shown in Fig. S1. GA serves as a strong antioxidant owing to its three hydroxyl groups (-OH) and the property of allowing straightforward copolymerization through its carboxylic (-COOH) group [2]. GA has antibiotic, anti- inflammatory, and anti-cancer properties [2]–[5]. GA acts as a quality indicator of GT during its standardization as pharmaceutical supplement [6] and is a major part in the composition of the biologically active compounds of GT. GA interferes with high pressure drugs and can add to the danger of cardiovascular diseases. Hence, monitoring the daily intake of GA is important.

Some of the traditional ways of determining GA content in food and beverages include reversed phase high- performance liquid chromatography [7], flow injection analysis [8], chemiluminescence [9], thin-layer chromatography [10] and chronoamperometry [11]. However, the usage of toxic organic solvents while performing experiments, extreme cost of the high-end instruments, long time of operation, requirement of skilled laborers for the execution of the experiment lead to

Manuscript received September 29, 2020; accepted November 2, 2020. Date of publication November 9, 2020; date of current version February 5, 2021. This work was supported by the Department of Science and Technology (DST), Government of West Bengal, India, under Grant ST/P/S&T/6G-19/2017. The associate editor coordinating the review of this article and approving it for publication was Prof. Bhaskar Choubey. *(Corresponding author: Runu Banerjee Roy.)*

Debangana Das, Runu Banerjee Roy, and Bipan Tudu are with the Department of Instrumentation and Electronics Engineering, Jadavpur University, Kolkata 700106, India (e-mail: debanganadas4@gmail.com; runuroy@yahoo.com; bipantudu@gmail.com).

Don Biswas is with the Department of Instrumentation and Electronics Engineering, Jadavpur University, Kolkata 700106, India, and also with the University Science Instrumentation Centre (USIC), HNB Garhwal University, Srinagar 249161, India (e-mail: donusic06@gmail.com).

Ajanto Kumar Hazarika and Santanu Sabhapondit are with the Tocklai Tea Research Institute, Jorhat 785008, India (e-mail: ajantohazarika65@gmail.com; santanusabhapondit1@gmail.com).

Rajib Bandyopadhyay is with the Department of Instrumentation and Electronics Engineering, Jadavpur University, Kolkata 700106, India, and also with the Laboratory of Artificial Sensory Systems, ITMO University, 190005 Saint Petersburg, Russia (e-mail: bandyopadhyay.rajib@gmail.com).

This article has supplementary downloadable material available at https://ieeexplore.ieee.org, provided by the authors.

Digital Object Identifier 10.1109/JSEN.2020.3036663

1558-1748 © 2020 IEEE. Personal use is permitted, but republication/redistribution requires IEEE permission.
See https://www.ieee.org/publications/rights/index.html for more information.

Authorized licensed use limited to: INDIAN INSTITUTE OF TECHNOLOGY GUWAHATI. Downloaded on February 15,2021 at 11:29:50 UTC from IEEE Xplore. Restrictions apply.

their stifled application [4], [5]. Although the above methods are available, some of them are complex, sensitivity is unknown [11], limit of detection (LOD) is unknown, lacks versatility, simplicity and portability. To overcome these limitations, electrochemical methods for the detection of GA have been put forward due to their intrinsic properties of good selectivity [12]. A number of electrodes based on carbon materials have been fabricated for the detection of GA in any food or beverage [13], [14]. For better electrochemical performance, electrodes were modified with nanomaterials [4], [5], [12], [15], [16]. However, these electrodes exhibited instability, low sensitivity, low reliability and the precursors used were costly, thus necessitating the adoption of MIP technology. Materials with recognition sites complementary in shape to the target molecule are formed. On subjecting these MIPs to the target analyte, molecules get trapped in the cavities and thus get detected. In [17], GA-imprinted electrodes were formed by the cyclic voltammetric deposition of a polypyrrole film on a GCE. Though it showed a stable response, yet LOD was not determined and the sensitivity was low. In [18], a sensor has been designed for the detection of GA by MIP wherein LOD obtained is 47nM and prior to real time analysis, sample preparation is required. MIPs on magnetic mesoporous silica [19] and carbon nanotubes [20] have been proposed for determination of GA in fruit juices and wine. However, selectivity or LOD in [19], [20] was unsatisfactory. Apart from electrochemical detection, an interesting application of MIP includes novel capacitive sensors for detection of 2-Furfuraldehyde in transformer oil [21], [22]. In [22], a unique comb type MIP capacitive sensor was fabricated with improved sensitivity. Successful electrochemical determinations of catechins and caffeine have also been reported using MIP technique [23], [24].

This work portrays development of an economic and reproducible electrode for the effective determination of GA in GT samples utilizing MIP technology. The matrix has been synthesized by co-polymerisation of itaconic acid (IA) and EGDMA using benzoyl peroxide (BP) as the polymerisation initiator. The sample has been modified with CuO NPs to increase the oxidation efficiency, the surface area of the electrode which in turn enhances the electrochemical performance of the sensor, stability of the sensor and biocompatibility.

Novelty of the proposed method is its low cost, quick synthesis, availability of the precursors and the reproducible nature of the MIP-CuO electrode. Also, the thermal stability of CuO NPs [25], [26] contributes towards the usage of the MIP-CuO electrode in any environmental condition. The electrode has been found to be selective, repeatable, stable and reproducible. It exhibited two linear ranges and a more sensitive detection limit as compared to other studies [16], [17], [20], [26] –[28]. No pre-treatment is needed prior to the electrochemical experimentation. Hence, the electrode can be dipped directly in any sample which is a major advantage for it to be deployable in industries. On the basis of GA content, GT samples were segregated using PCA. The quantitative measure of separability amongst the tea samples has been established by calculating the SI. Fig. S2 illustrates the work flow associated post development of the electrode. A detailed analysis of the predictive ability of MIP-CuO electrode has been investigated by developing PLSR model and PCR model. After calibration, these models were utilized to quantify the amount of GA in unknown GT samples.

II. Experimental

A. Reagents and Materials

Graphite powder (99%), EGDMA, GA, IA, acrylamide (AAM), maleic acid (MA), catechin (CAT) and ascorbic acid (AA) were purchased from Sigma Aldrich, India. BP was obtained from Sisco Research Laboratories Pvt. Ltd, India. Copper chloride ($CuCl_2$), ethanol, cetylpyridinium chloride ($C_{21}H_{38}NCl$), sodium hydroxide (NaOH), and paraffin oil were purchased from Merck & Co, India. Deionized water (Resistance 18 MΩ), obtained from Milli-Q water purification system was used for cleaning the electrode.

B. Equipment and Characterization

A Phillips PW 1710 X-ray diffractometer is used to obtain powder X ray diffraction (PXRD) patterns of CuO samples. The diffractometer is operated at 40kV and 40 mA with CuKα radiation (λ =1.5406 Å) in a continuous scan mode from 10° to 75°. The ultra violet-visible (UV-Vis) absorption measurements were done using Shimadzu UV-3600. The HPLC analysis was performed using UHPLC "DIONEX Ultimate 3000" for GA estimation. Scanning electron microscope (SEM) coupled with Oxford energy dispersive X-ray spectroscopy detector (EDX) (manufactured by ZEISS) were used to study the morphology and chemical composition. Fourier transform infra-red spectroscopic (FTIR) analysis was carried out using a MAGNA 550 FTIR spectrometer (Nicolet, USA) of the powder samples using KBr pellets. A three electrode system has been used to explore the behavior of electrode with Autolab Potentiostat/ Galvanostat 101 (Netherlands). As a counter electrode, the platinum (Pt) electrode is used and Ag/AgCl electrode is used as reference electrode. The DPV and cyclic voltammetry (CV) were carried out in the voltage range of 0.0 V to 1.0 V.

C. GA Estimation in HPLC

The chromatographic separation of GA from tea samples was carried out at Tocklai Tea Research Institute (TTRI), Assam, India. The column used was Phenomenex C18 (250mm x 4.6mm, 5 μm) phenyl hexyl ligand column. 9 % (volume fraction) acetonitrile, 2 % (volume fraction) acetic acid with 20 μg/ml EDTA was used as solvent A and 80 % (volume fraction) acetonitrile, 2 % (volume fraction) acetic acid with 20 μg/ml EDTA as solvent B. Flow rate of 1 ml/min was maintained. The chromatographic conditions were 100 % solvent A for initial 10 min, gradient elution over 15 min to 38% solvent B followed by 10 min in this conditions, i.e., 62 % solvent A + 38 % solvent B. The peak of GA was identified and estimated by external standard method from response factor determined from GA standard [29].

Authorized licensed use limited to: INDIAN INSTITUTE OF TECHNOLOGY GUWAHATI. Downloaded on February 15,2021 at 11:29:50 UTC from IEEE Xplore. Restrictions apply.

D. Synthesis of CuO NPs

The synthesis of CuO NPs was carried out in the laboratory by sol gel method. The flowchart in Fig. S3 describes the step-wise synthesis of the CuO NPs.

E. Synthesis of GA Imprinted Polymer (MIP) and Non Imprinted Polymer (NIP)

The MIP samples were prepared following a standard method with little modifications [24]. A detailed flowchart for the synthesis of the MIP is given in Fig. S4. This methodology was followed to synthesize the NIP sample excluding the mixing of GA.

F. Fabrication of CuO Modified MIP and NIP Electrodes

For fabricating the GA imprinted (MIP) and NIP electrodes, CuO NPs were added to both the MIP and NIP powder. The ratio of the polymerized powder to the CuO NPs was maintained to be 4:1. The given ratio has been optimized by trial and error method. The maximum current has been obtained when the ratio of the polymer material and CuO NPs were maintained at 4:1. The mixtures were ground into a fine and smooth paste. The paste was delivered into capillary glass tubes having inner radius of 1.25 mm. To provide electrical contact to the electrode, copper wire was used.

III. Data Analysis

A. PCA and Class Separability Measure

PCA enables visualization of spatial distribution of multivariate data of any dimension. It is done by observing PC score plots [30], [31] thus allowing the study of the distribution of DPV responses. For analyzing the distribution of responses quantitatively, the SI has been calculated [30].

B. Partial Least Square Regression (PLSR)

PLSR relates the response matrix and the predictor matrix by a linear multivariate model [24], [32]. In this work, the leave one out cross validation (LOOCV) technique has been used. The value of model parameters viz., RMSEC, root mean square error of validation (RMSEV) and root mean square error of prediction (RMSEP) mirrors the degree of consistency between the actual and the predicted values [24].

C. Principal Component Regression (PCR)

PCR technique evaluates the PCs by employing PCA on the data matrix [33]. The linear model parameters viz., RMSEC, RMSEV and RMSEP are observed to optimize the number of latent variables (LVs) that are best suited for a good prediction.

IV. Results and Discussions

A. UV-Visible Spectroscopy

The removal of GA from the polymer network was affirmed by UV-Vis spectroscopy. The scanning was done in the wavelength window of 200-800 nm. As observed from the spectrum (Fig. 1 (a)), two visible absorbance peaks are present corresponding to the GA molecule [33], one at 217 nm and other at 272 nm for the dried powder material before extraction of the target molecule (BRT). After extraction of GA (ART) from BRT material, both the peaks are absent in spectrum ascertaining the complete removal of GA from MIP material.

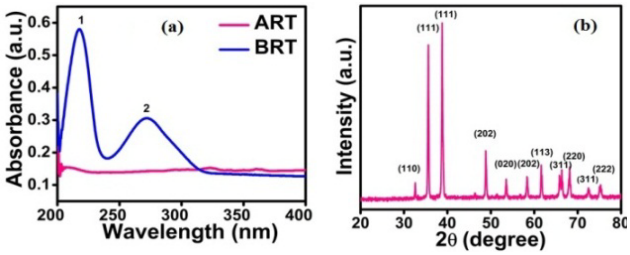

Fig. 1. (a) UV-vis absorbtion spectra of the 1mM GA solution before (BRT) and after (ART) removal of template (b) Powder XRD pattern of CuO NPs.

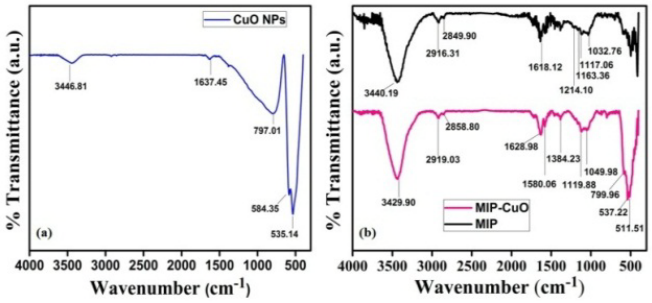

Fig. 2. FTIR analysis of (a) CuO NPs and (b) MIP and MIP-CuO.

B. XRD Analysis of the Prepared CuO NPs

The formation of CuO NPs was confirmed from JCPDS No. 80-1916, where diffraction peaks were obtained at 32.47°, 35.49°, 38.68°, 38.89°, 46.19°, 48.65°, 53.40°, 61.45°, 66.10°, 68.00°, 72.32° and 75.12°, respectively. These can be assigned to the (110), (111), (202), (020), (113), (311) and (222) planes and structure of CuO NPs is monoclinic in nature. The absence of any other peaks in the XRD spectra of the samples shown in Fig. 1 (b) indicates that the corresponding CuO so formed is free from the impure phases. The crystallite size of the NPs was calculated to be 41.6 ± 7.70 nm by applying the Debye-Scherer method as stated in [35].

C. FTIR Analysis

FTIR spectrum of CuO NPs in Fig. 2 (a) reveals several absorption bands around 535.14 cm^{-1} and 584.35 cm^{-1}, which can be assigned as the characteristic stretching vibrations of Cu(II)-O bonds [36]. Moreover, a broad absorption peak at 3446.81 cm^{-1} is the characteristic of O-H bond as CuO NPs absorb moisture because of their high surface to volume ratio [37]. Fig. 2 (b) shows the FTIR spectrum of MIP and MIP-CuO. In the case of MIP, characteristic stretching vibrations corresponding to the polymer in the 'Finger Print' region ($\sim$ 1000-1400 cm^{-1}) originating from the backbone structure of the polymer is observed [38]. Several characteristic stretching vibrations at 1618.12 cm^{-1}, 2849 cm^{-1}, 2916.31 cm^{-1} and 3440.19 cm^{-1}originating from the -COOH functionality of IA, -OH functionality of EGDMA have been observed. For the case of MIP-CuO, the FTIR spectrum

Authorized licensed use limited to: INDIAN INSTITUTE OF TECHNOLOGY GUWAHATI. Downloaded on February 15,2021 at 11:29:50 UTC from IEEE Xplore. Restrictions apply.

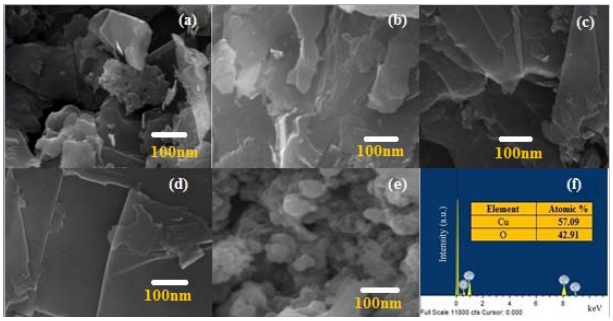

Fig. 3. SEM image of (a) MIP-CuO (b) NIP-CuO (c) MIP-unmodified (d) NIP-unmodified (e) CuO NPs and (f) EDX spectrum of CuO NPs.

shows absorption bands at 511.51 cm^{-1} and 537.22 cm^{-1}, which are the characteristic stretching vibrations of Cu(II)-O bonds. The characteristic stretching frequencies corresponding to pure CuO NPs have been shifted, which suggests an interaction between MIP and CuO NPs. Stretching vibrations corresponding to the polymer in the 'Finger Print' region ($\sim$ 700-1400 cm^{-1}) originating from the backbone structure of the polymer has been observed. Moreover, characteristic stretching vibrations at 1580.06 cm^{-1}, 1628.98 cm^{-1}, 2858.80 cm^{-1} and 3429.90 cm^{-1}, are also shifted as compared to MIP sample suggesting a strong interaction between MIP and CuO NPs. These stretching vibrations in this case has originated from the -COOH functionality of IA, -OH functionality of EGDMA (acrylate groups) corresponding to MIP sample.

D. SEM and Energy Dispersive Spectroscopy Studies

SEM micrographs of MIP-CuO, NIP-CuO, MIP-unmodified, NIP-unmodified and CuO NPs are shown in Fig. 2. In Fig. 3 (a) and 3 (c), the rough surfaces probably indicate that GA molecule has been leached out, thus hampering the smooth surface of the polymer. In Fig. 3 (b), the smooth surfaces of the NIP material in both cases reveal that no extraction process has been carried out. Fig. 3 (e) shows the SEM image of the CuO NPs. The elementary composition and purity of CuO NPs were investigated by EDX analysis (Fig. 3 (f)).

E. Optimization of the Experimental Conditions

1) Influence of Monomer Variation: The MIP material was prepared with three different monomers namely IA, AA and AAM. From Fig. 4 (a), it is observed that the current response for IA was the highest (26.39 μA) using MIP-CuO electrode. This is probably because IA contains two COOH groups; these will react with two OH groups of GA forming two covalent bonds, whereas AA will form one covalent linkage. On the other hand, AAM will establish only H-bonding between COOH group of GA and $CONH_2$ group of AAM.

2) Influence of Buffer and pH: The MIP-CuO electrode has been dipped in 1mM GA in different buffers of pH 5, viz., citrate buffer (CB), acetate buffer (ABS) and phosphate buffer solution (PBS), respectively. As shown in Fig. 4 (b), the oxidation peak current (19.56 μA) is highest for PBS. CV tests are performed to ascertain the impact of pH on the

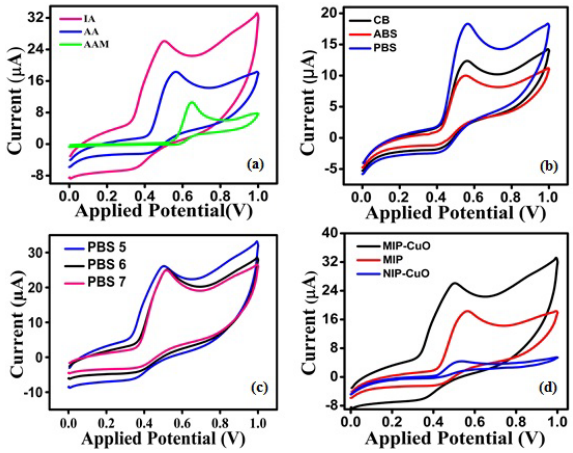

Fig. 4. Voltammograms obtained for 1 mM GA (a) using IA, AA and AAM monomers (b) in citrate, acetate and phosphate buffer solutions (c) with PBS of pH values 5, 6 and 7 (d) with MIP-CuO, MIP and NIP-CuO electrode.

MIP-CuO electrode using PBS of pH 5, 6, 7, respectively. The corresponding response curves are illustrated in Fig. 4(c). It is imperative that maximum current has been delivered by the electrode in case of PBS 5, thereby justifying its selection as the test solution. To examine the performance of the MIP- CuO electrode, unmodified MIP and NIP-CuO, CV responses were captured in 1 mM GA solution with the respective electrodes. Fig. 4(d) portrays the current response profile wherefrom it is derivable that the MIP-CuO electrode showed a considerable rise in peak current (26.20 μA) at 0.50 V when compared to the unmodified MIP electrode (18.30 μA) at 0.56 V. This surge in peak current is observed due to the high specific surface area CuO NPs [25]. It is also observed from Fig. 4(d) that the oxidation peak potential of the GA molecule on the MIP-CuO electrode surface is shifted negatively to 0.50 V as compared to that on the unmodified electrode. This phenomenon is observed possibly due to the presence of CuO NPs which facilitate faster transfer of electrons during electrochemical process [26]. For simple MIP electrode, owing to the absence of CuO NPs, the rate of electron transfer is assumed to considerably reduce. It can be inferred from Fig. 4(d) that the peak current of the NIP-CuO electrode is comparatively lower than that of the MIP-CuO electrode even though the respective electrode has responded proportionately to GA. The probable reason behind this observation may be attributed to the lesser active sites on NIP-CuO electrode because of the absence of GA -like cavities.

3) Influence of Scan Rate: The impact of scan rate on the kinetics of the reaction system involved therein has been established by means of CV using the MIP-CuO electrode.

The electrode was employed to 1 mM GA solution at varying scan rates ranging from 0.01 to 0.4 Vs^{-1}, and the respective voltammograms are illustrated in Fig. 5 (a). This particular window of scan rate has been selected because the oxidation peak current are proportional to the scan rate with $R^2 = 0.97$ (Fig. 5 (b)) which demonstrates a surface controlled process [34]. The adsorption kinetics of the MIP-CuO electrode has been studied in details. It is evident from Fig. 5 (c), that the value of peak potential (E_p) shifts in the

Authorized licensed use limited to: INDIAN INSTITUTE OF TECHNOLOGY GUWAHATI. Downloaded on February 15,2021 at 11:29:50 UTC from IEEE Xplore. Restrictions apply.

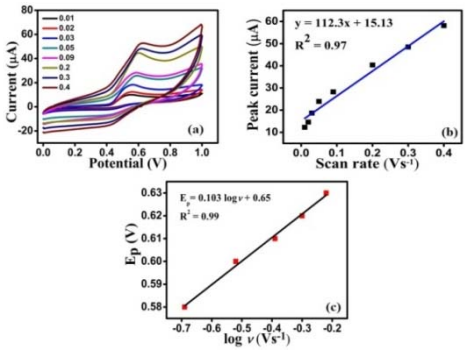

Fig. 5. (a) Variation of peak currents with different scan rates (0.01- 0.4 Vs-1) (b) Plot of peak current with scan rate (c) Relationship between oxidation potential and logarithm of scan rate (log ν).

positive direction and also increases linearly along with log ν. The surface concentration of the GA (Γ_c) and the number of electrons (n) transferred have been calculated using the following Eq. (1)

$$\mathrm{Ip} = \frac{\mathrm{nFQ}\nu}{4\mathrm{RT}} = \frac{\mathrm{n^2F^2A}\nu\Gamma_\mathrm{c}}{4\mathrm{RT}} \tag{1}$$

where, F, A and Q are Faraday's constant, area of the electrode, and quantity of charge consumed during the oxidation process, respectively. The value of n and Γ_c calculated from Eq. (1) are 1.87 (approximately equals 2) and 3.81x 10^{-9}mole cm^{-2}, respectively. This value of n and Γ_c is comparable to literature [39], thus indicates that the MIP-CuO electrode possesses excellent adsorption capacity towards the GA molecules. The regression equation of the calibration curve is given in Eq. (2) with $R^2 = 0.99$.

$$E_p = 0.103 \log \upsilon + 0.65 \tag{2}$$

The heterogeneous rate constant (k_s) of the oxidation reaction has been calculated as 1.127 s^{-1} using the Laviron's equation [24] and is found to be comparable as in [12]. The electron transfer coefficient (α) [39] was calculated from the slope of the calibration curve of Eq. (2) and found to be 0.42 [39].

4) Concentration Variation and Linearity: The current profile with increasing concentration of the GA in the analyte was monitored by performing DPV measurements using the MIP-CuO electrode. The experimental parameters viz., step potential, scan rate, modulation time, modulation amplitude and interval time were fixed at 0.01 V, 0.05 $Vs^{-}1$, 0.2 s, 0.005 V, and 0.4 s respectively. A prominent increase in current is observed in Fig. 6 (a) as the concentration of GA increases.

The calibration curve of GA (Fig. 6 (b)) reveals that there are two linear segments: one linear segment is from 1 μM to 100 μM, where the regression equation of $y = 0.128x + 4.43 (R^2 = 0.95)$ and a sensitivity of 2.56 μA $\mu M^{-1}\,cm^{-2}$ is obtained; the second linear segment is within the range of 100 μM and 900 μM, and the corresponding regression equation is $y = 0.0091x + 14.77 (R^2 = 0.96)$ with a sensitivity of 0.182 μA $\mu M^{-1} cm^{-2}$. Thus, as desirable, the MIP-CuO electrode has higher sensitivity in the lower linear range. The LOD of MIP-CuO electrode was calculated to be 12.6 nM based on 3Sy/x/m [24].

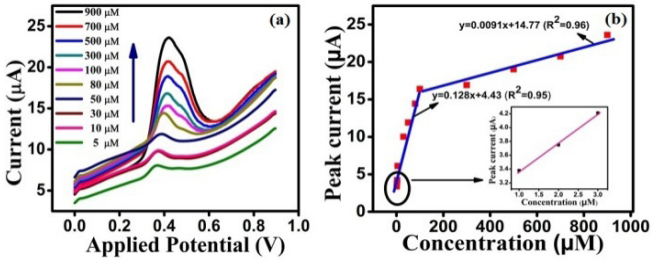

Fig. 6. (a) DPV plots obtained on the surface of the MIP-CuO electrode containing different concentrations of GA in PBS 5 (b) Variation of the peak current with concentration; the inset shows the magnified image of the encircled portion.

V. Sensory Parameters of the MIP - CuO Electrode

The MIP-CuO electrode has been subjected to 1mM of MA, AA and CAT, separately in order to measure the selectivity of theelectrode. The electrode showed a very little response when imbibed in MA and AA solutions with a negligible response towards CAT. The peak current obtained on imbibing the electrode to 1 mM GA, MA and AA has been plotted in Fig. S5 (a). Additionally, the MIP-CuO has been exposed to possible interferents (MA and AA) in the presence of GA to ensure the selectivity of the electrode in the mixture. The responses were obtained in the presence of 10-folds of each species interfering to 100 μM of the target analyte GA. Fig. S6 depicts the interference profile of MIP-CuO electrode. The relative change of signal due to presence of interfering agents has been plotted with respect to the response obtained without interference (only GA). The presence of either MA or AA over GA manifested no significant change of peak current with a tolerance limit of less than $\pm$5%.

CV responses were recorded to study the reproducibility of the electrode (Fig. S5 (b)) utilizing three similar electrodes. The electrodes showed acceptable reproducibility with relative standard deviation (% RSD) of 1.34. For repeatability, six CV measurements were in PBS 5. The nature of current response (Fig. S5 (c)) is repetitive with % RSD of 4.22. For stability analysis, DPV measurements were carried out in presence of 1 mM GA at an interval of 10 days for almost 3 months under similar environmental conditions. The performance of the electrode decreased by 0.94 % after 15 days (Fig. S5 (d)) and 2.9 % after 3 months.

VI. Real Sample Analysis

To comment on the practical application of the MIP-CuO electrode, it was employed to determine GA in ten varieties of GT samples by means of the developed PCR and PLSR models. The liquor for experimentation was prepared with modifications to a method stated in [24]. For each sample, eight repetitive DPV responses were recorded in the voltage range of 0.0 V – 1.0 V. The data matrix [179 x 80] so obtained on imbibing the MIP-CuO electrode to the GT samples was subjected to PCA [31], PLSR [32] and PCR [33] by using MATLAB R2014a.

A. Data Clustering Using PCA

Ten varieties of GT samples were discriminated and were visualized by means of PCA on the DPV datasets. It can be

Authorized licensed use limited to: INDIAN INSTITUTE OF TECHNOLOGY GUWAHATI. Downloaded on February 15,2021 at 11:29:50 UTC from IEEE Xplore. Restrictions apply.

TABLE I
ACTUAL AND PREDICTED GA CONTENT FROM PLSR AND PCR MODEL

S. No.	Actual GA (mg/g)	Predicted GA (mg/g)		Prediction accuracy (%)	
		PLSR	PCR	PLSR	PCR
1	0.11	0.116	0.113	94.54	97.27
2	0.12	0.124	0.127	96.66	94.16
3	0.05	0.057	0.068	86.00	80.00
4	0.1	0.102	0.092	98.00	92
5	0.05	0.065	0.071	80	60
6	0.1	0.11	0.107	90	93
7	0.13	0.12	0.123	92.30	94.16
8	0.08	0.10	0.098	75	77.5
9	0.13	0.121	0.113	93.84	87.6
10	0.06	0.07	0.062	83.33	96.66
Average prediction accuracy				**88.97**	**87.24**

observed from Fig. S7 that samples belonging to a definite class have formed segregated clusters. The first two PC loadings explain 95.93 % of the total variance in the dataset. On quantitative evaluation of the data nature, SI of 31.27 is obtained. This value of SI indicates that the interclass separability of the samples is reasonably good using the MIP-CuO electrode.

B. PLSR Analysis

The ability of the MIP-CuO electrode to predict the amount of GA has been analysed by developing PLSR model coupled with LOOCV technique. The matrix [179 x 80] so obtained as a result of the DPV response and the corresponding HPLC data were divided into two subsets, i.e., training set and testing set in the ratio of 70:30. The performance of the model has been estimated by observing correlation coefficient (R^2) and the root mean square error (RMSE) between predicted and experimental values. The latent variable (LV) has been selected corresponding to the lowest value of RMSE of calibration (RMSEC). As observed from Fig. S8 (a), the RMSEC value (1.35) is lowest for 14 LVs. For predicting the GA content (in mg/g) in GT samples, the PLSR model yielded a prediction accuracy of 88.97% on an average. Table I summarizes the comparison between the actual HPLC and predicted values of GA in the GT samples. The bar graph in Fig. S8(c) illustrates the comparative study for precise visualization. This plot affirms fair level of synonymity between the actual value and predicted value of GA content.

C. PCR Analysis

Through PCR analysis, a relation has been established between the principal components of the data matrix of size [179 x 80] and the corresponding HPLC data. As can be seen from Fig. S8 (b), the lowest RMSEC (1.38) has been obtained for 17 LVs. The average prediction accuracy obtained in this case is 87.24% (Table I). This has been graphically illustrated in Fig. S8 (c). Table II summarizes the statistical parameters, i.e., coefficient of determination for calibration ($R_c^2 = 0.93$), coefficient of determination of validation ($R_v^2 = 0.77$), RMSEC for both PLSR and PCR regression models. Hence, barring the sole dissimilarity of lesser quantity of LVs required for PLSR (14 LVs), both PCR and PLSR models furnish similar prediction accuracies.

TABLE II
PREDICTION OF GA CONCENTRATION IN UNKNOWN GT SAMPLES

Method	LV	Calibration		Validation		Prediction	
		RMSEC	R_c^2	RMSEV	R_v^2	RMSEP	R_p^2
PLSR	**14**	1.35	0.93	0.021	0.84	0.023	**0.82**
PCR	17	1.38	0.82	0.022	0.77	0.024	0.74

D. Prediction Using Linear Regression Models

Prediction was performed using an unknown dataset of size [179 x 20] by employing both the developed PLSR and PCR models. The results are tabulated below (Table II). The prediction results showed that on using the PLSR model, the RMSEP was found to be 0.023 with the coefficient of determination for prediction (R_p^2) as 0.82 with 14 LVs. Likewise for PCR, the RMSEP was established to be 0.024 with R_p^2being 0.74 with 17 LVs. The unknown dataset prediction results are in sync with the validation results, thereby suggesting that the PLSR model is the best option for analysing the GA content in any sample.

VII. COMPARISON OF THE PRESENT METHOD WITH EXISTING LITERATURE

The deep insight into literature has revealed a number of studies in which detection of GA has been sought (Table III). In this work, the detection limit has considerably improved in comparison to previous literature [12], [16], [18]–[20], [28]. The MIP – CuO sensor exhibited two wide linear ranges. Though few of the literature report low LOD or sensitive detection, yet the precursors and the processes involved in the preparation of the material are either costly, scarcely available or time consuming [40]. Some studies aimed to detect GA using MIP technology; however they have no detailed analysis of the analytical parameters, calculation of LOD or analysis of the linear range [4], [17]. The usage of excellently stable CuO NPs for the modification of the electrode contributed to an acceptable response in GT samples. The quantity of GA in tea samples roughly accounts to be 0.039- 6.7 mg/g; this is approximately 0.229 μM – 39.38 μM, noticeably higher than the LOD (12.6 nM) calculated. In essence, the electrode can be deployed as an efficient, cost-effective and electrochemically stable electrode for GA detection in any industry.

Authorized licensed use limited to: INDIAN INSTITUTE OF TECHNOLOGY GUWAHATI. Downloaded on February 15,2021 at 11:29:50 UTC from IEEE Xplore. Restrictions apply.

TABLE III
COMPARISON OF THE PRESENT METHOD WITH EXISTING LITERATURE

Techniques and electrode material	Linear range (μM)	LOD (nM)	References
DPV using Zirconia-choline chloride-gold NPs electrode.	0.22–55	25	[40]
DPV using carbon nanotubes modified electrode	0.5–15	300	[20]
CV and DPV Fe_2O_3/electro-reduced graphene oxide electrode	1 - 100	150	[12]
DPV using GA MIP sensor	0.12–380.0	47	[18]
CV and DPV using poly-(glutamic acid): graphene electrode	0.03–480	10	[34]
DPV using SiO_2 NPs modified electrode	0.8–100	250	[28]
CV and DPV using MIP-CuO electrode	**1-100 and 100-900**	**12.6**	**This work**

VIII. CONCLUSION

In the present work, the MIP material has been implanted with electrochemically active CuO NPs for effective detection of GA in GT by the concept of molecular imprinting. Two wide linear ranges are exhibited by the electrode (1 μM to 100 μM and 100 μM to 900 μM). Nanomolar detection of GA has been confirmed and LOD was calculated to be 12.6 nM which is markedly lower than the amount of GA in any product. The electrode has been found to be repeatable, selective and reproducible, having a stability of near about 3 months. Segregation between GT samples were confirmed from the PCA plot with SI value of 31.27. In addition, development and subsequent comparison of the prediction results obtained on implementation of PLSR and PCR with reference HPLC data have been done. This resulted in average prediction accuracy of 88.97 % and 87.24% of PLSR and PCR, respectively. Therefore, this study focuses on the development of a selective electrode and also on the quantitative analytical ability of the electrode. In a nutshell, this work puts a progressive step forward towards practical usability of the electrode as sensing material for qualitative estimation of tea in industries.

ACKNOWLEDGMENT

The authors would like to acknowledge the HNB Garhwal University, Srinagar, India, for their SEM facility and Central Glass and Ceramic Research Institute, Kolkata, for providing the XRD support. They also grateful to Prof. Arup Ranjan Bhattacharyya, Department of Metallurgical Engineering and Materials Science, IIT Bombay, for helping them throughout with the FTIR analysis. They also thank the Tocklai Tea Research Institute, Assam, India, for providing green tea samples and HPLC data.

REFERENCES

[1] Y. Zuo, "Simultaneous determination of catechins, caffeine and gallic acids in green, oolong, black and pu-erh teas using HPLC with a photodiode array detector," *Talanta*, vol. 57, no. 2, pp. 307–316, May 2002.

[2] R. V. Lith and G. A. Ameer, "Antioxidant polymers as biomaterials," *Oxidative stress Biomater.*, vol. 10, pp. 251–296, 2016.

[3] P. Carloni *et al.*, "Antioxidant activity of white, green and black tea obtained from the same tea cultivar," *Food Res. Int.*, vol. 53, no. 2, pp. 900–908, Oct. 2013.

[4] H. G. Valery, A. Chtaini, and B. Loura, "Voltammetric sensor based on electrodes modified by Poly(vinyl alcohol)-natural clay film, for the detection of gallic acid," *Portugaliae Electrochimica Acta*, vol. 37, no. 5, pp. 327–333, 2019.

[5] S. Sarafraz, H.-A. Rafiee-Pour, M. Khayatkashani, and A. Ebrahimi, "Electrochemical determination of gallic acid in Camellia sinensis (L.) Kuntze, Viola odorata L., Commiphora Wightii (Arn.) Bhandari, and Vitex agnus-castus L. by MWCNTs-COOH Modified CPE," *J. Nanostruct.*, vol. 9, no. 2, pp. 384–395, 2019.

[6] V. Armoskaite *et al.*, "The analysis of quality and antioxidant activity of green tea extracts," *J. Med. Plants Res*, vol. 5, no. 5, pp. 811–816, 2011.

[7] L. Wang, M. S. Halquist, and D. H. Sweet, "Simultaneous determination of gallic acid and gentisic acid in organic anion transporter expressing cells by liquid chromatography–tandem mass spectrometry," *J. Chromatogr. B*, vol. 937, pp. 91–96, Oct. 2013.

[8] W. Ma *et al.*, "Rapid and specific sensing of gallic acid with a photoelectrochemical platform based on polyaniline-reduced graphene oxide-TiO_2," *Chem. Commun.*, vol. 49, no. 71, pp. 7842–7844, 2013.

[9] X. Wang, J. Wang, and N. Yang, "Flow injection chemiluminescent detection of gallic acid in olive fruits," *Food Chem.*, vol. 105, no. 1, pp. 340–345, 2007.

[10] K. Dhalwal, V. M. Shinde, Y. S. Biradar, and K. R. Mahadik, "Simultaneous quantification of Bergenin, catechin, and gallic acid from Bergenia ciliata and Bergenia ligulata by using thin-layer chromatography," *J. Food Composition Anal.*, vol. 21, no. 6, pp. 496–500, Sep. 2008.

[11] R. de Queiroz Ferreira and L. A. Avaca, "Electrochemical determination of the antioxidant capacity: The ceric reducing/antioxidant capacity (CRAC) assay," *Electroanalysis*, vol. 20, no. 12, pp. 1323–1329, Jun. 2008.

[12] F. Gao *et al.*, "An electrochemical sensor for gallic acid based on Fe_2O_3/electro-reduced graphene oxide composite: Estimation for the antioxidant capacity index of wines," *Mater. Sci. Eng., C*, vol. 57, pp. 279–287, Dec. 2015.

[13] S. Sundaram, M. Jagannathan, M. R. A. Kadir, S. Palanivel, T. Hadibarata, and A. R. M. Yusoff, "A new electro-generated O-dianisidine derivative stabilized MWCNT-modified GCE for low potential gallic acid detection," *RSC Adv.*, vol. 5, no. 57, pp. 45996–46006, 2015.

[14] M. Kahl and T. D. Golden, "Electrochemical determination of phenolic acids at a Zn/Al layered double hydroxide film modified glassy carbon electrode," *Electroanalysis*, vol. 26, no. 8, pp. 1664–1670, Aug. 2014.

[15] D. Das *et al.*, "Development of a highly selective nickel cobalt oxide nanoparticles modified molecular imprinted polymer based sensor for detection of gallic acid in green tea," in *Proc. IEEE Int. Symp. Olfaction Electron. Nose (ISOEN)*, May 2019, pp. 1–4.

[16] M. Chen, "Determination of gallic acid in tea by a graphene modified glassy carbon electrode," *Int. J. Electrochem. Sci.*, vol. 14, pp. 4852–4860, Apr. 2019.

[17] P. Jara-Ulloa, P. Salgado-Figueroa, R. Moscoso, and J. A. Squella, "Polypyrrole molecularly imprinted modified glassy carbon electrode for the recognition of gallic acid," *J. Electrochem.*, vol. 160, no. 4, pp. 243–246, 2013.

[18] S. Shojaei, N. Nasirizadeh, M. Entezam, M. Koosha, and M. Azimzadeh, "An electrochemical nanosensor based on molecularly imprinted polymer (MIP) for detection of gallic acid in fruit juices," *Food Anal. Methods*, vol. 9, no. 10, pp. 2721–2731, Oct. 2016.

[19] X. Hu *et al.*, "Hydrophilic gallic acid–imprinted polymers over magnetic mesoporous silica microspheres with excellent molecular recognition ability in aqueous fruit juices," *Food Chem.*, vol. 179, pp. 206–212, Jul. 2015.

[20] L. P. Souza, F. Calegari, A. J. G. Zarbin, L. H. Marcolino-Juúnior, and M. F. Bergamini, "Voltammetric determination of the antioxidant capacity in wine samples using a carbon nanotube modified electrode," *J. Agricult. Food Chem.*, vol. 59, no. 14, pp. 7620–7625, Jul. 2011.

[21] M. M. Nezami, S. A. Wani, S. A. Khan, N. Khera, and S. Sohail, "An MIP-based novel capacitive sensor to detect 2-FAL concentration in transformer oil," *IEEE Sensors J.*, vol. 18, no. 19, pp. 7924–7931, Oct. 2018.

Authorized licensed use limited to: INDIAN INSTITUTE OF TECHNOLOGY GUWAHATI. Downloaded on February 15,2021 at 11:29:50 UTC from IEEE Xplore. Restrictions apply.

[22] Md. M. Nezami, S. A. Wani, S. Khan, N. Khera, and S. Sohail, "A comb type capacitive 2-FAL sensor for transformer oil with improved sensitivity," *IEEE Trans. Instrum. Meas.*, vol. 69, no. 7, pp. 4524–4532, 2020.

[23] T. Nandy Chatterjee *et al.*, "Molecular imprinted polymer based electrode for sensing catechin (+C) in green tea," *IEEE Sensors J.*, vol. 18, no. 6, pp. 2236–2244, Mar. 2018.

[24] D. Das *et al.*, "Titanium oxide nanocubes embedded molecularly imprinted polymer-based electrode for selective detection of caffeine in green tea," *IEEE Sensors J.*, vol. 20, no. 12, pp. 6240–6247, Jun. 2020.

[25] M. Ghaedi *et al.*, "CuO nanoparticles intermixed with chemically modified multiwalled carbon nanotubes as a novel electrode for Cu^{2+} ion determination," *IEEE Sensor J.*, vol. 15, pp. 2882–2890, 2015.

[26] R. Khan *et al.*, "Glucose-assisted synthesis of Cu_2O shuriken-like nanostructures and their application as nonenzymatic glucose biosensors," *Sens. Actuators B, Chem.*, vol. 203, pp. 471–476, Nov. 2014.

[27] B. B. Petković, D. Stanković, M. Milčić, S. P. Sovilj, and D. Manojlović, "Dinuclear copper(II) octaazamacrocyclic complex in a PVC coated GCE and graphite as a voltammetric sensor for determination of gallic acid and antioxidant capacity of wine samples," *Talanta*, vol. 132, pp. 513–519, Jan. 2015.

[28] J. Tashkhourian and S. F. Nami-Ana, "A sensitive electrochemical sensor for determination of gallic acid based on SiO_2 nanoparticle modified carbon paste electrode," *Mater. Sci. Eng., C*, vol. 52, pp. 103–110, Jul. 2015.

[29] *Determination of Substances Characteristic of Green and Black Tea—Part 2: Content of Catechins in Green Tea-Method Using High-Performance Liquid Chromatography*, ISO Standard 14502-2:2005, 2005.

[30] M. Palit *et al.*, "Classification of black tea taste and correlation with tea Taster's mark using voltammetric electronic tongue," *IEEE Trans. Instrum. Meas.*, vol. 59, no. 8, pp. 2230–2239, Aug. 2010.

[31] P. B. Garcia-Allende, O. M. Conde, J. Mirapeix, A. M. Cubillas, and J. M. Lopez-Higuera, "Data processing method applying principal component analysis and spectral angle mapper for imaging spectroscopic sensors," *IEEE Sensors J.*, vol. 8, no. 7, pp. 1310–1316, Jul. 2008.

[32] F. Harrou, Y. Sun, M. Madakyaru, and B. Bouyedou, "An improved multivariate chart using partial least squares with continuous ranked probability score," *IEEE Sensors J.*, vol. 18, no. 16, pp. 6715–6726, Aug. 2018.

[33] U. Depczynski, V. J. Frost, and K. Molt, "Genetic algorithms applied to the selection of factors in principal component regression," *Anal. Chim. Acta*, vol. 420, no. 2, pp. 217–227, Sep. 2000.

[34] J. J. Feminus, R. Manikandan, S. S. Narayanan, and P. N. Deepa, "Determination of gallic acid using poly(glutamic acid): Graphene modified electrode," *J. Chem. Sci.*, vol. 131, no. 2, pp. 1–10, Feb. 2019.

[35] B. D. Cullity and S. R. Stock, *Elements of X-Ray Diffraction*. Boston, MA, USA: Addison-Wesley, 2001.

[36] A. A. Radhakrishnan and B. B. Beena, "Structural and optical absorption analysis of CuO nanoparticles," *Indian J. Adv. Chem. Sci.*, vol. 2, no. 2, pp. 158–161, 2018.

[37] M. Elango, M. Deepa, R. Subramanian, and A. M. Musthafa, "Synthesis, characterization, and antibacterial activity of polyindole/Ag-Cuo nanocomposites by reflux condensation method," *Polym.-Plastics Technol. Eng.*, vol. 57, no. 14, pp. 1440–1451, 2018, doi: 10.1080/03602559.2017.1410832.

[38] C. Wang, P. Wang, Q. Xu, Z. Wei, and Y. Wu, "Synthesis and characterization of poly (itaconic acid-M-Phenylenediamine)," in *Proc. Int. Conf. Innov. Mater. Sci. Technol. (IMST)*, 2016, pp. 18–24.

[39] Z. Liang *et al.*, "A simple, ultrasensitive sensor for gallic acid and uric acid based on gold microclusters/sulfonate functionalized graphene modified glassy carbon electrode," *Sens. Actuators B, Chem.*, vol. 224, pp. 915–925, Mar. 2016.

[40] S. A. Shahamirifard, M. Ghaedi, Z. Razmi, and S. Hajati, "A simple ultrasensitive electrochemical sensor for simultaneous determination of gallic acid and uric acid in human urine and fruit juices based on zirconia-choline chloride-gold nanoparticles-modified carbon paste electrode," *Biosensors Bioelectron.*, vol. 114, pp. 30–36, Aug. 2018.

Authorized licensed use limited to: INDIAN INSTITUTE OF TECHNOLOGY GUWAHATI. Downloaded on February 15,2021 at 11:29:50 UTC from IEEE Xplore. Restrictions apply.

Materials Today: Proceedings 44 (2021) 3946–3950

Contents lists available at ScienceDirect

Materials Today: Proceedings

journal homepage: www.elsevier.com/locate/matpr

Post deposition annealing dependent structural and C-V characteristics of $(Ta_2O_5)_{0.965}$-$(TiO_2)_{0.035}$ thin films

Prashant Thapliyal [a,b,*], Alok S. Kandari [c], Vijendra Lingwal [d], N.S. Panwar [a], G. Mohan Rao [b]

[a] Department of Instrumentation Engineering, H.N.B. Garhwal University, Srinagar Garhwal, Uttarakhand 246174, India
[b] Department of Instrumentation and Applied Physics, Indian Institute of Science, Bangalore 560012, India
[c] Department of Physics, Govt. PG College New Tehri, Uttarakhand 249001, India
[d] Department of Physics, Pt. L.M.S. Govt. PG College Rishikesh, Dehradun, Uttarakhand 249201, India

ARTICLE INFO

Article history:
Received 23 August 2020
Received in revised form 6 September 2020
Accepted 12 September 2020
Available online 22 October 2020

Keywords:
Sputtering
Dielectric constant
MOS capacitors
Dielectric loss
Ta_2O_5
TiO_2

ABSTRACT

$(Ta_2O_5)_{1-x}$-$(TiO_2)_x$ (TTO) thin films, with x = 0.035, were deposited onto the P/boron-silicon (100) semiconducting substrates by reactive direct current (DC) magnetron sputtering of mosaic Ta and Ti metal targets, at ambient temperature. As-deposited films have been passed through the process of annealing at the temperatures, ranging from 500 to 800 °C. X-ray diffraction measurements, generally, show the formation of Ta_2O_5 structure of the annealed films. Metal–oxide–semiconductor (MOS) structure of Ag/$(Ta_2O_5)_{1-x}$-$(TiO_2)_x$/p-Si (Ag/TTO/p-Si), with x = 0.035, was formed, and capacitance of the structure was measured, at room temperature and 1 MHz. Capacitance of prepared MOS structure was measured, and found generally, increasing with annealing temperature. Among the prepared films, maximum value of dielectric constant was found 45, at 1 MHz, for the films annealed at 700 °C. Frequency dependent behaviour of dielectric loss was observed, and was found minimum value of 0.022, at 200 kHz, for the films deposited at room temperature.
© 2020 Elsevier Ltd. All rights reserved.
Selection and peer-review under responsibility of the scientific committee of the International Conference on Advances in Materials Processing & Manufacturing Applications.

1. Introduction

The consumer interest in miniaturization of electronic memory devices initiated the search of high dielectric constant materials. Some of the high dielectric constant metal oxides, like tantalum pentoxide (Ta_2O_5), titanium oxide (TiO_2), etc. [1–4], have been explored for this purpose, which have the potential to replace the basic silicon based dielectrics, e.g. SiO_2, SiO_xN_y, etc. The high dielectric constant and compatibility with the silicon devices [5], made Ta_2O_5 a preferred choice as a gate dielectric. The dielectric properties have been reportedly observed enhanced with the addition of other metal oxides to Ta_2O_5 [6]. The dielectric constant of bulk Ta_2O_5 was found considerably raised, from 35 to 126, by adding 8% (mole) TiO_2 [7]. The maximum dielectric constant 55, was reported by Gan et al. [8], for the annealed films deposited by sputtering of $(TiO_2)_x$-$(Ta_2O_5)_{1-x}$ bulk targets with x = 0.08. Along with the doping, the significant effect of substrate temperature as well as post-deposition annealing was reportedly observed for the improved microstructure and better quality of the film [9]. In the present piece of work TTO thin films, with x = 0.035 were deposited on the silicon (p-type) substrates by direct current (DC) magnetron sputtering of Ta and Ti metal targets in oxygen ambient. This report comprises the observed structural and dielectric properties of the deposited films.

2. Experimental

(Ta_2O_5)-(TiO_2) composite thin films were deposited onto the boron-doped silicon (100) substrates by reactive DC magnetron sputtering. The silicon substrates were washed with the help of deionised water, acetone and hydrogen fluoride (HF), followed by the ultrasonication for 5 min in the deionised water to eliminate surface impurities. The chemically cleaned and dried silicon substrates immediately placed in a vacuum chamber for deposition. Mosaic target assembly of Ta (purity 99.99%) and Ti (purity 99.99%) metals were used for sputtering in such a way that the composition of Ta and Ti may be obtained in the resultant thin film samples. Each target was having the dimension of 2 in. diameter, and 1 mm thickness. The horizontally rotating substrate holder

* Corresponding author.
E-mail address: pra.thapli1986@gmail.com (P. Thapliyal).

https://doi.org/10.1016/j.matpr.2020.09.297
2214-7853/© 2020 Elsevier Ltd. All rights reserved.
Selection and peer-review under responsibility of the scientific committee of the International Conference on Advances in Materials Processing & Manufacturing Applications.

was used to ensure the homogeneous composition of the deposited films. At first an ultimate pressure of 1×10^{-5} mbar was achieved in the vacuum chamber, followed by the pre-sputtering for 3–5 min, using a shutter to mask the substrates, to clean the exposed surface of the targets, before starting the deposition. The required oxide film deposition was performed using the high purity (>99.999%) oxygen and argon as the reactive and sputtering gases, respectively. Argon and oxygen pressures in the vacuum chamber were regulated with the help of needle valves. The sputtering pressure was maintained 5×10^{-3} mbar, while the oxygen pressure was kept 5% of the sputtering pressure, during deposition. The distance between substrates and targets assembly was maintained 50 mm, during deposition. The thin film samples deposited at room temperature (RT) were followed by annealing in ambient air, in the temperature range from 500 to 800 °C for 1.5 h. The prepared films were deposited at DC power of 45 Watt.

X-ray diffractometer (PANalytical, X'PERT PRO), using 1.5405980 Å wavelength of Cu Kα1 radiation, was used for analysing the crystallographic structure of the prepared films. Scanning electron microscope with energy dispersive spectrometer (SEM-EDS) (CARL ZEISS, MA15/EVO18) and X-ray photoelectron spectroscopy (XPS) (Kratos Axis Ultra DLD, monochromatic Al *K*α radiation 1486.6 eV), were used for the elemental study. Spectroscopic ellipsometer (SENTECH, SE800) was used to measure the thickness of the prepared films and it was found to be about 280 ± 10 nm. MOS capacitors (having area of 0.19625 mm^2) were fabricated with the prepared films by depositing silver as electrodes, Fig. 1. The capacitance-voltage measurements of MOS capacitors were performed by RLC meter (Fluke–PM6306), at 1 MHz.

3. Results and discussion

The observed XRD patterns of the prepared TTO thin films, with x = 0.035, have been shown in Fig. 2. TTO films, x = 0.035, annealed at and above 700 °C, was observed to form orthorhombic Ta_2O_5 structure, Fig. 2. The (*h k l*) planes associated with observed diffraction peaks were indexed as (001), (200), (201), (002) and (202), and were found consistent with reported results [10–12].

Fig. 3 shows the observed SEM-EDS spectrum of prepared TTO thin films, with x = 0.035, deposited at room temperature (RT), indicating the characteristic peaks of Ta, Ti and O. Atomic percentage of Ta, Ti and O obtained from SEM-EDS measurements, were used to determine the composition (x) of the prepared TTO films, which are shown in Table 1. The elemental peaks detected by SEM-EDS measurements were also found with the XPS measurements, Fig. 4.

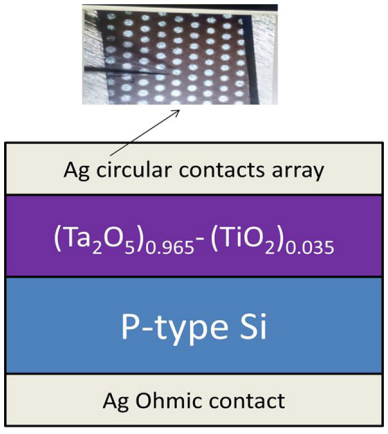

Fig. 1. Schematic diagram of MOS capacitor.

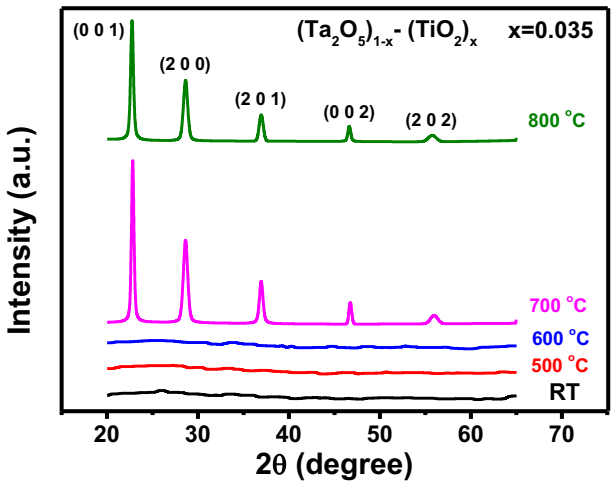

Fig. 2. XRD patterns of $(Ta_2O_5)_{0.965}$-$(TiO_2)_{0.035}$, films annealed at different temperatures.

The observed XPS survey scan spectrum of the deposited TTO thin films, with x = 0.035, has been shown in Fig. 4. The characteristic peaks of tantalum Ta 4f, Ta 4d, titanium Ti 2p and oxygen O 1 s, were observed at their corresponding positions about 26–29 eV, about 230–240 eV, about 454–465 eV and about 530 eV, respectively [12,13]. Additional carbon C 1 s peak was observed at 284.6 eV, which may be due to the air contaminated surface of the samples before measurements.

MOS structure was formed by depositing metal (Ag) onto the annealed TTO thin films, with x = 0.035. The capacitance-voltage (C–V) measurements were performed by the bi-directional sweep of the applied DC voltage (i.e., ±10 V), with a small AC signal voltage of 50 mV, at 1 MHz. The observed C-V characteristics of Ag/TTO/p-Si, x = 0.035, assisted MOS structures show typical accumulation, depletion and inversion regions, Fig. 5(a). For negative voltage sweep, holes collected at the surface of the silicon semiconductor (p-type) compensate the opposite charge of electrons, at the gate, which measures the capacitance of the deposited film (C_o). For positive voltage sweep, the surface of semiconductor becomes depleted from the holes, and produced extra space charge capacitance (C_s) is added in series to the C_o. The shifting along the voltage axis, towards negative bias in C-V characteristics was observed, and may be attributed to the presence of fixed oxide positive charge ($+Q_f$) near the semiconductor-deposited film interface [14]. Among the prepared film structures, maximum value of capacitance was found 281 pF, at 1 MHz, for Ag/$(Ta_2O_5)_{0.965}$-$(TiO_2)_{0.035}$/Si capacitors, films annealed at 700 °C, Fig. 5(a). From the accumulation region of the C-V characteristics, dielectric constant of the prepared capacitors was calculated and found 13, 14, 45 and 43 for the films, have been annealed at temperature 500, 600, 700 and 800 °C, respectively, at 1 MHz.

The variation of the dielectric constant of Ag/ TTO/ Si capacitors, x = 0.035, with annealing temperature has been shown in Fig. 5(b). For the annealing temperature ≤ 700 °C, the dielectric constant was observed increasing with the increases of annealing, and was observed decreased with further increase in annealing temperature (at 800 °C), [8] Fig. 5(b). This observed enhancement in the dielectric constant may be due to the improved crystallization of the deposited films with annealing, upto 700 °C. For higher annealing condition (≥800 °C), there might be a possibility of oxygen diffusion from the film layer to the film-substrate interface, which might have formed a low dielectric constant interfacial oxide layer with the silicon substrate, and thus the dielectric constant of the structure was observed reduced [15].

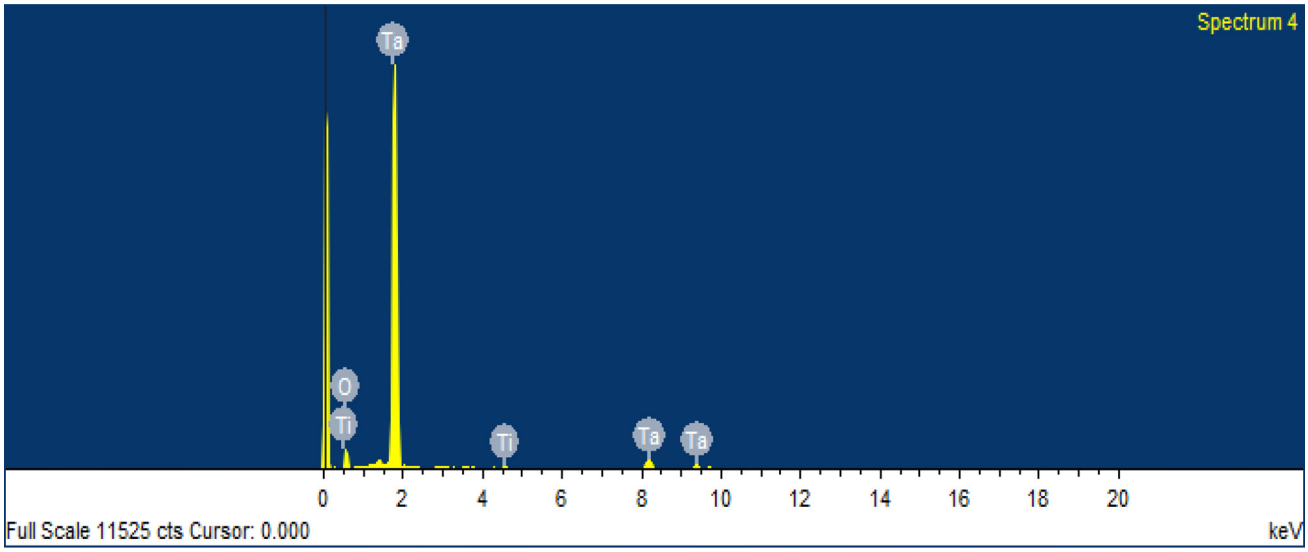

Fig. 3. SEM-EDS spectrum of TTO thin films, with x = 0.035.

Table 1
Composition (x) of the prepared TTO films.

S. No.	x	Ti (atomic %)	Ta (atomic %)	O (atomic %)
1.	0.035	0.53	37.94	61.53

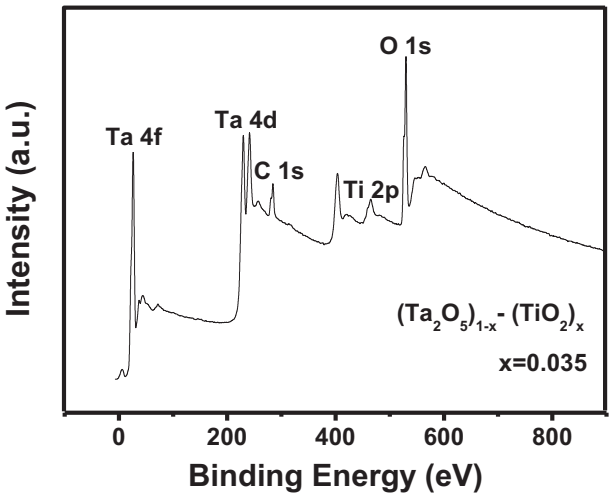

Fig. 4. XPS survey scan spectrum of TTO thin films, with x = 0.035.

Fig. 6(a) shows the capacitance vs frequency variation of TTO films, with x = 0.035, annealed at different temperatures. Generally, the capacitance was observed decreasing with increasing frequency, for all the annealing temperatures. Fig. 6(b) shows the variation of dielectric loss (tan δ) with the applied frequency of the TTO films, x = 0.035, for different annealing temperatures. The tan δ loss was observed decreasing with increasing frequency in the range of 10 kHz to 200 kHz, almost for all the annealing temperatures. At 200 kHz, the value of minimum dielectric loss was observed 0.022, for the films deposited at room temperature. At lower frequencies, the observed high dielectric loss may be due to the built-up of the free charge at the oxide film/ metal electrode interface. At higher frequencies, due to the fast altering polarity of the electric field, there is less possibility to accumulate the excess free charge in the field direction, results the decrease in the dielectric loss [16]. The dielectric loss was observed increasing with further increasing the frequency (>200 kHz). This increased dielectric loss may be attributed to the resonance condition induced with the effect of interfacial barrier or the frequency depending property of the dielectric or the effect of electrodes. The effect of resistance produced by the internal or external sources, contributing in series combination with the oxide film may vary the dielectric properties at high frequency [17–20].

4. Conclusions

Reactive DC magnetron sputtered composite thin films of TTO, with x = 0.035, were deposited onto the semiconducting silicon substrates by sputtering of the mosaic Ta and Ti metal targets, at room temperature. The as-deposited films have been annealed at the temperature ranging from 500 to 800 °C, in air ambient. X-ray diffraction results show formation of orthorhombic Ta_2O_5 structure. Capacitance of Ag/ TTO/ p-Si, x = 0.035, MOS structure, using the prepared films, was measured at 1 MHz, and was observed varying with the annealing temperature. The dielectric constant was observed increasing with increasing annealing temperature upto 700 °C, and decreased thereafter at the higher annealing temperature, 800 °C. Among the prepared thin films annealed at different temperatures, the maximum dielectric constant 45 was found for the films annealed at 700 °C. The frequency dependent dielectric properties were measured for capacitance and dielectric loss. Capacitance of the prepared MOS structure was observed decreasing with increasing the frequency, for all the annealing temperatures. Dielectric loss was found decreasing with increasing the frequency in the frequency range (~10–200 kHz), and was observed increasing for the further increase of frequency (>200 kHz). The increase in the dielectric loss in the higher frequency may be attributed to the resonance phenomena induced due to the intrinsic or extrinsic sources. Structural and C-V characteristics of the deposited TTO films, with x = 0.035, were observed strongly affected by the treatment of post-deposition

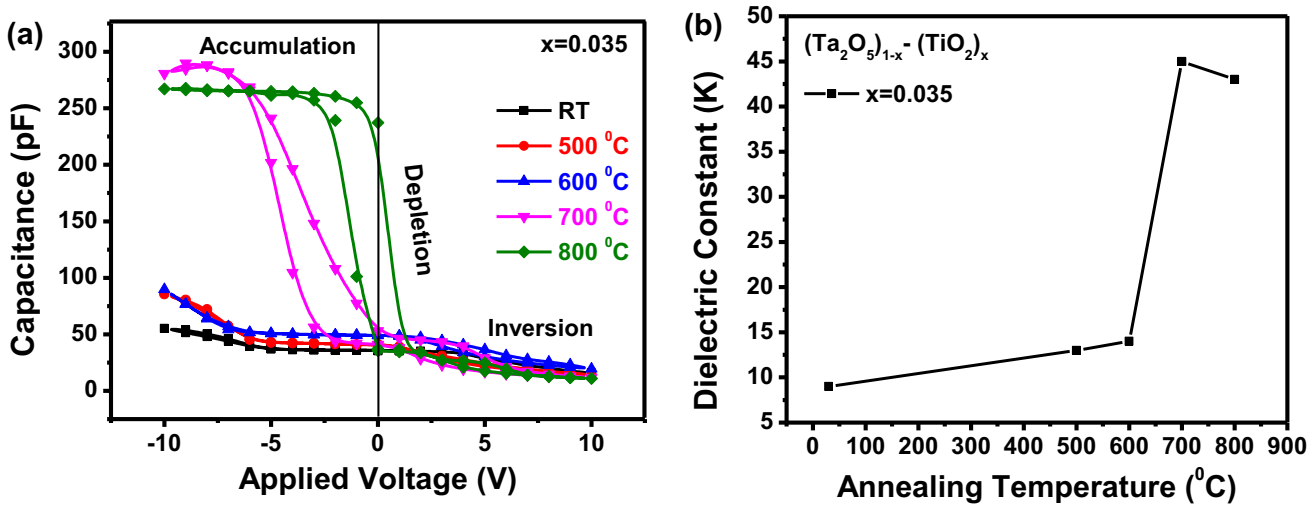

Fig. 5. (a) C-V characteristics; (b) Dielectric constant of Ag/TTO/Si capacitors, x = 0.035, for different annealing temperatures.

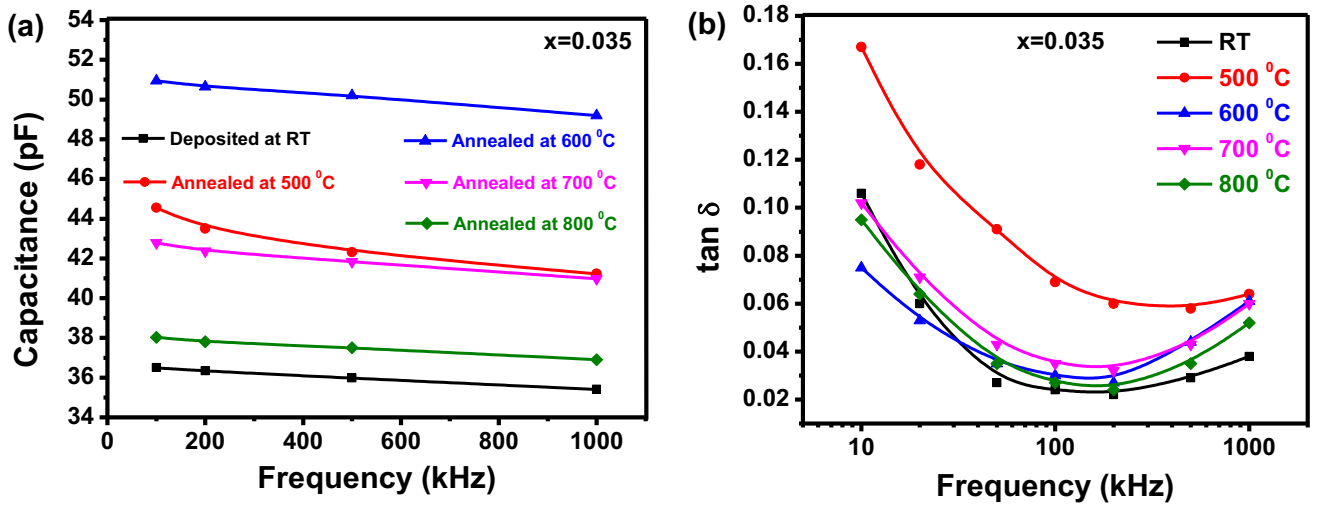

Fig. 6. Frequency dependent (a) capacitance; (b) Dielectric loss of Ag/TTO/Si capacitors, with x = 0.035, for different annealing temperatures.

annealing, in this report. For the presently deposited composition $(Ta_2O_5)_{0.965}$-$(TiO_2)_{0.035}$, films annealed at 700 °C, may have a preferred potential as high dielectric constant gate material to the memory devices.

CRediT authorship contribution statement

Prashant Thapliyal: Conceptualization, Methodology, Formal analysis, Investigation, Writing - original draft. **Alok S. Kandari:** Methodology, Investigation. **Vijendra Lingwal:** Validation, Formal analysis, Visualization. **N.S. Panwar:** Conceptualization, Resources, Writing - review & editing, Supervision. **G. Mohan Rao:** Conceptualization, Resources, Visualization, Supervision.

Declaration of Competing Interest

The authors declare that they have no known competing financial interests or personal relationships that could have appeared to influence the work reported in this paper.

Acknowledgements

Authors are very thankful to H.N.B. Garhwal University, Srinagar Garhwal, Uttarakhand to facilitate the 'Analytical Instruments Facility' in the department, where sample preparation and characterizations have been carried out. We convey our heartiest thanks to Indian Institute of Science, Bangalore for providing the facility of X-ray photoelectron spectroscopy.

References

[1] M. Kadoshima, M. Hiratani, Y. Shimamoto, K. Torii, H. Miki, S. Kimura, T. Nabatame, Thin Solid Films 424 (2003) 224–228.
[2] S. Ramanathan, C.M. Park, P.C. McIntyre, J. Appl. Phys. 91 (2002) 4521–4527.
[3] A. Callegari, E. Cartier, M. Gribelyuk, H.F.O. Schmidt, T. Zabel, J. Appl. Phys. 90 (2001) 6466–6475.
[4] G.B. Alers, D.J. Werder, Y. Chabal, H.C. Lu, E.P. Gusev, E. Garfunkel, T. Gustafsson, R. Urdahl, Appl. Phys. Lett. 73 (1998) 1517–1519.
[5] H. Shinriki, M. Nakata, IEEE Trans. Electron Dev. 38 (1991) 455–462.
[6] L. Manchanda, M.D. Morris, M.L. Green, R.B. van Dover, F. Klemens, T.W. Sorsch, P.J. Silverman, G. Wilk, B. Busch, S. Aravamudhan, Microelectron. Eng. 59 (2001) 351–359.
[7] R.F. Cava, W.F. Peck Jr., J.J. Krajewski, Nature 377 (1995) 215–217.
[8] J.-Y. Gan, Y.C. Chang, T.B. Wu, Appl. Phys. Lett. 72 (1998) 332–334.

[9] S.V.J. Chandra, P.S. Reddy, G.M. Rao, S. Uthanna, Res. Lett. Mater. Sci. 2007 (2007) 1–5.
[10] T.J. Bright, J.I. Watjen, Z.M. Zhang, C. Muratore, A.A. Voevodin, D.I. Koukis, D.B. Tanner, D.J. Arenas, J. Appl. Phys. 114 (2013), 083515-083515-10.
[11] W. Miao, M.M. Zhu, Z.C. Li, Z.J. Zhang, Mater. Trans. 49 (2008) 2288–2291.
[12] M. Chandra Sekhar, N. Nanda Kumar Reddy, V.K. Verma, S. Uthanna, Ceramics Int. 42 (2016), 18870-18870-9.
[13] Y. Kuo, J. Electrochem. Soc. 139 (1992) 579–583.
[14] S.M. Sze, Physics of Semiconductor Devices, second ed., Wiley, New York, 1981.
[15] Chyuan Haur Kao, Pei Lun Lai, Hsin Yuan Wang, Surf. Coatings Technol. 231 (2013) 512–516.
[16] M. Chandra Sekhar, P. Kondaiah, S.V. Jagadeesh Chandra, G. Mohan Rao, S. Uthanna, Appl. Surf. Sci. 258 (2011) 1789–1796.
[17] P.C. Joshi, M.W. Cole, J. Appl. Phys. 86 (1999) 871–880.
[18] M. Sayer, A. Mansingh, A.K. Arora, A. Lo, Integr. Ferroelectr. 1 (1992) 129–146.
[19] P.C. Joshi, S.B. Desu, Appl. Phys. Lett. 73 (1998) 1080–1082.
[20] P.C. Joshi, S.B. Desu, J. Appl. Phys. 80 (1996) 2349–2357.

Ferroelectrics

ISSN: 0015-0193 (Print) 1563-5112 (Online) Journal homepage: https://www.tandfonline.com/loi/gfer20

Effect of Li doping on dielectric properties of $Na_{1-x}K_xNbO_3$, x = 0.500, morphotropic phase region

Surendra Singh & N. S. Panwar

To cite this article: Surendra Singh & N. S. Panwar (2021) Effect of Li doping on dielectric properties of $Na_{1-x}K_xNbO_3$, x = 0.500, morphotropic phase region, Ferroelectrics, 570:1, 122-131

To link to this article: https://doi.org/10.1080/00150193.2020.1839263

Published online: 11 Jan 2021.

Submit your article to this journal

View related articles

View Crossmark data

Full Terms & Conditions of access and use can be found at
https://www.tandfonline.com/action/journalInformation?journalCode=gfer20

FERROELECTRICS
2021, VOL. 570, 122–131
https://doi.org/10.1080/00150193.2020.1839263

Taylor & Francis
Taylor & Francis Group

Check for updates

Effect of Li doping on dielectric properties of $Na_{1-x}K_xNbO_3$, x = 0.500, morphotropic phase region

Surendra Singh[a] and N. S. Panwar[b]

[a]Department of Physics, H. N. B. Garhwal University, Srinagar, India; [b]University Science Instrumentation Centre, H. N. B. Garhwal University, Srinagar, India

ABSTRACT

Li doped sodium-potassium niobate $(Na_{0.5}K_{0.5})_{1-y}Li_yNbO_3$ ceramic pellets, with y = 0 to 7 (mole) %, were prepared by solid state reaction method with double sintering. With varying lithium content (y), dielectric properties, and X-ray diffraction (XRD) peaks shifting pattern exhibit strong compositional dependence. Among the prepared Composition, a break in XRD peaks shifting tendency, and maximum dielectric constant, electric conductivity were obsreved at the composition with y = 0.06.

ARTICLE HISTORY
Received 4 January 2020
Accepted 14 July 2020

KEYWORDS
Ferroelectric; perovskite; dielectric properties; morphotropic phase transition

1. Introduction

The ABO_3 perovskite structure is important because of its capability of adjusting to a mismatch of the equilibrium bond lengths between and within the A and B sites, to both cation and anion vacancies, to cooperative orbital ordering or atomic displacements, to cation ordering, and to the formation of intergrowth structures. This capability makes it possible to tune a physical property of interest [1]. Perovskite (ABO_3) type ferroelectric materials are an important class of functional materials and a crucial important topic in materials science. One of the major challenges in this field is to build exact and collective structure-property relationships to better understand the morphotropic phase boundary (MPB) where physical properties are enhanced anomalously. Ferroelectrics with switchable spontaneous polarization and an intrinsic ability to convert electrical energy to mechanical energy and vice versa have found numerous applications in modern electronic devices ranging from nonvolatile memories to sensors in aeronautical applications. The piezoelectric device last two decades dominated by lead containing $Pb(Zr_{1-x},Ti_x)O_3$ (PZT) based materials due to their different and strong functional properties [2].

Very high piezoelectric and electromechanical properties have been achieved in a series of lead based ferro electric solid solution single crystals, such as $Pb(Mg_{1/3}Nb_{2/3})O_3$-$PbTiO_3$, $Pb(Zn_{1/3}Nb_{2/3})O_3$–$PbTiO_3$ (PZNT), and $BiScO_3$-$PbTiO_3$ (BSPT) [3,4]. The toxicity of lead, however, has raised health and environmental concerns and in the last two decades, Researchers efforts to find the suitable lead-free PZT alternative materials. The search for alternative piezoelectric materials is now focused on alkali niobates, and

CONTACT Surendra Singh jhinkwan.surendra@gmail.com.
© 2021 Taylor & Francis Group, LLC

modified alkali niobates, and systems in which an MPB occurs [5–8]. Among them, $(Na_{0.5}K_{0.5})NbO_3$ (NKN) has been considered a good candidate for lead-free piezoelectric ceramics because of its strong piezoelectricity and ferroelectricity. The hot pressed NKN ceramics (∼ 99% of the theoretical density) have been reported to possess a high Curie temperature (T_C, 420 °C), a large piezoelectric longitudinal response (d_{33}, 160 pC/N), and a high planar coupling coefficient (k_p, 45%) [9–12]. In spite of the significant focus on NKN-based ceramics and the successive wave of scientific publications, commercial realization of its piezoelectric properties has not been forthcoming due to the difficult processing of the material in the bulk ceramic form. The main problem of NKN ceramics synthesis is the difficulty in achieving high bulk density and reproducible electrical properties [13–16].

A number of studies have been carried out to improve the properties of NKN ceramics by ordinary processing; these include the formation of solid solutions of NKN with other ABO_3-type ferroelectrics or non-ferroelectrics, e.g., NKN-$LiNbO_3$ [17], NKN-$BaTiO_3$ [18], Li- and Ta-modified NKN [19,20], NKN-$Li(Nb,Ta,Sb)O_3$ [21], NKN-$LiSbO_3$ [22,23], NKN-$Bi_{0.5}Na_{0.5}TiO_3$ [24]. Most studies have been focused on modifying the system by doping various dopants [17–25] while keeping K/Na ratio of 50/50.

Present study was focused on the dielectric properties of $(Na_{0.5}K_{0.5})_{1-y}Li_yNbO_3$ ceramic pellets, with y = 0, 1, 2, 3, 4, 5, 6, and 7 (mole) %, composition Pellet samples were prepared by solid state reaction route using double sintering. XRD of the $(Na_{0.5}K_{0.5})_{1-y}Li_yNbO_3$ samples with y = 0, 1, 2, 3, 4, 5, 6, and 7 (mole) %, was carried out, in RT. Dielectric constant, dielectric loss and electrical conductivity of the prepared samples were measured in MIM configuration, at RT.

2. Methods

The preparation method of $(Na_{0.5}K_{0.5})_{1-y}Li_yNbO_3$ ceramic pellets, have been described in a previous communication [25]. XRD measurements of all the prepared samples were taken, at room temperature, by an X-ray diffractometer (PANalytical, X'PERT PRO), using Cu $K_{\alpha 1}$ radiation of wavelength 1.5405980 Å radiation, in a wide range of 2θ ($20^\circ < 2\theta < 70^\circ$) at a scanning rate of 6°/min. Sintered pellets were electroded, with air dryable conducting paste of silver, in metal- insulator- metal (MIM) configuration, for dielectric measurements. Dielectric constant (ε) and Electric conductivity (σ) of the prepared samples were measured, in MIM configuration, by RLC meter (Fluke, PM 6306), in the frequency range from 1 KHz to 1 MHz, at different temperatures.

3. Results and discussion

3.1. XRD Results

The observed XRD patterns of different prepared compositions of $(Na_{0.5}K_{0.5})_{1-y}Li_yNbO_3$ are shown in Fig. 1. The XRD patterns show polycrystalline behavior of the prepared samples, and have been found in good agreement with the Inorganic Crystal Structure Database – (ICSD) (00-061-0315) data of $Na_{0.5}K_{0.5}NbO_3$, for y = 0, 1, 2, 3, 4, and 5 (mole) %, while for samples y = 6 and 7 (mole) % have been found in good agreement with ICSD (00-060-0328) data of $K_{0.47}Na_{0.47}Li_{0.06}Nb_{0.94}Ta_{0.06}O_3$ with peaks

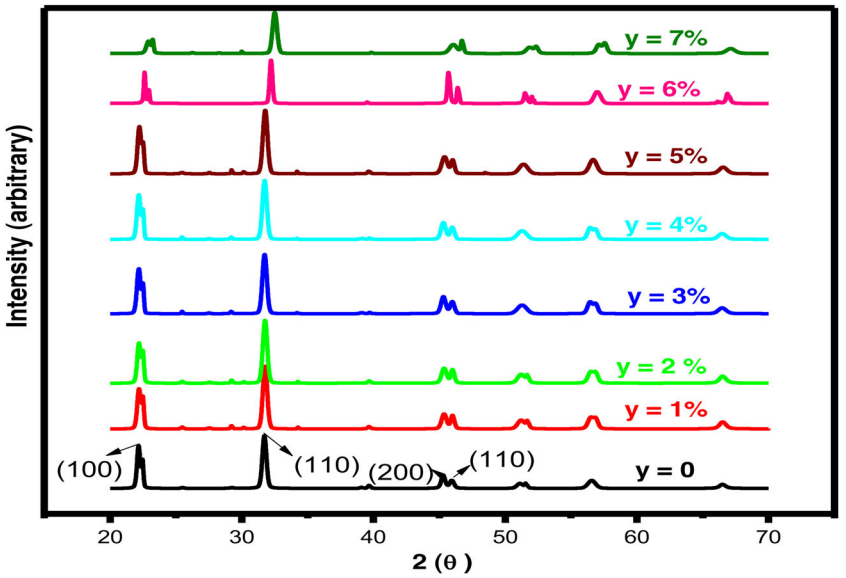

Figure 1. XRD patterns of $(Na_{0.5}K_{0.5})_{1-y}Li_yNbO_3$ $(0 \leq y \leq 0.07)$.

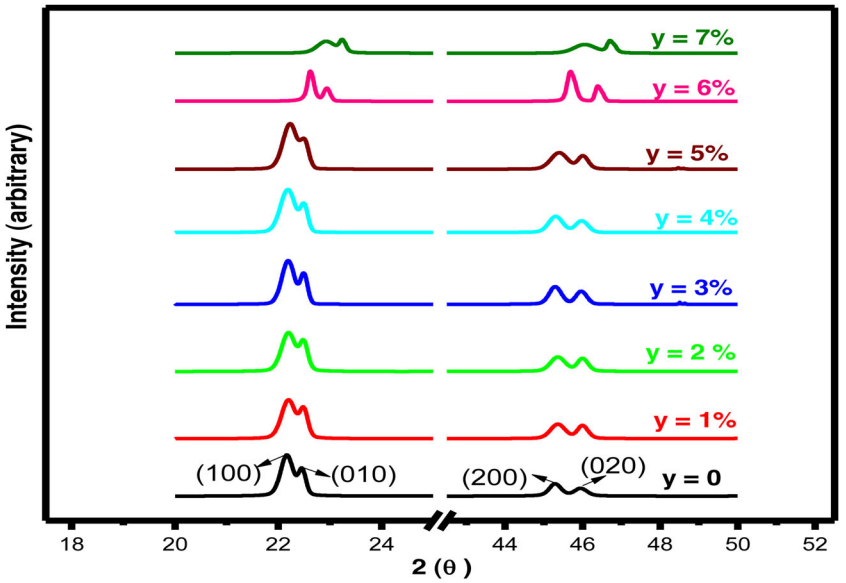

Figure 2. XRD patterns of $(Na_{0.5}K_{0.5})_{1-y}Li_yNbO_3$ $(0 \leq y \leq 0.07)$, Showing the peaks shifting tendency with y.

corresponding to (100), (010), (200), etc. In the observed composition range $(0 \leq y \leq 0.07)$, a continuous shifting of the most intense peaks, (100), (010), (200), and (020) was observed, with varying Lithium concentration (y value), Fig. 2. For compositions with $y \leq 0.06$, these peaks were observed shifting to higher angles with increasing y, showing a break in the peak shifting pattern at the composition with $y = 0.06$. Similar break in the peak shifting tendency has been reportedly observed, in $Na_{1-x}K_xNbO_3$, near

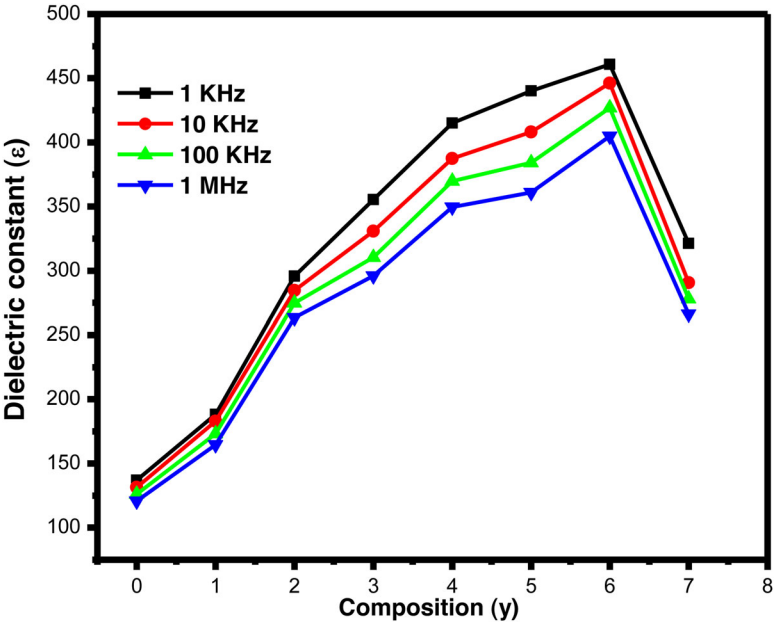

Figure 3. Variation of dielectric constant (ε) with composition (y), in $(Na_{0.5}K_{0.5})_{1-y}Li_yNbO_3$ ($0 \leq y \leq 0.07$), at room temperature.

$x = 0.175$, 0.32, 0.475, and 0.500 compositions [25–29]. After 5 (mole)% all peaks are shifted toward higher angles and for 7 (mole)% peaks (100), (010), (200), and (020) were observed inverted with respect to observed peaks in lower lithium concentration, which is indicates the structure change monoclinic to tetragonal. $Na_{0.5}K_{0.5}NbO_3$ has the perovskite structure with monoclinic symmetry [25]. $LiNbO_3$ however has the lithium niobate structure, which can be described as a heavily distorted perovskite [30] so it is evident that these effects on the structure of NKN ceramics have been observed in $(Na_{0.5}K_{0.5})_{1-y}Li_yNbO_3$ ceramics. At lower $LiNbO_3$ concentrations, Li mainly replaces Na and K in the A sites of ABO_3 perovskite structure (i.e., form a solid solution), leading to a linear shift of Curie point (T_C) to higher temperature. However, the structure of solid solution transforms from monoclinic to tetragonal symmetry due to the large distortion caused by Li^+. A multi-phase transition region was observed by Yan and Ren [31] with three phases, tetragonal, orthorhombic and rhombohedral, around room temperature at $0.65 \leq y \leq 0.8$. Yiping Guo et al. [17] shows a morphotropic phase boundary between orthorhombic and tetragonal phases is found at $0.05 \leq y \leq 0.07$.

3.2. Dielectric properties

The observed composition dependence of ε and σ, for different frequencies at RT, has been shown in Figs. 3 and 4. At all the applied frequencies, a remarkable maximum in ε and σ, at the composition with $y = 0.06$, indicates a strong feature- the morphotropic transition driven by the composition rather than frequency or temperature. Raevskii et al. [32] observed composition dependence of electrical conductivity and explained the

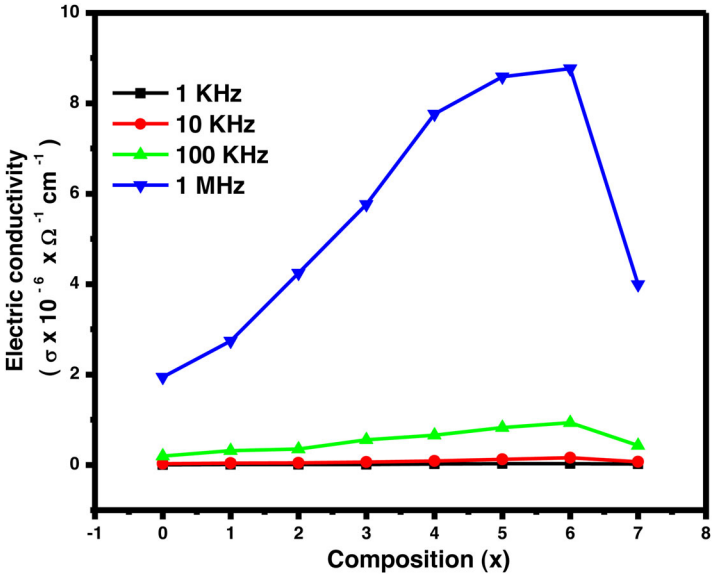

Figure 4. Variation of electric conductivity (σ) with composition (y), in $(Na_{0.5}K_{0.5})_{1-y}Li_yNbO_3$ ($0 \leq y \leq 0.07$), at room temperature.

MPT, for the compositions exhibiting maxima, in $(Na_{0.5}K_{0.5})_{1-y}Li_yNbO_3$. At 1 MHz, the observed composition ($0 \leq y \leq 0.07$) dependence of ε and σ, at different temperatures, has been shown in Figs. 5 and 6. With increasing temperature, in the measured range, ε and σ of all the prepared samples were found increasing. For all the measured temperatures, ε and σ increasing upto 6 (mole)% further decrease at 7 (mole)% ε and σ have maximum, indicates an MPT, for the ceramics with $y = 0.06$.

The observed composition ($0 \leq y \leq 0.07$) dependence of dielectric constant (ε), loss tangent (tan δ) and electric conductivity (σ) of $(Na_{0.5}K_{0.5})_{1-y}Li_yNbO_3$ ceramics, at room temperature (RT) and different frequencies has been given in Figs. 7–9. For all the prepared compositions, generally, ε and tan δ were observed decreasing and σ increasing, with increasing frequency. These observations are in good agreement with the earlier reported results [11,12,33,34]. Observed composition dependence of electrical conductivity and explained the MPT, for the compositions exhibiting maxima, in $(Na_{0.5}K_{0.5})_{1-y}Li_yNbO_3$. The composition dependent structural anomaly and the escape of alkali ions may be held responsible for the observed dielectric behavior of $(Na_{0.5}K_{0.5})_{1-y}Li_yNbO_3$ ($0 \leq y \leq 0.07$) system. Because of the increased presence of non-ferroelectric low permittivity grain boundaries dielectric constant, generally, decreases with decreasing grain size [35]. The loss decreases due to the reduction in the number of grain boundaries with increasing grain size. Moreover, the interplay of porosity, grain size, liquid phase presence, ordering, etc. may be held responsible for the observed dielectric behavior in these perovskite ceramics.

The ABO_3 perovskites may have two major defects, *viz.*, A-site, and O-site vacancies [36], and there is no concrete evidence of vacancies reported at B-site. Electrical properties are significantly affected by the presence of these vacancies [25–29]. With isovalent substitution of Li at Na/K site, at room temperature, resulting increased effective

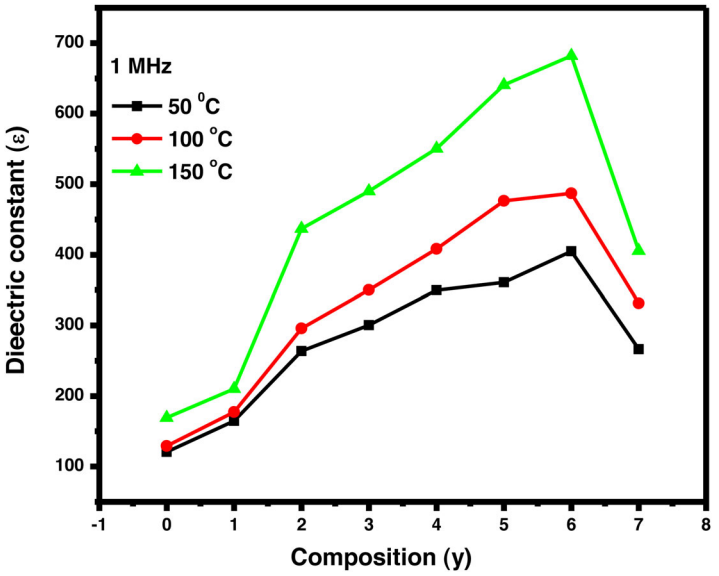

Figure 5. Variation of dielectric constant (ε) with composition (y), in $(Na_{0.5}K_{0.5})_{1-y}Li_yNbO_3$, at different temperatures.

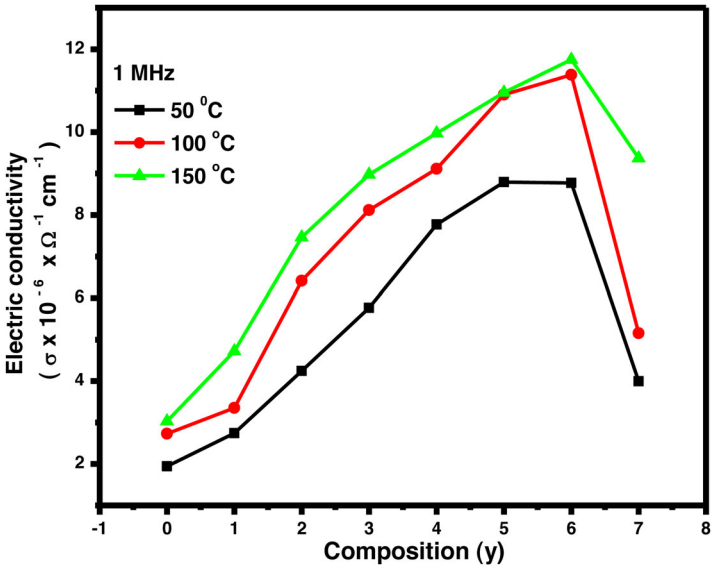

Figure 6. Variation of Electric conductivity (σ) with composition (x), in $(Na_{0.5}K_{0.5})_{1-y}Li_yNbO_3$, at different temperatures.

polarization and thereby increases in conductivity, in general, however, near MR it is observed markedly high. In these oxides the conduction process may be explained on the basis of the majority of acceptor or donor concentration. Due to the deficiency of electron the A-site vacancy contributes 'hole', and due to the excess of electrons the O-site vacancy contributes extra electrons for conduction in the solid. In that way if there are only A-site vacancies, the solid should show p-type behavior, or if there are

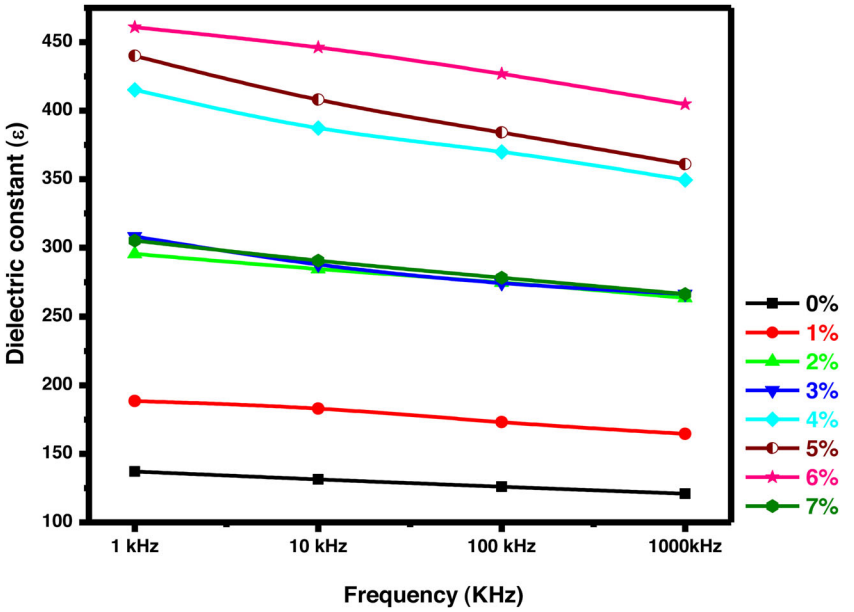

Figure 7. Variation of dielectric constant (ε) with frequency, in $(Na_{0.5}K_{0.5})_{1-y}Li_yNbO_3$ $(0 \leq y \leq 0.07)$.

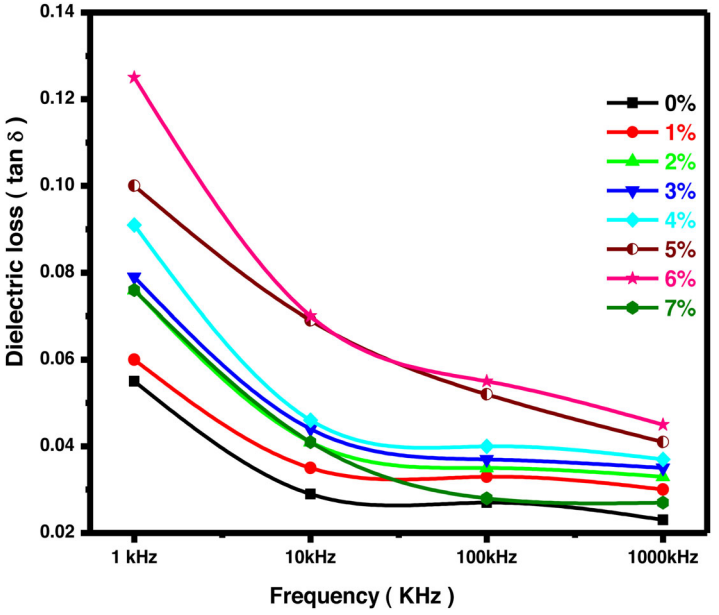

Figure 8. Variation of dielectric loss (tan δ) with frequency, in $(Na_{0.5}K_{0.5})_{1-y}Li_yNbO_3$ $(0 \leq y \leq 0.07)$.

only O-site vacancies it should behave as n-type. Majority of A- or O-site vacancies decides the majority of charge carriers, and thereby the p- or n-type nature of the conduction. The alkali ions escaping were observed significantly higher than oxygen escaping [25]. Due to the excess of the vacancies at A-site than that at O-site, p-type conduction is envisaged in the present $(Na_{0.5}K_{0.5})_{1-y}Li_yNbO_3$ compositions. The A-site

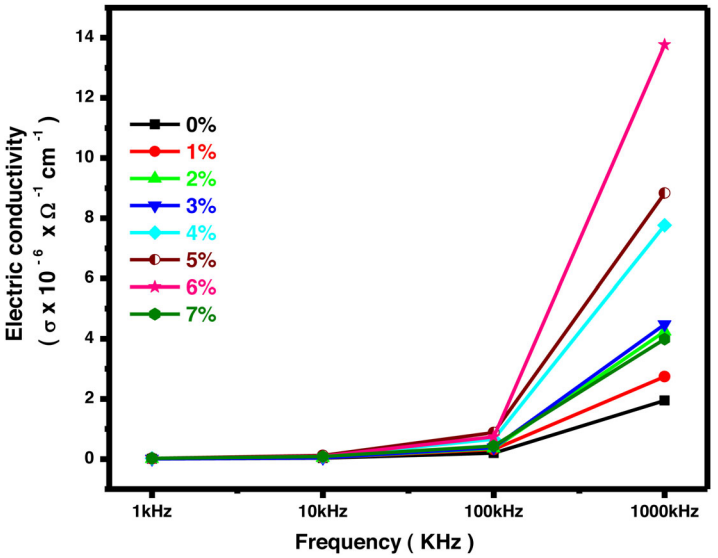

Figure 9. Variation of Electric conductivity (σ) with frequency, in $(Na_{0.5}K_{0.5})_{1-y}Li_yNbO_3$ ($0 \leq y \leq 0.07$).

vacancy attracts electron and acts as acceptor, and due to the electron deficiency the A-site vacancy behaves as 'hole' in the lattice. Due to the less escaping of the alkali ions less number of 'holes' will be available for conduction, resulting lower conductivity in the compositions with $x = 0.500$, than other compositions. The p- type conductivity is reportedly observed in many oxides, viz., $Pb(Ti, Zr)O_3$, ZrO_2, etc. [37] where 'superoxidation', i.e., excess of A-site vacancies over the O-site vacancies, is more probable.

4. Conclusion

Presently, with a decrease in A-site vacancy concentration for the composition, near MR with $y = 0.06$, a distinct conductivity maximum was observed, which agrees with the above given supposition. For the composition near MR, it seems that during sintering of the samples the intensification of diffusion processes remarkably reduces the possibility of escape of highly volatile alkali metal ions from the lattice. The properties of ceramics depend on the preparation process, and are subject to systematic and statistical fluctuations in the samples of a given batch. These fluctuations may be due to inhomogeneity in microchemistry, mechanical differences in the forming process, chemical modification and varying shrinkage at the time of sintering.

The reported and present observations show that preparation process, composition and structure greatly influence the electrical behavior of the ceramics. Structural anomaly may be attributed to the observed highest values of the dielectric constant and electric conductivity of the composition with $y = 0.06$, among the prepared compositions, which indicates that the occurrence of morphotropic phase boundary (MPB).

ORCID

Surendra Singh http://orcid.org/0000-0002-2958-4594

References

[1] J. B. Goodenough, Electronic and ionic transport properties and other physical aspects of perovskites, *Rep. Prog. Phys.* **67** (11), 1915 (2004). DOI: 10.1088/0034-4885/67/11/R01.

[2] J. Rödel *et al.*, Perspective on the development of lead-free piezoceramics, *J. Am. Ceram. Soc.* **92** (6), 1153 (2009). DOI: 10.1111/j.1551-2916.2009.03061.x.

[3] J. Kuwata, K. Uchino, and S. Nomura, Dielectric and piezoelectric properties of $0.91Pb(Zn_{1/3}Nb_{2/3})O_3$-$0.09PbTiO_3$ single crystals, *Jpn. J. Appl. Phys.* **21** (Part 1, No. 9), 1298 (1982). DOI: 10.1143/JJAP.21.1298.

[4] S. E. Park and T. R. Shrout, Ultrahigh strain and piezoelectric behavior in relaxor based ferroelectric single crystals, *J. Appl. Phys.* **82** (4), 1804 (1997). DOI: 10.1063/1.365983.

[5] Y.-M. Chiang, G. W. Farrey, and A. N. Soukhojak, Lead-free high-strain single-crystal piezoelectrics in the alkaline–bismuth–titanate perovskite family, *Appl. Phys. Lett.* **73** (25), 3683 (1998). DOI: 10.1063/1.122862.

[6] B. Chu *et al.*, Electrical properties of $Na_{1/2}Bi_{1/2}TiO_3$–$BaTiO_3$ ceramics, *J. Eur. Ceram. Soc.* **22** (13), 2115 (2002). DOI: 10.1016/S0955-2219(02)00027-4.

[7] S.-E. Park, S.-J. Chung, and I.-T. Kim, Ferroic phase transitions in $(Na_{1/2}Bi_{1/2})TiO_3$ crystals, *J. Am. Ceram. Soc.* **79** (5), 1290 (1996). DOI: 10.1111/j.1151-2916.1996.tb08586.x.

[8] K. Kakimoto, I. Masuda, and H. Ohsato, Ferroelectric and piezoelectric properties of $KNbO_3$ ceramics containing small amounts of $LaFeO_3$, *Jpn. J. Appl. Phys.* **42** (Part 1, No. 9B), 6102 (2003). DOI: 10.1143/JJAP.42.6102.

[9] G. Shirane, R. Newnham, and R. Pepinsky, Dielectric properties and phase transitions of $NaNbO_3$ and $(Na,K)NbO_3$, *Phys. Rev.* **96** (3), 581 (1954). DOI: 10.1103/PhysRev.96.581.

[10] L. Egerton and D. M. Dillon, Piezoelectric and dielectric properties of ceramics in the system potassium-sodium niobate, *J. Am. Ceram. Soc.* **42** (9), 438 (1959). DOI: 10.1111/j.1151-2916.1959.tb12971.x.

[11] R. E. Jaeger and L. Egerton, Hot pressing of potassium-sodium niobates, *J. Am. Ceram. Soc.* **45** (5), 209 (1962). DOI: 10.1111/j.1151-2916.1962.tb11127.x.

[12] G. H. Haertling, Properties of hot-pressed ferroelectric alkali niobate ceramics, *J. Am. Ceram. Soc.* **50** (6), 329 (1967). DOI: 10.1111/j.1151-2916.1967.tb15121.x.

[13] B. Malic *et al.*, Sintering of lead-free piezoelectric sodium potassium niobate ceramics, *Materials* **8** (12), 8117 (2015). DOI: 10.3390/ma8125449.

[14] I. Coondoo, N. Panwar, and A. Kholkin, Lead-free piezoelectrics: current status and perspectives, *J. Adv. Dielect.* **03** (02), 1330002 (2013). DOI: 10.1142/S2010135X13300028.

[15] D. W. Baker *et al.*, Comprehensive study of the phase diagram of $K_xNa_{1-x}NbO_3$, *Appl. Phys. Lett.* **95** (9), 091903 (2009). DOI: 10.1063/1.3212861.

[16] L. Wu *et al.*, Influence of compositional ratio K/Na on physical properties in $(K_xNa_{1-x})NbO_3$ ceramics, *J. Appl. Phys.* **103** (8), 084116 (2008). DOI: 10.1063/1.2907866.

[17] Y. Guo, K. Kakimoto, and H. Ohsato, Phase transitional behavior and piezoelectric properties of $(Na_{0.5}K_{0.5})NbO_3$–$LiNbO_3$ ceramics, *Appl. Phys. Lett.* **85** (18), 4121 (2004). DOI: 10.1063/1.1813636.

[18] H. Y. Park *et al.*, Microstructure and piezoelectric properties of $0.95(Na_{0.5}K_{0.5})NbO_3$–$0.05BaTiO_3$ ceramics, *Appl. Phys. Lett.* **89** (6), 062906 (2006). DOI: 10.1063/1.2335816.

[19] E. Hollenstein *et al.*, Piezoelectric properties of Li- and Ta-modified $(K_{0.5}Na_{0.5})NbO_3$, *Appl. Phys. Lett.* **87** (18), 182905 (2005). DOI: 10.1063/1.2123387.

[20] Y. Dai, X. Zhang, and G. Zhou, Phase transitional behavior in $K_{0.5}Na_{0.5}NbO_3$–$LiTaO_3$ ceramics, *Appl. Phys. Lett.* **90** (26), 262903 (2007). DOI: 10.1063/1.2751607.

[21] Y. Saito *et al.*, Lead-free piezoceramics, *Nature* **432** (7013), 84 (2004). DOI: 10.1038/nature03028.

[22] G. Z. Zang *et al.*, Perovskite $(Na_{0.5}K_{0.5})_{1-}x(LiSb)_xNb_{1-x}O_3$ lead-free piezoceramics, *Appl. Phys. Lett.* **88** (21), 212908 (2006). DOI: 10.1063/1.2206554.

[23] S. Zhang *et al.*, Piezoelectric properties in perovskite $0.948(K_{0.5}Na_{0.5})NbO_3$–$0.052LiSbO_3$ lead-free ceramics, *J. Appl. Phys.* **100** (10), 104108 (2006). DOI: 10.1063/1.2382348.

[24] S. Zhang *et al.*, Characterization of lead free $(K_{0.5}Na_{0.5})NbO_3$–$LiSbO_3$ piezoceramic, *Solid State Commun.* **141** (12), 675 (2007). DOI: 10.1016/j.ssc.2007.01.007.
[25] S. Singh, J. Negi, and N. S. Panwar, Dielectric properties of $Na_{1-x}K_xNbO_3$, near x = 0.5 morphotropic phase region, *J. Phys. Chem. Solids* **123**, 311 (2018). DOI: 10.1016/j.jpcs.2018.08.018.
[26] J. Negi, S. Singh, and N. S. Panwar, Structural and dielectric anomaly in $Na_{1-X}K_xNbO_3$, at x = 0.315, *Phase Transit.*, **92** (2), 149 (2019). DOI: 10.1080/01411594.2018.1563789.
[27] S. Singh, J. Negi, and N. S. Panwar, Temperature dependent dielectric properties of (Na, K) NbO_3, near equimolar composition, *Ceram. Int.* **45** (10), 13067 (2019). DOI: 10.1016/j.ceramint.2019.03.238.
[28] A. S. Kandari, V. Lingwal, and N. S. Panwar, Morphotropic phase boundary in Na1-xKxNbO3, near x = 0.32, *Solid State Commun.*, **150** (1-2), 74 (2010). DOI: 10.1016/j.ssc.2009.10.002.[ ]
[29] A. S. Kandari *et al.*, Composition dependent dielectric anomaly in $Na_{1-x}K_xNbO_3$, at x = 0.475, *Ferroelectrics* **393** (1), 121 (2009). DOI: 10.1080/00150190903413190.
[30] E. A. Wood, Polymorphism in potassium niobate, sodium niobate, and other ABO_3 compounds, *Acta Cryst.* **4** (4), 353 (1951). DOI: 10.1107/S0365110X51001112.
[31] K. Yan, and X. Ren, Multi-phase transition behaviour and large electrostrain in lead-free (K, Na, Li)NbO_3 ceramics, *J. Phys. D Appl. Phys.* **47** (1), 015309 (2014). DOI: 10.1088/0022-3727/47/1/015309.
[32] I. P. Raevskii, L. A. Reznichenko, and O. I. Prokopalo, Phase-transition and electrical-properties of ferroelectric sodium niobate-based solid-solutions, *Izv. Akad. Nauk SSSR* **15**, 872 (1979).
[33] S. Narayana Murty, K. Umakantham, and A. Bhanumathi, Ferroelectric behaviour of lanthanum doped (NaK)$Nb0_3$ ceramics, *Ferroelectrics* **82** (1), 141 (1988). DOI: 10.1080/00150198808201348.
[34] L. E. Cross, Electric double hysteresis in $(K_xNa_{1-x})NbO_3$ single crystals, *Nature* **181** (4603), 178 (1958). DOI: 10.1038/181178a0.
[35] M. H. Frey *et al.*, The role of interfaces on an apparent grain size effeect on the dielectric properties for ferroelectric barium titanate ceramics, *Ferroelectrics* **206** (1), 337 (1998). DOI: 10.1080/00150199808009168.
[36] B. Jaffe, W. R. Cook, and J. H. Jaffe, *Piezoelectric Ceramics* (Academic, New York, 1971).
[37] J. Z. Rudolph, About the conduction mechanism of oxidic semiconductors at high temperatures, *Naturforsch* **14a**, 727 (1959).

ECS Journal of Solid State Science and Technology, 2021 **10** 033002
2162-8777/2021/10(3)/033002/7/$40.00 © 2021 The Electrochemical Society ("ECS"). Published on behalf of ECS by IOP Publishing Limited

Composition Dependent Electrical Properties of $(Ba_{1-x}CaxZr_{0.1}Ti_{0.9})O_3$ Ceramics, Near Morphotropic Phase Boundary ($0.140 \leqslant x \leqslant 0.160$)

Don Biswas,[1,z] Prolay Sharma,[2] and N. S. Panwar[1]

[1]*Instrumentation Engg.-USIC. H. N. B. Garhwal University, Srinagar—246174, India*
[2]*Instrumentation and Electronics Engg. Jadavpur University, Kolkata, India*

In this work, pellet samples of $(Ba_{1-x}Ca_xZr_{0.1}Ti_{0.9})O_3$, $(0.140 \leqslant x \leqslant 0.160)$ were prepared using solid-state reaction route with double sintering. The dielectric and structural properties of the prepared samples were measured, from room temperature to 250 °C, at different frequencies, in the range 10–1000 KHz. A peak shifting anomaly in the X-ray diffraction peaks patterns, an anomalous change in the slope of c/a *vs* x plot, and the observed minimum values of dielectric constant, loss and conductivity of the prepared compositions show a strong compositional dependent dielectric and structural properties, indicating a morphotropic phase transition type behavior, at the composition with $x = 0.150$.
© 2021 The Electrochemical Society ("ECS"). Published on behalf of ECS by IOP Publishing Limited. [DOI: 10.1149/2162-8777/abea61]

Manuscript submitted December 25, 2020; revised manuscript received February 24, 2021. Published March 10, 2021.

Supplementary material for this article is available online

Perovskite ABO_3 type ferroelectric compounds are technologically important and show significant electrical and optical properties.[1] A series of binary and tertiary perovskite solutions can be prepared by replacing A-and or B-site atoms, with compatible valence and tolerance. Among these ferroelectric materials, barium calcium zirconate titanate (BCZT) based system may have the significant potential to replace lead-based ceramics used in various dielectric and ferroelectric devices.[2–4] Solid solutions of $(Ba_{1-x}Ca_xZr_yTi_{1-y})O_3$ (BCZT) system may be produced for all values of x and y (x, y = 0 to 1), permitting a great extent of tailorability in dielectric and piezoelectric properties. Ba can be replaced by Ca, and Ti with Zr, in the BCZT system, to form binary solid solutions. In the solid solutions of perovskite type compounds, a composition-dependent transition in physical properties is termed as a morphotropic phase boundary (MPB),[5] which shows an irregular change in lattice parameters with extremal physical properties.[6] The extremal physical properties, near the MPB, have significant technological potential.[7,8] Due to the symmetry-allowed polarization extension, the large electromechanical response has been associated to the MPB.[9–11] Jaffe et al.[12] observed the anomaly in the dielectric and piezoelectric properties in lead zirconate titanate (PZT) ceramics, near the MPB, which appeared due to the separation of the tetragonal and rhombohedral phases across the MPB. The morphotropic phase region contained mixed tetragonal and rhombohedral phases. The tetragonal and rhombohedral structures have 6 and 8 possible polarization directions, respectively. Therefore, a morphotropic phase boundary, consisting of both phases, has 14 possible polarization directions, resulting in large contribution towards electromechanical coupling factor (k_s) and extremal remanent polarization.[13] An extermal dielectric constant may be associated with the extremal remanent polarization, near MPB.

For $(Ba_{1-x}Ca_xZr_{0.1}Ti_{0.9})O_3$ ceramics, the orthorhombic to tetragonal (O-T) phase transition point ($T_{O-T} \sim 125°$) was reportedly found shifting towards lower temperature with the increase in x, from 0.140 to 0.160.[14] With a variation in Ba/Ca ratio, the composition-dependent behavior of electrical properties suggested the existence of a typical MPB, in $(Ba_{1-x}Ca_xZr_{0.1}Ti_{0.9})O_3$ ceramics, near $x = 0.150$.[14] The reported anomalous dielectric behavior was found composition dependent rather than temperature and frequency, in $(Ba_{1-x}Ca_xZr_{0.1}Ti_{0.9})O_3$, near $x = 0.150$.[15] In MPB region, the factors like polarization extension, polarization rotation, and elastic softening of lattice significantly contribute to the dielectric properties BCZT ceramics, near MPB.[14,16] Mondal et al.[15] observed increased resistivity with the substitution of Ba by Ca in BCZT compounds. A decrease in the mobility of the charge carriers was observed, which attributed to the lattice distortion in BCZT $(Ba_{1-x}Ca_xZr_{0.1}Ti_{0.9})O_3$ ceramics, at $x = 0.150$. An anomalous peak shifting in X-ray diffraction patterns have been reported close to the MPT (Morphotropic phase transition) region.[17] The dielectric and structural properties of $Ba_{1-x}Ca_xTiO_3$- $BaZr_yTi_{1-y}O_3$ (BCT-BZT) system have been explored by Tuan et al., near MPB.[18] Hanani et al.[19] reported enhanced dielectric properties of $(Ba_{1-x}Ca_xZr_{0.1}Ti_{0.9})O_3$ ceramics, at $x = 0.150$. Considerable enhancement in electrical properties with longer sintering time has been reported in this system.[20–22] The reportedly observed enhanced dielectric and piezoelectric properties of the BCZT system, near MPB, have been associated to the coexistence of two different phases.[23–25] The dielectric constant and electrical conductivity were reportedly found extremal, in the $(Na,K)(Nb,Ta)O_3$ system, near MPB.[17,26,27]

The electrical properties of the perovskite materials significantly altered with the change in the preparation conditions and compositions of solid solution systems. In MPB, the separation of two different ferroelectric phases with different lattice parameters may result significant enhancement of electrical properties.[28,29] From the composition-property diagram of solid solution systems, at morphotropic phase boundary (MPB), the ferro-composition has two-or more phases and has extremal electro-physical properties.[16,30–33] The width of the coexistence region has been also associated to the particle size[34] and depends on the processing conditions. On change of composition, MPT exhibits anomalous dielectric and piezoelectric properties.[17]

In the present study, ceramic samples of $(Ba_{1-x}Ca_xZr_{0.1}Ti_{0.9})O_3$ were prepared, near the morphotropic phase boundary, $(0.140 \leqslant x \leqslant 0.160)$, using the solid-state reaction route with double sintering,. The dielectric constant (ε), loss tangent (tan δ), and electric conductivity (σ) of the prepared composition samples were measured at 10, 100 and 1000 KHz. X-ray diffraction (XRD) and scanning electron microscopy (SEM) measurements of the prepared compositions were carried out at room temperature (RT). The observed composition dependent dielectric behavior of the prepared pellet samples is presented.

Experimental

In this study, high purity (>99.5%) powders of barium carbonate ($BaCO_3$), calcium carbonate ($CaCO_3$), titanium oxide (TiO_2) and zirconium oxide (ZrO_2) were used as raw materials. The compositions of BCZT ceramics were prepared using solid-state reaction route with double sintering.[35] The dissolved moisture was removed

[z]E-mail: donusic06@gmail.com

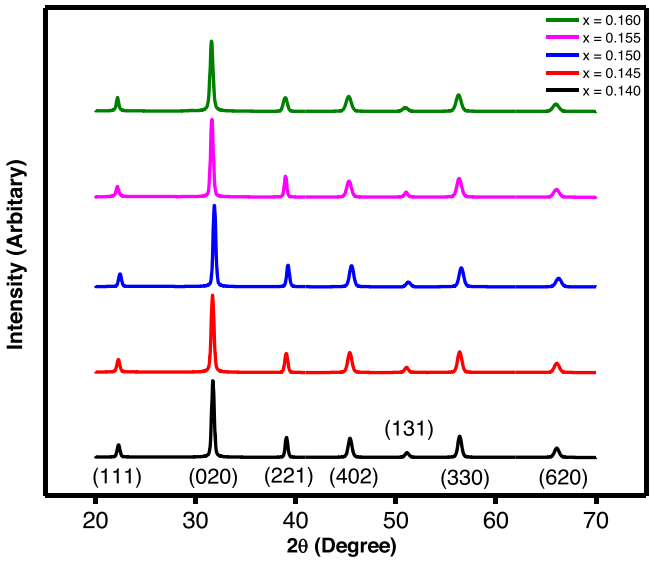

Figure 1. XRD patterns of $(Ba_{1-x}Ca_xZr_{0.1}Ti_{0.9})O_3$, $(0.140 \leqslant x \leqslant 0.160)$ powder samples, at RT.

from the raw powders by drying them in an oven, at 200 °C for 2 h, and then the dried powders were weighed in the stoichiometric ratio to prepare the desired $(Ba_{1-x}Ca_xZr_{0.1}Ti_{0.9})O_3$, $(0.140 \leqslant x \leqslant 0.160)$ compositions. The mixture was manually dry mixed and ground for 4 h, and then with methanol for another 2 h. The agate mullet mortar and pestle were used for grinding. The mixed ground powder was calcined in the ambient air at 1100 °C, in the alumina crucible, to remove carbon dioxide. The calcined power was taken out from the furnace when it cooled to room temperature. The calcined power was weighed to check complete carbon dioxide removal. The calcined power was pressed into pellets with the longitudinal pressure of 0.2 GPa. The pellets of the prepared compositions were sintered at 1300 °C, for 4 h. The sintered pellets were crushed and ground further into powder. This ground powder was further pressed into pellets (8 mm dia, ∼ 2 mm thick), at 0.2 GPa. These pellets were further sintered at 1300 °C, for 4 h. The BCZT ceramic samples reportedly show maximum density when double sintered at 1300 °C.[36,37]

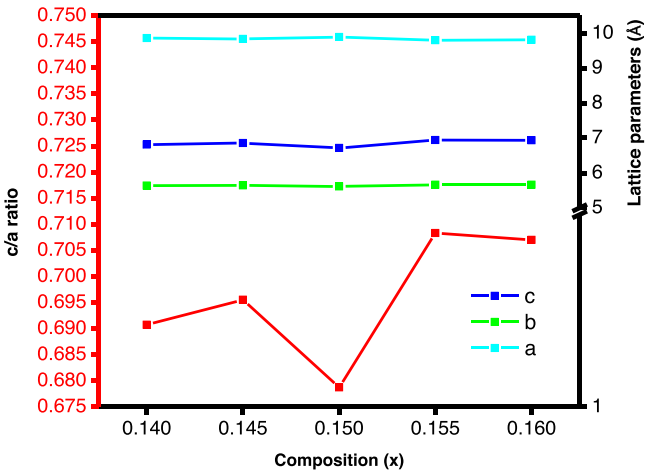

Figure 3. Lattice parameters and c/a (ratio of lattice parameters, c and (a) change with composition (x), in $(Ba_{1-x}Ca_xZr_{0.1}Ti_{0.9})O_3$, $(0.140 \leqslant x \leqslant 0.160)$ ceramics.

The XRD patterns of all prepared powder samples were measured, at room temperature (RT), with the help of PANalytical PW340 X-ray diffractometer, having a wavelength 1.54060 A. The XRD data was taken at a scan speed of 0.3 s per step with the step size of 0.025°. For all the prepared ceramics, the dielectric properties (ε, tan δ, and σ) were observed, near the MPB region $(0.160 \leqslant x \leqslant 0.200)$. For dielectric measurements, specimens were electroded, with conducting silver paste, in a metal-insulator-metal (MIM) configuration. With RLC meter (PM 6306, Fluke), the dielectric measurements were carried out with increasing temperature, from RT to 250 °C, and in the frequency range from 1 to 1000 KHz. SEM images were observed to study surface morphology and grain size using EVO 18 Special Edition (CARL ZEISS).

Results and Discussion

XRD measurements.—The observed room temperature XRD patterns of the prepared $(Ba_{1-x}Ca_xZr_{0.1}Ti_{0.9})O_3$, $(0.140 \leqslant x \leqslant 0.160)$ pellet samples have been given in Figs. 1–2. The XRD patterns show perovskite structure of the prepared BCZT compositions with orthorhombic symmetry. The observed XRD data are consistent with the Inorganic Crystal Structure Database (ICSD)—

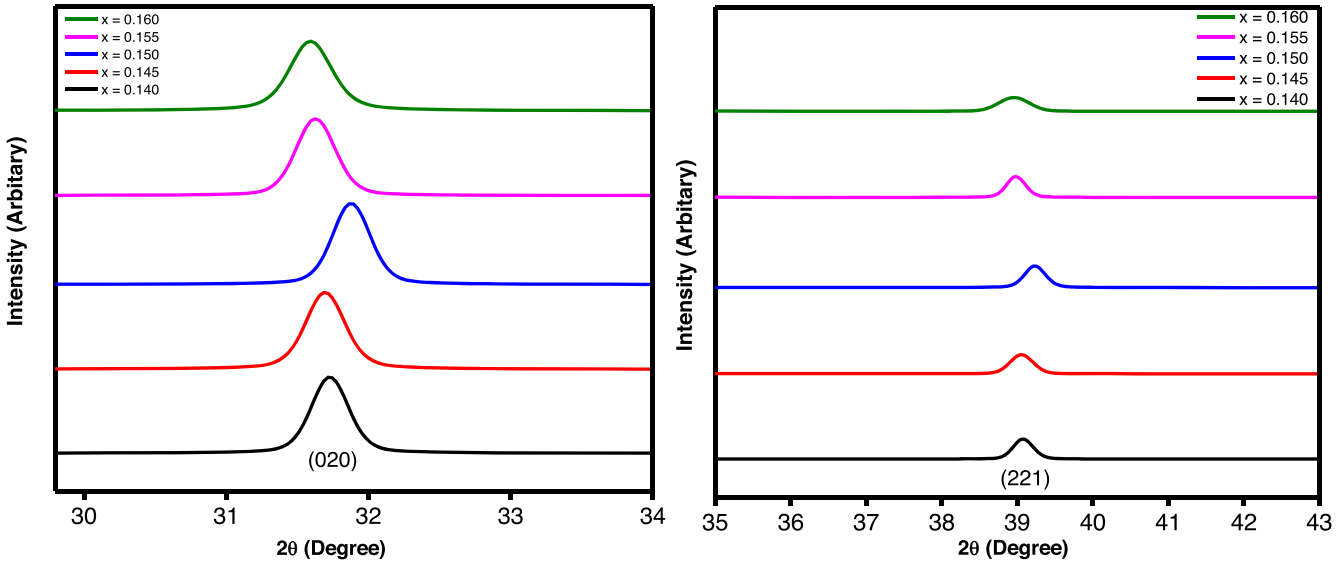

Figure 2. XRD patterns of $(Ba_{1-x}Ca_xZr_{0.1}Ti_{0.9})O_3$, $(0.140 \leqslant x \leqslant 0.160)$ powder samples, at RT, showing break in peaks shifting tendency, at x = 0.150 composition.

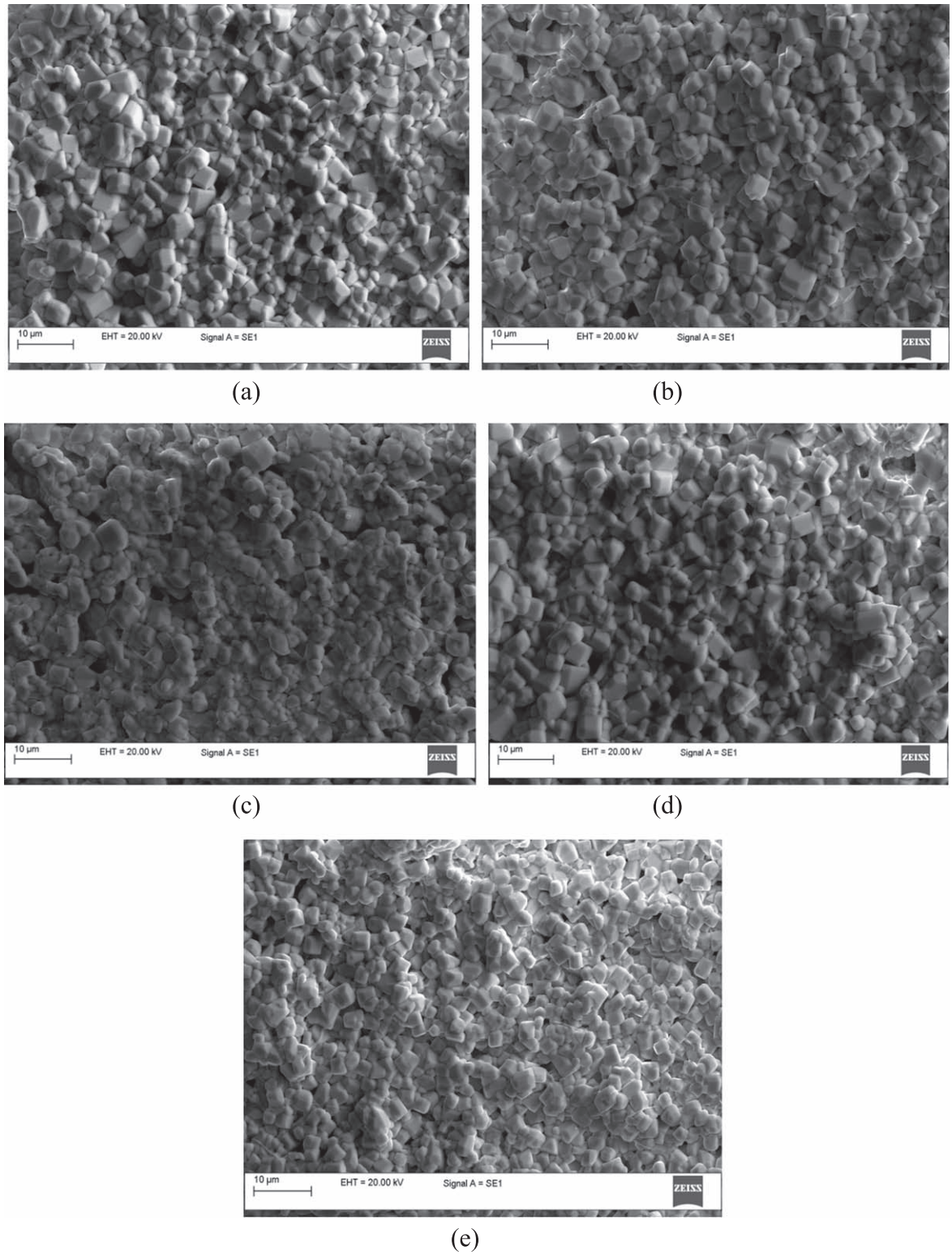

Figure 4. SEM images of $(Ba_{1-x}Ca_xZr_{0.1}Ti_{0.9})O_3$, for x = 0.140 (a), 0.145 (b), 0.150 (c), 0.155 (d), 0.160 (e).

(code 00–056–1033) records of $(Ba_{1-x}Ca_xZr_{0.1}Ti_{0.9})O_3$, with peaks corresponding to (020), (221), (402), and (330), etc.[38]

Among the prepared compositions, a continuous peak shifting was observed, in the most intense peaks (020), (221), (402), and (330), with the increment in the value of calcium concentration (x). In the XRD patterns of BCZT ceramics, the most intense peaks were observed shifting to a lower angle with increasing x, except for the composition with x = 0.150, where the peaks moved to the higher angle, indicating anomalous structural behavior at this composition-a break was noticed in the peak shifting tendency. A similar tendency was also observed by other workers.[17,26,27] The lattice parameters were calculated from the observed XRD data. The variation of lattice parameters (a, b, and c), and c/a ratio with composition (x), has been given in Fig. 3. The slope of the c/a *vs* x graph changed, from negative to positive, at the composition with x = 0.150, which indicates a structural abnormality, at this

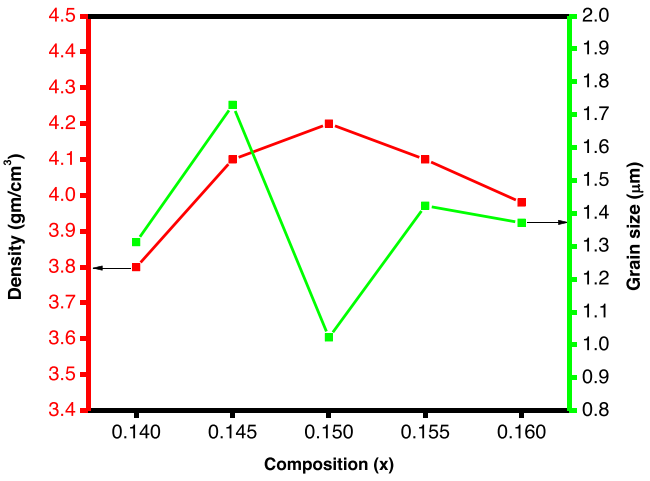

Figure 5. Composition (x) variation of grain size and density, in $(Ba_{1-x}Ca_xZr_{0.1}Ti_{0.9})O_3$, $(0.140 \leqslant x \leqslant 0.160)$.

composition-a composition dependent behavior, an MPB region. Sen et al. have reported change in the lattice parameters with the varying composition (x), in $(Ba_{1-x}Ca_xZr_{0.1}Ti_{0.9})O_3$ ceramics.[38] A similar break in the peaks shifting tendency has been reportedly observed in $Na_{1-x}K_xNbO_3$, near x = 0.17, 0.32, and 0.50 compositions.[17,26,27]

SEM measurements.—The SEM images of the prepared pellet samples of $(Ba_{1-x}Ca_xZr_{0.1}Ti_{0.9})O_3$, $(0.140 \leqslant x \leqslant 0.160)$ have been shown in Fig. 4. All the samples were found homogeneous and fine-grained. The average grain size of the prepared BCZT ceramics was determined by dividing the across length of the SEM photograph in terms of the scale by the numbers of grains in that length. Density of the sintered pellets was measured using Archimedes method. Generally, density of the pellets was found proportionally varying with grain size; except for the composition with x = 0.150, where the density was found maximum and grain size minimum, among the prepared compositions, Fig. 5. The grain size and density significantly influence the dielectric properties of ceramics.[39,40]

During the sintering process, the mechanism of densification and grain growth needs material transportation and that may happen via grain boundary diffusion, lattice diffusion, surface diffusion, evaporation, and viscous flow.[41] A two-stage sintering method was chosen to achieve the densification of ceramic bodies without significant grain growth.[42] Ceramics of intermediate density and fine grain size have been reported for perovskite compounds, like $BaTiO_3$, using two-stage sintering method.[43,44] The double sintered ceramic samples show a significant increase in dielectric constant than those prepared with usual single sintering. The double sintering is a simple and cost-effective method to obtain higher density materials with controlled grain growth without adding any dopants. Sintering significantly affects the densification of ceramics and thereby their dielectric properties.[45] The double sintering process was applied in the present study to improve the density of the ceramics inhibiting grain growth. It triggers different sintering mechanisms in different temperature ranges. After the first sintering (at 1300 °C) pellets with poor density with developed cracks were obtained. The minimum activation energy of surface diffusion exhibits excessive grain growth during the start of the sintering process, which triggers grain coarsening, and the total surface area reduces because of larger grains. The driving force is the observed change in surface area. Moreover, due to early grain growth, the reduced driving force appears before the composition enters the main sintering process.[46,47] Once that coarsening occurs, the pore removal becomes quite difficult, resulting in poor densification, in the single sintering. The double sintering was chosen to activate different sintering mechanisms in different temperature ranges, and to suppress grain growth and improve densification. After the second stage sintering the present pellet samples were hard enough with improved density.

The material grain growth, free surfaces, the reaction of grain boundaries, and the change in lattice may be significantly altered with the function of sintering and the involvement of different mechanisms. For every diffusing species, whether it is volatile or non-volatile, are ions of different charges and responsible for contributing different diffusion rates. Different diffusing species or ions may have different vapor pressures, diffusion paths, and different diffusion rates, and their collective effort greatly alters the measured density and grain size of prepared compositions.

The EDAX results show considerable escaping of alkaline metal (Ba and Ca) ions from the prepared compositions of BCZT $(Ba_{1-x}Ca_xZr_{0.1}Ti_{0.9})O_3$, $(0.140 \leqslant x \leqslant 0.160)$ ceramics, with a lowest for the compositions with x = 0.150, Table I. The EDAX analysis show more escaping of calcium (Ca) than barium (Ba), which may be due to the higher equilibrium vapor pressure of the former.[48] A small variation in the stoichiometry triggers a sensitive effect in the density, grain size, and morphology of BCZT ceramics.[49]

Dielectric measurements.—At RT, the observed composition dependence $(0.140 \leqslant x \leqslant 0.160)$ of dielectric properties (ε, tan δ, and σ) of $(Ba_{1-x}Ca_xZr_{0.1}Ti_{0.9})O_3$ ceramics, at different frequencies, has been shown in Figs. 6a–6c. With the increase in frequency, normally, ε and tan δ were found decreasing, and σ increasing, for the prepared compositions. These observations are in consistency with the previous publications.[17,26,27,35] Figures 7–8 show the measured composition dependence $(0.140 \leqslant x \leqslant 0.160)$ of ε, tan δ, and σ of BCZT ceramics, at different temperatures, at 1 MHz. With the increase in temperature, the dielectric constant (ε) was found increasing, and dielectric conductivity (σ) and loss tangent (tan δ) decreasing, for all the prepared compositions. Among the prepared compositions, an irregular decrease was found in the dielectric properties, near MPB, with anomalously lower values of ε, tan δ, and σ, at x = 0.150. The measured composition $(0.140 \leqslant x \leqslant 0.160)$ dependence of ε, tan δ, and σ, at different frequencies with RT, has been given in Figs. 9–10. A drastic change was observed in the dielectric properties (ε, tan δ, and σ) at x = 0.150, at all the measured frequencies. Figures 7–10 show that the dielectric properties of the BCZT are significantly composition dependent. A drastic minimum in the dielectric properties (ε, tan δ, and σ), shows a typical morphotropic phase transition type behavior, at the compositions with x = 0.150, which is composition dependent rather than

Table I. EDAX results of the prepared $(Ba_{1-x}Ca_xZr_{0.1}Ti_{0.9})O_3$, $(0.140 \leqslant x \leqslant 0.160)$ compositions.

	Atomic % (Measured)				Atomic % (Calculated)				Escaping of Ba and Ca (%)	
Composition (x)	Ba/Ca	Ba	Ca	O	Ba/Ca	Ba	Ca	O	Ba	Ca
0.140	6.04	13.90	2.30	64.66	6.14	17.2	2.8	60	19.18	17.85
0.145	6.15	14.47	2.35	65.15	5.89	17.1	2.9	60	15.38	18.96
0.150	6.18	15.21	2.46	66.10	5.66	17.0	3.0	60	10.52	18.00
0.155	6.43	14.92	2.32	63.29	5.45	16.9	3.1	60	11.71	25.16
0.160	6.47	13.99	2.17	68.04	5.25	16.8	3.2	60	16.72	32.80

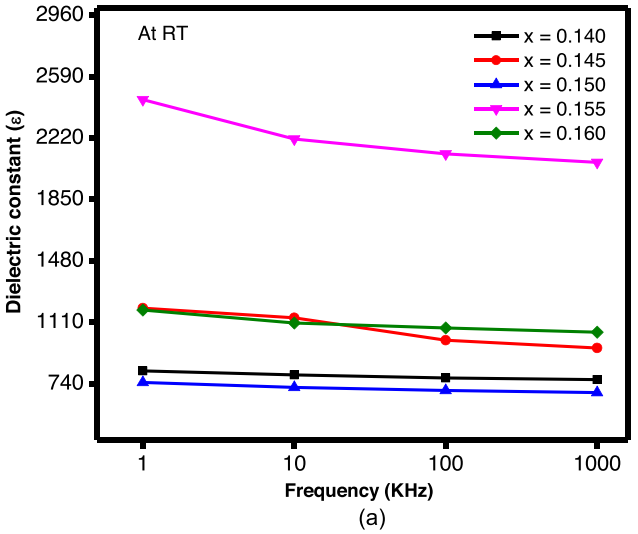

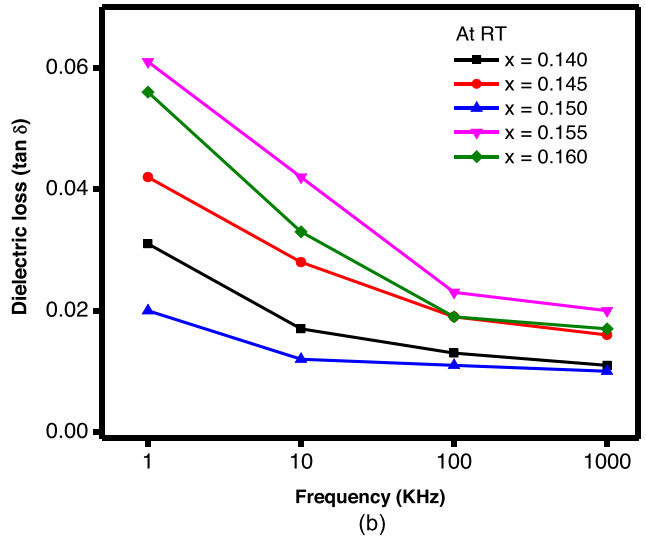

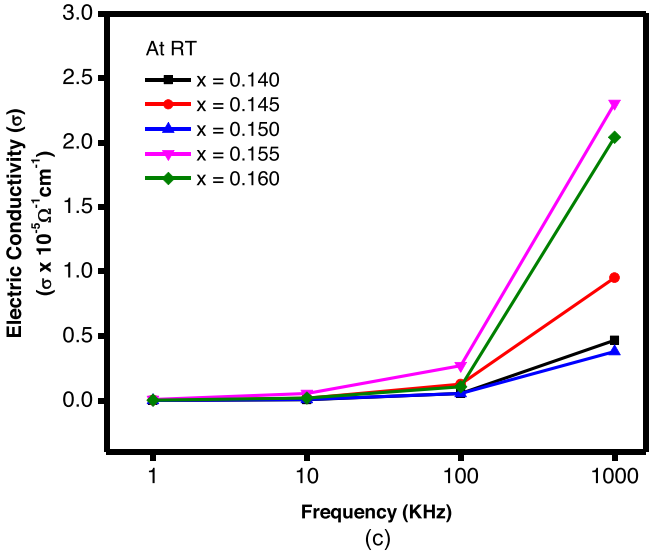

Figure 6. (a). Variation of dielectric constant (ε) with frequency, in $(Ba_{1-x}Ca_xZr_{0.1}Ti_{0.9})O_3$, ($0.140 \leqslant x \leqslant 0.160$), at RT. (b): Variation of dielectric loss (tan δ) with frequency, in $(Ba_{1-x}Ca_xZr_{0.1}Ti_{0.9})O_3$, ($0.140 \leqslant x \leqslant 0.160$), at RT. (c). Variation of electric conductivity (σ) with frequency, in $(Ba_{1-x}Ca_xZr_{0.1}Ti_{0.9})O_3$, ($0.140 \leqslant x \leqslant 0.160$), at RT.

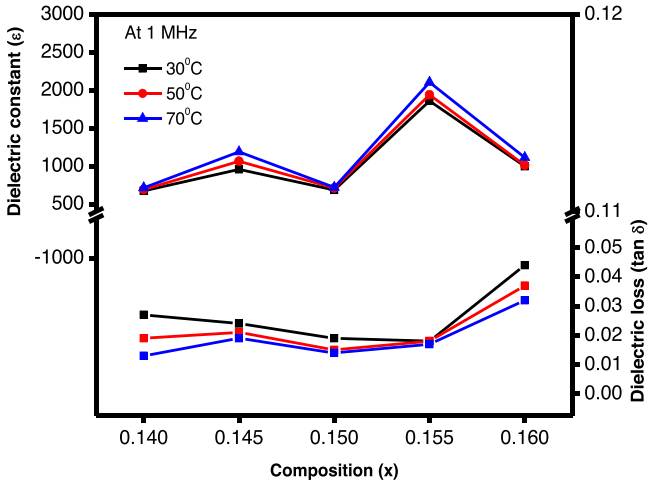

Figure 7. Composition variation of dielectric constant (ε) and dielectric loss (tan δ), in $(Ba_{1-x}Ca_xZr_{0.1}Ti_{0.9})O_3$, ($0.140 \leqslant x \leqslant 0.160$), at different temperatures.

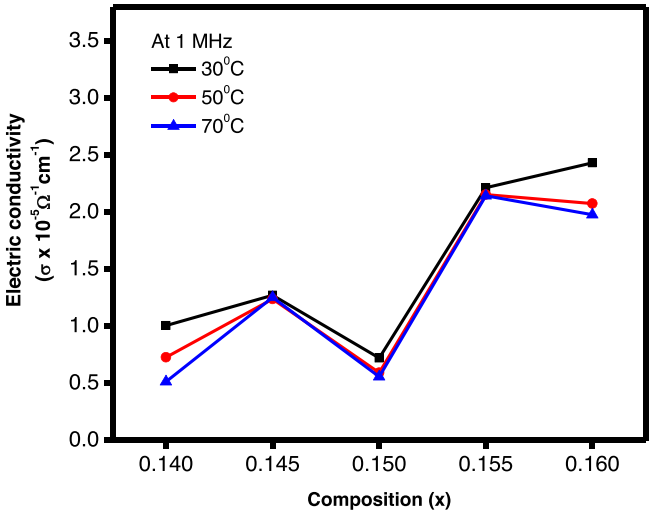

Figure 8. Composition variation of electric conductivity (σ), in $(Ba_{1-x}Ca_xZr_{0.1}Ti_{0.9})O_3$, ($0.140 \leqslant x \leqslant 0.160$), at different temperatures.

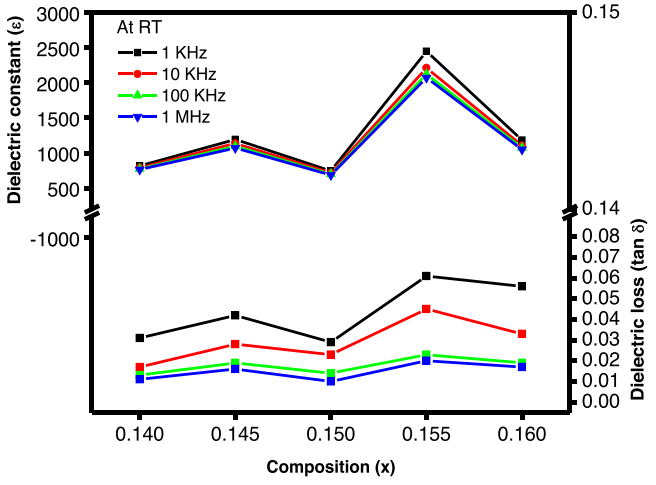

Figure 9. Composition variation of dielectric constant (ε) and dielectric loss (tan δ), in $(Ba_{1-x}Ca_xZr_{0.1}Ti_{0.9})O_3$, ($0.140 \leqslant x \leqslant 0.160$), at different frequencies.

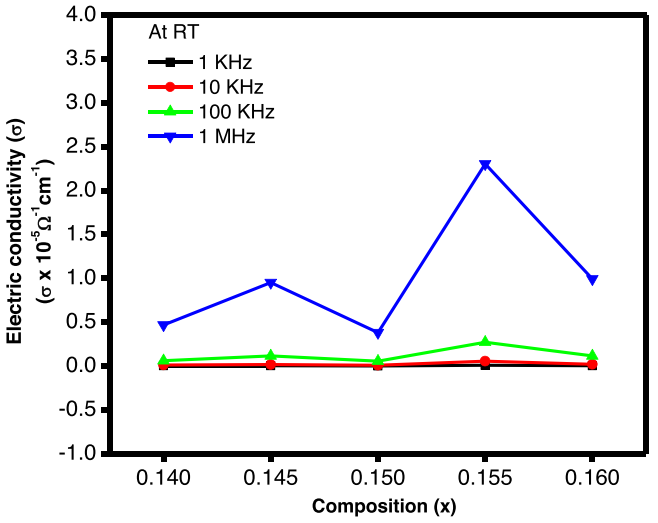

Figure 10. Composition variation of electric conductivity (σ), in $(Ba_{1-x}Ca_xZr_{0.1}Ti_{0.9})O_3$, ($0.140 \leqslant x \leqslant 0.160$), at different frequencies.

temperature and frequency.[15] However, the microstructure, grain size, voids, porosity and density greatly affect the dielectric properties of the pellet samples.[39,50] The contribution of escaping of alkaline ions and composition-dependent structural anomaly may be the responsible factors for the observed dielectric anomaly in the prepared BCZT ceramics. The dielectric constant decreases with decreasing grain size, which arises because of the increased occurrence of non-ferroelectric low permittivity grain boundaries.[50] With increasing grain size, number of grain boundaries decreases and results in the decreased loss. Also, the presence of liquid phase, internal stress, etc may contribute to the observed dielectric behavior in BCZT samples.

There are two types of defects found in perovskite ABO_3 type compounds, viz., vacancies at A-, and O-site.[28] These vacancies are significantly responsible to affect the electrical properties[17,26,27,51] of oxides. The conduction process in these oxides may be understood with the behavior of the majority of acceptor or donor concentration. In ABO_3 type perovskite compounds, A-site vacancy behaves as an acceptor of electron, that is equivalent of saying that it may donate a hole for conduction; and the O-site vacancy behaves as an electron donor, it may donate electron for conduction. If the number of vacancies at A-site is more than that at O-site, the solids may behave as p-type, or if there is majority of O-site vacancies, it may behave as the n-type. The majority of A-or O-site vacancies will be the deciding factor to determine whether a solid will behave as p-type or n-type. More A-site vacancies will donate more holes for conduction and the hole conductivity will increase, whereas more O-site vacancies will contribute more electrons for conduction and electron conductivity of the solid will increase. The EDAX results of the prepared $(Ba_{1-x}Ca_xZr_{0.1}Ti_{0.9})O_3$ ceramics show considerable escaping of alkaline (Ba and Ca) ions from the samples, having minimum for the composition with $x = 0.150$, Table I. The oxygen escaping was observed lower than the escaping of alkaline (Ba and Ca) ions. Therefore, A-site vacancies are in excess than that at O-site, envisaging the dominance of p-type conduction in the present $(Ba_{1-x}Ca_xZr_{0.1}Ti_{0.9})O_3$ ceramics. The deficiency of A-site vacancies is lowest, so less number of holes are available for conduction, and thereby the conductivity is minimum for the samples with $x = 0.150$, than the other prepared compositions.

Many researchers reported the p-type conductivity in various oxides, viz., ZrO_2, $Na_{1-x}K_xNbO_3$, etc.[17,26,52] In the present study, a distinct conductivity minimum was observed, with a decrease in A-site vacancy concentration, near MPB, with $x = 0.150$. Among the prepared compositions, it appears that during the sintering of the pellet samples, the intensification of diffusion processes distinctively decreases the possibility of escaping of volatile alkaline ions, near MPB region.[17,26]

With increase in density the dielectric constant of ceramics increases.[53,54] In the present study, the dielectric constant was found minimum even the density was maximum, for the composition with $x = 0.150$, among the prepared compositions, which indicates the control of composition than the density, near MPB region. The dielectric properties of ceramics may depend on the preparation process, because of its mechanical distinctions in the forming process, inhomogeneity in microchemistry, varying shrinkage, and chemical modification during sintering.

These observations indicate that the composition, structure, and the preparation process significantly affect the electrical properties of BCZT ceramics. For the composition near MPB, the structural anomaly and a decrease in A-site vacancy concentration in the p-type oxides may be the responsible factors for the observed minimum values of ε, tan δ, and σ, at $x = 0.150$, among the prepared compositions.

Conclusions

$(Ba_{1-x}Ca_xZr_{0.1}Ti_{0.9})O_3$, ($0.140 \leqslant x \leqslant 0.160$) compositions were prepared by double sintering method. Among the prepared compositions structural anomaly was observed; and the dielectric constant, loss tangent and electric conductivity were found minimum, at all the measured frequencies and temperatures, for the composition with $x = 0.150$, showing morphotropic-like phase boundary at this composition. A significant escaping of alkali earth metal (Ba and Ca) ions was observed in the sintered pellets, with a minimum for the composition with $x = 0.150$. The composition dependent structural anomaly and decreased A-site vacancies may be held responsible for the observed morphotropic like behavior, in these p-type perovskite compositions, at $x = 0.150$.

ORCID

Don Biswas https://orcid.org/0000-0001-5130-087X

References

1. G. A. Samara, *Ferroelectrics*, **73**, 145 (1987).
2. Y. Saito, H. Takao, T. Tani, T. Nonoyama, K. Takatori, T. Homma, T. Nagaya, and M. Nakamura, *Nature*, **432**, 84 (2004).
3. M. Dawber, K. M. Rabe, and J. F. Scott, *Rev. Mod. Phys.*, **77**, 1083 (2005).
4. P. Kantha and K. Pengpat, *Curr. Appl Phys.*, **9**, 460 (2009).
5. M. Ahtee and A. M. Glazer, *Acta Cryst.*, **A32**, 434 (1976).
6. R. Guo, L. E. Cross, S. E. Park, B. Noheda, D. E. Cox, and G. Shirane, *Phys. Rev. Lett.*, **84**, 5423 (2000).
7. S. E. Park and T. R. Shrout, *J. Appl. Phys.*, **82**, 1804 (1997).
8. B. Noheda, *Curr. Opin. Solid State Mater. Sci.*, **6**, 27 (2002).
9. H. Fu and R. E. Cohen, *Nature*, **403**, 281 (2000).
10. R. E. Cohen, *Nature*, **441**, 941 (2006).
11. M. Ahart, M. Somayazulu, R. E. Cohen, P. Ganesh, P. Dera, H. K. Mao, R. J. Hemley, Y. Ren, P. Liermann, and Z. Wu, *Nature*, **451**, 545 (2008).
12. B. Jaffe, R. S. Roth, and S. Marzullo, *J. Res. Natl. Bur. Standard*, **55**, 239 (1955).
13. S. Somiya, *Encyclopedia of Physical Science and Technology* (Academic Press, New York) 3rd ed., p. 578 (2003), https://doi.org/10.1016/B0-12-227410-5/00092-2.
14. Y. Tian, L. Wei, X. Chao, Z. Liu, and Z. Yang, *J. Am. Ceram. Soc.*, **96**, 496 (2013).
15. T. Mondal, S. Das, T. Badapanda, T. P. Sinha, and P. M. Sarun, *Physica B: Physics of Condensed Matter*, **508**, 124 (2017).
16. D. Xue, Y. Zhou, H. Bao, C. Zhou, J. Gao, and X. Ren, *J. Appl. Phys.*, **109**, 054110 (2011).
17. S. Singh, J. Negi, and N. S. Panwar, *J. Phys. Chem. Solids*, **123**, 311 (2018).
18. D. A. Tuan, V. Tung, T. V. Choung, N. T. Tinh, and N. T. M. Huong, *Indian J. Pure Appl. Phys.*, **53**, 409 (2015).
19. Z. Hanani, D. Mezzane, M. Amjoud, S. Fourcade, A. G. Razumnaya, I. A. Luk'yanchuk, and M. Gouné, *Superlattices Microstruct.*, **127**, 109 (2019).
20. P. Wang, Y. Li, and Y. Lu, *J. Eur. Ceram. Soc.*, **31**, 2005 (2011).
21. J. Wu, D. Xiao, B. Wu, W. Wu, J. Zhu, Z. Yang, and J. Wang, *Mater. Res. Bull.*, **47**, 1281 (2012).
22. J. Wu, D. Xiao, W. Wu, J. Zhu, and J. Wang, *J. Alloys Compd.*, **509**, L359 (2011).
23. W. Li, Z. Xu, R. Chu, P. Fu, and G. Zang, *J. Am. Ceram. Soc.*, **93**, 2942 (2010).
24. W. Li, Z. Xu, R. Chu, P. Fu, and G. Zang, *Mater. Lett.*, **64**, 2325 (2010).
25. S. W. Zhang, H. L. Zhang, B. P. Zhang, and S. Yang, *J. Alloys Compd.*, **506**, 131 (2010).
26. D. Biswas, P. Sharma, and N. S. Panwar, *Ferroelectrics*, **571**, 214 (2021).
27. J. Negi, S. Singh, and N. S. Panwar, *Phase Transitions*, **92**, 149 (2019).
28. B. Jaffe, R. S. Roth, and S. Marzullo, *J. Appl. Phys.*, **25**, 809 (1954).

29. D. Damjanovic, *Rep. Prog. Phys.*, **61**, 1267 (1998).
30. A. M. Glazer, P. A. Thomas, K. Z. Baba-Kishi, G. K. H. Pang, and C. W. Tai, *Phys. Rev. B*, **70**, 184123 (2004).
31. B. Jaffe, W. R. Cook, and J. H. Jaffe, *Piezoelectric ceramics* (Academic Press, New York) (1971), https://doi.org/10.1016/B978-0-12-379550-2.X5001-7.
32. A. J. Moulson and J. M. Herbert, *Electroceramics: Materials, Properties, Applications* (Wiley, England) 2nd ed. (2003).
33. Y. Ishibashia and M. Iwata, *Jpn. J. Appl. Phys.*, **Part1 38**, 800 (1999).
34. W. Cao and L. E. Cross, *Phys. Rev. B*, **47**, 4285 (1993).
35. D. Biswas, P. Sharma, and N. S. Panwar, "Structural and electrical properties of lead free $Na_{1-x}K_xNbO_3$ ($0.160 \leqslant x \leqslant 0.200$) ceramics." *Ceram. Int.* (2021), https://www.sciencedirect.com/science/article/pii/S0272884221002832?via%3Dihub.
36. D. Biswas, N. S. Panwar, and P. Sharma, *Ferroelectrics*, **568**, 95 (2020).
37. N. Buatip, Promsawat, N. Pisitpipathsin, O. Namsar, P. Pawasri, K. Ounsung, K. Phabsimma, S. T. Rattanachan, P. Janphuang, and S. Projprapai, *Integr. Ferroelectr.*, **187**, 45 (2018).
38. S. Sen and R. Choudhay, *J. Mater. Sci., Mater. Electron.*, **15**, 671 (2004).
39. K. Kinoshita and A. Yamaji, *J. Appl. Phys.*, **47**, 371 (1976).
40. Y. Hirata, A. Nitta, S. Sameshima, and Y. Kamino, *Mater. Lett.*, **29**, 229 (1996).
41. B. Malic, J. Koruza, J. Hrescak, J. Bernard, K. Wang, J. G. Fisher, and A. Bencan, *Materials*, **8**, 8117 (2015).
42. I. W. Chen and X. H. Wang, *Nature*, **404**, 168 (2000).
43. H. T. Kim and Y. H. Han, *Ceram. Int.*, **30**, 1719 (2004).
44. W. Chaisan, R. Yimnirun, and S. Ananta, *Ferroelectrics*, **346**, 84 (2007).
45. U. Sutharsini, M. Thanihaichelvan, and R. Singh, *Sintering of Functional Materials*, ed. I. Shishkovsky (Intechopen Ltd, London) 2nd, ed. (2017), https://www.intechopen.com/books/sintering-of-functional-materials.
46. J. Koruza and B. Malic, *J. Eur. Ceram. Soc.*, **34**, 1971 (2014).
47. R. M. German and Z. A. Munir, *J. Am. Ceram. Soc.*, **59**, 379 (1976).
48. J. Bohdanskya and H. E. J. Schins, *J. Phys. Chem.*, **71**, 215 (1967).
49. N. Pisitpipathsin, P. Kantha, K. Pengpat, and G. Rujijanagul, *Ceram. Int.*, **39**, S35 (2013).
50. M. H. Frey, Z. Xu, P. Han, and D. A. Payne, *Ferroelectrics*, **206**, 337 (1998).
51. E. V. Bursyan, *Nonlinear Crystal-Barium Titanate* (Nauka Press, Moskva) (1974).
52. J. Z. Rudolph, *Naturforsch*, **14a**, 727 (1959).
53. H. Chen, C. Yang, C. Fu, L. Zhao, and Z. Gao, *Appl. Surface Sci.*, **252**, 4171 (2006).
54. Q. Xu, X. F. Zhang, H. X. Liu, W. Chen, M. Chen, and B. H. Kim, *Mater. Des.*, **32**, 1200 (2011).

Ceramics International 47 (2021) 16746–16751

Contents lists available at ScienceDirect

Ceramics International

journal homepage: www.elsevier.com/locate/ceramint

Influence of post-deposition annealing on electrical and optical properties of $(Ta_2O_5)_{1-x}$ - $(TiO_2)_x$ thin films, $x \leq 0.08$

Prashant Thapliyal [a,b,*], N.S. Panwar [a], G. Mohan Rao [b]

[a] Department of Instrumentation Engineering, H.N.B. Garhwal University, Srinagar Garhwal, Uttarakhand, India
[b] Department of Instrumentation and Applied Physics, Indian Institute of Science, Bangalore, India

ARTICLE INFO

Keywords:
DC magnetron Sputtering
Leakage current density
Conduction mechanism
Refractive index
Optical band gap
Dielectric constant

ABSTRACT

Tantalum (Ta) and titanium (Ti) metal targets were direct current (DC) magnetron sputtered in the oxygen environment by varying its relative areas to deposit $(Ta_2O_5)_{1-x}$- $(TiO_2)_x$ (TTO_x) thin films, with $x = 0$, 0.03, 0.06, and 0.08, onto the boron-doped p-silicon (1 0 0) and optically polished quartz substrates, at room temperature; and were annealed at 500, 600, 700, and 800 °C, for 1.5 h. The thin films annealed at and above 600 °C show the Ta_2O_5 structure. The leakage current density and capacitance-voltage (C–V) characteristics were measured for TTO_x, $x \leq 0.08$, assisted Ag/TTO_x/p-Si metal– oxide– semiconductor (MOS) structures. The leakage current density was found minimum, for the films annealed at 800 °C, for all the prepared TTO_x films, $x \leq 0.08$. The minimum leakage current density 1.6×10^{-8} A/cm^2, at 3.5×10^5 V/cm electric field, was observed for $x = 0.03$, annealed at 800 °C, among the prepared compositions. The prepared $TTO_{0.03}$ films, annealed at 700 °C show maximum dielectric constant 39, at 1 MHz. The optical parameters, viz., refractive index (n), extinction coefficient (k), and optical band gap (E_g) of the films, with $x = 0.03$, prepared on quartz substrates, were determined from their optical transmittance plots. The values of n and k of the crystalline films were observed increasing from 2.123 to 2.143, and 0.099 to 0.130, respectively, at 550 nm wavelength; and E_g decreasing from 3.95 to 3.89 eV with the increasing annealing temperature, from 600 to 800 °C. Ohmic emission, in the lower electric field; Schottky and space-charge- limited current conduction mechanisms, in the intermediate to higher electric fields, were generally envisaged from the current-voltage characteristics in the prepared Ag/$TTO_{0.03}$/p-Si structures.

1. Introduction

The semiconductor industry has developed rapidly in recent times, demanding the large-scale integration of capacitors into high-density memory devices. Leakage current density, temperature and frequency-dependent dielectric constant, breakdown strengths, etc., are the parameters of the technological interest in these devices [1]. Having good compatibility with silicon-based semiconductors, SiO_2 has been used widely for many years as a primary gate dielectric in semiconductor devices. But the demand for miniaturization [2], low power consumption, and low leakage current technologically limit the application of SiO_2 in the semiconductor industry [3]. The existing SiO_2 based gate dielectrics in the microelectronic industry may be replaced by using the materials of high dielectric constant, viz., barium strontium titanate, titanium dioxide, tantalum pentoxide, hafnium oxide [4–7], etc. Tantalum pentoxide (Ta_2O_5) was reportedly observed as one of the most popular materials among other oxides due to its wide applications in the fields of optics and electronics [8–10]. Ta_2O_5 thin layers have wide applications in the various fields, e.g., as a high-k dielectric in microelectronics [11,12], a highly transparent and refracting material in optics [13], a catalyst in optoelectronics [14,15], anti-reflective coatings [16], and optical waveguides [17,18].

The physical properties of oxide thin films mainly depend on the deposition methods and processing conditions [19,20]. The films' microstructure and quality improved when deposited at elevated substrate temperature and post-deposition annealing [21]. Annealing results increase in packing density, reduction in the film's oxygen vacancy and defect density due to the phase transformation from amorphous to crystalline [22]. A crucial role of annealing condition was observed in the structural, surface morphological, and optical properties of Ta_2O_5 thin film [23,24]. Along with the annealing process and conditions, the doping of metal oxides (e.g., TiO_2, Y_2O_3) into Ta_2O_5 can enhance the

* Corresponding author. Department of Instrumentation Engineering, H.N.B. Garhwal University, Srinagar Garhwal, Uttarakhand, India
E-mail address: pra.thapli1986@gmail.com (P. Thapliyal).

https://doi.org/10.1016/j.ceramint.2021.02.246
Received 23 January 2021; Received in revised form 24 February 2021; Accepted 26 February 2021
Available online 27 February 2021
0272-8842/© 2021 Elsevier Ltd and Techna Group S.r.l. All rights reserved.

dielectric and electrical properties of pure Ta_2O_5 [25–27] due to reduced oxygen vacancies in Ta_2O_5 by the doped material. Nanoparticle TiO_2 thin films have reportedly shown potential in photocatalytic and solar cell applications [28,29]. Moreover, the researchers have studied the electrical and optical properties of (Ta_2O_5 - TiO_2) thin films, prepared with different methods, for various applications [30–33]. In the present report, TTO_x, $x \leq 0.08$, thin films were deposited on (1 0 0) P/boron-silicon and quartz (n = 1.51, T = 92%) by magnetron DC sputtering of the varying areas of metallic Ta and Ti targets in the presence of oxygen. This report exhibits observed electrical and optical properties of the prepared films and underlying possible conduction mechanisms in the prepared structures.

2. Experimental

The composite oxide thin films of tantalum (Ta) and titanium (Ti) were deposited onto the p-silicon with (1 0 0) orientation, and both sides optically polished quartz (15 mm × 10 mm, 1 mm thick) substrates by DC reactive magnetron sputtering. By arranging identical star-shaped radially cut Ti and Ta targets over a continuous circular Ta target, the target assembly was formed for sputtering. All the sputtering targets had an equal dimension (diameter 2-inch, and thickness 1 mm) and the same purity (99.99%). The target assembly was then varied for each deposition in such a way that the exposed area of the Ti target was gradually increased to form sputtered TTO_x compositions. Gradually varying the relative sputtering areas of metal targets gives greater flexibility to deposit the desired composition than sputtering separate ceramic targets for each composition. The details of the experimental setup of the thin film preparation and measuring instruments have been described elsewhere [34,35].

The prepared samples' transmission spectra were measured in a 190–1000 nm wavelength range, using an ultraviolet–visible spectrophotometer (UV–Vis) (Specord S600– 212C291) with a resolution of 0.5 nm. Optical transmittance data was used to calculate the optical coefficients using Swanepoel's envelope method [36]. The thickness (~260–280 nm) of the prepared film samples measured from transmission spectra was found consistent with (280 ± 10 nm) obtained from the spectroscopic ellipsometer.

3. Results and discussion

The XRD measurements of the prepared TTO_x, ($0 \leq x \leq 0.08$), thin films show the increasing crystallizing annealing temperature with increasing x [35]. Fig. 1 shows the observed XRD peak patterns of the deposited thin films of the select composition with x = 0.03, annealed at different temperatures.

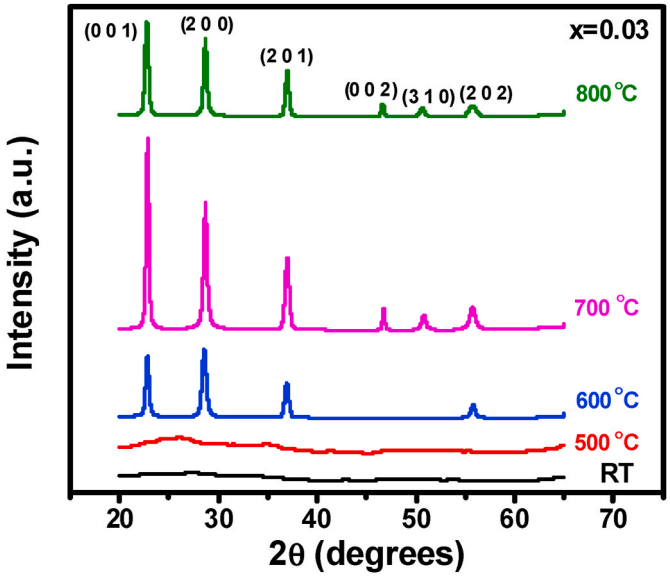

Fig. 1. XRD patterns of $TTO_{0.03}$ thin films, annealed at different temperatures.

For the deposited MOS Ag/TTO_x/p-Si structures, with $x \leq 0.08$, the leakage current density (J) was measured at 3.5 × 10^5 V/cm. The observed variation of leakage current density with composition and annealing temperature is given in Table 1. The observed decreasing leakage current density, up to 700 °C, with increasing annealing temperature may be due to the enhanced crystallinity and decreased oxygen vacancies [37]. The leakage current density was observed drastically decreased by an order of ~3, with further annealing at 800 °C, for all the prepared compositions. The formation of an additional silicon dioxide layer at the film-silicon interface, and improved quality of the interface, resulting in higher barrier heights at the interface [38], may be held responsible for the observed decrease in leakage current. For the prepared films of different compositions, the observed leakage current density, at applied 10 V, has been given in Table 1. The minimum leakage current density was found for x = 0.03, films annealed at 800 °C, among the prepared compositions. Fig. 2 shows the variation of leakage current density with the electric field (J-E plot) for the prepared MOS structures, films annealed at 800 °C.

Due to the observed minimum leakage current density for the $TTO_{0.03}$ thin-film structures, among the prepared compositions, the dielectric and optical properties were further investigated to understand the current conduction mechanisms in the prepared system.

The observed capacitance-voltage (C–V) characteristics of the $TTO_{0.03}$ assisted MOS capacitors, measured with the DC bias voltage sweeping from +10 to −10 V, using a 50 mV, 1 MHz signal, have been shown in Fig. 3(a). The usual inversion, depletion, and accumulation regions observed in the C–V characteristics indicate the charge mobility mechanisms with varying biasing conditions, Fig. 3(a) [34,39]. The dielectric constant of $TTO_{0.03}$ assisted MOS capacitors were calculated from C–V characteristics and found 10, 38, 39, and 23 for the films annealed at 500, 600, 700, and 800 °C, respectively, Fig. 3(b). With increasing annealing, the observed improving dielectric constant may be associated with the improved crystallinity of the prepared films; however, the decreased dielectric constant, at 800 °C annealing, may be due to the formation of the SiO_2 layer at the oxide film-substrate interface [34,35,40,41].

Fig. 4 shows the transmittance versus wavelength spectra of $TTO_{0.03}$ thin films, deposited onto the quartz substrates and annealed at 600, 700, and 800 °C. The high transmittance (~79–87%) was observed (for the wavelength > 400 nm) for the films annealed at 600 °C. Further, the transmittance was found slightly decreased (~74–85%) with increasing annealing temperature (≤800 °C). The observed decrease in the transmittance may be due to the increase of oxygen deficiency [42,43] and trap concentration [44] at the higher annealing temperatures (>600 °C).

The refractive index (n) and extinction coefficient (k) of the crystalline $TTO_{0.03}$ films were calculated from the transmittance spectra using Swanepoel's envelope method [36]. The variation of n and k with wavelength has been shown in Fig. 5. Generally, both the n and k values

Table 1
Leakage current density of prepared MOS capacitors, films annealed at different temperatures, at 3.5 × 10^5 V/cm.

Annealing temperature	Leakage current density (A/cm^2) for different compositions (x), at E = 3.5 × 10^5 V/cm (Corresponds to 10 V)			
	x = 0	x = 0.03	x = 0.06	x = 0.08
As-deposited	7.5×10^{-5}	1.1×10^{-4}	4.1×10^{-4}	8.3×10^{-5}
500 °C	2.7×10^{-5}	8.8×10^{-5}	8.3×10^{-5}	5.9×10^{-5}
600 °C	2.6×10^{-5}	2.2×10^{-5}	7.1×10^{-5}	5.3×10^{-5}
700 °C	3.7×10^{-5}	2.3×10^{-5}	3.4×10^{-5}	4.5×10^{-5}
800 °C	4.2×10^{-8}	1.6×10^{-8}	2.7×10^{-8}	3.0×10^{-8}

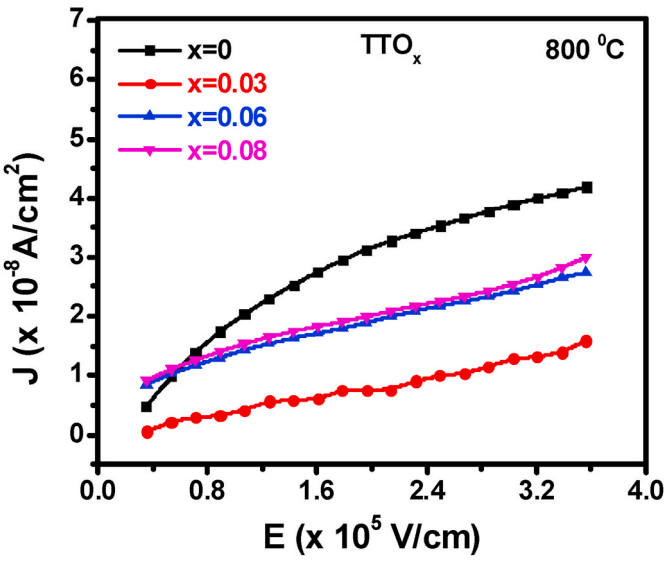

Fig. 2. The variation of leakage current density with the electric field for Ag/TTO_x/Si capacitors ($0 \leq x \leq 0.08$), films annealed at 800 °C.

decreased with increasing the wavelength for the annealed films. At 550 nm wavelength, the refractive index was found to increase from 2.123 to 2.143, with increasing annealing from 600 to 800 °C, Fig. 5(a), which may be due to the improved packing density and crystallization, with increasing the annealing temperature [42,44]. Also, thin films' refractive index may be influenced by imperfection, voids, interaction at the substrate-film interface and growth conditions, etc. [44]. The values of k, at 550 nm, were observed increasing from 0.099 to 0.130 with annealing, from 600 to 800 °C, Fig. 5(b). As the annealing temperature increases, the diffusion of oxygen away from the film volume may result in more absorption and increased extinction coefficient [43].

One of the important parameters, the optical band gap (E_g), can be derived from the optical transmittance plots by using Tauc's equation [45,46]:

$$\alpha h\nu = A(h\nu - E_g)^m \quad (1)$$

where A is the constant, α and hν are the absorption coefficient and photon energy, respectively. The value of constant m suggests the allowed transition in the thin film samples. In the presently prepared $TTO_{0.03}$ films, Tauc's equation (1) gives the best fit for the value m = ½, which indicates the direct transition due to photon-electron interaction. Following the photon-electron interaction, the optical band gaps were illustrated by using the linear (straight line) portion of the plots of α^2 versus hc/λ, near to the absorption edge, which intersects the x-axis (energy axis), Fig. 6(a–c). In the transmittance plot (Fig. 4), the optical absorption edge is observed at about 280 nm, which is observed shifting towards the higher wavelength, indicating the decrease in the band gap from 3.95 to 3.89 eV, with increasing annealing from 600 to 800 °C. The decreased value of the E_g may be related to the phase separation [47] and the increase in the crystalline nature [42], with increasing the annealing temperature. The observed E_g values of annealed $TTO_{0.03}$ thin films show a red shift with increasing the annealing temperature [47].

Fig. 7 shows the variation of leakage current density with the electric field for crystalline $TTO_{0.03}$ films. The leakage current density linearly increasing with the increasing electric field at the lower field region ($E < 1.0 \times 10^5$ V/cm) indicates the ohmic emission [48], which may be caused by the hopping of electrons [49].

Various plots illustrate the possible current conduction mechanisms in the crystalline $TTO_{0.03}$ films. For the films annealed at 600 and 700 °C, the plots of J/d versus E^2/d^2 were found linear in the higher electric field region (2.0×10^5 V/cm $\leq E \leq 3.4 \times 10^5$ V/cm), suggesting the possibility of space-charge- limited (SCL) current conduction mechanism, Fig. 8. The accumulated charge carriers near the conducting contact in the oxide film are injected into the oxide with no compensating charge on electric field application, results in space-charge-limited current conduction mechanism [49].

The prepared $TTO_{0.03}$ thin films, annealed at 800 °C show a linear graph between Ln J and $E^{1/2}$, in the electric field region (1.0×10^5 V/cm $\leq E \leq 3.5 \times 10^5$ V/cm), indicating the possibility of Schottky emission

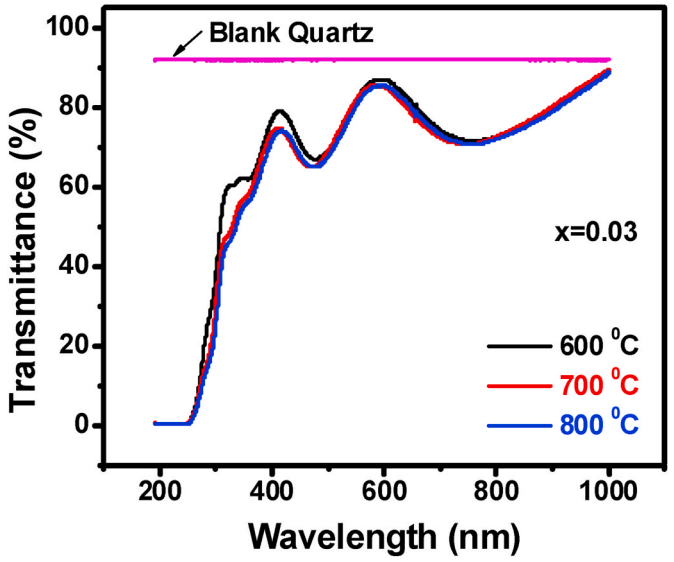

Fig. 4. Transmittance versus wavelength spectra of crystalline $TTO_{0.03}$ thin films.

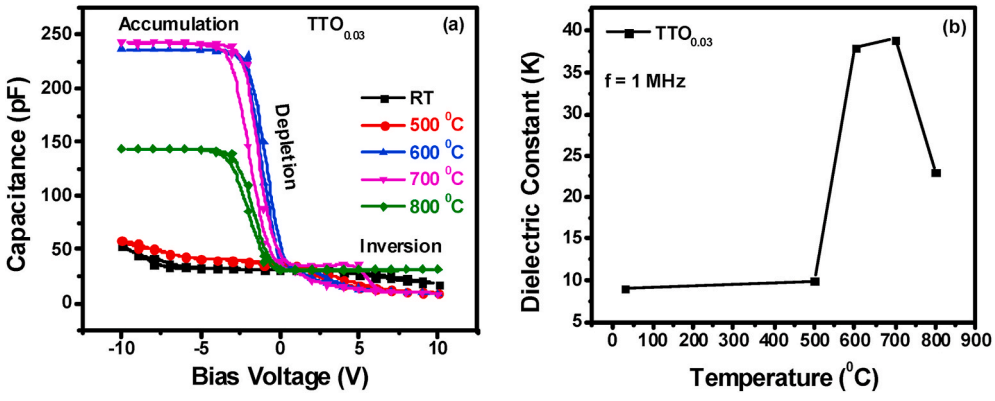

Fig. 3. The plots of (a) C–V characteristics, (b) Dielectric constant of $TTO_{0.03}$ films, at different annealing temperatures.

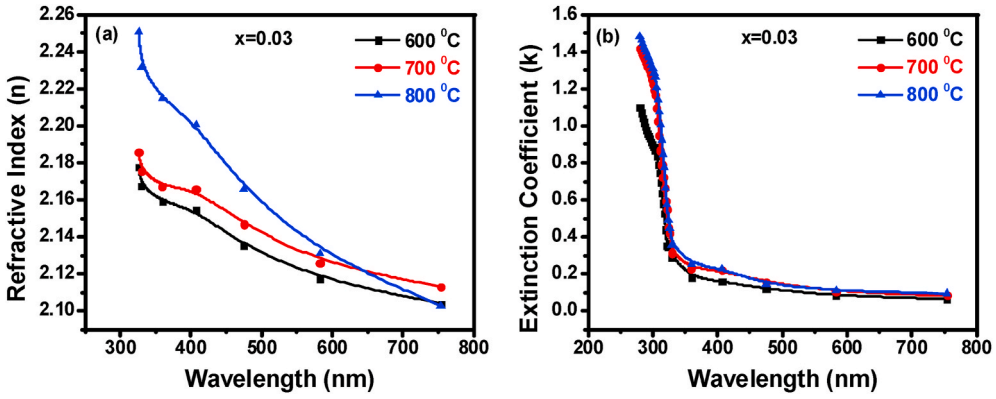

Fig. 5. Wavelength variation of (a) refractive index, (b) extinction coefficient of crystalline $TTO_{0.03}$ thin films.

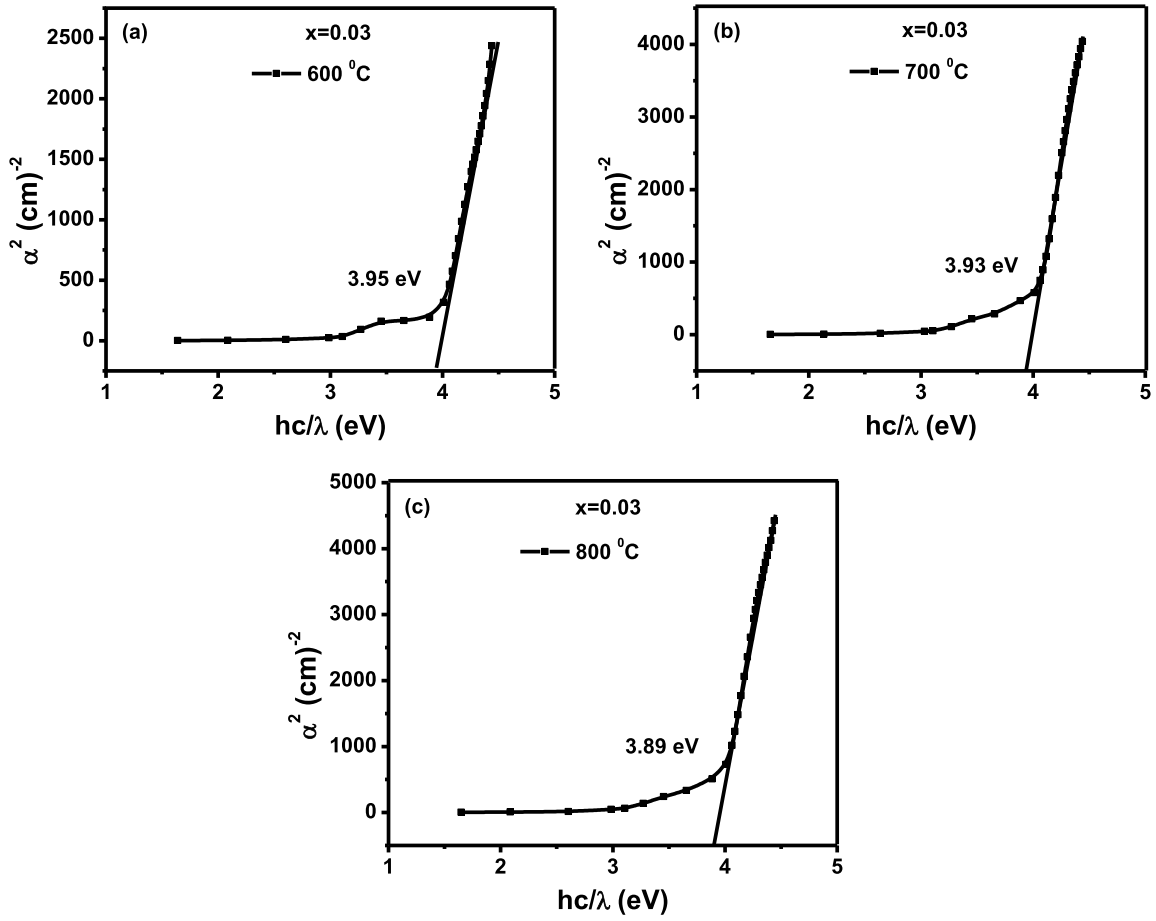

Fig. 6. α^2 versus hc/λ plots for $TTO_{0.03}$ films, annealed at (a) 600, (b) 700, and (c) 800 °C.

conduction mechanism, Fig. 9. The dynamic dielectric constant (K_r) and the refractive index (n) ($n = \sqrt{K_r}$), calculated from the slope of Ln J versus $E^{1/2}$ plot, were used and compared with the refractive index (n_{opt}) obtained from the optical measurements to confirm Schottky emission conduction mechanism in the moderate and higher electric field regions. From the optical measurements (discussed in the previous section of this paper), at 550 nm, the refractive index of $TTO_{0.03}$ thin films, annealed at 800 °C was found 2.143, which is in good agreement with the reported results [50,51]. For the composition x = 0.03, the refractive index at 550 nm, obtained from the optical measurements, was observed closer to the refractive index extracted from the plot of Ln J versus $E^{1/2}$, for the sample annealed at 800 °C, which indicates the confirmation of Schottky emission conduction mechanism in the field regimes (1.0×10^5 V/cm ≤ E ≤ 3.5×10^5 V/cm). Schottky emission occurs by lowering the barrier height due to the image force and the applied electric field at the interface between the insulating film and metal electrode [49,52].

In the Ag/$TTO_{0.03}$/Si capacitors, ohmic emission was observed in the lower electric field range (E < 1.0×10^5 V/cm) for the crystalline films. Space-charge- limited current conduction, in the higher field region (2.0×10^5 V/cm ≤ E ≤ 3.4×10^5 V/cm), for the films annealed at 600 and 700 °C; and Schottky emission, in 1.0×10^5 V/cm to 3.5×10^5 V/cm applied electric field region, for the films annealed at 800 °C, were dominantly observed.

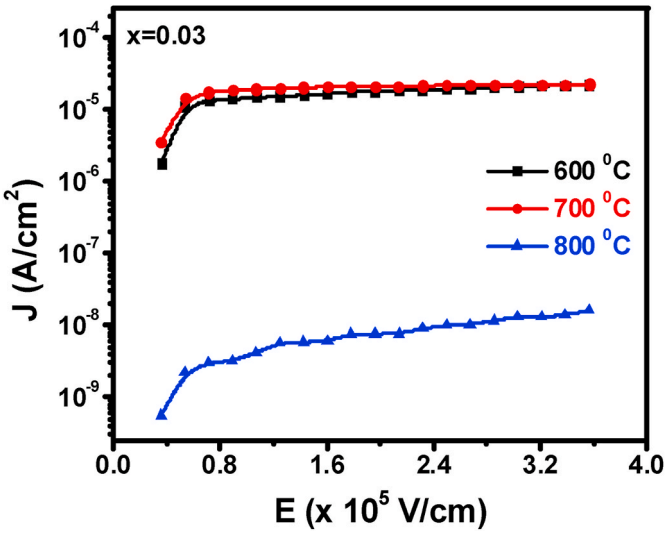

Fig. 7. The J-E plots of crystalline $TTO_{0.03}$ films.

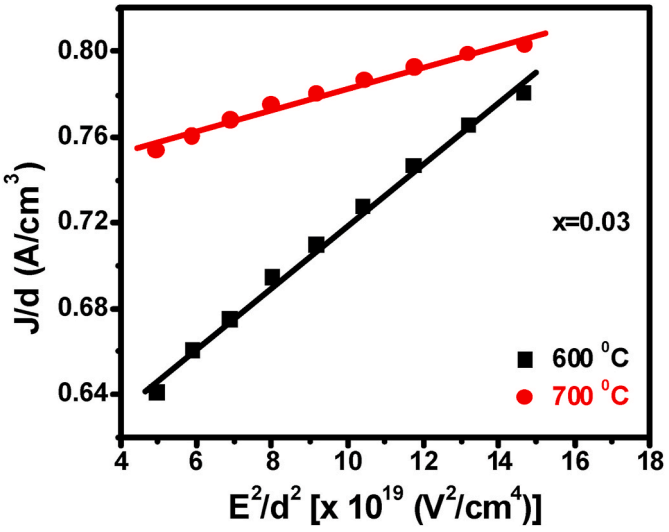

Fig. 8. The plots of J/d versus E^2/d^2 of $TTO_{0.03}$ films, annealed at 600 and 700 °C (Space-charge- limited current conduction mechanism).

4. Conclusions

Ta and Ti metal targets, with varying its relative sputtering areas, were sputtered in the oxygen environment to deposit TTO_x films, with x = 0, 0.03, 0.06, and 0.08, onto the p-Si (1 0 0) and quartz substrates, at room temperature. The films deposited at room temperature were followed by post-deposition annealing at 500, 600, 700, and 800 °C. The crystalline Ta_2O_5 structure was observed for the films, annealed at and above 600 °C. The leakage current density drastically reduced when the annealing temperature increased from 700 to 800 °C, which may be due to the interfacial SiO_2 layer formation. At 3.5×10^5 V/cm electric field, the minimum leakage current density was observed 1.6×10^{-8} A/cm^2, for $TTO_{0.03}$ films, annealed at 800 °C, among the prepared compositions. From the C–V characteristics, the maximum dielectric constant of $TTO_{0.03}$ thin films was found 39 for the films annealed at 700 °C.

Optical properties, e.g., transmittance, refractive index, extinction coefficient, and optical band gap of $TTO_{0.03}$ thin films were measured for the films annealed at different temperatures. The observed decrease in transmittance, with increasing the annealing temperature from 600 to 800 °C, for the prepared $TTO_{0.03}$ thin films, may be attributed to the

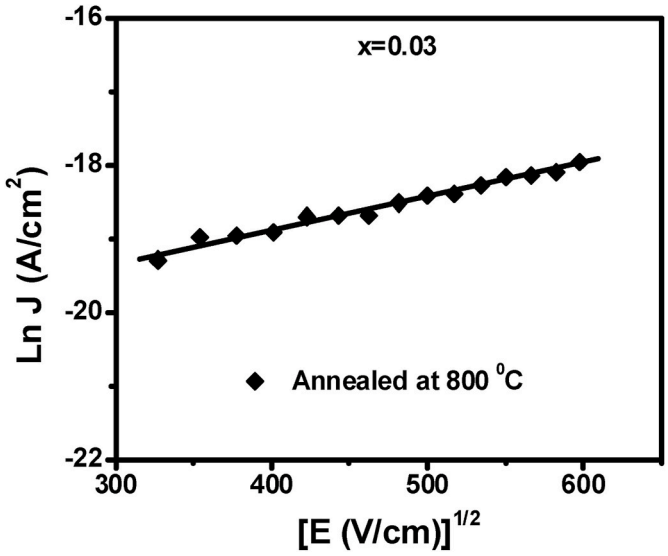

Fig. 9. The plot of Ln J versus $E^{1/2}$ of $TTO_{0.03}$ films, annealed at 800 °C (Schottky emission conduction mechanism).

increased oxygen deficiency due to its diffusion from the film volume. With increasing annealing temperature from 600 to 800 °C, the refractive index of the $TTO_{0.03}$ thin films, at the 550 nm wavelength, increased from 2.123 to 2.143, which may be considered due to the improvement in the packing density and crystal structure upon annealing. Also, the extinction coefficient increased from 0.099 to 0.130 with annealing, from 600 to 800 °C, due to the deficiency of oxygen in the film volume, on annealing. The optical band gap of $TTO_{0.03}$ thin films decreased from 3.95 to 3.89 eV, with increasing annealing temperature, from 600 to 800 °C.

At the lower electric field region, ohmic emission was observed for all the crystalline films; space-charge- limited current conduction, in the higher electric field regimes, for the films annealed at 600 and 700 °C; whereas Schottky emission in the moderate and higher electric fields, for the films annealed at 800 °C, were observed dominating.

Declaration of competing interest

The authors declare that they have no known competing financial interests or personal relationships that could have appeared to influence the work reported in this paper.

Acknowledgments

The authors are thankful to Hemvati Nandan Bahuguna Garhwal University, Uttarakhand, to provide a well-equipped research lab and 'Central Analytical Instruments facility' in the Department of Instrumentation Engineering-USIC, where preparation of samples and characterizations have been executed. We express our heartiest gratitude to the Indian Institute of Science, Bangalore, for facilitating the XPS and UV–Vis spectrophotometer.

References

[1] S. Ezhilvalavan, T.Y. Tseng, Preparation and properties of tantalum pentoxide (Ta_2O_5) thin films for ultra large scale integrated circuits (ULSIs) application – a review, J. Mater. Sci. Mater. Electron. 10 (1999) 9–31.
[2] K.W. Kwon, C.S. Kang, S.O. Park, H.K. Kang, S.T. Ahn, Thermally robust Ta_2O_5 capacitor for the 256-mbit DRAM, IEEE Trans. Electron. Dev. 43 (6) (1996) 919–923.
[3] G. Lucovsky, A. Mooradian, W. Taylor, G.B. Wright, R.C. Keezer, Identification of the fundamental vibrational modes of trigonal, α - monoclinic and amorphous selenium, Solid State Commun. 5 (2) (1967) 113–117.
[4] A.I. Kingon, J.P. Maria, S.K. Streiffer, Alternative dielectrics to silicon dioxide for memory and logic devices, Nature 406 (2000) 1032–1038.

[5] M. Kumar, M. Kumar, D. Kumar, The deposition of nanocrystalline TiO_2 thin film on silicon using sol–gel technique and its characterization, Microelectron. Eng. 87 (2010) 447–450.

[6] A. Cappellani, J.L. Keddie, N.P. Barradas, S.M. Jackson, Processing and characterisation of sol–gel deposited Ta_2O_5 and TiO_2– Ta_2O_5 dielectric thin films, Solid State Electron. 43 (1999) 1095–1099.

[7] I.R. Kaufmann, A. Pick, M.B. Pereira, H. Boudinov, Metal-insulator-SiC Schottky structures using HfO_2 and TiO_2 dielectrics, Thin Solid Films 621 (2017) 184–187.

[8] M.C. Sekhar, N.K. Reddy, H.S. Akkera, B.P. Reddy, V. Rajendar, S. Uthanna, S. H. Park, Role of interfacial oxide layer thickness and annealing temperature on structural and electronic properties of Al/Ta_2O_5/TiO_2/Si metal-insulator-semiconductor structure, J. Alloy, Compd 718 (2017) 104–111.

[9] J. Lee, W.D. Lu, E. Kioupakis, Electronic and optical properties of oxygen vacancies in amorphous Ta_2O_5 from first principles, Nanoscale 9 (2017) 1120–1127.

[10] R. Shakoury, R.R. Willey, Optimization of Ta_2O_5 optical thin film deposited by radio frequency magnetron sputtering, Appl. Optic. 55 (2016) 5353–5357.

[11] C. Chaneliere, S. Four, J.L. Autran, R.A.B. Devine, Comparison between the properties of amorphous and crystalline Ta_2O_5 thin films deposited on Si, Microelectron. Reliab. 39 (1999) 261–268.

[12] C.H. Kao, P.L. Lai, H.Y. Wang, The comparison between Ta_2O_5 and Ti-doped Ta_2O_5 dielectrics, Surf. Coating. Technol. 231 (2013) 512–516.

[13] J.-C. Zhou, D.-T. Luo, Y.-Z. Li, Z. Liu, Effect of sputtering pressure and rapid thermal annealing on optical properties of Ta_2O_5 thin films, Trans. Nonferrous Metals Soc. China 19 (2009) 359–363.

[14] G. Guo, J. Huang, Preparation of mesoporous tantalum oxide and its enhanced photocatalytic activity, Mater. Lett. 65 (2011) 64–66.

[15] K. Koc, F.Z. Tepehan, G.G. Tepehan, Antireflecting coating from Ta_2O_5 and SiO_2 multilayer films, J. Mater. Sci. 40 (2005) 1363–1366.

[16] F. Rubio, J. Denis, J.M. Albella, J.M. Martinez-Duart, Sputtered Ta_2O_5 antireflection coatings for silicon solar cells, Thin Solid Films 90 (1982) 405–408.

[17] W.M. Paulson, F.S. Hickernell, R.L. Davis, Effects of deposition parameters on optical loss for rf sputtered Ta_2O_5 and Si_3N_4 waveguides, J. Vac. Sci. Technol. 16 (2) (1979) 307–310.

[18] H. Terui, M. Kobayashi, Refractive-index-adjustable SiO_2-Ta_2O_5 films for integrated optical circuits, Appl. Phys. Lett. 32 (10) (1978) 666–668.

[19] Y.-H. Pai, C.-C. Chou, F.-S. Shieu, Preparation and optical properties of Ta_2O_{5-x} thin films, Mater. Chem. Phys. 107 (2008) 524–527.

[20] E. Atanassova, D. Spassov, X-ray photoelectron spectroscopy of thermal thin Ta_2O_5 films on Si, Appl. Surf. Sci. 135 (1998) 71–82.

[21] S.V.J. Chandra, P.S. Reddy, G.M. Rao, S. Uthanna, Effect of postdeposition annealing on the structural, electrical, and optical properties of dc magnetron sputtered Ta_2O_5 films, Res. Lett. Mater. Sci. (2007) 1–5, 2007.

[22] J.S. Lee, S.J. Chang, J.F. Chen, S.C. Sun, C.H. Liu, U.H. Liaw, Effects of O_2 thermal annealing on the properties of CVD Ta_2O_5 thin films, Mater. Chem. Phys. 77 (2002) 242–247.

[23] C. Xu, Q. Xiao, J. Ma, Y. Jin, J. Shao, Z. Fan, High temperature annealing effect on structure, optical property and laser-induced damage threshold of Ta_2O_5 films, Appl. Surf. Sci. 254 (2008) 6554–6559.

[24] R. Rabady, I. Avrutsky, Titania, silicon dioxide, and tantalum pentoxide waveguides and optical resonant filters prepared with radio-frequency magnetron sputtering and annealing, Appl. Optic. 44 (2005) 378–383.

[25] L. Manchanda, M.D. Morris, M.L. Green, R.B. van Dover, F. Klemens, T.W. Sorsch, P.J. Silverman, G. Wilk, B. Busch, S. Aravamudhan, Multi-component high- K gate dielectrics for the silicon industry, Microelectron. Eng. 59 (2001) 351–359.

[26] D.H. Triyoso, R.I. Hegde, S. Zollner, M.E. Ramon, S. Kalpat, R. Gregory, X.D. Wang, J. Jiang, M. Raymond, R. Rai, D. Werho, D. Roan, B.E. White Jr., P.J. Tobin, Impact of titanium addition on film characteristics of HfO_2 gate dielectrics deposited by atomic layer deposition, J. Appl. Phys. 98 (2005), 054104–054104-8.

[27] K.M.A. Salam, H. Fukuda, S. Nomura, Effects of additive elements on improvement of the dielectric properties of Ta_2O_5 films formed by metalorganic decomposition, J. Appl. Phys. 93 (2003) 1169–1175.

[28] U. Nwankwo, R. Bucher, A.B.C. Ekwealor, S. Khamlich, Maaza Malik, Fabian I. Ezema, Synthesis and characterizations of rutile-TiO_2 nanoparticles derived from chitin for potential photocatalytic applications, Vacuum 161 (2019) 49–54.

[29] C.G. Ezema, A.C. Nwanya, B.E. Ezema, B.H. Patil, R.N. Bulakhe, P.O. Ukoha, C. D. Lokhande, Maaza Malik, Fabian I. Ezema, Photo-electrochemical studies of chemically deposited nanocrystalline meso-porous n-type TiO_2 thin films for dyesensitized solar cell (DSSC) using simple synthesized azo dye, Appl. Phys. A 122 (2016), 435-435-10.

[30] P. Mazzolini, P. Gondoni, V. Russo, D. Chrastina, C.S. Casari, A. Li Bassi, Tuning of electrical and optical properties of highly conducting and transparent Ta-doped TiO_2 polycrystalline films, J. Phys. Chem. C 119 (2015) 6988–6997.

[31] Nobuyuki Koike, Koji Sasaki, Takatoshi Yamada, Naoki Hanashima, Akio Takada, Motofumi Suzuki, Optical properties and microstructures of inorganic wave plates prepared by serial bideposition, J. Nanophotonics 8 (2014), 083991-083991-7.

[32] M. Neubert, S. Cornelius, J. Fiedler, T. Gebel, H. Liepack, A. Kolitsch, M. Vinnichenko, Overcoming challenges to the formation of high-quality polycrystalline TiO_2:Ta transparent conducting films by magnetron sputtering, J. Appl. Phys. 114 (2013), 083707-083707-7.

[33] Anjana Devi, Malte Hellwig, Davide Barreca, Parala Harish, Reji Thomas, Hans-Werner Becker, Ram.S. Katiyar, A. Fischer Roland, Eugenio tondello, growth and characterization of Ti-Ta-O thin films on Si substrates by liquid injection MOCVD for high-k applications from modified titanium and tantalum precursors, Chem. Vap. Depos. 16 (2010) 157–165.

[34] Prashant Thapliyal, Alok S. Kandari, Vijendra Lingwal, N.S. Panwar, G. Mohan Rao, Post deposition annealing dependent structural and C-V characteristics of $(Ta_2O_5)_{0.965}$-$(TiO_2)_{0.035}$ thin films, Mater. Today: Proceedings (2020), https://doi.org/10.1016/j.matpr.2020.09.297.

[35] Prashant Thapliyal, Alok S. Kandari, Vijendra Lingwal, N.S. Panwar, G. Mohan Rao, Annealing temperature-dependent structural and electrical properties of $(Ta_2O_5)_{1-x}$- $(TiO_2)_x$ thin films, $x \leq 0.11$, Ceram. Int. (2021), https://doi.org/10.1016/j.ceramint.2021.01.050.

[36] R. Swanepoel, Determination of the thickness and optical constants of amorphous silicon, J. Phys. E Sci. Instrum. 16 (1983) 1214–1222.

[37] E. Atanassova, M. Kalitzova, G. Zollo, A. Paskaleva, A. Peeva, M. Georgieva, G. Vitali, High temperature-induced crystallization in tantalum pentoxide layers and its influence on the electrical properties, Thin Solid Films 426 (2003) 191–199.

[38] T. Dimitrova, K. Arshak, E. Atanassova, Crystallization effects in oxygen annealed Ta_2O_5 thin films on Si, Thin Solid Films 381 (2001) 31–38.

[39] M. Chandra Sekhar, N. Nanda Kumar Reddy, V.K. Verma, S. Uthanna, Structural, optical and electrical properties of DC reactive magnetron sputtered $(Ta_2O_5)_{1-x}(TiO_2)_x$ thin films, Ceram. Int. 42 (2016), 18870-18870-9.

[40] Chyuan Haur Kao, Pei Lun Lai, Hsin Yuan Wang, The comparison between Ta_2O_5 and Ti-doped Ta_2O_5 dielectrics, Surf. Coating. Technol. 231 (2013) 512–516.

[41] J.-Y. Gan, Y.C. Chang, T.B. Wu, Dielectric property of $(TiO_2)_x$-$(Ta_2O_5)_{1-x}$ thin films, Appl. Phys. Lett. 72 (1998) 332–334.

[42] S.V. Jagadeesh Chandra a, S. Uthanna a, G. Mohan Rao, Effect of substrate temperature on the structural, optical and electrical properties of dc magnetron sputtered tantalum oxide films, Appl. Surf. Sci. 254 (2008) 1953–1960.

[43] Jianchao Li, Wanmin Yang, Junhong Su, Chen Yang, Junqi Xu, Shenjiang Wu, Effect of temperature fields on optical properties of $La_2Ti_2O_7$ thin films, Mater. Res. Express 6 (2019), 026404-026404-8.

[44] P.C. Joshi, M.W. Cole, Influence of postdeposition annealing on the enhanced structural and electrical properties of amorphous and crystalline Ta_2O_5 thin films for dynamic random access memory applications, J. Appl. Phys. 86 (1999) 871–880.

[45] O.A. Azim, M.M. Abdel-Aziz, I.S. Yahia, Structure and optical analysis of Ta_2O_5 deposited on infrasil substrate, Appl. Surf. Sci. 255 (2009) 4829–4835.

[46] J. Tauc, R. Grigorovici, A. Vancu, Optical properties and electronic structure of amorphous germanium, Phys. Status Solidi B 15 (1966) 627–637.

[47] D.Y. Jiang, D.Z. Shen, K.W. Liu, C.X. Shan, Y.M. Zhao, T. Yan, B. Yao, Y.M. Lu, J. Y. Zhang, Effect of post annealing on the band gap of $Mg_xZn_{1-x}O$ thin films, Semicond. Sci. Technol. 23 (2008), 035002-035002-5.

[48] P.L. Young, DC electrical conduction in thin Ta_2O_5 films. I. Bulk-limited conduction, J. Appl. Phys. 47 (1976) 235–241.

[49] S.M. Sze, Physics of Semiconductor Devices, second ed., Wiley, New York, 1981.

[50] Mahesh Kumar Agarwal, Aradhana Bhandari, Y. Singh, N.S. Panwar, Optical properties of amorphous $[Ta_2O_5]_{1-x}$-$[TiO_2]_x$ (x=0.08) thin films, International Journal of Research and Innovations in Science and Technology 1 (2014) 23–29.

[51] M. Chandra Sekhar, N. Nanda Kumar Reddy, B. Purusottam Reddy, B. Poorna Prakash, Harish Sharma Akkera, S. Uthanna, Si-Hyun Park, Influence of substrate bias voltage on crystallographic structure, optical and electronic properties of Al/$(Ta_2O_5)_{0.85}(TiO_2)_{0.15}$/p-Si MIS Schottky barrier diodes fabricated by dc magnetron sputtering, Mater. Sci. Semicond. Process. 76 (2018) 80–86.

[52] R. Brazis, Electron transport in Ta_2O_5 films, J. Mater. Sci. Lett. 9 (1990) 266–267.

Ceramics International 47 (2021) 13814–13819

Contents lists available at ScienceDirect

Ceramics International

journal homepage: www.elsevier.com/locate/ceramint

Structural and electrical properties of lead free $Na_{1-x}K_xNbO_3$ ($0.160 \leq x \leq 0.200$) ceramics

Don Biswas [a,*], Prolay Sharma [b], N.S. Panwar [a]

[a] University Science Instrumentation Centre, H.N.B. Garhwal University, Srinagar, 246174, India
[b] Instrumentation and Electronics Engg, Jadavpur University, Kolkata, India

ARTICLE INFO

Keywords:
Phase transition
Solid state reaction
Dielectric constant
Electric conductivity

ABSTRACT

In this study, pellet samples of $Na_{1-x}K_xNbO_3$ (NKN) ($0.160 \leq x \leq 0.200$) were prepared using the solid-state reaction method with double sintering. For the prepared compositions, the dielectric measurements were carried out from room temperature to 480 °C, at 10, 100, and 1000 kHz. Dielectric measurements of the prepared samples indicated anomalies around 210, 380, and 450 °C. High temperature X-ray diffraction (HT-XRD) measurements were carried out to analyze the structural properties of the samples, with $x = 0.175$. Consistent with the dielectric behavior, HT-XRD measurements of the prepared samples, with $x = 0.175$, indicated monoclinic phase, between room temperature and 210 °C; tetragonal phase, between 210 and 380 °C; tetragonal phase with a change in the lattice, between 380 and 460 °C; and cubic phase above 460 °C, in the measured temperature range.

1. Introduction

In $(Na_{1-x}K_x)NbO_3$ based system, abbreviated as NKN, morphotropic phase transition boundary plays an important role in determining the behavior of composition. At high temperatures, the NKN based system shows cubic structure, a para-electric phase [1,2]. Sodium-potassium niobate, (Na, K)NbO_3, has quite interesting distinct phases [3–6]. Megaw found cubic structure in the high temperature range and several other distinct ferroelectric phases in (Na, K)NbO_3 system [1]. The High-temperature phases of $NaNbO_3$–$KNbO_3$ solid solutions were studied by Ahtee et al. [3]. Nobre et al. [4,5] found four different phase transitions, in the temperature range from room temperature (RT) to 750 °C, in polycrystalline samples $Na_{1-x}Li_xNbO_3$ and $Na_{1-x}K_xNbO_3$ ($x = 0.15$). Dabin Lin et al. [6] found tetragonal to tetragonal transition at 405 °C, and tetragonal to cubic phase transition at 496 °C, for $(Na_{1-x}K_x)NbO_3$ ($x = 0.11$) crystals. Some researchers found only two phase transitions from the dielectric measurements, one at 200 °C and another at around 400 °C [7–9]. The dielectric properties of the ABO_3 depend significantly on the low frequency optical soft mode [10,11], which influences the transition temperature (Tc), and is responsible for the anomalous dielectric behavior of these materials near the phase transition. The soft mode frequency tends to zero, and the lattice displacement associated with it becomes unstable-triggering phase transition, and results anomalous dielectric behavior of these materials, near Tc. The distinct structural phase transitions are the static manifestations of the dynamic soft mode, resulting the tilting of the BO_6 octahedra in this system [2,12].

NKN solid solutions have significant potential to substitute the lead based oxides in delay-lines and piezoelectric applications [13–17]. Promising piezoelectric properties in alkali niobates are believed to arise from the coexistence of thermodynamically equivalent phases at the morphotropic phase boundary (MPB) composition. At MPB, enhanced piezoelectric responses are found due to the ease of polarization rotation under the external electric field [18].

The phase diagrams of the $Na_{1-x}K_xNbO_3$ system were presented by Jaffe et al. [19], Tennery and Hang [20], and Ahtee and Glazer [3], showing the distinct phases. Ahtee et al. indicated the existence of phase X, though suspicious, in the phase diagram, in the composition range $0.2 < x < 0.5$, above 400 °C. Nevertheless, it is highly suspicious. However, at the higher temperatures, beyond the phase X, the existence of cubic phase is well established [3]. It is reportedly observed that with change in potassium (x) percentage in $Na_{1-x}K_xNbO_3$, a possible shifting in the transition temperature has been occurred.[12].

Researchers practice a number of synthesis methods for the preparation of ceramic powders, which include solid state reaction, sol-gel processing, co-precipitation method, hydrothermal method, spray

* Corresponding author.
E-mail address: d.biswas@hnbgu.ac.in (D. Biswas).

https://doi.org/10.1016/j.ceramint.2021.01.246
Received 26 November 2020; Received in revised form 4 January 2021; Accepted 24 January 2021
Available online 28 January 2021
0272-8842/© 2021 Elsevier Ltd and Techna Group S.r.l. All rights reserved.

drying, microwave heating, etc., methods [21,22]. Every method has its advantages and limitations. The solid state reaction method is simple, inexpensive and fast to synthesize the perovskite oxides, and the present ceramic pellets were prepared by this method. This study explores different structural phase transitions, in the NKN system. Presently the temperature-dependent dielectric properties of $Na_{1-x}K_xNbO_3$ ($0.160 \leq x \leq 0.200$) ceramic pellet samples have been studied. The dielectric constant, loss tangent, and dielectric conductivity of the $Na_{1-x}K_xNbO_3$ ($0.160 \leq x \leq 0.200$) pellet samples were measured from room temperature (RT) to 480 °C, at 10, 100, and 1000 kHz. For the samples with $x = 0.175$, the HT-XRD was carried out in the temperature range from RT to 480 °C. The HT-XRD results show different structural phases of the NKN system, in the measured temperature range.

2. Experimentation

The ceramic pellets were prepared using the solid-state reaction method. The preparation methodology has been described in a previous communication [23–25]. For the present study, raw materials used for preparing the composition were sodium carbonate (Na_2CO_3), potassium carbonate (K_2CO_3) and niobium pentoxide (Nb_2O_5), all of 99.99% pure. For the prepared pellet samples, temperature-dependent dielectric properties were measured. The compositions were calcined first in a crucible in the air at 900 °C to remove carbonate. The calcined powder was well ground and pressed at 0.2 GPa to form 8 mm diameter, ~2mm thick pellets. The pellets of $Na_{1-x}K_xNbO_3$ ($0.160 \leq x \leq 0.200$) were prepared and sintered for 4 hrs, at temperatures between 1130 and 1136 °C, with decreasing x (K content). The melting point of $NaNbO_3$ is 1422 °C, and that of $KNbO_3$ is 1040 °C, so the sintering temperatures of the $Na_{1-x}K_xNbO_3$ compositions were chosen according to their melting points. The sintered NKN pellets were crushed further, fine ground, and pressed into pellets at 0.2 GPa. The pellets were further sintered at the chosen temperatures according to their melting temperatures, each for 4 hours.

The dielectric constant (ε), dielectric loss (tan δ) and electric conductivity (σ) of the sintered pellets were observed systematically. For this purpose, first, they were electroded, with air dryable conducting paste of silver, in metal-insulator-metal (MIM) configuration, by RLC meter (Fluke, PM 6306), with increasing temperature cycles, at 10, 100, and 1000 kHz.

To analyze different phases, the X-ray diffractions were measured, from room temperature (RT) to 480 °C, for the samples with $x = 0.175$. The X-ray diffractometer used was PANalytical, X'PERT PRO, having $CuK_{\alpha 1}$ radiation of wavelength 1.54060 Å. The 2θ angle has been selected from 20 to 70°. For HT- XRD measurement, data was collected at a scan speed of 0.1 s per step with the step size of 0.01°. To heat the sample up to desired temperature, the heating rate was kept 5 °C/s. The XRD data were collected after a holding time of 5 min.

3. Results and discussion

3.1. Dielectric measurements

At room temperature (RT), the observed composition dependence of dielectric properties (ε, tan δ, and σ) of NKN ceramics ($Na_{1-x}K_x$) NbO_3 ($0.160 \leq x \leq 0.200$) are shown in Figs. 1–3, at different frequencies. With the increase in frequency, normally, ε and tan δ were decreasing and σ increasing for the prepared compositions. Moreover, these outcomes are consistent with the previous publications [26–28]. Among the prepared compositions, the dielectric constant, loss tangent and electric conductivity was observed minimum, at all the measured frequencies, for the composition with $x = 0.175$, showing morphotropic- like phase boundary at this composition [29]. The dielectric constant and loss tangent of the ($Na_{1-x}K_x$) NbO_3 ($0.160 \leq x \leq 0.200$) ceramics were measured as a function of temperature with different frequencies (at 10, 100 and 1000 KHz). The results are presented in Figs. 4–8. The data

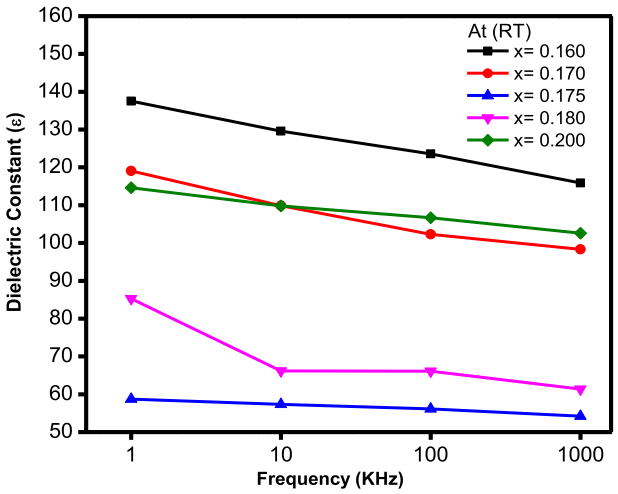

Fig. 1. Variation of dielectric constant (ε) with frequency, in $Na_{1-x}K_xNbO_3$ ($0.160 \leq x \leq 0.200$).

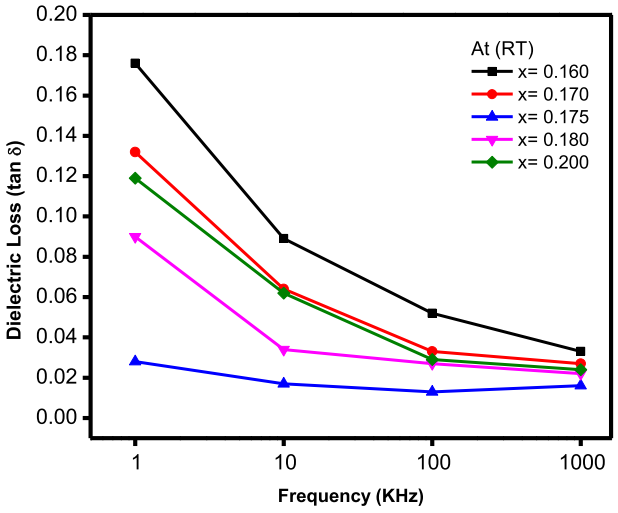

Fig. 2. Variation of dielectric loss (tan δ) with frequency, in $Na_{1-x}K_xNbO_3$ ($0.160 \leq x \leq 0.200$).

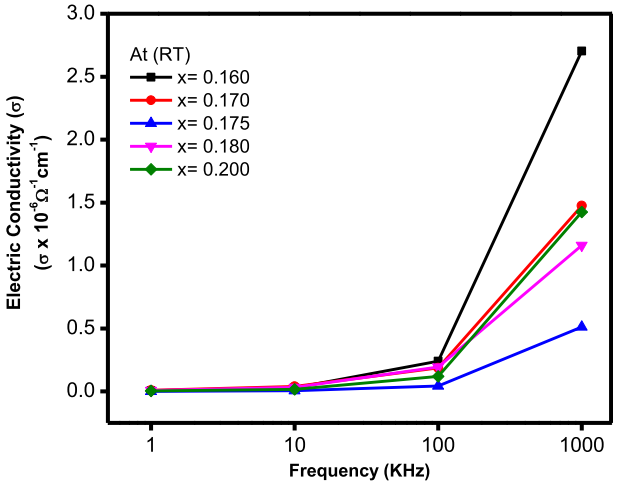

Fig. 3. Variation of electric conductivity (σ) with frequency, in $Na_{1-x}K_xNbO_3$ ($0.160 \leq x \leq 0.200$).

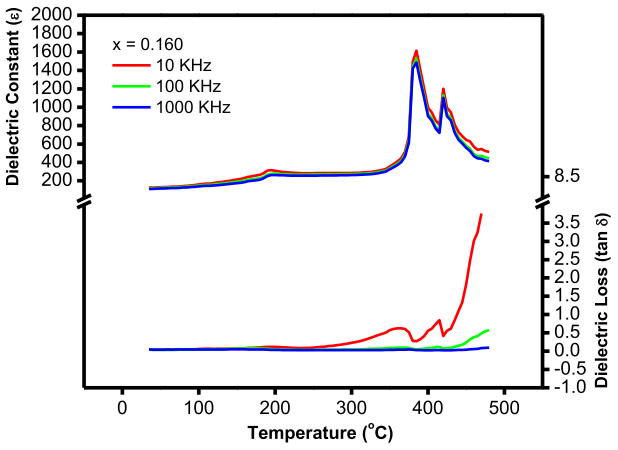

Fig. 4. Temperature variation of the dielectric constant and tangent loss observed for $Na_{1-x}K_xNbO_3$ (x = 0.160), at different frequencies.

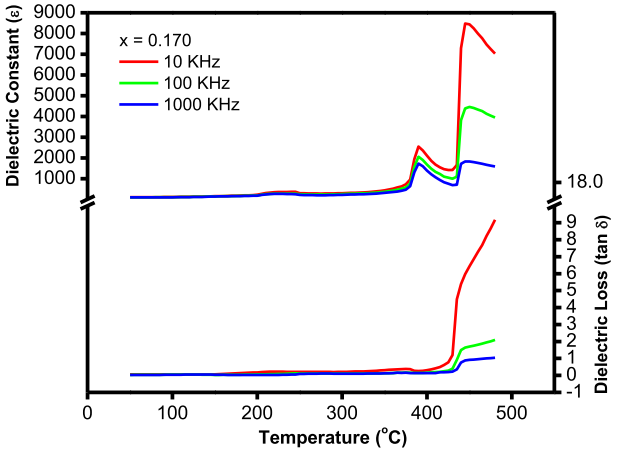

Fig. 5. Temperature variation of the dielectric constant and tangent loss observed for $Na_{1-x}K_xNbO_3$ (x = 0.170), at different frequencies.

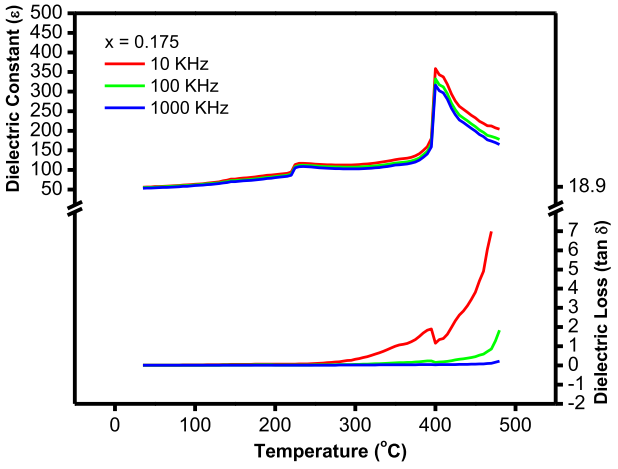

Fig. 6. Temperature variation of the dielectric constant and tangent loss observed for $Na_{1-x}K_xNbO_3$ (x = 0.175), at different frequencies.

shows that the ε and tan δ curves shift downward as the frequency has been increased from 10 kHz to 1000 kHz for all the prepared samples. The decreasing peak strength at a particular temperature may be attributed to the damping out of successive relaxation modes in the lattice [30]. For all the prepared compositions, the dielectric constant

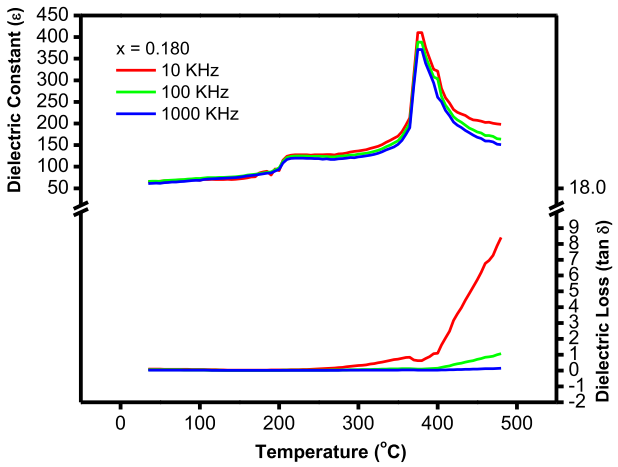

Fig. 7. Temperature variation of the dielectric constant and tangent loss observed for $Na_{1-x}K_xNbO_3$ (x = 0.180), at different frequencies.

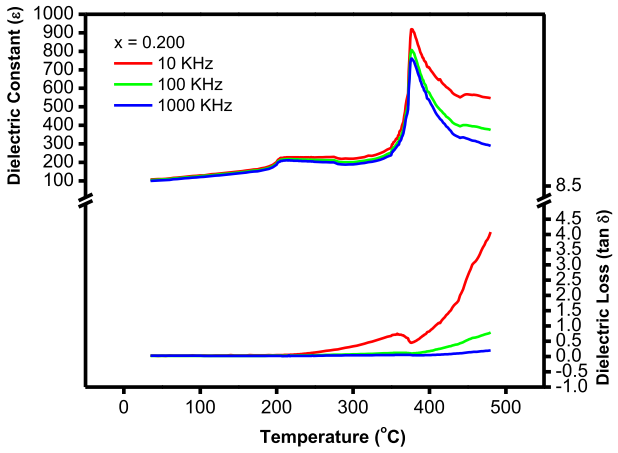

Fig. 8. Temperature variation of the dielectric constant and tangent loss observed for $Na_{1-x}K_xNbO_3$ (x = 0.200), at different frequencies.

was found increasing for all the prepared compositions, with increasing temperature, but with anomalously higher values at around 210, 380, and 450 °C, indicating distinct phase transitions at these temperatures [31].

Effective ionic sizes and the forces that govern ions' arrangement in a crystal are both temperature-dependent. They may change sufficiently for a particular structure to become unstable and to transform to a new one structure with a lattice change. The temperature at which both forms are in equilibrium is called a transition temperature. Crystal dimensions may change and generate internal stresses, particularly at the crystallite boundaries in a ceramic. The electrical conductivity of the samples may change by several orders of magnitude. In some respects, crystal structure transitions are similar to the more familiar phase transitions, melting, vaporization, and when, with the temperature and pressure constant, there are changes in entropy and volume [32].

In this study, the temperature-dependent dielectric constant and electrical conductivity of the $Na_{1-x}K_xNbO_3$ ($0.160 \leq x \leq 0.200$) were observed at 1 MHz. For the prepared compositions, the measured data of dielectric constant as a function of temperature at 1 MHz, are shown in Fig. 9. For all the prepared compositions, dielectric constant was observed gradually increasing with increasing temperature, but with significant large values at around 210, 380, and 450 °C, indicating distinct phase transitions at these temperatures [19,30]. The temperature dependent electrical conductivity of NKN system, at 1 MHz, has been shown in Fig. 10. Fig. 11 shows the dielectric properties expanded

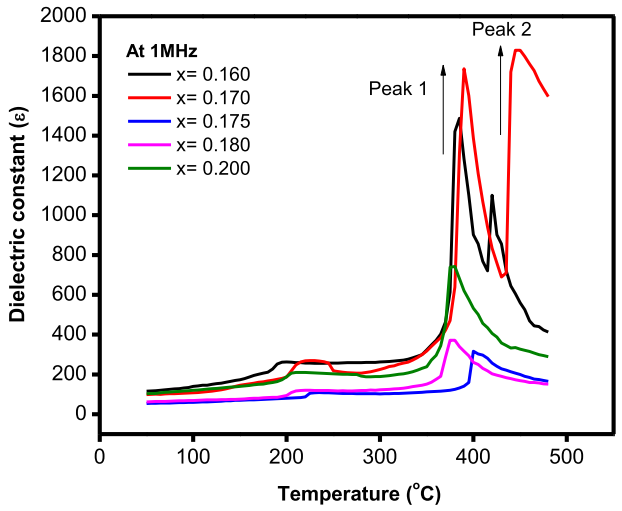

Fig. 9. Temperature variation of the dielectric constant (ε) of $Na_{1-x}K_xNbO_3$ ($0.160 \leq x \leq 0.200$), for different compositions (x), at 1 MHz.

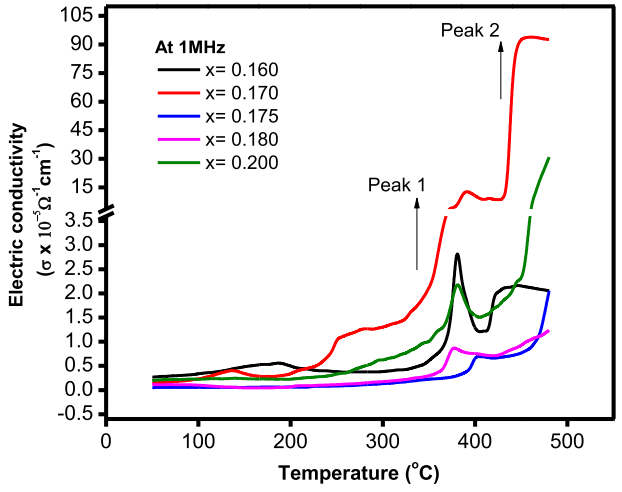

Fig. 10. Temperature variation of the electric conductivity (σ) of $Na_{1-x}K_xNbO_3$ ($0.160 \leq x \leq 0.200$), for different compositions (x), at 1 MHz.

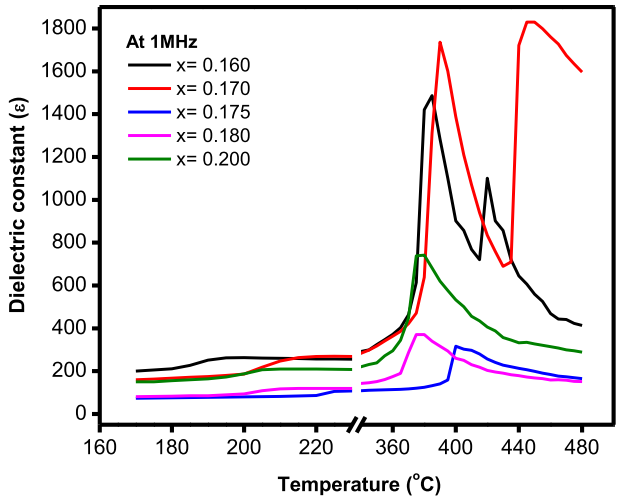

Fig. 11. (a): Dependence of dielectric constant with the temperature, expanded view in temperature range of 170- 230 °C and 340- 480 °C, at 1 MHz.

view with peaks at around 210, 380, and 450 °C, respectively. As K content increases at the A-site, the observed dielectric anomaly shifted to a lower temperature, indicating decrease in T_c. It was observed that with increasing value of x ($0.160 \leq x \leq 0.200$), the first transition temperature was shifted from 230 to 210 °C, the second from 400 to 375 °C, and the third from 450 to 410 °C. For the prepared compositions, two most intense peaks were observed at around 400 and 450 °C. The peaks (at around 400 and 450 °C) were observed shifted, towards lower temperature, as the concentration of x increased, from 0.160 to 0.200, Fig. 11.

From the soft mode theory of perovskites, the dielectric permittivity is obtained proportional to the inverse of the square of the active phonon mode frequency [33]. In $NaNbO_3$, when Na is substituted by K atoms, the force constant changes due to the modification of bond length, ionic radius, cell parameters, etc., leading to frequency shift. The randomly distributed K in the $NaNbO_3$ lattice results variation in mass and force constant, which leads to the frequency shift of the soft mode and thereby to the observed change in the dielectric constant, with the substitution of Na by K in the lattice. The respective dielectric conductivity peaks were observed shifted to a slightly lower temperature than the dielectric constant peaks (at T_c) at the ferro-to para-electric transition temperature, for composition $x = 0.160$, and at the same temperatures as observed from the respective dielectric constant peaks (at T_c) for rest of the compositions. The dielectric anomaly, near the T_c, can be explained by the fact that soft mode frequency softens, giving rise to a considerable value of dielectric constant and dielectric conductivity. However, due to the resultant effect of structural change, grain boundary barrier heights, and activation energy of surface terms, respective dielectric conductivity peaks were observed at slightly lower temperatures than those observed from dielectric constant peaks for the compositions with $x = 0.160$. For the rest of the prepared compositions, the respective dielectric conductivity and dielectric constant peaks were observed at the same temperatures.

The barrier heights depend on the dielectric constant of bulk grains, $T\text{-}T_c$ (from high symmetry phase side); increasing dielectric constant leads to a decrease in the barrier heights, which results an exponential increase in conductivity. In the region $T < T_c$, grain boundary barrier heights are diminished due to the compensation of the grain boundary charge by spontaneous polarization [34] or due to the disappearance of localized states at the grain boundaries in the observed phase [35]. Near but below T_c, the diminishing barrier heights leading to a high loss in the prepared samples; the loss is determined by the softening of the optical mode [10,36] rather than barrier heights. At T_c, dielectric loss is observed minimum, which indicates that barrier heights have not been fully diminished at this temperature. They have a dominating effect rather than the optical mode softening [10,36–38] and the activation energy of surface terms. The dominating barriers might be allowing the least current to pass through, which results lowest dielectric loss at T_c. With increasing temperature, above T_c, activation energy of surface terms increases, and dielectric loss increases with temperature. Near but above T_c, dielectric constant decreases with increasing temperature, leading to an increase in barrier heights, which leads to an increase in resistivity with the rise of temperature, until the activation energy becomes equal to or greater than the potential barrier. Beyond that temperature, resistivity starts decreasing with further temperature rise, as in the semiconductors.

Effect of grain boundary potential barriers seems to dominate more than the effect of the softening of the ferroelectric mode and structural change, for the observed dielectric conductivity and loss behavior of the prepared samples, around the transition temperature. For the compositions near $x = 0.175$, the respective dielectric constant peak and conductivity peak were observed at the same temperature [39].

3.2. Phase transition behavior and HT- X-Ray diffractometer measurements for $N_{1-x}K_xNbO_3$ (x = 0.175)

For the samples with x = 0.175, the HT- XRD patterns were measured near transition temperatures to investigate the anomalies encountered in the dielectric measurements. Among the prepared compositions, only one composition was taken up due to a similar dielectric anomaly. The observed HT-XRD patterns have been shown in Fig. 12. HT-XRD data collected at different temperatures were compared with the dielectric anomaly. The various parameters have been observed from Rietveld refinement and are given in Table 1. For the sample x = 0.175, lattice parameters of HT-XRD refinement are shown in Fig. 13.

From the room temperature XRD patterns (x = 0.175), the samples show monoclinic phase, between RT and around 210 °C, and is consistent with ICSD- (01-074-2025) and (01-074-2024) data, and in good agreement with the measurements of reference [31]. Between 210 and 380 °C, it reflects tetragonal phase, consistent with ICSD- (01-077-0037) data, between 380 and 460 °C, tetragonal phase with change in lattice, consistent with ICSD- (00-077-0037) data, and reference [4]; and above 460 °C, it shows cubic phase and compatible with ICSD- (01-078-5547) data, data of reference [3].

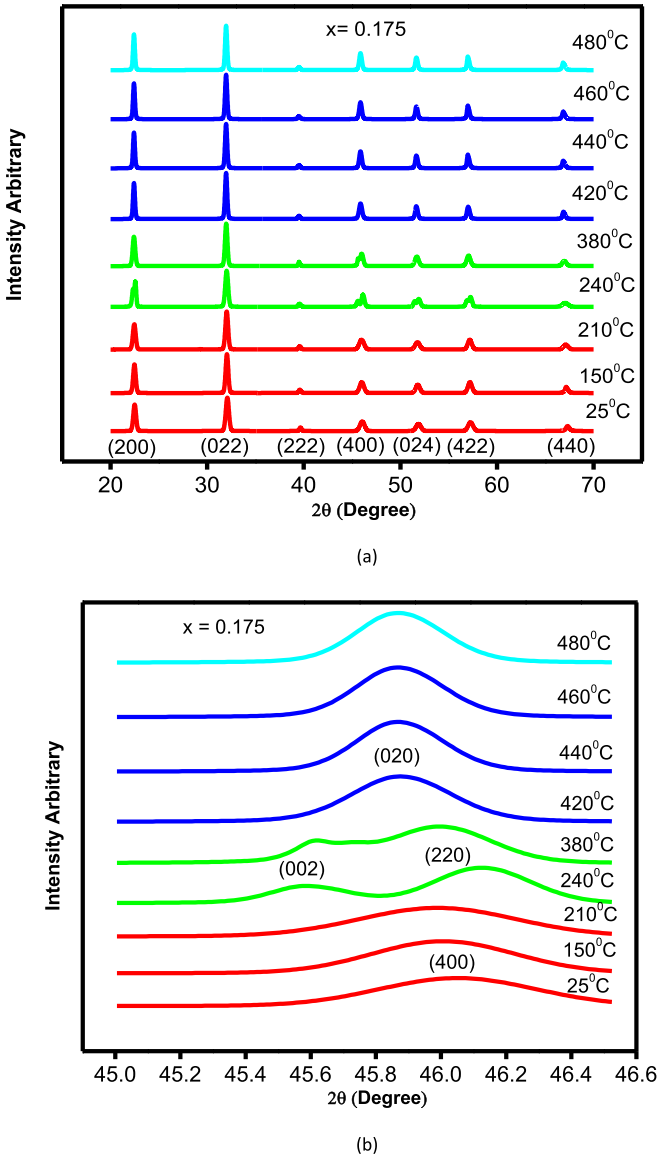

Fig. 12. XRD patterns of $Na_{1-x}K_xNbO_3$ (x = 0.175) with variation in temperature (a), expanded angle view (45°- 46.6°) (b). Monoclinic phase were observed, between RT and around 210 °C with ICSD- (01-074-2025); between 210 and 380 °C, it reflects tetragonal phase with ICSD- (01-077-0037) data; and further, between 380 and 460 °C, tetragonal phase with a change in the lattice, and above 460 °C, it shows cubic phase and consistent with ICSD- (01-078-5547) data.

With the help of HT- XRD data, the demonstration of peaks at 2θ ~ 45°, with different temperatures, are shown in Fig. 12 (b). The X-ray diffraction pattern of NKN has been refined with monoclinic (P6mm) space group (ICSD 01-074-2025) and Tetragonal (P4/mbm) space group (ICSD 01-077-0037), with peak (400), with dominated monoclinic phase (97%), as 25 °C (NKN) approached [31]. Tetragonal (P4/mbm) space group (ICSD 01-077-0037) is characterized by the split of the peak at 2θ ~ 46°, with peak (220) at higher (2θ ~ 46.091°) Bragg angle and peak (002) at lower (45.56°) Bragg angle as 240 °C (NKN) approached [4]. Again, the tetragonal (P4/mbm) space group (ICSD 01-077-0037) is characterized with decreased lattice, peak (020) with Bragg angle 2θ ~ 45.841°, as around 380 °C (NKN) approached [4]. The peak (020) characterizes cubic phase (ICSD 01-078-5547) at lower 2θ Bragg angle (2θ = 45.837°), as 460 °C (NKN) approached [3].

A continuous peak shifting was observed in the most intense peaks (200), (022), (400), and (024) with the change in temperature in $Na_{1-x}K_xNbO_3$ (x = 0.175). For x = 0.175, the peaks were observed shifting to a lower angle with increasing temperature, between RT to 210 °C and above 210 °C these peaks were observed shifting to lower angle, and further, above 380 °C, peaks (002) and (220) vanished and above 460 °C, the remaining peaks were observed slightly shifting towards a lower angle, Fig. 12 (b). From the measured HT-XRD patterns, the four distinguishable phases, exhibiting transitions, consistent with dielectric measurements, at near 210, 380 and 460 °C, were observed.

The lattice parameters were processed by High Score Plus software, using the Rietveld method, and the background was modeled using the Legendre polynom, and the peaks' profiles were processed using a pseudo-Voigt function [40,41]. The selected space groups for these refinements were monoclinic Pm6 and tetragonal P4mm/mbm, respectively [42]. The tetragonal phases have a similar space group, i. e., P4mm/mbm, but have small changes in their lattice. Beyond temperature 460 °C, the HT- XRD shows the cubic phase. The processed lattice parameters and angle (β for monoclinic symmetry) are shown in Fig. 13 and suggest the three abrupt changes in the structure of NKN (x = 0.175). The measured XRD patterns make it visible to differentiate the monoclinic, tetragonal, tetragonal (with different lattice parameters), and cubic symmetries, in different temperature ranges. The observed HT- XRD results support the transitions observed from the dielectric constant and electric conductivity measurements of $Na_{1-x}K_xNbO_3$ ($0.160 \leq x \leq 0.200$) pellets. From these observations it is evident that the so called X phase exists as the tetragonal phase, between 380 and 460 °C, in the measured compositions [43].

4. Conclusion

The observed dielectric constant and electric conductivity exhibit minimum values for the samples with x = 0.175, at 1 MHz frequency. For the samples with x = 0.175, HT-XRD indicate the existence of four distinct phases, viz., monoclinic, between room temperature (RT) and 210 °C; tetragonal, between 210 and 380 °C; and above 380 °C, tetragonal with the change in lattice, between 380 and 460 °C; and above 460 °C, cubic structure. The monoclinic to tetragonal phase transition at around 210 °C, and tetragonal to tetragonal (with the change in lattice) at around 380 °C, and tetragonal to cubic (with decreased lattice) at around 450 °C, were distinctly observed from dielectric and HT- XRD measurements in the present study.

Declaration of competing interest

The authors declare that they have no known competing financial interests or personal relationships that could have appeared to influence

Table 1
Lattice and other parameters of $Na_{1-x}K_xNbO_3$ system, with x = 0.175 (at various temperatures).

Lattice & other Parameters (X = 0.175)	Temp. (25 °C)	Temp. (150 °C)	Temp. (210 °C)	Temp. (240 °C)	Temp. (380 °C)	Temp. (420 °C)	Temp. (440 °C)	Temp. (460 °C)	Temp. (480 °C)
a/Å	7.495 (3)	7.92 (3)	7.92 (3)	5.616 (1)	5.607 (1)	5.582 (1)	5.5744 (9)	5.581 (1)	3.9475 (6)
b/Å	7.524 (3)	7.83 (3)	7.82 (3)	5.616 (1)	5.607 (1)	5.582 (1)	5.5744 (9)	5.581 (1)	3.9475 (6)
c/Å	7.672 (5)	7.91 (9)	7.86 (9)	3.9381 (6)	3.9445 (5)	3.9515 (3)	3.9541 (4)	3.9517 (3)	3.9582 (7)
alpha/°	90	90	90	90	90	90	90	90	90
beta/°	90.51 (4)	90.3 (3)	90.4 (4)	90	90	90	90	90	90
gamma/°	90	90	90	90	90	90	90	90	90
R (Bragg)/%	66.89249	92.82535	92.58818	38.97279	40.56617	41.24910	39.44897	41.03093	37.22320

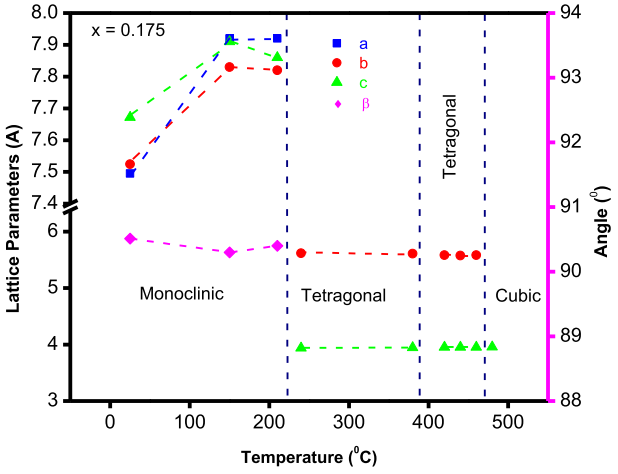

Fig. 13. Variation of lattice parameters with temperature, in $Na_{1-x}K_xNbO_3$ (x = 0.175).

the work reported in this paper.

References

[1] H.D. Megaw, The seven phases of sodium niobate, Ferroelectrics 7 (1974) 87–89.
[2] A.M. Glazer, K. Ishida, Cation displacements and octahedral tilts in $NaNbO_3$ Part I Determination from x-ray difference reflections, Ferroelectrics 6 (1974) 219–1224.
[3] M. Ahtee, A.M. Glazer, High-temperature phases of sodium niobate- potassium niobate solid solutions, Ferroelectrics 12 (1976) 205–206.
[4] M.A.L. Nobre, S. Lanfredi, Impedance spectroscopy analysis of high- temperature phase transitions in sodium lithium niobate ceramics, J. Phys. Condens. Matter 12 (2000) 7833–7841.
[5] M.A.L. Nobre, S. Lanfredi, Phase transition in sodium lithium niobate polycrystal: an overview based on impedance spectroscopy, J. Phys. Chem. Solid. 62 (2001) 1999–2006.
[6] D. Lin, Z. Li, F. Li, C. Cai, W. Liu, S. Zhang, Tetragonal- to- tetragonal phase transition in lead- free $(K_xNa_{1-x})NbO_3$ (x = 0.11 and 0.17) crystals, Crystals 4 (2014) 113–122.
[7] A.S. Kandari, A. Bhandari, A.A. Bourai, N.S. Panwar, Electrical properties of $Na_{1-x}K_xNbO_3$ ($0.28 \leq x \leq 0.40$), Ferroelectrics 386 (2009) 139–151.
[8] V. Lingwal, B.S. Semwal, N.S. Panwar, Relaxational behavior of mixed $NaNbO_{[3]}$-$KNbO_{[3]}$ system, Ferroelectrics 332 (2006) 219–225.
[9] Y. Zhen, J.F. Li, Normal sintering of (K, Na)$NbO_{[3]}$- based ceramics: influence of sintering temperature on densification, microstructure, and electrical properties, J. Am. Ceram. Soc. 89 (2006) 3669–3675.
[10] N.S. Panwar, T.C. Upadhyay, B.S. Semwal, Soft mode dynamics of perovskite type crystals, Pramana - J. Phys. 33 (1989) 603–616.
[11] E. Pytte, Theory of perovskite ferroelectrics, Phys. Rev. B5 (1972) 3758–3769.
[12] M. Ahtee, A.W. Hewat, Structural phase transition in sodium-potassium niobate solid solutions by neutron powder diffraction, Acta Crystallogr. A34 (1978) 309–317.
[13] L. Egerton, Dolores M. Dillon, Piezoelectric and dielectric properties of ceramics in the system potassium-sodium niobate, J. Am. Soc. 42 (1959) 438–442.
[14] S.Y. Chu, W. Water, Y.D. Juang, J.T. Liaw, S.B. Dai, Piezoelectric and dielectric characteristics of lithium potassium niobate ceramic system, Ferroelectrics 297 (2003) 11–17.
[15] H. Zhang, Y. Zhu, P. Fan, M.A. Mawat, W. Ma, K. Liu, H. Liu, B. Xie, K. Wang, J. Koruza, Temperature-insensitive electric-field-induced strain and enhanced piezoelectric properties of <001> textured (K, Na)NbO_3-based lead-free piezoceramics, Acta Mater. 156 (2018) 389–398.
[16] P. Fan, Y. Zhang, Q. Zhang, B. Xiea, Y. Zhua, M. Ali Mawat, W. Ma, K. Liu, J. Xiao, Haibo Zhang, Large strain with low hysteresis in $Bi_4Ti_3O_{12}$ modified $Bi_{1/2}(Na_{[0.82]}K_{[0.18]})_{1/2}TiO_{[3]}$ lead-free Piezoceramics, J. Eur. Ceram. Soc. 38 (2018) 4404–4413.
[17] H. Zhang, P. Xu, E. Patterson, J. Zang, S. Jiang, J. Rödel, Preparation and enhanced electrical properties of grain-oriented $(Bi_{1/2}Na_{1/2})TiO_{[3]}$- based lead-free incipient piezoceramics, J. Eur. Ceram. Soc. 35 (9) (2015) 2501–2512.
[18] S.E. Park, T.R. Shrout, Ultrahigh strain and piezoelectric behavior in relaxor based ferroelectric single crystals, J. Appl. Phys. 82 (1997) 1804–1811.
[19] B. Jaffe, W.R. Cook, J.H. Jaffe, Piezoelectric Ceramics, Academic, New York, 1971.
[20] V.J. Tennery, K.W. Hang, Thermal and X-ray diffraction studies of the $NaNbO_3$-$KNbO_3$ system, J. Appl. Phys. 39 (1968) 4749–4753.
[21] D.D. Athayde, D.F. Souza, A.M.A. Silva, D. Vasconcelos, E.H.M. Nunes, J.C. Costa, W.L. Vasconcelos, Review of perovskite ceramic synthesis and membrane preparation methods, Ceram. Int. 42 (2016) 6555–6571.
[22] E.C. Subbarao, Science and Technology of Rare Earth Materials, Academic Press, New York, 1980.
[23] D. Biswas, G.S. Kathait, P. Thapliyal, V. Rohilla, S. Singh, J. Negi, Converse piezoelectric properties of K and Na-modified $(Na_{1-x}K_x)$ NbO_3 lead free ceramics for x = 0.08 and 0.17, Ferroelectrics 550 (2019) 228–232.
[24] D. Biswas, G.S. Kathait, P. Thapliyal, V. Rohilla, S. Singh, Temperature dependence of dielectric properties of sodium potassium niobate ceramics for different values of x ($Na_{1-x}K_xNbO_3$), Ferroelectrics 526 (2018) 168–175.
[25] D. Biswas, N.S. Panwar, P. Sharma, Converse piezoelectric properties of lead free $Ba_{1-x}Ca_xZr_{0.1}Ti_{0.9}O_3$ (x = 0.055) ceramics using double sintered method, Ferroelectrics 568 (2020) 95–103.
[26] R.E. Jaeger, L. Egerton, Hot pressing of potassium-sodium niobates, J. Am. Ceram. Soc. 45 (1962) 209–213.
[27] G.H. Heartling, Properties of hot-pressed ferroelectric alkali niobate ceramics, J. Am. Ceram. Soc. 50 (1967) 329–330.
[28] L.E. Cross, Electric double hysteresis in (K_xNa_{1-x}) NbO_3 single crystals, Nature 181 (1958) 178–179.
[29] A.S. Kandari, V. Lingwal, N.S. Panwar, Morphotropic Region in $Na_{1-x}K_xNbO_3$, between x= 0.17 and 0.18, Ferroelectrics 396 (2010) 18–26.
[30] R.C. Buchanan, M. Dekker, Ceramic Materials for Electronics: Processing, Properties, and Applications, second ed., Inc., New York, 1991, p. 532.
[31] G. Shirane, R. Newnham, R. Pepinsky, Dielectric properties and phase transitions of $NaNbO_3$ and $(Na,K)NbO_3$, Phys. Rev. 96 (1954) 581–588.
[32] A.J. Moulson, J.M. Herbert, Electroceramics, Wiley, England, 2003.
[33] X. Gonze, C. Lee, Dynamical matrices, Born effective charges, dielectric permittivity tensors, and interatomic force constants from density-functional perturbation theory, Phys. Rev. B 55 (1997) 10355–10368.
[34] W. Heywang, Structural engineering of ferroelectrics, Ferroelectrics 49 (1983) 3–14.
[35] V.B. Kraskov, K.S. Valeev, On the model of positor effect in conducting barium titanate, Bull. Acad. Sci. USSR, Phys. Ser. 39 (1975) 166.
[36] W. Cochran, Crystal stability and the theory of Ferroelectricity, Adv. Phys. 9 (1960) 89.
[37] B.S. Semwal, N.S. Panwar, Dielectric properties of perovskite crystals, Bull. Mater. Sci. 15 (1992) 237.
[38] G.A. Samara, P.S. Peercy, The Study of Soft-Mode Transitions at High Pressure, Solid State Physics, vol. 36, Academic Press, New York, 1982, pp. 1–118.
[39] A.S. Kandari, A. Bhandari, A.A. Bourai, et al., Electrical properties of $Na_{1-x}K_xNbO_3$ ($0.28 \leq x \leq 0.40$), Ferroelectrics 386 (2009) 139–151.
[40] J. Tellier, B. Malic, B. Dkhil, D. Jenko, J. Cilensek, M. Kosec, Crystal structure and phase transitions of sodium potassium niobate perovskites, Solid State Sci. 11 (2009) 320–324.
[41] L.V. Azaroff, Elements of X-Ray Crystallography, McGraw Hill Book Company, New York, 1968.
[42] J. Attia, L. Bellaiche, P. Gemeiner, Study of potassium-sodium-niobate alloys: a combined experimental and theoretical approach, J. Phys. IV - Proc. 128 (2005) 55–60.
[43] S. Singh, J. Negi, N.S. Panwar, Temperature dependent dielectric properties of (Na, K) NbO3, near equimolar composition 45 (2019) 13067–13071.

Journal of Applied Physics

Electrical and optical properties of $(Ta_2O_5)_{1-x}$–$(TiO_2)_x$ films, x = 0.035, prepared by sputtering of ceramic and mosaic (Ta, Ti) metal targets

Cite as: J. Appl. Phys. **130**, 035304 (2021); https://doi.org/10.1063/5.0055725
Submitted: 02 May 2021 . Accepted: 03 July 2021 . Published Online: 21 July 2021

Prashant Thapliyal, N. S. Panwar, and G. Mohan Rao

View Online Export Citation CrossMark

Challenge us.
What are your needs for periodic signal detection?
Watch
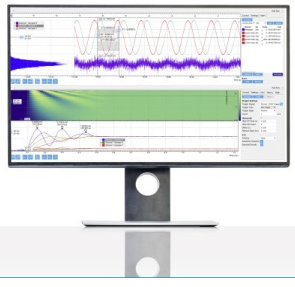
Zurich Instruments

© 2021 Author(s).

Journal of Applied Physics ARTICLE scitation.org/journal/jap

Electrical and optical properties of $(Ta_2O_5)_{1-x}$–$(TiO_2)_x$ films, x = 0.035, prepared by sputtering of ceramic and mosaic (Ta, Ti) metal targets

Cite as: J. Appl. Phys. **130**, 035304 (2021); doi: 10.1063/5.0055725
Submitted: 2 May 2021 · Accepted: 3 July 2021 ·
Published Online: 21 July 2021

View Online Export Citation CrossMark

Prashant Thapliyal,[1,2,a)] N. S. Panwar,[1] and G. Mohan Rao[2]

AFFILIATIONS

[1]Department of Instrumentation Engineering, H.N.B. Garhwal University, Srinagar, Garhwal 246174, India
[2]Department of Instrumentation and Applied Physics, Indian Institute of Science, Bangalore 560012, India

[a)]**Author to whom correspondence should be addressed:** pra.thapli1986@gmail.com

ABSTRACT

$(Ta_2O_5)_{1-x}$–$(TiO_2)_x$, with x = 0.035, thin films were deposited onto p-type silicon and quartz substrates following two different routes: first, by the sputtering of the ceramic target and, second, by sputtering of mosaic (Ta, Ti) metal target in the presence of oxygen (hereafter referred to as CT and MT, respectively). The deposited films were found to crystallize on annealing at and above 700 °C. The dielectric constant of the prepared films was found to increase with increasing annealing temperature, up to 700 °C, and on annealing at 800 °C, it was found to decrease. The dielectric constant of the CT was observed to be higher than that of the MT film structures at each annealing temperature. From the transmittance measurements, different optical parameters of the deposited crystalline films were calculated. The leakage current density of the CT films was found to increase with the annealing temperature, whereas in the MT films, it drastically decreased by an order of ~3 when the annealing temperature was increased from 700 to 800 °C. Different conduction mechanisms were observed in the different applied field regions in the prepared film structure. The observed electrical properties of the prepared film structure seem to depend on the status of the growing interfacial oxide layer on annealing.

Published under an exclusive license by AIP Publishing. https://doi.org/10.1063/5.0055725

I. INTRODUCTION

Fast-growing semiconductor-based microelectronic industries have set their high-performance criteria to fulfill the requirements to overcome the challenges from other competitors in the field. Among these, the performance criteria based on characteristics, viz., high dielectric constant, low leakage current density ($<10^{-8}$ A/cm^2), high breakdown strength, low switching voltage, and material fabrication processes available at a low temperature, have been focused on mainly.[1–3] Due to their compatibility with the manufacturing infrastructure, silicon (Si) based dielectrics, e.g., SiO_2 and SiO_xN_y, have been extensively used in dynamic random access memory (DRAM) and complementary metal–oxide–semiconductor (CMOS) applications in the microelectronics industry until the last couple of decades. However, the high power consumption, high leakage current,[4,5] and limitation of physical dimensions due to the use of these low dielectric constant (K) dielectrics[6] push researchers to explore compatible high-K oxide materials, such as HfO_2, ZrO_2, TiO_2, and Ta_2O_5.[7–10]

Tantalum pentoxide (Ta_2O_5) was identified as the most promising candidate among the proposed and investigated high-K oxides due to its high dielectric constant and chemical stability that may potentially replace Si-based dielectrics in storage capacitors.[9,11–15] However, the structural and dielectric properties of Ta_2O_5 insulating films have been reportedly found to be intensely dependent on the nature of the depositing substrate, fabrication method, post-deposition annealing conditions, and electrode material.[16–19] In particular, Ta_2O_5 amorphous films were observed to be better than crystalline films with regard to leakage current and breakdown strength.[20] Titanium dioxide (TiO_2), which may be another possible choice in the electronic semiconductor industry, has various applications in lithium-ion batteries,[21] photovoltaic cells, and solar collectors as antireflection coatings,[22] electrochromic displays,[23] humidity, and gas sensors.[24,25] TiO_2, reportedly having a high dielectric constant (~100) and comparatively smaller bandgap (~3.5 eV)[26] than the other metal oxides, exhibits a large

Published under an exclusive license by AIP Publishing

leakage current and unstable contact with Si.[27] In recent years, the technological trend of using TiO_2 doped composites of other metal oxides, such as Ta_2O_5, HfO_2, and ZrO_2,[28–30] has increased drastically. In general, it is associated with the assumption that doping concentration acts as a network modifier and quenches the dangling bonds of excess oxygen in metal oxides,[31] resulting in reduced leakage current and trap density. Also, doping may be held responsible for increasing the transition temperature of the amorphous-to-crystalline phase change.[32] With the doping process, the dielectric properties of Ta_2O_5 were observed to improve, and the crystallization temperature shifts toward the higher temperature,[33] which may lower the leakage current after high-temperature annealing treatment.[34–37] For $[(Ta_2O_5)_{1-x}–(TiO_2)_x]$ (TTO_x) ceramics, high dielectric constant values have been reported as 126 for $x = 0.08$,[34] 340 for $x = 0.056$,[38] and 280 for $x = 0.08$.[39] To achieve a high dielectric constant in TTO_x films also, some attempts have been made by the researchers and have obtained $K = 55$, using $(TiO_2)_x–(Ta_2O_5)_{1-x}$ ceramic target with $x = 0.08$,[40] and $K = 71$, using metal TTO_x target with $x = 0.06$.[33] A lower-K interfacial layer was observed in between the Si substrate and the Ta_2O_5 film, which forms a thermodynamically unstable contact at the interface like many other transition metal oxides.[11,41,42] The crystallizing high-temperature (>600 °C) heat treatment results in thicker unavoidable interfacial oxide (SiO_2) layer in between Si and Ta_2O_5 films[9,43] and reduces the breakdown strength.[44,45] Various optical materials have been investigated and used as optical lamps.[46,47] The desirable optical properties of the thin-film materials, e.g., high transmittance and refractive index, and high mechanical and temperature stability, must be tested for the different applications.[48] Ta_2O_5 was reported with its beautiful applications in optics as highly transparent and refracting material,[49] as anti-reflecting coatings,[50] and as optical waveguides.[51,52] Sputter deposition was reported as a better choice among other deposition methods due to its reasonable control over the microstructure, composition, electrical and optical properties, and other deposition parameters.[53] In the present study, $TTO_{0.035}$ films were separately prepared by magnetron sputtering of the ceramic and mosaic (Ta, Ti) metal targets in the presence of oxygen onto silicon and quartz substrates. The as-deposited films were annealed at different temperatures (≤800 °C). The structural, electrical, and optical properties of prepared films were studied, and the observed results of the crystalline films are presented here.

II. EXPERIMENTAL

A ceramic pellet target of TTO_x, with $x = 0.08$, was prepared by the conventional solid-state reaction method due to the reported enhanced dielectric properties in bulk for this composition.[34,39,54] High purity (99.99%) tantalum pentoxide (Ta_2O_5) and titanium dioxide (TiO_2) powders were used as the initial materials. The initial materials were dried at 200 °C for 2 h to remove the possible moisture content. The initial powder materials were weighed in stoichiometric ratio to prepare TTO_x ($x = 0.08$). The powder materials were ground for a total of 8 h to get the homogeneity, with 5 h wet grinding in methanol and 3 h dry grinding, using an agate-mullet mortar and pestle. The ground powder mixture was kept in a high-temperature alumina crucible. The mixture carrying crucible was kept in a muffle furnace for heating, at 1400 °C, for 14 h, at the atmospheric pressure. The powder mixture was further ground for 2 h after it was cooled to room temperature. By pressing the ground powder at 0.2 GPa, a pellet target with a diameter of 2 in. and a thickness of about 4 mm was prepared. The pellet target was carefully removed from the die assembly and kept for sintering at 1400 °C for 15 h. After slow cooling to room temperature, in a controlled manner, the prepared pellet target was taken out of the furnace. This ceramic target was radio frequency (RF) magnetron sputtered, and the TTO_x, $x = 0.035$, thin films, were deposited. Also, a similar TTO_x film composition was deposited by direct current (DC) magnetron sputtering of a suitably arranged mosaic (Ta, Ti) metal target in the presence of oxygen, where the sputtering areas of the Ta and Ti metals were arranged such that the TTO_x films with $x = 0.035$ could be deposited. For depositing the composite metal–oxide films, the mosaic assembly[33] of Ta and Ti metals (2 in. diameter, 1 mm thick, and 99.99% pure solid Ta, and star-shaped Ti and Ta) was used as a target (Fig. 1). Mono-crystalline p-type (1 0 0) oriented silicon and optically polished quartz were used as substrates to deposit the TTO_x thin films. The substrates (silicon and quartz) were rinsed by the solution of de-ionized water and acetone. The silicon substrates were additionally treated with a 1:20 hydrogen fluoride (HF) solution to remove the oxide layer. Finally, the substrates (silicon and quartz) were rinsed sufficiently with de-ionized water followed by ultrasonication before loading into the vacuum chamber. A high-speed turbo molecular pump with the combination of the rotary pump was used to evacuate the sputtering chamber up to base pressure (1.0×10^{-5} mbar). The needle valves were used to regulate the flow of sputtering (argon with 99.999% purity) and reactive (oxygen with 99.999% purity) gases; the pressure in the vacuum chamber was measured using the Pirani and Penning gauges. In both cases, the target was pre-sputtered to get a clean sputtering surface by masking the substrate for 5 min before it was exposed for depositing a film onto it. It was done by using a substrate masking assembly, which facilitates the masking of the substrate during pre-sputtering of the target. After 5 min of pre-sputtering, the mask was removed, and the substrate was exposed for the deposition of sputtered material onto it. During the deposition, the substrate holder was horizontally rotated for the deposition of homogeneous composition.

Targets were sputtered at different conditions after optimizing the preparation conditions, separately, for ceramic and mosaic metal targets. First, the ceramic target was loaded into the vacuum chamber, and the chamber was evacuated to the base pressure of 1.0×10^{-5} mbar. Keeping the target substrate distance (TSD) of 40 mm, the ceramic target was RF sputtered, with 110 W, at 7.0×10^{-3} mbar argon working pressure to deposit the films onto the Si and quartz substrates. Similarly, with 50 mm TSD, the mosaic (Ta, Ti) metal target was DC sputtered, with 750 V, 60 mA, at 5.0×10^{-3} mbar working pressure, in the presence of oxygen with 2.5×10^{-4} mbar partial pressure. In reactive sputtering, the oxygen partial pressure was optimized such that the sputtering sustains at the lower working pressure. The higher presence of oxygen may poison the metals of the target, and it may scatter the sputtered atoms resulting in a reduced deposition rate.[48] The working pressure, in either case, was chosen to yield the best deposition rate with maintaining the sputtering process throughout. At higher

Published under an exclusive license by AIP Publishing

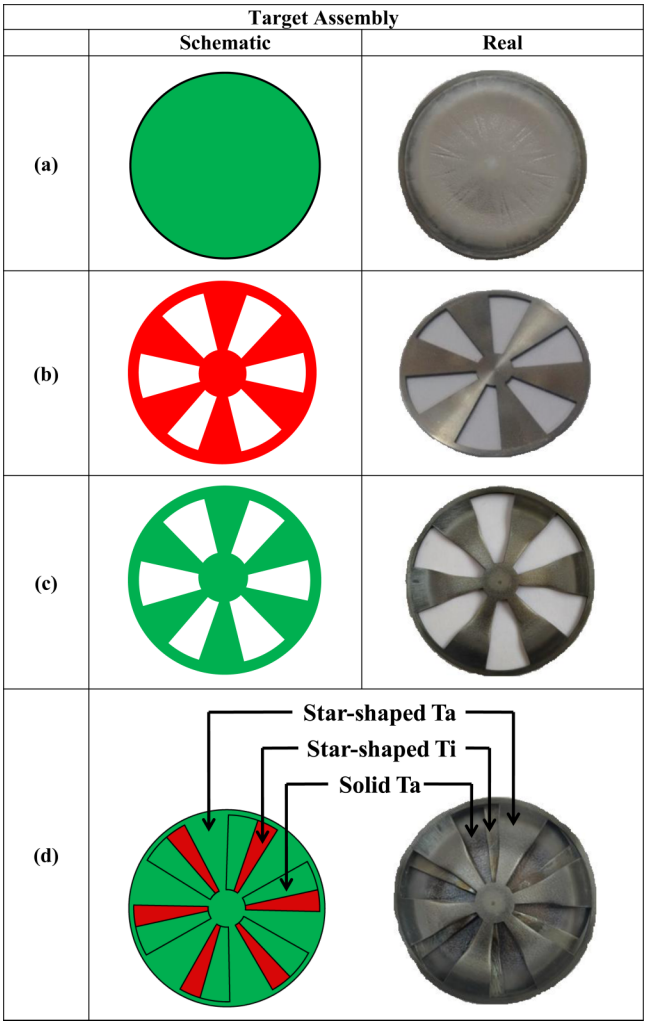

FIG. 1. (a) Solid Ta target, (b) star-shaped Ti target, (c) star-shaped Ta target, and (d) solid Ta-star shaped Ti-star shaped Ta mosaic target assembly.

working pressure, the deposition rate slows down due to the scattering of the sputtered atoms by ambient gas. From ellipsometric measurements, CT films were 350 ± 10 nm thick and MT films were 280 ± 10 nm thick. The as-deposited CT and MT films were annealed for 1.5 h, at temperatures of 500, 600, 700, and 800 °C. Using a shadow mask (holes with 0.5 mm diameter), silver (Ag) was sputter-deposited onto the top of the deposited films to fabricate the Ag/$TTO_{0.035}$/p-Si metal–oxide–semiconductor (MOS) structures. The bottom ohmic contact was formed by using sputter-deposited silver (Ag) metal at the back side of the silicon substrate.

Different measuring instruments were used for various measurements, viz., x-ray diffractometer to determine crystal structure, scanning electron microscope-energy dispersive spectrometer (SEM-EDS) and x-ray photoelectron spectroscopy (XPS) for elemental identification and concentration in the films, RLC meter for capacitance–voltage (C–V) measurements, ferroelectric PE loop tracer with piezometer for current–voltage (I–V) measurements, ultraviolet–visible (UV–Vis) spectrophotometer for optical measurements, and spectroscopic ellipsometer for thickness measurements. The composition of the prepared films was determined using SEM-EDS (make: CARL ZEISS, model: MA15/EVO18) with the electron beam energy of 20 keV. The concentration of elements with EDS measurements was determined using "Oxford INCA" software. The EDS results were found to be consistent with XPS measurements, using monochromatic Al Kα radiation (1486.6 eV) as an x-ray source and a hybrid (electromagnetic and electrostatic) lens (make: Kratos, model: Axis Ultra DLD). The wide (survey) scan and individual narrow (high-resolution) spectra were recorded at the pass energy of 160 and 20 eV, respectively. The wide scan and individual narrow spectra were obtained at an energy step size of 1 and 0.1 eV, respectively. CASA XPS tool was used to calibrate or relocate the elemental peaks at their corresponding binding energy positions with reference to the standard carbon C 1s peak at 284.6 eV. The EDS and XPS measurements of the as-deposited films were carried out before depositing conducting silver (Ag) contacts onto the films. The details of other instruments used in these measurements have been described elsewhere.[33,55,56]

III. RESULTS AND DISCUSSION

Figure 2 shows the XRD patterns with h k l planes of the crystalline CT and MT films, annealed at 700 and 800 °C. The orthorhombic Ta_2O_5 structure for both CT and MT films was observed, including three major peaks at their corresponding positions[57] in the XRD peak patterns [source: Inorganic Crystal Structure Database (ICSD) (01-089-2843)] [Figs. 2(a) and 2(b)]. For both the CT and MT films, the peak height was observed decreasing as annealing temperature was increased from 700 to 800 °C, which shows decreasing crystallite size (from 18.32 to 14.87 nm, for CT films and from 18.29 to 17.24 nm, for MT films, calculated by using the Debye–Scherrer[58] formula), on increasing the annealing temperature. The peak height of the CT films was observed higher than the MT films, which may be due to the larger thickness of the former.

Figure 3 shows the EDS patterns of the as-deposited CT and MT films with the characteristic peaks of the detected elements. To determine the composition of the CT and MT films, the atomic percentage obtained from SEM-EDS measurements was used (Table I). Although the starting materials were weighed stoichiometrically to prepare a ceramic target, with x = 0.08, reportedly having the highest dielectric constant TTO_x composition,[34,39] the EDS and XPS results of the sputter-deposited films show the composition, with x = 0.035. The observed lower x in the deposited films than the target may be due to the re-sputtering of lighter Ti atoms from the growing film by the momentum transfer of the sputtered heavier Ta atoms.[59]

The XPS wide spectrum and narrow spectra of Ta 4f, Ti 2p, and O 1s, associated with the as-deposited films, have been shown in Figs. 4(a)–4(d). In the XPS wide spectrum, the characteristic peaks of tantalum Ta 4f, at about 26–29 eV, titanium Ti 2p, at about 454–465 eV; and the distinct peak of oxygen O 1s, at

Published under an exclusive license by AIP Publishing

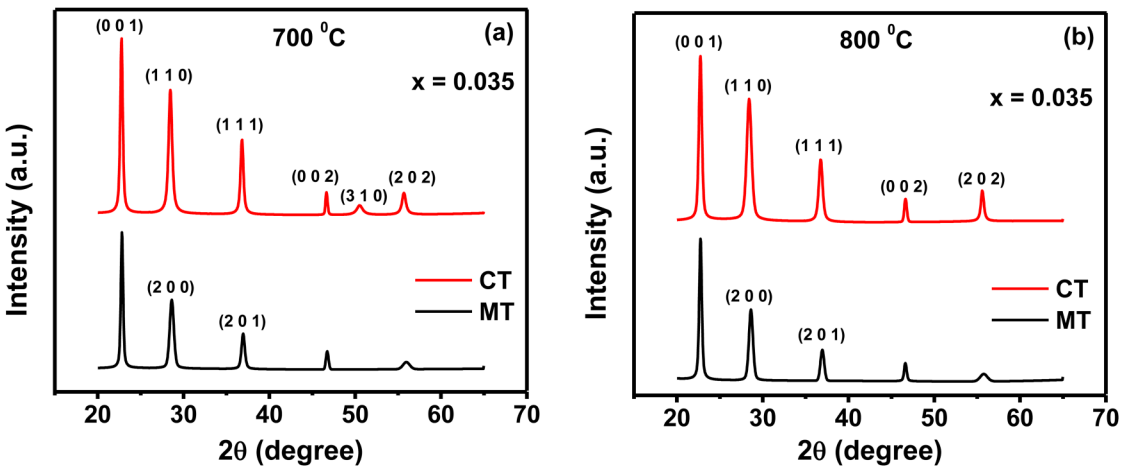

FIG. 2. XRD patterns of CT and MT films, annealed at (a) 700 and (b) 800 °C.

about 530 eV, and carbon C 1s, at about 284.6 eV, were observed [Fig. 4(a)].[33,55,60]

XPS narrow spectrum of the deposited films shows the core-level binding energy of Ta 4f in the 29–26 eV range. In this range, two peaks corresponding to Ta $4f_{5/2}$ and Ta $4f_{7/2}$ were observed at 28.4 and 26.6 eV, respectively [Fig. 4(b)], indicating the fully oxidized state of tantalum.[14] Ta $4f_{5/2}$ and Ta $4f_{7/2}$ peaks were separated by 1.8 eV, which is very close to the reported results.[14,60] XPS narrow spectrum of Ti 2p of the deposited films is shown in Fig. 4(c). The core-level binding energy of Ti $2p_{1/2}$ and Ti $2p_{3/2}$ were found at 462.5 and 454.6 eV, respectively, which were separated by 7.9 eV from each other.[60] In the XPS narrow spectrum of oxygen [Fig. 4(d)], the characteristic peak of O 1s was observed at 530.4 eV, which is consistent with the reported results.[15,60]

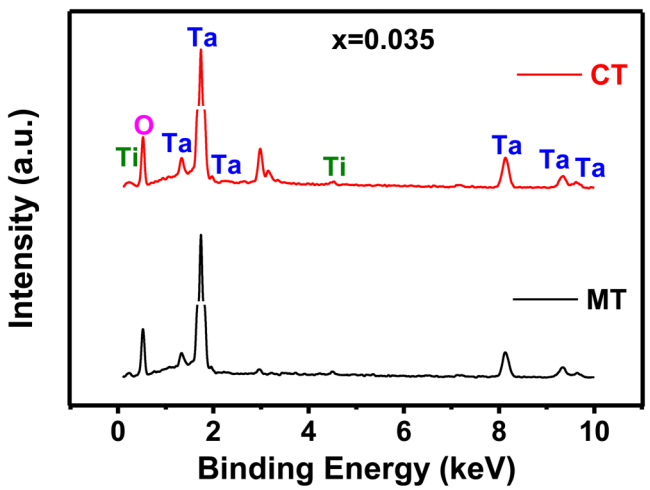

FIG. 3. The observed EDS spectra of as-deposited CT and MT films.

The C–V characteristics of the capacitors, prepared using the as-deposited and films annealed at 500, 600, 700, and 800 °C, were measured with an RLC meter (Fluke–PM6306). The C–V characteristics were plotted at 1 MHz, by employing a to-and-fro sweep of applied DC voltage (between +10 and −10 V), with a 50 mV oscillating signal. The measured C–V characteristics of the CT and MT films, annealed at 700 and 800 °C, are shown in Figs. 5(a) and 5(b). The three usual regions named accumulation, depletion, and inversion [shown in Fig. 5(b)] were observed in the C–V plots.[55,60] When the negative bias voltage is applied, the negative charge of electrons at the gate is compensated by the positive charge of holes collected at the surface of the silicon semiconductor (p-type), which measures the capacitance (C) of the capacitor formed by the deposited film. On the other hand, for the positively biased structure, the surface of the semiconductor becomes depleted with the holes and produces an extra space charge capacitance (C_s), which is added in series to the capacitance C. The change in potential at the gate in the strong inversion region is determined by the presence of electrons at the metal–semiconductor interface. The observed shifting in the C–V plot of the MT films toward the more negative bias may be attributed to the presence of a positive fixed oxide charge at the silicon–oxide film interface.[33,61] Moreover, the MT films were deposited in the presence of oxygen, which may initiate the trapping of more oxide charges at the interface. Also, in the presence of oxygen, an oxide layer is formed at the film–substrate interface, and the equivalent capacitance of the MT film-assisted MOS capacitor was found lower than that of the CT assisted one. The series

TABLE I. Atomic percentage obtained from the EDS measurements for CT and MT films.

Sample	x	Ti (at. %)	Ta (at. %)	O (at. %)
CT films	0.035	0.53	38.54	60.92
MT films	0.035	0.53	37.94	61.53

Published under an exclusive license by AIP Publishing

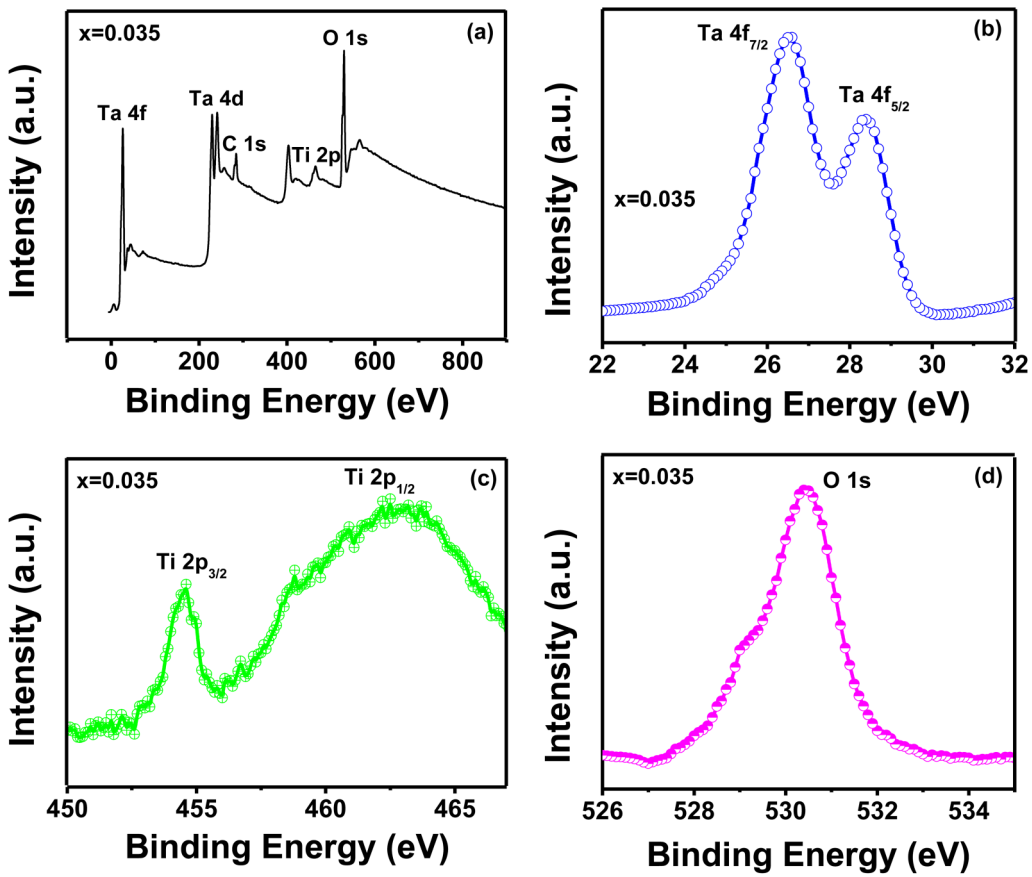

FIG. 4. XPS spectra of as-deposited films: (a) wide spectrum; narrow spectra of (b) Ta 4f, (c) Ti 2p, and (d) O 1s.

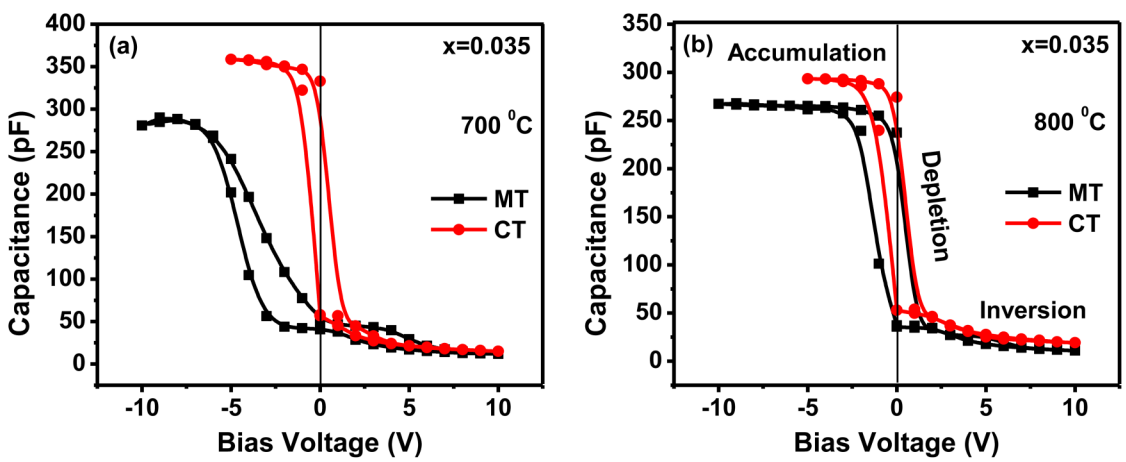

FIG. 5. C–V characteristics of CT and MT films annealed at (a) 700 and (b) 800 °C.

Published under an exclusive license by AIP Publishing

capacitor formed by the oxide layer results in lower equivalent capacitance of the MT film-assisted MOS structures. The CT film-assisted MOS capacitors were prepared in the absence of oxygen, and there was a faint possibility of the formation of such an interfacial oxide layer, resulting in less trapped oxide charges and thereby shifting of the C–V plot to less negative bias and more equivalent MOS capacitance (Fig. 5).

The C–V characteristics of the prepared MOS structure are significantly influenced by the interfacial SiO_2 layer, which is formed at the interface of Si substrate and the deposited TTO_x film. The thickness of this SiO_2 interfacial layer depends on the concentration of oxygen- and thermal-environment of the silicon substrate. Also, the interfacial layer thickness increases with increasing annealing temperature.[15] Presently, the approximate value of the thickness of the interfacial SiO_2 layer was assumed on the basis of the reported studies. The measured capacitance of a prepared structure is the series equivalent of the capacitors formed by the deposited $TTO_{0.035}$ film and the interfacial SiO_2 layer. From the measured capacitance in the accumulation region of the C–V characteristics, effective dielectric constant (K_{eff}) was calculated using the relation[62]

$$K_{eff} = (Cd)/A\varepsilon_o, \quad (1)$$

where C is the measured effective capacitance (in Farad) in the accumulation region, d is the thickness (in meter) of the prepared film, A is the area (in m^2) of the fabricated capacitor, and ε_o (8.854×10^{-12} F/m) is the permittivity of free space.

The effective dielectric constant (K_{eff}) of the MT film structures was observed to be 9, 13, 14, 45, and 43 for the as-deposited films and those annealed at the 500, 600, 700, and 800 °C, respectively. Researchers reported the thickness (d_S) of the interfacial SiO_2 layer in the range of 2.4–3 nm for the Ta_2O_5 film structures, deposited at 10% oxygen concentration,[15,63] which further thickens (up to 4.7 nm) during post-deposition high-temperature (at 850 °C) annealing process.[15] Assuming linear growth in the thickness of the interfacial SiO_2 layer with increasing annealing temperature, the growth of the interfacial layer thickness, in the MT film structures, at annealing temperatures of 500, 600, 700, and 800 °C was extracted, from the straight line connecting the interfacial layer thickness points at room temperature (2.4 nm) and 850 °C (4.7 nm), as 3.7, 4.0, 4.3, and 4.6 nm, respectively. Using the two-layer model,[63] the actual dielectric constant (K_T) of the deposited $TTO_{0.035}$ thin-film material was obtained from the relation

$$K_T = [K_{eff}K_S d]/[K_S(d + d_S) - K_{eff}d_S], \quad (2)$$

where K_S (3.9) is the dielectric constant of the interfacial SiO_2 layer, and d is the thickness of the deposited $TTO_{0.035}$ film. Using the two-layer model, the dielectric constant of the $TTO_{0.035}$ MT film material was found to be 9.1, 13.4, 14.5, 53.7, and 51.5 for the as-deposited films and those annealed at 500, 600, 700, and 800 °C, respectively. The dielectric constant of MT films annealed at 800 °C was observed to decrease compared to the films annealed at 700 °C, which may be attributed to the reduced density of the films with increasing annealing temperature from 700 to 800 °C. The lattice constants (a–c) obtained from the XRD measurements show an increased unit cell volume of the MT films, indicating the release of internal stress and reduced density, on increasing the annealing temperature from 700 to 800 °C (discussed in the section on refractive index measurement).

The CT films were deposited in the absence of active oxygen. The effective dielectric constant of the CT films was observed to be 38, 40, 41, 58, and 47 for the as-deposited films and those annealed at 500, 600, 700, and 800 °C, respectively. Nishioka *et al.*[63] reported that an ~0.7 nm thick native oxide (SiO_2) layer is generally formed onto the Si substrate, which on high-temperature annealing may thicken in the proportion as formed in the case of MT films. By drawing a line parallel to that for the MT films, passing through 0.7 nm (as the CT films were presently deposited in the absence of oxygen) for the as-deposited films, the thickness of the interfacial SiO_2 layer for the CT film structures annealed at 500, 600, 700, and 800 °C was assumed to be 2.0, 2.3, 2.6, and 2.9 nm, respectively. Using the two-layer model, the actual dielectric constant of the prepared $TTO_{0.035}$ CT film material was found to be 38.7, 42.2, 43.7, 64.7, and 51.7 for the as-deposited and films annealed at 500, 600, 700, and 800 °C, respectively. Also, on increasing the annealing temperature, from 700 to 800 °C, the XRD measurements show increased geometrical volume of the unit cell of CT films. However, the refractive index measurements show the improved density of the CT films due to improved oxygen stoichiometry on increasing the annealing temperature, from 700 to 800 °C. The reducing oxygen vacancies seem to be more dominating to increase the density than the decreasing density due to the increasing geometrical unit cell volume of the CT films on annealing at 800 °C. Despite the increased density of the CT films, the decreased dielectric constant of the CT films was observed with increasing annealing temperature from 700 to 800 °C. This may be attributed to the

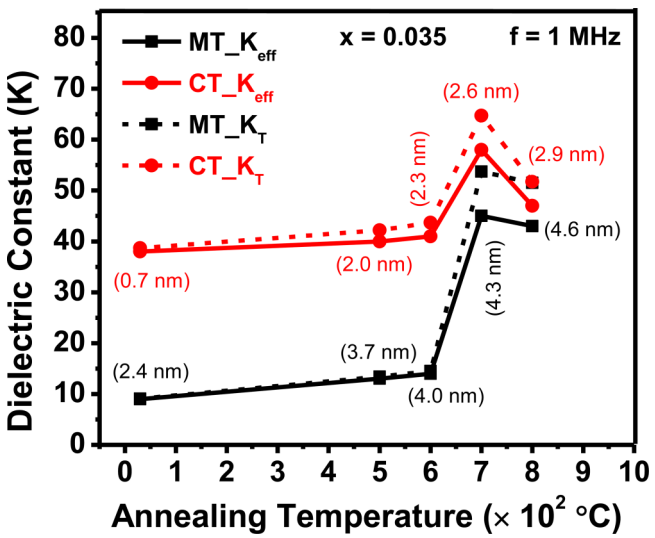

FIG. 6. The values of K_{eff} and K_T of the CT and MT films, annealed at different temperatures (value inside the brackets is the assumed thickness of the interfacial SiO_2 layer at the corresponding annealing temperature).

Published under an exclusive license by AIP Publishing

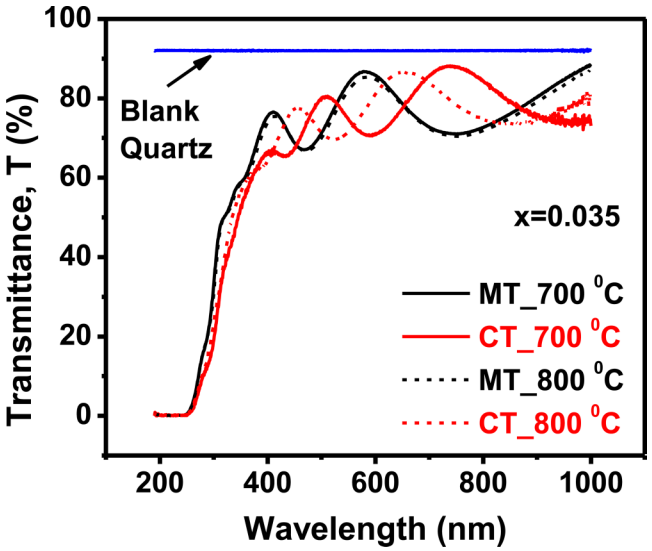

FIG. 7. Transmittance vs wavelength plots of crystalline CT and MT films.

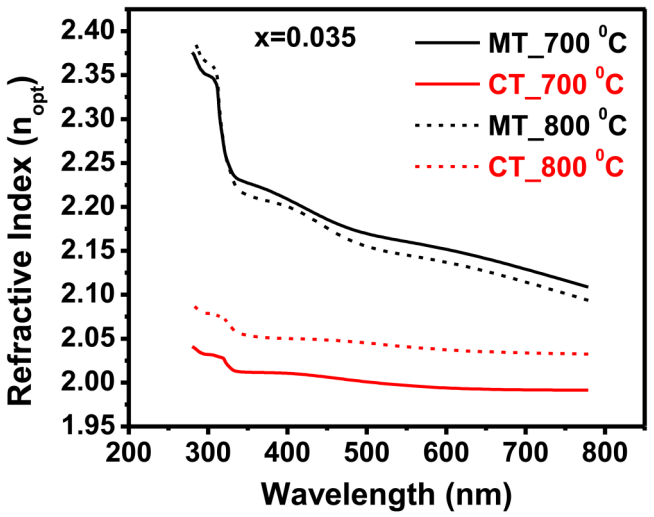

FIG. 8. Refractive index vs wavelength plots for crystalline CT and MT films.

reduced charged oxygen vacancies on annealing at higher temperature, which leads to the reduced polarization in the film volume and results in a decreased dielectric constant. The values of K_{eff} and K_T of CT and MT films, annealed at different temperatures, have been shown in Fig. 6.

Figure 7 shows the wavelength (λ) dependent transmittance (T) plots of $TTO_{0.035}$, CT, and MT films, annealed at 700 and 800 °C. The slightly higher transmittance of the MT films than the CT films may be due to the better oxygen stoichiometry in the former (Table I). For the MT crystalline films, the transmittance was observed (for λ > 400 nm) to decrease (from ~86.74% to 85.40%) as annealing was increased from 700 to 800 °C, which may be due to the reorientation of atoms, reduced crystallite size, and the more oxygen escaping from the film volume than supplied, at the higher annealing temperature.[56,64,65] A slight increase was observed in the transmittance of the CT crystalline films, as annealing temperature increased from 700 to 800 °C, which may be due to improved oxygen stoichiometry on the increased annealing temperature. For the films annealed at 700 °C, the transmittance of the MT films (~86.74%) was observed to be higher than the CT films (~82.67%), which may be due to the deposition of MT films in the oxygen-rich environment. However, for the films annealed at 800 °C, the transmittance of CT films (~86.94%) was observed to increase slightly compared to the MT films (~85.40%), which may be attributed to the repair of more oxygen vacancies in the former.

From the transmittance plots and by using Swanepoel's envelope method, the refractive index (n_{opt}) and the extinction coefficient (k) of the prepared films were calculated.[66] The refractive index (n_{opt}) vs wavelength plots of $TTO_{0.035}$, CT, and MT crystalline films are shown in Fig. 8. For the CT films annealed at 700 and 800 °C, the value of n_{opt}, at 550 nm wavelength (2.000 and 2.044, respectively) was observed to be less than that of the MT films (2.160 and 2.144, respectively). The lattice constants (a–c) and the volume (V) of the crystalline CT and MT films were calculated from the XRD measurements and were found to be consistent with the reported results.[67] For the films annealed at 700 °C, the lattice constants of MT films were found as a = 6.236 Å, b = 3.595 Å, c = 3.896 Å, and the volume of the cell V = 87.342 Å^3, for CT films, they were a = 6.182 Å, b = 3.627 Å, c = 3.905 Å, and V = 87.558 Å^3. For the films annealed at 800 °C, the lattice constants of MT films were a = 6.236 Å, b = 3.585 Å, c = 3.909 Å, and V = 87.389 Å^3, and for CT films, they were a = 6.182 Å, b = 3.633 Å, c = 3.912 Å, and V = 87.860 Å^3. At both the annealing temperatures, 700 and 800 °C, the increased volume of the CT films, compared to the MT films, shows reduced density and results in a lower refractive index of the former. However, the refractive index of the CT films was observed to increase with increasing annealing temperature, which may be attributed to the increased density due to the improving oxygen stoichiometry, though the unit cell volume increases with annealing at 800 °C. The improving oxygen stoichiometry seems to be more dominating to increase the density than the decreasing density due to the increasing geometrical unit cell volume of the CT films, on annealing at 800 °C.[2,64]

Figure 9 shows the wavelength-dependent extinction coefficient (k) plots for CT and MT crystalline films. On annealing at 700 °C, the value of k for the CT films (0.135) was observed to be higher than the MT films (0.093), at the 550 nm wavelength, due to the higher transmittance of the latter [Fig. 9(a)]. However, for the films annealed at 800 °C, the k value was observed to be slightly higher for the MT films (0.118) than that for the CT films (0.116) due to the very small higher transmittance of the latter [Fig. 9(b)].

The bandgap (E_g) was determined from the transmittance vs wavelength plot using Tauc's equation,[68,69]

$$\alpha h\nu = A(h\nu - E_g)^m, \quad (3)$$

where α, hν, and A are the coefficient of absorption, the energy of the photon, and a constant, respectively. The bandgap of the CT

Published under an exclusive license by AIP Publishing

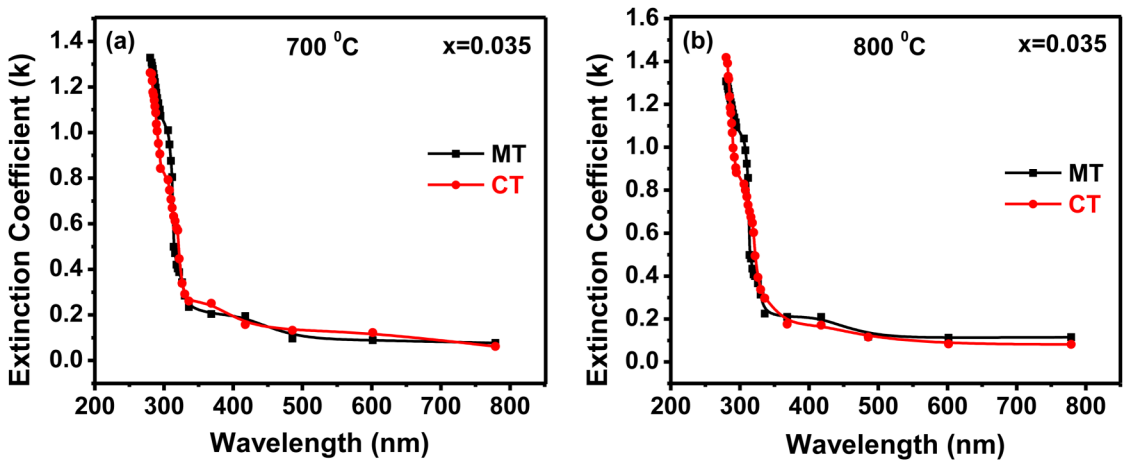

FIG. 9. Extinction coefficient vs wavelength plots for CT and MT films annealed at (a) 700 and (b) 800 °C.

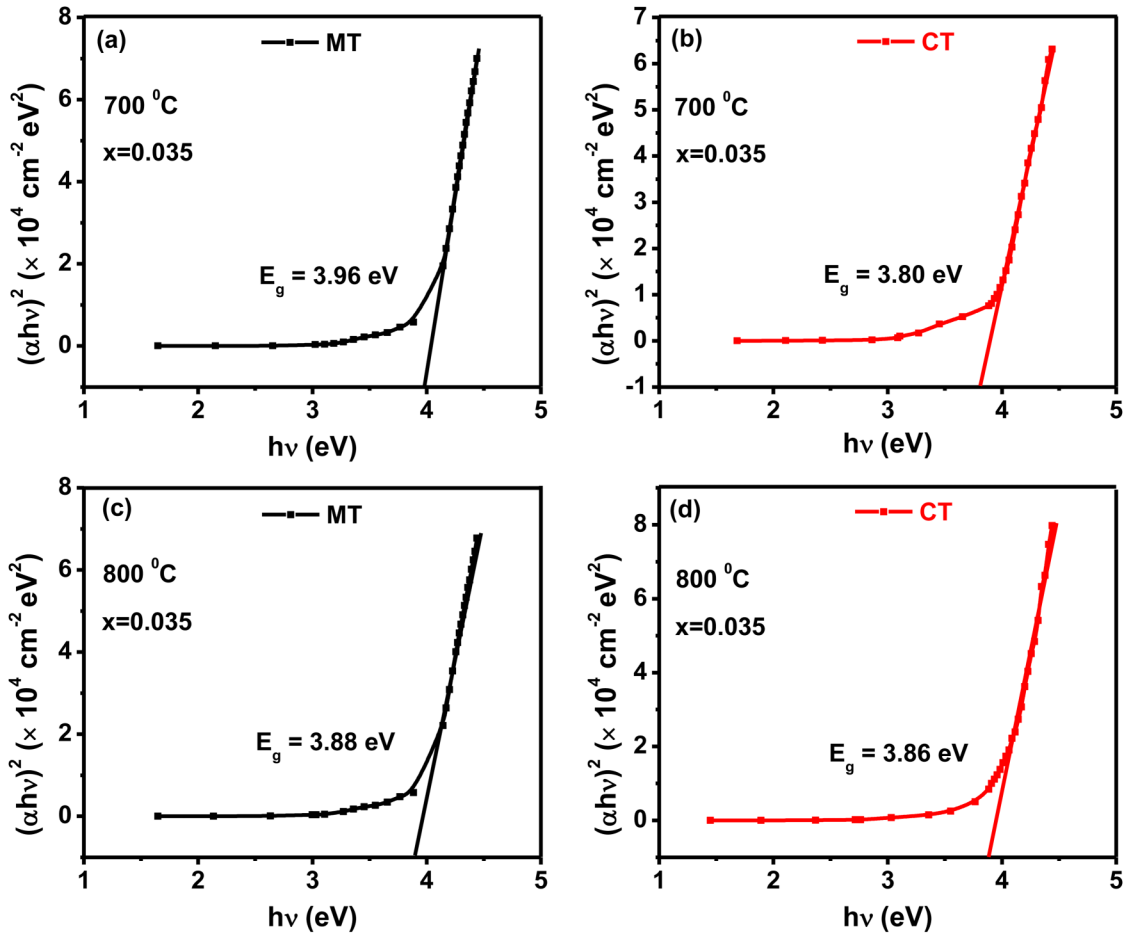

FIG. 10. $(\alpha h\nu)^2$ vs $h\nu$ plots for films annealed at 700 °C: (a) MT films and (b) CT films; and for films annealed at 800 °C: (c) MT films and (d) CT films.

Published under an exclusive license by AIP Publishing

and MT films calculated from the transmittance plot is shown in Fig. 10. The allowed transition in the films is suggested by the value of constant m, which satisfies Eq. (3). If Eq. (3) is satisfied for m = ½, it indicates the transitions due to the photon–electron interaction. The straight line portion of the $(\alpha h\nu)^2$ vs hν plot intersecting the energy axis determines the optical bandgap [Figs. 10(a)–10(d)]. The bandgap was observed to be decreasing for the MT films and increasing for the CT films with increasing annealing temperature. The bandgaps of the MT and CT films were observed to be 3.96 and 3.80 eV, respectively, for 700 °C annealing and 3.88 and 3.86 eV, respectively, for 800 °C annealing. The variation of the bandgap of the crystalline $TTO_{0.035}$ films was observed to be strongly depending on the oxygen stoichiometry. For the MT films (Fig. 7), the transmittance was observed to decrease with increasing annealing temperature, from 700 to 800 °C, which indicates the degrading insulating nature of the films, resulting in the decreased bandgap, due to the increased charged oxygen vacancies in the MT films, on increasing annealing temperature. There seems to be more oxygen escaping from the film volume than that is supplied on annealing, whereas the transmittance of the CT films (Fig. 7) was observed to be increasing with increasing annealing temperature, from 700 to 800 °C, which indicates reduced charged oxygen vacancies resulting in the increased bandgap of the CT films on increasing annealing temperature. Also, the increasing bandgap of the CT films may be associated with improving oxygen stoichiometry and decreasing mid-band levels with decreasing oxygen vacancies, with increasing annealing temperature. The observed larger bandgap of MT films with respect to CT films may be attributed to better oxygen stoichiometry in the former. The MT films were prepared in oxygen by sputtering of mosaic (Ta, Ti) metal target, leaving fewer oxygen vacancies and thereby less intermediate energy levels in between valence and conduction band.

Measured leakage current density (J) vs electric field (E) plots for CT and MT films, annealed at 700 and 800 °C, have been shown in Fig. 11. In the MT films, at the measured electric field 2.8×10^5 V/cm, a drastic decrease of the order of ∼3 was observed in the value of J, which may be due to the formation of an SiO_2 layer at the interface, with increasing annealing temperature, from 700 to 800 °C, which improves the quality of the interface and higher barrier height at the interface.[70] From the XRD measurements, the average crystallite size in CT films was observed to reduce, from 18.32 to 14.87 nm, on increasing the annealing temperature, from 700 to 800 °C. The increased number of grain boundaries due to the decreased crystallites size[2,71] may be held responsible for the increased leakage current density on increasing annealing temperature, from 700 to 800 °C, in the CT films at 2.8×10^5 V/cm. The increased number of grain boundaries may provide more paths to the flow of leakage current and results in increased leakage current; on increasing annealing temperature, from 700 to 800 °C. At 700 °C, the leakage current density of the MT and CT films was observed to be comparable; however, the small differences may be due to the dissimilar impurity levels, homogeneity, stress, etc.[2] On annealing at 800 °C, a significant decrement (an order of ∼3) was observed in the MT films compared to the CT films. The substantial improvement in the decrease of leakage current in the MT films may be attributed to the formation of a thicker SiO_2 layer at the film–substrate interface, resulting in

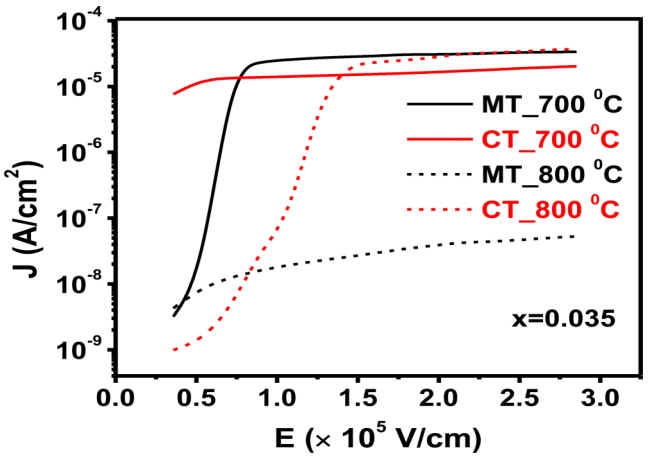

FIG. 11. J vs E plots for crystalline CT and MT films.

increased barrier height at the interface. The thickening of the interfacial SiO_2 layer in the reactive magnetron sputtered MT films may be assisted by the active oxygen during the film deposition and also by the migration of oxygen from the film volume to the Si–film interface, on annealing at 800 °C. As the CT films were deposited in the absence of oxygen, the SiO_2 interfacial layer may tend to form; however, the formation of the interfacial SiO_2 layer seems to be immature in the CT films on annealing, even at 800 °C.

Various plots, derived from the J–E characteristics of crystalline CT and MT films, have been used to determine the different current conduction mechanisms.[61] In the electric field region, $E < 1.0 \times 10^5$ and $E \leq 2.1 \times 10^5$ V/cm, the linear variation of current with the applied electric field indicates the ohmic emission[61,72] in the MT films annealed at 700 and 800 °C, respectively. All the crystalline CT films show the ohmic conduction in the lower electric field region, $E < 1.2 \times 10^5$ V/cm. Among the other mechanisms, ln J vs $\sqrt{E}$ and ln (J/E) vs $\sqrt{E}$ plots corresponding to Schottky emission and the Poole–Frenkel effect, respectively, have been plotted for the prepared CT and MT films [Figs. 12(a) and 12(b)]. The linear plots were observed in the intermediate to higher electric field range ($E \geq 1.0 \times 10^5$ V/cm) for the CT and MT films annealed at different temperatures. The linear ln J vs $\sqrt{E}$ and ln (J/E) vs $\sqrt{E}$ plots indicate the possibility of Schottky emission[73] and the Poole–Frenkel effect,[74] respectively, in the intermediate to higher fields. The refractive index (n_{opt}) obtained from the optical measurements and the refractive index (n) extracted from the slopes of the electrical [ln J vs $\sqrt{E}$ and ln (J/E) vs $\sqrt{E}$] plots were found to be far away from each other for the crystalline CT and MT films (Table II). The consistency of these two refractive indices with each other plays a deciding role to determine the dominance of Schottky emission or the Poole–Frenkel effect in the prepared film samples[75] in the linearity range. In the present study, the inconsistency in the values of n_{opt} with n for the crystalline CT and MT films discards the possibility of both Schottky and Poole–Frenkel conduction mechanisms in the intermediate to higher electric field range.

The observed linear J/d vs E^2/d^2 plots, in the field ranges 1.0×10^5 V/cm $\leq E < 1.9 \times 10^5$ V/cm and $E > 2.1 \times 10^5$ V/cm, for

Published under an exclusive license by AIP Publishing

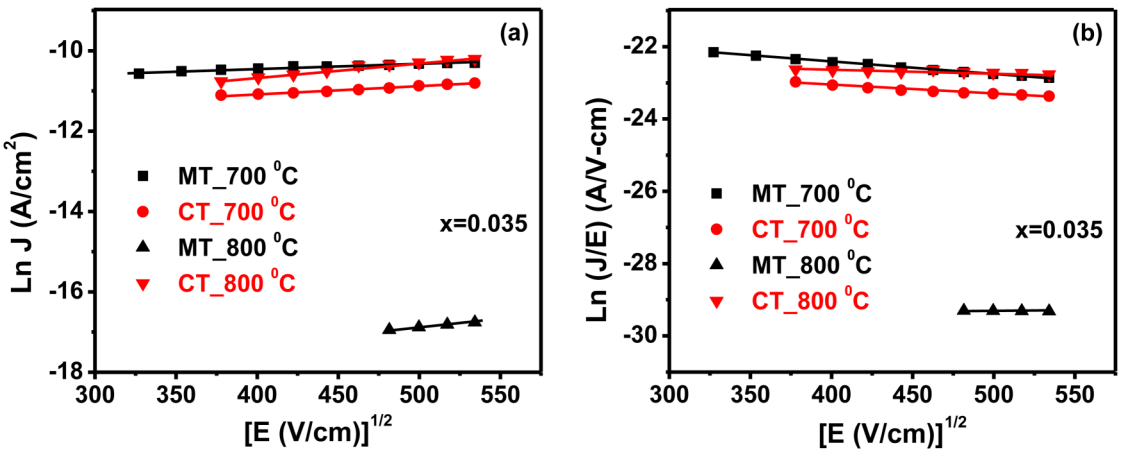

FIG. 12. (a) Ln J vs $\sqrt{E}$ (Schottky emission) and (b) ln (J/E) vs $\sqrt{E}$ (Poole–Frenkel effect) plots for crystalline CT and MT films.

the MT films annealed at 700 and 800 °C, respectively [Figs. 13(a) and 13(b)] suggest the space-charge-limited (SCL) current conduction.[61] The linearity of the J/d vs E^2/d^2 plots, in the field range $E > 1.2 \times 10^5$ V/cm and 1.2×10^5 V/cm $< E < 2.1 \times 10^5$ V/cm, for the CT films annealed at 700 and 800 °C, respectively, indicate the possibility of space-charge-limited current conduction in the respective regions [Figs. 13(c) and 13(d)].

Furthermore, in higher electric fields, the possibility of other conduction mechanisms was explored for the crystalline MT and CT films. In the higher fields, the linearity of ln (J/E^2) vs 1/E plots indicates the possibility of tunneling conduction[13,43,61] in the MT films annealed at 700 °C and the CT films annealed at 800 °C (Fig. 14). The possible different tunneling conductions [double barrier, direct, and Fowler–Nordheim (FN)] in the Ta_2O_5 MOS structures were described by Chaneliere *et al.*[76] There may be a possibility to follow one of these tunneling conductions in the presently prepared MT films annealed at 700 °C and CT films annealed at 800 °C. The chances of tunneling through the film volume may be neglected in the present case due to quite a higher thickness of the prepared films (~280 and ~350 nm). Therefore, the tunneling mechanism through the thin SiO_2 interfacial layer may be considered dominating in the presently deposited films. In the MT films annealed at 700 °C and CT films annealed at 800 °C, since the possibility of Schottky and Poole–Frenkel conductions has been ruled out, the chances of trap assisted tunneling (double barrier and direct) are very rare. These observations indicate the possibility that Fowler–Nordheim (FN) tunneling dominates in the MT films annealed at 700 °C, in the electric field range $E \geq 1.9 \times 10^5$ V/cm, and in the CT films annealed at 800 °C, in the field region $E \geq 2.1 \times 10^5$ V/cm, through the very thin interfacial SiO_2 layer [Figs. 14(a) and 14(b)], whereas in the 800 °C annealed MT films, the possibility of tunneling in the higher electric fields may be ruled out through the thicker SiO_2 layer at the interface. Though in the CT films annealed at 700 °C there may be a possibility of tunneling in the higher fields, the extended SCL conduction up to higher fields and more linearity of J/d vs E^2/d^2 plot as compared to the ln (J/E^2) vs 1/E plot discard the possibility of the dominance of tunneling conduction in these film structures. Moreover, the higher leakage current in the 800 °C annealed films than in the 700 °C annealed films may assist to dominate FN tunneling in the 800 °C annealed CT films.

In short, the various conduction mechanisms in the different electric field regions have been explored in the crystalline CT and MT films. In the CT films annealed at 700 °C, ohmic conduction in the lower fields, $E \leq 1.2 \times 10^5$ V/cm, and SCL current in the intermediate to higher fields, $E > 1.2 \times 10^5$ V/cm, control the conduction. In the CT films annealed at 800 °C, ohmic conduction in the lower fields, $E < 1.2 \times 10^5$ V/cm; SCL current in the intermediate fields, 1.2×10^5 V/cm $< E < 2.1 \times 10^5$ V/cm; and FN tunneling in the higher electric fields, $E \geq 2.1 \times 10^5$ V/cm, were found to be prominent. In the MT films annealed at 700 °C, ohmic conduction in the

TABLE II. Schottky and Poole–Frenkel current conductions in the CT and MT $TTO_{0.035}$ thin films.

Label parameters	Calculated from Schottky plots	Calculated from Poole–Frenkel plots[a]	
		r = 1[a]	r = 2
CT_700 °C (n_{opt} = 2.000)			
$n = \sqrt{K_r}$	6.29	16.60	8.30
K_r	39.56	275.56	68.89
CT_800 °C (n_{opt} = 2.044)			
$n = \sqrt{K_r}$	4.42	15.93	7.96
K_r	19.53	253.76	63.36
MT_700 °C (n_{opt} = 2.160)			
$n = \sqrt{K_r}$	13.72	8.57	4.28
K_r	188.23	73.44	18.31
MT_800 °C (n_{opt} = 2.144)			
$n = \sqrt{K_r}$	3.30	88.95	44.47
K_r	10.89	7912.10	1977.58

[a]r = 1, for normal Poole–Frenkel and r = 2 for modified Poole–Frenkel effect. K_r = dynamic dielectric constant.[75]

Published under an exclusive license by AIP Publishing

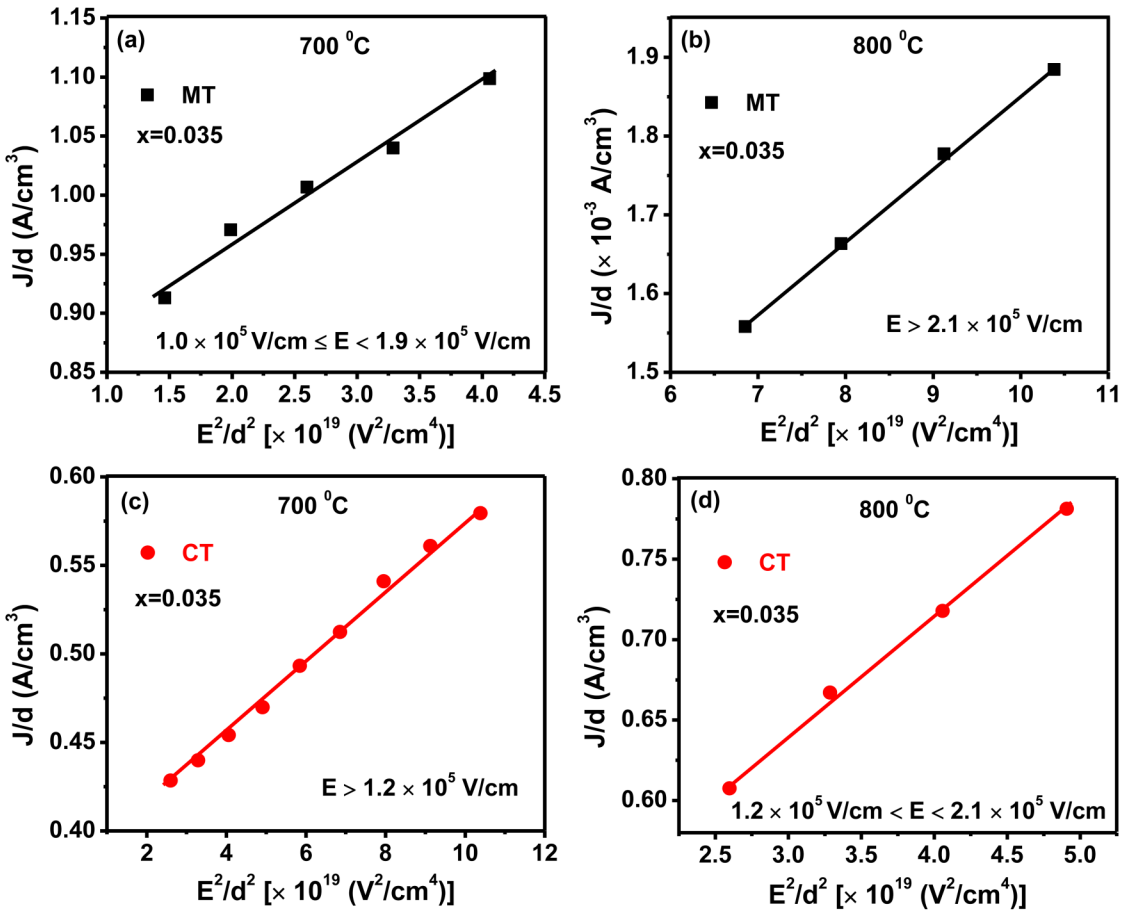

FIG. 13. J/d vs E^2/d^2 plots (space-charge-limited current conduction) for MT films annealed at (a) 700 and (b) 800 °C; and for CT films annealed at (c) 700 and (d) 800 °C.

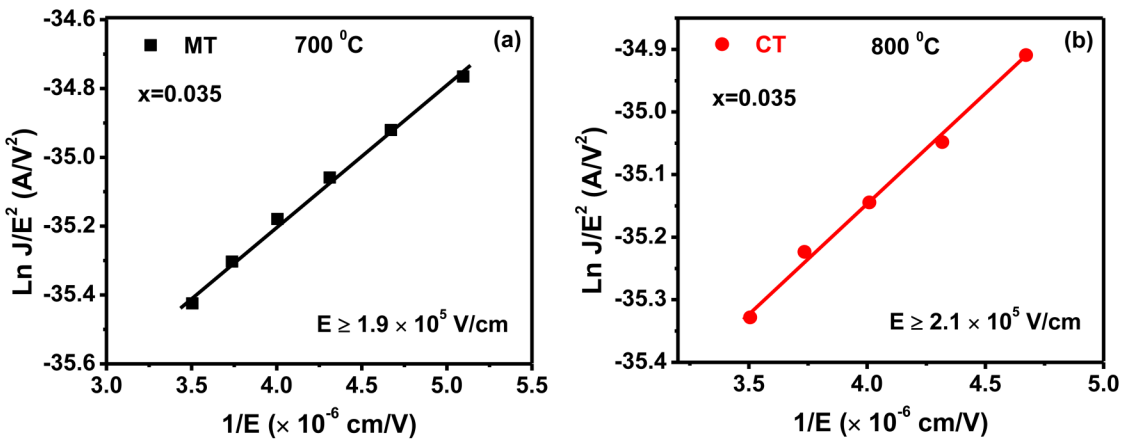

FIG. 14. ln (J/E^2) vs 1/E plots (Fowler–Nordheim tunneling) for (a) MT films annealed at 700 °C and (b) CT films annealed at 800 °C.

Published under an exclusive license by AIP Publishing

lower fields, $E < 1.0 \times 10^5$ V/cm; SCL current in the intermediate fields, 1.0×10^5 V/cm $\leq E < 1.9 \times 10^5$ V/cm; and FN tunneling conduction in the higher electric fields, $E \geq 1.9 \times 10^5$ V/cm, were observed to be dominating. In the MT films annealed at 800 °C, ohmic conduction in the lower intermediate fields, $E \leq 2.1 \times 10^5$ V/cm, and SCL current conduction in the higher fields, $E > 2.1 \times 10^5$ V/cm, were found to be dominating to control the conduction.

IV. CONCLUSIONS

TTO_x, x = 0.035, thin-film samples were prepared onto the p-Si and quartz substrates at ambient temperature following two separate routes: first, by RF magnetron sputtering of a $TTO_{0.08}$ ceramic target and, second, by DC magnetron sputtering of a mosaic assembly of (Ta, Ti) metals, in the presence of oxygen. The as-deposited films were annealed at 500, 600, 700, and 800 °C. XRD measurements show crystallization of the deposited films when annealed at and above 700 °C in both cases. The electrical and optical properties of the prepared crystalline films were measured. For the films annealed at 700 °C, the measured (effective) dielectric constant of the CT films (58) was observed higher than that of the MT films (45). As the MT films were deposited in the presence of oxygen, the earlier growing oxide layer at the film–Si interface may be a reason for the lower values of the observed capacitance of the capacitor and so the dielectric constant of these films. On annealing at 800 °C, due to the more grown oxide layer at the film–Si interface, the capacitance of the MOS capacitors prepared using these films was observed to decrease and so was the dielectric constant. Considering the effect of the series capacitance of the interfacial SiO_2 layer, the dielectric constant of the deposited CT and MT film materials was found to be 64.7 and 53.7 for the films annealed at 700 °C, respectively, and 51.7 and 51.5 for the films annealed at 800 °C, respectively. At any annealing temperature, the status of the growing interfacial oxide layer was found to be a deciding factor for the observed dielectric properties and conduction mechanisms in these films. Except for the effect of the interfacial layer, the electrical and optical properties and conduction mechanisms in the films prepared from the two different routes were found to be quite comparable. Sputtering a composite ceramic target or an alloy target in the presence of oxygen is the simplest approach to prepare the composite oxide films. However, this inflexible and expensive approach renders deposition of only one possible composition. Furthermore, a mosaic target has the flexibility of varying the relative sputtering areas of the participating metals within a single holder assembly. To get any desired film composition, the relative sputtering areas of the participating metals can be varied. This enhanced flexibility makes the metals' mosaic target assembly cost-effective by many folds and that too with comparable CT quality films if the formation of the interfacial oxide layer is taken care of in the former.

DATA AVAILABILITY

The data that support the findings of this study are available from the corresponding author upon reasonable request.

REFERENCES

[1]V. Mikhelashvili and G. Eisenstein, Microelectron. Reliab. **40**, 657 (2000).
[2]P. C. Joshi and M. W. Cole, J. Appl. Phys. **86**, 871 (1999).
[3]S. Ezhilvalavan and T. Y. Tseng, J. Mater. Sci. Mater. Electron. **10**, 9 (1999).
[4]A. T. Kobayashi, O. Maida, M. Inoue, M. Takahashi, Y. Todokoro, and H. Kobayashi, Appl. Phys. Lett. **81**, 3410 (2002).
[5]Y. C. Yeo, T. J. King, and C. Hu, Appl. Phys. Lett. **81**, 2091 (2002).
[6]K. W. Kwon, C. S. Kang, S. O. Park, H. K. Kang, and S. T. Ahn, IEEE Trans. Electron. Devices **43**, 919 (1996).
[7]R. Thomas, R. Bhakta, A. Milanov, A. Devi, and P. Ehrhart, Chem. Vap. Deposition **13**, 98 (2007).
[8]R. Thomas, E. Rije, P. Ehrhart, A. Milanov, R. Bhakta, A. Bauneman, A. Devi, R. Fischer, and R. Waser, J. Electrochem. Soc. **154**, G77 (2007).
[9]C. Chaneliere, J. L. Autran, R. A. B. Devine, and B. Balland, Mater. Sci. Eng. R Rep. **22**, 269 (1998).
[10]M. Kadoshima, M. Hiratani, Y. Shimamoto, K. Torii, H. Miki, S. Kimura, and T. Nabatame, Thin Solid Films **424**, 224 (2003).
[11]The International Technology Roadmap for Semiconductors (ITRS), 2006, see http://public.itrs.net.
[12]M. Matsui, H. Nagayoshi, G. Muto, S. Tanimoto, K. Kuroiwa, and Y. Tauri, Jpn. J. Appl. Phys. **29**, 62 (1990).
[13]G. Q. Lo, D. L. Kwong, and S. Lee, Appl. Phys. Lett. **60**, 3286 (1992).
[14]E. Atanassova and D. Spassov, Appl. Surf. Sci. **135**, 71 (1998).
[15]E. Atanassova, Microelectron. Reliab. **39**, 1185 (1999).
[16]B. H. Lee, L. Kang, R. Nieh, W. J. Qi, and J. C. Lee, Appl. Phys. Lett. **76**, 1926 (2000).
[17]A. Pignolet, G. Mohan Rao, and S. B. Krupanidhi, Thin Solid Films **258**, 230 (1995).
[18]S. W. Park and H. B. Im, Thin Solid Films **207**, 258 (1992).
[19]F. C. Chiu, J. J. Wang, J. Y. Lee, and S. C. Wu, J. Appl. Phys. **81**, 6911 (1997).
[20]I. S. Kim, S. J. Jeong, J. S. Song, and P. S. Shin, Met. Mater. Int. **8**, 577 (2002).
[21]S. Y. Huang, L. Kavan, I. Exnar, and M. Gratzel, J. Electrochem. Soc. **142**, L142 (1995).
[22]V. P. S. Perera, P. V. V. Jayaweera, P. K. D. D. P. Pitigala, P. K. M. Bandaranayake, G. Hastings, A. G. U. Perera, and K. Tennakone, Synth. Met. **143**, 283 (2004).
[23]A. E. Aliev and H. W. Shin, Displays **23**, 239 (2002).
[24]W. P. Tai and J. H. Oh, Sens. Actuators B **85**, 154 (2002).
[25]L. Francioso, D. S. Presicce, A. M. Taurino, R. Rella, P. Siciliano, and A. Ficarella, Sens. Actuators B **95**, 66 (2003).
[26]S. J. Rhee, C. S. Kang, C. H. Choi, C. Y. Kang, S. Krishnan, M. Zhang, M. S. Akbar, and J. C. Lee, in *IEDM Technical Digest. IEEE International Electron Devices Meeting, 2004* (IEEE, 2004), p. 837.
[27]M. C. Sekhar, N. K. Reddy, H. S. Akkera, B. P. Reddy, V. Rajendar, S. Uthanna, and S. H. Park, J. Alloys Compd. **718**, 104 (2017).
[28]S. K. Streiffer and A. I. Kingon, Nature **377**, 194 (1995).
[29]Q. Fang, J.-Y. Zhang, Z. M. Wang, J. X. Wu, B. J. O'Sullivan, P. K. Hurley, T. L. Leedham, H. Davies, M. A. Audier, C. Jimenez, J.-P. Senateur, and I. W. Boyd, Thin Solid Films **428**, 263 (2003).
[30]H. Bensouyad, H. Sedrati, H. Dehdouh, M. Brahimi, F. Abbas, H. Akkari, and R. Bensaha, Thin Solid Films **519**, 96 (2010).
[31]L. Manchanda, M. D. Morris, M. L. Green, R. B. van Dover, F. Klemens, T. W. Sorsch, P. J. Silverman, G. Wilk, B. Busch, and S. Aravamudhan, Microelectron. Eng. **59**, 351 (2001).
[32]J. Y. Tewg, Y. Kuo, J. Lu, and B. Schueler, J. Electrochem. Soc. **151**, F59 (2004).
[33]P. Thapliyal, A. S. Kandari, V. Lingwal, N. S. Panwar, and G. Mohan Rao, Ceram. Int. **47**, 12066 (2021).
[34]R. F. Cava, W. F. Peck, Jr., and J. J. Krajewski, Nature **377**, 215 (1995).
[35]K. C. Chiang, C. C. Huang, H. C. Pan, C. N. Hsiao, J. W. Lin, I. J. Hsieh, C. H. Cheng, C. P. Chou, A. Chin, H. L. Hwang, and S. P. McAlister, J. Electrochem. Soc. **154**, G54 (2007).
[36]K. C. Chiang, C. H. Lai, A. Chin, T. J. Wang, H. F. Chiu, J. R. Chen, S. P. McAlister, and C. C. Chi, IEEE Electron Device Lett. **26**, 728 (2005).

Published under an exclusive license by AIP Publishing

[37]M. Li, Z. Zhang, S. A. Campbell, H. J. Li, and J. J. Peterson, J. Appl. Phys. **101**, 044509 (2007).
[38]D. Makovec, J. Zuo, R. Twesten, and D. A. Payne, J. Solid State Chem. **179**, 1782 (2006).
[39]G. L. Brennecka and D. A. Payne, J. Am. Ceram. Soc. **89**, 2089 (2006).
[40]J.-Y. Gan, Y. C. Chang, and T. B. Wu, Appl. Phys. Lett. **72**, 332 (1998).
[41]G. D. Wilk, R. M. Wallace, and J. M. Anthony, J. Appl. Phys. **89**, 5243 (2001).
[42]E. Atanassova and T. Dimitrova, in *Handbook of Surface and Interfaces of Materials*, edited by H. S. Nalwa (Academic Press, San Diego, CA, 2001), Vol. 4, p. 439.
[43]E. Atanassova, N. Novkovski, A. Paskaleva, and M. Pecovska-Gjorgjevich, Solid State Electron. **46**, 1887 (2002).
[44]A. P. Huang, S. L. Xu, M. K. Zhu, B. Wang, H. Yan, and T. Liu, Appl. Phys. Lett. **83**, 3278 (2003).
[45]S. Roberts, J. Ryan, and L. Nesbit, J. Electrochem. Soc. **133**, 1405 (1986).
[46]R. S. Bergman and T. G. Parham, IEEE Proc. A **140**, 418 (1993).
[47]H. Kostlin, G. Frank, G. Hebbinghaus, H. Auding, and K. Denissen, J. Non-Cryst. Solids **218**, 347 (1997).
[48]A. Ritz, Surf. Coat. Technol. **174–175**, 651 (2003).
[49]J.-C. Zhou, D.-T. Luo, Y.-Z. Li, and Z. Liu, Trans. Nonferrous Met. Soc. China **19**, 359 (2009).
[50]F. Rubio, J. Denis, J. M. Albella, and J. M. Martinez-Duart, Thin Solid Films **90**, 405 (1982).
[51]W. M. Paulson, F. S. Hickernell, and R. L. Davis, J. Vac. Sci. Technol. **16**, 307 (1979).
[52]H. Terui and M. Kobayashi, Appl. Phys. Lett. **32**, 666 (1978).
[53]C. Corbella, M. Vives, A. Pinyol, I. Porqueras, C. Person, and E. Bertran, Solid State Ionics **165**, 15 (2003).
[54]A. Bhandari, A. S. Kandari, M. K. Agarwal, V. Lingwal, and N. S. Panwar, Ferroelectr. Lett. **37**, 43 (2010).
[55]P. Thapliyal, A. S. Kandari, V. Lingwal, N. S. Panwar, and G. Mohan Rao, Mater. Today **44**, 3946 (2021).
[56]P. Thapliyal, N. S. Panwar, and G. Mohan Rao, Ceram. Int. **47**, 16746 (2021).
[57]S. J. Wu, B. Houng, and B. Huang, J. Alloys Compd. **475**, 488 (2009).
[58]B. D. Cullity, *Elements of X-Ray Diffraction*, 2nd ed. (Addison Wesley, London, 1978).
[59]V. Lingwal and N. S. Panwar, J. Appl. Phys. **97**, 104902 (2005).
[60]M. C. Sekhar, N. K. Reddy, V. K. Verma, and S. Uthanna, Ceram. Int. **42**, 18870 (2016).
[61]S. M. Sze, *Physics of Semiconductor Devices*, 2nd ed. (Wiley, New York, 1981).
[62]V. Lingwal and N. S. Panwar, Ferroelectrics **300**, 3 (2004).
[63]Y. Nishioka, S. Kimura, H. Shinriki, and K. Mukai, J. Electrochem. Soc. **134**, 410 (1987).
[64]S. V. J. Chandra, S. Uthanna, and G. Mohan Rao, Appl. Surf. Sci. **254**, 1953 (2008).
[65]J. Li, W. Yang, J. Su, C. Yang, J. Xu, and S. Wu, Mater. Res. Express **6**, 026404 (2019).
[66]R. Swanepoel, "Determination of the thickness and optical constants of amorphous silicon," J. Phys. E: Sci. Instrum. **16**, 1214 (1983).
[67]S. Lee, J. Kim, S. J. Kim, S. Kim, and G. Park, Phys. Rev. Lett. **110**, 235502 (2013).
[68]O. A. Azim, M. M. Abdel-Aziz, and I. S. Yahia, Appl. Surf. Sci. **255**, 4829 (2009).
[69]J. Tauc, R. Grigorovici, and A. Vancu, Phys. Status Solidi B **15**, 627 (1966).
[70]T. Dimitrova, K. Arshak, and E. Atanassova, Thin Solid Films **381**, 31 (2001).
[71]B. K. Moon, C. Isobe, and J. Aoyama, J. Appl. Phys. **85**, 1731 (1999).
[72]P. L. Young, J. Appl. Phys. **47**, 235 (1976).
[73]R. Brazis, P. Pipinys, A. Rimeika, and V. Lapeika, Mater. Sci. Lett. **9**, 266 (1990).
[74]C. Isobe and M. Saitoh, Appl. Phys. Lett. **56**, 907 (1990).
[75]C. Chaneliere, S. Four, J. L. Autran, R. A. B. Devine, and N. P. Sandler, J. Appl. Phys. **83**, 4823 (1998).
[76]C. Chaneliere, J. L. Autran, and R. A. B. Devine, J. Appl. Phys. **86**, 480 (1999).

Published under an exclusive license by AIP Publishing

J. Mountain Res. P-ISSN: 0974-3030, E-ISSN: 2582-5011 DOI: https://doi.org/10.51220/jmr.v16i2.34
Vol. 16(2) Special Issue ICRAMS-2021, (2021), 279-286

Investigation on Dielectric and Optical Properties of $Ba_{1-x}Ca_xZr_{0.1}Ti_{0.9}O_3$ (x = 0.150) Ferroelectric Ceramics

Don Biswas[1,2*] • Surendra Singh[1] • Prashant Thapliyal[1] • Vishal Rohilla[1] • G S Kathait[1] • N S Panwar[1] • Prolay Sharma[2]

[1]*Instrumentation Engg.-USIC, H.N.B. Garhwal University, Srinagar – 246174, India.*
[2]*Instrumentation and Electronics Engg., Jadavpur University, Kolkata, India.*

***Corresponding author Email:** donusic06@gmail.com

Received: 29.8.2011; Revised: 22.11.2021; Accepted: 27.11.2021
©Society for Himalayan Action Research and Development

Abstract: Pellet samples of $(Ba_{1-x}Ca_xZr_{1-y}Ti_y)O_3$ (x = 0.150, y = 0.90) were prepared using the solid-state reaction method following double sintering. The electrical and optical properties of $(Ba_{1-x}Ca_xZr_{1-y}Ti_y)O_3$ (x = 0.150, y = 0.90) ceramics were studied. For $(Ba_{0.85}Ca_{0.15}Zr_{0.1}Ti_{0.9})O_3$ ferroelectric perovskite ceramics, the dielectric and structural properties were explored. The prepared composition of BCZT ceramics were calcined at 1100 ºC. The sintering temperature was 1300 ºC. Dielectric properties were observed from room temperature (RT) to 150 ºC, at 1 MHz. The powder of the sintered samples has been taken for reflectance measurement at UV-Vis range. From the observed tauc plot, the band-gap is calculated. The measured band- gap is 3.19 eV.

Keywords- Dielectric constant; Electric conductivity; Reflectance; UV-Vis.

Introduction

Perovskite compounds are of considerable interest due to their high extent of tailorability in physical properties and application in the field of sensors. Their contributions in the field of sensors are significant due to their large piezoelectric properties. Ferroelectric/ABO_3 type materials may generate voltage if external voltage or pressure has been applied to it. These compounds possess spontaneous polarization.

Researchers investigated the dielectrics properties of $(Ba_{1-x}Ca_xZr_{1-y}Ti_y)O_3$ (x = 0.150, y = 0.90) ceramics, near morphotropic phase boundary (MPB) region (Tian et al., 2013; Mondal et al., 2017; Hennings and Schnell, 1982; Yu et al., 2002; Wang et al., 2012; Wu et al., 2012). The BCZT ceramics show significant dielectric properties, at x = 0.150. At x = 0.150, Tian et al. observed co-existence of two different phases in BCZT ceramics (Tian et al., 2013). For $(Ba_{0.85}Ca_{0.15}Zr_{0.1}Ti_{0.9})O_3$ samples, O ("Orthorhombic")- T ("Tetragonal") transition point has been observed near 120 ºC (Tian et al., 2013). The presence of these phases may create several possible polarization directions. Therefore, this MPB consisting of both phases and may have maximum possible polarization directions, which may contribute towards k_s (coupling

factor). A significant dielectric constant may be seen because of its large remnant polarization, which increases due to its large coupling factor (Yamashita and Shimanuki, 1996; Yamashita et al., 1996; Yamashita et al., 1998).

In this study, the $(Ba_{1-x}Ca_xZr_{1-y}Ti_y)O_3$ (x = 0.150, y = 0.90) samples were prepared using the conventional "solid- state reaction" method with double sintering. The pellet samples were sintered at 1300 °C for 4 hrs. For dielectric measurement, the pellet samples were electroded with conducting silver paste, in M-I-M configuration. For XRD measurement, the prepared powder sample of BCZT composition was taken. Furthermore, PANalytical, X'PERT PRO X-ray machine has been used to measure XRD patterns. It has Cu$K_{\alpha 1}$ radiation of wavelength 1.54060 Å. The range of 2θ angle was selected from 20 to 70°, at a scanning rate 0.3 sec per step with step size 0.03°.

Experimental details

The pellet samples of $(Ba_{1-x}Ca_xZr_{1-y}Ti_y)O_3$ (x = 0.150, y = 0.90) were prepared using solid-state reaction method with double sintering. Raw materials of Barium carbonate ($BaCO_3$), Calcium carbonate ($CaCO_3$), Zirconium oxide (ZrO_2), and Titanium oxide (TiO_2) were taken with purity 99.99%, were dried at 200 °C for 2 hours to remove the absorbed moisture. The methodology has been described in a previous communication (Biswas et al., 2020; Biswas et al., 2021; Biswas et al., 2019; Biswas et al., 2018; Biswas et al., 2021; Singh et al., 2018; Singh et al., 2019).

Result and discussion

X- Ray Diffraction result

The XRD measurement was carried out for the $(Ba_{1-x}Ca_xZr_{1-y}Ti_y)O_3$ (x = 0.150, y = 0.90) composition, at the selected 2θ angle range. It has been shown in Fig. 1. For the prepared composition, powder sample was found in good consistency with "Inorganic Crystal Structure Database" (ICSD file No. 00-056-1033) data (Sen and Choudhary, 2004), with peaks corresponding to (020), (221), (402). The measured RT- XRD data of the $(Ba_{0.85}Ca_{0.15}Zr_{0.1}Ti_{0.9})O_3$ powder samples exhibit orthorhombic phase.

The lattice parameters were measured manually. The selected space group is 'C' type. For the prepared powder samples, the measured X- ray diffraction data were matched with "Inorganic Crystal Structure Database" (ICSD) data. The ICSD data will give the information of the orthorhombic unit cell (a, b and c parameters) and volume. The manually calculated values (a, b and c parameters) must be in more close approximation to those values. At first, the positions of the observed x- ray peaks were

identified. For a corresponding peak, the d-spacing and (hkl) has been noted from the ICSD data. The equation for an interplaner spacing for an orthorhombic unit cell was used to calculate the lattice parameters. To work with the above interplaner equation, the h, k, l, and d values were noted and further, the lattice parameters were measured. The lattice parameters were given in Table 1.

Table 1. Lattice parameters of $(Ba_{1-x}Ca_xZr_{1-y}Ti_y)O_3$ (x = 0.150, y = 0.90) samples and peaks used in the present calculation were (111), (020) and (402).

Cell Constants (Calculated)

$(Ba_{0.85}Ca_{0.15}Zr_{0.1}Ti_{0.9})O_3$	a (Å)	b (Å)	c (Å)	c/a (Å)
0.150	9.89054	5.61610	6.71288	0.67871

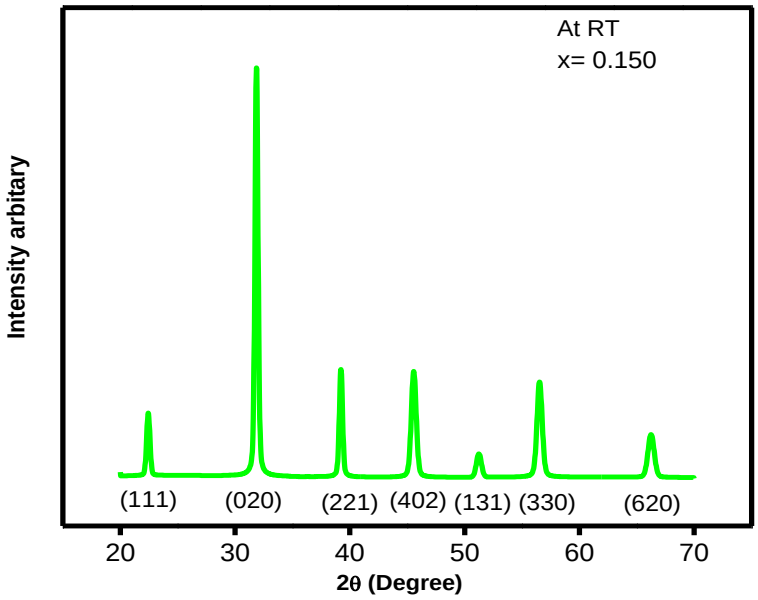

Fig. 1. XRD patterns of $(Ba_{1-x}Ca_xZr_{1-y}Ti_y)O_3$ (x = 0.150, y = 0.90) ceramics, at room temperature.

Dielectric and morphology results

In this study, the relative permittivity (K), loss tangent (tan δ), and dielectric conductivity (σ) were observed systematically. For the prepared samples, K, tan δ, and σ were measured from temperature 30 and 140 ºC, at 1 MHz (Figs. 2- 3). The micro- structure show fine grain and homogeneous structure of the $(Ba_{0.85}Ca_{0.15}Zr_{0.1}Ti_{0.9})O_3$ samples. The grain size was observed between 0.7 and 1.0 µm (Fig. 4). The average grain size was measured 1.15 µm. The dielectric constant was found maximum near 120 ºC.

Furthermore, the dielectric constant has been decreasing with an increase in temperature. The large value of the dielectric constant indicates a phase change near 120 °C. The transition is also observed from the data of electric conductivity. The electric conductivity was suddenly increased near 120 °C and further, it decreases. The loss of the prepared composition is very small at high frequency.

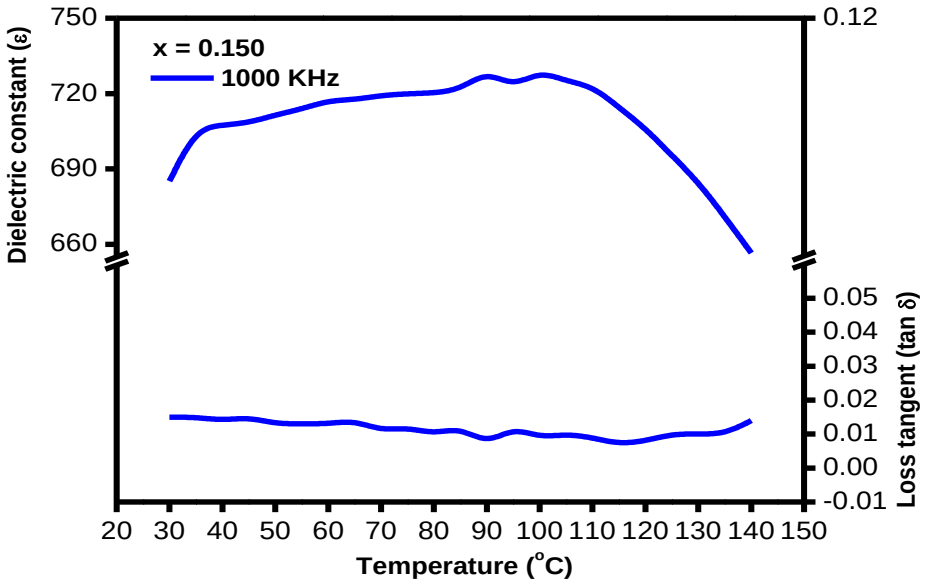

Fig. 2. Temperature- dependent dielectric constant and loss tangent of the $(Ba_{1-x}Ca_xZr_{1-y}Ti_y)O_3$ (x = 0.150, y = 0.90) sample, at 1 MHz.

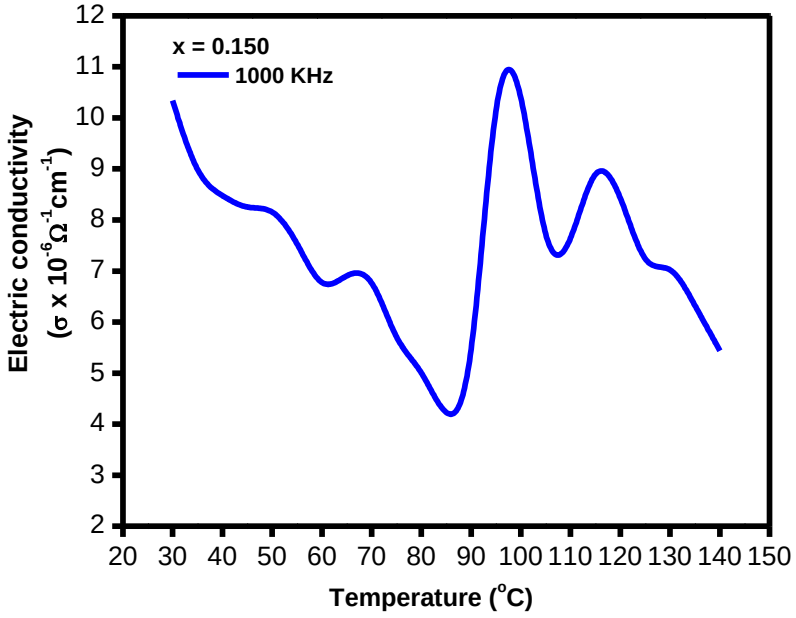

Fig. 3. Temperature- dependent electric conductivity of the $(Ba_{1-x}Ca_xZr_{1-y}Ti_y)O_3$ (x = 0.150, y = 0.90) ceramics, at 1 MHz.

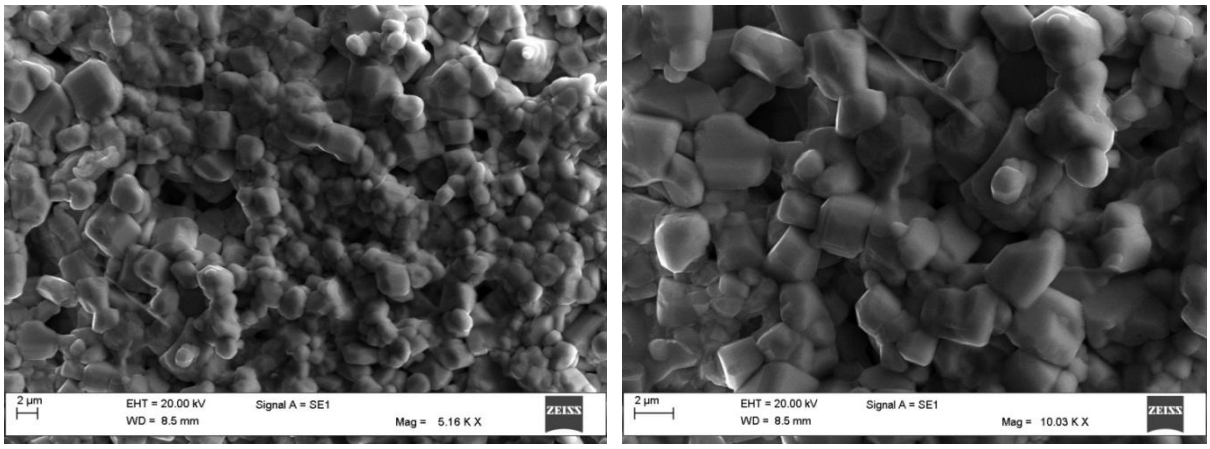

Fig. 4. SEM images of $(Ba_{1-x}Ca_xZr_{1-y}Ti_y)O_3$ (x = 0.150, y = 0.90) ceramics, at different magnification.

Table 2: Energy dispersive X- ray results of the $(Ba_{1-x}Ca_xZr_{1-y}Ti_y)O_3$ (x = 0.150, y = 0.90) system and spectrum analysis.

ELEMENT	WEIGHT%	ATOMIC%
O K	25.69	66.10
Ca K	2.39	2.46
Ti K	16.36	14.06
Zr L	4.81	2.17
Ba L	50.75	15.21
Totals	100.00	

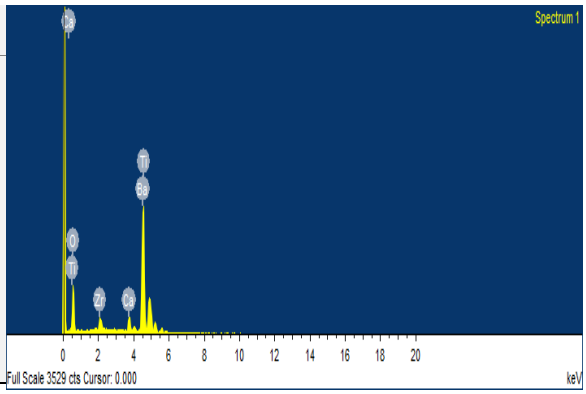

Table 3. Standards selected in EDAX analysis of the $(Ba_{1-x}Ca_xZr_{1-y}Ti_y)O_3$ (x = 0.150, y = 0.90) ceramics.

STANDARD DETAILS			
O	SiO2	01.06.1999	12 AM
Ca	Wollastonite	01.06.1999	12 AM
Ti	Ti	01.06.1999	12 AM
Zr	Zr	01.06.1999	12AM
Ba	BaF2	01.06.1999	12 AM

Lossy dielectric can be characterized with the help of a circuit analog of a resistance in parallel with a capacitor (Haertling, 1967). When the input signal is taken as a sinusoidal signal, the capacitor always show low reactance path at higher frequencies, leading to minimization in conduction losses. Therefore, dielectric loss has been decreasing with an increase in frequency, which is consistent with the previous reports (Haertling, 1967; Jaeger and Egerton, 1962). The EDAX results confirmed the atomic percentage of the elements. The data has been given in Table 2. From the spectrum of EDAX, the presence of the elements can be confirmed. The standard details were given below in Table 3.

Reflectance results

The optical properties of the prepared composition have been observed (Figs. 5-6). The band-gap was measured 3.19 eV (Tunc et al., 2019). The band-gap is calculated using tauc function. Fig. 4 indicates the reflectance graph with the variation in wavelength. The reflectance is 75% at around 900 nm (UV range) and 10% at around 350 nm (Vis range). A sharp downfall may be observed in reflectance plot at around 350 nm. Teflon is taken as the standard material.

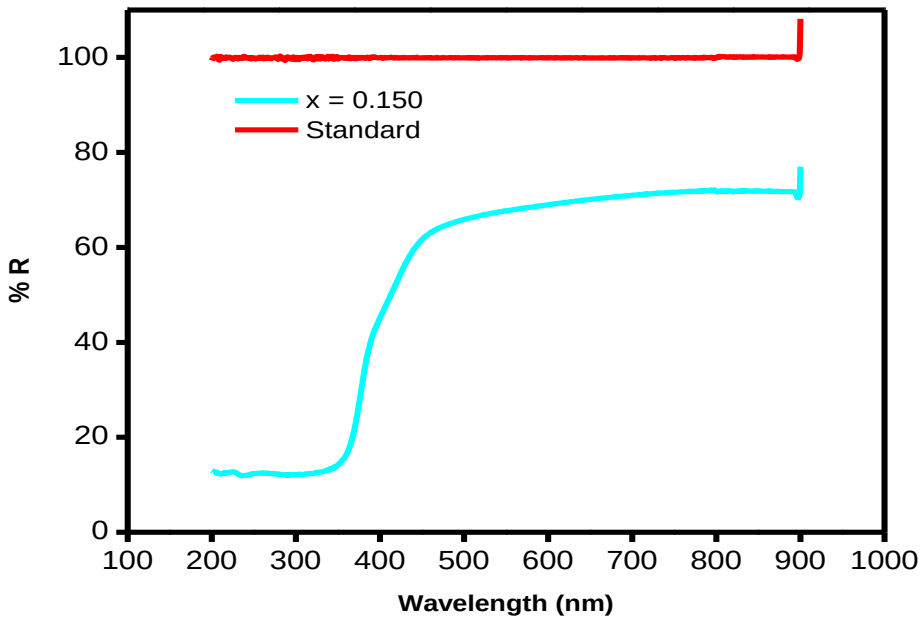

Fig. 5. Variation in reflectance with the wavelength, in $(Ba_{1-x}Ca_xZr_{1-y}Ti_y)O_3$ (x = 0.150, y = 0.90) ceramics, at 1 MHz.

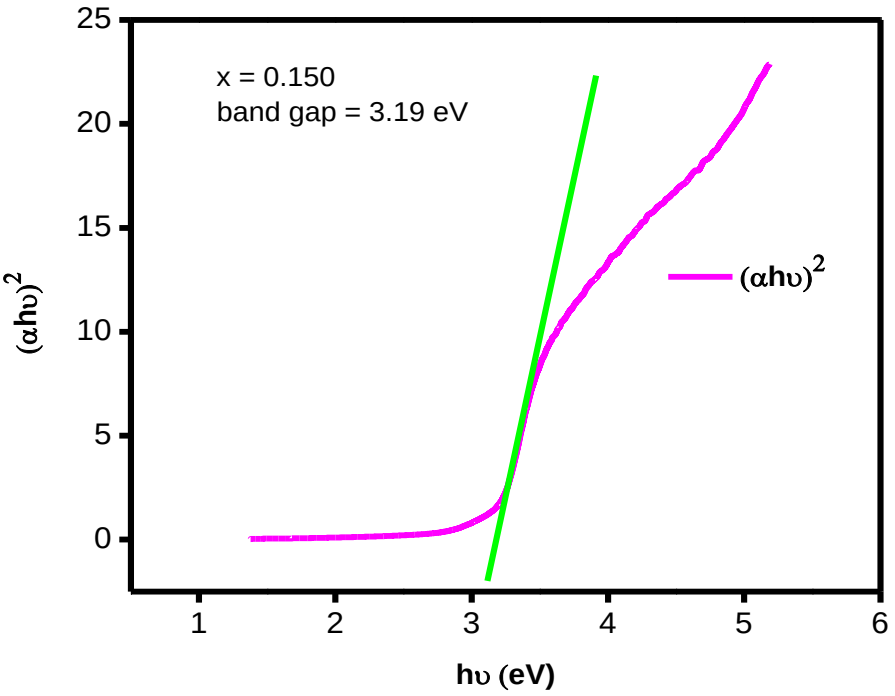

Fig. 6. Tauc plot of the $(Ba_{1-x}Ca_xZr_{1-y}Ti_y)O_3$ (x = 0.150, y = 0.90) powder samples.

Conclusion

The dielectric and optical properties of the ferroelectric perovskite $(Ba_{0.85}Ca_{0.15}Zr_{0.1}Ti_{0.9})O_3$ ceramics were observed. The composition shows polycrystalline structure. The observed maximum dielectric constant is measured 729, at around 100 ^oC. Also grain size is in µm range. From the observed optical properties, the reflectance was observed 80% near UV wavelength and 10% near visible range. The band-gap of the prepared composition is 3.19 eV.

References

Biswas D, Panwar NS and Sharma P (2020). Converse piezoelectric properties of lead free $Ba_{1-x}Ca_xZr_{0.1}Ti_{0.9}O_3$ (x = 0.055) ceramics using double sintered method. *Ferroelectrics* 568: 95-103.

Biswas D, Sharma P and Panwar NS (2021). Dielectric properties of $Na_{1-x}K_xNbO_3$ (NKN) (0.160 ≤ x ≤ 0.200) ceramics synthesized by double sintered method. *Ferroelectrics* 571: 214- 229.

Biswas D, Kathait GS, Thapliyal P, Rohilla V, Singh S and Negi J (2019). Converse piezoelectric properties of K and Na-modified $(Na_{1-x}K_x)$ NbO_3 lead free ceramics for x = 0.08 and 0.17. *Ferroelectrics* 550: 228–232.

Biswas D, Kathait GS, Thapliyal P, Rohilla V and Singh S (2018). Temperature dependence of dielectric properties of sodium potassium niobate ceramics for different values of x $(Na_{1-x}K_xNbO_3)$. *Ferroelectrics* 526: 168-175.

Biswas D, Sharma P and Panwar NS (2021). Structural and electrical properties of lead free $Na_{1-x}K_xNbO_3$ (0.160 ≤ x

≤ 0.200) ceramics. *Ceramics International* 47: 13814–13819.

Haertling GH (1967). Properties of hot-pressed ferroelectric alkali niobate ceramics. *J. Am. Ceram. Soc.* 50: 329.

Hennings D and Schnell A (1982). Diffuse Ferroelectric Phase Transitions in $Ba(Ti_{1-y}, Zr_y)O_3$ Ceramics. *J. Am. Ceram. Soc.* 65: 539–44.

Jaeger RE and Egerton L (1962). Hot pressing of potassium-sodium niobates. *J. Am. Ceram. Soc.* 45: 209.

Mondal T, Das S, Badapanda T, Sinha TP and Sarun PM (2017). Effect of Ca^{2+} substitution on impedance and electrical conduction mechanism of $Ba_{1-x}Ca_xZr_{0.1}Ti_{0.9}O_3$ ($0.00 \leq x \leq 0.20$) ceramics. *Physica B.* 508: 124-135.

Negi J and Panwar NS (2021). Structural and electrical properties of lead-free $Na_{0.685}K_{0.315}Nb_{1-y}Ta_yO_3$ ($0 \leq y \leq 0.05$) ceramics. *Journal of Physics and Chemistry of Solids* 151: 109853.

Singh S, Negi J and Panwar NS (2018). Dielectric properties of $Na_{1-x}K_xNbO_3$, near x = 0.5 morphotropic phase region. *Journal of Physics and Chemistry of Solids* 123: 311-317.

Singh S, Negi J and Panwar NS (2019). Temperature dependent dielectric properties of (Na, K) NbO_3, near equimolar composition, *Ceramics International* 45: 13067–13071.

Sen S and Choudhary R (2004). Effect of doping Ca ions on structural and electrical properties of $Ba(Zr_{0.05}Ti_{0.95})O_3$ electroceramics. *J. Mater. Sci.: Mater Electron* 15: 671-675.

Tian Y, Wei L, Chao X, Liu Z and Yang Z (2013). Phase Transition Behavior and Large Piezoelectricity Near the Morphotropic Phase Boundary of Lead-Free $(Ba_{0.85}Ca_{0.15})(Zr_{0.1}Ti_{0.9})O_3$ Ceramics. *J. Am. Ceram. Soc.* 96: 496–502.

Tunc S, Sonmez NA, Cetin SS and Ozcelik S (2019). Influences of annealing temperature on anti-reflective performance of amorphous Ta_2O_5 thin films. *Ceramics International* 45: 11-18.

Wang P, Li Y and Lu Y (2011). Enhanced piezoelectric properties of $(Ba_{0.85}Ca_{0.15})(Ti_{0.9}Zr_{0.1})O_3$ lead-free ceramics by optimizing calcination and sintering temperature. *J. Eur. Ceram. Soc.* 31: 2005–2012.

Wu J, Xiao D, Wu B, Wu W, Zhu J, Yang Z and Wang J (2012). Sintering temperature-induced electrical properties of $(Ba_{0.90}Ca_{0.10})(Ti_{0.85}Zr_{0.15})O_3$ lead-free ceramics. *Mater. Res. Bull.* 47: 1281–1284.

Yamashita Y and Shimanuki S (1996), Synthesis of lead scandium niobate-lead titanate pseudo binary system single crystals. *Mater. Res. Bull.* 31: 887–895.

Yamashita Y, Harada K, Tao T and Ichinose N (1996). Piezoelectric properties of the $Pb(Sc_{1/2}Nb_{1/2})$ O_3-$Pb(Mg_{1/3}Nb_{2/3})$ O_3-$PbTiO_3$ ternary ceramic materials near the morphotropic phase boundary. *Integrated Ferroelectrics* 13: 9–16.

Yamashita Y, Harada K, Hosono Y, Natsume S and Ichinose N (1998). Effects of B-site Ions on the Electromechanical Coupling Factors of $Pb(B'B'')O_3$–$PbTiO_3$ Piezoelectric Materials. *Jpn. J. Appl. Phys.* 37: 5288–5291.

Yu Z, Ang C, Guo R and Bhalla AS (2002). Piezoelectric and Strain Properties of $Ba(Ti_{1-x}Zr_x)O_3$ Ceramics. *J. Appl. Phys.* 92: 1489–93.

Environment, Development and Sustainability
https://doi.org/10.1007/s10668-021-01388-y

Investigation of microplastic pollution in river Alaknanda stretch of Uttarakhand

Jaspal Singh Chauhan[1] · Deepti Semwal[1] · Mamta Nainwal[1] · Neha Badola[1] · Prashant Thapliyal[2]

Received: 2 March 2020 / Accepted: 1 April 2021
© The Author(s), under exclusive licence to Springer Nature B.V. 2021

Abstract

Microplastic pollution research is conducted at a rapid rate throughout the world. However, microplastics (MPs) research in the freshwater ecosystem especially riverine ecosystem is lacking in India. This study is the pioneer to explore the occurrence of MPs in an Indian river. For the present investigation a stretch of river Alaknanda which is a major stream of river Ganga was selected. This stretch was divided into five sampling sites from which five water samples and four sediment samples were collected. The samples were filtered, oxidized, density separated and finally studied under compound microscope and Scanning Electron Microscope. Further, Energy-Dispersive X-ray Spectrum was also conducted to analyze the elemental status of the samples. The result of this research study recorded a total of 955 MPs. Among which 566 particles of the MPs were in water samples while 389 particles were found in sediment samples. In this study threads/fibers were the dominating type, i.e., 412 particles and particle size less than 1 mm was the most abundant type of MPs. Presence of such fine size of plastic particles increases the effect of exposure and interaction of particles with aquatic organisms and possesses a bigger threat for aquatic life. Metals like sodium, potassium, aluminum, calcium, titanium and magnesium were found attached with the MPs, indicating the potential risks to the living organisms.

Keywords Alaknanda · Heavy metals · Microplastics · Plastic · River ecosystem

✉ Jaspal Singh Chauhan
jaspal.env@gmail.com

Deepti Semwal
kaku97.0.6.semwal.deepti@gmail.com

Mamta Nainwal
mamtanainwal09@gmail.com

Neha Badola
badola.neha05@gmail.com

Prashant Thapliyal
pra.thapli1986@gmail.com

[1] Aquatic Biodiversity Lab, Department of Himalayan Aquatic Biodiversity, H.N.B Garhwal University, Srinagar, Uttarakhand 246174, India

[2] Department of Instrumentation Engineering, H.N.B Garhwal University, Srinagar, Uttarakhand 246174, India

Published online: 06 April 2021

1 Introduction

Plastic pollutants are rapidly imposing a long term and widespread threat to aquatic ecosystems and hence warrant an urgent need for its remediation. Plastics while entering the aquatic ecosystem undergoes degradation by various physical, chemical and biological processes. The fragmented particles of size < 5 mm are classified as MPs and their smaller size make them more potent to impair the quality of any aquatic ecosystem (Imhof et al., 2013; Thompson, 2015; Tudor & Williams, 2004). MPs originate from a variety of sources and can be broadly categorized as primary (MPs released directly from source) and secondary (MPs resulted from the fragmentation of larger items) MPs (Andrady, 2011; Cole et al., 2011; Hidalgo et al., 2012). Earlier, only the marine ecosystems were extensively investigated for the research on MPs but recently, interest in the occurrence and effects of the MPs has extended towards the freshwater ecosystems also (Kleinet al., 2015; Lambert & Martin, 2018; Sruthy & Ramasamay, 2016; Zhang et al., 2015). Freshwater ecosystems like rivers majorly contribute to MPs pollution in the ocean. A model prediction says that the Chinese Yangtze River is the largest contributor of plastic discharged into the East China Sea, followed by the River Ganga catchment between India and Bangladesh (Lebreton et al., 2017). There are many evidences which highlighted that MPs are ubiquitous and its concentrations with long-term exposure may pose a high risk to the aquatic ecosystems and its health (Biginagwa et al., 2016; Farrell & Nelson, 2013; Murray & Cowie, 2011; Scherer et al., 2017; Setälä et al., 2014). Further, adsorption of surrounding pollutants (hydrophobic contaminants, metals, etc.) by MPs on its surface enhances the level of threat to the aquatic life (Delle, 2001). There are investigations that noticed MPs potential to cause direct and indirect harms to the aquatic organism like toxicological impacts, physical blockages, tissue inflammation, digestive cell impairment as well as it can act as a potential substrate for the transport of elements, pathogens and algae (Besseling et al., 2013; Lambert & Martin, 2018; Moos et al., 2012; Rosenkranz et al., 2009). MPs also shows the risk of entering into the aquatic food web and get biomagnified to the higher trophic level (Farrell & Nelson, 2013).

Internationally, researches have been conducted to assess MPs in the fresh water ecosystems like rivers (Blair et al., 2019; Wang et al., 2017) and lakes (Wang et al., 2017; Zbyszewski & Corcoran, 2011; Zhang et al., 2016) but in India very few studies are conducted on the freshwater ecosystems. A research conducted by Central Inland Fisheries Research Institute, Kolkata, confirmed the presence of MPs in the sediment of eastern part of river Ganga (Sarkar et al., 2019). Similarly, Napper et al., (2021) identified different types of MPs particles from 10 sites along a 2575 km stretch of the Ganga river, which are considered to be the possible source of MPs pollution in the ocean. Another study conducted by Singh et al. (2021) in the river Ganga recorded 17 to 36 items/kg dry weight of sediments and 380 to 684 items/1000 m3 in the water samples. Before 2019, research work in this field was mostly conducted for plastic availability on beaches. A study by Jayasiri et al. (2013) quantified plastic litter in four sandy beaches of Mumbai and recorded the mean abundance of 7.49 g and 68.83 items per square meter, in which 41.85% MPs were predominated. In another research Karthik et al. (2018) evaluate the MPs distribution over the 25 sandy beaches along Tamil Nadu coast and found that the beaches adjacent to rivers recorded a relatively higher abundance of MPs as compared to distant one. Reddy et al. (2006) studied the small fragments of plastic debris in the intertidal sediments of a yard in Alang-Sosiys, India, and recorded 81 g of MPs in per kg of sediments. Few researchers have tried to work on the quality

and type of MPs found in the aquatic system. Veerasingam et al. (2016) studied the distribution of MPs pellets in the six beaches of Goa and recorded polyethylene (PE) and polypropylene (PP) as the dominant polymer. Similarly, Veerasingam et al. (2016) researched MPs along the Chennai coast of India and recorded white MPs as dominant type plastics. Scientists suggested that tourist activities and fishing practices are the possible sources of the MPs debris on beaches and rivers. Vidyasakar et al. (2018) collected marine sediment sample along the coastal areas of tourist place Rameswaram Island, Gulf of Mannar, India, and their results showed the highest abundance of white-colored and irregular-shaped plastic debris in the study area.

No study till date has assessed the occurrence, interaction, and risk associated with MPs in the riverine system of India. Among the freshwater ecosystems, rivers are considered as a lifeline for a huge population in India as it serves the demand of drinking water for them. But these rivers are now mostly polluted with organic or inorganic matter which is posing a risk to the dependent population. Plastic pollution has already invaded in all of the freshwater ecosystems specially rivers and thereby disturbing the ecological balance (Blair et al., 2019; Imhof et al., 2013; Tudor & Williams, 2004; Wang, Ndungu, et al., 2017; Wang, Peng, et al., 2017; Zbyszewski & Corcoran, 2011; Zhang et al., 2016). One such river that is lifeline of many villages and town is river Alaknanda. It is one of the major source streams of the River Ganga which provides drinking water for many populated towns of Uttarakhand and also supports the different agricultural activities. Hence, this study was designed to record the status of MPs in the water and sediment sample of river Alaknanda so that a baseline information may be provided to the researchers for further work.

2 Materials and methods

2.1 Study area

Approximately, 10 km stretch of the river Alaknanda at city Srinagar Garhwal was selected for this study. Srinagar Garhwal is situated in foothills of the Kumaon Himalayas and located at the banks of Alaknanda River in the Uttarakhand state of India. Srinagar Garhwal region comes under the Shivalik's ranges of the Himalaya. The latitude and longitude of Srinagar are 30.22°N and 78.78°E with an average elevation of 560metres (1837ft). The Alaknanda River is one of the two head-streams of holy River Ganga originate from the Satopanth Glacier and the Bhagirathi Kharak Glacier. The length of this river is approximately 190 km and the basin is about 10,882 km square. The towns along the banks of this river are Badrinath, Vishnuprayag, Joshimath, Chamoli, Nandaprayag, Karnaprayag, Rudraprayag, Srinagar and Devprayag (end point of this river). These major towns are mostly situated at the bank of river with dense population and hence are contributing for plastic pollution. This study area was selected due to the extensive human activity and other external interferences in this region. The study area was subdivided into 5 major sites as mentioned in Fig. 1. The water and sediment samples from the major sites were collected for analysis (Table 1).

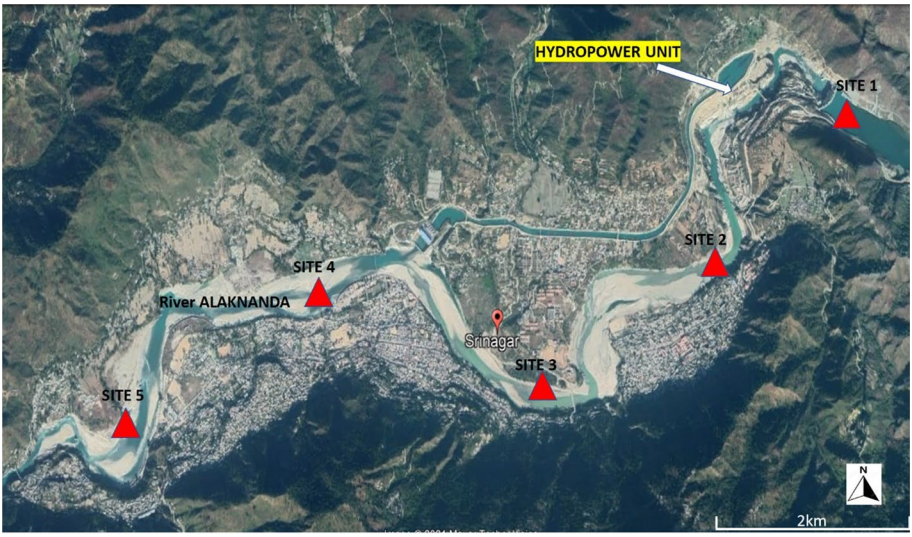

Fig. 1 Sampling sites in the study area Source: Google Earth

2.2 Sampling

Sampling was done in the months of April 2019. Total 9 samples were taken from five sampling sites among which 5 were water samples while 4 were sediment samples. For the standards, known samples of 6 types of plastic particles, i.e., Poly Ethylene Terephthalate (PET), High Density Ethylene (HDPE), Poly Vinyl Chloride (PVC), Low Density Polyethylene (LDPE), PP and Polystyrene (PS) were used.

2.2.1 Sediment

Sediment samples were taken from the four sites (Site 2, Site 3, Site 4 and Site 5) of the Alaknanda River stretch. The low depth region of the sites was selected to collect sediment samples. The site 1 is hydropower site with high depth and hence due to unavailability of official permission sediment sample was not taken. Quadrat of size 0.5*0.5 m was laid randomly and sediment samples were taken to a depth of 2–5 cm roughly at each site using Grab sampler and then transferred into a sample container.

2.2.2 Water

Water samples were collected from all the selected sites (Site 1, Site 2, Site 3, Site 4 and Site 5). A fifty liter of water sample was collected and filtered through 100 µm plankton net. Filtered material were collected in the well labeled glass vials and taken to laboratory for further analysis.

Table 1 Details of sampling sites in the river Alaknanda stretch of Srinagar, Garhwal

Site number	Site name	Location	Type of sampling	Source of interference
Site 1	Upstream Srinagar dam	$30^{0'}$ 14′17″ N 78^{0} 49′ 57″ E	Water	Temple, 04 hotel
Site 2	Srikot	30^{0} 13′ 46″ N 78^{0} 49′ 20″ E	Water	Apprx 50 houses, Temple, domestic waste water discharge, construction factory and school
		30°13′39.55″ N 78°49′08.05″ E	Sediment	
Site 3	Chauras Bridge	30^{0} 13′ 14″ N 78^{0} 48′ 24″ E	Water	20–30 hotels, Temple, construction site, Hotel, approximately 80–150 houses
		30°13′12.64″ N 78°48′07.15″ E	Sediment	
Site 4	Naithana Bridge	30^{0} 13′ 29″ N 78^{0} 45′ 59″ E	Water	Schools, temple, approximately 150–250 houses
		30°13′41.88″ N 78°47′15.06″ E	Sediment	
Site 5	Shri Yantra tapu Kirtinagar	30^{0} 13′ 50″ N 78^{0} 47′ 30″ E	Water	03 Hotels, temples, schools, approximately 150–200 houses
		30°13′09.58″ N 78°45′46.98″ E	Sediment	

2.3 Analysis

For the analysis of both sediment and water samples the standard protocol of National Oceanic Atmospheric Administration (NOAA) was followed (Masura et al., 2015).

2.3.1 Sediment

Sediment samples were wet sieved through a 5 mm stainless steel mesh sieve and ensured all material has been well washed, drained, and sorted. All the material retained on 5 mm sieve was discarded. After this Wet Peroxide Oxidation (WPO) of sediment samples were done by adding 20 ml of 30% hydrogen peroxide in the sample and then the mixtures were left at room temperature for 24 h. The process was repeated to ensure complete digestion of organic matter from the sample. After the WPO, all the samples were processed for density separation using salt (NaCl) to increase the density of the aqueous solution (~ 5 M NaCl) and then allowed solids to settle overnight. After settling, floating solid samples were filtered through 5 µm membrane filter (Whatman AE98) and the residual sediments from the beaker was discarded. The samples were air dried and weight of the samples was taken and finally sample was examined under the Stereo microscope at 40X magnification. Further, for the microparticle analysis the SEM and EDS were done at University Science and Instrument Center (USIC) at HNB Garhwal University. The plastic particles observed were categorized under 5 classes based on size; < 1 mm, 1–2 mm, 2–3 mm, 3–4 mm and 4–5 mm. Less than 1 mm size range includes all MPs of size less than 1 mm which we were able to see under compound microscope and SEM.

2.3.2 Water

The filtered material that was retained in the plankton net was wet sieved through a 5 mm stainless steel mesh sieve. The residue was discarded and the filtrate was processed for WPO by adding 20 ml of 30% hydrogen peroxide at room temperature and kept for 24 h. The process was repeated to ensure complete digestion of organic matter from the sample. After the WPO, all the samples were processed for density separation using NaCl to increase the density of the aqueous solution (~ 5 M NaCl) and then allowed solids to settle overnight. After settling, floating solid samples filtered through 5 µm membrane filter (Whatman AE98) and the residual sediments from the beaker was discarded. After covering samples with aluminum foil, the sample was air dried. Dried weight of the samples was taken and finally sample was examined under the Stereo microscope at 40X magnification. Further, in the microparticle analysis the SEM and EDS were done at USIC, HNB Garhwal University. The plastic particles observed were categorized under 5 classes based on size; < 1 mm, 1–2 mm, 2–3 mm, 3–4 mm and 4–5 mm. Less than 1 mm size range includes all MPs of size less than 1 mm which we were able to see under compound microscope.

3 Results and discussion

3.1 Morphological study

Morphological characterization based on different shape and size of MPs was investigated with the help of microscope. We recorded five types (fragments, films, foam, fiber/line and pellets) of MPs from the study area (Table 2). Since SEM is a good tool to get high resolution structure of surface of the particles (Wang et al., 2017), its analysis provided the images of MPs having different shapes and sizes from few microns to 5 mm (Fig. 2). Total number of MPs found in overall study was 955 particles. Among the total MPs, 566 were found in water and 389 were found in the sediment samples. Further this study, recorded threads/fibers count as highest, i.e., 766 as compared to the other category of MPs namely fragments (79), pellets (28) and films (73) and the foam. The MPs of foam type were observed in least quantity, i.e., 9 (Table 2). Similar results indicating high number of threads MPs was recorded by Wang et al. (2017) and Wu et al. (2019) for lakes and rivers of Wuhan, and two estuaries in Bohai Bay, China, respectively. The domestic effluent is considered as an important source of fiber and thread that is usually released from washing of cloths and other items (Browne et al. 2011). Recently, Napper et al. (2021) also found the fibers as highest particles (91%) and fragment (9%) in waters samples of the river Ganga. Similarly, Sarkar et al. (2019) observed film and fiber to be the dominant types of MPs in the sediments of Ganga River. Contrastingly, Wu et al. (2020) recorded fragment as dominant in both water and sediment samples of Maozhou River. The dominancy of the particles may be attributed to the sources of water pollution available in the study region. Our study recorded the MPs having size less than 1 mm were in significant amount as compared to the other categories. Wu et al. (2019) also observed high number of smaller sizes microplastics in surface water and sediments of Maozhou River. Smaller size MPs can easily access the different food chains of any aquatic ecosystem and hence can potentially affect it (Jeong et al., 2016).

In the sediment samples the most dominant MP at every site was fiber/threads with a total number of 354 particles while Foam plastic was absent. The total number of fragments, films and pellets were 17, 10 and 8, respectively. In sediment sample the highest number of MPs was found at site 3 with 122 MPs and the least was found at the site 5 with 74 MPs (Table 2). According to size MPs were categorized under 5 categories (size less than 1 mm, 1–2 mm, 2–3 mm, 3–4 mm and 4–5 mm). Particles less than 1 mm in size were dominating type in sediment sample contributing about 24% of total samples, followed by 2–3 mm (23%), 3–4 mm (21%), 1–2 mm (18%) and 4–5 (14%) (Fig. 3(a)). MPs of smaller size may pose serious threat to the aquatic organisms since it is capable to adsorb pollutants as a result of relatively large surface areas (Jeong et al., 2016).

In the water samples the dominant MP at every site was fiber/line with total number of 412 particles while foam plastic was noticed to be lowest in count with the total number of 9 particles. The results of Lahens et al., (2018) also show fibers and fragments as predominate while assessing MPs in the Saigon River and in the four urban canals. The total number of fragments, films and pellets in the water samples were 62, 63 and 20, respectively. The MPs of fragments and foams shapes are widely used in cosmetic products or transportation packages (Yan et al., 2019). Further, for the water samples the highest number of MPs was found at site 4 with 153 MPs and the least was found at site 3 with 101 MPs (Table 2). Pellets type of MPs were absent at site 3, site 4 and foam was absent at

Table 2 Number of MPs of different shape recorded during the study

Types of MPs	Site 1	Site 2		Site 3		Site 4		Site 5		Total
	Water	Water	Sediments	Water	Sediments	Water	Sediments	Water	Sediments	
Fragments	11	12	5	17	4	9	1	13	7	79
Threads/Fibers	79	71	74	60	113	124	103	78	64	766
Pellets	7	5	1	0	3	0	2	8	2	28
Films	5	14	3	21	2	17	4	6	1	73
Foam	2	1	0	3	0	3	0	0	0	9
Total	104	103	83	101	122	153	110	105	74	955

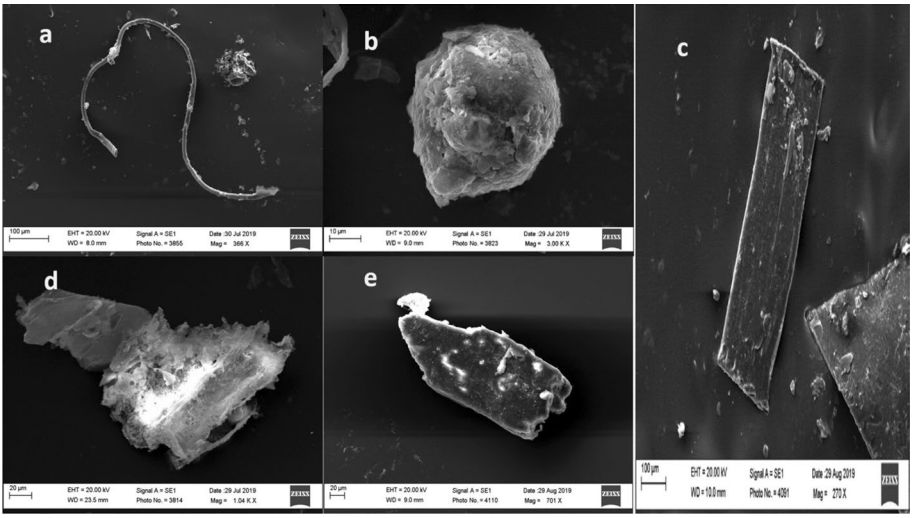

Fig. 2 Images of different shape (**a**. threads, **b**. pellets, **c**. film, **d**. foam, **e**. fragments) of microplastic observed in the study

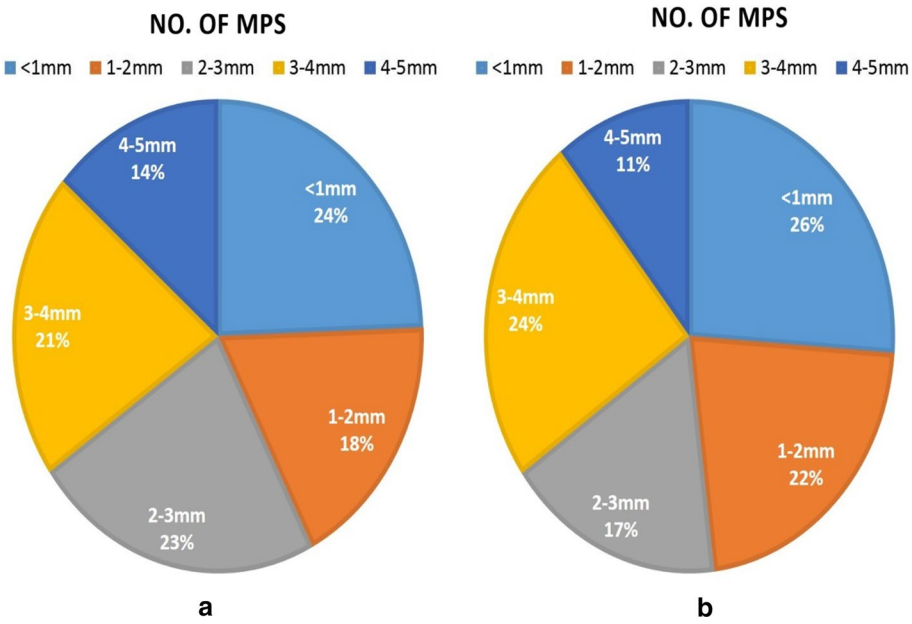

Fig. 3 Percentage of MPs of different size found in (**a**) sediment samples (**b**) water samples

site 5. Particles less than 1 mm were dominating with 26% of total sample followed by 3–4 mm (24%), 1–2 mm (22%), 2–3 (17%) and 4–5 (11%) (Fig. 3(b)). Other researcher also found small size MPs to be prevalent in their study area. Lahens et al. (2018) recorded less than 0.25 mm MPs to be dominant in the Saigon River (Vietnam). Similarly, Baldwin

et al. (2016) observed a major part (72%) of the MPs were in the size range of (0.35–0.99) mm while analyzing 29 great lakes tributaries worldwide.

All the study sites were highly disturbed due to human activities like direct dumping of domestic waste, untreated sewage drain, washing clothes, influence of solid commercial waste and construction waste. The city Srinagar is also a center point for tourists, because many famous religious destinations are connected by the highway which passes through it. So, it faces great rush of the tourists in the different seasons, contributing to plastic pollution. This study provides the baseline information about the availability of MPs in the river Alaknanda. A few studies in the different countries have also proved the presence of MPs in water and sediments of lakes like lakes in Vembanad, Kerala (Sruthy & Ramasamay, 2016); Tibet plateau, China (Zhang et al., 2016) and Huron, Canada (Zbyszewski & Corcoran, 2011) but river is still lesser-known area of study in this field.

3.2 Identification and characterization

An effort was made to identify and understand the basic chemical characterization of the standard sediment and water sample with the help of EDS. EDS was done for standard samples and field samples so that resemblance could be found. The EDS report shows that selected 6 standards (PT, HDPE, PVC, LDPE, PP and PS) and samples (water and sediments) were having high peak of Carbon. In the graph of PT, HDP, LDP and PP carbon weight percentage were found 92.43%, 89.90%, 96.51% and 95.70%, respectively, while in PVC and PS carbon weight percentage was 53.88% and 63.79%. Other than carbon, oxygen was also found in all the standard samples. This presence of oxygen can also attribute to the sample's exposure to atmospheric oxygen besides being a constituent of plastic formation. Peak of silicon and calcium was observed in standard of PT and HDPE while in PVC,

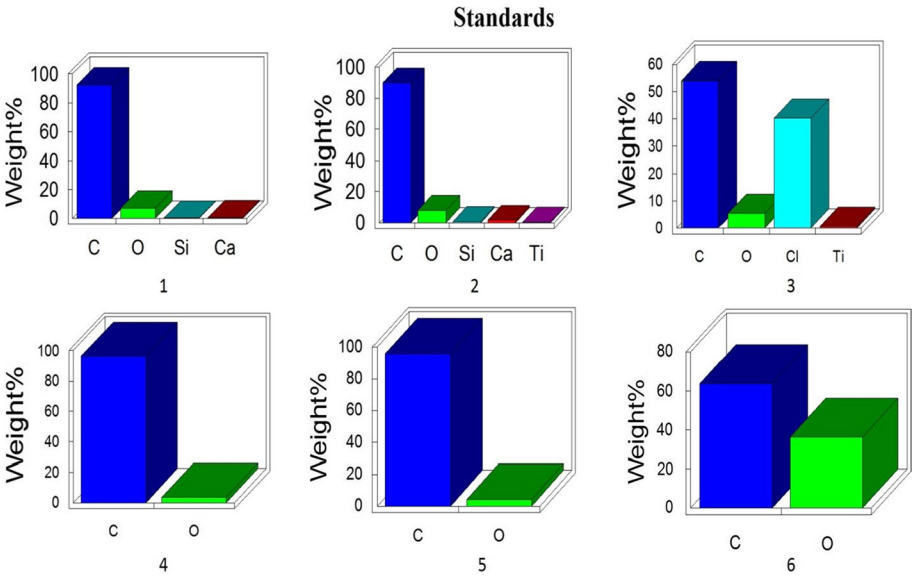

Fig. 4 Graph showing weight percentage of the standard samples of different types (1. PET, 2. HDPE, 3. PVC, 4. LDPE, 5. PP and 6. PS)

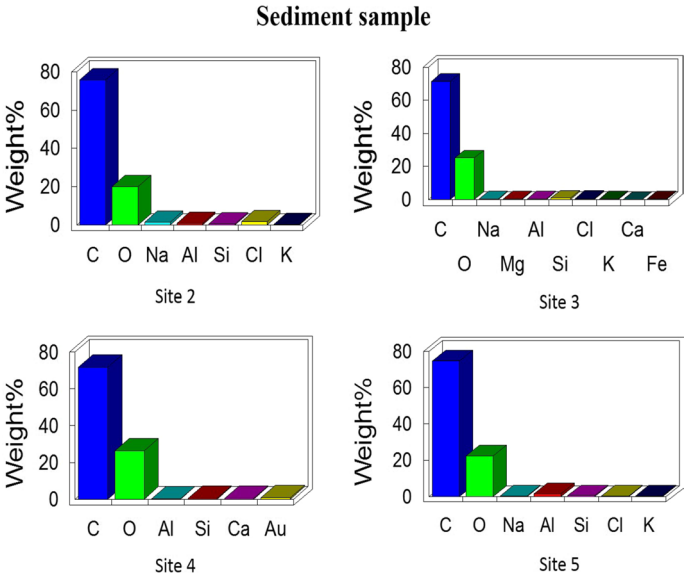

Fig. 5 Graph showing weight percentage of the different elements in the sediment samples

peak of chlorine and titanium was observed. In the standard of LDPE, PP and PS only carbon and oxygen were found no other element was observed (Fig. 4).

In the EDS reports of both water and sediment sample; high peak of carbon is obtained as like standards so we can state that tested particles have a high probability of being plastic

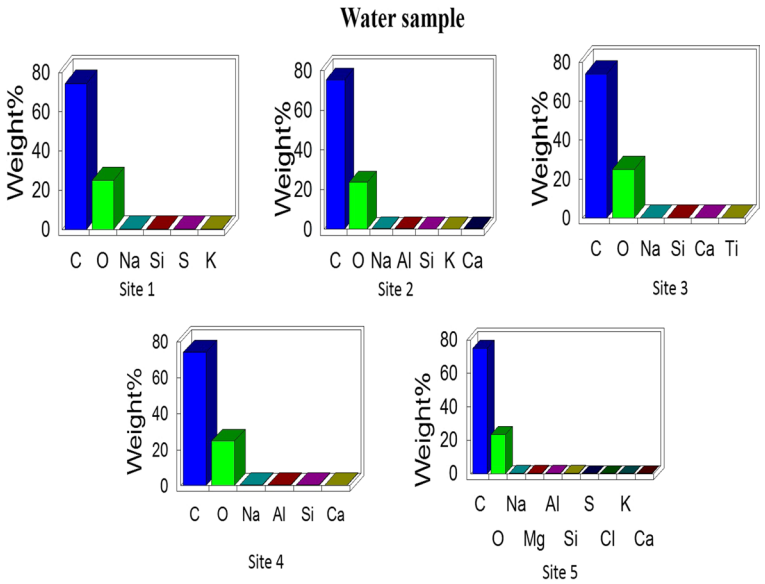

Fig. 6 Graph showing weight percentage of the different elements in the water samples

particles. Similar results statement was given by Blair et al. (2019) on the basis of the high peak of carbon in his study. In the sediment sample percentage weight of carbon found at site 2, site 3, site 4 and site 5 was75.68%, 71.30%, 71.70% and 74.71%, respectively (Fig. 5). While in water samples the carbon weight percent at site 1, site 2, site 3, site 4 and site 5 was 74.43%, 75.31%, 74.20%, 74.16% and 74.90% (Fig. 6). When carbon weight percent of sample and standards were compared, none of them matched exactly. The possible reason was sample were taken from the contaminated ecosystem while the standards were taken from pure sources. But it was observed that samples were having an average carbon weight % of approx. 74%, which was falling in the range of standards between PS 63.8% and HDPE 89%. So, it may be chance that the samples were a degradation product of PS or HDPE. A Fourier-transform infrared spectroscopy analysis is required to further confirm it.

3.3 Interaction with metals

In the EDS analysis of samples, many other elements were found other than carbon and oxygen, such as silicon, calcium, potassium, sodium, titanium, magnesium, aluminum. Among these elements' sodium, potassium, aluminum, calcium, titanium, magnesium were metals. In the sediment samples aluminum was found at all sites within the range 0.21% to 1.51% while in water samples it's ranged from 0.24 to 0.32% (Figs. 5 and 6). Titanium was found only at site 3 in water sample which was 0.23% (Fig. 6). Titanium dioxide is used as pigment in plastic industry to give white color to plastics hence its presence in sample maybe marked to validate the presence of plastic particle (Wang, Wagner, et al., 2017). Titanium was also noticed in the study done by Wu et al. (2020) along with lead (Pb) and zinc (Zn). Detection of metal proves capabilities of plastic particle to bind metals, including heavy metals on its surface. As plastics have a long life, they do not degrade easily and therefore continuously interact with different elements, and act as adsorbent for them (Wang, Peng, et al., 2017). Since Al, Fe, Si, Ca, and K are commonly found elements in any aquatic environment and their presence on MPs indicate that MPs can attach different element on its surface (Wu et al., 2020). Thus, these MPs particles can easily carry toxic elements to aquatic food chains as a result of bio magnification. The common metal found attached with MPs as observed in different studies were Al, Fe, Mn, Cd, Cr, Ni, Cu, Zn, Ni, Cd, Pb and Ti (Ashton et al., 2010; Brennecke et al., 2016; Dobardaran et al., 2018; Massos & Turner, 2017; Wang, Peng, et al., 2017).

4 Conclusion

Rivers are the important source of the drinking water and hence any substance that changes its quality abruptly must be researched properly. This study was aimed to assess the occurrence and quantification of MPs in the river Alaknanda, one of the major tributaries of the river Ganga that contribute significant amount of its water for drinking purpose. Our finding indicates the presence of high level of MPs in the water and sediment of the river Alaknanda. Further, these MPs were of different shape and size which indirectly explains different source of origin. High level of threads in sample explains the domestic source of release (such as activities of washing clothes) in the region. The MPs found were able to adsorb metals on their surfaces capable of posing high risks to the living organisms. This river stretch water is also commonly pumped for drinking purpose at Srinagar Town hence it is possible that these MPs may reach human beings and affect their health. Moreover,

the MPs can easily enter the food web of river ecosystem and can impair its quality. This study is a base line study that proves the occurrence of different shape and size of MPs in the river. Further researches are required to understand the level of toxicity that MPs can pose to the aquatic ecosystem and human beings. More study with advance technology is demanded on this topic for building a better perspective and understanding about the problem and to find out every possible solution.

Supplementary Information The online version contains supplementary material available at https://doi.org/10.1007/s10668-021-01388-y.

Acknowledgement Research facilities received from USIC, Hemvati Nandan Bahuguna Garhwal university (A Central university) Srinagar Garhwal Uttarakhand, India, is gratefully acknowledged. Authors are grateful to the anonymous reviewers for their valuable suggestions that helped us to improve this work.

References

Andrady, A. L. (2011). Microplastics in the marine environment. *Marine Pollution Bulletin, 62*, 1596–1605.

Ashton, K., Holmes, L., & Turner, A. (2010). Association of metals with plastic production pellets in the marine environment. *Marine Pollution Bulletin, 60*, 2050–2055.

Besseling, E., Wegner, A., Foekema, E. M., Van, D. H. G. M. J., & Koelmans, A. A. (2013). Effects of microplastic on fitness and PCB bioaccumulation by the Lugworm Arenicola marina (L.). *Environment Science and Technology, 47*, 593–600.

Biginagwa, F. J., Mayoma, B. S., Shashoua, Y., Syberg, K., & Khan, F. R. (2016). First evidence of microplastics in the African Great Lakes: Recovery from Lake Victoria Nile perch and Nile tilapia. *Journal of Great Lakes Research, 42*, 146–149.

Bladwin, A., Corsi, S., & Mason, S. (2016). Plastic debris in 29 great lakes tributaries: Relations to watershed attributes and hydrology. *Environmental Science and Technology, 50*, 10377–10385.

Blair, R. M., Waldron, S., Phoenix, V. R., & Lindsay, C. G. (2019). Microscopy and elemental analysis characterization of microplastics in sediments of a freshwater urban river in Scotland, UK. *Environmental Science and Pollution Research, 26*, 12491–1250.

Brennecke, D., Duarte, B., Paiva, F., Caçador, I., & Canning-Clode, J. (2016). Microplastics as vector for heavy metal contamination from the marine environment. *Estuarine Coastal and Shelf Science, 178*(5), 189–195.

Browne, M. A., Crump, P., Niven, S. J., Teuten, E., Tonkin, A., & Galleway, T. (2011). Accumulation of microplastic on shorelines worldwide: Sources and sinks. *Environmental Science & Technology, 45*, 9175–9179.

Cole, M., Lindeque, P., Halsband, C., & Galloway, T. S. (2011). Microplastics as contaminants in the marine environment: A review. *Marine Pollution Bulletin, 62*, 2588–2597.

Delle, S. A. (2001). Factors affecting sorption of organic compounds in natural sorbent/water systems and sorption coefficients for selected pollutants: A review. *The Journal of Physics and Chemistry Reference Data, 30*, 187–439.

Dobardaran, S., Schmidt, T. C., Nabipour, I., Khajeahmadi, N., Tajbakhsh, S., Saeedi, R., Mohammadi, M. J., Keshtkar, M., Khorsand, M., & Ghasemi, F. F. (2018). Characterization of plastic debris and association of metals with microplastics in coastline along the Persian Gulf. *Water Management, 78*, 649–658.

Farrell, P., & Nelson, K. (2013). Trophic level transfer of microplastic: Mytilus edulis (L.) to Carcinusmaenas (L.). *Environmental Pollution, 177*, 1–3.

Hidalgo, R. V., Gutow, L., Thompson, R. C., & Thiel, M. (2012). Microplastics in the marine environment: A review of the methods used for identification and quantification. *Environmental Science & Technology, 46*, 3060–3075.

Imhof, H. K., Schmid, J., Niessner, R., Ivleva, N. P., & Laforsch, C. (2013). Contamination of beach sediments of a subalpine lake with microplastic particles. *Current Biology, 23*, 867–868.

Jayasiri, H. B., Purushothaman, C. S., & Vennila, A. (2013). Quantitative analysis of plastic debris on recreational beaches in Mumbai, India. *Marine Pollution Bulletin, 77*, 107–112.

Jeong, C. B., Won, E. J., Kang, H. M., Lee, M. C., Hwang, D. S., Hwang, U. K., Zhou, B., Souissi, S., Lee, S. J., & Lee, J. S. (2016). Microplastic size-dependent toxicity, oxidative stress induction, and

p-JNK and p-p38 activation in the monogonont rotifer (Brachionus koreanus). *Environmental Science and Technology, 50*, 8849–8857.

Karthik, R., Robin, R. S., Puevaja, R., Ganguly, D., Anandavelu, I., Raghuraman, R., Hariharan, G., Ramakrishna, A., & Ramesh, R. (2018). Microplastic along the beaches of southeast coast of India. *Science of the Total Environment, 645*, 1388–1399.

Klein, S., Worch, E., & Knepper, T. P. (2015). Occurrence and spatial distribution of microplastics in river shore sediments of the Rhine-main area in Germany. *Environmental Science & Technology, 49*, 6070–6076.

Lambert, S., & Martin, W. (2018). Microplastics are contaminants of emerging concern in freshwater environments: An overview. *Freshwater Microplastics: Emerging Environmental Contaminants, The Handbook of Environmental Chemistry, 58*, 1–23.

Lahens, L., Strady, E., Kieu-Le, T. C., Dris, R., Boukerma, K., Rinnert, E., Gasperi, J., & Tassin, B. (2018). Macroplastic and microplastic contamination assessment of a tropical river (Saigon River, Vietnam) transversed by a developing megacity. *Environment Pollution, 236*, 661–671.

Lebreton, L. C., Van Der Zwet, J., Damsteeg, J. W., Slat, B., Andrady, A., & Reisser, J. (2017). River plastic emissions to the world's oceans. *Nature Communications, 8*(1), 1–10.

Massos, A., & Turner, A. (2017). Cadmium, lead and bromine in beached microplastics. *Environmental Pollution, 227*, 139–145.

Masura, J., Baker, J., Foster, G., Arthur, C., Herring, C. (2015). Laboratory methods for the analysis of microplastics in the marine environment: recommendations for quantifying synthetic particles in waters and sediments. *NOAA Technical Memorandum NOS-OR&R*-48.

Moos, N. V., Holm, P. B., & Kohler, A. (2012). Uptake and effects of microplastics on cells and tissue of the Blue mussel Mytilus edulis L. after an experimental exposure. *Environmental Science & Technology, 46*, 11327-e11335.

Murray, F., & Cowie, P. R. (2011). Plastic contamination in the decapods crustacean Nephropsnorvegicus (Linnaeus, 1758). *Marine Pollution Bulletin, 62*, 1207–1217.

Napper, I. E., Baroth, A., Barrett, A. C., Bhola, S., Chowdhury, G. W., Davies, B. F., Duncan, E. M., Kumar, S., Nelms, S. E., Niloy, M. N. H., Nishat, B., Maddalene, T., Thompson, R. C., & Koldewey, H. (2021). From sea to source: The abundance and characteristics of microplastics in surface water in the transboundary Ganges River. *Environmental Pollution, 274*, 116348.

Reddy, M. S., Basha, S., Adimurthy, S., & Ramachandraiah, G. (2006). Description of the small plastics fragment in marine sediments along the Alang-Sosiys ship-breaking yard, India. *Estuarine coastal and Shelf Science, 68*, 656–660.

Rosenkranz, P., Chaudhry, Q., Stone, V., & Fernandes, T. F. (2009). A comparison of nanoparticle and fine particle uptake by Daphnia magna. *Environmental Toxicology and Chemistry, 28*, 2142–2149.

Sarkar, D. J., Sarkar, S. D., Das, B. K., Manna, R. K., Behera, B. K., & Samanta, S. (2019). Spatial distribution of meso and microplastics in the sediments of river Ganga at eastern India. *Science of the Total Environment, 694*, 133712.

Scherer, C., Weber, A., Lambert, S., & Wagner, M. (2017). Interactions of microplastics with freshwater biota. *Freshwater Microplastic, Handbook of Environmental Chemistry, 58*, 1–23.

Setälä, O., Fleming-Lehtinen, V., & Lehtiniemi, M. (2014). Ingestion and transfer of microplastics in the planktonic food web. *Environmental Pollution, 185*, 77–83.

Singh, N., Mondal, A., Bagri, A., Tiwari, E., Khandelwal, N., Monikh, F. A., & Darbha, G. K. (2021). Characteristics and spatial distribution of microplastics in the lower Ganga River water and sediment. *Marine Pollution Bulletin, 163*, 111960.

Sruthy, S., & Ramasamay, E. V. (2016). Microplastic pollution in Vembanad Lake, Kerala, India: the first report of microplastics in lake and estuarine sediments in India. *Environmental Pollution, 222*, 315–322.

Thompson, R. C. (2015). Microplastics in the marine environment: Sources, consequences and solutions. In L. Gutow, M. Klages, & M. Bergmann (Eds.), *Marine anthropogenic litter.* (pp. 185–200). Cham: Springer.

Tudor, D. T., & Williams, A. T. (2004). Development of a 'matrix scoring technique' to determine litter sources at a Bristol channel beach. *Journal of Coastal Conservation, 10*, 119–127.

Veerasingam, S., Saha, M., Suneel, V., Vethamony, P., Rodrigues, A. C., Bhattacharyya, S., & Naik, B. G. (2016). Characteristics, seasonal distribution and surface degradation features of microplastic pellets along the Goa coast, India. *Chemosphere, 159*, 496–505.

Veerasingam, S., Mugilarasan, M., Venkatachalapathy, R., & Vethamony, P. (2016). Influence of 2015 flood on the distribution and occurrence of microplastic pellets along the Chennai coast, India. *Marine Pollution Bulletin, 109*, 196–204.

Vidyasakar, A., Neelavannan, K., Krishnakumar, S., Prabaharan, G., Sathiyabama Alias Priyanka, T., Magesh, N. S., Godson, P. S., & Srinivasalu, S. (2018). Macrodebris and microplastic distribution in the beaches of Rameshwaram Coral Island, Gulf of Mannar, Southeast coast of India: A first report. *Marine Pollution Bulletin, 137*, 610–616.

Wang, J., Peng, J., Tan, Z., Gao, Y., Zhan, Z., Chen, Q., & Cai, L. (2017). Microplastics in the surface sediments from the Beijiang River littoral zone: Composition, abundance, surface textures and interaction with heavy metals. *Chemosphere, 171*, 248–258.

Wang, W., Ndungu, A. W., Li, Z., & Wang, J. (2017). Microplastics pollution in inland freshwaters of China: A case study in urban surface waters of Wuhan, China. *Science of the Total Environment, 575*, 1369–1374.

Wang, Z. M., Wagner, J., Ghosal, S., Bedi, G., & Wall, S. (2017). SEM/EDS and optical microscopy analyses of microplastics in ocean trawl and fish guts. *Science of The Total Environment, 603*, 616–626.

Wu, N., Zhang, Y., Zhao, Z., He, J., Li, W., Ma, Y., & Niu, Z. (2019). Occurrence and distribution of microplastics in the surface water and sediment of two typical estuariesin Bohai Bay, China. *Environmental Science: Processes & Impacts, 21*, 1143–1155.

Wu, P., Tang, Y., Dang, M., Wang, S., Jin, H., Liu, Y., Jing, H., Zheng, C., Yi, S., & Cai, Z. (2020). Spatial-temporal distribution of microplastics in surface water and sediments of Maozhou River within Guangdong-Hong Kong-Macao Greater Bay Area. *Science of the Total Environment, 717*, 135187.

Yan, M., Nie, H., Xu, K., He, Y., Hu, Y., Huang, Y., & Wang, J. (2019). Microplastic abundance, distribution and composition in the Pearl River along Guangzhou city and Pearl River estuary, China. *Chemosphere, 217*, 879–886.

Zbyszewski, M., & Corcoran, P. L. (2011). Distribution and degradation of fresh water plastic particles along the beaches of Lake Huron, Canada. *Water Air Soil Pollution, 220*, 365–372.

Zhang, K., Gong, W., Lv, J., Xiong, X., & Wu, C. (2015). Accumulation of floating microplastics behind the three Gorges Dam. *Environmental Pollution, 204*, 117–123.

Zhang, K., Su, J., Xiong, X., Wu, X., Wu, C., & Liu, J. (2016). Microplastic pollution of lakeshore sediments from remote lakes in Tibet plateau, China. *Environmental Pollution, 219*, 450–455.

Publisher's Note Springer Nature remains neutral with regard to jurisdictional claims in published maps and institutional affiliations.

Superlattices and Microstructures 158 (2021) 107008

Contents lists available at ScienceDirect

Superlattices and Microstructures

journal homepage: www.elsevier.com/locate/superlattices

Optical properties and current conduction in annealed $(Ta_2O_5)_{0.94}$ – $(TiO_2)_{0.06}$ thin films

Prashant Thapliyal [a,b,*], N.S. Panwar [a], G. Mohan Rao [b]

[a] Department of Instrumentation Engineering, H.N.B. Garhwal University, Srinagar Garhwal, Uttarakhand, India
[b] Department of Instrumentation and Applied Physics, Indian Institute of Science, Bangalore, India

ARTICLE INFO

Keywords:
Refractive index
Sputtering
Optical bandgap
Tunneling
Conduction mechanism

ABSTRACT

By sputtering the mosaic assembly of tantalum (Ta) and titanium (Ti) metal targets in the oxygen environment, $(Ta_2O_5)_{1-x}$–$(TiO_2)_x$, x = 0.06, thin films were deposited onto the quartz, and P/boron-silicon (1 0 0) substrates, at room temperature (RT). The RT deposited films were annealed for 1.5 h, from 500 to 800 °C. Formation of the crystal structure in the films was observed at and above 700 °C annealing. Optical transmittance data, measured with the UV–Vis spectrophotometer, were used to find out the extinction coefficient (k), refractive index (n_{opt}), and optical bandgap (E_g) of the prepared films. With the increasing annealing temperature, both the n_{opt} and E_g values were observed, decreasing from 2.218 to 2.160, and 4.23 to 4.02 eV, respectively. The extinction coefficient of amorphous films was observed lesser than the crystalline films. The current–voltage characteristics of the prepared film assisted metal–oxide–semiconductor (MOS) structures manifest different conductions, viz., ohmic at the lower electric fields; and Schottky, Poole–Frenkel, Fowler–Nordheim tunneling and space–charge–limited current, in the intermediate to higher fields, for different annealing treatments.

1. Introduction

The increasing demand for high-performance and high-storage electronic gadgets has initiated the integration of capacitors into high-memory devices. SiO_2, the most common dielectric used in semiconductor memories, needs to be replaced due to its low relative permittivity [1] and large leakage current [2]. Many high dielectric constant metal oxides have been suggested to reduce the memory device size with improved performance [3–6]. Among the suggested oxides, tantalum pentoxide (Ta_2O_5) is one of the most commonly recommended, owing to its optics and electronics applications [7–9]. Ta_2O_5 thin films have promising applications, as highly transparent and refracting coatings [10], as anti-reflector in silicon solar cells [11], and optical waveguides [12,13].

The microstructure and quality of the film can be improved either with substrate heating during deposition or post-deposition annealing [14]. However, the high crystallization temperature (≥600 °C) of Ta_2O_5 facilitates interaction between the Si substrate and Ta_2O_5 film and reduces breakdown strength [15–17]. In MOS structures, an unavoidable thin interfacial SiO_2 layer is formed between Si and the metal oxide film [18], which further thickens with post-deposition treatment [19]. Conduction in the MOS structures may be affected by the formed interfacial SiO_2 layer at the interface [19]. Post-deposition annealing crystallization improves the structural and optical properties of Ta_2O_5 thin films [20,21], which is attributed to the reduced oxygen vacancies and defects [22]. Besides annealing, the admixing of TiO_2 or Y_2O_3 into Ta_2O_5 shows a significant enhancement in the dielectric and electrical properties

* Corresponding author. Department of Instrumentation Engineering, H.N.B. Garhwal University, Srinagar Garhwal, Uttarakhand, India.
E-mail address: pra.thapli1986@gmail.com (P. Thapliyal).

https://doi.org/10.1016/j.spmi.2021.107008
Received 3 May 2021; Received in revised form 4 August 2021; Accepted 15 August 2021
Available online 17 August 2021
0749-6036/© 2021 Elsevier Ltd. All rights reserved.

[23–25]. The high dielectric constant, 55 and 71, was reportedly observed for the annealed $(TiO_2)_{0.08}$–$(Ta_2O_5)_{0.92}$ films, deposited with the sputtering of the ceramic target [26]; and annealed $(Ta_2O_5)_{0.94}$–$(TiO_2)_{0.06}$ films, deposited with the sputtering of (Ta, Ti) metal targets [27], respectively. Chandra et al. [28] studied the optical and electrical properties of Ti-doped Ta_2O_5. Knowledge of the bandgap is extremely important for understanding the ambient energy-material interaction, and the electrical properties of a thin film material, and is, therefore, of great practical interest. The current transport phenomena in dielectrics need to be explored for complete understanding of charge conduction through the material structures. Since, these phenomena are of great importance for electronic applications, further efforts would be needed to enhance the understanding of the underlying current conduction mechanisms. A thorough understanding of the different conduction mechanisms in the metal–oxide–semiconductor (MOS) structures would help to reduce the level of the leakage current through them. The present manuscript describes the annealing temperature dependent growth of the interfacial SiO_2 layer, which significantly affects the current conduction and hence the leakage current through the prepared films [29].

In the present study, the $(Ta_2O_5)_{0.94}$–$(TiO_2)_{0.06}$ (hereafter referred to as $TTO_{0.06}$) thin films were deposited onto the quartz (refractive index = 1.51, transmittance = 92% in the visible range) and silicon substrates, by reactive direct current (DC) magnetron sputtering of the mosaic Ta and Ti metal targets. The $TTO_{0.06}$ films deposited by sputtering were annealed at different temperatures ranging from 500 to 800 °C. The transmittance variation with wavelength was measured for the films deposited onto the quartz substrates. The $TTO_{0.06}$ film-assisted MOS structures were prepared and their current–voltage (I–V) characteristics were measured. The optical parameters and bandgap calculated from the observed transmittance of the deposited films, and the conduction mechanisms manifested by the I–V characteristics of the prepared MOS structures have been presented in this paper.

2. Experimentation

Optically polished quartz plates (1 mm thick), and (1 0 0) oriented p-silicon substrates were used to deposit the (Ta_2O_5) – (TiO_2) composite thin films employing reactive magnetron DC sputtering. The quartz and silicon substrates were rinsed with acetone, hydrogen fluoride (HF), and de-ionized water, following the standard procedure. The relative sputtering areas of the mosaic Ta and Ti targets were arranged in such a way that the $TTO_{0.06}$ composition of the deposited films is achieved [27]. The star-shaped targets were cut from the solid plates with a diameter of 2-inches and a thickness of 1 mm. All the targets used were having purity ~99.99%. The mosaic Ta–Ti target assembly was sputtered by argon (5×10^{-3} mbar working pressure) in the presence of oxygen (5% of working pressure). The sputter-deposited thin films were annealed for 1.5 h in ambient air, at 500, 600, 700, and 800 °C. The thin film preparation setup and conditions, their structural and compositional characteristics, and relevant measuring instruments details have been reported in the previous communications [27,30].

The thickness (d) of the prepared films was measured about 280 ± 10 nm using the ellipsometric method. The transmission spectra of prepared films were obtained, in the 190–1000 nm wavelength range, with a 0.5 nm step, using a UV–Vis spectrophotometer (Specord S600–212C291). Swanepoel's envelope approach [31] was used to estimate optical parameters from optical transmittance plots. Using a shadow mask (with holes diameter of 0.5 mm), silver (Ag) was sputter deposited to fabricate Ag/$TTO_{0.06}$/p-Si MOS capacitors. The current–voltage (I–V) characteristics of the prepared MOS structures were determined using a P–E loop tracer with piezometer (make: aixACCT Systems GmbH, model: aixPES).

3. Results and discussion

In continuation of the previous communication [27], due to its best dielectric and electrical properties, among the prepared TTO_x compositions, presently, the composition with x = 0.06 was chosen to study the optical properties and I–V characteristics of the

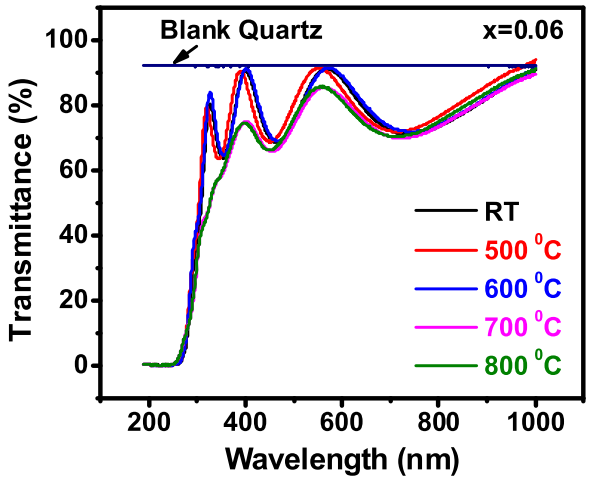

Fig. 1. The transmittance vs wavelength plots of prepared $TTO_{0.06}$ thin films.

prepared capacitors. X-ray diffraction results show sputter-deposited films remain amorphous even when annealed, up to 600 °C; and on annealing at and above 700 °C, the films show crystalline structure [27]. Fig. 1 shows the observed transmittance vs wavelength plot of the prepared $TTO_{0.06}$ optical films. Very high transmittance (~90.5–91.8%), closer to the transmittance of blank quartz substrate (i.e., 92%), was observed, for the as-deposited and the films annealed up to 600 °C, in the measured wavelength range >400 nm. For the amorphous films, the transmittance was observed increasing on increasing annealing (≤600 °C), which may be due to the improved oxygen stoichiometry and film quality, on annealing. However, the observed enhancement was less in the transmittance of amorphous films, with increasing annealing up to 600 °C. On further annealing (at and above 700 °C), the transmittance was found to decrease (~75–87%), which may be due to the formation of crystalline structure, and the reorientation of the atoms in the crystal lattice caused by the amorphous-to-crystalline phase transformation, with annealing (≥700 °C) [27], may result in the scattering of incident photons and thereby decreased transmittance. In the crystalline films (annealed at 700 and 800 °C), no significant change in the transmittance was observed, on annealing, Fig. 1.

Using Swanepoel's envelope method [31], refractive index (n_{opt}) and extinction coefficient (k) were calculated from the optical transmittance plots. For all the prepared films, generally, both the refractive index (n_{opt}) and extinction coefficient (k) were found to decrease as the wavelength was increased [32], Fig. 2. With increasing annealing temperature, the refractive index, at 550 nm, was found to decrease from 2.218 to 2.160 and was found consistent with the reported values [33–35]. A considerable change in the refractive index was observed between amorphous and crystalline films, Fig. 2(a). The crystalline films' refractive index was observed to decrease drastically compared to the amorphous films. On annealing, the release of internal stress and crystallization may be held responsible for the observed drastic change in the refractive index. On the release of internal stress, the films' density reduces, and the refractive index decreases [10]. From the XRD measurement [27], the lattice constants of the crystalline films were obtained as, a = 6.235 Å, b = 3.590 Å, c = 3.900 Å, and V = 87.296 $Å^3$, for 700 °C annealed films; and a = 6.233 Å, b = 3.593 Å, c = 3.904 Å, and V = 87.431 $Å^3$, for 800 °C annealed films. At the higher annealing temperature, the increasing unit cell volume of the films tending towards the unit cell volume of the bulk (a = 6.200 Å, b = 3.660 Å, c = 3.890 Å, and V = 88.272 $Å^3$) [source: Inorganic Crystal Structure Database (ICSD) – (01-089-2843)], indicates the release of stress in the films. The release of stress in the films may reduce the density and thereby observed decreasing the refractive index, with increasing annealing temperature. The refractive index may also be affected by voids, imperfections, the film–substrate interfacial interactions, film growth conditions, etc. [36]. At 550 nm wavelength, for the amorphous films, no distinguishable change was observed in the values of k (which remains near to 0.017) on annealing (up to 600 °C); whereas on crystallization, with annealing at 700 and 800 °C, k increased to 0.120, without any significant change on annealing, Fig. 2(b). Reorientation of atoms, and increased oxygen loss in the crystal volume [37], at 700 and 800 °C, may result in further absorption, resulting in an increased extinction coefficient of crystalline films as compared to the amorphous films.

The bandgap (E_g) was determined from the transmittance vs wavelength plot, using the well known Tauc's equation [38,39]:

$$\alpha h\nu = A(h\nu - E_g)^m, \quad (1)$$

where α, hν and A stand for the coefficient of absorption, the energy of the photon, and a constant, respectively. The allowed transition in the films is suggested by the value of constant m, which satisfies Eq. (1), for m = ½, and indicates the photon–electron interaction. In the $(\alpha h\nu)^2$ vs hν plots, the straight-line portion, which intersects the energy axis when expanding, gives the energy bandgap, Figs. 3 (a–e). At around 300 nm, a sharp optical absorption edge was observed, Fig. 1. As the annealing temperature was increased, the bandgap was observed to decrease from 4.23 to 4.02 eV, which may be attributed to the phase separation [40] and increased crystalline structure [41] with increasing annealing. With increasing the annealing temperature, the energy bandgap decreased, showing the red shifting bandgap in the prepared $TTO_{0.06}$ films [40]. The transitions overcoming this energy gap are dominated by the photon–electron interactions.

Fig. 4 shows the leakage current density (J) vs the electric field (E) plot for the prepared Ag/$TTO_{0.06}$/Si capacitors. In the lower electric fields ($E \leq 1.2 \times 10^5$ V/cm), the linear variation of leakage current indicates the ohmic conduction in all the prepared film

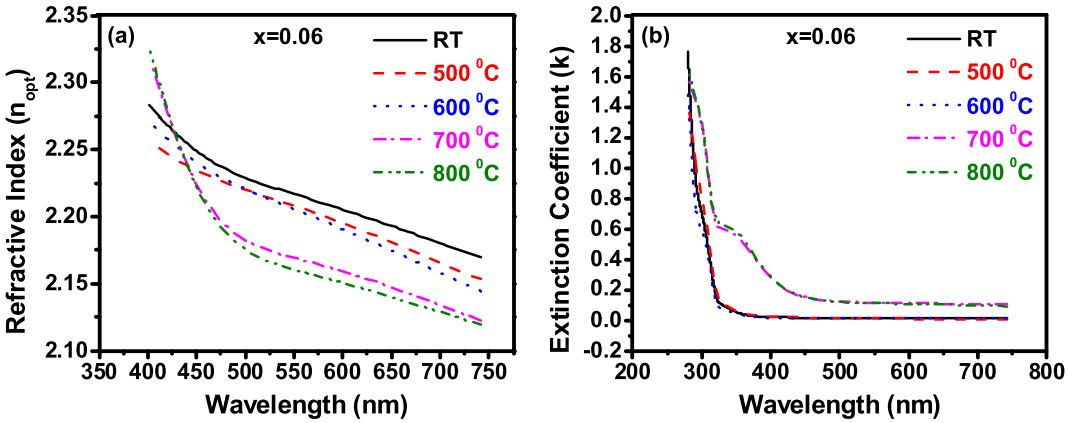

Fig. 2. Wavelength dependent (a) refractive index and (b) extinction coefficient plots of annealed $TTO_{0.06}$ thin films.

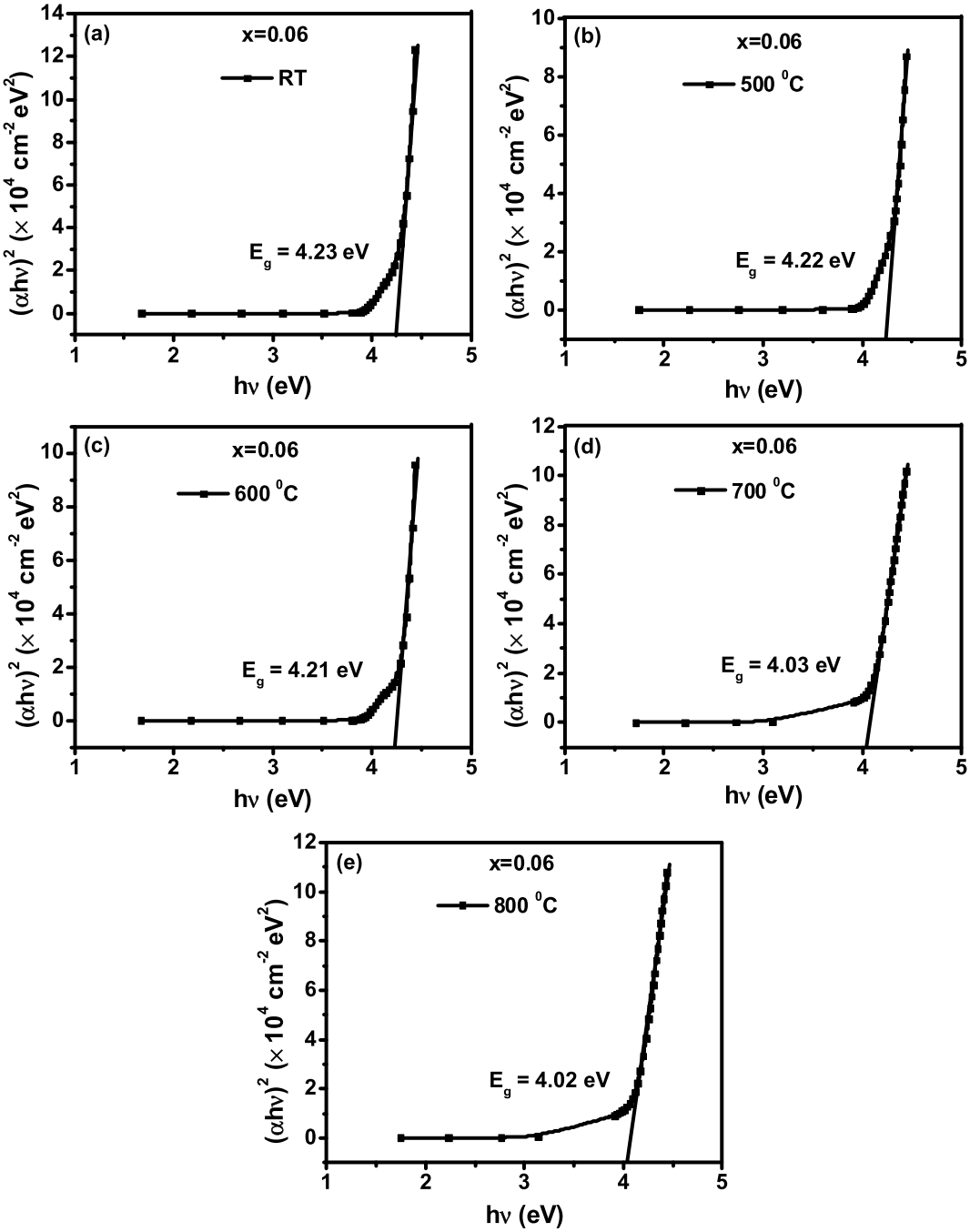

Fig. 3. $(\alpha h\nu)^2$ vs hν plots for $TTO_{0.06}$ films deposited at (a) RT; and annealed at (b) 500, (c) 600, (d) 700, and (e) 800 °C.

samples [42,43].

To find out the other possible conduction mechanisms in Ag/$TTO_{0.06}$/Si MOS structures, in the intermediate to higher field regions, various plots [43] have been drawn for the prepared film structures. In the measured field range (above 1.2 × 10^5 V/cm, for the as-deposited and the films annealed up to 700 °C; and above 2 × 10^5 V/cm, for the films annealed at 800 °C), the plots of Ln J vs $\sqrt{E}$, and Ln (J/E) vs $\sqrt{E}$ were observed linear, which indicate the possibility of Schottky emission (SE) or Poole–Frenkel (PF) conductions, respectively, in these films, Figs. 5(a) and 5(b). To explore the dominating conduction in the measured field regions, the refractive indices (n), ($n = \sqrt{K_r}$, K_r is the dynamic dielectric constant), were determined from the slopes of SE and PF plots, Figs. 5(a) and 5(b), respectively [44]. The obtained refractive indices were compared with the optically measured refractive index (n_{opt}), Table 1. Among all the prepared films, only for the 600 °C annealed films, the optically measured n_{opt} values, at 550 nm, were found comparable to the

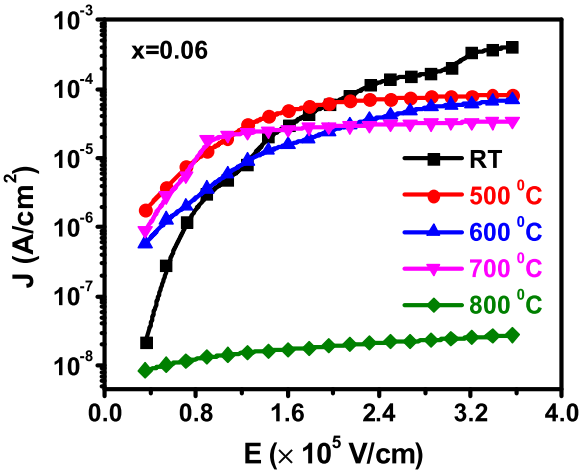

Fig. 4. J vs E plots for prepared $TTO_{0.06}$ MOS capacitors.

refractive index derived from the Ln J vs $\sqrt{E}$ plot, which indicated the dominance of SE, and discards the possibility of PF conduction, in the field regime, 1.2×10^5 V/cm $< E \leq 3.5 \times 10^5$ V/cm, for the 600 °C annealed films. Schottky emission is a thermionic emission of electrons at the interface between an insulating film and a metal electrode when the barrier height is lowered by an applied electric field and image force [43,45]. Further, the linear plot between Ln (J/E^2) and 1/E, observed in the higher electric fields, $E \geq 2.8 \times 10^5$ V/cm, indicates the possibility of tunneling conduction, in the films annealed at 600 °C, Fig. 6. The linearity of the plots and the consistency of refractive indices obtained from different approaches indicate the dominance of ohmic conduction in the lower fields ($\leq 1.2 \times 10^5$ V/cm), Schottky emission in the intermediate to higher fields (1.2×10^5 V/cm $< E \leq 3.5 \times 10^5$ V/cm), and also the possibility of tunneling conduction in the higher fields ($\geq 2.8 \times 10^5$ V/cm), for the 600 °C annealed films.

For the as-deposited films, the optically measured refractive index, at 550 nm, was found consistent with the refractive index derived from the Ln (J/E) vs $\sqrt{E}$ plot, which indicated the dominance of normal Poole–Frenkel effect [44] rather than Schottky emission, in the applied field range, 1.2×10^5 V/cm $< E \leq 3.5 \times 10^5$ V/cm, Table 1. Poole–Frenkel effect is associated with the migration of trapped charge carriers into the insulator's conduction band, caused by the field enhanced thermal excitation [43,46].

For the 500 and 700 °C annealed films, the refractive indices extracted from the electrical plots were not found comparable with the n_{opt}, which discards the possibility of SE and PF conductions in the field range, 1.2×10^5 V/cm $< E \leq 3.5 \times 10^5$ V/cm, in these films, Table 1. The linear J/d vs E^2/d^2 plots, (where d is the thickness of prepared films) indicate the possibility of space-charge-limited (SCL) current conduction in the lower intermediate field region, 1.2×10^5 V/cm $\leq E < 2.0 \times 10^5$ V/cm, for the 500 and 700 °C annealed films, Fig. 7(a). In the higher electric field area, $E \geq 2.0 \times 10^5$ V/cm, the Ln (J/E^2) vs 1/E plots were observed linear, which suggests the prominence of tunneling conduction in the 500 and 700 °C annealed films, Fig. 7(b). The tunneling conduction mechanism is caused by the tunneling of electrons from the Fermi energy level of metal into the insulator conduction band or by the migration of trap carriers into the conduction band due to field ionization [19,43,47]. Chaneliere et al. [48] described the possibility of different tunneling conduction mechanisms (double barrier, direct, and Fowler–Nordheim) contributing to the Ta_2O_5 MOS structures. These tunneling mechanisms may contribute to the current conduction in the 500 and 700 °C annealed films. Since the deposited film thickness was

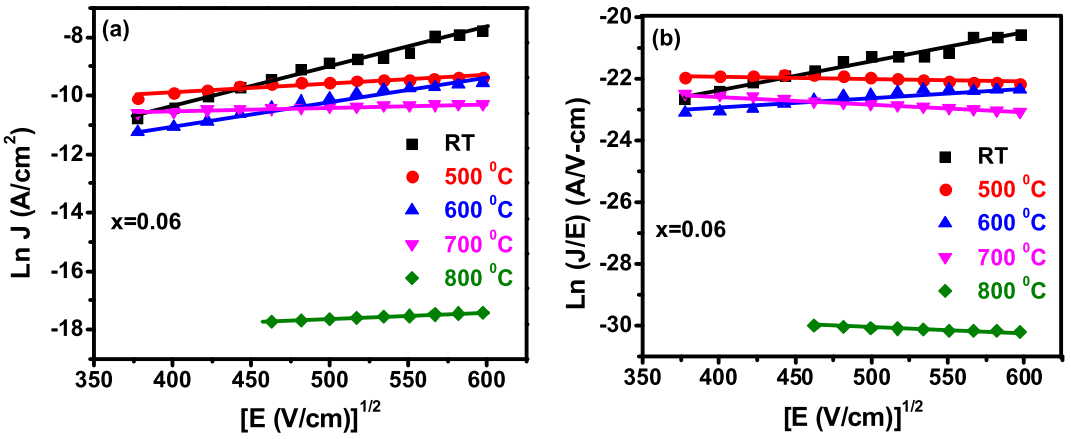

Fig. 5. (a) Ln J vs $\sqrt{E}$ (Schottky emission), and (b) Ln (J/E) vs $\sqrt{E}$ (Poole–Frenkel effect) plots, for annealed $TTO_{0.06}$ films.

Table 1
Schottky and Poole–Frenkel conductions in the prepared $TTO_{0.06}$ thin films.

Label Parameters	Calculated from Schottky Plots	[a]Calculated from Poole–Frenkel Plots	
		r = 1	r = 2
Films deposited at RT ($n_{opt} = 2.218$)			
$n = \sqrt{K_r}$	0.87	2.46	1.23
K_r	0.76	6.05	1.51
Annealed at 500 °C ($n_{opt} = 2.209$)			
$n = \sqrt{K_r}$	9.70	12.28	6.14
K_r	94.09	150.79	37.69
Annealed at 600 °C ($n_{opt} = 2.204$)			
$n = \sqrt{K_r}$	2.15	10.12	5.06
K_r	4.62	102.41	25.60
Annealed at 700 °C ($n_{opt} = 2.169$)			
$n = \sqrt{K_r}$	13.21	11.47	5.74
K_r	174.50	131.56	32.94
Annealed at 800 °C ($n_{opt} = 2.160$)			
$n = \sqrt{K_r}$	5.95	22.76	11.38
K_r	35.40	518.01	129.50

[a] r = 1, for normal Poole–Frenkel; and r = 2, for modified Poole–Frenkel effect [44].

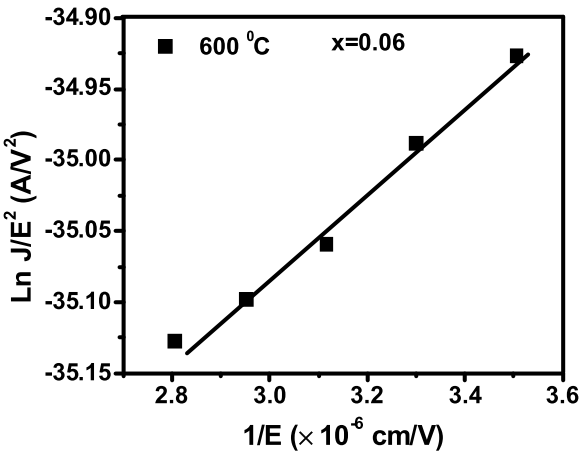

Fig. 6. Ln (J/E^2) vs 1/E plot in the field range, $E \geq 2.8 \times 10^5$ V/cm, for the $TTO_{0.06}$ films, annealed at 600 °C (Fowler–Nordheim tunneling).

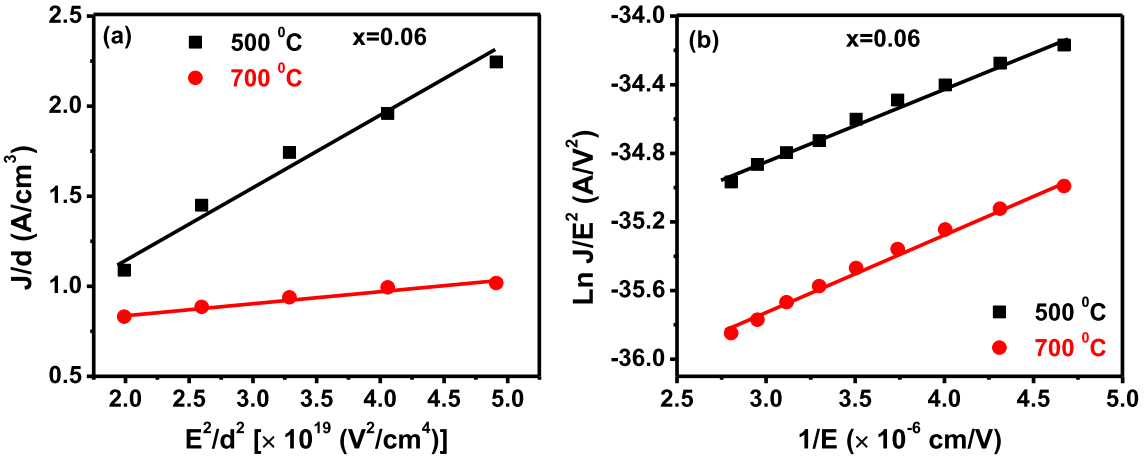

Fig. 7. (a) J/d vs E^2/d^2 (1.2×10^5 V/cm $\leq E < 2.0 \times 10^5$ V/cm), and (b) Ln (J/E^2) vs 1/E ($E \geq 2.0 \times 10^5$ V/cm) plots for $TTO_{0.06}$ films, annealed at 500 and 700 °C.

quite high (around 280 nm) in the present study; the chances of tunneling through the film volume are very faint. The possibility of tunneling may be significant through the very thin films (<50 nm). The observed tunneling may be understood by the fact that a very thin interfacial SiO_2 layer is formed on the silicon substrate and with increasing annealing temperature thickness of this layer increases [18,19]. In the amorphous films, tunneling conduction dominantly controls the conduction at the higher electric fields, $E \geq 2.0 \times 10^5$ V/cm, in the 500 °C annealed films, Fig. 7(b); and also a possibility of tunneling conduction was indicated by the linear Ln (J/E^2) vs 1/E plot for the amorphous films, annealed at 600 °C, at the higher fields ($\geq 2.8 \times 10^5$ V/cm), Fig. 6. With increasing annealing temperature increased interfacial SiO_2 layer increases the field to observe tunneling conduction, in the amorphous films. On annealing, at and above 700 °C, films crystallize. Tunneling conduction is found dominating, at the higher fields ($\geq 2.0 \times 10^5$ V/cm) in the crystalline films, annealed at 700 °C; however, due to increased thickness of interfacial SiO_2 layer, the possibility of tunneling conduction becomes meagre, in the 800 °C annealed films. Since there is no possibility of Schottky and Poole–Frenkel conductions, in the 500 and 700 °C annealed films, the trap assisted tunneling (double barrier and direct) through the anode to the cathode may be ruled out. These observations suggest the dominance of Fowler–Nordheim (FN) tunneling from the electrode's Fermi energy level into the insulator's conduction band, through very thin interfacial SiO_2 layer, without hopping of trap electrons, in the 500 and 700 °C annealed $TTO_{0.06}$ films, in the higher fields, $E \geq 2.0 \times 10^5$ V/cm.

$TTO_{0.06}$ films annealed at 800 °C show linear plots of Ln J vs $\sqrt{E}$, and Ln (J/E) vs $\sqrt{E}$ only in the higher field region, Fig. 5. However, the refractive index measured from the optical method (n_{opt}) was not found consistent with the refractive indices obtained from electrical plots, Ln J vs $\sqrt{E}$, and Ln (J/E) vs $\sqrt{E}$, which indicate the rare possibility of SE or PF mechanism in the 800 °C annealed films, Table 1. At 800 °C annealing, the interfacial SiO_2 layer, due to the migration of oxygen from film volume, becomes thicker to allow tunneling conduction. The effect of the thickened oxide layer, at 800 °C annealing, was also observed in the C–V and I–V characteristics of the $TTO_{0.06}$ films [27]. Due to the formation of a thicker SiO_2 layer, the possibility of FN tunneling can be ruled out in these films, annealed at 800 °C. The linear J vs E plot indicates the ohmic conduction in the field region, $E < 2.0 \times 10^5$ V/cm, for the 800 °C annealed films, Fig. 8(a). In the measured higher electric field range, $E \geq 2.0 \times 10^5$ V/cm, the linear J/d vs E^2/d^2 plot suggests the dominance of space-charge-limited (SCL) current conduction in the films annealed at 800 °C, Fig. 8(b). The SCL current conduction is a bulk-limited mechanism due to the carriers' non-uniform transportation from the metal contact to the oxide film. Due to the non-uniform injection of charge carriers from contact to film, space-charge cloud develops, and further charge injection slows down [43,49].

Summarily, in the formed Ag/$TTO_{0.06}$/Si MOS structures, the ohmic conduction for all the prepared films was observed in the lower field region, $E \leq 1.2 \times 10^5$ V/cm. In the field region, 1.2×10^5 V/cm $< E \leq 3.5 \times 10^5$ V/cm, Poole–Frenkel effect, in the as-deposited films; while Schottky emission, in the 600 °C annealed films, was found dominating. For the 500 and 700 °C annealed films, SCL current conduction, in the lower intermediate fields, 1.2×10^5 V/cm $\leq E < 2.0 \times 10^5$ V/cm, and FN tunneling conduction in the higher fields, $E \geq 2.0 \times 10^5$ V/cm, respectively, were observed dominating. In the annealed films at 800 °C, the ohmic conduction was observed in the lower intermediate field range, $E < 2.0 \times 10^5$ V/cm, whereas, space-charge-limited current conduction was observed dominating, for the electric fields, $E \geq 2.0 \times 10^5$ V/cm, in the measured range.

4. Conclusions

Variable areas of Ta and Ti metal targets were simultaneously sputtered in an oxygen environment to deposit $TTO_{0.06}$ films, at room temperature, onto the quartz and silicon substrates. The RT deposited films were annealed at 500, 600, 700, and 800 °C. The films remain amorphous when annealed up to 600 °C, and crystallize on annealing at and above 700 °C. Refractive index, extinction coefficient, and optical bandgap were calculated from the observed transmittance of the prepared films. With increasing the annealing temperature, the transmittance was observed increasing for the amorphous films and decreased for the crystalline films. In the amorphous films, the decrease of oxygen vacancies with increasing annealing temperature improves transmittance, whereas, on crystallization, the decreased transmittance may be attributed to the rearrangement of atoms and different orientations of the film crystallites. The refractive index of the $TTO_{0.06}$ thin films, at the wavelength of 550 nm, was found to decrease, from 2.218 to 2.160, with increasing annealing temperature, which may be due to the release of internal stress, enhanced crystallization, and reduced film density on annealing. With increasing annealing temperature, the optical bandgap decreased from 4.23 to 4.02 eV. On crystallizing, the extinction coefficient increased as compared to the amorphous films.

The ohmic emission in the lower electric field was found to prevail in all the prepared films. In the intermediate to higher field region, Poole–Frenkel conduction, in the as-deposited films, and Schottky emission, in the films annealed at 600 °C, was found dominating. Also, at the higher fields, the possibility of tunneling conduction was observed in the 600 °C annealed films. For the 500 and 700 °C annealed films, in the intermediate fields, SCL conduction, while in the higher fields, FN tunneling conduction was observed dominating. For the 800 °C annealed films, the ohmic conduction, in the lower intermediate fields, and SCL conduction mechanism, in the measured higher fields, was found dominant. The $TTO_{0.06}$ films with high transmittance and refractive index show its applications as anti-reflecting or anti-transmitting coatings in silicon solar cells, energy conservation systems, optical waveguides, etc. The high dielectric constant and low leakage current density of the annealed films of $TTO_{0.06}$ indicate its preferred potential to use as a dielectric in the semiconductor memory devices.

Declaration of competing interest

The authors declare that they have no known competing financial interests or personal relationships that could have appeared to influence the work reported in this paper.

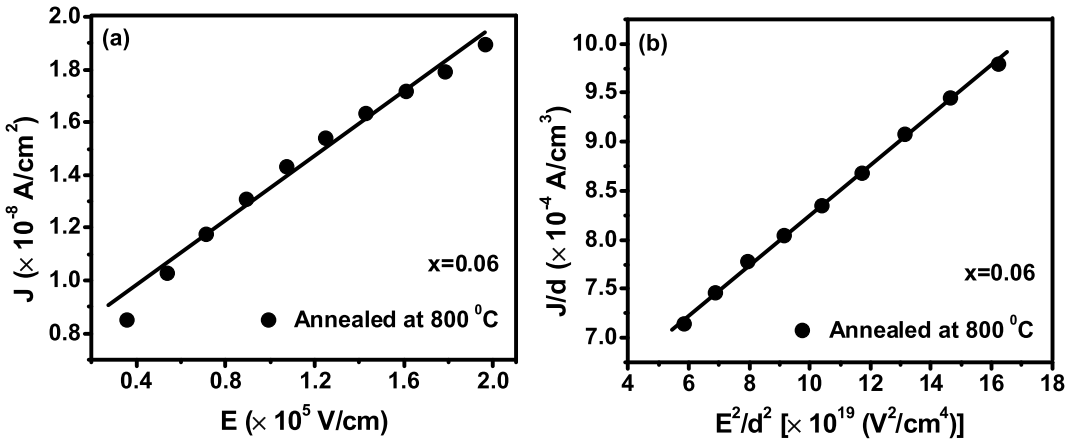

Fig. 8. (a) J vs E ($E < 2.0 \times 10^5$ V/cm), and (b) J/d vs E^2/d^2 ($E \geq 2.0 \times 10^5$ V/cm) plots for 800 °C annealed $TTO_{0.06}$ films.

References

[1] K.W. Kwon, C.S. Kang, S.O. Park, H.K. Kang, S.T. Ahn, Thermally robust Ta_2O_5 capacitor for the 256-mbit DRAM, IEEE Trans. Electron. Dev. 43 (6) (1996) 919–923.

[2] G. Lucovsky, A. Mooradian, W. Taylor, G.B. Wright, R.C. Keezer, Identification of the fundamental vibrational modes of trigonal, α-monoclinic and amorphous selenium, Solid State Commun. 5 (2) (1967) 113–117.

[3] A.I. Kingon, J.P. Maria, S.K. Streiffer, Alternative dielectrics to silicon dioxide for memory and logic devices, Nature 406 (2000) 1032–1038.

[4] M. Kumar, M. Kumar, D. Kumar, The deposition of nanocrystalline TiO_2 thin film on silicon using sol–gel technique and its characterization, Microelectron. Eng. 87 (2010) 447–450.

[5] A. Cappellani, J.L. Keddie, N.P. Barradas, S.M. Jackson, Processing and characterisation of sol–gel deposited Ta_2O_5 and TiO_2–Ta_2O_5 dielectric thin films, Solid State Electron. 43 (1999) 1095–1099.

[6] I.R. Kaufmann, A. Pick, M.B. Pereira, H. Boudinov, Metal-insulator-SiC Schottky structures using HfO_2 and TiO_2 dielectrics, Thin Solid Films 621 (2017) 184–187.

[7] M.C. Sekhar, N.K. Reddy, H.S. Akkera, B.P. Reddy, V. Rajendar, S. Uthanna, S.H. Park, Role of interfacial oxide layer thickness and annealing temperature on structural and electronic properties of Al/Ta_2O_5/TiO_2/Si metal-insulator-semiconductor structure, J. Alloys Compd. 718 (2017) 104–111.

[8] J. Lee, W.D. Lu, E. Kioupakis, Electronic and optical properties of oxygen vacancies in amorphous Ta_2O_5 from first principles, Nanoscale 9 (2017) 1120–1127.

[9] R. Shakoury, R.R. Willey, Optimization of Ta_2O_5 optical thin film deposited by radio frequency magnetron sputtering, Appl. Opt. 55 (2016) 5353–5357.

[10] J.-C. Zhou, D.-T. Luo, Y.-Z. Li, Z. Liu, Effect of sputtering pressure and rapid thermal annealing on optical properties of Ta_2O_5 thin films, Trans. Nonferrous Metals Soc. China 19 (2009) 359–363.

[11] F. Rubio, J. Denis, J.M. Albella, J.M. Martinez-Duart, Sputtered Ta_2O_5 antireflection coatings for silicon solar cells, Thin Solid Films 90 (1982) 405–408.

[12] W.M. Paulson, F.S. Hickernell, R.L. Davis, Effects of deposition parameters on optical loss for rf sputtered Ta_2O_5 and Si_3N_4 waveguides, J. Vac. Sci. Technol. 16 (2) (1979) 307–310.

[13] H. Terui, M. Kobayashi, Refractive index adjustable SiO_2-Ta_2O_5 films for integrated optical circuits, Appl. Phys. Lett. 32 (10) (1978) 666–668.

[14] S.V.J. Chandra, P.S. Reddy, G.M. Rao, S. Uthanna, Effect of postdeposition annealing on the structural, electrical, and optical properties of dc magnetron sputtered Ta_2O_5 films, Res. Lett. Mater. Sci. (2007) 1–5, 2007.

[15] Shin-ichiro Kimura, Yasushiro Nishioka, Akira Shintani, Kiichiro Mukai, Leakage-current increasein amorphous films due to pinhole growth during annealing below 600 C, J. Electrochem. Soc. 130 (12) (1983) 2414–2418.

[16] S. Roberts, J. Ryan, L. Nesbit, Selective studies of crystalline Ta_2O_5 films, J. Electrochem. Soc. 133 (7) (1986) 1405–1410.

[17] A.P. Huang, Paul K. Chu, Crystallization improvement of Ta_2O_5 thin films by the addition of water vapor, J. Cryst. Growth 274 (2005) 73–77.

[18] C. Chaneliere, J.L. Autran, R.A.B. Devine, B. Balland, Tantalum pentoxide (Ta_2O_5) thin films for advanced dielectric applications, Mater. Sci. Eng. R Rep. 22 (6) (1998) 269–322.

[19] E. Atanassova, N. Novkovski, A. Paskaleva, M. Pecovska-Gjorgjevich, Oxygen annealing modification of conduction mechanism in thin rf sputtered Ta_2O_5 on Si, Solid State Electron. 46 (2002) 1887–1898.

[20] C. Xu, Q. Xiao, J. Ma, Y. Jin, J. Shao, Z. Fan, High temperature annealing effect on structure, optical property and laser-induced damage threshold of Ta_2O_5 films, Appl. Surf. Sci. 254 (2008) 6554–6559.

[21] R. Rabady, I. Avrutsky, Titania, silicon dioxide, and tantalum pentoxide waveguides and optical resonant filters prepared with radio-frequency magnetron sputtering and annealing, Appl. Opt. 44 (2005) 378–383.

[22] J.S. Lee, S.J. Chang, J.F. Chen, S.C. Sun, C.H. Liu, U.H. Liaw, Effects of O_2 thermal annealing on the properties of CVD Ta_2O_5 thin films, Mater. Chem. Phys. 77 (2002) 242–247.

[23] L. Manchanda, M.D. Morris, M.L. Green, R.B. van Dover, F. Klemens, T.W. Sorsch, P.J. Silverman, G. Wilk, B. Busch, S. Aravamudhan, Multi-component high- K gate dielectrics for the silicon industry, Microelectron. Eng. 59 (2001) 351–359.

[24] D.H. Triyoso, R.I. Hegde, S. Zollner, M.E. Ramon, S. Kalpat, R. Gregory, X.D. Wang, J. Jiang, M. Raymond, R. Rai, D. Werho, D. Roan, B.E. White Jr., P.J. Tobin, Impact of titanium addition on film characteristics of HfO_2 gate dielectrics deposited by atomic layer deposition, J. Appl. Phys. 98 (2005), 054104–054104-8.

[25] K.M.A. Salam, H. Fukuda, S. Nomura, Effects of additive elements on improvement of the dielectric properties of Ta_2O_5 films formed by metalorganic decomposition, J. Appl. Phys. 93 (2003) 1169–1175.

[26] J.-Y. Gan, Y.C. Chang, T.B. Wu, Dielectric property of $(TiO_2)_x$-$(Ta_2O_5)_{1-x}$ thin films, Appl. Phys. Lett. 72 (1998) 332–334.

[27] Prashant Thapliyal, Alok S. Kandari, Vijendra Lingwal, N.S. Panwar, G. Mohan Rao, Annealing temperature-dependent structural and electrical properties of $(Ta_2O_5)_{1-x}$ - $(TiO_2)_x$ thin films, $x \leq 0.11$, Ceram. Int. 47 (2021) 12066–12071.

[28] M. Chandra Sekhar, N. Nanda Kumar Reddy, V.K. Verma, S. Uthanna, Structural, optical and electrical properties of DC reactive magnetron sputtered $(Ta_2O_5)_{1-x}(TiO_2)_x$ thin films, Ceram. Int. 42 (2016), 18870-18870-9.

[29] Prashant Thapliyal, N.S. Panwar, G. Mohan Rao, Electrical and optical properties of $(Ta_2O_5)_{1-x}$- $(TiO_2)_x$ films, $x = 0.035$, prepared by sputtering of ceramic and mosaic (Ta, Ti) metal targets, J. Appl. Phys. 130 (2021), 035304-035304-13.

[30] Prashant Thapliyal, Alok S. Kandari, Vijendra Lingwal, N.S. Panwar, G. Mohan Rao, Post deposition annealing dependent structural and C-V characteristics of $(Ta_2O_5)_{0.965}$- $(TiO_2)_{0.035}$ thin films, Mater. Today: Proc. 44 (2021) 3946–3950.

[31] R. Swanepoel, Determination of the thickness and optical constants of amorphous silicon, J. Phys. E Sci. Instrum. 16 (1983) 1214–1222.

[32] C. Corbella, M. Vives, A. Pinyol, I. Porqueras, C. Person, E. Bertran, Influence of the porosity of RF sputtered Ta_2O_5 thin films on their optical properties for electrochromic applications, Solid State Ionics 165 (2003) 15–22.
[33] Mahesh Kumar Agarwal, Aradhana Bhandari, Y. Singh, N.S. Panwar, Optical properties of amorphous $[Ta_2O_5]_{1-x}$-$[TiO_2]_x$ (x = 0.08) thin films, Int. J. Res. Innov. Sci. Technol. 1 (2014) 23–29.
[34] M. Chandra Sekhar, N. Nanda Kumar Reddy, B. Purusottam Reddy, B. Poorna Prakash, Harish Sharma Akkera, S. Uthanna, Si-Hyun Park, Influence of substrate bias voltage on crystallographic structure, optical and electronic properties of $Al/(Ta_2O_5)_{0.85}(TiO_2)_{0.15}$/p-Si MIS Schottky barrier diodes fabricated by dc magnetron sputtering, Mater. Sci. Semicond. Process. 76 (2018) 80–86.
[35] Prashant Thapliyal, N.S. Panwar, G. Mohan Rao, Influence of post-deposition annealing on electrical and optical properties of $(Ta_2O_5)_{1-x}$- $(TiO_2)_x$ thin films, $x \leq 0.08$, Ceram. Int. 47 (2021) 16746–16751.
[36] P.C. Joshi, M.W. Cole, Influence of postdeposition annealing on the enhanced structural and electrical properties of amorphous and crystalline Ta_2O_5 thin films for dynamic random access memory applications, J. Appl. Phys. 86 (1999) 871–880.
[37] Jianchao Li, Wanmin Yang, Junhong Su, Chen Yang, Junqi Xu, Shenjiang Wu, Effect of temperature fields on optical properties of $La_2Ti_2O_7$ thin films, Mater. Res. Express 6 (2019), 026404-026404-8.
[38] O.A. Azim, M.M. Abdel-Aziz, I.S. Yahia, Structure and optical analysis of Ta_2O_5 deposited on infrasil substrate, Appl. Surf. Sci. 255 (2009) 4829–4835.
[39] J. Tauc, R. Grigorovici, A. Vancu, Optical properties and electronic structure of amorphous germanium, Phys. Status Solidi B 15 (1966) 627–637.
[40] D.Y. Jiang, D.Z. Shen, K.W. Liu, C.X. Shan, Y.M. Zhao, T. Yan, B. Yao, Y.M. Lu, J.Y. Zhang, Effect of post annealing on the band gap of $Mg_xZn_{1-x}O$ thin films, Semicond. Sci. Technol. 23 (2008), 035002-035002-5.
[41] S.V. Jagadeesh Chandra, S. Uthanna, G. Mohan Rao, Effect of substrate temperature on the structural, optical and electrical properties of dc magnetron sputtered tantalum oxide films, Appl. Surf. Sci. 254 (2008) 1953–1960.
[42] P.L. Young, DC electrical conduction in thin Ta_2O_5 films. I. Bulk-limited conduction, J. Appl. Phys. 47 (1976) 235–241.
[43] S.M. Sze, Physics of Semiconductor Devices, second ed., Wiley, New York, 1981.
[44] C. Chaneliere, S. Four, J.L. Autran, R.A.B. Devine, N.P. Sandler, Properties of amorphous and crystalline Ta_2O_5 thin films deposited on Si from a $Ta(OC_2H_5)_5$ precursor, J. Appl. Phys. 83 (1998) 4823–4829.
[45] R. Brazis, Electron transport in Ta_2O_5 films, J. Mater. Sci. Lett. 9 (1990) 266–267.
[46] C. Isobe, M. Saitoh, Effect of ozone annealing on the dielectric properties of tantalum oxide thin films grown by chemical vapor deposition, Appl. Phys. Lett. 56 (1990) 907–909.
[47] G.Q. Lo, D.L. Kwong, S. Lee, Metal-oxide-semiconductor characteristics of chemical vapor deposited Ta_2O_5 films, Appl. Phys. Lett. 60 (1992) 3286–3288.
[48] C. Chaneliere, J.L. Autran, R.A.B. Devine, Conduction mechanisms in Ta_2O_5/SiO_2 and Ta_2O_5/Si_3N_4 stacked structures on Si, J. Appl. Phys. 86 (1) (1999) 480–486.
[49] Milton Ohring, The Materials Science of Thin Films, Academic Press, San Diego, California, 1992.

Indian Journal of Pure & Applied Physics
Vol. 60, February 2022, pp. 111-116

Structural and Piezoelectric Properties of $(Ba_{1-x}Ca_xZr_{0.1}Ti_{0.9})O_3$ Ceramics, Near Morphotropic Phase Boundary ($0.140 \leq x \leq 0.160$)

Don Biswas,[a,b] Prolay Sharma[b*] & N S Panwar[a]

[a]Instrumentation Engg.-USIC, H.N.B. Garhwal University, Srinagar (Garhwal)-246 174 India

[b]Instrumentation and Electronics Engg., Jadavpur University, Kolkata-700 032 India

Received 23 November 2021; accepted 20 January 2022

Ceramic pellet samples of $(Ba_{1-x}Ca_xZr_{1-y}Ti_y)O_3$ (x = 0.140- 0.160, y = 0.9), were prepared using the conventional solid-state reaction method followed by double sintering. Structural and piezoelectric measurements of the prepared compositions were carried out at room temperature. For the compositions with $x \leq 0.150$, the converse piezoelectric constant (d_{33}*), strain (%), coercive field (E_c) and remnant polarization (P_r), were found increasing with x, which were found anomalously to decrease with further increase in x above 0.150. Among the prepared compositions, maximum value of d_{33}* was found 342 pm/V, for the samples with x = 0.150. The measured maximum values of strain (%), piezoelectric constant (d_{33}*) and break in XRD peak shifting patterns of the prepared samples indicate composition dependent piezoelectric properties, showing morphotropic- like phase boundary (MPB), near x = 0.150 composition. The prepared compositions of lead- free BCZT ceramics will extend the possibilities to use this compound in the field of piezoelectric sensors.

Keywords: Ferroelectrics; solid state reaction; piezoelectric constant; X- ray diffraction

1 Introduction

ABO_3 type barium–calcium zirconate–titanate (BCZT) ferroelectric ceramics are interesting due to their wide electrical properties and non- toxic nature[1-3]. Though the large piezoelectric constant lead- based perovskite ferroelectric compounds, e.g., lead zirconate titanate (PZT) and $Pb(B'B'')O_3$, (B' = Zn, Mg, In and Sc and B'' = Nb, Mo, Ta, and W),[4-5] are available, but due to their toxic nature, they are less preferred to utilize, and the search for high piezoelectric constant lead- free compounds has attracted the attention recently[1,6-10].

Significant piezoelectric constant has been found in $(Ba_{1-x}Ca_xZr_{1-y}Ti_y)O_3$, (x, y = 0 to 1) ceramics, near the morphotropic phase boundary[11,12]. The structural and electrical properties of BCZT system have been investigated by Hennings[13] & Yu *et al.*[14]. Tian *et al.*[15] studied the composition variation of piezoelectric and structural properties by varying the Ba/Ca ratio in $(Ba_{1-x}Ca_x)(Ti_{0.9}Zr_{0.1})O_3$, for the compositions with x = 0 to 0.20, and reported the existence of a typical MPB, near x = 0.150. The mechanism of the enhanced piezoelectricity around the MPB is of considerable significance. The polarization extension and rotation, presence of intermediate phases, and elastic softening of lattice are the contributing factors to large piezoelectricity in $(Ba_{1-x}Ca_xTi_{0.9}Zr_{0.1})O_3$ ceramics, at morphotropic phase boundary[15]. Thereby, great efforts have been devoted to studying the high level of piezoelectricity and the origin of this large piezoelectricity. The $(Ba_{1-x}Ca_x)(Ti_{0.9}Zr_{0.1})O_3$ ceramic systems receive significant attention because of the development of several possible polarization directions, at MPB, which may contribute to a large extremal remanent polarization and electromechanical coupling factor (k_s)[5]. Mondal *et al.*[16] observed enhanced electrical properties in BCZT ceramics due to the cell deformation, near MPB region. An anomalous break in the peak shifting pattern has been reportedly observed, at MPB[17]. Hanani *et al.*[18] found technologically potential piezoelectric properties of $(Ba_{1-x}Ca_xTi_{0.9}Zr_{0.1})O_3$ compositions, near x = 0.150. Wang *et al.*[19] observed significant piezoelectric properties of $(Ba_{1-x}Ca_xTi_{0.9}Zr_{0.1})O_3$ lead-free ceramics with x = 0.150. Wu *et al.*[20,21] observed the effect of sintering dwell time on piezoelectric properties of $(Ba_{1-x}Ca_x)(Ti_{0.9}Zr_{0.1})O_3$ compounds, near x = 0.150, the morphotropic phase boundary. The enhanced electrical properties of the $(Ba_{1-x}Ca_x)(Ti_{0.9}Zr_{0.1})O_3$ compounds, near morphotropic phase boundary (MPB), may be attributed to the separation of two ferroelectric phases with different crystallographic

*Corresponding author: (E-mail: prolaysharma08@gmail.com)

parameters[22-24]. Therefore, ABO_3 type compounds are attracting considerable attention due to the significant hike in their piezoelectric properties, near the MPB.

Presently, $(Ba_{1-x}Ca_xZr_{1-y}Ti_y)O_3$ (x = 0.140- 0.160, y = 0.9), samples of BCZT ceramics have been prepared by solid- state reaction method following double sintering, at 1300 °C, for 4 hrs, each cycle. The structural behavior and piezoelectric properties of the prepared $(Ba_{1-x}Ca_xZr_{1-y}Ti_y)O_3$ compositions were observed. The composition dependence of structure, converse piezoelectric constant (d_{33}*), strain (%), coercive field, polarization current, and remnant polarization of the BCZT samples were measured, for the compositions near MPB, x = 0.150.

2 Experimental procedure

The samples of $(Ba_{1-x}Ca_xZr_{1-y}Ti_y)O_3$ (x = 0.140- 0.160, y = 0.9) ceramics were prepared using solid- state reaction technique with double sintering. For this purpose, raw powders of $BaCO_3$, $CaCO_3$, TiO_2 and ZrO_2 were selected. All the selected raw powders have purity greater than 99.5% (from MERCK, Germany). Initially, the powders were dried separately to remove the absorbed moisture, at 200 °C for 2 hours. Furthermore, they were weighed in the stoichiometric ratio to prepare the compositions of $(Ba_{1-x}Ca_xZr_{1-y}Ti_y)O_3$ ceramics. The compositions were manually ground for 2 hrs in acetone, and then dry for 4 hrs. To remove carbonate, the compositions were calcined at 1100 °C for 4 hrs. The calcined mixture was ground for 1 hour. Furthermore, the compositions were pressed into pellets with ~ 2 mm thick and 8 mm diameter, at 0.2 GPa pressure. The prepared pellets of $(Ba_{1-x}Ca_xZr_{1-y}Ti_y)O_3$ (x = 0.140- 0.160, y = 0.9) were sintered for 4 hours, at 1300 °C temperature. Furthermore, the sintered samples were crushed and taken for another cycle of sintering process[25]. The sintered compositions were electroded, with conducting paste of silver, in metal-insulator-metal (MIM) configuration. For piezoelectric and polarization measurements of the prepared compositions, piezo-meter (AixACCT Systems, GmbH) and PE loop tracer are used, respectively. For structural analysis, X- ray diffractometer (PANalytical, X'PERT PRO, with Cu$K\alpha_1$ radiation of wavelength 1.5406 Å) is used to measure the XRD patterns of $(Ba_{1-x}Ca_xZr_{1-y}Ti_y)O_3$ (x = 0.140- 0.160, y = 0.9). The X- ray machine collect the data at a scanning rate of 6°/min.

3 Results and discussion

The X- ray diffraction (XRD) patterns of the prepared BCZT compositions, observed at room temperature, were shown in Fig. 1. The X-ray diffraction patterns of BCZT pellet samples were found matched with "Inorganic Crystal Structure Database" (ICSD), data code 01-075-1608[26]. The prepared compositions of BCZT ceramics show pure orthorhombic structure with (111), (102), (022), and (220), *etc*. peaks.

In the prepared composition range, the prominent peaks were, generally, found shifting to smaller angle with rising x, except for the samples with x = 0.150. For the composition with x = 0.150, a break in the peaks shifting pattern was observed, the peaks shift to higher angle, representing an abnormal structural nature for this sample. Fig. 2 exhibits the peak (111) shifting pattern. The observed break in the peak shifting patterns may be attributed to the lattice change. Workers observed similar incident for the pellet samples of (Na, K)NbO_3 ceramics, near MPB[17,27].

The lattice parameters of BCZT ceramics were evaluated from the measured X- ray diffraction data, Table 1. In a/b ratio *vs*. composition (x) plot, an anomalous dip was observed for the samples with x = 0.150, showing an abrupt sample dependent structural change at this x, Fig. 3. Shirane *et al*. observed similar variations of a/b ratio with sample (x), in BCZT ceramics[26]. The lattice parameters were measured manually. The selected space group is 'Amm2' type.

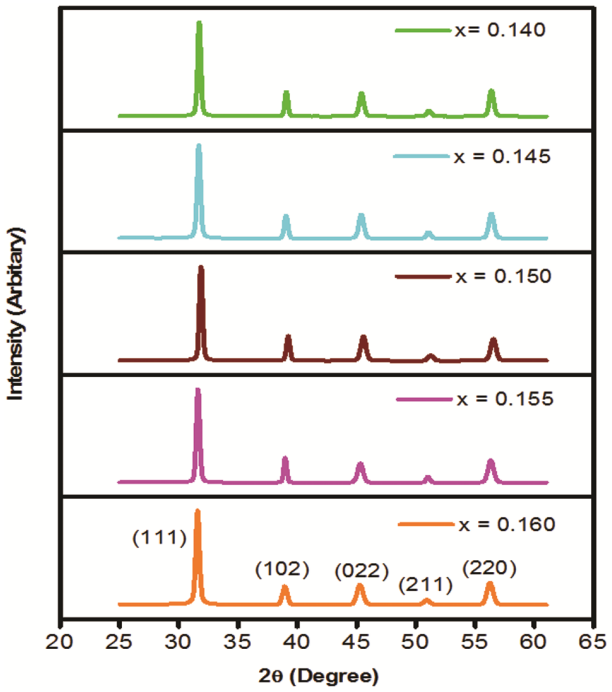

Fig. 1 — X-ray diffraction patterns of $(Ba_{1-x}Ca_xZr_{1-y}Ti_y)O_3$ (x = 0.140- 0.160, y = 0.9) ceramics.

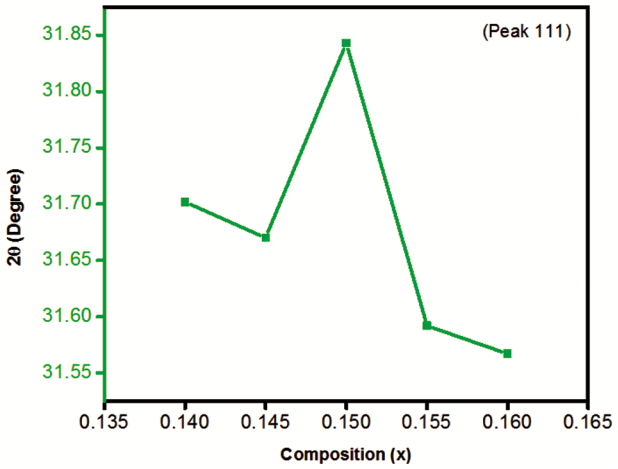

Fig. 2 — Peak (111) shifting tendency with sample (x), in $(Ba_{1-x}Ca_xZr_{1-y}Ti_y)O_3$ (x = 0.140- 0.160, y = 0.9) ceramics.

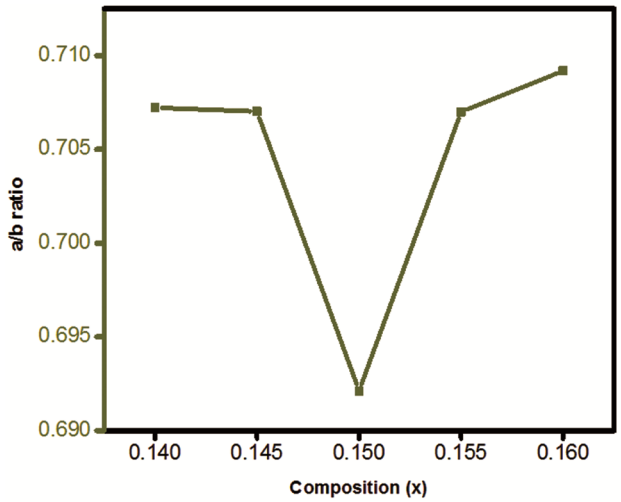

Fig. 3 — Variation of a/b ratio with sample (x), in $(Ba_{1-x}Ca_xZr_{1-y}Ti_y)O_3$ (x = 0.140- 0.160, y = 0.9) ceramics.

Table 1 — Lattice parameters of $(Ba_{1-x}Ca_xZr_{1-y}Ti_y)O_3$ (x = 0.140- 0.160, y = 0.9) ceramics.

Composition (x)	Lattice Parameters (Calculated) a (Å)	b (Å)	c (Å)
0.140	3.9976	5.6525	5.6424
0.145	3.9975	5.6539	5.6469
0.150	3.9661	5.7304	5.5363
0.155	4.0013	5.6594	5.6617
0.160	4.0048	5.6470	5.6627

The polarization *vs*. electric field (P- E) hysteresis loops of the prepared BCZT samples were measured at room temperature, at 1 Hz frequency (triangular wave), with an applied peak electric field of 8.28 kV/cm. The observed P- E hysteresis loops for the prepared compositions have been shown in Fig. 4. The hysteresis loops show a good ferroelectric nature of the prepared ceramics. Fig. 5 shows the observed

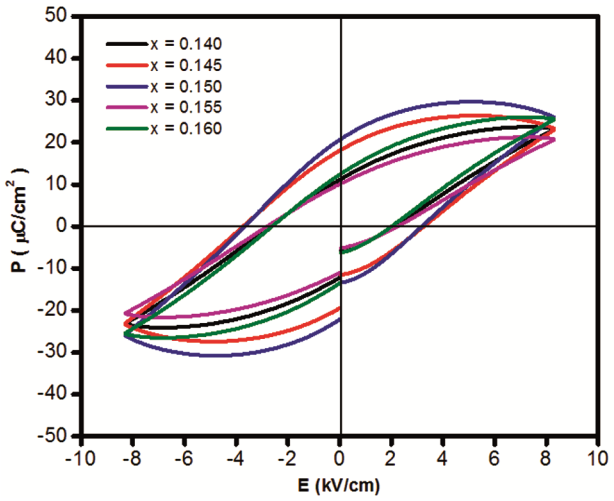

Fig. 4 — Polarization vs. electric field (P- E) hysteresis loops of $(Ba_{1-x}Ca_xZr_{1-y}Ti_y)O_3$ (x = 0.140- 0.160, y = 0.9) ceramics.

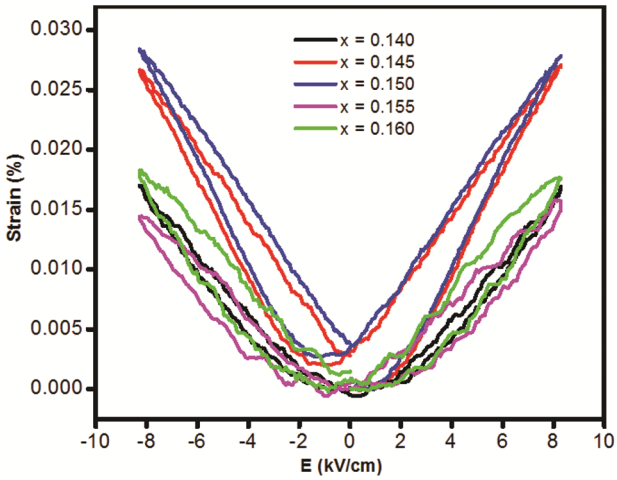

Fig. 5 — Plot of strain (%) with electric field, in $(Ba_{1-x}Ca_xZr_{1-y}Ti_y)O_3$ (x = 0.140- 0.160, y = 0.9)

strain (%) *vs*. electric field characteristics of the prepared BCZT samples. The observed butterfly loops show the hard domain reorientation characteristic of the prepared samples[28].

Generally, electroceramics have two main categories. They are called dielectric and conductive ceramics. The electroceramics may show mechanical strain upon applying an applied electric field and vice versa. The observed electric field- induced strain experience two types of contribution. The intrinsic contributions are responsible to exhibit electrostriction and piezoelectric effects, while the extrinsic contributions may show domain wall movement in materials having ferroelectric domain structures. The converse piezoelectric effect exhibits a

mechanical strain upon applying an electric field. The converse effect consists of a linear dependence of the strain upon the applied electric field, which can be elongation or contraction depending on the relative direction of the applied electric field and the material's polarity[28]. The ferroelectric domain may change when an electric field was applied on the prepared ceramics. The domain walls simultaneously contribute to the changes in polarization and strain. The observed strain is firmly negative exhibiting that the compositions experiences elongation along the electric field direction. Furthermore, strain response, piezoelectric effect and electrostriction, incorporates the contribution of domain wall movement, which contributes increase to a complex nonlinear and hysteretic nature, with a typical strain- electric field loop similar to a butterfly- like shape[28].

For the prepared compositions, highest value of strain (%) was observed for the composition with x = 0.150. The converse piezoelectric constant (d_{33}*) is obtained as the ratio of the strain (maximum) to the electric field (maximum), *i.e.*, S_{max}/E_{max}[29], and was calculated from the butterfly characteristics of the BCZT ceramics. For the prepared compositions, a plot of the piezoelectric constant (d_{33}*) with composition (x), at RT, has been shown in Fig. 6. The value of (d_{33}*) was found maximum to be 342 pm/V, for the compositions with x = 0.150, among the prepared compositions. Singh *et al.* observed similar piezoelectric characteristics for the pellet samples of (Na, K)NbO_3 ceramics, near MPB[30]. The observed distinct change in converse piezoelectric properties, at x = 0.150, may be attributed to the lattice change, near the MPB.

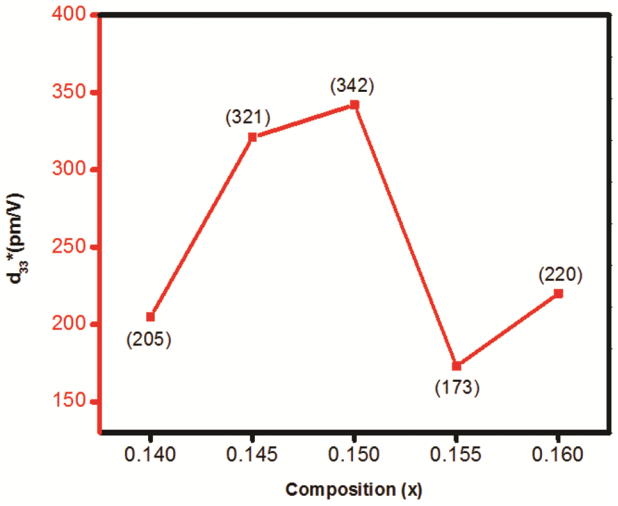

Fig. 6 — Plot of converse piezoelectric constant (d_{33}^*) with sample (x), in $(Ba_{1-x}Ca_xZr_{1-y}Ti_y)O_3$ (x = 0.140- 0.160, y = 0.9) ceramics.

For the prepared BCZT compositions, the observed variation of coercive field (E_c) and remnant polarization (P_r) with Ca content (x) have been shown in Fig. 7. In the prepared composition range, maximum value of remnant polarization (P_r) was found 20.82 μC/cm^2; and maximum coercive field (E_c), 3.384 kV/cm, for the samples with x = 0.150. These observations may be attributed to the greater deformation in the lattice of the BCZT ceramics, near MPB, at x = 0.150[15,31]. The variation of polarization current with the applied electric field was shown in Fig. 8. The highest magnitude (3.48 x 10^{-5} A) was observed for the compositions with x = 0.150, among the prepared samples.

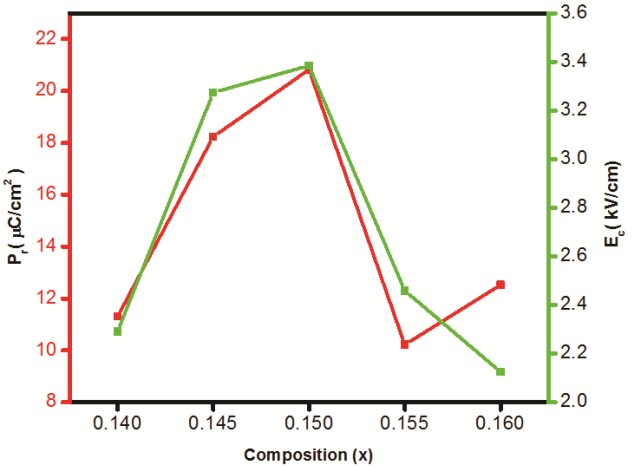

Fig. 7 — Variations of coercive field (E_c) and remnant polarization (P_r) with sample (x), in $(Ba_{1-x}Ca_xZr_{1-y}Ti_y)O_3$ (x = 0.140- 0.160, y = 0.9) ceramics.

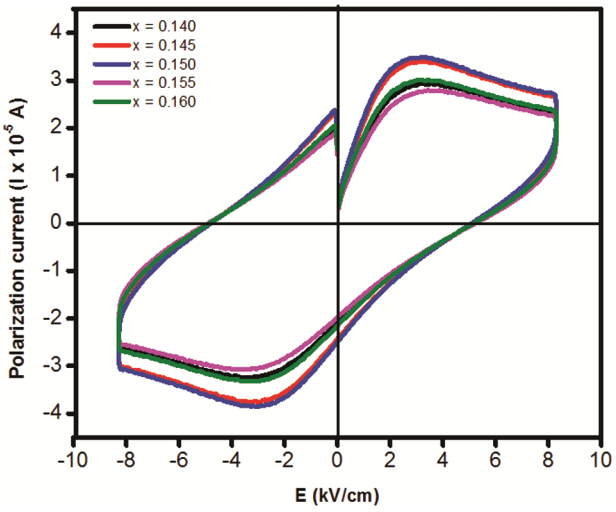

Fig. 8 — Variations of polarization current with electric field, in $(Ba_{1-x}Ca_xZr_{1-y}Ti_y)O_3$ (x = 0.140- 0.160, y = 0.9) ceramics.

The internal stress, defects, and morphology of the ceramics considerably depend on the processing conditions[32], and on the purity as well as on the grain size of the starting materials[33]. The electrical properties considerably depend on the crystallographic information, grain size and density of the prepared samples[34,35]. The low permittivity of the grain boundary contributes low polarization in the ferroelectrics. Also the available space charges at the grain boundary may help to exclude polarization charges on the grain surface, and may result polarization discontinuity. Therefore, a depolarization field appears and further the polarization reduces, in the smaller grain ceramics. With increasing Ca component (x), the density of the BCZT ceramics was reportedly found to increase, reaching maximum for x = 0.150, which decreases with further increase in x; whereas the grain size was found having opposite variation, *i.e.*, it decreased with increasing x, reaching minimum for x = 0.150, and increases with further increase in x[36]. The increase or decrease in the number of grain boundaries depends on the grain size of the ceramics, while larger grains result less no. of grain boundaries and vice versa. The smaller grain size, for x = 0.150 composition, would have more number of grain boundaries, and result to reduced polarization, in the BCZT ceramics. But the observed remnant polarization (P_r) and coercive field (E_c) were found maximum for the sample with x = 0.150, which shows that these parameters are a composition dependent property rather than the density or the grain size of the BCZT ceramics. A similar observation on the dielectric properties of BCZT ceramics has been reported in a previous communication[36].

For the prepared composition range, these measurements indicate that the structure, strain (%), converse piezoelectric constant (d_{33}*), remnant polarization and coercive field of the BCZT ceramics significantly depend on composition and show morphotropic- like boundary near x = 0.150 composition.

4 Conclusion

$(Ba_{1-x}Ca_xZr_{1-y}Ti_y)O_3$ (x = 0.140- 0.160, y = 0.9) samples were prepared using solid- state reaction method with double sintering. The piezoelectric and structural properties were observed for BCZT ceramic samples. For the prepared BCZT ceramics, a continuous XRD peaks shifting pattern was observed with varying x, with a break for the samples with x = 0.150, which indicated a strong composition dependent structural anomaly. Among the prepared compositions, the piezoelectric constant (d_{33}*), strain (%), remnant polarization, polarization current and coercive field were observed maximum, for the sample with x = 0.150. The structural anomaly, and extremal values of converse piezoelectric constant (d_{33}*), strain (%), remnant polarization, and coercive field show a MPB- like composition, near x = 0.150, in the prepared BCZT ceramics.

References

1 Saito Y, Takao H, Tani T, Nonoyama T, Takatori K, Homma T, Nagaya T & Nakamura M, *Nature,* 432 (2004) 84.
2 Dawber M, Rabe K M & Scott J F, *Rev Mod.Phys*, 77 (2005) 1083.
3 Kantha P & Pengpat K, *Curr Appl Phys*, 9 (2009) 460.
4 Du X, Zheng J, Belegundu U & Uchino K, *Appl Phys Lett*, 72 (1998) 2421.
5 Somiya S, *Encyclopedia of physical science and technology*, Academic press, (2003) 578.
6 Cross E, *Nature*, 432 (2004) 24.
7 Liu W F & Ren X B, *Phys Rev Lett*, 103 (2009) 257602.
8 Bao H X, Zhou C, Xue D Z, Gao J H & Ren X B, *J Phys D: Appl Phys*, 43 (2010) 465401.
9 Fu J, Zuo R Z & Xu Z K, *Appl Phys Lett*, 99 (2011) 062901.
10 Xue D Z, Zhou Y M, Bao H X, Zhou C, Gao J H & Ren X B, *J Appl Phys*, 109 (2011) 054110.
11 Swain A B, Kumar S D, Subramanian V & Murugavel P, *J All Comp*, 787 (2019) 990.
12 Tian Y, Gong Y, Meng D, Li Y & Kuang B, *J Elec Mater*, 44 (2015) 2890.
13 Hennings D & Schnell A, *J Am Ceram Soc*, 65 (1982) 539.
14 Yu Z, Ang C, Guo R & Bhalla A S, *J Appl Phys*, 92 (2002) 1489.
15 Tian Y, Wei L, Chao X, Liu Z & Yang Z, *J Am Ceram Soc*, 96 (2013) 496.
16 Mondal T, Das S, Badapanda T, Sinha T P & Sarun P M, *Phys B: Phys Cond Matter*, 508 (2017) 124.
17 Singh S, Negi J & Panwar N S, *J Phys Chem Sol*, 123 (2018) 311.
18 Hanani Z, Mezzane D, Amjoud M, Fourcade S, Razumnaya A G, Luk'yanchuk I A & Gouné M, *Superlatt Microstruct*, 127 (2019) 109.
19 Wang P, Li Y & Lu Y, *J Eur Ceram Soc*, 31 (2011) 2005.
20 Wu J, Xiao D, Wu B, Wu W, Zhu J, Yang Z & Wang J, *Mater Res Bull*, 47 (2012) 1281.
21 Wu J, Xiao D, Wu W, Zhu J & Wang J, *J Alloys Comp*, 509 (2011) L359.
22 Li W, Xu Z, Chu R, Fu P & Zang G, *J Am Ceram Soc*, 93 (2010) 2942.
23 Li W, Xu Z, Chu R, Fu P & Zang G, *Mater Lett*, 64 (2010) 2325.
24 Zhang S W, Zhang H L, Zhang B P & Yang S, *J Alloys Compd*, 506 (2010) 131.
25 Biswas D, Sharma P & Panwar N S, *Ceram Int*, 47 (2021) 13814.
26 Shirane G, Denner H & Pepkinsky R, *Phys Rev*, 105 (1957) 856.

27 Negi J & Panwar N S, *J Phys Chem Sol*, 151 (2021) 109853.
28 Viola G, Saunders T, Wei X, Chong K B, Luo H, Reece M J & Yan H, *J Adv Dielectr*, 3 (2013) 1350007.
29 Jalalian A, Grishin A M, Wang X L, Cheng Z X & Dou S X, *Appl Phys Lett*, 104 (2014) 103112.
30 Singh S & Panwar N S, *Ferroelectrics*, 558 (2020) 240.
31 Xu G, Wen J, Stock C & Gehring P M, *Nat Mater*, 7 (2008) 562.
32 Mitra S, Kulkarni A R & Prakash O, *J Appl Phys*, 114 (2013) 064106.
33 Nalwa H S, *Handbook Nanostruct Mater Nanotechnol*, (1999) 1.
34 Mudinepalli V R, Feng L, Lin W C & Murty B S, *J Adv Ceram*, 4 (2015) 46.
35 Shen Z Y & Li J F, *J Ceram Soc Jpn*, 118 (2010) 940.
36 Biswas D, Sharma P & Panwar N S, *ECS J Solid State Sci Technol*, 10 (2021) 033002.

ECS Journal of Solid State Science and Technology, 2022 **11** 043007
2162-8777/2022/11(4)/043007/7/$40.00 © 2022 The Electrochemical Society ("ECS"). Published on behalf of ECS by IOP Publishing Limited

Temperature Dependent Dielectric and Structural Properties of $(Ba_{1-x}Ca_x)(Zr_{0.1}Ti_{0.9})O_3$, $(0.140 \leqslant x \leqslant 0.160)$ Ceramics

Don Biswas,[1,2,z] Prolay Sharma,[2] and N. S. Panwar[1]

[1]*Department of Instrumentation Engineering, H.N.B. Garhwal University, Srinagar (Garhwal), India*
[2]*Department of Instrumentation and Electronics Engineering, Jadavpur University, Kolkata, India*

Ceramic pellets of $(Ba_{1-x}Ca_x)(Zr_{1-y}Ti_y)O_3$, (x = 0.140 to 0.160, y = 0.9), were prepared via solid- state reaction method followed by double sintering. Dielectric properties (ε, tan δ, and σ) of the prepared compositions were measured, in the temperature range from RT (room temperature) to 450 °C, at various frequencies (12–1000 kHz). The dielectric measurements show a single phase transition, around 100 °C, for the prepared $(Ba_{1-x}Ca_x)(Zr_{1-y}Ti_y)O_3$ (BCZT) compositions, in the measured temperature range. The structural variation was studied using high temperature X- ray diffraction (HT- XRD) measurements of the compositions with x = 0.150 and 0.155. The HT- XRD results were found consistent with the dielectric measurements, showing structural anomaly at around 100 °C; showing tetragonal phase, between RT and around 100 °C; and cubic phase, above 100 °C, in the measured temperature range.
© 2022 The Electrochemical Society ("ECS"). Published on behalf of ECS by IOP Publishing Limited. [DOI: 10.1149/2162-8777/ac62f3]

Manuscript submitted January 18, 2022; revised manuscript received March 29, 2022. Published April 12, 2022.

The distinct dielectric properties of the perovskite (ABO_3 type) ferroelectric compounds attract to investigate them for industrial applications. Their high dielectric constant and piezo-coefficient make them potential candidates to be used in the field of capacitors and transducers. The ABO_3 based materials are also promising candidates for energy storage applications.[1,2] Recently, with the increasing environment awareness, the lead (Pb) based high piezo-constant materials (e.g., $PbZr_{1-x}Ti_xO_3$ (PZT), etc.) are being abandoned due to their toxic nature,[3] and a surge in the investigation of the environment friendly lead- free piezo- materials is being observed. The PZT ceramics show large dielectric and piezoelectric constant due to the presence of structurally rhombohedral and tetragonal bridging phases,[4–6] a morphotropic phase boundary (MPB), near certain composition (x). Presence of structurally bridging phases may result several possible polarization directions, near MPB. Extremal electro- physical properties have been observed due to the occurrence of different crystal phases, near MPB.[7–12] It may be attributed to the instability appeared in the polarization state or abrupt structural changes, leading to the alteration of the ferro-electric domains, at the MPB.

With the consideration of the structure- property correlation of the lead based compounds, near MPB, many lead free compounds enable themselves as a suitable alternative of various lead based compounds. Consequently, researchers have been trying to develop new ferroelectric materials, with extremal electro- physical properties, for the applications of sensors, actuators, and transducers. Many lead- free compounds, like NKN (sodium potassium niobate), BST (barium strontium titanate), BCZT (barium calcium zirconate titanate), etc. have been tried to replace the lead based piezo-materials,[13–18] but piezoelectricity in the NKN and BST compounds was found lower than that of the lead- based compounds.[16] The perovskite lead free non-toxic BCZT system shows compatibly high piezo-properties, like PZT, with piezo-constant ($d_{33} \sim$ 620 pC/N).[17,18] The perovskite ABO_3 structure is maintained, when Ba is replaced by Ca, and/or Ti by Zr, in the $BaTiO_3$, to prepare $(Ba_{1-x}Ca_x)(Zr_{1-y}Ti_y)O_3$, (x, y = 0 to 1), system.[19] The physical properties of this system can be significantly altered with this replacement at A- and/or B- site, with $x \sim 0.150$, and $y \sim 0.1$, near the morphotropic phase boundary.

In a previous communication, dielectric properties (ε, tan δ, and σ) of $(Ba_{1-x}Ca_x)(Zr_{1-y}Ti_y)O_3$, (x = 0.140–0.160, y = 0.9) were found lowest for the samples with x = 0.150, among the prepared compositions, at all measured frequencies and temperatures.[20] The observed results exhibit a strong composition dependence of dielectric properties- a morphotropic—like phase boundary in $(Ba_{1-x}Ca_x)(Zr_{1-y}Ti_y)O_3$, (x = 0.140–0.160, y = 0.9), ceramics, at x = 0.150. The composition variation of this system also shows structural anomaly, near x = 0.150. The polarization rotation and extension, and the elastic softening of the lattice may be the factors for the composition dependent anomaly, near the MPB.[21] Also, near the MPB, presence of two or more phases can significantly change the physical or structural properties of the $(Ba_{1-x}Ca_x)(Zr_{1-y}Ti_y)O_3$ ceramics.[22,23] Depending on the composition (x), $(Ba_{1-x}Ca_x)(Zr_{1-y}Ti_y)O_3$, system shows cubic, tetragonal or orthorhombic phases.[18] The $(Ba_{1-x}Ca_x)(Zr_{1-y}Ti_y)O_3$ ceramics also exhibit poly-morphic phases depending on the temperature and composition (x).[24] In the previous communications, the sintering dependent density and dielectric properties of $(Ba_{1-x}Ca_x)(Zr_{1-y}Ti_y)O_3$ compositions were reported.[20,25] The study was further extended and the observed temperature dependent dielectric and structural properties of the double sintered $(Ba_{1-x}Ca_x)(Zr_{1-y}Ti_y)O_3$ compositions are being reported presently.

The pellet samples of $(Ba_{1-x}Ca_x)(Zr_{1-y}Ti_y)O_3$, were prepared for the compositions, x = 0.140–0.160, y = 0.9, near MPB, following the solid- state reaction route with double sintering. The dielectric constant, loss tangent, and dielectric conductivity of the prepared compositions were measured, from RT to 450 °C, at different frequencies. As the representative of the present BCZT system, the HT- XRD measurements were carried out for two compositions, with x = 0.150 and 0.155, in the temperature range RT to 450 °C.

Experimental

The preparation methodology of the $(Ba_{1-x}Ca_x)(Zr_{1-y}Ti_y)O_3$ pellet samples, their X- ray diffraction (XRD) patterns, scanning electron micrograph (SEM) images, composition- dependent di-electric properties, density, etc. were described in a previous communication.[20] Presently, the dielectric constant, loss tangent and electric conductivity of the prepared compositions, measured at different frequencies in the temperature range, from RT to 450 °C, using an impedance analyzer (Keysight, E49990), have been reported. For dielectric measurements, specimens were electroded, with conducting silver paste, in a metal- insulator-metal (MIM) configuration.

To study different phases of the prepared BCZT ceramics, HT-XRD were measured, from RT to 450 °C, for the compositions with x = 0.150 and 0.155, by an X- ray diffractometer (PANalytical, X'PERT PRO), using Cu$K_{\alpha 1}$ radiation of wavelength 1.54060 Å. The scan speed of the diffractometer was 0.1 sec per step with step size of 0.01°. The composition was heated up at a heating rate of 5 °C s^{-1}. The desired temperature was held for 2 min, before the XRD measurement, at each measuring temperature.

[z]E-mail: d.biswas@hnbgu.ac.in

Results and Discussion

Dielectric results.—Presently, the thermal variation of the dielectric properties, the dielectric constant (ε), tangent loss (tan δ) and electric conductivity (σ), of the prepared BCZT samples were measured, in the temperature range from RT to 450 °C, at different frequencies (12–1000 kHz). Figures 1, 2 and 3 show the measured temperature- dependence of ε, tan δ, and σ of the BCZT ceramics. The dielectric constant (ε) was found increasing with increase in temperature, but with anomalously large value at around 100 °C, indicating a phase transition at this temperature. Similarly, the tangent loss and electric conductivity anomaly, Figs. 2 and 3, respectively, confirm the occurrence of phase transition at around 100 °C, in these compositions. The insets of Figs. 1–2 show the anomaly. The wide dielectric constant peaks were observed at 99, 99, 84, 99, and 94 °C, Fig. 1; and electric conductivity peaks at 104, 104, 89, 99, and 94 °C, Fig. 3, for the compositions with x = 0.140, 0.145, 0.150, 0.155, 0.160, respectively. The dielectric constant, loss tangent and the electric conductivity anomaly were observed at the same temperature for all the measuring frequencies, for an individual composition, Figs. 1–3. However, for the compositions with x ⩽ 0.150, the dielectric constant and electric conductivity peaks were not observed at the same temperature, for an individual composition. The observed wide

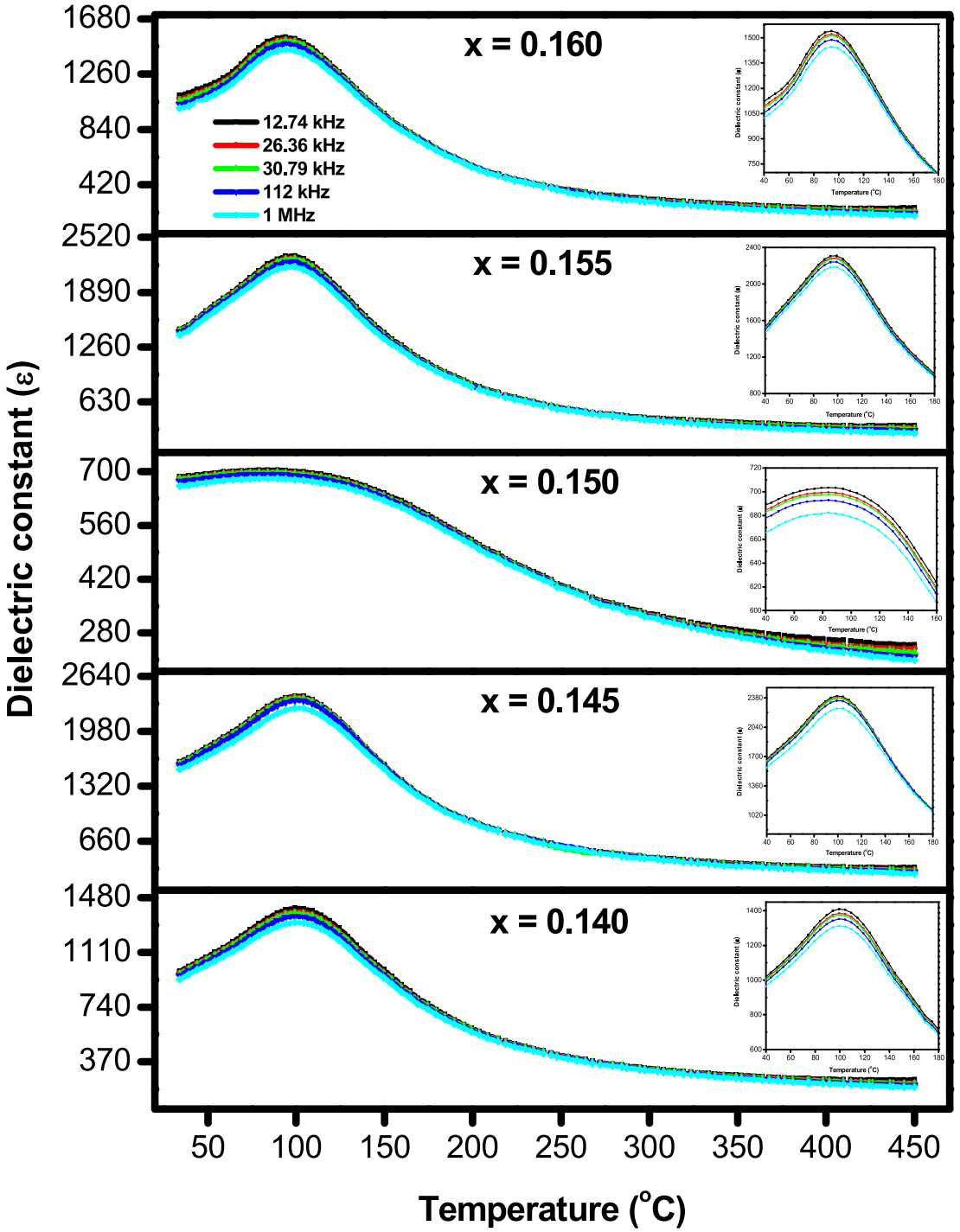

Figure 1. Temperature variation of dielectric constant (ε), in $(Ba_{1-x}Ca_x)(Zr_{1-y}Ti_y)O_3$, (x = 0.140–0.160, y = 0.9), at different frequencies. The inset of Fig. 1 shows the dielectric anomaly.

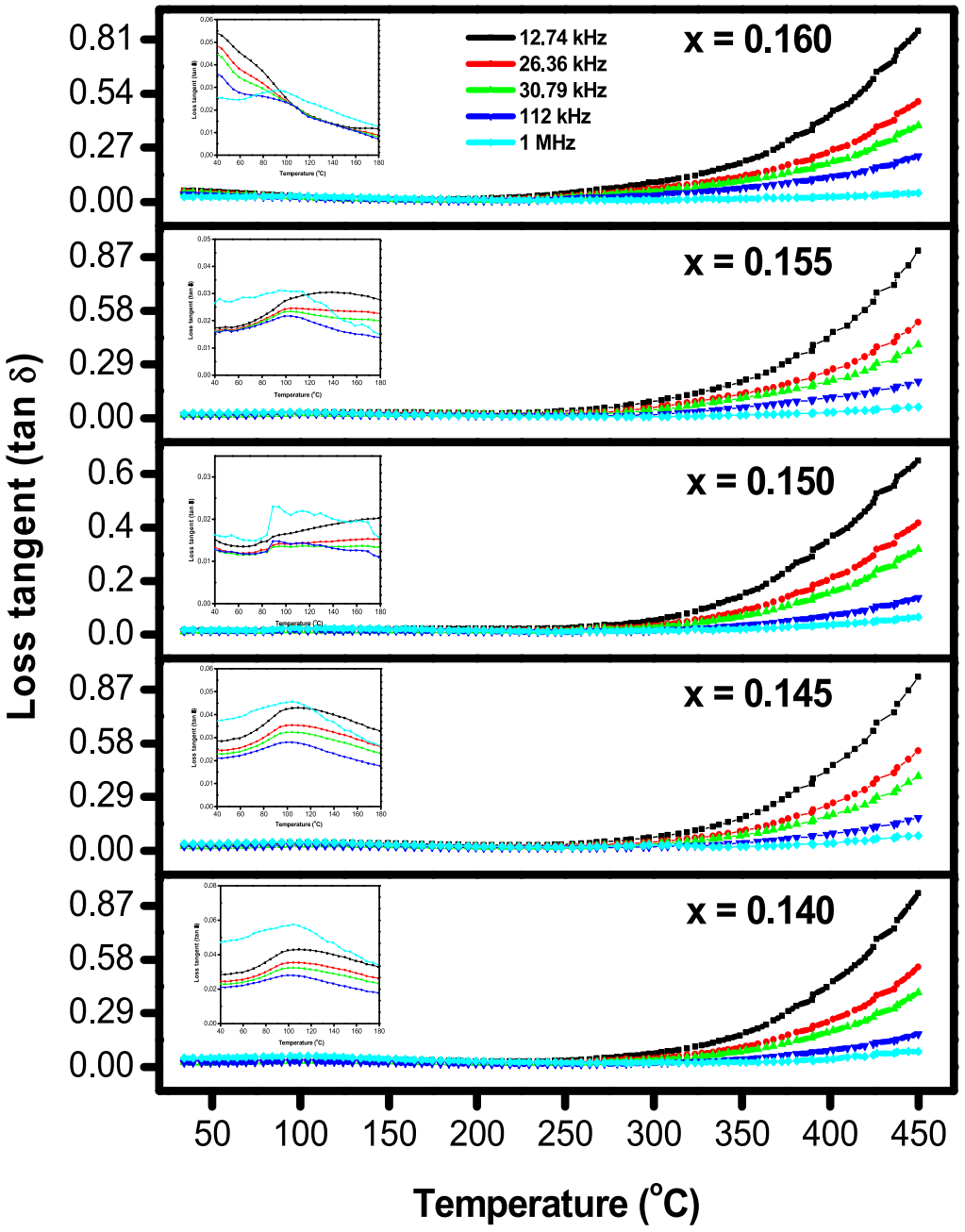

Figure 2. Temperature variation of dielectric loss (tan δ), in $(Ba_{1-x}Ca_x)(Zr_{1-y}Ti_y)O_3$, (x = 0.140–0.160, y = 0.9), at different frequencies. The inset of Fig. 2 shows the loss anomaly.

dielectric peaks indicate the relaxor-type behavior, whereas the occurrence of frequency independent transition temperature shows non- relaxor nature of the prepared material.[26] For a relaxor, the wide dielectric constant peak shifts to higher temperature with increasing frequency, due to the increasing relaxation time with temperature.[26] The occurrence of wide dielectric constant and electric conductivity peaks, and small variation in the temperature of these peaks may be the resulting effect of the structural change, barrier heights at the grain boundary, activation energy and other interactions,[27] resulting maximum for one grain at one temperature and for another grain at another temperature, in the ceramic sample, near the transition temperature of that composition. Near x = 0.150, the BCZT ceramics shows morphotropic- type phase boundary (MPB), comprising of two or more phases.[28] A combination of these phases may initiate different polarization directions, which might have also contributed to the observed wide dielectric peaks, for the compositions near MPB.

With increase in the measuring frequency the observed decrease in dielectric constant (ε) and loss tangent (tan δ), and increase in the electric conductivity were found consistent with the reported results,[20,29,30] which may be attributed to the damping out of successive relaxation modes in the lattice.[31]

The Curie point indicates the transition temperature where the material observes paraelectric to ferroelectric transition. The paraelectric phase is a high symmetry phase and the ferroelectric a low symmetry phase. Thus, this phase transition is associated with the structural phase transition in the perovskite- type ferroelectrics.[32] The dielectric properties of the perovskites are associated to a significantly temperature dependent vibrational mode—the soft mode.[33] The frequency of vibrational modes in a crystal depends on the long—and shor—range interactions among the vibrating species. At the transition temperature, the frequency of the soft mode tends to zero, and the lattice observes a displacement leading to the

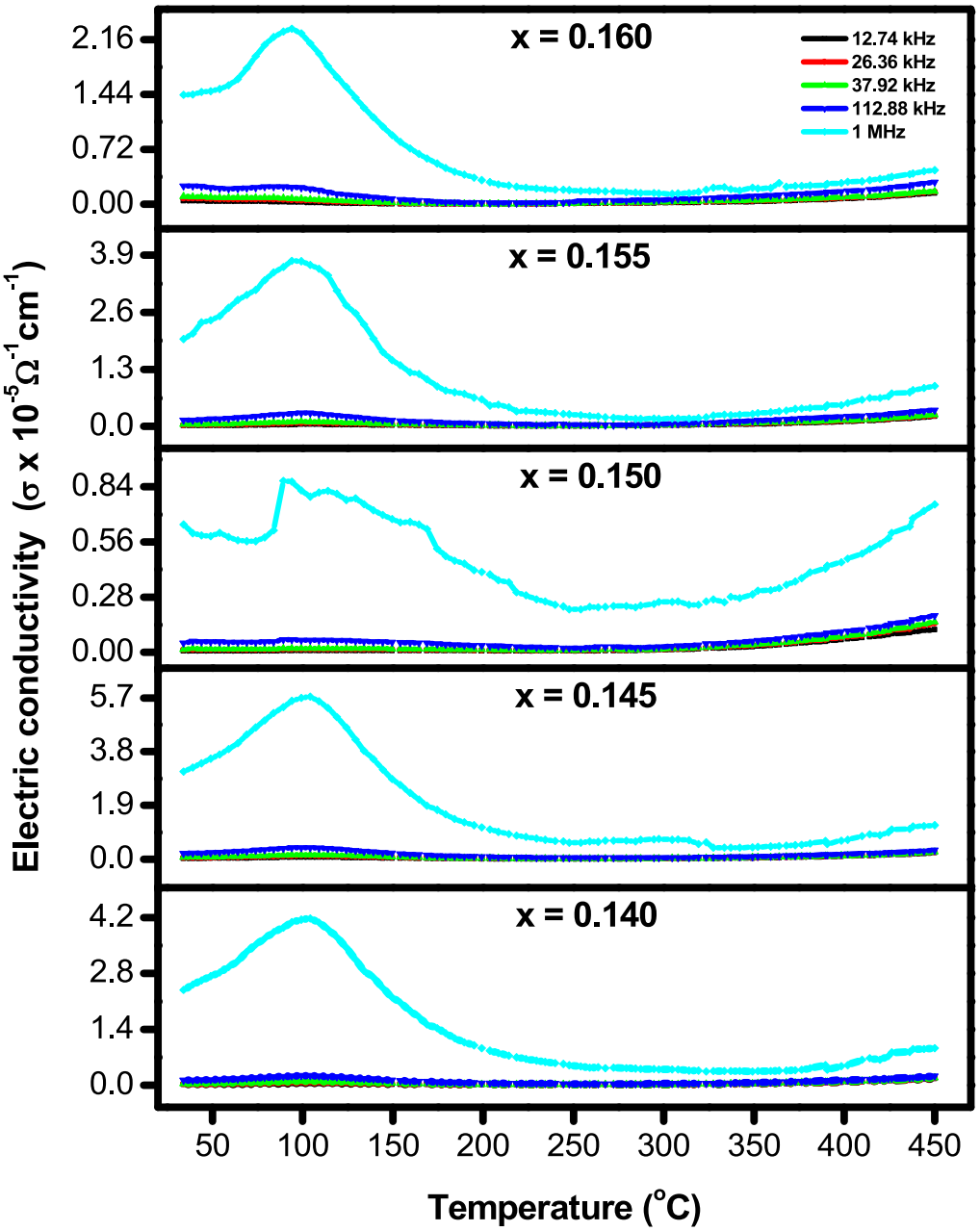

Figure 3. Temperature variation of electric conductivity (σ), in $(Ba_{1-x}Ca_x)(Zr_{1-y}Ti_y)O_3$, (x = 0.140–0.160, y = 0.9), at different frequencies.

structural anomaly- the structural phase transition.[33,34] According to the soft mode theory, the dielectric permittivity of perovskites is proportional to the inverse of the square of the soft mode frequency.[35] When Ba atoms are replaced by Ca atoms, in the ABO_3 type $Ba(Zr,Ti)O_3$, the change in the mass, force constant and other interactions result change in the soft mode frequency. With the random allocation of varied (Ca) mass at different lattice sites (A- site), the force constant and other interactions vary randomly, resulting change in the soft mode frequency accordingly and, thereby to the change in the observed dielectric constant with the substitution of Ba by Ca in the lattice.

Figure 4 shows the temperature—dependence of dielectric permittivity and conductivity, at 1 MHz, in the measured temperature range. The dielectric anomaly was observed near 100 °C, for the prepared BCZT compositions. The observed anomaly in the dielectric properties indicates the transition temperature.[32] This transition is attributed to the tetragonal to cubic structural change.[36] The dielectric anomaly was observed varying with the Ca doping (x), at the A- site, in the $(Ba_{1-x}Ca_x)(Zr_{1-y}Ti_y)O_3$, (x = 0.140–0.160, y = 0.9) ceramics, as shown in Figs. 1–3. Apart from the softening of the active phonon mode, the polarization extension and rotation mechanism, porosity, microstructure and grain morphology of $(Ba_{1-x}Ca_x)(Zr_{1-y}Ti_y)O_3$ ceramic samples, of a composition, may contribute to its observed dielectric nature.[37]

HT- X-ray diffractometer measurements.—The dielectric measurements of the prepared BCZT compositions indicate the phase transition at around 100 °C. To study the structural variation with temperature, the high temperature X-ray diffraction (HT- XRD) measurements were carried on the samples with composition x = 0.150 and 0.155, in the temperature range from RT to 450 °C. These two compositions (x = 0.150 and 0.155) were selected as the representatives of the prepared compositions due to their similar observed dielectric anomaly, near T_c. The HT- XRD patterns obtained for $(Ba_{1-x}Ca_x)(Zr_{1-y}Ti_y)O_3$, x = 0.150 and 0.155, pellet samples have been shown in Figs. 5 and 6, respectively. The

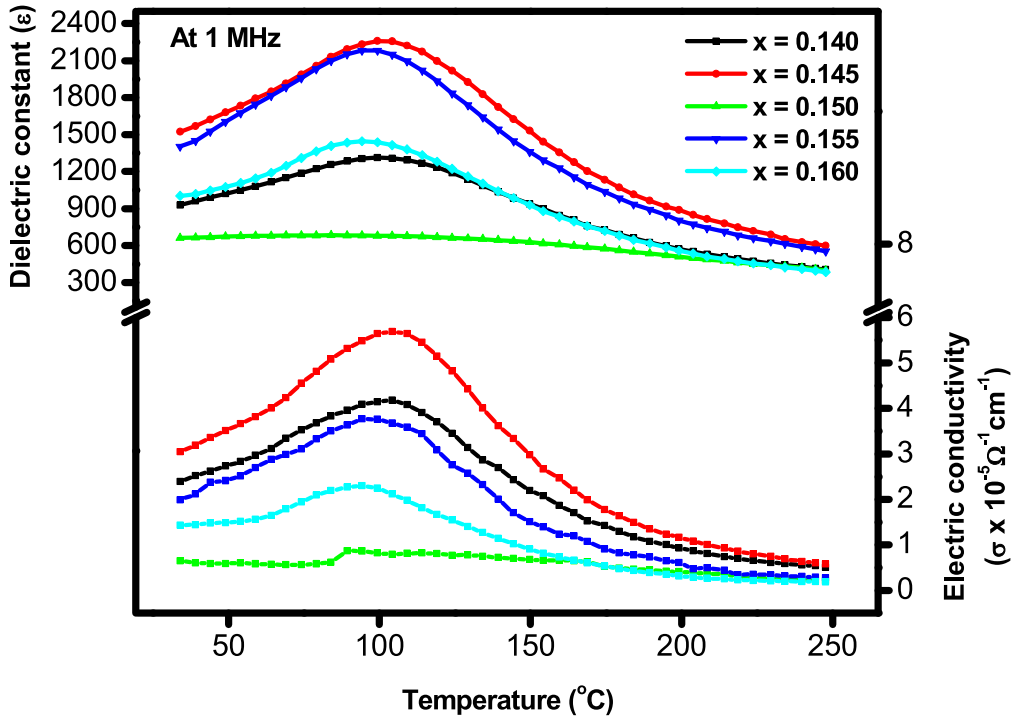

Figure 4. Variation of dielectric constant (ε) and electric conductivity (σ) with temperature, in $(Ba_{1-x}Ca_x)(Zr_{1-y}Ti_y)O_3$, (x = 0.140–0.160, y = 0.9), at 1 MHz.

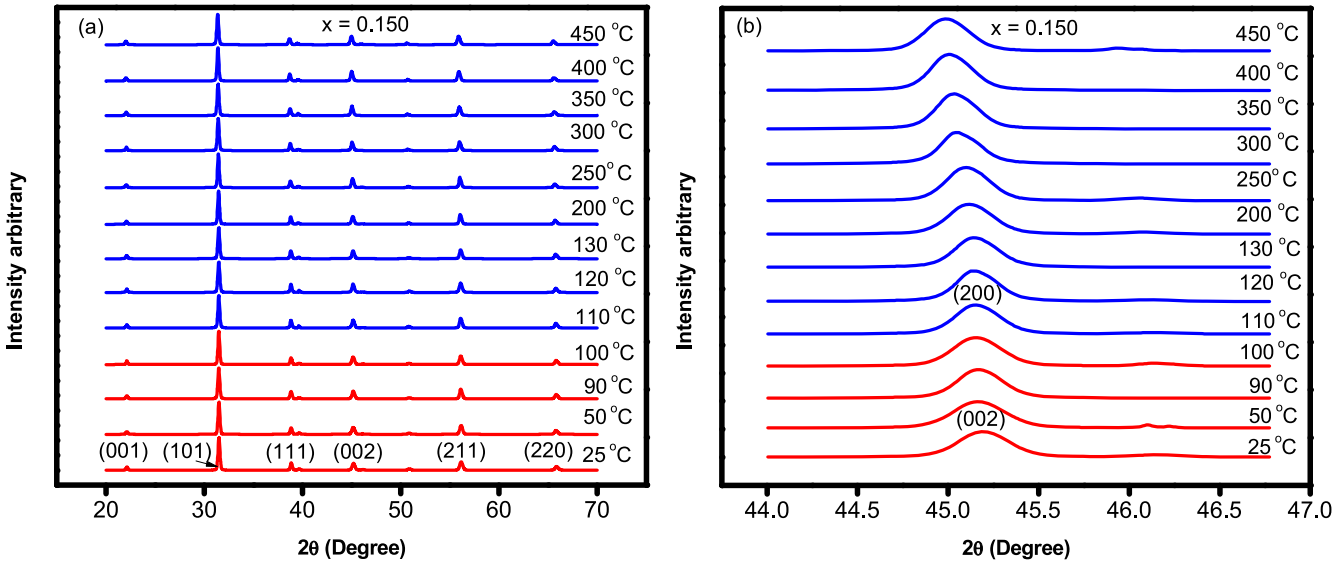

Figure 5. (a) HT-XRD patterns of $(Ba_{0.85}Ca_{0.15})(Zr_{0.1}Ti_{0.9})O_3$ ceramics, (b) expanded angle view (44°−47°).

measured XRD peaks have been indexed with the help of Inorganic Crystal Structure Database (ICSD). The HT- XRD of the ceramics indicates polycrystalline nature. The HT- XRD patterns measured near the transition temperatures were compared with the observed dielectric anomaly. The observed phase transition from the HT-XRD data and dielectric anomaly were found consistent to each other. The lattice parameters of BCZT ceramics were refined using the Rietveld method. The space groups for these refinements were P4mm and Pm-3m, respectively.[38–41]

From the observed XRD patterns of these compositions exhibit tetragonal phase, between room temperature and about 100 °C, which is compatible with the ICSD—(code 01–083–1875) and (code 01–079–2265) data;[38,39] and above about 100 °C, they exhibit cubic symmetry, consistent with ICSD—(01–074–1962),[40] ICSD—(01–075–0216),[42] and ICSD—(01–078–4475) data.[41]

In the HT-XRD patterns of $(Ba_{1-x}Ca_x)(Zr_{1-y}Ti_y)O_3$, (x = 0.150), a continuous shifting of the most intense peaks (101), (111), (002), and (211), to the lower angle was observed with increasing temperature, in the measured temperature range, Fig. 5. A similar fashion was also observed for the composition x = 0.155, Fig. 6. The measured HT-XRD patterns exhibit a structural transition, from tetragonal (ferroelectric) to cubic (paraelectric) phase, at around 100 °C, which is consistent with the dielectric measurements. The peaks' profiles were refined using a pseudo-Voigt function and background was modeled using the Legendre polynomial. Furthermore, lattice parameters were refined by High Score Plus software, using the Rietveld analysis.[43] Ba and Ca ions were located and shared at the same A-site (0,0,0), Ti and Zr ions were shared at B-site (½,½,½) and oxygen ions were located at the O-site (½,½,0), respectively.[36] Furthermore, the occupancies of Ba: Ca ions that

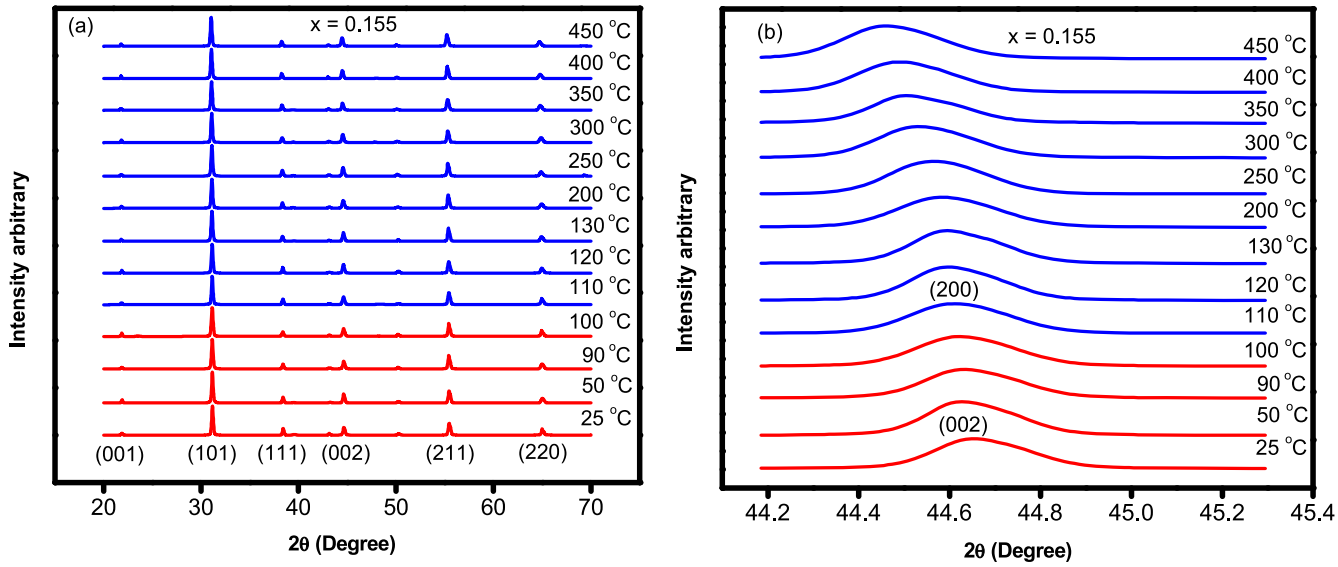

Figure 6. (a) HT-XRD patterns of $(Ba_{0.845}Ca_{0.155})(Zr_{0.1}Ti_{0.9})O_3$ ceramics, (b) expanded angle view (44°−47°).

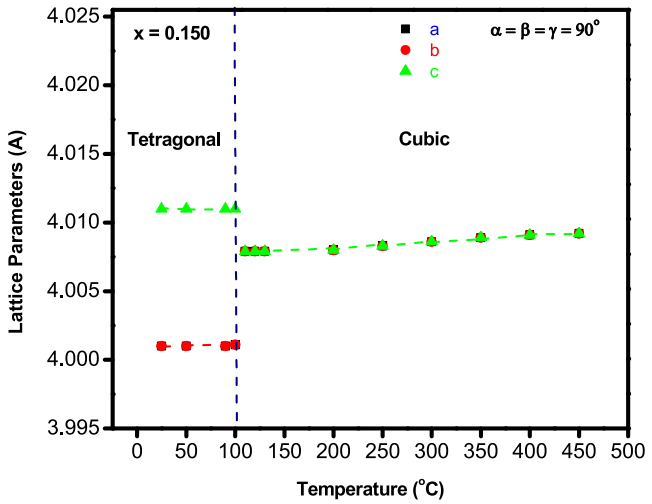

Figure 7. Variation of lattice parameters with temperature, in $(Ba_{1-x}Ca_x)(Zr_{1-y}Ti_y)O_3$, (x = 0.150, y = 0.9).

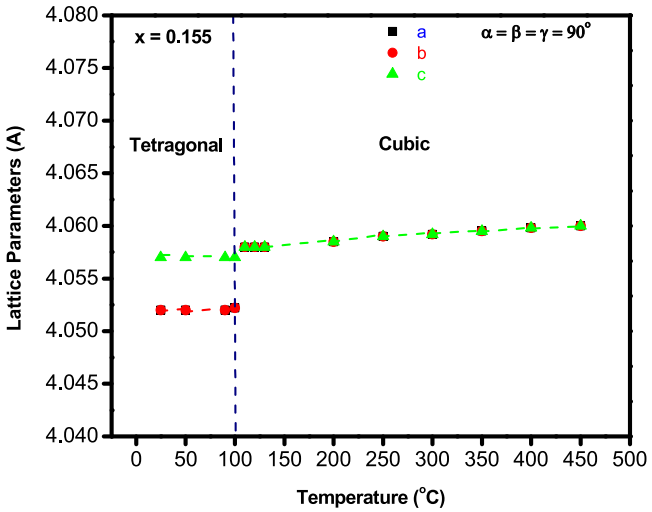

Figure 8. Variation of lattice parameters with temperature, in $(Ba_{1-x}Ca_x)(Zr_{1-y}Ti_y)O_3$, (x = 0.155, y = 0.9).

were shared at the same location were fixed as 85: 15 (for x = 0.150 composition), and 845: 155 (for x = 0.155 composition); and for Ti: Zr ions 90: 10, according to their molar ratios. The observed temperature variations in lattice parameters are shown in Figs. 7 and 8, for the compositions with x = 0.150 and 0.155, respectively.

Conclusions

The dielectric properties and high temperature X- ray diffraction (HT-XRD) of the $(Ba_{1-x}Ca_x)(Zr_{1-y}Ti_y)O_3$, (x = 0.140–0.160, y = 0.9) ceramics were measured. At all the measured frequencies, the observed electric conductivity and dielectric constant exhibit minimum values for the compositions with x = 0.150, among the prepared compositions. The HT-XRD of the BCZT ceramic samples with x = 0.150 and 0.155 were measured. The HT-XRD measurements show distinct phase transition, from tetragonal to cubic phase, at around 100 °C, which is consistent with the dielectric measurements.

ORCID

Don Biswas https://orcid.org/0000-0001-5130-087X

References

1. W. B. Li, D. Zhou, L. X. Pang, R. Xu, and H. H. Guoa, "Novel barium titanate based capacitors with high energy density and fast discharge performance." *J. Mater. Chem. A*, **5**, 19607 (2017).
2. W. B. Li, D. Zhou, and L. X. Pang, "Enhanced energy storage density by inducing defect dipoles in lead free relaxor ferroelectric $BaTiO_3$-based ceramics." *Appl. Phys. Lett.*, **110**, 132902 (2017).
3. P. K. Panda and B. Sahoo, "PZT to lead free piezo ceramics: a review." *Ferroelectrics*, **474**, 128 (2015).
4. P. Kantha and K. Pengpat, "Phase formation and electrical properties of BNLT–BZT lead-free piezoelectric ceramic system." *Curr. Appl Phys.*, **9**, 460 (2009).
5. Y. Tian, Y. Gong, D. Meng, Y. Li, and B. Kuang, "Dielectric dispersion, diffuse phase transition, and electrical properties of BCT–BZT ceramics sintered at a low-temperature." *Journal of Elec. Mater.*, **44**, 2890 (2015).
6. E. Cross, "Material science: lead free at last." *Nature*, **432**, 24 (2004).
7. A. M. Glazer, P. A. Thomas, K. Z. Baba- Kishi, G. K. H. Pang, and C. W. Tai, "Influence of short range and long-range order on the evolution of the morphotropic phase boundary in $Pb(Zr_{1-x}Ti_x)O_3$." *Phys. Rev. B*, **70**, 184123 (2004), (1-9).
8. K. Kakimoto, K. Akao, Y. Guo, and H. Ohsato, "Raman scattering study of piezoelectric $(Na_{0.5}K_{0.5})NbO_3$-$LiNbO_3$ Ceramics." *Jpn. J. Appl. Phys.*, **44**, 7064 (2005).
9. B. Jaffe, W. R. Cook, and J. H. Jaffe, *Piezoelectric Ceramics* (Academic, New York) (1971).
10. A. J. Moulson and J. M. Herbert, *Electroceramics: Materials, Properties, Applications* (Wiley, United Kingdom) (2003).
11. Y. Ishibashi and M. Iwata, "A theory of morphotropic phase boundary in solid-solution systems of perovskite-type oxide ferroelectrics." *Jpn. J. Appl. Phys.*, **38**, 800 (1999).

12. N. Klein, E. Hollenstein, D. Damjanovic, H. J. Trodahl, N. Setter, and M. Kuball, "A study of the phase diagram of (K, Na, Li)NbO_3 determined by dielectric and piezoelectric measurements, and Raman spectroscopy." *J. Appl. Phys.*, **102**, 014112 (2007).
13. D. Biswas, G. S. Kathait, P. Thapliyal, V. Rohilla, S. Singh, and J. Negi, "Converse piezoelectric properties of K and Na-modified ($Na_{1-x}K_x$) NbO_3 lead free ceramics for x = 0.08 and 0.17." *Ferroelectrics*, **550**, 228 (2019).
14. G. S. Kathait, N. S. Panwar, P. Thapliyal, D. Biswas, V. Rohilla, and S. Singh, "Sintering effect on electrical properties and morphology of lead-free $Na_{0.92}K_{0.08}NbO_3$ ceramics." *Sci. Sinter.*, **51**, 421 (2019).
15. D. Biswas, G. S. Kathait, P. Thapliyal, V. Rohilla, and S. Singh, "Temperature dependence of dielectric properties of sodium potassium niobate ceramics for different values of x ($Na_{1-x}K_xNbO_3$)." *Ferroelectrics*, **526**, 168 (2018).
16. T. R. Shrout and S. J. Zhang, "Lead-free piezoelectric ceramics: alternatives for PZT?" *J. Electroceram.*, **19**, 113 (2007).
17. A. Frattini, A. D. Loreto, O. D. Sanctis, and E. R. Benavidez, "BCZT ceramics prepared from activated powders." *Procedia Materials Science*, **1**, 359 (2012).
18. W. Liu and X. Ren, "Large piezoelectric effect in Pb-free ceramics." *Phys. Rev. Lett.*, **103**, 257602 (2009).
19. M. McQuarrie and F. W. Behnke, "Structural and dielectric studies in the system (Ba, Ca)(Ti, Zr)O_3." *J. Am. Ceram. Soc.*, **37**, 539 (1954).
20. D. Biswas, P. Sharma, and N. S. Panwar, "Composition dependent electrical properties of $(Ba_{1-x}Ca_xZr_{0.1}Ti_{0.9})O_3$ ceramics, near morphotropic phase boundary ($0.140 \leqslant x \leqslant 0.160$)." *ECS J. Solid State Sci. Technol.*, **10**, 033002 (2021).
21. Y. Ishibashi, "Theory of the morphotropic phase boundary." *Ferroelectrics*, **264**, 197 (2001).
22. W. Li, Z. Xu, R. Chu, P. Fu, and G. Zang, "Piezoelectric and dielectric properties of $(Ba_{1-x}Ca_x)(Ti_{0.95}Zr_{0.05})O_3$ lead-free ceramics." *J. Am. Ceram. Soc.*, **93**, 2942 (2010).
23. W. Li, Z. Xu, R. Chu, P. Fu, and G. Zang, "High piezoelectric d_{33} coefficient in $(Ba_{1-x}Ca_x)(Ti_{0.98}Zr_{0.02})O_3$ lead-free ceramics with relative high curie temperature." *Mater. Lett.*, **64**, 2325 (2010).
24. G. Singh, V. S. Tiwari, and P. K. Gupta, "Evaluating the polymorphic phase transition in calcium-doped Ba $(Zr_{0.05}Ti_{0.95})O_3$: a lead-free piezoelectric ceramic." *J. Appl. Crystallogr.*, **46**, 324 (2013).
25. D. Biswas, N. S. Panwar, and P. Sharma, "Converse piezoelectric properties of lead free $Ba_{1-x}Ca_xZr_{0.1}Ti_{0.9}O_3$ (x = 0.055) ceramics using double sintered method." *Ferroelectrics*, **568**, 95 (2020).
26. A. Peláiz-Barranco, F. Calderón-Piñar, O. García-Zaldívar, and Y. González-Abreu, "Relaxor behaviour in ferroelectric ceramics." *Advances in Ferroelectrics* (Intech open Ltd, London) 86 (2012).
27. J. Negi and N. S. Panwar, "Structural and electrical properties of lead-free $Na_{0.685}K_{0.315}Nb_{1-y}Ta_yO_3$ ($0 \leqslant y \leqslant 0.05$) Ceramics." *J. Phys. Chem. Solids*, **151**, 109853 (2021).
28. S. Somiya, *Encyclopedia of Physical Science and Technology* (Academic press, New York) p. 578 (2003).
29. S. Singh, J. Negi, and N. S. Panwar, "Dielectric properties of $Na_{1-x}K_xNbO_3$, near x = 0.5 morphotropic phase region." *J. Phys. Chem. Solids*, **123**, 311 (2018).
30. A. S. Kandari, K. Kandari, and V. Lingwal, "Composition dependent dielectric anomaly in $Na_{1-x}K_xNbO_3$, at x = 0.475." *Ferroelectrics*, **393**, 121 (2009).
31. R. C. Buchanan and M. Dekker, *Inc., Ceramic Materials for Electronics: Processing, Properties, and Applications* (Wiley, New York) Vol. 43, p. 180 (1991).
32. S. Singh, J. Negi, and N. S. Panwar, "Temperature dependent dielectric properties of (Na, K) NbO3, near equimolar composition." *Ceram. Int.*, **45**, 13067 (2019).
33. N. S. Panwar, T. C. Upadhyay, and B. S. Semwal, "Soft mode dynamics of perovskite type crystals." *Pramana- J. Phys.*, **33**, 603 (1989).
34. E. Pytte, "Theory of perovskite ferroelectrics." *Phys. Rev. B*, **5**, 3758 (1972).
35. X. Gonze and C. Lee, "Dynamical matrices, born effective charges, dielectric permittivity tensors, and interatomic force constants from density-functional perturbation theory." *Phys. Rev. B*, **55**, 10355 (1997).
36. K. N. D. K. Muhsen, R. A. M. Osman, and M. S. Idris, "Structure refinement and impedance analysis of $Ba_{0.85}Ca_{0.15}Zr_{0.10}Ti_{0.90}O_3$ ceramics sintered in air and nitrogen." *J. Mater. Sci., Mater. Electron.*, **30**, 20673 (2019).
37. G. Goodman, R. C. Buchanan, and T. G. Reynolds III, *Ceramic Materials for Electronics: Processing, Properties, and Applications* (Marcel Dekker Inc, New York) 32 (1991).
38. R. Waesche, W. Denner, and H. Schulz, "Influence of high hydrostatic pressure on the crystal structure of barium titanate ($BaTiO_3$)." *Mater. Res. Bull.*, **16**, 497 (1981).
39. R. H. Buttner and E. N. Maslen, "Structural parameters and electron difference density in $BaTiO_3$." *Acta Crystallogr.*, **48**, 764 (1992).
40. S. Miyake and R. Ueda, "On phase transformation of $BaTiO_3$." *J. Phys. Soc. Jpn.*, **2**, 93 (1947).
41. H. D. Megaw, "Crystal structure of barium titanate." *Nature (London)*, **155**, 484 (1945).
42. J. W. Edwards, R. Speiser, and H. L. Johnston, "Structure of barium titanate at elevated temperatures." *J. Am. Chem. Soc.*, **73**, 2934 (1951).
43. L. V. Azaroff, *Elements of X- ray Crystallography* (McGraw Hill Book Company, New York) (1968).

Science of Sintering, **54** (2022) 201-209

https://doi.org/10.2298/SOS2202201B

UDK: 622.785; 546.824; 676.014.8

Effect of Sintering on the Piezoelectric Properties and Microstructure of Lead Free ($Ba_{1-x}Ca_xZr_{0.1}Ti_{0.9}O_3$) (x = 0.065) Ceramics

Don Biswas[1,2*)], Prolay Sharma[2*], N. S. Panwar[1]

[1]Instrumentation Engg.-USIC Dept., H. N. B. Garhwal University, Srinagar Garhwal, India.

[2]Instrumentation and Electronics Engg., Jadavpur University, Kolkata, India.

Abstract:

In this work, pellet samples of barium calcium zirconate titanate ($Ba_{1-x}Ca_xZr_{0.1}Ti_{0.9}O_3$, x=0.065) were prepared using solid state reaction route with double sintering. The structural and piezoelectric properties were measured. Further, SEM and EDAX analysis were observed. With different sintering temperature, the density and grain size of the prepared pellet samples were changed and further, their effect in piezoelectric properties has been observed. For the prepared samples, the converse piezoelectric constant (d_{33}^*) has been decreased with the increase in sintering temperature. The piezoelectric constant (d_{33}^*) was measured highest (153 pm/V) at 1300°C.

Keywords*: Ferroelectrics; Piezoelectric constant; Perovskite; 2- step sintering.*

1. Introduction

Perovskite type materials are of huge interest because of their large piezoelectric and dielectric properties [1]. They are important due to their spontaneous polarization characteristics. Their contributions in the field of sensors and transducers are very important. The ABO_3 compounds also have the ferroelectric property [1]. Ferroelectric/ABO_3 type materials may generate voltage by applying pressure on it and produce stress due to applying electric field. Lead based compounds have been widely used because of its large electrical properties. One widely used compound is lead zirconate titanate (PZT). The PZT type compounds show a large piezoelectric value. It may be due to the coexistence of two phases (rhombohedral and tetragonal) at the MPB region [2-4]. But due to its toxic 'nature', PZT is prohibited and scientists are going for lead free piezoelectric materials [4]. Now, for the replacement of Lead- based compounds, lead free ABO_3 type compounds have been widely used. Their dielectric and piezoelectric properties aren't comparable with PZT, but these lead free ferroelectric/ABO_3 materials have been extensively used as a replacement. Further, lead free ABO_3 materials have been used in the various fields of sensors and transducers, etc.

Many researchers studied the PZT system. It has high piezoelectric properties near morphotropic phase boundary (MPB) [3]. It may be occurred because of the abrupt transformation of the polarization state leads to unstable state, at the MPB region. The ferroelectric domains may be altered or several ferroelectric domains may appear due to that reason, which results large piezoelectric properties [3].

*) **Corresponding author:** prolaysharma08@gmail.com

Several ferroelectric compounds such as $BaTiO_3$, KTN, KNN, NKN etc. have been studied [5]. But, they reflect the minimum value of piezoelectric coefficient as compared to PZT. One prominent lead free compound is (K, Na) NbO_3 or sodium potassium niobate based system, which has been reviewed as a good ferroelectric material for lead-based compounds [6]. They have good electrical properties, and further, their properties can be enhanced by using different technologies.

Another important lead free compound is the barium calcium zirconate titanate (BCZT) based system. It may have the significant potential to replace lead-based ceramics used in various dielectric and ferroelectric devices. Their electrical properties may be comparable to the PZT system. BCZT ceramics have been considered for various applications due to their large electrical properties [6]. With a variation in sintering temperature, the piezoelectric properties of BCZT ceramics significantly changed. Buatip et al. [7] reported that if the sintering temperature has been increased above 1300°C, then the piezoelectric coefficient of BCZT ceramics has been reduced. Villafuerte-Castrejón and Tian et al. [8, 9] reported about the piezoelectric coefficient of BCZT ($Ba_{1-x}Ca_xZr_{0.1}Ti_{0.9}O_3$) ceramics, which have a range from 160 pC/N - 600 pC/N.

Further, this research has been done to investigate the piezoelectric properties and grain size variation with the introduction of two - step sintering process. The pellet samples were sintered for 4 hrs with different sintering temperatures. The sintering temperatures were selected 1300, 1400, and 1450°C. Moreover, with variation in sintering temperature conditions, the structure, microstructure, and piezoelectric properties of the synthesized ($Ba_{0.935}Ca_{0.065}Zr_{0.1}Ti_{0.9}O_3$, x = 0.065) pellet samples of BCZT ceramics were investigated. The composition x = 0.065 was selected to see and compare the piezoelectric properties, density and grain size. However, with composition x = 0.075, the sintering effect was already observed and their properties were compared in this study [7].

2. Materials and Experimental Procedures

The pellet samples of BCZT ($Ba_{0.935}Ca_{0.065}Zr_{0.1}Ti_{0.9}O_3$) ceramics were prepared using solid-state reaction route with double sintering [10,11]. Raw materials of Barium carbonate ($BaCO_3$), Calcium carbonate ($CaCO_3$), Zirconium oxide (ZrO_2), and Titanium oxide (TiO_2) were taken with purity greater than 99.99 %. The materials were dried at 200°C for 2 h, to remove the absorbed moisture. A proper stoichiometric ratio has been maintained to prepare the compositions. An agate mullet mortar and pestle is used to ground. The powders were ground with acetone for 2 h and further, 'dry' for 4 h. After 6 hrs, the grinding cycle has been completed. The mixture was calcined in a crucible at 1100°C to remove all carbonate. The pre-sintered mixture was ground and pressed into the disk of 8 mm diameter and 2 mm thickness at 0.2 GPa. The ceramic pellet samples were sintered at 1100°C for 4 h. The sintered pellets were crushed and ground further into powder. This ground powder was further pressed into the disk of 8 mm diameter and 2 mm thickness, at 0.2 GPa. The ceramic pellet samples were sintered again with same conditions. The ceramic pellets were collected from the furnace and cooled it down to room temperature.

The X–ray diffraction patterns were observed at room temperature. For the prepared compositions, powder and pellet samples of BCZT ($Ba_{0.0935}Ca_{0.065}Zr_{0.1}Ti_{0.9}O_3$) ceramics were used. The XRD measurements were taken using PANalytical, X'PERT PRO with Cu$K_{\alpha 1}$ radiation of wavelength 0.1541 nm. The 2θ angle has been selected from 20° to 70°, at a scan speed of 0.3 sec per step with step size 0.03°.

Scanning Electron Microscopy (SEM) has been used to view the microstructure and grain size of the prepared pellet samples, by ZEISS EVO 18 SEM equipped with energy dispersive X-ray Analyzer (EDAX) system.

For piezoelectric measurements, the sintered pellet samples were electrode, with air drying silver paste, in metal – insulator - metal (MIM) configuration. The piezoelectric constant 'd_{33}^{*}' was measured using the aixACCT system GMBH.

3. Results and Discussion

The XRD measurements were carried out for the powder and 'pellet' samples at different sintering temperatures as shown in Fig. 1 and Fig. 2, respectively. A pure perovskite structure has been observed for all the prepared pellet samples. No other phases were observed. The pellet samples have been shown polycrystalline behavior. They were found in good consistency with Inorganic Crystal Structure Database (ICSD) - (00-056-1033), with peaks corresponding to (111), (020), (221), etc. [12]. The RT - XRD of the pellet samples BCZT ($Ba_{0.0935}Ca_{0.065}Zr_{0.1}Ti_{0.9}O_3$) show orthorhombic phase with matched ICSD file No. 00-056-1033 (Fig. 2).

The lattice parameters were calculated manually. The selected space group is 'C' type. For the prepared powder samples, the observed XRD data were matched with Inorganic Crystal Structure Database (ICSD). The ICSD data will give the information of the orthorhombic unit cell (a, b and c parameters) and volume. The manually calculated values (a, b and c parameters) must be in more close approximation to those values. At first, the positions of the observed x- ray peaks were identified. For a corresponding peak, the d-spacing and (hkl) has been noted from the ICSD data. The equation for an interplanar spacing for an orthorhombic unit cell was used to calculate the lattice parameters. To work with the above interplanar equation, the h, k, l, and d values were noted and further, the lattice parameters were calculated. The lattice parameters were shown in Table I.

Tab. I Lattice parameters of BCZT ($Ba_{0.0935}Ca_{0.065}Zr_{0.1}Ti_{0.9}O_3$) ceramics.

	a(Å)	**b(Å)**	**c(Å)**
BCZT Lattice parameters in (Å)	9.807	5.651	6.893

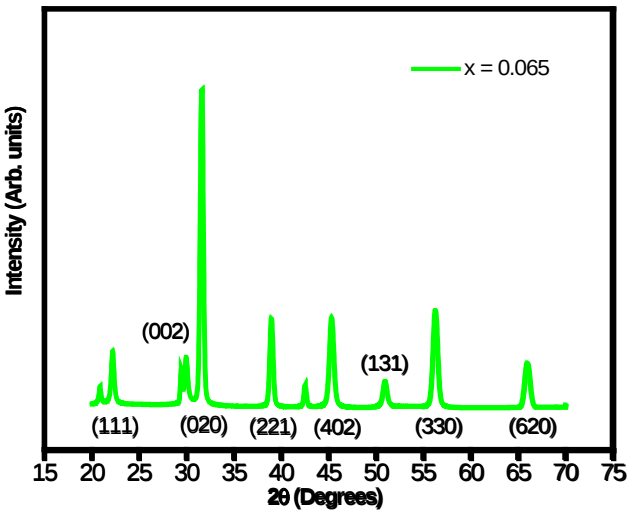

Fig. 1. XRD pattern of the powder sample of BCZT ($Ba_{0.0935}Ca_{0.065}Zr_{0.1}Ti_{0.9}O_3$), at room temperature.

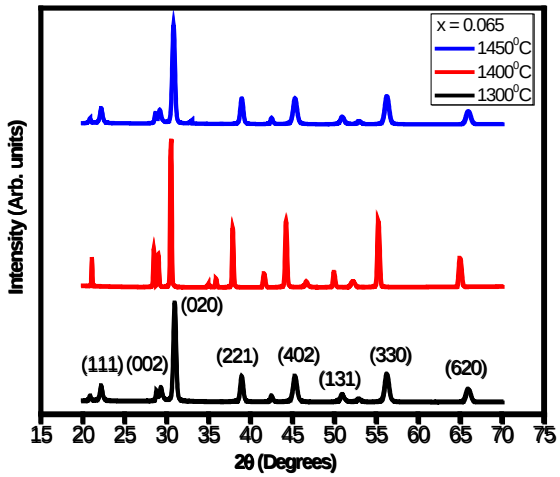

Fig. 2. XRD patterns of pellet samples of BCZT ($Ba_{0.0935}Ca_{0.065}Zr_{0.1}Ti_{0.9}O_3$), at different sintering temperatures.

With the change in grain size, the piezoelectric properties of the prepared compositions were also altered. The SEM images of the sintered pellets were shown in Fig. 3-5. The influences of two-step sintering on the lead- free BCZT ($Ba_{0.0935}Ca_{0.065}Zr_{0.1}Ti_{0.9}O_3$) ceramics with different sintering temperatures were analyzed. The density decreases as the sintering temperature increases (Table II). Further, if the sintering temperature has been increased then the grain size of the sintered pellet samples has been increased, leading to small grain boundary. Also, the porosity has been increased. The EDAX (Energy dispersive X-ray analyzer) measurements of the sintered pellet samples of BCZT ceramics has been shown in Tables III-V. From the EDAX results of the prepared compositions, the atomic percentage of barium and calcium has been observed. For an increase in sintering temperature, the atomic percentage of barium was decreased at 'A' site and further, the percentage of calcium has been increased at the 'B' site (Fig. 3-5). Calcium escaping has been reduced and escaping of barium was increased as the sintering temperature increased. For BCZT ceramics, grain growth has been seen with an inhomogeneous rate, due to the variation in the sintering temperature from 1300 to 1450°C. The reason is longer dwelling time and atoms of the pellet samples were getting more time to diffuse into adjoining grains, at the grain boundary, and the resulting in the grain growth of BCZT ceramics [13-15]. The measured grain size has been shown in Table II.

Tab. II Physical properties of BCZT ($Ba_{0.0935}Ca_{0.065}Zr_{0.1}Ti_{0.9}O_3$) ceramics sintered at various temperatures.

	Sintering temperature (°C)	Density (gm/cm^3)	Grain size (μm)
BCZT	1300	3.49	0.59-2.60
	1400	3.08	0.78-3.00
	1450	2.56	1.30-4.30

During the start of sintering, due to the low activation energy of the samples, extreme grain growth appears and grain coarsening has been introduced. So, the total surface area has been reduced due to an increase of the average size of the particles or grains. The driving force is basically changing surface area. Here, it is 'surface energy' and surface area both are changing. This is also another possibility, but in principle, this is not feasible because once

these larger particles are there, the sintering itself becomes difficult and further, it may not reduce its pores so easily, until one may go to a very high temperature. Once that coarsening takes place, the pore removal becomes quite difficult and resulting in poor densification [16-18].

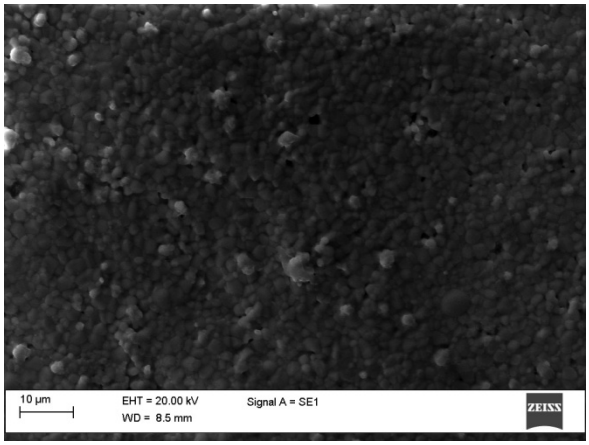

Fig. 3. SEM image of BCZT ($Ba_{0.0935}Ca_{0.065}Zr_{0.1}Ti_{0.9}O_3$) ceramics, at 1300^{o}C temperature.

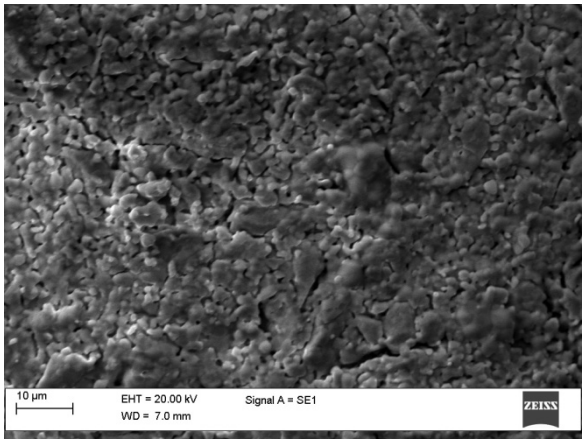

Fig. 4. SEM image of BCZT ($Ba_{0.0935}Ca_{0.065}Zr_{0.1}Ti_{0.9}O_3$) ceramics, at 1400^{o}C temperature.

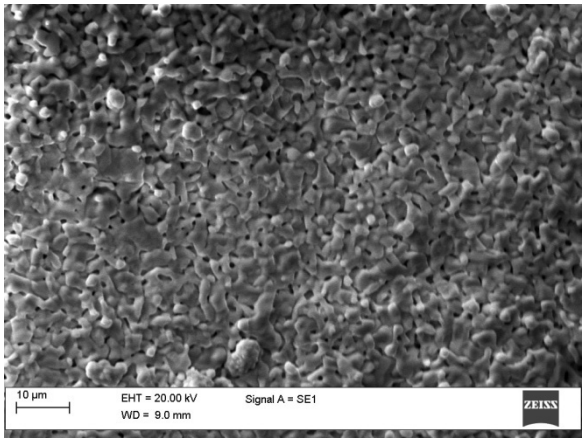

Fig. 5. SEM images of BCZT ($Ba_{0.0935}Ca_{0.065}Zr_{0.1}Ti_{0.9}O_3$) ceramics, at 1450^{o}C temperature.

Tab. III EDAX result of BCZT ($Ba_{0.0935}Ca_{0.065}Zr_{0.1}Ti_{0.9}O_3$) ceramics, at 1300°C temperature.

Element	Weight %	Atomic %
O	25.51	64.23
Ca	4.22	3.23
Ti	18.53	15.50
Zr	0.62	0.24
Ba	51.65	15.32
Total	100.00	

Tab. IV EDAX result of BCZT ($Ba_{0.0935}Ca_{0.065}Zr_{0.1}Ti_{0.9}O_3$) ceramics, at 1400 °C temperature.

Element	Weight %	Atomic %
O	28.94	65.56
Ca	5.12	4.12
Ti	18.80	14.21
Zr	0.37	0.18
Ba	46.44	12.26
Total	100.00	

Tab. V EDAX result of BCZT ($Ba_{0.0935}Ca_{0.065}Zr_{0.1}Ti_{0.9}O_3$) ceramics, at 1450°C temperature.

Element	Weight %	Atomic %
O	30.75	66.11
Ca	6.45	5.75
Ti	18.95	15.78
Zr	0.27	0.12
Ba	43.58	11.04
Total	100.00	

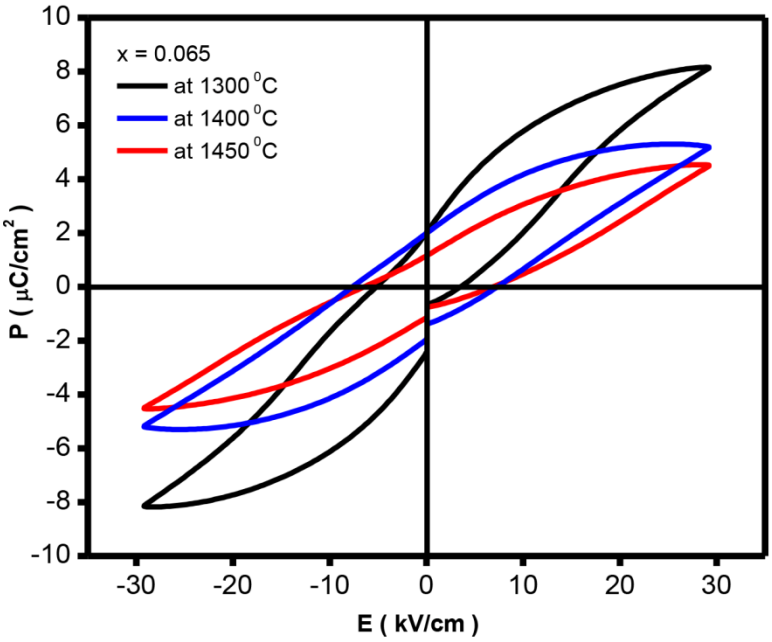

Fig. 6. P- E loops of BCZT ($Ba_{0.0935}Ca_{0.065}Zr_{0.1}Ti_{0.9}O_3$) ceramics, at different sintering temperature, at an applied field 14.73 (kV/cm).

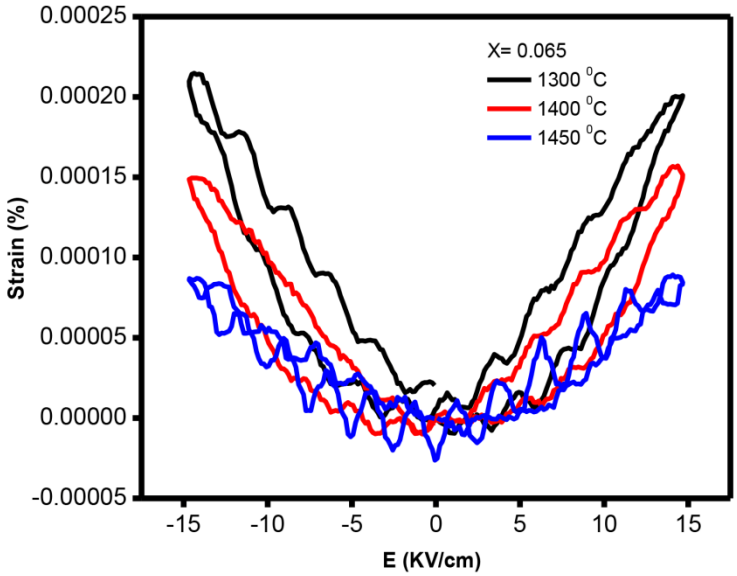

Fig. 7. Strain (%) with change in the electric field of BCZT ($Ba_{0.0935}Ca_{0.065}Zr_{0.1}Ti_{0.9}O_3$) ceramics, at different sintering temperature, at an applied field 14.73 (kV/cm).

The P-E hysteresis loops of prepared BCZT ($Ba_{0.0935}Ca_{0.065}Zr_{0.1}Ti_{0.9}O_3$) ceramics pellet samples were shown in Fig. 6. The piezoelectric measurements were carried out at room temperature (RT), and applied field 14.73 (kV/cm). For the prepared compositions, the hysteresis loops show a good ferroelectric nature. From P-E hysteresis loops, the value of the remnant polarization (P_r) was 2.074 μC/cm^2 and the corresponding coercive field was 3.63 kV/cm (E_C), with sample x = 0.065, sintered at 1300^{o}C. For the double sintering pellet samples, 'well saturated' loops were observed for the BCZT ($Ba_{0.0935}Ca_{0.065}Zr_{0.1}Ti_{0.9}O_3$) ceramics, with a temperature range from 1300 to 1450^{o}C. For the prepared pellet samples, 'well saturated' loops were measured due to high density and low porosity, at different sintering temperatures [7].

P-E strain% loops for the BCZT ($Ba_{0.0935}Ca_{0.065}Zr_{0.1}Ti_{0.9}O_3$) ceramics pellet samples were shown in Fig. 7. The converse piezoelectric coefficient has been calculated for the BCZT pellet samples sintered at different temperatures, and has been shown in Table VI. They were observed at an electric field 14.73 (KV/cm). The effect of variation in sintering temperature has been observed, and found that the piezoelectric constant has been decreasing as the sintering temperature is increased beyond 1300^{o}C, and further, it may arise due to its low density which may be seen from the SEM images [7]. Also, at higher temperatures, grain size has been increased and further, grain boundary decreases. Further, porosity has been appeared at higher sintering temperature. For the pellet samples of BCZT ($Ba_{0.0935}Ca_{0.065}Zr_{0.1}Ti_{0.9}O_3$) ceramics sintered at different temperatures, the strain percentage was found maximum at 1300^{o}C. Buatip et al. [7] found similar results and said that with an increase in sintering temperature, the piezoelectric properties get minimized. Buatip et al. reported the various properties of BCZT ceramics, Table VII.

Tab. VI Converse piezoelectric properties of BCZT ($Ba_{0.0935}Ca_{0.065}Zr_{0.1}Ti_{0.9}O_3$) ceramics, for x = 0.065, at an applied field 14.73 (kV/cm).

	Sintering temperature (^{o}C)	**Converse piezoelectric constant (d_{33}*) (pm/V)**
BCZT	1300	153
	1400	121
	1450	73

Therefore, from the observed data, the grain size and piezoelectric properties are more or less equal. However, remnant polarization and coercive field were found higher compared with the present study. The density was greater than the present data (3.49 gm/cm^3, sintered at 1300^{o}C, 4 h).

Tab. VII Piezoelectric properties and grain size of BCZT ($Ba_{0.0925}Ca_{0.075}Zr_{0.1}Ti_{0.9}O_3$) ceramics [7].

	$T_{sint.}$ (^{o}C)	Piezoelectric constant (d_{33}) (pC/N)	Grain size (μm)	Density (gm/cm^3)	Remnant polarization (μC/cm^2)	Coercive field (kV/cm)
($Ba_{0.0925}Ca_{0.075}Zr_{0.1}Ti_{0.9}O_3$)	1250	14	0.86 ± 0.41	5.48 ± 0.08	1.70	5.13
	1300	167	2.19 ± 0.87	5.62 ± 0.02	5.84	4.22
	1350	16	0.68 ± 0.19	5.52 ± 0.08	1.43	4.32

4. Conclusion

For the prepared compositions, the value of the converse piezoelectric properties has been decreased as the sintering temperature has been increased. The XRD patterns show that BCZT ceramics have a perovskite structure for all sintering conditions. The grain size tends to increase and further, density decreases for the prepared pellet samples with an increase in sintering temperature. The sintering conditions greatly alter the piezoelectric properties and microstructure of the BCZT ceramics. This may be due to its density and grain size effect on the domain switch ability and alignment. BCZT ceramics sintered at 1300^{o}C for 4 h, exhibited an optimum density (3.49 g/cm^3, ~72 % of theoretical density), grain size (average 2.01 ± 0.59 μm) and piezoelectric properties (2.074 μC/cm^2 and d_{33}* = 153 pC/N).

5. References

1. P. K. Panda, B. Sahoo, PZT to Lead Free Piezo Ceramics: A Review, Ferroelectrics, 474 (2015) 128-143.
2. P. Kantha, K. Pengpat, Phase formation and electrical properties of BNLT–BZT lead-free piezoelectric ceramic system, Current Applied Physics, 9 (2009) 460.
3. Y. Tian, Y. Gong, D. Meng, Y. Li, B. Kuang, Dielectric Dispersion, Diffuse Phase Transition, and Electrical Properties of BCT–BZT Ceramics Sintered at a Low-Temperature, Journal of Elec. Mater., 44 (2015) 2890.
4. E. Cross, Material Science: Lead free at last, 432 (2004) 24.
5. D. Biswas, G. S. Kathait, P. Thapliyal, V. Rohilla, S. Singh, J. Negi, Converse piezoelectric properties of K and Na-modified ($Na_{1-x}K_x$) NbO_3 lead free ceramics for x = 0.08 and 0.17, Ferroelectrics, 550 (2019) 228-232.
6. A. Frattini, A. D. Loreto, O. D. Sanctis, E. R. Benavidez, BCZT ceramics prepared from activated powders, Procedia Materials Science, 1 (2012) 359-365.
7. N. Buatip, N. Promsawat, N. Pisitpipathsin, O. Namsar, P. Pawasri, K. Ounsung, K. Phabsimma, S. T. Rattanachan, P. Janphuang, S. Projprapai, Investigation on electrical properties of BCZT ferroelectric ceramics prepared at various sintering conditions, Integrated Ferroelectrics, 187 (2018) 45-52.

8. M. E. Villafuerte-Castrejón, E. Morán, A. Reyes-Montero, R. Vivar-Ocampo, J. A. Peña- Jiménez, S.O. Rea-López, L. Pardo, Towards Lead-Free Piezoceramics: Facing a Synthesis Challenge, Materials, 9 (2016) 1-27.
9. Y. Tian, L. Wei, X. Chao, Z. Liu, Z. Yang, Phase transition behavior and large piezoelectricity near the morphotropic phase boundary of lead-free $(Ba_{0.85}Ca_{0.15})(Zr_{0.1}Ti_{0.9})O_3$ ceramics, J. Am. Ceram. Soc., 96 (2013) 496-502.
10. D. Biswas, G. S. Kathait, P. Thapliyal, V. Rohilla, S. Singh, Temperature dependence of dielectric properties of sodium potassium niobate ceramics for different values of x $(Na_{1-x}K_xNbO_3)$, Ferroelectrics, 526 (2018) 168-175.
11. G. S. Kathait, M. K. Panda, N. S. Panwar, Effect of Modified Two-step Sintering Approaches on Potassium Tantalum Niobate–Barium Titanate (KTN-BT) Ceramics and Their Dielectric and Piezoelectric Properties, Science of sintering, 52 (2020) 97-107.
12. S. Sen, R. Choudhay, Effect of doping Ca ions on structural and electrical properties of $Ba(Zr_{0.05}Ti_{0.95})O_3$ electroceramics, J. Mater. Sci.: Mater Electron., 15 (2004) 671-675.
13. P. Wang, Y. X. Li, Y. Q. Lu, Enhanced piezoelectric properties of $(Ba_{0.85}Ca_{0.15})(Ti_{0.9}Zr_{0.1})O_3$ lead-free ceramics by optimizing calcination and sintering temperature, J Eur. Ceram Soc., 31 (2011) 2005-2012.
14. J. Wu, D. Xiao, B. Wu, W. Wu, J. Zhu, Z. Yang, J. Wang, Sintering temperature-induced electrical properties of $(Ba_{0.90}Ca_{0.10})(Ti_{0.85}Zr_{0.15})O_3$ lead-free ceramics, Mater. Res. Bull., 47 (2012) 1281-1284.
15. J. Wu, D. Xiao, W. Wu, J. Zhu, J. Wang, Effect of dwell time during sintering on piezoelectric properties of $(Ba_{0.85}Ca_{0.15})(Ti_{0.90}Zr_{0.10})O_3$ lead-free ceramics, J. Alloys Compd., 509 (2011) L359-L361.
16. J. Koruza, B. Malic, Initial stage sintering mechanism of $NaNbO_3$ and implications regarding the densification of alkaline niobates, J. Eur. Ceram. Soc., 34 (2014) 1971-1979.
17. R. M. German, Z. A. Munir, Surface-area reduction during isothermal sintering, J. Am. Ceram. Soc., 59 (1976) 379-383.
18. G. S. Kathait, N. S. Panwar, P. Thapliyal, D. Biswas, V. Rohilla, S. Singh, Sintering effect on Electrical Properties and Morphology of Lead-Free $Na_{0.92}K_{0.08}NbO_3$ Ceramics, Science of Sintering, 51 (2019) 421-428.

Сажетак: *У овом раду, припремљени су узорци титаната ($Ba_{1-x}Ca_xZr_{0.1}Ti_{0.9}O_3$, $x = 0.065$) реакцијом у чврстом стању двостепеним синтеровањем. Одређена су структурна и пиезоелектрична својства. Примењене су и методе SEM и EDAX анализе. Са различитим температурама синтеровања, густина и величина зрна су се мењале, и посматран је њихов утицај на пиезоелектрична својства. Конверзна пиезоелетрична константа (d_{33}^*) је опадала са порастом температуре синтеровања. Највиша вредност од 153 pm/V је измерена на 1300°C.*

Кључне речи*: фероелектрици; пиезоелектрична константа; перовскит; двостепено синтеровање.*

© 2022 Authors. Published by association for ETRAN Society. This article is an open access article distributed under the terms and conditions of the Creative Commons — Attribution 4.0 International license (https://creativecommons.org/licenses/by/4.0/).